Proton Improvement Plan-II

Preliminary Design Report

March 22, 2019

1

Authors

J. Adetunji,[3] J. Anderson,[3] R. Andrews,[3] C. Baffes,[3] M. Ball,[3] T. Banaszkiewicz,[5] S. Belomestnykh,[3] S. Chandrasekaran,[3] B. Chase,[3] A. Chen,[3] M. Convery,[3] Z. Conway,[1] R. Crawford,[3] E. Cullerton,[3] J. Czajkowksi,[3] A. Dalesandro,[3] P.F. Derwent,[3] J. Dey,[3] S. Dixon,[3] N. Eddy,[3] J. Einstein-Curtis,[3] F.G. Garcia,[3] I. Gonin,[3] A. Grassellino,[3] T. Hamerla,[3] T. Hamilton,[3] B. Hanna,[3] B. Hansen,[3] E. Harms,[3] S. Holmes,[3] J. Holzbauer,[3] E. Huedem,[3] J. Hunt,[3] A. Ibrahim,[3] A. Jain,[4] D. Johnson,[3] M. Kaducak,[3] S. Kazakov,[3] T. Khabiboulline,[3] A. Klebaner,[3] I. Kourbanis,[3] M. Lad,[4] L. Lari,[3] V. Lebedev,[3] J. Leibfritz,[3] A. Lunin,[3] M. Martinello,[3] A. Martinez,[3] L. Merminga,[3] J.K. Mishra,[2] D. Morris,[3] A. Olson,[3] J. Ozelis,[3] M. Pande,[2] M. Parise,[3] D. Passarelli,[3] J. Patrick,[3] L. Pei,[3] W. Pellico,[3] D. Peterson,[3] Y. Pischalnikov,[3] J. Polinski,[5] E. Pozdeyev,[3] R. Prakash,[4] P. Prieto,[3] L. Prost,[3] B.V. Ramarao,[2] J. Reid,[3] V. Roger,[3] A. Rowe,[3] A. Saini,[3] V. Scarpine,[3] A. Shemyakin,[3] S. Singh,[2] N. Solyak,[3] J. Steimel,[3] A. Sukhanov,[3] I. Terechkine,[3] R. Thurman-Keup,[3] R. Wang,[3] A. Warner,[3] C. Worel,[3] G. Wu,[3] M. Xiao,[3] V. Yakovlev,[3] and R. Zifko[3]

[1] *Argonne National Laboratory, Lemont, IL 60439, USA*
[2] *Bhabha Atomic Research Center, Mumbai, India*
[3] *Fermi National Accelerator Laboratory, Batavia, IL 60510, USA*
[4] *Raja Rammana Center for Advanced Technology, Indore, India*
[5] *Wroclaw University of Science and Technology, Wroclaw, Poland*

Contents

List of Figures

List of Tables

Todo list

Chapter 1

Executive Summary

The PIP-II project at Fermilab is building a superconducting Linac to fuel the next generation of intensity frontier experiments. Capitalizing on advances in superconducting radio-frequency (SRF) technology, five families of superconducting cavities will accelerate H^- ions to 800 MeV for injection into the Booster. Upgrades to the existing Booster, Main Injector, and Recycler rings will enable them to operate at a 20 Hz repetition rate and will provide a 1.2 MW proton beam for the Long Baseline Neutrino Facility.

The Particle Physics Project Prioritization Panel stated in 2014, "The PIP-II project at Fermilab is a necessary investment in physics capability, enabling the world's most intense neutrino beam, providing the wideband capability for LBNF, as well as high proton intensities for other opportunities..." and recommended the project to proceed immediately [1].

The strong expertise Fermilab has developed in 1.3 GHz SRF, leads naturally to the PIP-II Linac designed around 162.5, 325 and the 650 MHz cavities of the same harmonic family. Cryogenic infrastructure and expertise from Tevatron operations also provide an advantage. The choice of a superconducting Linac compatible with continuous-wave operation allows an upgrade path for a second-generation Mu2e experiment [2].

International partnerships have been formed with the Department of Atomic Energy in India, the Istituto Nazionale di Fisica Nucleare in Italy, the Atomic Energy Commission and CNRS National Institute of Nuclear and Particle Physics in France and the Science and Technology Facilities Council in the UK, for in-kind contributions of SRF cavities and other significant components. The success of the PIP-II injector test to date, has relied on components such as magnets from India, for the medium-energy beam transport.

Future upgrades for Mu2e and for 2 MW beam power to LBNF are supported by the location and the technologies employed within the Linac. The enclosure for the beamline, connecting the Linac to the existing Booster, will include a short extension to allow for a future beamline to serve Mu2e. The Linac site also takes advantage of electrical, water, and cryogenic infrastructure already available in the vicinity.

Building on the accomplishments of the Proton Improvement Plan [3], PIP-II will provide additional modifications to the existing accelerator complex. Modifications under the PIP-II project will allow injections into the Booster at higher energy, thereby mitigating space-charge forces at higher beam intensities. Systems will be upgraded for beam operations at 20 Hz to support the 8-GeV program including Mu2e and short-baseline neutrinos. Main-Injector RF will be enhanced to support 1.2 MW beam power. Upgrades designed to lower beam losses, such as Booster dampers, collimators, and a Main-Injector γ_t-jump system, which are needed to increase beam power to the NOvA experiment, will be operational several years before the commissioning of PIP-II beam in the Booster and Main Injector. This will reduce the time needed to reach 1.2 MW with PIP-II.

This report presents a preliminary design for the PIP-II project. It is also intended to describe how the accelerator will be used to carry out a scientific program at Fermilab. Different systems and subsystems are at different levels of design maturity, and in some cases, the report describes plans for a design, rather than the design itself. The beam physics design is mature and defines requirements for the technical components and support systems. The design for these subsystems will be finalized in the next phase of the project.

The Preliminary Design Report is organized as follows: Chapter 2 gives an overview of the PIP-II project, followed by a discussion of beam physics in Chapter 3. Upgrades to the existing accelerator complex are discussed in Chapter 4. The next three chapters describe the warm front end and the SRF Linac and RF systems. Chapters 9, 10 and 11 cover beam instrumentation, magnets and power supplies and the integrated control system, respectively. Cryogenics, vacuum systems, test stands and safety systems are discussed in Chapters 13, 14, 15 and 16, respectively. Chapter 17 describes the conventional facilities. Chapters 18 and 19 cover safety and quality management while Chapters 20 and 21 describe integration and commissioning.

Chapter 2

Overview

2.1 Design requirements

The P5 report and the Mission Need Statement call for a performance upgrade of the Fermilab accelerator complex to support a world-leading neutrino program, while maintaining high-reliability operations through the rejuvenation of aging systems within this complex and providing a platform for future enhancements. The project configuration and development has proceeded with the following functional requirements:

- Deliver 1.2 MW of proton beam power from the Fermilab Main Injector, over the energy range 60 - 120 GeV, at the start of operations of the LBNF/DUNE program;
- Sustain high reliability operations of the Fermilab accelerator complex throughout the initial phase of LBNF/DUNE operations;
- Support the currently operating and envisioned 8 GeV program at Fermilab including Mu2e, g-2, and the suite of short-baseline neutrino experiments;
- Provide a platform for eventual extension of beam power to LBNF/DUNE to >2 MW;
- Provide a flexible platform for long-range development of the Fermilab complex; in particular, provide an upgrade path for a factor of ∼10 increase in beam power to the Mu2e experiment and for extension of accelerator capabilities to include flexible high-bandwidth pulse formatting/high beam power operations.

The Proton improvement plan (PIP)-II is the proposed road map to enhance the capabilities of the existing Fermilab accelerator complex to support the delivery of 1.2 MW beam power to the LBNF production target while simultaneously providing a platform for subsequent upgrade of the accelerator complex to a multi mega-watt accelerator facility. PIP-II is primarily based on building a new 800 MeV superconducting (SC) linear accelerator (Linac) that will replace the

existing normal conducting 400 MeV Linac. The Linac will be located in close proximity to the existing Booster as shown in Figure 2.1. This siting offers several advantages in terms of minimizing cost while retaining options for future development; in particular, the site affords direct access to significant electrical, water and cryogenic infrastructure while providing a straightforward path for eventual replacement of the Booster, which is required to support beam powers in excess of 2 MW. Table 2.1 summarizes the high-level objectives and performance parameters for both PIP-II and PIP. Some considerations for future developments are discussed in Section 2.3.

Table 2.1:

Performance Parameter	PIP	PIP-II	Unit
Linac Beam Energy	400	800	MeV
Linac Beam Current (chopped)	25	2	mA
Linac Pulse Length	0.03	0.54	ms
Linac Pulse Repetition Rate	15	20	Hz
Linac Upgrade Potential	N/A	CW	
Booster Protons per Pulse (extracted)	4.2	6.5	10^{12}
Booster Pulse Repetition Rate	15	20	Hz
Booster Beam Power @ 8 GeV	80	166	kW
8 GeV Beam Power to LBNF	N/A	83-142*	kW
Beam Power to 8 GeV Program	30	83-24*	kW
Main Injector Protons per Pulse (extracted)	4.9	7.5	10^{13}
Main Injector Cycle Time @ 120 GeV	1.33	1.2	sec
Main Injector Cycle Time @ 60 GeV	N/A	0.7	sec
Beam Power @ 60 GeV	N/A	1	MW
Beam Power @ 120 GeV	0.7	1.2	MW
Upgrade Potential @ 80-120 GeV	N/A	2.4	MW
* the first number refers to Main Injector operations at 120 GeV, second number to 60 GeV			

Foremost, bottlenecks that limit the beam power below 1.2 MW to the LBNF target in the PIP operational regimes are as followed:

- The apparent limitation arises from the present Booster injection energy of 400 MeV. The Booster beam experiences a force from its own electromagnetic field, distorting the optics in an intensity-dependent way. This effect results in an amplitude dependent defocusing that leads to a tune spread of the beam particles. Tune spread ($\Delta\nu$) can be expressed as:

$$\Delta\nu = \frac{\pi\lambda r_0 R}{2\epsilon_n \beta\gamma^2} \tag{2.1}$$

  where, λ is the line charge density, r_0 is the classical proton radius, R is the vacuum pipe radius, β and γ are relativistic factors and ϵ is the normalized emittance. Beam loss at injection driven by space charge forces limit the number of protons per Booster pulse to roughly 5×10^{12} at this energy.

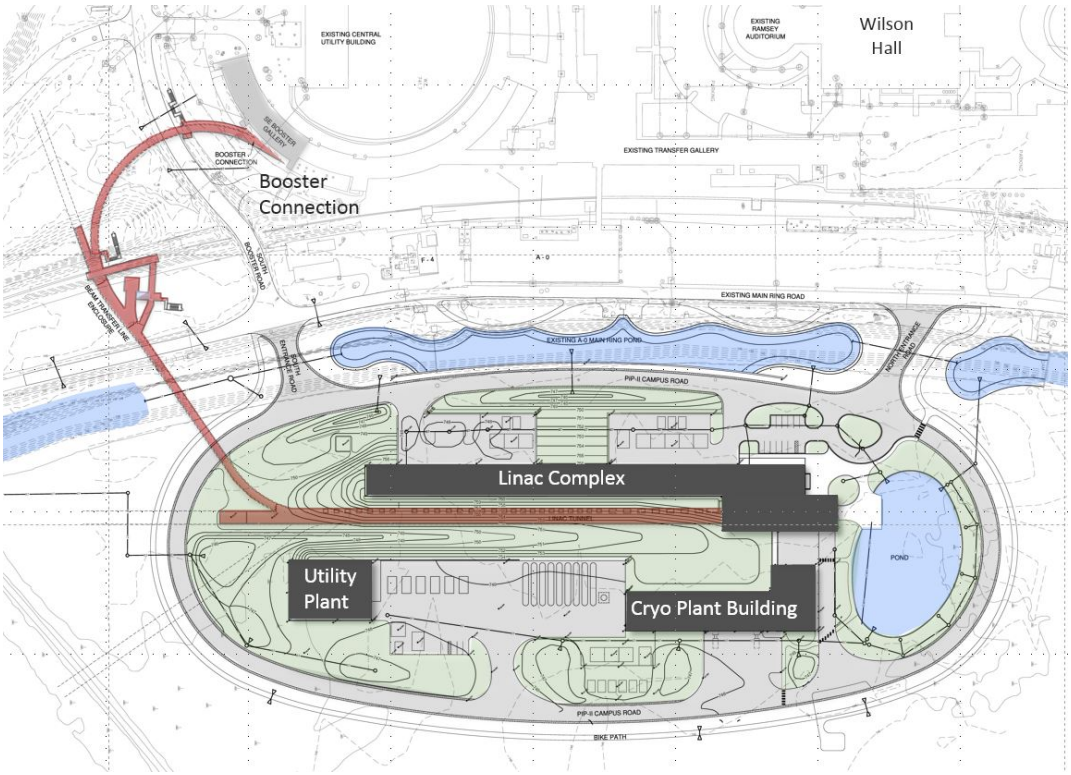

Figure 2.1: Site location in the Main Ring infield.

- The second limitation arises from the slip-stacking of twelve Booster pulses in the Recycler. This performance is determined jointly be characteristics of the Recycler itself as well as the characteristic of the beam from the Booster.

The PIP-II SC Linac will double the Booster injection energy that will support about a 50% increase in Booster beam intensity accompanied by a 30% reduction in space charge tune shift in comparison to current operation. In addition, the Linac will deliver a high-quality beam with lower emittances. This will allow beam painting at injection in all the three degrees of freedom, further reducing the space charge force and beam losses at high intensity. Furthermore, the Booster repetition rate will be increased from 15 to 20 Hz. This is extremely helpful for reduction of beam losses during slip-stacking in the Recycler due to the larger momentum difference between the two streams of slip-stacked bunches. The repetition rate increase also enhances the overall particle flux through the Booster and yields higher power for the 8-GeV experimental program.

Besides higher injection energy to the Booster, the PIP-II SC Linac will deliver an effective beam temporal structure that will facilitate an efficient beam injection to the Booster. Beam temporal pattern is prepared using a bunch-by-bunch chopping system deployed in the Medium Energy Beam Transport (MEBT) in the PIP-II Linac. It allows the removal of bunches arriving at the Booster RF bucket boundaries and therefore, minimizes the beam loss at injection. The same chopper creates a three-bunch long extraction gap as well.

2.2 Linac design considerations and choices

The design criteria, as represented by the project functional requirements, drive design considerations. The total protons per second necessary for 1.2 MW to the LBNF target, coupled with the existing Booster, Recycler, and Main Injector operational parameters, flows into the beam current considerations. Booster loss limits, space charge tune shift, and higher pulse intensity point toward a higher injection energy. An injection energy of 800 MeV gives a 30% reduction in space charge tune shift at injection. The provisions for higher beam power and future flexible platforms flow into consideration of continuous wave (CW) operation, higher output energy, and bunch selection. Support for CW operations leads to the design choice of utilizing superconducting RF cavities for acceleration to 800 MeV, starting at the lowest practical energy. With the development and implementation of performance improvements in 1.3 GHz cavities for XFEL and LCLS-II, a natural design choice for PIP-II is to operate with sub-harmonics of 1.3 GHz.

Considering bunch selection and flexible time structures, it makes sense to do selection at the lowest possible energy, minimizing radiation and energy deposition. As SRF cavities are very sensitive to losses and particulates, such selection needs to be done in a warm section. Given the sub-harmonics of 1.3 GHz, individual selection of 325 MHz bunches (a 3.07 nanosecond period) seems beyond state of the art while individual selection of 162.5 MHz bunches (6.15 nanosecond period) is considered feasible. As a result, the fundamental bunching frequency is 162.5 MHz. To minimize activation and simplify maintenance in the area of the selection, the energy (2.1 MeV) from the Radio Frequency Quadrupole (RFQ) is chosen to be below neutron production threshold in most materials.

The superconducting Linac now has a set of frequencies (162.5 MHz, 325 MHz, 650 MHz) and energy range (2.1 MeV to 800 MeV). The relativistic β for the H^- ions goes from 0.07 to 0.85 over this energy range. Taking into consideration the number of cavities, acceleration efficiencies, cavity types and performance with an eye to costs, the design choices of a half wave resonator, two types of single spoke resonators, and two types of elliptical cavities is made.

Transverse focusing considerations then enter into the choices for groupings into cryomodules. Lower energy matches to a short focusing period. This consideration led to the choice of superconducting solenoids, with strong fields and radial focusing, internal to the cryomodules. As the energy increases, the focusing period increases, enabling fewer solenoids per accelerating cavity. Once the energy reaches a certain threshold, it becomes more cost effective to use short cryomodules and and warm quadrupoles in between cryomodules for focusing elements.

2.3 Configuration

Given the criteria and considerations, a configuration was devised that meets the stated requirements:

- An 800 MeV superconducting H^- Linac, with CW RF operational capability, and operating

initially in pulsed beam mode.

- Beam transport of 800 MeV H^- from the Linac to the Booster, including accommodation of a beam dump capable of accommodating full intensity at low (1%) duty factor and future delivery of beam to the Muon Campus.

- A new injection area in the Booster to accommodate 800 MeV injection.

- Modifications to the Main Injector and Recycler Ring to support acceleration of high intensity/high power proton beams over the range of 60-120 GeV.

- Associated conventional facilities including enclosures, equipment galleries and utilities.

A simple technology map of the Linac is shown in Figure 2.2. The Linac has a room temperature front end, starting with a 30 keV DC H^- ion source. A radio-frequency quadrupole at 162.5 MHz bunches the H^- and accelerates it to 2.1 MeV. A bunch-by-bunch chopper allows for the creation of a programmable 162.5 MHz bunch pattern.

There are five different superconducting RF cavities, at three different frequencies, to accommodate the changing beam velocity as discussed in Section 2.2. In order of increasing energy, there is a half wave resonator (HWR) operating at 162.5 MHz, two types of single spoke resonators (SSR1, SSR2) at 325 MHz and two types of elliptical cavities (LB650, HB650) at 650 MHz. Focusing elements in the HWR, SSR1 and SSR2 sections are superconducting solenoids located inside the cryomodules, focusing elements in the LB650 and HB650 sections are quadrupole doublets located in between the cryomodules. For cavity and cryomodule configurations, see Table 2.2 and Table 2.3.

The Linac is followed by a beam transport line to bring the H^- beam to the Booster. This line includes an arc bending the beam by about 210°. The line includes elements to send the H^- beam to an absorber capable of handling full intensity at a 1% duty factor or to a future line to the Mu2e experiment. The bending radius of the arc is maintained above 23 meters to prevent stripping of the H^- beam prior to Booster injection.

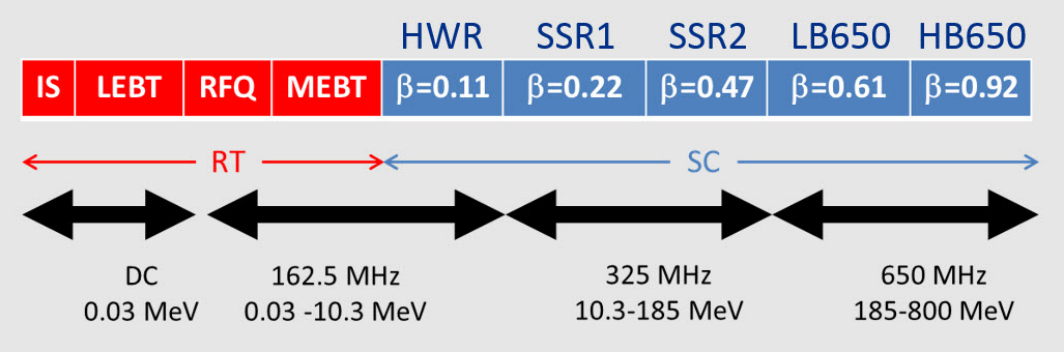

Figure 2.2: The Linac technology map. The optimal betas are shown for HWR, SSR1 and SSR2, while the geometric betas, β_g are shown for the LB650 and HB650. The energies are shown for the transitions between frequencies.

The Linac energy is selected to support a 50% increase in Booster beam intensity, accompanied by

a 30% reduction in the space-charge tune shift as compared to the current operations. The Linac is constructed entirely of components that are capable of operating in continuous wave (CW) mode. Initial operation will be with CW RF power and pulsed beam in order to minimize effects from Lorentz Force Detuning (LFD).

Table 2.2: Superconducting RF cavity configurations. β_g for the elliptic cavities is defined as the ratio of regular cell length to half-wavelength. Energy gain and beam current set peak power levels. β_{opt} is the value where the transit time factor is maximum.

Cavity name	β_g	β_{opt}	Freq. (MHz)	Cavity type	Energy gain at β_{opt} per cavity (MeV)	Energy range (MeV)
HWR	0.094	0.112	162.5	Half wave resonator	2	2.1 - 10.3
SSR1	0.186	0.222	325	Single-spoke resonator	2.05	10.3 - 35
SSR2	0.398	0.475	325	Single-spoke resonator	5	35 - 185
LB650	0.61	0.65	650	Elliptic 5-cell cavity	11.9	185 - 500
HB650	0.92	0.971	650	Elliptic 5-cell cavity	19.9	500 - 800

Table 2.3: Superconducting cryomodule configurations - "s" stands for solenoid, "c" stands for cavity.

CM type	Cavities per CM	Number of CMs	CM configuration
HWR	8	1	8 x (sc)
SSR1	8	2	4 x (csc)
SSR2	5	7	sccsccsc
LB650	3	11	ccc
HB650	6	4	cccccc

The Booster repetition rate will be increased from 15 to 20 Hz. Protons will be injected into the Booster using multi-turn strip-injection similar to the injection method used in the SNS [4]. The number of injection turns is equal to about 300. Although the number of injection turns is much larger than what is presently used in the Booster, it is still about three times less than that used in the SNS. The large number of injection turns and small emittances of the SC Linac beam allow painting of transverse and longitudinal distributions resulting in a significant reduction of space-charge effects. In contrast to present operations, beam injection will proceed at non-zero RF voltage. This allows one to avoid adiabatic bunching, which is problematic because of the long bunching time. To reduce beam losses during Booster injection the Linac bunches arriving at the RF bucket boundaries are removed by a bunch-by-bunch chopper located in the Medium Energy Beam Transport (MEBT) of the Linac. The same chopper creates a three-bunch long extraction gap. Slip-stacking in the Recycler and acceleration in the Main Injector will be done in a manner similar to that presently used for NOvA [5]. The increase in repetition rate reduces the rate of beam losses during slip-stacking in the Recycler due to the larger momentum difference between the two streams of slip-stacked bunches. The repetition rate increase also increases overall particle flux through the Booster and yields higher power for the 8 GeV experimental program.

Upgrades to a number of systems in the Booster, Recycler, and Main Injector will be required in order to support the higher Booster injection energy and higher beam intensities. These include upgrades to the Booster injection system and the RF systems in the Recycler and Main Injector.

Existing shielding and active loss monitor systems are expected to sufficient for operation at the higher intensities.

The location of the PIP-II Linac is driven primarily by the requirement for close proximity to the existing Booster accelerator and access to existing infrastructure, see Figure 2.3. The location in the Main Ring infield, adjacent to the Footprint area of the Fermilab campus, allows direct access to existing electrical, water and cryogenic infrastructure currently located in the vicinity. The Main Ring infield location is well suited to extensions of chilled water service from the existing Central Utility Building (CUB). At the same time, the Main Ring infield location provides space for future expansion opportunities.

While requirements are not defined at this time, the guiding principles for future opportunities are:

- Provide a platform for eventual extension of beam power to LBNF/DUNE to >2 MW;
- Provide a flexible platform for long-range development of the Fermilab complex; in particular, provide an upgrade path for a factor of 10 increase in beam power to the Mu2e experiment and for extension of accelerator capabilities to include flexible high-bandwidth pulse formatting/high beam power operations.

To reach a power level >2 MW for the long baseline program requires approximately another doubling of the intensity to the production target (e.g., 1.5×10^{14} protons every 1.2 seconds at 120 GeV corresponds to 2.4 MW). The operational model of utilizing slip stacking in the Recycler will need to change, as the slip stacking process is inherently too lossy at these intensities. Boxcar stacking (from a rapid cycling synchrotron) or direct injection from an 8 GeV Linac is feasible. The Booster, no matter the injection energy or other machine upgrades, is also not capable of accelerating the required intensities. Extending the Linac to higher energies (2-3 GeV) and retaining the CW capability could open new physics opportunities.

To reach injection energy for the Recycler or Main Injector, a pulsed 8 GeV Linac or 8 GeV rapid cycling synchrotron could be developed. Due to stripping of H^- in magnetic fields, the maximum bend radius is constrained for higher energy Linacs. Due to space constraints in the Main Injector, a lower injection energy can not take place in the MI10 area. It is possible to accommodate a 3 GeV, a 6 GeV and a 8 GeV Linac, with injection in the MI-60 region of the Main Injector, in the Main Ring infield starting from the planned PIP-II location.

A configuration for delivery of Linac beam to a second generation Mu2e experiment has been developed. The experiment requests a burst, not more than 200 nsec in duration, then a gap of with population $< 10^{-11}$ with respect to intensity in the burst. The full cycle time is 1.69 μsec. With the Linac parameters as in Table 2.1, the full cycle is 275 162.5 MHz buckets. Power is limited to approximately 85 kW, which corresponds to 6 populated 162.5 MHz buckets and 269 empty 162.5 MHz buckets. As the Booster cycles take up 1.1% of the Linac, these cycles could run in the remaining 98%.

An additional consideration in the siting of the PIP-II facility is the impact to existing known wetlands within the Main Ring (Tevatron) infield as well as conformation with the 2015 Fermilab

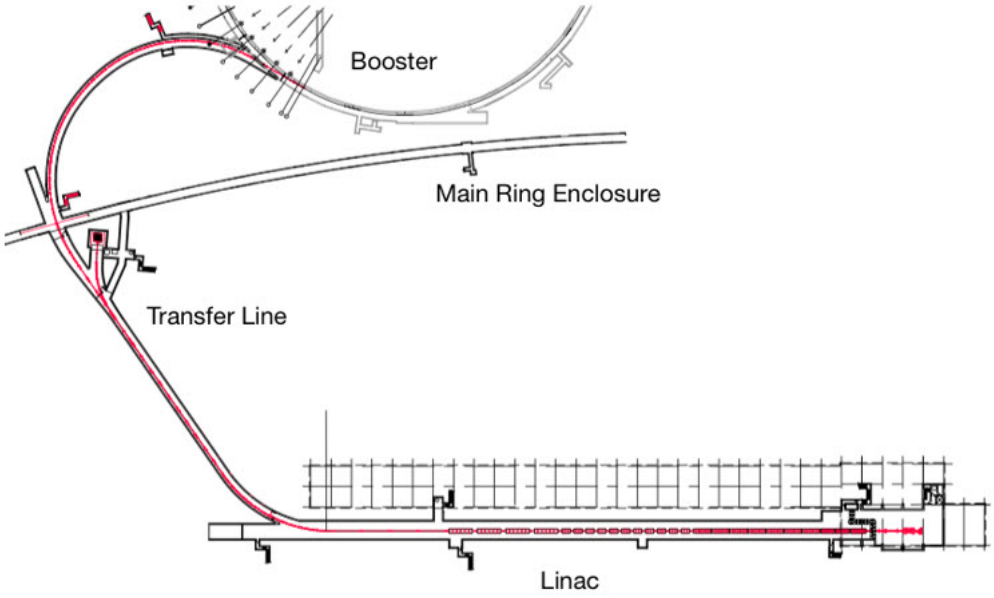

Figure 2.3: Configuration layout of the Linac and transfer line.

Campus Master Plan which has designated the area east of Wilson Hall as the Superconducting Linac Complex, see Figure 2.1.

Surface construction for the PIP-II facility includes new buildings, site improvements, roadwork and parking to allow access from the Fermilab Central Campus. Underground construction includes the Linac Tunnel, the Beam Transfer Line enclosure, and Beam Dump enclosure. The Linac enclosure will be constructed with a length to accommodate at least two HB650 cryomodules beyond the nominal compliment required for 800 MeV. There is a provision for installation of an RF separator and septum at the Linac end. These could be utilized to support the operation of multiple experiments following future Linac upgrades.

The Linac Tunnel is sited at the same elevation as the existing Booster and the Main Ring tunnel. The Beam Transfer Line enclosure will cross the Main Ring tunnel which holds the existing 120 GeV transfer line used for beam delivery to the Fixed Target Area Switchyard, which is assumed to continue its operation in the PIP-II era. The floors of the two tunnels will be on the same elevation, but the PIP-II Beam Transfer Line will rise up, cross the existing Main Ring enclosure near its ceiling, and then come down in the vicinity of the existing 120 GeV line.

Chapter 3

Beam Physics

3.1 Overview

The new superconducting (SC) linear accelerator (Linac) that is the heart of PIP-II is designed to deliver an H^- ion beam with a final kinetic energy of 800 MeV and an average current of 2 mA. The Linac is endowed with a special and flexible time structure to satisfy diverse experimental needs and will be capable of operations in a continuous wave (CW) regime. A list of operational parameters of the PIP-II SC Linac is summarized in Table 3.1.

Table 3.1: PIP-II superconducting Linac operational parameters

Parameter	Requirement	Units
Particle species	H^-	
Input beam energy (kinetic)	2.1	MeV
Output beam energy (kinetic)	800	MeV
Bunch repetition rate	162.5	MHz
RF pulse length	pulsed-to-CW	
Beam pulse length	0.55	msec
Sequence of bunches	Programmable	
Average beam current in SC Linac	2	mA
Final rms norm. transverse emittance, $\epsilon_x = \epsilon_y$	≤ 0.3	mm-mrad
Final rms norm. longitudinal emittance	≤ 0.35 (1.1)	mm-mrad (keV-ns)
Rms bunch length at the SC Linac end	< 4	ps

3.2 Linac architecture

The baseline configuration of the PIP-II Linac is delineated in Figure 3.1. On the basis of operating temperature, the Linac is segmented in two parts, i.e., the room temperature (RT) front-end and the SC Linac. The front-end includes an ion source, a Low Energy Beam Transport (LEBT) section, a 162.5 MHz Radio Frequency Quadrupole (RFQ), and a Medium Energy Beam Transport (MEBT). The SC Linac comprises five families of superconducting cavities to accelerate the H^- ions from a kinetic energy of 2.1 MeV to 800 MeV. Based on these families, the SC Linac is further segmented into five sections named the Half Wave Resonator (HWR), Single Spoke Resonator (SSR)-1 & 2, Low Beta (LB), and High Beta (HB). The operating frequency and energy range of each section are also shown in Figure 3.1.

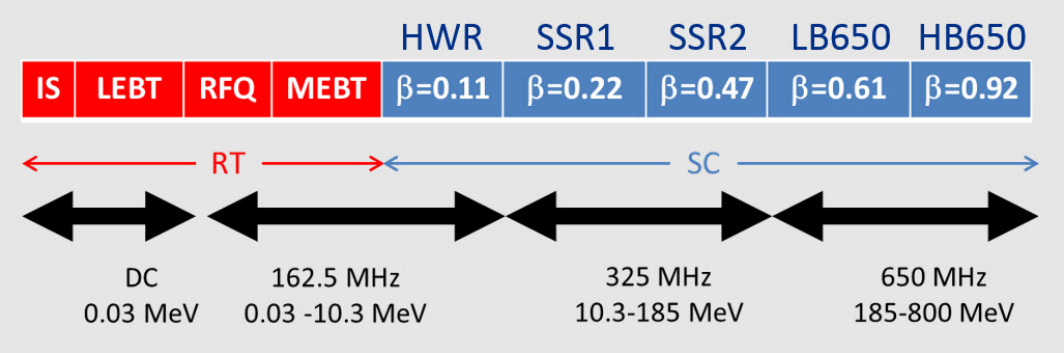

Figure 3.1: A schematic of the acceleration scheme in the PIP-II Linac. Red colored blocks represent normal conducting sections while blue colored represent superconducting accelerating sections in the PIP-II Linac. β (v/c) depicts the normalized optimal (first three SC sections) or geometric (last two SC sections) beam velocity in the respective sections.

In order to minimize the beam losses through the Linac as well as at Booster injection, it is crucial to limit emittance growth along the Linac. Thus, preservation of the beam quality in the course of it its acceleration along the Linac is the utmost design objective. Table 3.2 summarizes maximum tolerable normalized RMS beam emittances at critical locations in the Linac. In subsequent sections of this report we provide a detailed description of the Linac design and explain choices made for beamline elements and their operating parameters.

Table 3.2: RMS emittance budget through the PIP-II Linac for nominal peak beam current of 5 mA

	Normalized RMS beam emittance (mm-mrad)	
	Transverse	Longitudinal
Ion source	0.14	-
RFQ entrance	0.18	-
RFQ exit	0.20	0.28
MEBT exit	0.23	0.31
Exit of SC Linac	0.3	0.35

3.2.1 Room temperature front end

The room temperature front-end prepares the beam for injection into the SC Linac for further acceleration. All essential beam manipulations such as beam pulse-length preparation, peak current, generation/preparation of arbitrary bunch patterns using a beam-chopper assembly, etc., happen at this part of the Linac. Thus, the front-end comprises critical elements whose performance outlines the overall reliability of the Linac.

3.2.1.1 Ion source and LEBT

The PIP-II ion source is capable of delivering a 15 mA beam of H^- ions at 30 KeV in both CW and pulsed regimes. The choice of output beam energy of 30 KeV is made to balance emittance growth between longitudinal and transverse planes. Note that a low beam energy results in an increase in transverse emittance at the LEBT and RFQ due to space charge effects. However, a low injection energy at the RFQ leads to a lower longitudinal emittance at exit of the RFQ. This implies that the energy choice is a compromise that is made to minimize final emittance growth in all three degrees of freedom (horizontal, vertical and longitudinal) at the exit of the front-end.

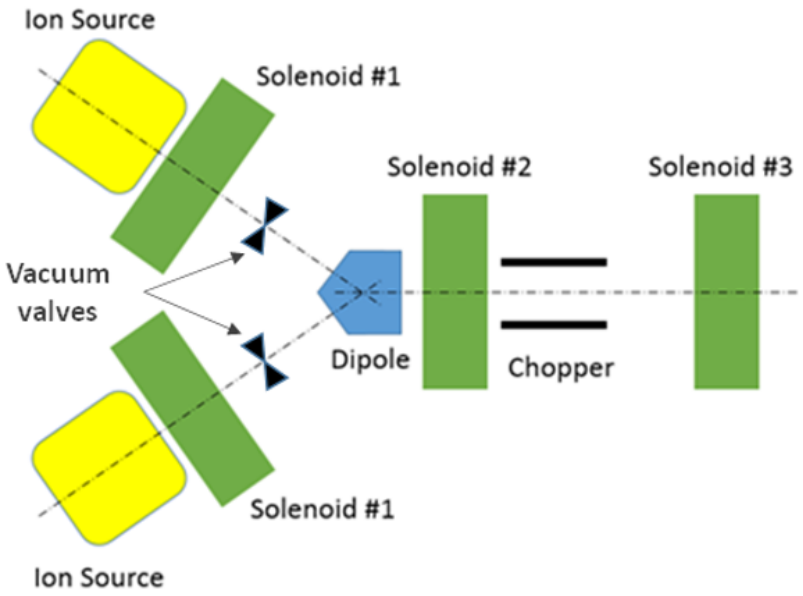

Figure 3.2: Conceptual schematic of the PIP-II LEBT with two ion sources.

In order to enhance the beam availability, the baseline design of the Linac utilizes two ion sources that are installed in a "Y"-configuration with a slow switching dipole bending magnet. Vacuum valves isolate the ion sources from the rest of the LEBT. Thus, each source can be removed for repairs, reinstalled, and conditioned without interrupting operation of the other. Figure 3.2 shows a schematic of the ion source and LEBT line. The 3-solenoid LEBT transports the beam from the exit of the ion source to the entrance of the RFQ and matches the beam's optical functions to the ones required for a low-loss acceleration in the RFQ. In addition, a slow chopping system with rise and fall times in range of 100 ns is also placed in the LEBT to facilitate formation of a low duty

factor beam required particularly during the machine commissioning and tuning in pulsed mode. Furthermore, the chopping system is deployed as a part of the Machine Protection System (MPS) that, depending on MPS permit status, could interrupt nominal beam operation by prohibiting the beam from further acceleration in the RFQ.

While designing the LEBT, the utmost importance is given to safeguarding the reliability of the front-end and its critical components. Consequently, a fairly long LEBT (2 m) is envisioned to guarantee a good vacuum region in the RFQ that allows minimizing bombardments of particles on the RFQ vanes and therefore the rate of the sparking occurrence. Also, good vacuum in the LEBT reduces the likelihood of stripping of the H^- ions. Note that the resulting protons from H^- ion stripping could be accelerated through the RFQ and lead to a significant uncontrolled beam loss at the high-energy portion of the Linac. Thus, isolating the RFQ region from inherently bad vacuum around the ion source is one of the main functional requirements of the LEBT design. A detailed description of the Functional Requirement Specifications (FRS) for the LEBT is presented in Ref. [6]. It can also be noted from Figure 3.2 that the dipole bend of 30° between the first two solenoids ensures there is no direct line of sight between the ion sources and the RFQ (as well as the superconducting elements further downstream). This in turn, greatly reduces the bombardment of fast neutrals on the RFQ vane surface. Thus, the configuration presented here further improves the overall reliability of the RFQ.

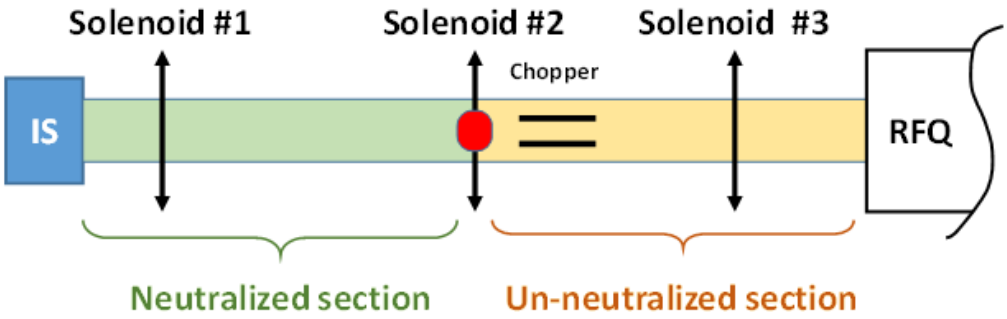

Figure 3.3: Beam transport scheme through LEBT.

As the beam propagates through the LEBT, it ionizes residual gas molecules. The resulting secondary charged particles might get trapped in the beam potential and therefore neutralize the beam's space charge. Because the neutralization process is not instantaneous, often the front of the beam pulse is not neutralized as it propagates through the LEBT, and it may exhibit different Twiss parameters from its steady state. This implies that optics tuned for a short beam pulse length (needed for the machine commissioning) differs from a long pulse or DC beam operation. Also, for nominal beam operation when the optics of the machine are tuned for neutralized transport through the LEBT, the un-neutralized front of the pulse may result in an increase in the beam loss along the LEBT and the following beamline. In order to minimize this effect and to obtain a transport scheme where the beam envelope is mostly time-independent through the beam pulse, an atypical transport scheme with an un-neutralized section at the downstream portion of the LEBT is implemented.

Figure 3.3 illustrates the concept of the transport scheme through the LEBT. As vacuum is quite poor near the ion source, it results in a relatively short neutralization time, and therefore nearly a full beam space charge neutralization take place in the neutralized section. Then, transition to the un-neutralized section is obtained by applying an electrical potential barrier (red oval on Figure 3.3) that confines thermal ions upstream, and a clearing electric field that sweeps compensating ions out of the beam path downstream of the potential barrier. The clearing electric field is created by a negative DC offset on one of the chopper plates. In addition, low vacuum pressure is maintained between the potential barrier and the RFQ to limit the ionization process. The corresponding beam optics are shown in Fig. 3.4. These optics have been implemented at the PIP-II Injector Test [7, 8, 9], where a low emittance beam ($\epsilon_n \leq 0.18$ mm mrad, rms) with Twiss parameters adequate for injection into the RFQ was obtained at the end of LEBT.

The location of the chopper, between solenoids #2 and #3, is relatively far from the RFQ entrance, and conforms to the principles expressed previously for achieving high reliability (i.e., good vacuum in the RFQ and low particle bombardment of the vanes). In addition, it leaves space for diagnostics both before and after solenoid #3, as well as provides room for a vacuum pump. Note that unlike many other LEBT designs, where a chopping system is located just upstream of the RFQ, the PIP-II LEBT layout provides sufficient room for a simple and robust chopper.

Finally, it is essential to reiterate again that the PIP-II LEBT design was driven not only by the beam optics requirements but also by the need of stable and reliable operation of the critical components. The presented LEBT design is very robust and successfully meets (1) good vacuum in the RFQ, (2) a simple and reliable chopper scheme, (3) a beam transport scheme that provides optics tuning independent of the beam pulse length, and (4) availability of sufficient space for the beam diagnostics.

3.2.1.2 RFQ

The RFQ operates in CW mode at a frequency of 162.5 MHz and accelerates the beam from 30 keV to 2.1 MeV. It is designed to handle a beam current up to 10 mA in CW regime. Figure 3.5 shows the beam transmission through the RFQ for input beam current ranging from 1 mA to 15 mA. For the nominal beam current of 5 mA, simulation suggests 99.8% beam transmission. The RFQ design parameters are summarized in Table 3.3.

Beam transmission through the RFQ was estimated by comparing beam currents measured using three identical toroids placed at both sides of the RFQ. These toroids were calibrated using the same source, and therefore provide a reliable estimation. For a nominal beam current of 5 mA and RFQ voltage of 60 kV, beam transmission through the RFQ was found to 98%. Note that the design specification for the RFQ transmission was $> 95\%$. A simulation study of the RFQ performed using the beam distribution measured at the LEBT suggested that only 1% of DC beam coming out the RFQ would accelerate, and the rest of the particles would have energy in the range of 30-40 keV. These particles get lost immediately after the first focusing magnet which are set to transport nominal beam of 2.1 MeV. Thus, DC tails coming from the RFQ could be estimated by comparing currents in two toroids located at the exit of the RFQ and downstream of the second doublet in the MEBT. It was found that current signals in both toroids were identical,

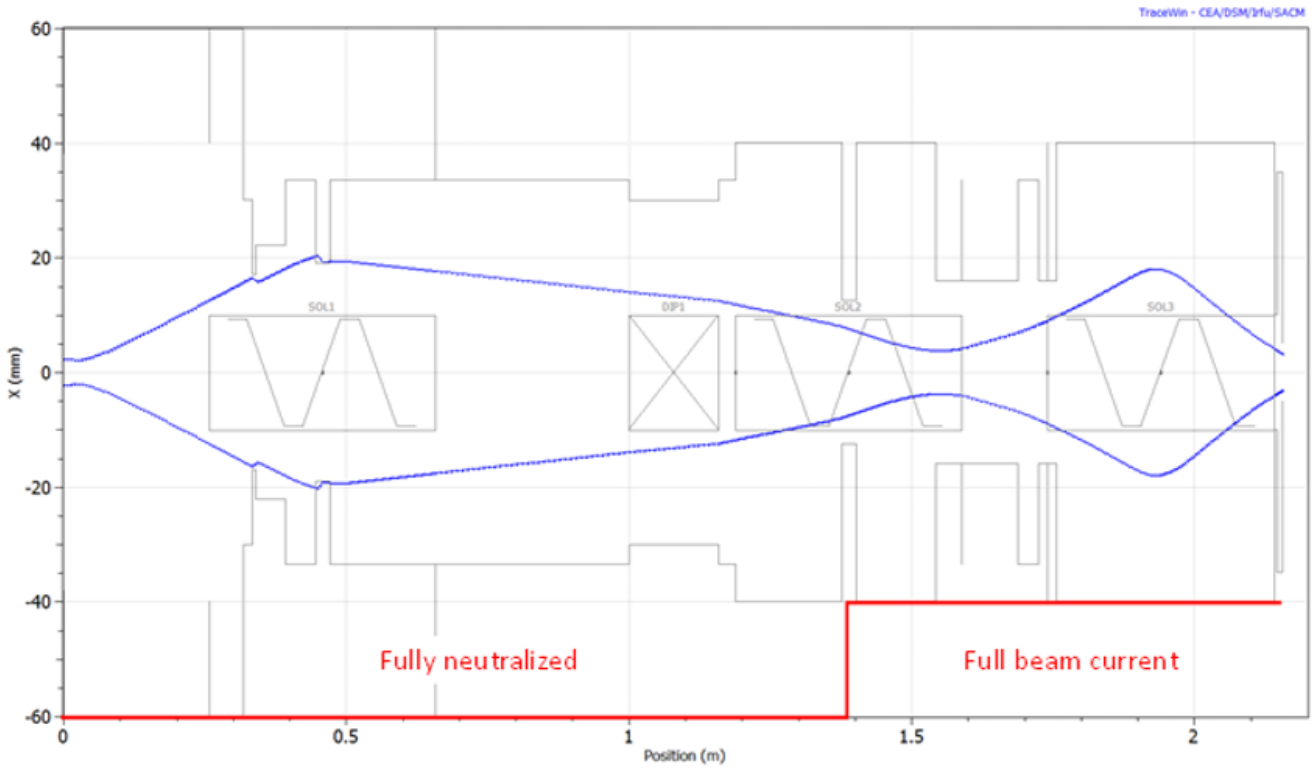

Figure 3.4: Beam horizontal envelope (2.5σ) for the partially un-neutralized LEBT optics solution simulated with TraceWin. The grey lines show aperture limitations. The red line indicates the level of neutralization (from fully neutralized to full beam current of 5 mA). Focusing is nearly symmetric which makes the vertical envelope quite close to the horizontal one. The initial distribution was derived from measurements of the ion source phase space carried out initially at LBNL [10] and later at the PIP-II Injector Test (PIP2IT).

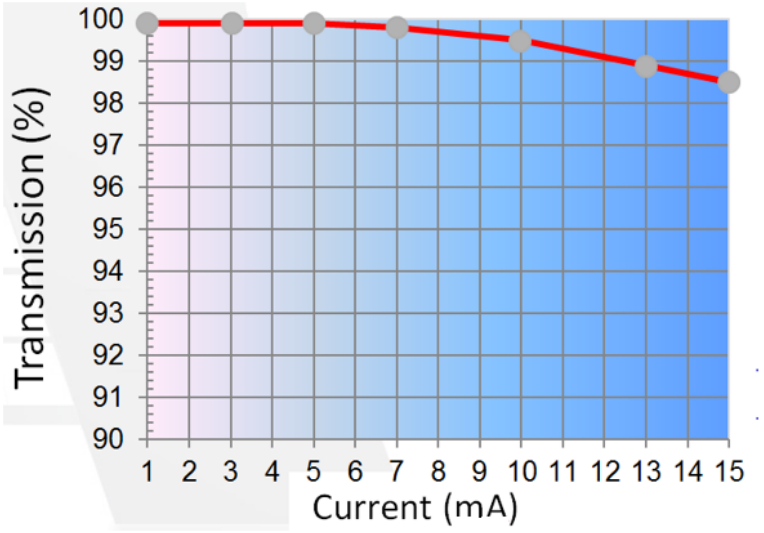

Figure 3.5: Dependence of the calculated RFQ transmission on the beam current

which implies that the DC beam current is below the measurement accuracy of 2%.

Table 3.3: Operational Parameters of the PIP-II RFQ

Parameter	Value	Unit
Input energy	30	kV
Output Energy	2.1	MeV
Duty Factor	100	%
Frequency	162.5	MHz
Beam Current	5 (nominal); 1-10	mA
Transmission (1-10 mA)	> 95	%
Output Transverse Emittance (1-10 mA)	< 0.25	mm-mrad
Output Longitudinal Emittance (1-10 mA)	0.8-1.0 (0.26-0.32)	keV-nsec (mm-mrad)

The requirement of CW operation forces the design optimization to be aimed at the minimization of RF power loss in the structure. Since most of the RF power is dissipated on the cavity walls, it creates a significant thermal load. Consequently, a relatively modest nominal vane-tip-to-vane-tip voltage of 60 kV was adopted to limit the overall RF power requirement, which yields a manageable thermal load of the RFQ structure. The RF design is based on detailed simulations including 3D electro-magnetic simulations of the entire RFQ. Mode stabilization with pi-mode rods significantly reduces the structure sensitivity to manufacturing errors. The geometry of the vane ends (vane-to-end-plate transition) was adjusted to achieve good field flatness [11] along the RFQ. The RFQ is also supported by 80 slug tuners to compensate manufacturing errors and imperfections of simulations.

The beam dynamics design of the RFQ was simulated using PARMTEQ [12] and it either meets or exceeds primary requirements of capture efficiency, transmission efficiency and emittance growth. Figure 3.6 shows a PARMTEQ simulation for a 5 mA beam, ideally matched into the RFQ. The transmission is 99.8% and the output longitudinal emittance is 0.7 keV−ns. For an input transverse rms emittance of 0.11 mm mrad, the output emittance is 0.15 mm mrad, a 35% increase but still well below the budget specified in Table 3.3. In addition, an error analysis (e.g., mismatch, centroid offsets, field errors...) was carried out that indicates a robust and error-tolerant design. Results of simulations of the transverse and longitudinal emittances as functions of the beam current (assuming a 0.11 mm−mrad rms normalized emittance at the RFQ entrance) are presented in Fig. 3.7.

Excessive longitudinal tails can result in beam losses in the course of acceleration and can limit the beam extinction of removed bunches[1]. The latter is an important requirement for future high duty factor experiments. Figure 3.8 presents the longitudinal distribution at the exit of the RFQ over the longitudinal Courant-Snyder invariant expressed using following equation,

[1]A non-zero value for the beam extinction is associated with particles having large momentum deviation. These particles in the course of their motion from the kicker to the HWR are not captured in the MEBT RF bucket, and therefore can drift into a nearby already-emptied RF bucket. Then these particles are captured into the HWR RF, whose RF bucket height is significantly larger than the bucket height of the MEBT.

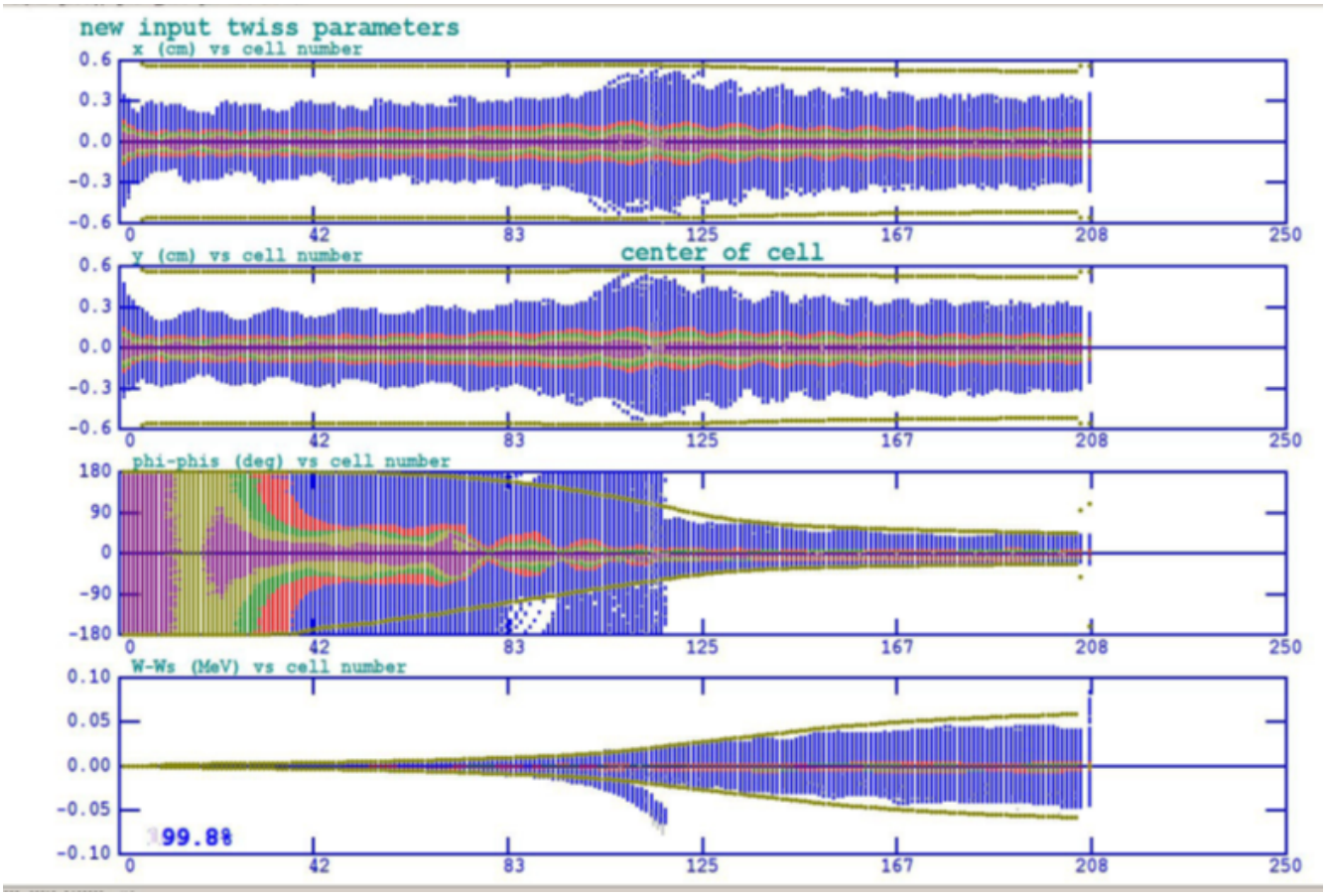

Figure 3.6: PARMTEQ simulation of a 5 mA beam using 100,000 macro-particles. The initial distribution was derived from the emittance measurements of the ion source performed during acceptance tests. The input Twiss parameters, however, are ideal.

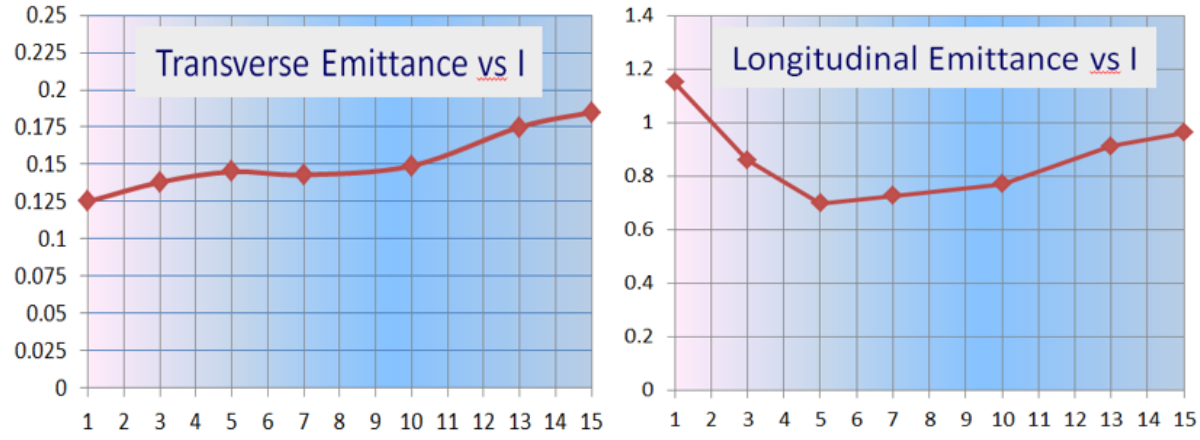

Figure 3.7: Dependence of the calculated transverse (left) and longitudinal (right) rms normalized emittances on the beam current (mA); the transverse emittance is presented in mm·mrad and the longitudinal one in keV·ns (1 keV·ns $\approx$ 0.32 mm·mrad).

$$\epsilon_s = (1+\alpha_s^2)s^2/\beta_s + 2\alpha_s s\Delta p/p + \beta_s(\Delta p/p)^2$$

and the integral of this distribution. Here β_s and α_s are the longitudinal beta- and alpha-functions, respectively, and s and $\Delta p/p$ are the deviations in the longitudinal coordinate and the relative momentum from the reference particle, respectively. Note from Fig. 3.8 that 3.1% of particles located in the halo with the Courant-Snyder invariant above three times the rms emittance[2] were not accounted for in the computation of β_s, α_s, and the rms emittance. Note also from Fig. 3.8 that about 2.5% of particles are in the non-Gaussian tails. This stresses the necessity of accounting for longitudinal tails in the computation of particle losses during further acceleration.

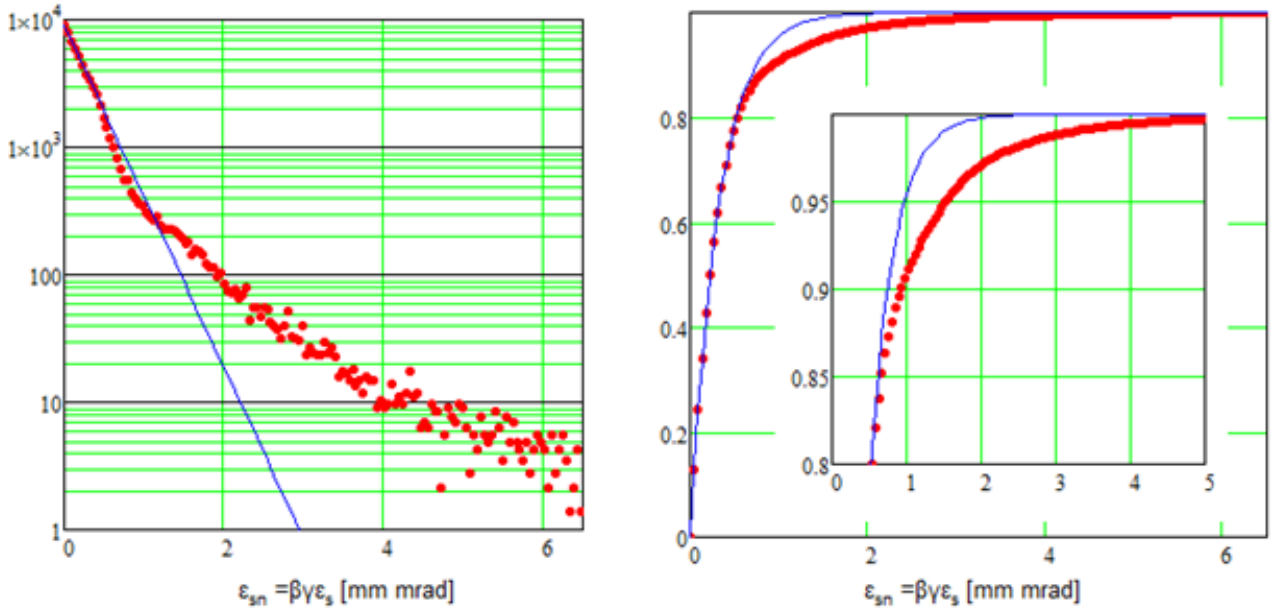

Figure 3.8: The particle longitudinal distribution (left) and its integral (right) at the end of the RFQ simulated for 5 mA beam current; $\beta_s = 1.69$ m, $\alpha_s = 0.087$, rms normalized emittance of 0.162 mm mrad. Blue lines show the Gaussian distribution and its integral built for longitudinal rms emittance computed from the particle distribution. 100,000 macro-particles were used in this simulation.

3.2.1.3 MEBT

The RFQ is followed by a MEBT which is designed to transport 2.1 MeV, 1-10 mA H^- beam between the RFQ and the HWR cryomodule with low emittance growth ($< 10\%$) and low beam losses. In a high-intensity ion Linac, the primary objective of a MEBT is to match the optical function between the RFQ and the main Linac. Furthermore, it also facilitates a beam diagnostic before injecting the beam to the SRF Linac. The PIP-II MEBT is envisioned to exhibit not only those features but also a chopping system that would provide a capability of removing any bunch

[2]Note that the average of Courant-Snyder invariants of all particles is twice larger than the corresponding rms beam emittance.

out of a true-CW beam coming out from the RFQ. This is one of the several eminent features of the PIP-II Linac design that enables not only optimizing injection into the Booster ring but also customizing the beam temporal pattern for any other potential users.

The chopper system includes a pair of wide-band kickers [13]-[14] and a beam absorber [15]. Two kickers are separated by ∼180° of betatraon phase advance and provide a vertical deflection to the beam. The absorber is positioned at ∼90° phase advance from the last kicker. This arrangement provides a maximum separation of 6σ between transmitted bunches and chopped out bunches at the absorber. Deposition of a high beam power density on the absorber makes it vulnerable to vacuum failures. Apart from the chopping system of length 5 m, a safe separation of the SRF section from the absorber is also required to deal with accidental vacuum failures. These accidental scenarios are considered in the MEBT design that leads to a significant elongation of the MEBT. Furthermore, the design also needs to address potential diffusion of particles and outgases, resulting from the chopping system, to the first SRF cryomodule, Half Wave Resonators (HWR). This is required to preserve surface quality of the SRF cavities, and therefore to ensure reliable operation of the cryomodule. Thus, it could be easily concluded by now that the chopping system is the most critical part of the MEBT, and its implementation drives the overall design concept of the MEBT. Some of the beam requirements in the MEBT are shown in Table 3.4.

Table 3.4: MEBT beam parameters. The output beam current is averaged over 2 μs.

Parameter	Value	Unit
Energy	2.1	MeV
Input Beam Current	0.5-10	mA
Output Beam Current	0-2	mA

The MEBT design also features a concrete wall to shield the front end from radiation coming from the main linac. This configuration, similar to one at the SNS MEBT, will facilitate personnel access to the front end for maintenance even during the machine's nominal operation. The complete list of the MEBT functional requirements is presented in Ref. [16]. A design of the PIP-II MEBT that satisfies these requirements has been developed [17]. This design is the result of several iterations taking into account feedback from optics simulations, mechanical design, and experience gained at the PIP-II Injector Test facility (PIP2IT) [18]. Figure 3.9 shows a schematic of the front end at the PIP2IT and at PIP-II. The concepts of both designs are very similar.

The resulting MEBT design is 14 m long. It consists of two quadrupole doublets and ten quadrupole triplets to provide transverse beam focusing while four quarter-wave resonators are used to provide longitudinal beam focusing. Each magnet package also includes a beam position monitor, as well as horizontal and vertical steering correctors. A focusing period of 1175 mm (center-to-center separation between successive triplets) is chosen to facilitate installation of the kickers and absorber between triplets. Note that only 650 mm is available between flange to flange. Figure 3.10 shows a detailed layout of the MEBT in the form of a block-diagram. In this figure, space available between successive transverse focusing units (such as between two neighbouring triplets or doublets) was addressed as a section in the MEBT.

The section labeled #6 in Fig. 3.10 is named "Differential Pumping Insert (DPI)". This section facilitates an ultra-high vacuum (UHV) in the 1×10^{-10} Torr range in close proximity of the

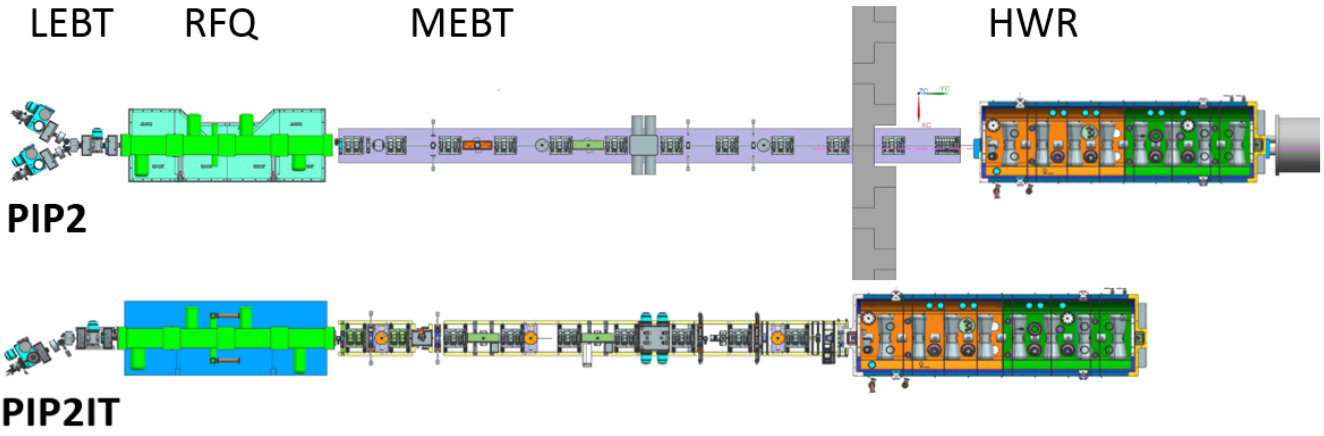

Figure 3.9: A schematic of the front-end of the PIP-II and PIP2IT. The PIP-II front-end design features a concrete wall envisioned at downstream of the MEBT. There is no such wall in the PIP2IT front-end due to space limitation.

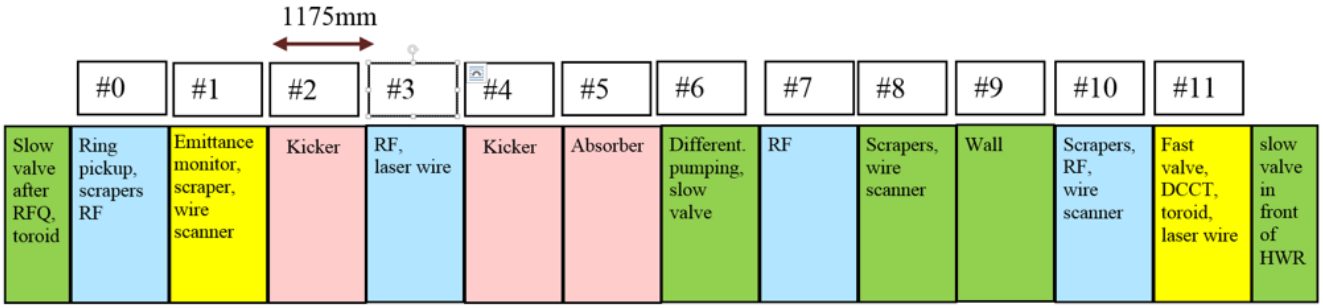

Figure 3.10: The MEBT structure. Sections are color-coded according to their main functions: vacuum (green), RF (blue), instrumentation (yellow), and chopper (pink).

SRF section and therefore minimizes potential condensation of gases at 2K surfaces. Note that outgassing from H^- beam deposited at the absorber was estimated to be up to 4×10^{-4} Torr-L/s. Thus, DPI provides a separation between UHV and high vacuum (HV) region in the MEBT. The DPI also imposes the transverse aperture limitation in the MEBT. A low-conductance aperture (10 mm diameter by 200 mm long) of the DPI is installed in the MEBT section just downstream of the absorber. The volume immediately downstream of the aperture is pumped by a 100 L/s ion pump. The DPI is electrically isolated such that any beam loss at the aperture restriction may be measured. Downstream of the DPI, all components are metal or ceramic, with no O-rings or elastomers.

The beam optics of the MEBT were developed using the beam dynamics code TRACEWIN. Figure 3.11 shows the betatron phase advance along the MEBT for 0 mA and 5 mA beam current. The beam tracking study was performed using a Gaussian beam distribution of macro particles truncated at 6σ with initial normalized RMS longitudinal and transverse beam emittance of 0.28 μm and 0.21 μm, respectively, to simulate a 5 mA beam current (average over the RF bucket). Initial beam energy used in this simulation was 2.1 MeV. The beam was tracked from the exit of the RFQ to the end of first focusing period in the HWR cryomodule. Figure 3.12 shows 3σ beam envelopes in respective planes through the MEBT. In the case of passing bunches there was zero voltage between kicker plates, while for the deflected bunches, voltages were -1000 V and 1000 V at the first and second kicker respectively. It can also be observed from Fig. 3.12 that the vertical trajectory of the passing beam is corrected using steering magnets to minimize beam loss at the kickers. Figure 3.13 shows the normalized RMS beam emittance evolution for the passing beam along the MEBT. There are no significant emittance growths in the elongated MEBT.

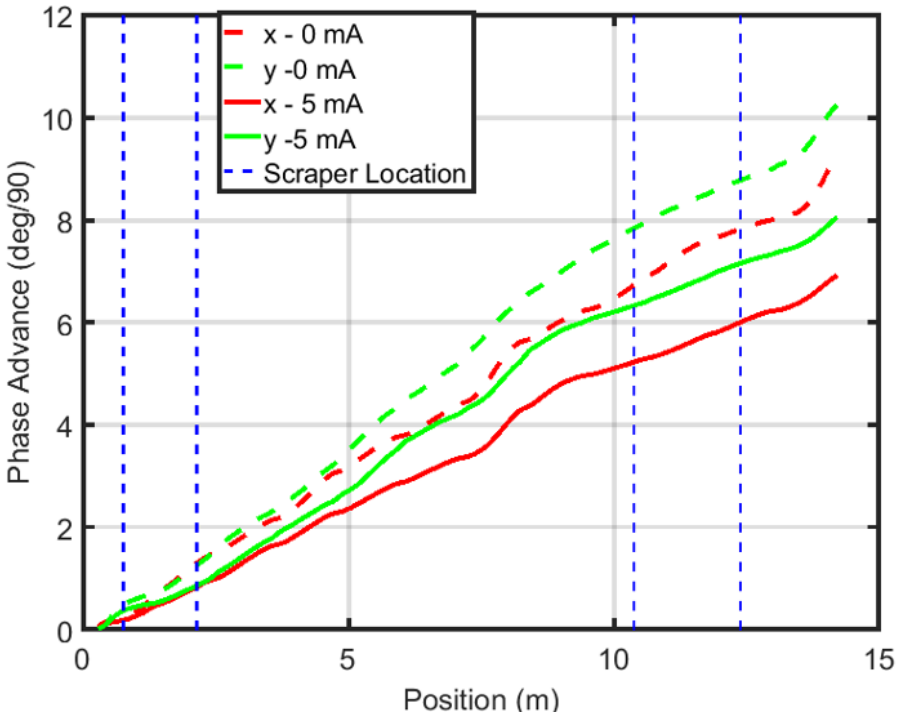

Figure 3.11: Horizontal (red) and vertical (green) betatron phase advance in the MEBT for 0 mA and 5 mA. Location of scraper assemblies are shown in blue vertical lines.

It can also be seen in Fig. 3.12 that the MEBT houses four scraper assemblies. Each assembly

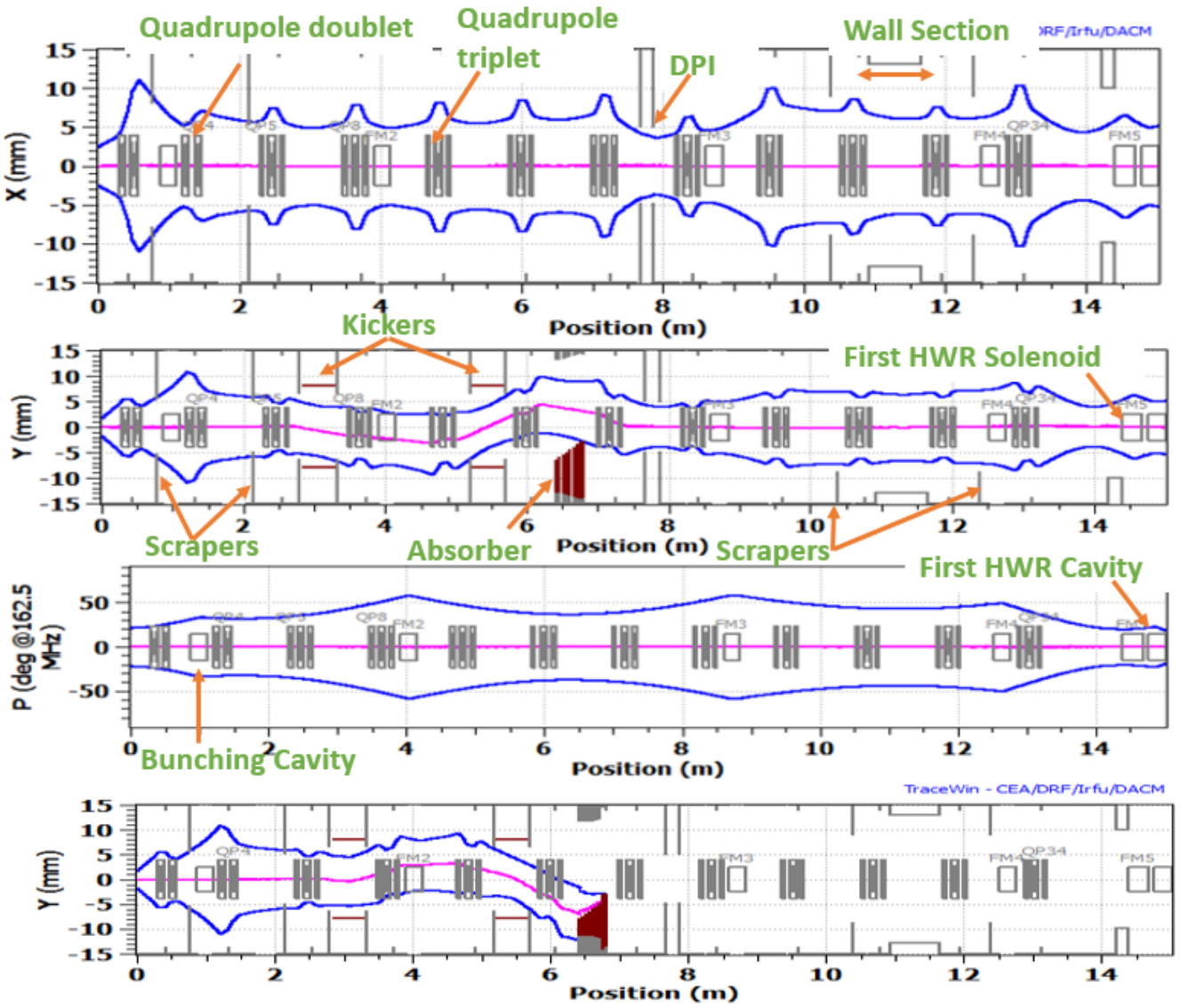

Figure 3.12: 3σ beam envelopes of 5 mA the passing bunch in the horizonal (x), vertical (y), and longitudinal (p) planes, and for the chopped-out bunch in the vertical plane along the MEBT. The magenta line in the plots indicates the beam centroid in respective planes.

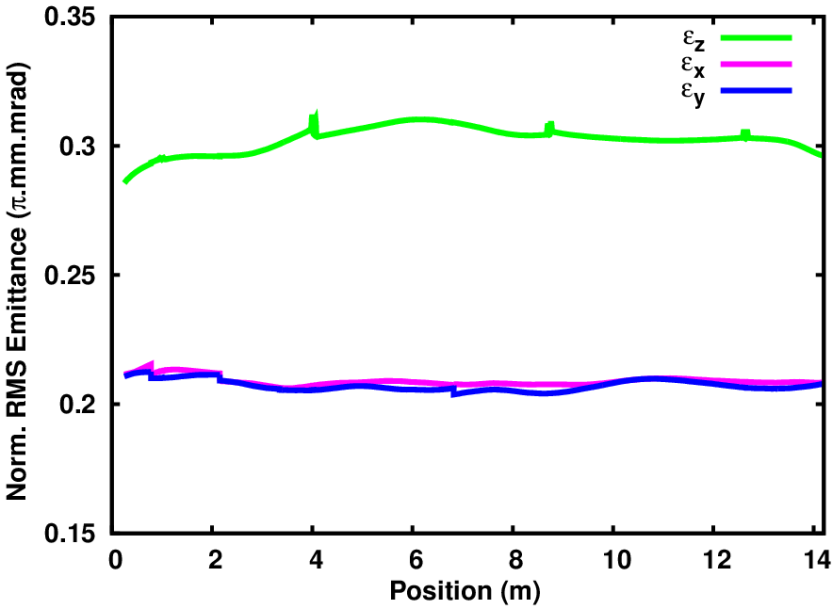

Figure 3.13: Longitudinal (green), vertical (blue) and horizontal (magenta) normalized RMS beam emittance along the MEBT.

consists of four scrapers named as left, right, top, and bottom scrapers. Note that a scraper is an electrically-insulated, 75 W-rated TZM plate that can move across the 30-mm MEBT aperture [19]. These scrapers serve several purposes such as:

- protection of downstream equipment from a beam loss caused by beam envelope and trajectory mismatches,
- cleaning of the beam by removing far tail particles in the distribution,
- preparation of a pencil beam for commissioning and measurements in SRF Linac (applicable only for a short pulse beam operation),
- supplementary diagnostic device for the beam distribution measurements. (applicable only for a short pulse beam operation).

In order to obtain effective removal of particles exhibiting large actions, successive scraper assemblies should be separated by 90° in betatron phase. However, implementation of this in the real transport line is challenged by space constraints and phase advance suppression due to space charge forces. In the PIP-II MEBT, locations of the scrapers are such that the beam phase advance between two nearest assemblies (i.e. phase advance between the pair of upstream assemblies or the pair of downstream assemblies) is ∼90° in the absence of space charge forces. Table 3.5 summarizes the phase advance between each assembly in the PIP-II MEBT. Furthermore, while intercepting a beam, the scraper results in outgassing and generates dust particles because of blistering and sputtering of its surface. Taking these into account, the design assumes that first two scraper assemblies intercept 1% of every bunch while last two intercept only ∼0.1%. This arrangement minimizes the likelihood of generation of dust particles in the vicinity of the SRF cavities. A

detailed description of the optics design of the scraper system for the PIP-II MEBT is presented in Ref. [20].

Table 3.5: Betatron phase advance between scraper assemblies in the PIP-II MEBT

Beam current		Scraper 1-2	Scraper 2-3	Scraper 3-4
0 mA	x	95.4°	488.0°	98.6°
	y	69.8°	592.6°	83.7°
5 mA	x	58.7°	394.2°	70.2°
	y	45.1°	491.3°	74.3°

3.2.2 Superconducting Linac

The MEBT is followed by the SRF Linac that accelerates the beam from a kinetic energy of 2.1 MeV to 800 MeV. Unlike other existing accelerator facilities, PIP-II utilizes SRF cavities directly downstream of the MEBT. Figure 3.14 shows the acceleration map in the Linac. Each block in the figure represents a section that was named after the type of SRF cavity to be used for the given range of acceleration.

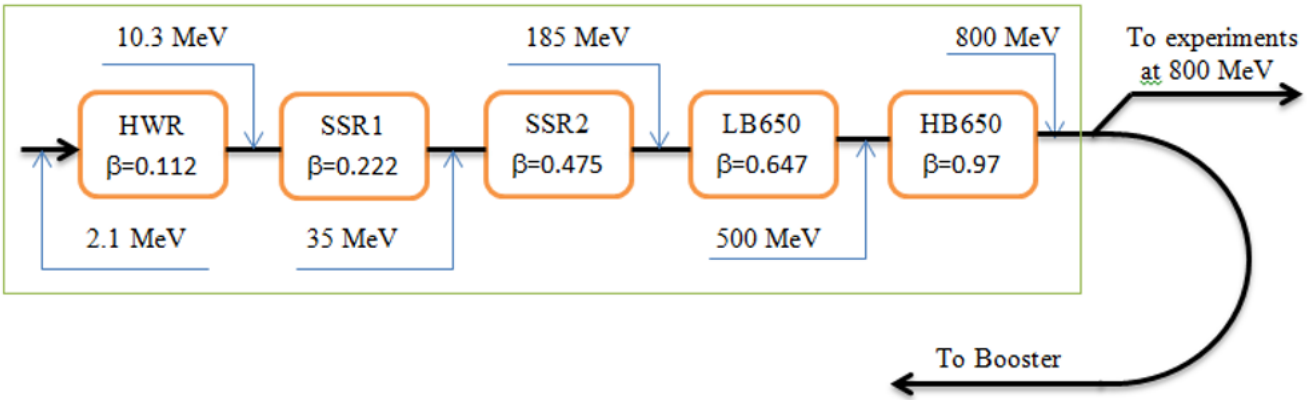

Figure 3.14: Schematic of acceleration scheme in the PIP-II SRF Linac. Beam energy at the entrance and exit of each section are indicated using a blue arrow. The β refers to the optimal beta of the respective cavity.

The first section in the Linac uses half-wave resonators (HWR) that operate at 162.5 MHz. It accelerates the beam up to 10 MeV. The following two sections, i.e., SSR1 and SSR2, utilize two types of single spoke resonators operating at 325 MHz (SSR1 and SSR2). They provide a combined acceleration from 10 MeV to 185 MeV. Finally, the LB650 and HB650 sections provide the remaining acceleration using two types of elliptical 5-cell cavities operating at 650 MHz. The transverse lattice of the Linac is composed of the superconducting solenoids and normal conducting quadrupoles. The HWR, SSR1 and SSR2 use three types of solenoids (one type for each section) while the last two sections use normal conducting quadrupoles arranged in doublet formation to provide transverse beam focusing. In the following, the choice of the beam line elements will be outlined and evaluated together with their respective beam dynamics performance.

3.2.2.1 Choice of transverse focusing element

An axially symmetric beam is less sensitive to space charge forces and more immune to coupling between transverse planes in the presence of the same phase advance for both planes (equipartition theorem). Thus, choices of transverse focusing elements were made to keep the beam round (same sizes in both horizontal and vertical planes) in the transverse planes along the PIP-II Linac. In the first three sections, i.e., HWR, SSR1 and SSR2, superconducting solenoids were chosen to provide transverse focusing. The choice of solenoids was made for the following reasons:

- A solenoid provides axial symmetric focusing. The quadrupole focusing in doublet/triplet configuration also provides an axial focusing but it requires more space in comparison to a solenoid. At the low energy part of the Linac where the space-charge force is most significant, a short focusing period is more desirable. Thus, a solenoidal focusing is preferred choice for the low energy sections.

- The focusing strength of a solenoid is expressed as:

$$\frac{1}{f_s} \approx \left(\frac{q}{2mc\beta\gamma}\right)^2 B^2 L$$

  where f_s is the focal length of the solenoid, B is the axial field strength, L is the length of the solenoid, β and γ are Lornetz factors, c is the velocity of light and m is the mass of the charged particle. Similarly, the focusing strength of the doublet is expressed as:

$$\frac{1}{f_d} \approx \left(\frac{qB}{mc\beta\gamma a}\right)^2 l^2 s$$

  where f_d is the focal length of the doublet, and l and s are the length and center-to-center separation of the quadrupoles, respectively. B is the field strength at the quadrupole poles and a is the pole radius. Using these equations, a comparison of their focusing strengths can be made. Considering a solenoid with length equivalent to a doublet system (sum of quadrupoles lengths and gap between them) and having the same field strengths, it is evident that a doublet focusing is much superior to a solenoid. Thus, quadrupole focusing is used for the LB650 and HB650 sections where the beam energy is higher and a relatively long focusing period is tolerable. However, a choice of solenoidal focusing for low energy is still preferred as it facilitates a large transverse aperture and a compact axial-symmetric focusing.

- Accelerating cavities also result in RF defocusing and generate a radial kick to the beam. This kick is inversely proportional to the square of the particle velocity. Thus, a radial focusing of the solenoid at low energy is an ideal choice to compensate RF defocusing of the cavity.

3.2.2.2 Choice of accelerating cavity

Most of the technological and the beam-dynamics complexities associated with an ion Linac are consequences of the non-relativistic nature of the accelerating particles. The ion velocity changes

significantly with acceleration along the Linac, and therefore the Linac needs several types of accelerating cavities optimized for different particle velocities. Although this arrangement provides an efficient acceleration scheme, it introduces a technological challenge of designing, building and commissioning a variety of accelerating cavities. Different lengths and operating frequencies of these accelerating cavities bring the beam dynamics aspect into consideration. Thus, a careful choice of accelerating structure is crucial for a cost-effective as well as a robust optics design of the Linac. In the following, we discuss the operational and beam-dynamics aspects in the framework of the PIP-II Linac that determine the choices of accelerating cavities in the SC Linac.

Accelerating Range and Maximum Energy Gain of the Accelerating Cavities

In modern accelerators, multi-cell accelerating cavities are used to maximize the energy gain per structure. The larger the number of cells, the larger the maximum energy gain per structure. However, the optimal energy gain through a structure decreases if the particle velocity differs significantly from the designed velocity of the structure. Note that a regular cell length is

$$L_{cell} = \beta_G \lambda / 2 \tag{3.1}$$

where β_G and λ are the design normalized particle velocity and the RF wavelength in free space, respectively. Because a particle with the design velocity takes half of the RF period to pass through a cell, it experiences maximum interaction with the accelerating RF field while traversing through it. As the particle velocity differs from the design velocity (as is the typical case for ions), particles not only interact less but might experience the decelerating field (wrong phase of the RF field). As a result, the total energy gain through an accelerating structure is reduced. This effect is accounted for using the transit-time factor $T(\beta)$. For a periodic structure with a harmonic distribution of electric field along the axis,

$$E \propto \sin\left(\omega z / \beta_G c\right) \exp\left(i\omega t\right), \tag{3.2}$$

the transit-time factor for a cavity operating at the π-mode can be expressed by the following formula:

$$T(\beta) = \frac{T_0(\beta)}{T_0(\beta_{opt})}, T_0(\beta) = \frac{2\beta}{\pi n}\left(\frac{\sin\left[\pi n(\beta-\beta_G)/(2\beta)\right]}{\beta-\beta_G} - (-1)^n \frac{\sin\left[\pi n(\beta+\beta_G)/(2\beta)\right]}{\beta+\beta_G}\right), \tag{3.3}$$

where n is the number of cells in a multi-cell cavity. Note that $T_0(\beta_G) = 1$, and $T_0(\beta)$ achieves its maximum (exceeding 1) at $\beta = \beta_{opt}$. That determines the normalization of $T(\beta)$ so that $T(\beta_{opt}) = 1$, where β_{opt} is called the optimal beta. The electric field for a typical SC cavity operating in the π-mode can be approximated as in Eq. 3.2. Consequently, Eq. 3.3 represents a good approximation for the transit time factor. For a sufficiently large number of cells per cavity, Eq. 3.3 indicates that the geometric and optimal betas are related as follows:

$$\beta_{opt} \approx \beta_G \left(1 + \frac{6}{\pi^2 n^2}\right) \tag{3.4}$$

Energy gain in an n-cell cavity is then expressed as:

$$\Delta u = n E_0 L_{cell} T(\beta) \tag{3.5}$$

where E_0 is the field amplitude. One can easily conclude from Eq. 3.5 and Fig. 3.15 that the larger the number of cells in a cavity, the larger the maximal energy gain [$T(\beta) = 1$]. The dependence of

the transit-time factors on the beam velocity, β (normalized to geometrical beta), and consequently, energy gain (normalized to maximal energy gain) in a multi-cell cavity are shown in Fig. 3.16 for different numbers of cells. It could be observed from the figure that a multi-cell cavity is efficient only for a certain range of the beam velocity, and this range increases for a small number of cells in a multi-cell cavity. Thus, the lower the number of cells, the wider the operating range of a multi-cell cavity. Furthermore, a cavity with a lower number of cells is easier to handle (such as surface processing, tuning, etc.) and is less sensitive to trapped modes. On the other hand, too few cells in a multi-cell cavity will lead to a large total number of cavities needed to obtain the final beam energy, which will cause an increase in the overall cost of the Linac. Also, the contribution from the end cells will be larger in a multi-cell cavity with a small number of cells, which further deteriorates the effective gradient. Thus, the choice of the number of cells in a multi-cell cavity is a trade-off between the maximum energy gain and the operating range of the cavity. In an ion Linac, a cavity with a lower number of cells is preferred at low energy, where the particle velocity changes very rapidly with acceleration (see Fig. 3.17). As the beam energy increases, the change in particle velocity with acceleration slows down. Thus, an increase in the number of cells in a cavity for the intermediate- and higher-energy part of the Linac is a more rational choice. This arrangement allows limiting the type of cavities required to achieve the final beam energy.

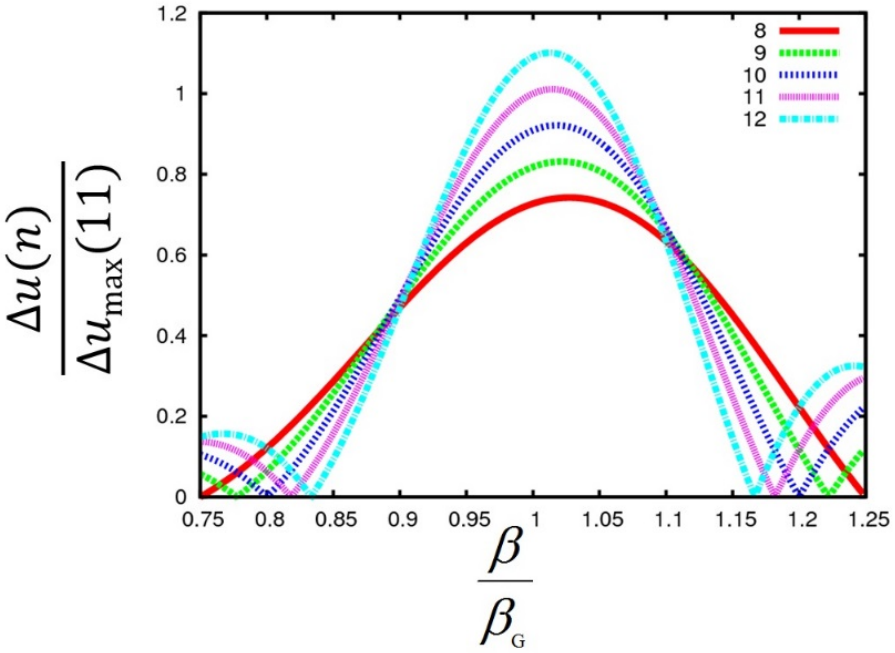

Figure 3.15: Energy gain in a multi-cell cavity. Particle velocity is normalized with respect to the geometrical beta, and energy gain is normalized to the maximal energy gain in a 11-cell cavity. The maximum energy gain for each case is shifted with respect to $\beta/\beta_G = 1$ as described by Eq. 3.4.

In the PIP-II SC Linac, we use five types of cavities. The HWR, SSR1, and SSR2 cavities were designed with two accelerating gaps while the LB650 and HB650 cavities were designed with five cells. Figure 3.18 shows the dependence of the transit time factor on particle velocity for the PIP-II cavities.

Choice of Operating Frequency

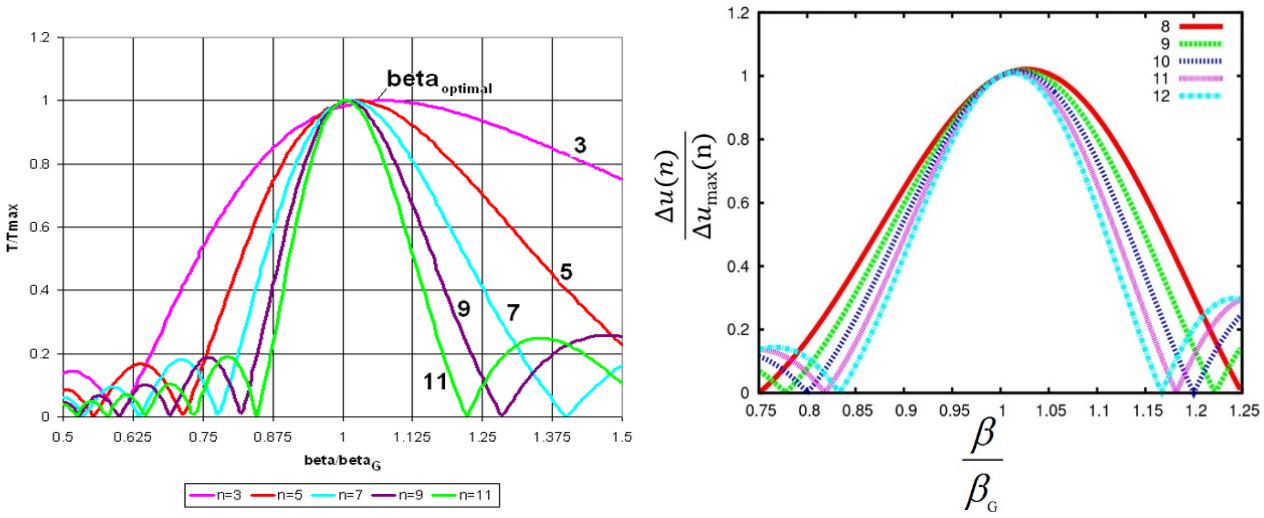

Figure 3.16: Variation in transit time factor (left) and normalized energy gain (right) with the particle velocity for different number of cells in a multi-cell cavity.

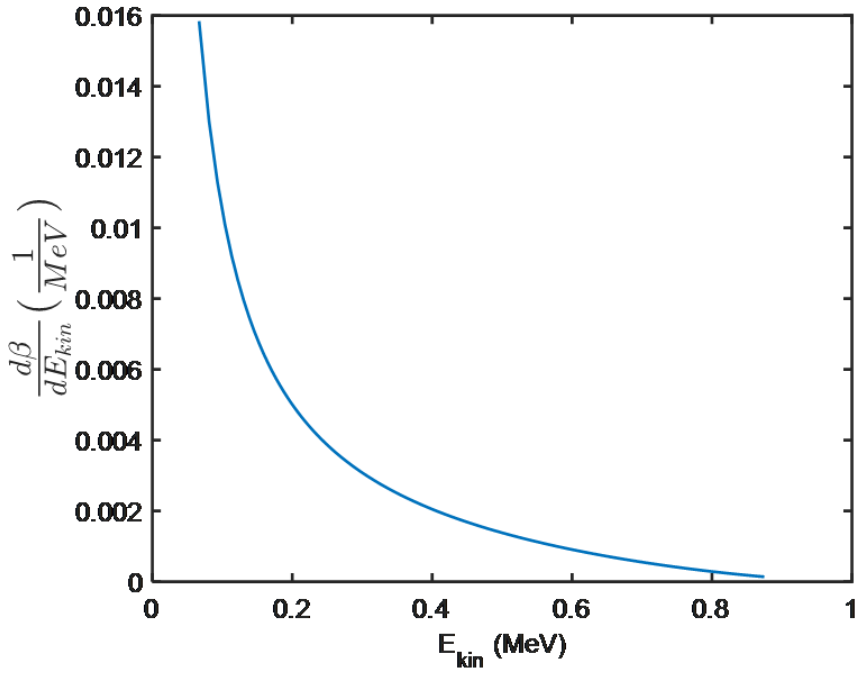

Figure 3.17: Variation in rate of change in beta with respect to kinetic energy of the H^- ion at different energies.

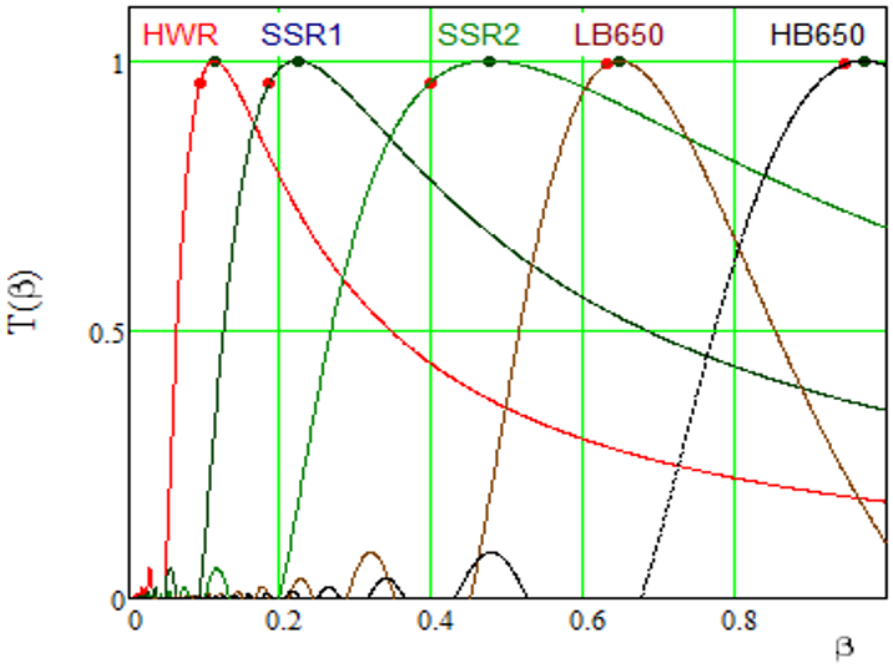

Figure 3.18: Variation in the transit time factor with beam velocity for the PIP-II cavities. Red dots mark the position of β_G, and blue dots the position of β_{opt}.

The following are considered while making the choice of an operating frequency for an accelerating cavity:

- For a TM-mode operating accelerating cavity, aperture is inversely proportional to the operating frequency. Thus, a lower frequency allows a larger aperture that in turn, provides a larger transverse acceptance. Note that a large transverse acceptance is essential to limiting beam loss.

- The beam traversing through an accelerating cavity receives a transverse RF kick. This kick [21] is expressed using the following:

$$\Delta(\gamma\beta r') = \pi V_{acc} \sin(\phi_s)/(mc^2\gamma_s^2\beta_s^2\lambda) \tag{3.6}$$

  where, ϕ_s is the synchronous RF phase, λ is the RF wavelength in free space. L and V_{acc} are the length and accelerating voltage of the cavity, respectively. T is the transit time factor. The subscript "s" represents the synchronous particle. Equation 3.6 shows that the kick is directly proportional to the frequency of the cavity. Thus, a lower operating frequency of the cavity is preferred especially at the low-energy part of the Linac where the RF kick is significantly larger (because of lower β) and might lead to a beam instability in a space charge dominated regime. As the beam velocity increases with acceleration, the RF defocusing kick is reduced and a higher operating frequency is favored for the cavities.

- A slow varying RF field is more effective at accelerating a non-relativistic charged particle,

as it provides a longer interaction of particles with the RF fields.

There are tradeoffs of using the low operating frequency application as well.

- Cavities operating at lower frequency are usually more expensive because of their large dimensions (and therefore, more niobium). Also, cryogenic losses per cavity are higher. However, the increased cost (fabrication and operating) per cavity is well compensated by the smaller number of cavities and RF sources.

- Microphonics is a more serious issue at lower frequencies and therefore, special care is needed for reliable operation of these cavities.

While making choices of operating frequencies of the accelerating cavities for the PIP-II Linac, it was also considered that 1300 MHz SRF technology has been widely adopted within the accelerator community across the world. Upcoming accelerator projects such as LCLS-II and XFEL are using this technology. Also, recent developments in 1300 MHz ILC technology at Fermilab [22] and elsewhere makes it a preferable choice for a high-energy upgrade of the PIP-II Linac. Perceiving this idea and above considerations, the PIP-II Linac uses three frequencies that are sub-harmonics of 1300 MHz. The HWR cavity operates at 162.5 MHz while both SSR1 and SSR2 operate at 325 MHz. The operating frequency of the last two families of cavities is 650 MHz.

Note that the RFQ operates at 162.5 MHz. This choice was outlined by a requirement of bunch-by-bunch chopping. Chopping at 325 MHz is presently beyond the "state-of-the art". This leaves 162.5 MHz as the only viable choice. This frequency is also used for the HWR. In comparison with the alternative of 325 MHz cavities, this choice results in reduced transverse defocusing and reduced longitudinal focusing from cavity fields, which otherwise would limit the accelerating gradient in the first SC cryomodule. The number of cavities and the Linac length required to accelerate the beam from 2.1 MeV to 10 MeV is reduced by more than a factor of two while using 162.5 MHz cavities in comparison to the alternative 325 MHz cavities. Beyond 10 MeV, a choice of 325 MHz and later 650 MHz were made for the cavities in the PIP-II Linac. These choices of frequencies results in a comparatively smooth frequency increase in the course of acceleration along the Linac, and therefore allow accommodating the bunch compression due to adiabatic damping.

Choice of Operating Gradient in Accelerating Cavity

Selection of the accelerating gradient in an accelerating structure is primarily driven by the choice of RF operation. In a low duty cycle RF pulsed regime, a choice of the maximum available accelerating gradient is made to achieve higher energy gain per cavity and the limitation mainly arises from the field emission onset, Lorentz-force detuning, and microphonics. However, in a long-duty or a CW RF regime, the cryogenic heat load is the main concern that determines the optimal accelerating gradient in a cavity. Thus, an accelerating gradient is chosen such that it links to a high-Q-high-accelerating gradient region. This arrangement allows minimizing the operating cost of the machine. Note that dynamic RF heat load is inversely proportional to the quality factor Q of the cavity.

Experience gained with operation of the cavities at different frequencies gives insight into potential high Q-slope onset for the PIP-II cavities. Figure 3.19 (taken from Ref. [23], see also Ref. [24])

shows high Q-slope onset in terms of the peak surface magnetic field at different frequencies. Using this information, limits on the peak surface magnetic fields for the PIP-II cavities were chosen as 50 mT and 60 mT for the HWR and SSR1 cavities, respectively, and 75 mT for the LB650 and HB 650 cavities. For all cavities, the peak surface electric fields were kept below 45 MV/m to reduce the likelihood of strong field emission.

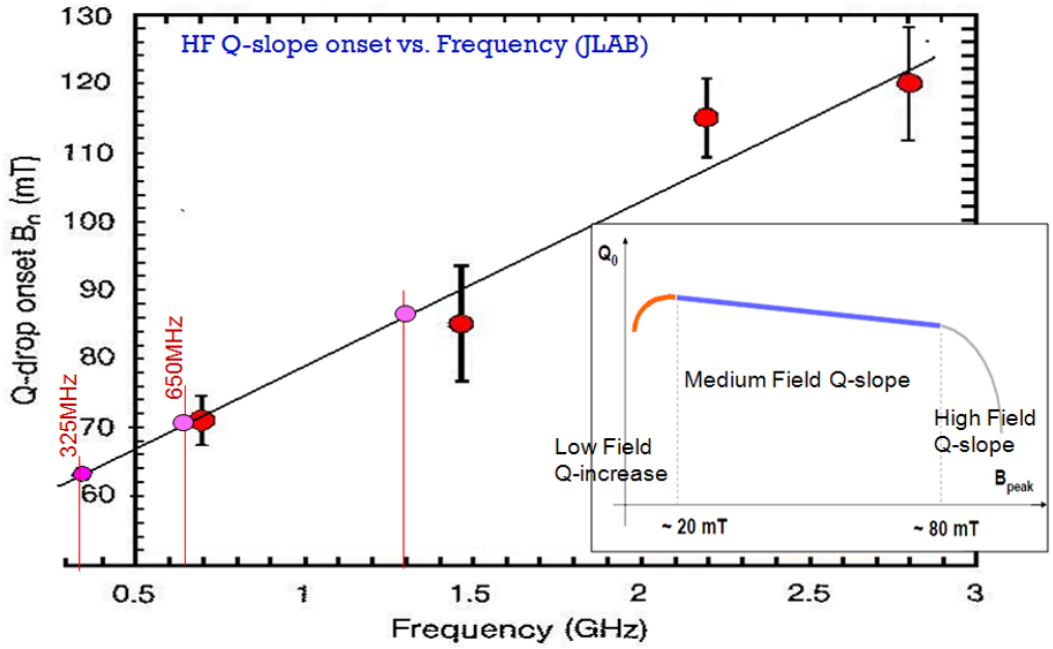

Figure 3.19: High field Q-slope onset versus frequency. Red points with error bars represent measurements of cavities at their respective frequencies while magneta points show the operating frequencies of the PIP-II cavities, including 1.3 GHz for a future upgrade.

Transition Energy between the Sections

Choice of the beam energy when switching from one family of cavity to another is quite critical for obtaining an efficient performance from the subsequent families of cavities. Transition at the wrong energy (due to the transit time factor) will dampen the real-state accelerating gradient (energy gain per unit length of the Linac). Consequently, more cavities are required to achieve the design energy. Thus, transition energies between different types of cavities were optimized to minimize the total number of cavities in the Linac. Because available accelerating voltage increases in subsequent families of cavities in the PIP-II Linac, transition between sections occurs before the transit-time factors for the two types are equal.

The HWR section accelerates the beam from 2.1 MeV to 10 MeV. Note that the initial beam energy is determined by the RFQ. The following two families of single spoke resonators accelerate the beam from 10 MeV to 185 MeV. At this energy, transition occurs to two families of 5-cell, 650 MHz, cavities for the rest of the beam acceleration. It is worth mentioning here that use of a single family of the elliptical cell cavities for the entire range of the acceleration will be inefficient. In order to obtain an optimal transition between two families of elliptical shape cavities, an analysis was performed to evaluate the total number of cavities required as a function of geometrical betas of the LB650 and HB650 cavities. The analysis assumed, (1) a linear dependence of the

field enhancement factors versus β [25], (2) the initial synchronous RF phase is -30°, and (3) the decrease in absolute value of the synchronous phase is inversely proportional to the square root of the energy to keep the desired RF bucket size.

The left pane in Fig. 3.20 shows the number of cavities as a function of beta of the LB650 and HB650 cavities. Note that the number of cavities is weakly dependent on beta in the vicinity of the minimum. This in turn, provides alternative options (in close proximity of the minimum) for choices of the geometrical beta of these cavities. Analysis suggests that the optimal choice of the geometrical betas for the LB650 and HB650 MHz cavities are 0.65 and 0.92, respectively, and the optimal transition energy is 466 MeV (as shown in the right pane in Fig. 3.20). However, a more accurate simulation that took realistic field enhancement factors into account resulted in an optimal choice of geometrical betas at 0.61 and 0.92.

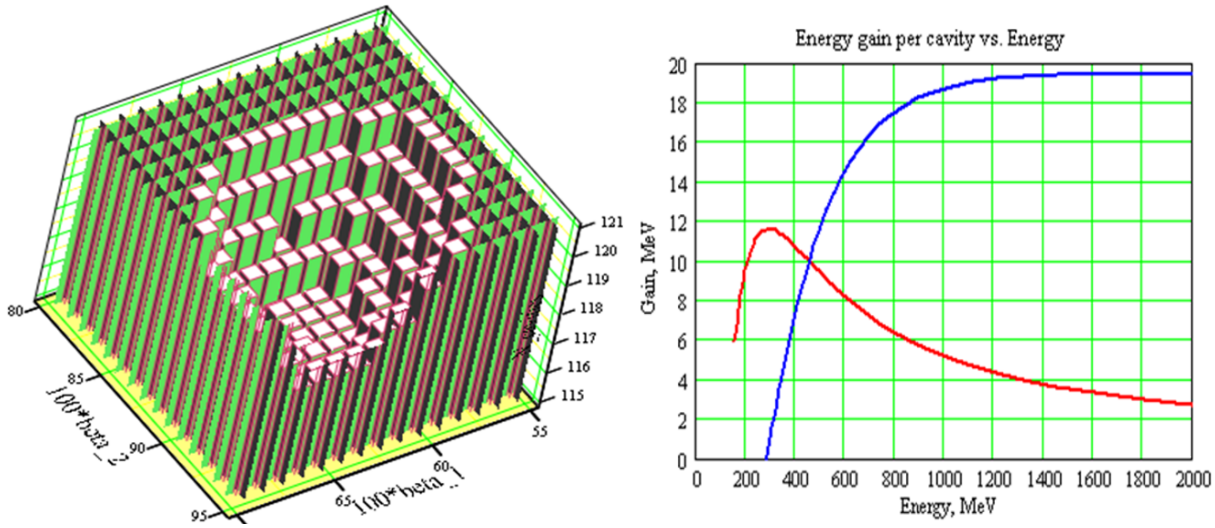

Figure 3.20: Number of cavities required for acceleration from 185 to 800 MeV versus cavity beta in the LB650 and HB650 sections (left) and the energy gain per cavity versus particle energy (right) for LB650 (red curve) and HB650 (blue curve) cavities.

Tables 3.6 and 3.7 summarize the families of cavities and their operating parameters in the PIP-II SC Linac. Note that throughout this document we define (R/Q) so that in the absence of cavity detuning and beam current, the RF power required to create the voltage amplitude U_0 is equal to: $P_g = (1+\beta_c)^2 U_0^2/[4\beta_c(R/Q)Q_0]$, where β_c is the coupling coefficient and Q_0 is the cavity unloaded quality factor.

3.3 Preliminary design of the PIP-II superconducting Linac

After making appropriate choices of the beamline elements and their operating parameters, the next objective is to develop a robust beamline that will preserve the beam quality (beam emittances, energy spread) along the Linac and deliver a beam with the designed parameters (such as current, energy, etc.). Experience with existing high-intensity Linac such as LANSCE [26] and SNS, as

Table 3.6: Accelerating cavities in the PIP-II Linac and their operating ranges in the Linac. ($\beta_g = \beta_G$ for the HWR, SSR1 and SSR2 cavities, β_g for the elliptic cavities is defined as the ratio of regular cell length to half-wavelength. Fitting to Eq. 3.3 for the elliptic cavities yields: $\beta_G = 0.64$ for LB650 and $\beta_G = 0.947$ for HB650.)

Cavity name	β_g	β_{opt}	Freq. (MHz)	Cavity type	Energy gain at β_{opt} per cavity (MeV)	Energy range (MeV)
HWR	-	0.112	162.5	Half wave resonator	2	2.1 - 10.3
SSR1	-	0.222	325	Single-spoke resonator	2.05	10.3 - 35
SSR2	-	0.475	325	Single-spoke resonator	5	35 - 185
LB650	0.61	0.65	650	Elliptic 5-cell cavity	11.9	185 - 500
HB650	0.92	0.971	650	Elliptic 5-cell cavity	19.9	500 - 800

Table 3.7: Main electro-dynamical parameters of SC cavities. (For energy gain per cavity presented in Table 3.6 where the cavity effective length was computed as $L_{eff} = \beta_{opt}\lambda n_{cell}/2$ for the HWR, SSR1 and SSR2 cavities, and as $L_{eff} = \beta_g\lambda n_{cell}/2$ for the LB650 and HB650 cavities.)

Cavity type	Aperture (diameter) (mm)	Effective length (cm)	Accelerating gradient (MV/m)	E_{peak} (MV/m)	B_{peak} (mT)	R/Q (Ω)	G (Ω)
HWR	33	20.7	9.7	44.9	48.3	272	48
SSR1	30	20.5	10	38.4	58.1	242	84
SSR2	40	43.8	11.4	40	64.5	297	115
LB650	88	70.3	16.9	40.3	74.6	341	193
HB650	118	106.1	18.8	38.9	73.1	610	260

well as past studies [27, 28, 29, 30], have led to a set of rules that helps in the design of a high intensity Linac. These rules in are discussed in the following:

- Adiabatic variation in phase advance: In a high-intensity ion Linac, non-linear space charge forces play a crucial role in beam stability. Thus, the lattice is designed with an adiabatic variation in the longitudinal and transverse focusing. This arrangement results in a gradual change in the beam sizes along the Linac, and therefore minimizes the impact of the non-linear forces along the Linac. Note that most of the optics elements operate in the linear regime, and therefore do not compensate non-linear forces effectively. Avoiding any abrupt changes in the phase advances per unit length of the Linac (i.e. deg/m) allows a balance to be maintained among all degrees of freedom.

- Focusing Period: The focusing period is kept short at the low energy part of the Linac. This is done to serve two purposes:

  - As can be observed from Eq. 3.6, transverse RF defocusing is proportional to the field amplitude in the cavity and its effect is foremost at low velocity. This in turn implies that a short focusing period, where a transverse focusing element follows (immediately or at a short interval) an RF cavity, is only way to obtain an efficient use of the available accelerating voltage in the cavity.

  - This minimizes the effect of the space charge forces by limiting the drift space a beam traverses through without focusing.

  - To enhance the real-state gradient in the Linac, the number of accelerating cavities per transverse focusing magnet is increased gradually along the Linac. Consequently, transverse focusing periods also increase. Figure 3.21 shows focusing periods in the HWR, SSR1, and SSR2 sections. In order to protect the HWR cavities from potential contamination coming from the MEBT, the period in the HWR cryomodule starts with a SC solenoid. The sequence of elements in the SSR1 and SSR2 cryomodules is chosen to minimize optics perturbations at the cryomodule-to-cryomodule transitions. Figure 3.22 shows periods the in LB650 and HB650 sections. Normal-conducting quadrupole doublets are utilized in the LB and HB sections to provide transverse beam focusing.

- Beam Matching: Each section in the Linac has different focusing periods, and therefore the Linac is not a periodic, but a quasi-periodic structure. A transition from one focusing period to another or transition from one cryomodule to another in the beamline might lead to abrupt changes in the beam envelopes that consequently could result in emittance growth and halo formation. Thus, a careful beam matching is required at these locations of discontinuities. It is usually performed by adjusting gradients and RF phases (for cavity only) of the outermost beamline elements in cryomodules to obtain a smooth beam envelope and an adiabatic phase advance variation while switching to a new focusing period.

- Robustness of the design: The Linac is composed of many optics elements. There is a high probability that fabrication errors and other technical aspects may affect their optimal performance. In such a case, they might not operate at their design parameters. This results

in a spread of the operating parameters over the length of the Linac. This aspect should be considered during the lattice design. The lattice should be capable of sustaining stable operation even in the presence of failure of at least one RF cavity or focusing magnet.

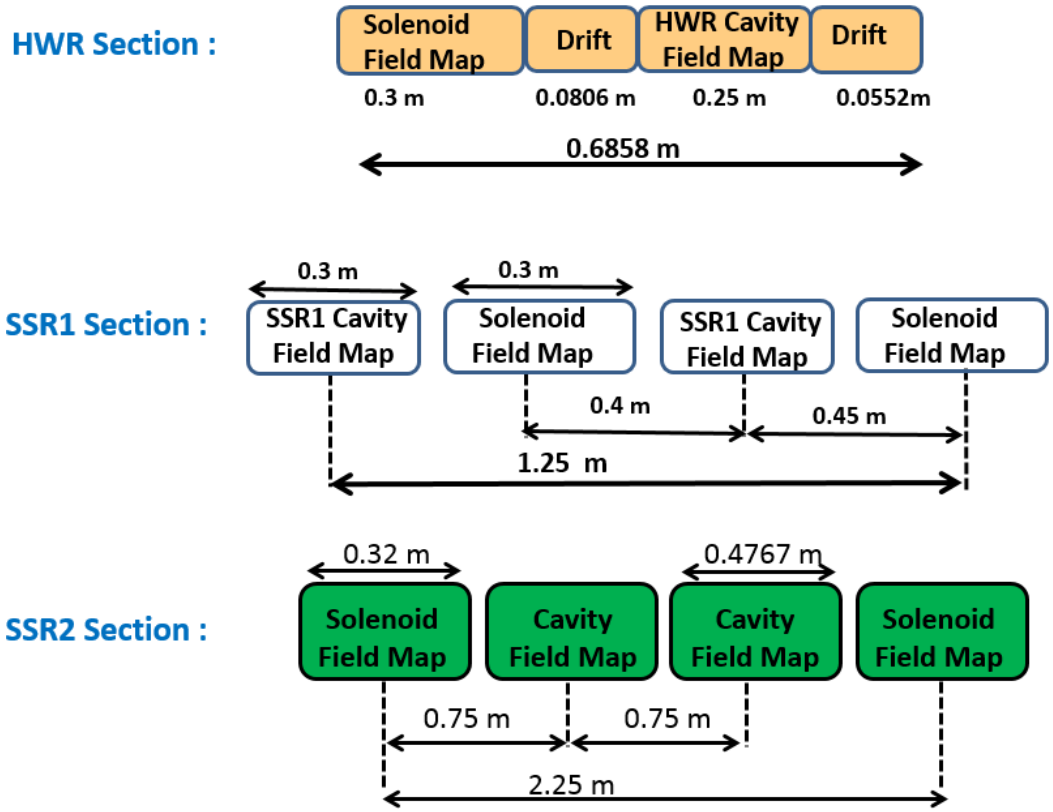

Figure 3.21: Focusing periods in HWR, SSR1 and SSR2 sections of the PIP-II Linac. Center-to-center separation of elements in HWR (top), SSR1 (center) and SSR2 (bottom) sections are also depicted. Note that element lengths are presented in terms of axial field map lengths which is typically longer than their physical lengths. This allows for accounting of the edge fields while performing optics studies. The structures of cryomodules are: (sc)×8 for HWR, (csc)×4 for SSR1, and (sccsccsc) for SSR2; where c and s denote cavities and solenoids, respectively.

Using the above considerations, a robust lattice for the PIP-II Linac was developed using the beam-dynamics codes TRACEWIN and TRACK. These codes account for the effect of space charge in the optics. A considerable effort was made to benchmark these codes with regard to the underlying physics and to ensure that they perform reliable calculations. There was no ambiguity in the beam physics between the codes. They were also benchmarked with experimental measurements as shown elsewhere [31, 32, 33].

Table 3.8 summarizes the total number of cryomodules, their configurations, lengths, and operating parameters. Note that the cavities' Q_0's are based on an operating temperature of 2K and a conservative approach toward the surface resistances that is based on values already obtained in operating cryomodules. Note also that the measured surface resistance values for the HWR and SSR1 cavities are considerably lower.

All cryomodules in the PIP-II Linac are separated by warm sections. These warm sections are

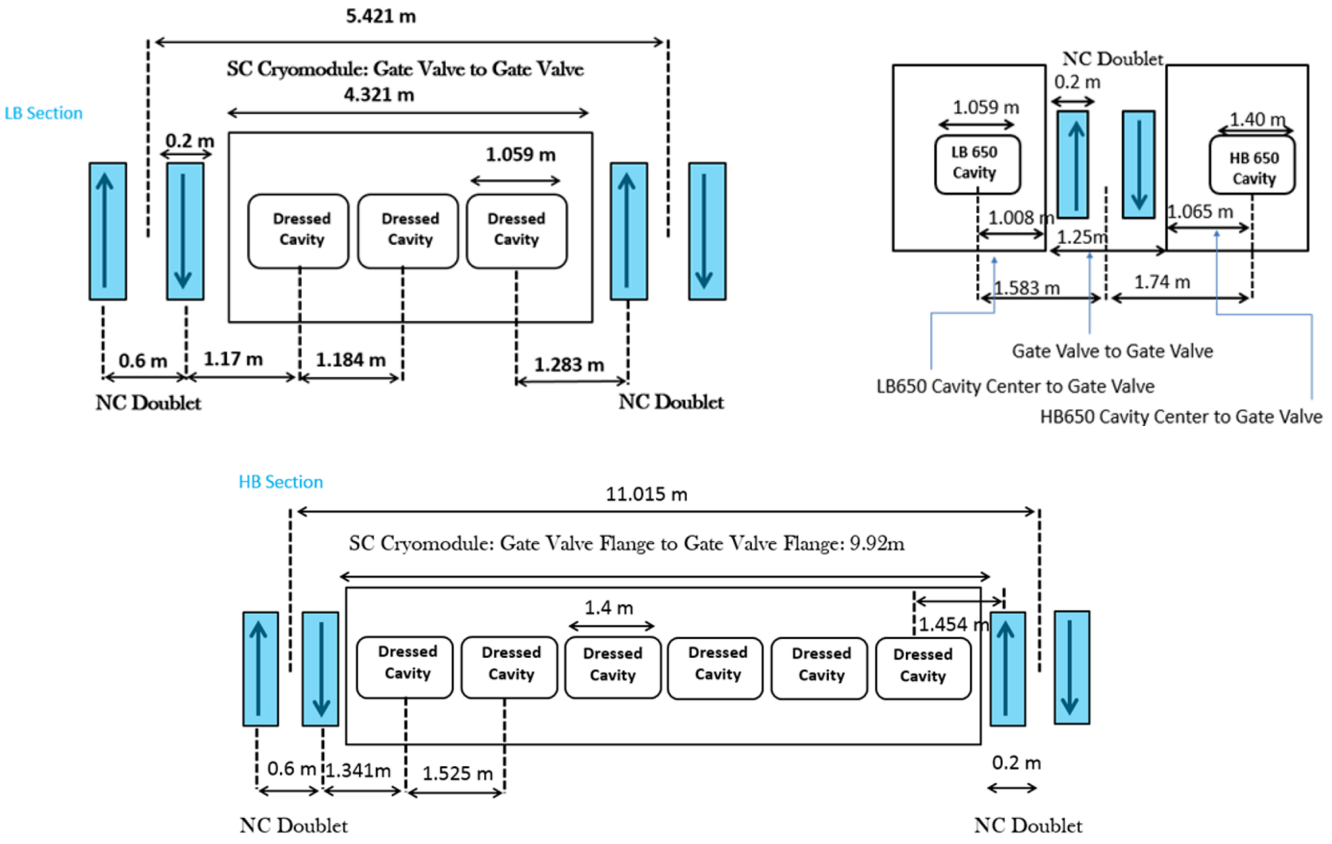

Figure 3.22: Transverse focusing periods in LB650 (top, left), HB650 (bottom) and the interface between LB650 and HB650 sections (top, right) used in the optics design. NC and SC abbreviate normal-conducting and superconducting, respectively. All dimensions are in unit of meters. The upward and downward arrows mark vertically and horizontally focusing quads, respectively.

Table 3.8: General parameters of SC cryomodules.
$^{+}$Within the cryomodule (CM) configuration column "c" refers to an individual accelerating cavity, and "s" to a focusing solenoid.
*This number represents the present estimate of the cryomodule lengths. It will be finalized with advances in the cryomodule design.
†Measured value based on recent measurements of two HWR cavities at 2 MV accelerating voltage.
‡Based on recent measurements of SSR1 cavities made of CABOT niobium. We expect to get better results for the SSR2 cavities to be made of material which satisfies Fermilab specifications [34].
$^{\triangle}$Loaded Qs have been selected to minimize the total RF power requirements in the respective sections.

CM type	Cavities per CM	Number of CMs	CM configuration^{+}	CM length (m)	Q_0 at 2K (10^{10})	Surface resistance, (nΩ)	Loaded Q$^{\triangle}$ (10^6)
HWR	8	1	8×(sc)	5.93	0.5	9.6 (2.75†)	2.32
SSR1	8	2	4×(csc)	5.3	0.6	14 (10‡)	3.02
SSR2	5	7	sccsccsc	6.5*	0.8	14.4	5.05
LB650	3	11	ccc	4.32*	2.15	9.0	10.36
HB650	6	4	cccccc	9.92*	3	8.7	9.92

used for additional diagnostics (bunch transverse and longitudinal profile monitors, beam loss monitors, etc.) and for beam collimators required to avoid uncontrolled beam losses inside the SC cryomodules. The composition of each of the warm insertions is determined by requirements of safe and reliable operations, diagnostics, collimation, and cryogenic segmentation constraints.

Figure 3.23 shows the field settings of the solenoids that correspond to the baseline optics of the PIP-II Linac. Three types of solenoids that differ in strengths and lengths are used. Each type is designed to operate at a maximum field amplitude of 6 T. Figure 3.24 shows the integrated fields in the quadrupoles along the Linac. Identical quadrupoles are used in the LB650 and HB650 sections and they are designed to provide a maximum integral field of 3 T.

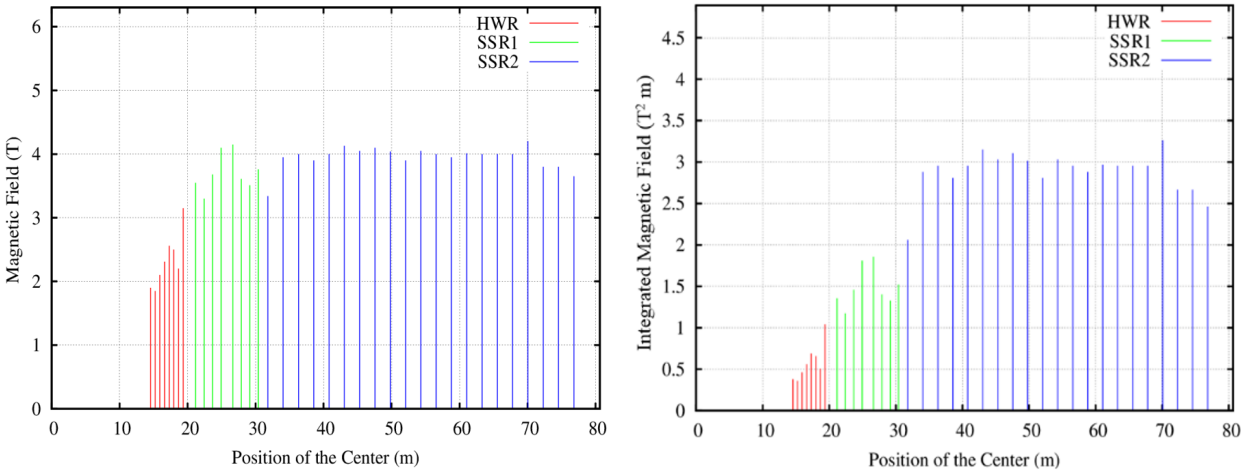

Figure 3.23: Magnetic field amplitude (left) and integral strength (right) of focusing solenoids in the HWR, SSR1, and SSR2 sections for the baseline design of the PIP-II Linac.

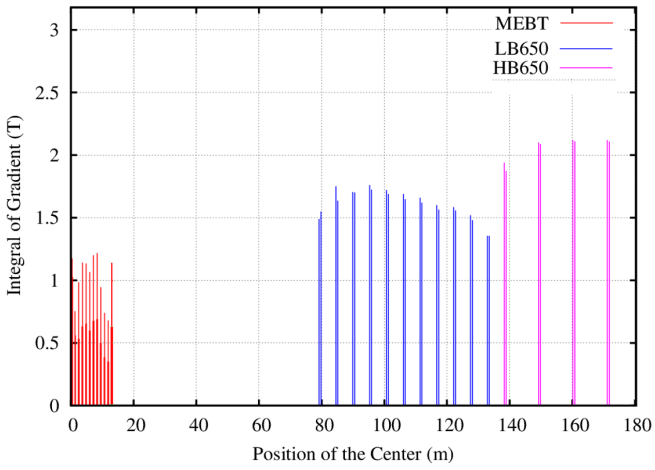

Figure 3.24: Integral strength of quadrupoles in the MEBT, LB650, and HB650 for the baseline design of the PIP-II Linac.

Each magnet package (i.e., solenoid or quadrupole doublet) includes vertical and horizontal correctors and a 3-coordinate beam position monitor[3] (BPM) required for beam steering and optics measurements.

[3]The BPM has 4 plates and allows measurements of both transverse beam positions, as well as longitudinal bunch position measured by bunch arrival time.

Figures 3.25 and 3.26 show the accelerating voltage and RF phases of the cavities along the Linac for the baseline optics. The phases in the cavities were determined such that the RF phases are large enough to accommodate a longitudinal beam of $6\sigma_z$, where σ_z is the RMS bunch length. Mote also that the location of sudden changes in RF phases in Fig. 3.26 represents the outermost cavities in the cryomodule, whose phases were varied to provide an additional longitudinal focusing to match the beam between the cryomodules. Figure 3.27 shows the evolution of the beam energy along the Linac for the above settings of the cavities.

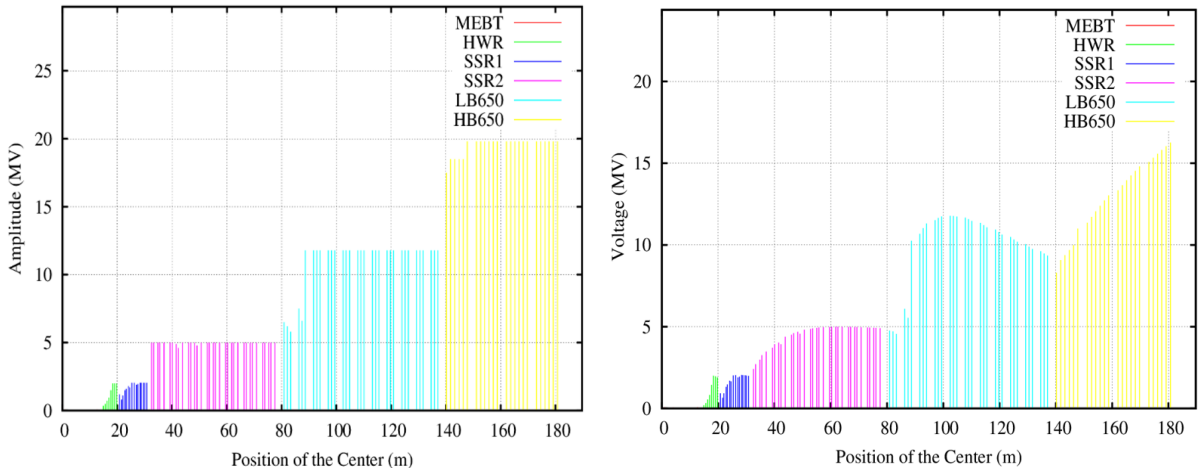

Figure 3.25: Accelerating voltage per cavity along the Linac corresponding to the baseline optics: (left) the voltage amplitude at the optimal beta and (right) the voltage amplitude with the transit-time factors accounted.

Note that the HWR, SSR1, and SSR2 cavities are not axially symmetric. Therefore, their quadrupole components cannot be compensated over the entire range of beam velocities. Figure 3.28 presents the dependence of the quadrupole effect on velocity. Numerical simulations verify that in the range of PIP-II parameters, the strength of the quadrupole field is proportional to the strength of the axially symmetric cavity defocusing. Both types of focusing are proportional to the sine of the accelerating phase. This motivates the definition of the focusing asymmetry parameter, Q, presented in Fig. 3.28. The stem in the HWR cavity is located in the horizontal plane and therefore this quadrupole field represents a normal quadrupole. Due to engineering limitations, mainly related to the RF couplers, the SSR1 and SSR2 cavities are rolled by 45°. Consequently, their quadrupole fields are also rolled and are equivalent to a skew-quadrupole field. The cavity quadrupole and skew-quadrupole fields have a small but non-negligible effect on the beam dynamics. To compensate these fields, the SSR1 and SSR2 cryomodules will have skew-quadrupole correction coils located inside the focusing solenoids. The skew-quadrupole field will be created by an imbalance in the currents of independently powered coils of x- and y-dipole correctors. Since the solenoids located in the HWR, SSR1, and SSR2 cryomodules rotate the plane of betatron motion, compensation can be improved by an appropriate choice of magnetic field signs in the solenoids. The eight cavities of the HWR cryomodule introduce little coupling, and therefore this cryomodule does not have coupling correction.

The quadrupole fields in the LB650 and HB650 cavities are related to the RF couplers. Compared to those in the HWR, SSR1, and SSR2, they are significantly smaller as can be seen in the bottom row of Figure 3.28. These quadrupole fields will be corrected by the main focusing quadrupoles

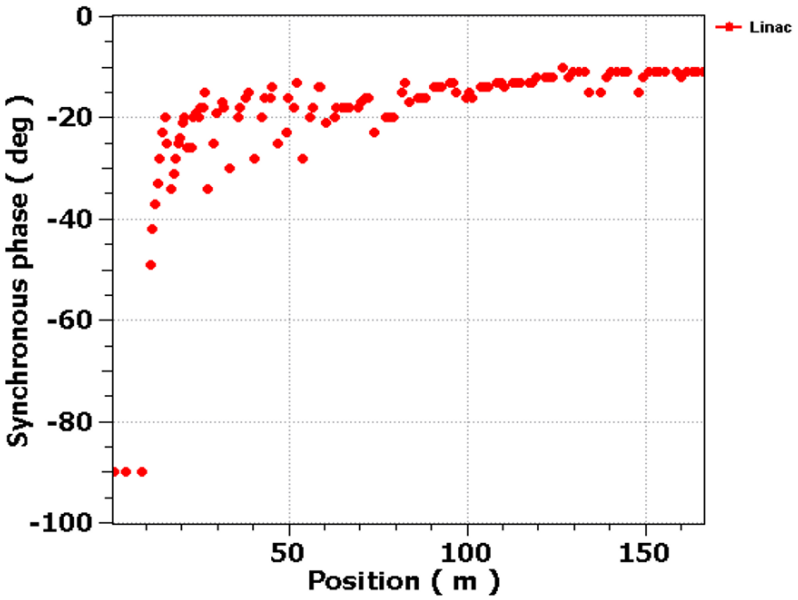

Figure 3.26: Accelerating phases of cavities corresponding to the baseline optics. The first three dots belong to the MEBT bunching cavities, which do not produce acceleration.

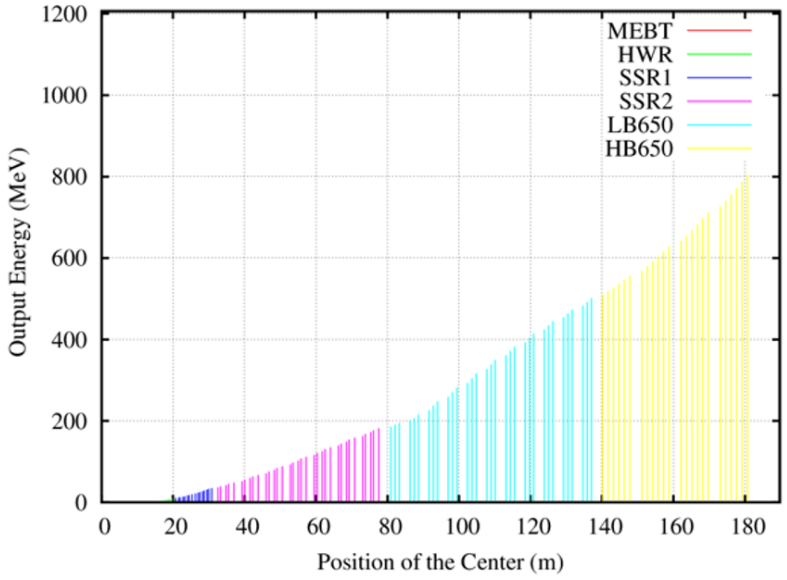

Figure 3.27: The beam energy along the Linac.

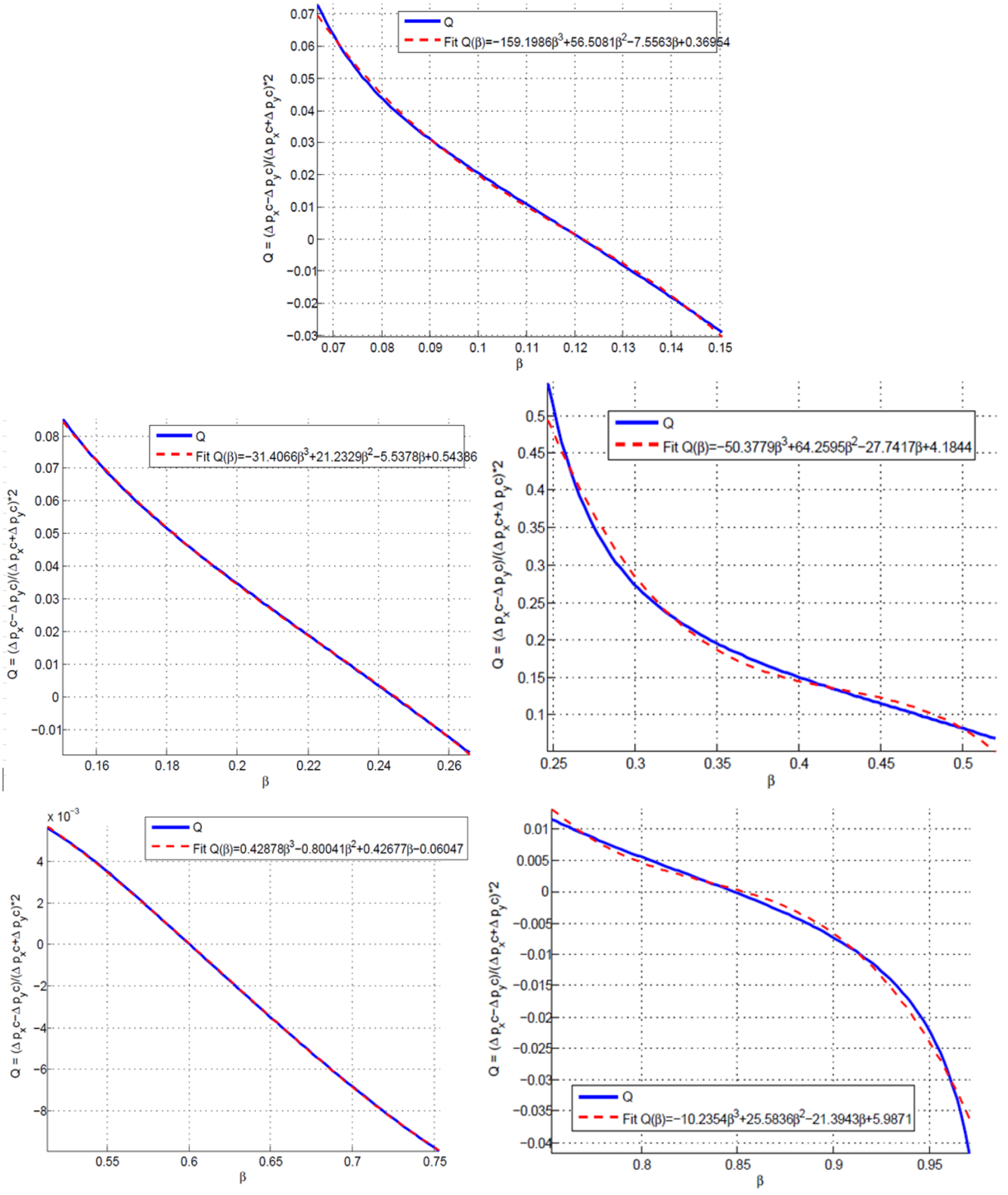

Figure 3.28: The focusing asymmetry parameters Q (ratio of quadrupolar to radial focusing) for HWR (top), SSR1 (middle-left), SSR2 (middle-right), LB650 (bottom-left) and HB650 (bottom-right) versus the particle velocity β in the operating domain; blue and red lines represent simulation results and a polynomial fit, respectively.

located between cryomodules. The RF couplers of the LB650 and HB650 cavities also create dipole fields resulting in dipole kicks which are also dependent on the beam velocity. The maximum kicks, $\Delta p_\perp c$, are about 3.6 keV for LB650 and 2.6 keV for HB650 cavities. The corresponding beam deflections are small and are not expected to produce any visible effect on the beam motion. The coupling accumulated in the Linac is corrected by four skew quadrupoles located at the Linac downstream end in two periods immediately following the last cryomodule. Two skew quadrupoles are placed on both sides of each doublet.

3.3.1 Beam dynamics study for baseline optics

Beam dynamics studies were performed for 5 mA peak beam current using 1M macro-particles with a 6σ Gaussian distribution. The beam tracking was performed from the exit of the RFQ to the end of the SC Linac. Figure 3.29 show the evolution of 1σ beam envelopes along the SC Linac for a nominal setting of the beamline elements. It can be observed that the transverse rms beam sizes change comparatively little along the Linac, and do not exceed 3 mm over the course of the entire acceleration. This weak dependence of beam sizes on the acceleration implies that the adiabatic reduction of beam transverse emittances with beam acceleration is compensated by a corresponding increase in the beta-functions. Figure 3.30 shows the beta functions along the Linac in all degrees of freedoms. The beta-functions[4] are computed from the rms beam sizes, angular spreads and emittances, and hence describe the beam transport with the beam space charge forces included. Note from Fig. 3.31 that there is an emittance growth in the Linac beginning where the space charge forces are significant. However, a simulation study showed that the growth is within budget, and there is a substantial margin for the final value of transverse emittance from its tolerance limit. Figure 3.32 depicts the phase space density projection of a bunch at the Linac end. Note there are no significant distortions in the bunch phase space. No beam losses were observed in the SC Linac. A small fraction of particles was intercepted at the scrapers in the MEBT. This study confirms that there are no particles beyond $\sim 6\sigma$. This result is supported by measurements performed at the SNS, which has a bunch brightness similar to what is expected in the PIP-II Linac.

Figure 3.33 presents the beam density projection in the horizontal plane and the aperture limitations along the Linac. In the HWR, SSR1, and SSR2 cryomodules, limitations are set to 33, 30 and 40 mm, respectively, by the apertures of the cavities. For the LB650 and HB650 cryomodules, the cavity apertures are 83 and 118 mm, respectively. Consequently, the aperture limits for these sections are set by the 46-mm aperture of the vacuum pipe (standard 2" pipe) in the quadrupoles.

Figure 3.34 shows the beam phase advances along the PIP-II Linac for the baseline optics. Table 3.9 summarizes the beam phase advances in all planes at the exit of each section.

[4] The longitudinal beta-function β_{st}, is introduced similarly to the transverse ones, so that: $\sigma_s = \sqrt{\beta_{st}\epsilon_{sn}/\beta\gamma}$, $\sigma_p = \sqrt{\epsilon_{sn}/(\beta_{st}\beta\gamma)}$. This definition implies that the phase advance of longitudinal (synchrotron) motion is $d\mu = dL/(\beta_s\gamma^2)$. Here ϵ_{sn} is the rms longitudinal emittance (normalized), σ_s is the rms bunch length, σ_p is the rms relative momentum spread, and β and γ are the relativistic factors.

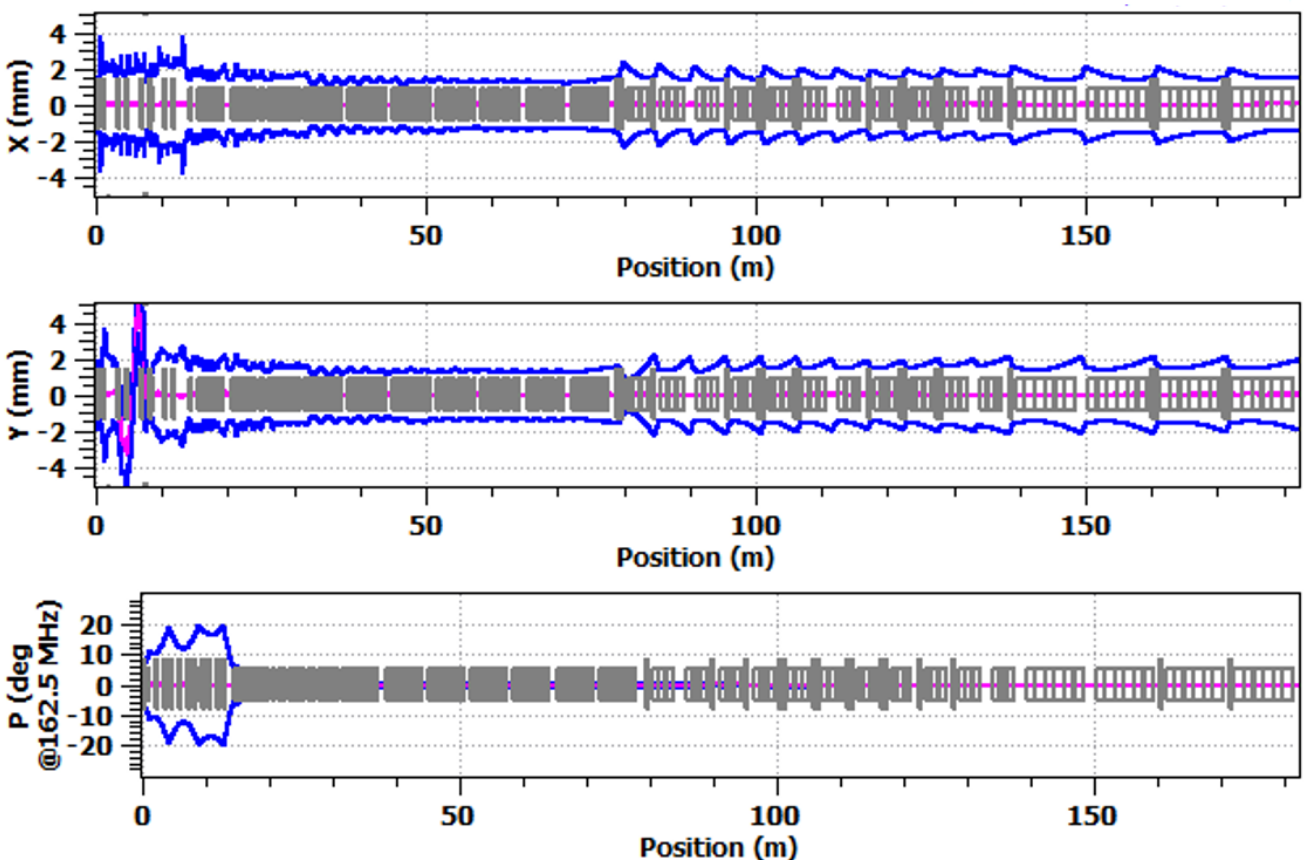

Figure 3.29: Horizontal (top) and vertical (center) rms bunch envelopes and rms bunch length (bottom) along the entire Linac (from the beginning of the MEBT to the end of the 0.8 GeV Linac); bunch population corresponds to the RFQ beam current of 5 mA. Magenta lines show displacements of the bunch centroid.

Table 3.9: Beam phase advance for 5 mA at the exit of each section in the Linac. Phase advances were normalized to 90°.

Parameter	X	Y	Z
HWR	4.1	4.1	5.6
SSR1	8.5	8.5	11.8
SSR2	20.0	20.0	21.2
LB650	25.1	25.9	27.6
HB650	27.5	28.6	30.2

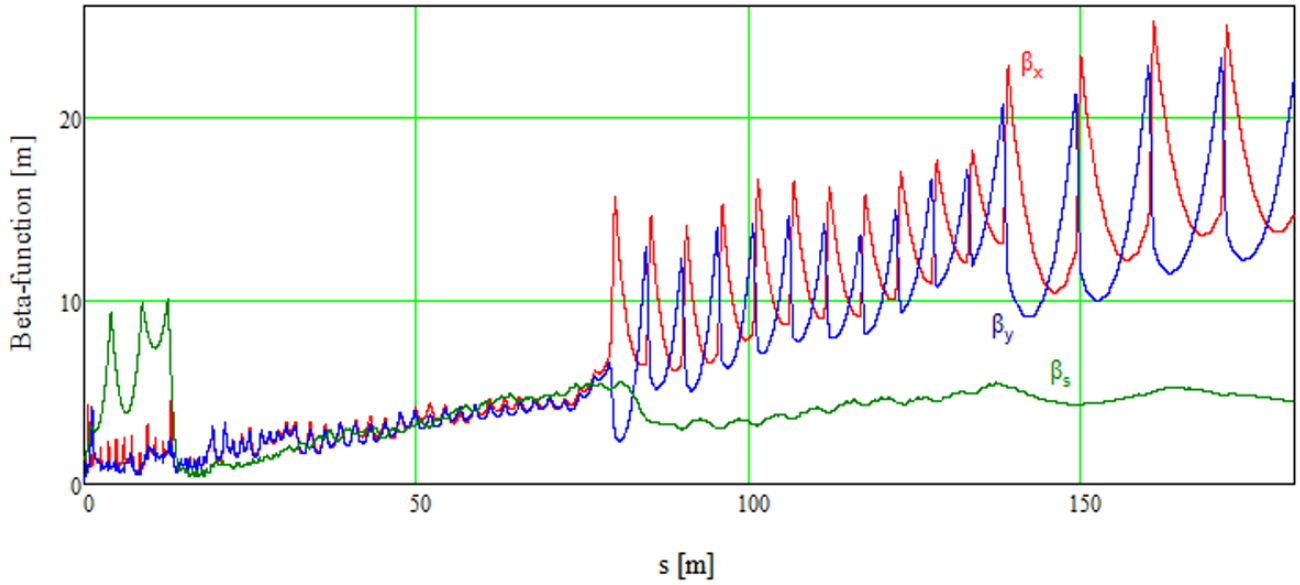

Figure 3.30: The beta functions for x, y, and s (longitudinal) planes along the Linac from the RFQ exit to the Linac end. The values were computed from rms beam sizes and emittances obtained by beam tracking with TraceWin for 5 mA beam current.

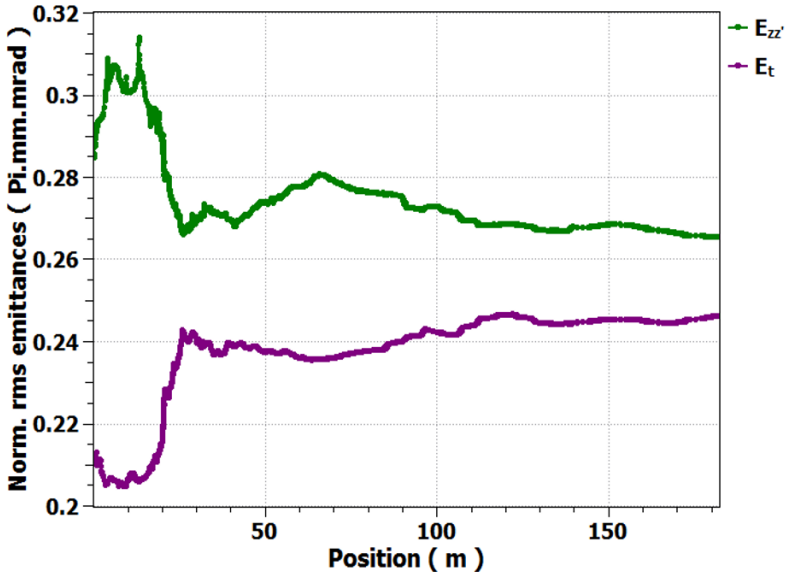

Figure 3.31: The rms normalized transverse (magenta, $\epsilon_x{=}\epsilon_y$) and longitudinal (green) emittances along the Linac (from the RFQ exit to the Linac end).

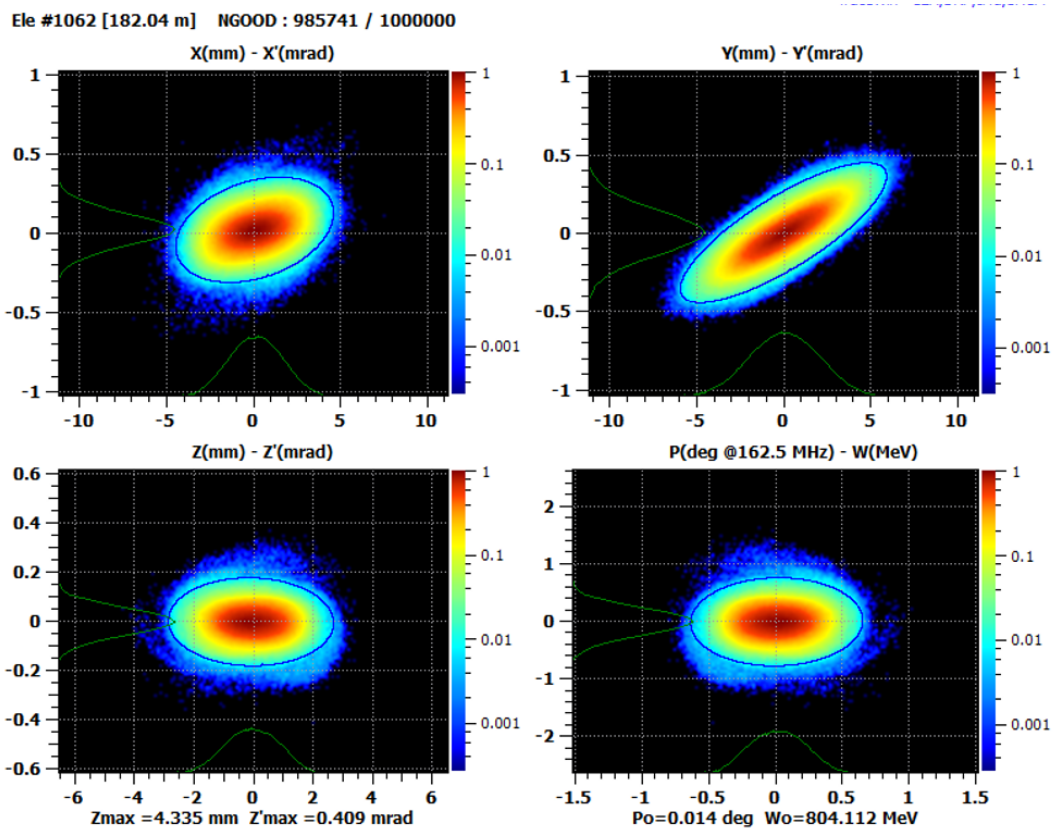

Figure 3.32: Phase space density of a bunch at the Linac end for the baseline optics.

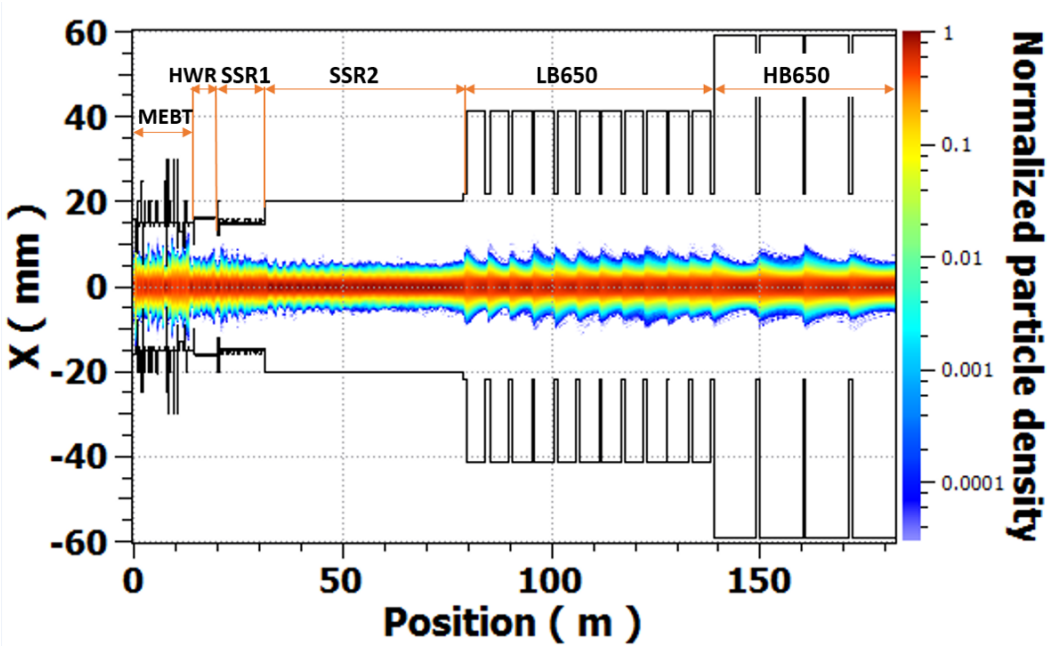

Figure 3.33: Beam density projection in the horizontal plane and aperture limitations along the Linac from the RFQ exit to the Linac end.

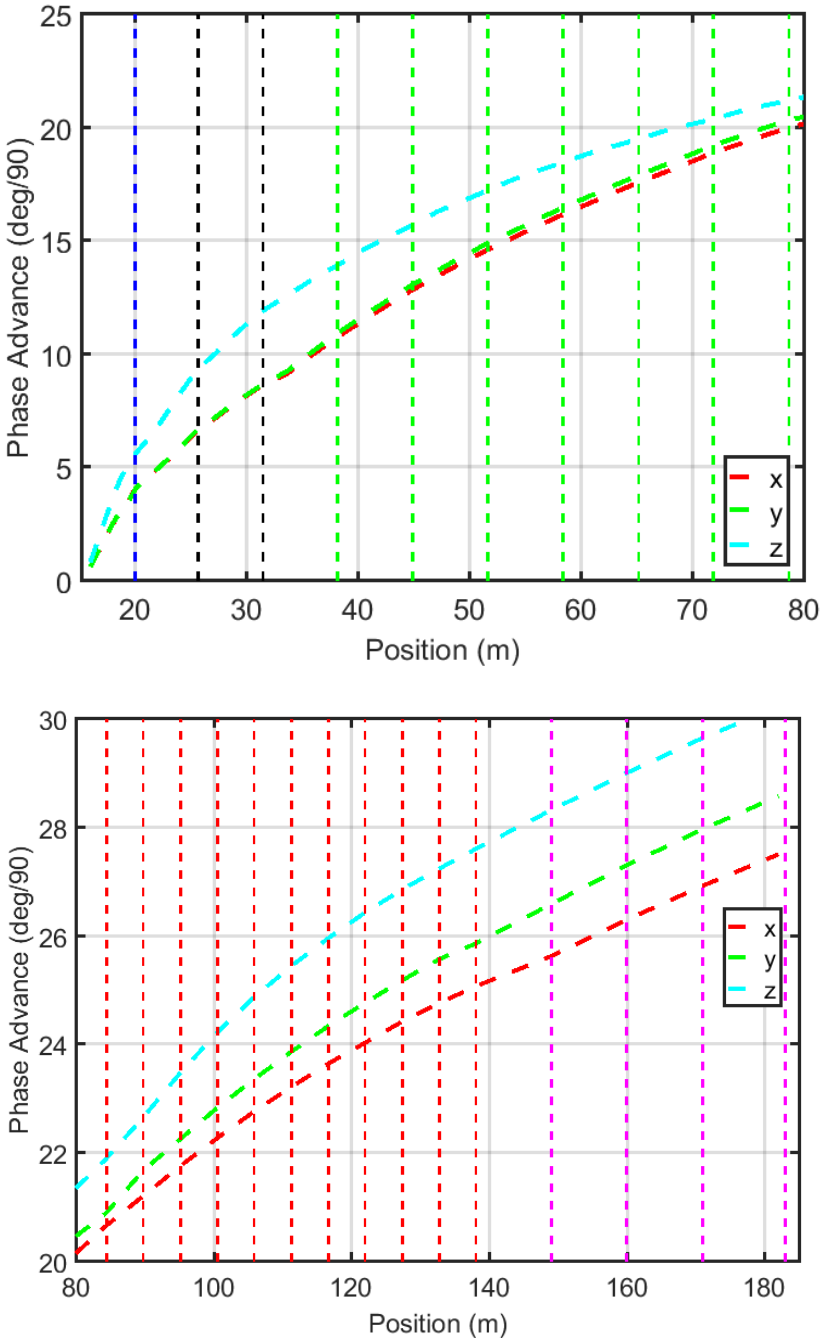

Figure 3.34: Beam phase advance in all planes for 5 mA along the PIP-II Linac. (Top) the beginning of the HWR to the exit of the SSR2 section and (bottom) LB650 to HB650 sections. Each vertical line represents the exit of cryomodule in the respective section.

3.3.2 Acceptance of the Linac

The acceptance is a vital means to measure the Linac performance. It is determined by the largest possible beam size that can be transmitted through the Linac without any beam losses. Thus, a large acceptance implies a higher tolerance against machine imperfections. In order to determine the longitudinal acceptance of the PIP-II Linac, an artificial initial beam distribution was created with a very large longitudinal emittance compared to nominal, and a relatively very small transverse emittance. The distribution was tracked from the HWR entrance to end of the Linac. Initial coordinates of surviving particles trace the acceptance of the machine. Figure 3.35 shows the longitudinal acceptance of the PIP-II Linac. It can be seen that the acceptance is substantially large enough to accommodate a 6σ beam easily. Note that the effects of space charge were excluded in this study. The transverse acceptance is primarily determined by aperture limitations in the Linac.

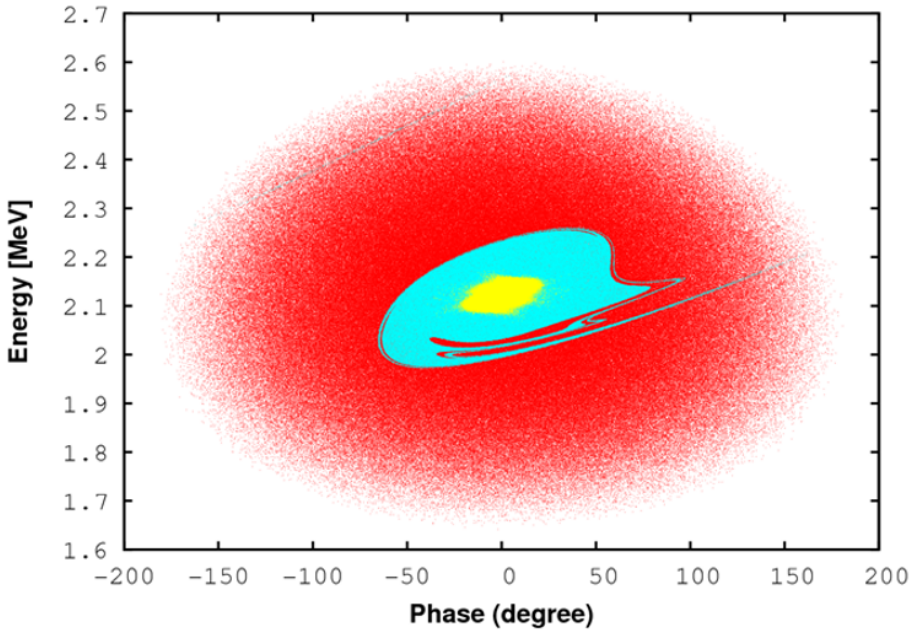

Figure 3.35: Longitudinal acceptance (cyan) for the baseline optics of the Linac. Nominal 6σ beam (yellow) at the entrance of the HWR is well confined in the Linac. The initial beam distribution is shown in red.

3.3.3 Misalignment studies

Misalignments of the beamline elements in the Linac severely affect the performance of the Linac. They result in a reduction of the geometrical machine acceptance, and in emittance growth due to spherical aberrations related to the non-linearity of focusing fields resulting from large beam offsets in focusing lenses. Both effects can trigger beam loss. This in turn requires stringent tolerances on alignment of the beamline elements in the Linac. Table 3.10 shows the rms alignment tolerances for the beamline elements in the PIP-II Linac. Note that "NC" in the table corresponds to normal-conducting. A study is underway to evaluate the implications of these misalignments on the beam.

Table 3.10: Alignment tolerances in the PIP-II SC Linac.

Error Source	RMS Error	Unit
Cavity X, Y misalignment w.r.t CM	0.5	mm
Solenoid X, Y misalignment w.r.t. CM	0.5	mm
BPMs X, Y misalignment w.r.t CM	0.5	mm
Cavity Z misalignment w.r.t CM	0.5	mm
Solenoid Z misalignment w.r.t. CM	0.5	mm
BPMs Z misalignment w.r.t CM	2	mm
Cavity Tilt misalignment w.r.t CM	1	mrad
Solenoid Tilt misalignment w.r.t. CM	0.5	mrad
BPMs tilt misalignment w.r.t CM	3	mrad
Quadrupole, NC solenoid, RFQ, X, Y, misalignment w.r.t survey line	0.25	mm
Quadrupole, NC solenoid, RFQ, Z misalignment w.r.t survey line	2	m
Quadrupole, NC solenoid tilt misalignment, w.r.t survey line	1	mrad
CM X, Y, misalignment w.r.t survey line	0.3	mm
CM Z, misalignment w.r.t survey line	2	mm
CM tilt, misalignment w.r.t survey line	0.05	mrad
RFQ tilt misalignment w.r.t survey line	0.05	mrad

3.3.4 Beam losses and collimation

In a high-intensity, MW-level accelerator facility, uncontrolled beam loss poses a severe threat for reliable and safe operation of the facility. Thus, having a low-loss beam transport is very critical in order to minimize the residual radiation in the tunnel, and therefore to facilitate hands-on maintenance. The currently accepted limit for beam loss that still allows for hands-on maintenance is 1 W/m and stems from the experience at LANSCE [26]. However, at energies about or above 1 GeV, a 1 W/m loss rate produces a peak contact residual dose rate of $\sim$ 150 mrem/hr at 30 cm on a bare beam pipe [35]. Although magnets shield the radiation and significantly reduce the residual activation on their external surfaces, still the radiation of unshielded pieces including magnet interfaces and instrumentation locations must be sufficiently small. Thus, it is more appropriate to set the maximum acceptable loss rate in the framework of these unshielded pieces. For the PIP-II Linac, it is highly preferred to keep the residual radiation below 15 mrem/h at 30 cm from a component surface. This in turn sets the limit of the beam loss rate to 0.1 W/m at energies in proximity of 1 GeV or above. In the baseline configuration, the PIP-II Linac will deliver 18 kW of beam power. Consequently, a fractional particle loss rate below 5×10^{-6} m^{-1} is required.

Experience with SNS operation [36, 37] suggests that intra-beam stripping is the main source of particle losses in a well-tuned Linac. A study was performed to evaluate the beam loss due to intra-beam stripping in the PIP-II Linac. It can be observed from Figure 3.36 that even for CW operation, the intra-beam stripping results in an integrated beam loss of about 10 W in the entire PIP-II Linac. Also, the differential losses were below 0.1 W/m everywhere along the Linac. Thus, it can be concluded that intra-beam stripping losses are well within specification.

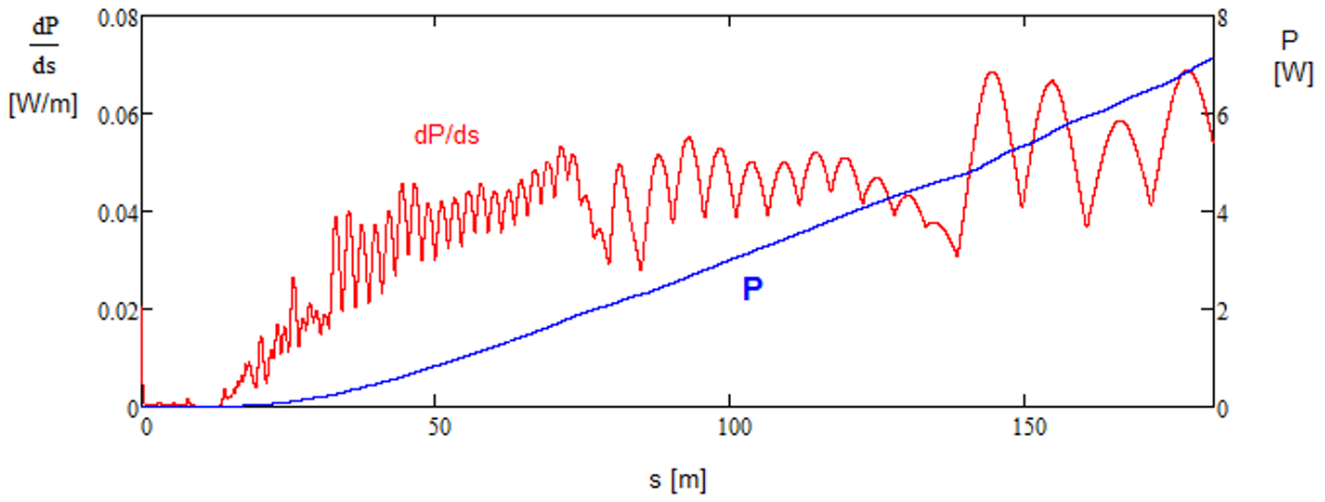

Figure 3.36: Beam power loss per unit length due to intrabeam stripping (red) and its integrated value along the Linac (blue) for a CW beam of 2 mA. (Note that, 60% of the 5 mA beam coming out of the RFQ was chopped off).

In addition to intra-beam stripping, the existence of beam halo is another important characteristic of a high-intensity ion Linac. The term, "halo" represents far-tail particles in the distribution. It is considered to be relatively easy to clean the transverse halo using dedicated collimators, but a major problem arises because of the longitudinal halo. It is well known that the longitudinal focusing is non-linear, and therefore far longitudinal tails experience a different force from the beam-core, resulting in phase slippage along the accelerator. These particles receive a strong (or weak depending on their energy with respect to core) transverse focusing from a magnetic element which is set for a reference particle (core particles). Consequently, the longitudinal halos are transformed into transverse halos over the course of acceleration, and are finally lost. A beam loss at the cold surface of cavities causes not only a degradation in cavity performance, but also an overall increase in the cryogenic heat load of the machine. Thus, additional care was taken to further minimize beam losses in the cryogenic environment in the PIP-II Linac using the following approaches:

- Limiting the maximum action of the beam distribution at the entrance of the SRF Linac is done using a dedicated scraper system in the MEBT that intercepts not only far-tail particles coming out from the RFQ, but also protects the SRF cavities from any unexpected scenarios such as accidental beam steering, or focusing errors in the MEBT. The scrapers are envisioned to be a part of the Machine Protection System (MPS) that trips off the beam permit when the beam losses on their surfaces increase above a threshold value. A study presented elsewhere [20] showed that the maximum action can be limited to 10 times the initial RMS beam emittance that corresponds to $\sim 3\sigma$ in the transverse beam size.

- Beam collimators are installed between each cryomodule in the HWR, SSR1, and SSR2 sections. Apertures in the collimators are chosen to be 3 mm smaller than the apertures of the downstream cryomodules. Their thickness increases with energy, reaching 4 cm of steel at the end of the SSR2 section. There are no dedicated collimators in the LB650 and HB650

sections. As in the SNS, the vacuum chambers in the quadrupoles will perform this role. Taking into account the comparatively small beam losses, it appears unnecessary to have additional radiation shielding around the collimators, which otherwise would require quite a large amount of shielding material.

3.3.5 Radiological design goals

The design goals for the PIP-II SC Linac and the Linac-to-Booster Beam Line meet or exceed the minimum requirements of the FRCM. The design goals are:

- Permit unlimited occupancy for all service buildings, shielding berms, parking lots, control rooms, and associated areas. By design, radiation levels are to be kept below 0.05 mrem/hr in all accessible locations outside of the beam enclosures for normal operating conditions, based upon an assumed continuous beam loss of 0.1 W/m.

- Permit inspection and maintenance activities within tunnel enclosures while maintaining personnel radiation exposure due to residual activation of accelerator components and beam enclosures at levels as low as reasonably achievable. At 0.1 W/m, the residual dose rates should not exceed about 15 mrem/hr at 30 cm from beam component surface.

- Limit radiation exposure due to air activation both within the beam enclosure during inspection and maintenance activities and at the site boundary.

- Limit ground water and surface water activation to levels well below regulatory standards.

- Prevent the activation of accelerator component surfaces to avoid the generation of removable radioactivity.

- Minimize the activation of accelerator components which can impact their useful service life.

3.3.5.1 Preliminary radiation shielding modeling

Above the PIP-II Linac tunnel, a passive shielding of 13.5 feet is considered and it will vary long the length of the enclosure from 13.5 feet at the north end to 18.5 feet at the south end. The Linac is followed by a stripping beam transfer line to bring the final proton beam to the Booster. The Linac-to-Booster will be crossing the Tevatron enclosure near its ceiling. Beam Transfer Line will be designed to accommodate up to 18.5 feet of earth shielding.

An established parameterization [38] is used to determine the radiation dose equivalent rate as a function of energy (GeV), distance (feet), and angle with respect to incident beam direction (degrees) from a low energy proton beam (<1 GeV) incident upon a target. The parameterization

determines the dose per incident proton (mrem) at one foot as:

$$(E, r, \Theta_s) = 2 \times 10^{-5}(1 + E^{0.6}) \left[\frac{1 - e^{-3.6E^{1.6}}}{\left[0.3048r \left[\Theta_s + \frac{40}{\sqrt{E}}\right]\right]^2} \right] \tag{3.7}$$

The neutrons produce a major fraction of the radiation behind the shield. For neutron energies below 1 GeV, the attenuation length in concrete strongly depends on the energy of neutrons. The mean free path of low energy neutrons relative to the high energy asymptote has been parameterized as:

$$\frac{\lambda_{LE}}{\lambda_{HE}} = 1 - 0.8e^{-5E} \tag{3.8}$$

The reduction in radiation dose rate as a function of energy (GeV) and concrete shield thickness (feet) is:

$$A(E, T_{conc}) = 10^{\frac{-T_{conc}}{3}/(1-0.8e^{-5R})} \tag{3.9}$$

In the dose rate estimates, the peak neutron energy, E (GeV), is taken to be equal to the beam energy. This simplification is conservative in that the actual neutron energies are necessarily lower and hence lead to better attenuation provided by the concrete shielding than indicated by the above equation. In addition, the dose equivalent per neutron conversion factor is taken as a constant value of 40 fSv/n over the full range of the neutron spectrum. Thus the resulting shielding estimates are implicitly conservative.

The radiation shielding required to limit radiation dose rates to 0.05 mrem/hr for beam energy in the range [0, 1] GeV and various levels of beam loss is shown in Figure 3.37. The shielding requirement varies with beam energy and assumed maximum beam power loss, and it is different for normal and accident conditions. The choice of shielding thickness will take into account a number of factors including the confidence level given to the Safety Analysis as described in the Radiation Safety section of the PIP-II Conceptual Design Report [39] including consideration of the projected loss mechanisms and the machine protection system. Results are in line with project passive shielding assumptions.

The PIP-II Linac tunnel will be connected to the Linac gallery through penetrations. The main penetrations between the PIP-II tunnel and gallery are supposed to house waveguide or coaxial lines for the powering of the Radio Frequency (RF) cavities. Additional penetrations are required for housing signal or general servicing cables as needed for the operation of the PIP-II accelerator.

To support the design of civil engineering and mechanical integration, preliminary estimation of radiation level at an operational beam loss limit of 0.1 W/m were calculated by means of Monte Carlo simulations with FLUKA [40][41] and MARS15 [42][43] codes. In particular the

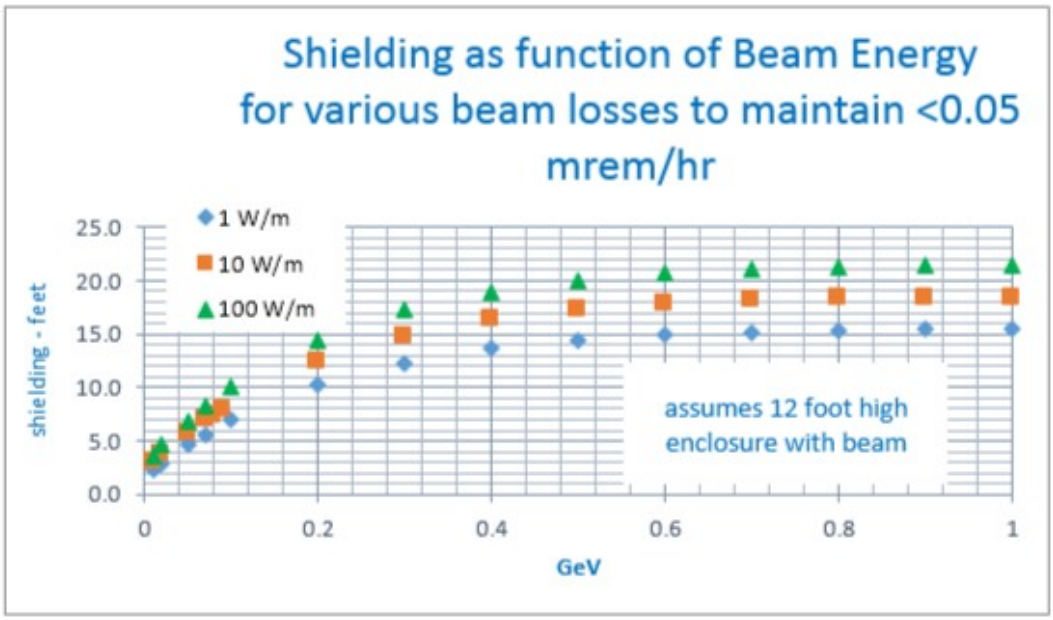

Figure 3.37: Radiation shielding requirements as a function of beam energy and beam power loss for a PIP-II beam enclosure.

FLUKA Monte Carlo code was used for the evaluation of the prompt radiation in the gallery for different penetration layouts, assuming 0.1 W/m proton losses uniformly distributed along the superconducting section and taking into account the different beam energies along the machine. As a conservative approach the impact angle was set to 3 mrad with respect to the beam direction. Three different cross section designs were studied, see Figure 3.38.

For the evaluation of the effect of the different layouts on the dose in the gallery at the exit of penetrations, a simplified approach was used. It consists of distributing the beam losses on the internal surface of a standard stainless steel beam vacuum pipe of 2 mm thickness, at diameter sized for the low β and high β sections. Simulation results identified the highest values of ambient dose equivalent in the gallery at the exit of the of the pentrations in the high β section. In particular at the locations of the penetrations that will be constructed to support the four extra high β cryomodules for the Linac PIP-II future upgrade, see Figure 3.39.

The simplified approach used is valid for comparing the three alternatives in terms of dose released in the gallery, but it is not giving realistic results. Indeed, the presence of beam elements can bring different estimations. For this reason, a comparison with a similar Linac, i.e. the European Spallation Source (ESS) one [44], was performed.

The effective dose in the MARS15 simulation results applied to ESS Linac with a complete beam line geometry, accelerating fields in cavities and magnetic fields in quadruapoles give 0.8×10^4 mrem/h in the tunnel at the penetration entrance. Corresponding effective dose calculated in this study with FLUKA without the beamline elements is 2×10^4 mrem/h. Both values are given at the 800 MeV longitudinal position and are based on a proton loss rate of 0.1 W/m. All the complexity of the realistic MARS15 modeling gives a reduction in dose of 2.5 with respect to the simplified bare-pipe FLUKA results.

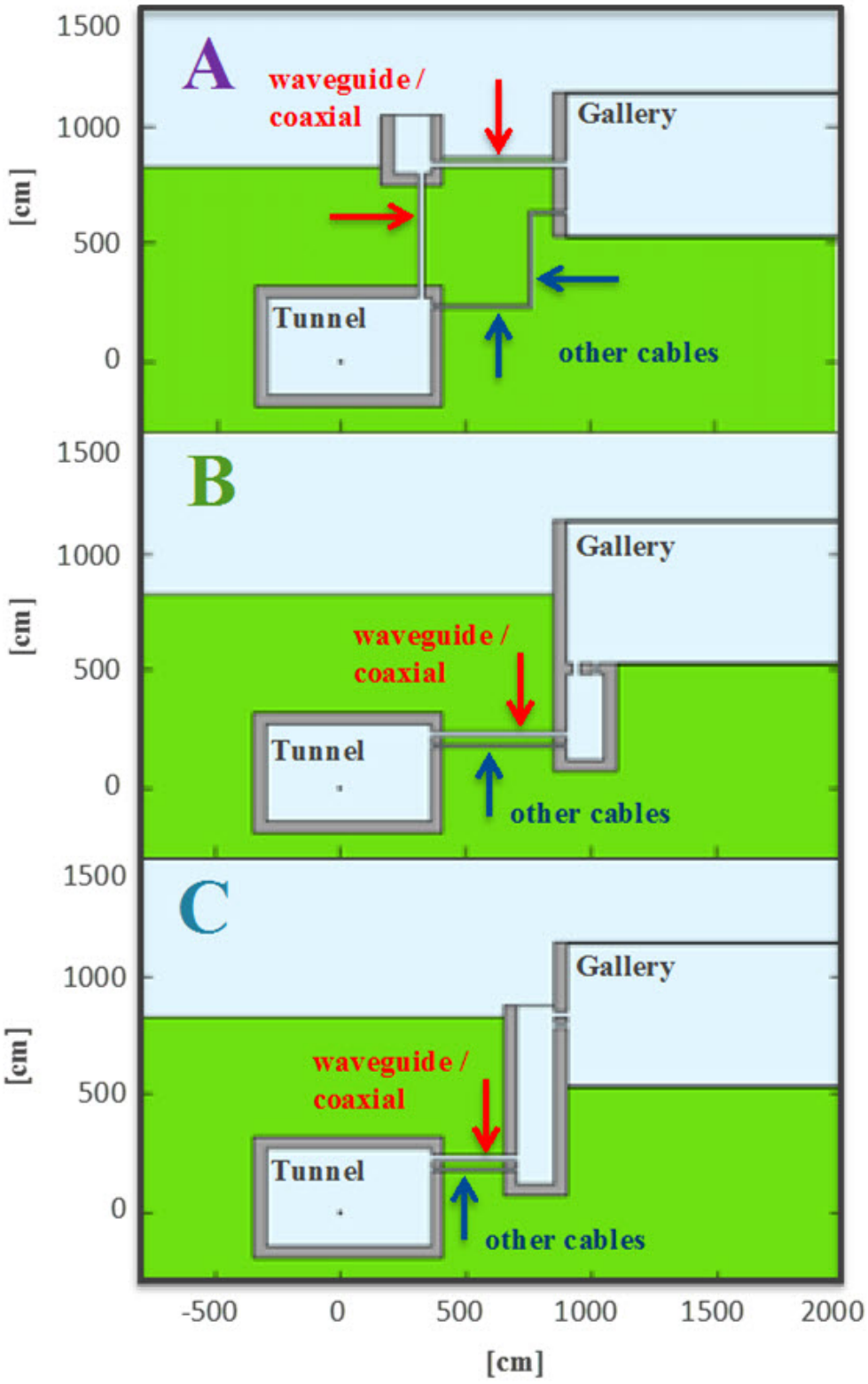

Figure 3.38: FLUKA models of alternatives A, B and C for penetrations. The model layout is built in FLUKA for radiation study purposes and based on civil engineering drawings. Location of waveguide/coaxial and other cables are shown for the different layouts. The average transverse aperture is 1000 cm^2 for waveguides, 500 cm^2 for coaxial lines and 100 cm^2 for other service cables.

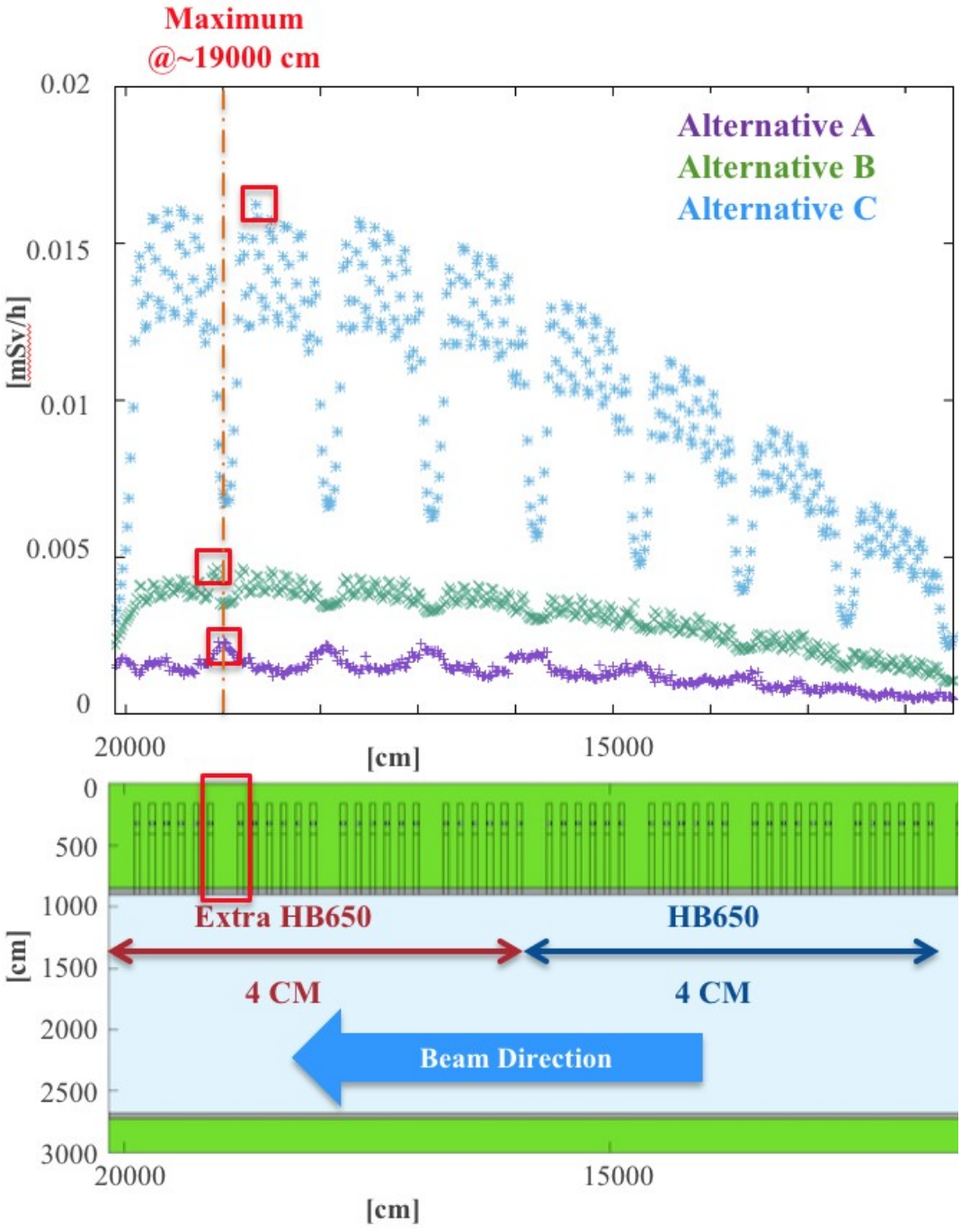

Figure 3.39: FLUKA averaged ambient does equivalent rate results in the gallery, near the penetration exits for the 3 alternatives (top plot). The maximum in the gallery is at the location in the tunnel situated at 190 m from HWR in the high bay section (bottom plot).

Based on the MARS15 dose in the tunnel and using the analytical calculations applied to the alternative A layout, one finds that the dose at this location in the gallery is safely below the unlimited occupancy criterion of 0.25 mrem/h, see Figure 3.40.

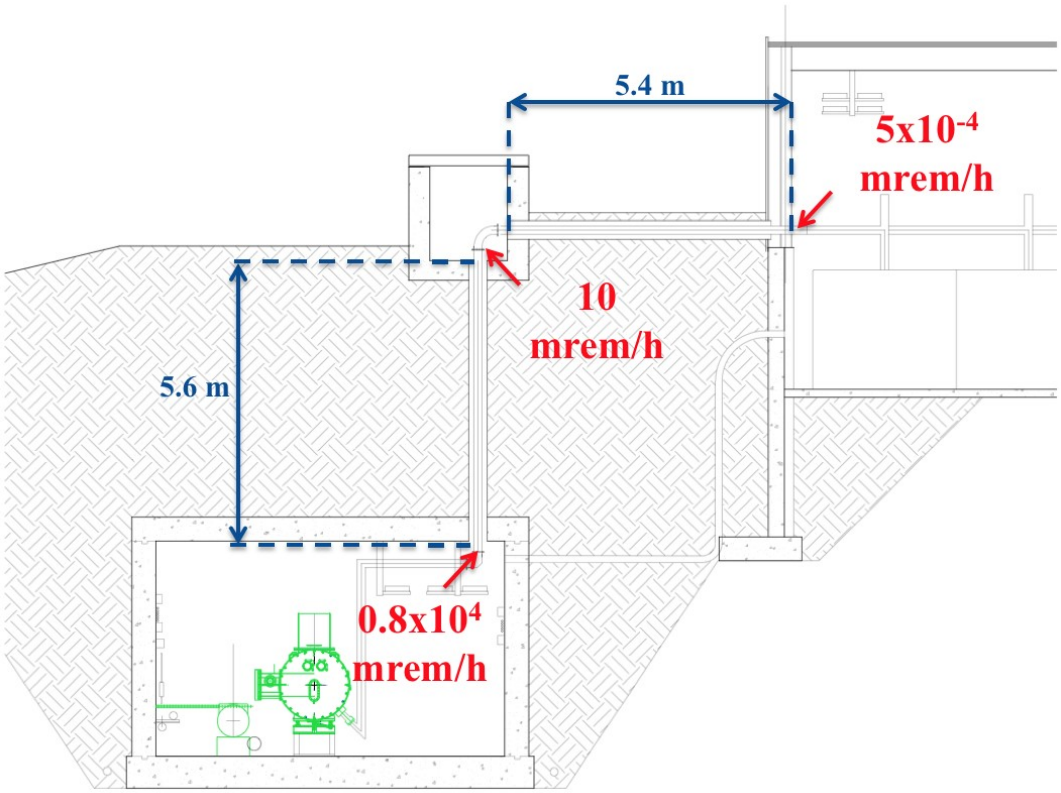

Figure 3.40: Alternative A cross section civil engineering drawing with values of effective does shown at the exit/entrance of the tunnel, ground level (inside the waveguide vault) and gallery. The estimates are based on analytical calculations with universal curves of does attenuation.

The FLUKA results in Figure 3.38 show that alternative A is the best choice to lower radiation in the PIP-II gallery. However civil engineering and mechanical constraints make the alternative B more suitable. The PIP-II integration is following the alternative B implementation, including studying of possible improvements such as extra shielding in the gallery penetration exit for the higher doses areas in order to bring the alternative B at the same level of radiation in the gallery as the alternative A. Detailed studies will follow this preliminary evaluation by the implementation of a realistic model of the PIP-II machine in the simulations and taking into account the filling factors for the penetrations and the on-going optimization of the mechanical and civil constructions designs.

3.3.5.2 Residual activation of accelerator components and structures

Residual radiation levels in beam transport lines and accelerators due to operational beam losses must be controlled in order to conduct maintenance activities while keeping personnel radiation exposure as low as reasonable achievable (ALARA). For 1.6 MW beam power, even 0.1% loss

would result in very high residual radiation levels which would render a beam enclosure access difficult and maintenance near loss points extraordinarily difficult. A sensitive machine protection system, which inhibits the beam operation when significant losses are present, is required to allow access and maintenance activities as historically enjoyed at Fermilab.

For design purposes, a loss rate of 3 to 10 W/m results in a dose rate of about 100 mR/hr at one foot from from beam line component within magnets following a 30 day irradiation period and 1 day of cool down. A loss of 0.25 W/m results in a dose rate of about 100 MR/hr at one foot from lows mass components such as beam pipes for the same irradiation/cooling period. Radiation levels considered acceptable are typically at least a factor of 5 less than these levels. For example, for a typical magnet beam loss location at 2 W/m, the fractional beam power loss is 1 ppm. A sensitive machine protection system will be required to quickly identify and suspend operation in the event such losses occur.

In the Safety Analysis, projected normal losses due to intrabeam scattering and other loss mechanisms are below 0.1 W/m. The machine protection system as presently conceived should limit beam loss to < 0.25 W/m. Consequently, residual activation of the accelerator, beam line components, and tunnel structures should be comparable to or less than levels tolerated in existing and previous Fermilab accelerators. While the machine protection system would serve to protect the accelerator and beam line components, the TLM system would serve in a parallel role as a personal safety system to limit residual activation of accelerator components.

3.3.5.3 Air activation

Air activation must also be characterized for the projected PIP-II operations. Based upon the anticipated losses described in the Safety Analysis, the combination of anticipated normal beam loss and the machine protection system should serve to limit the total beam loss levels at or below those produced at existing facilities. Based upon projected losses from the Safety Analysis, no significant air activation is anticipated. While the machine protection system would serve to protect the accelerator and beam line components, the TLM system would serve in a parallel role as a personnel safety system to limit air activation within accelerator enclosures.

3.3.5.4 Water activation

The site chosen for the new PIP-II accelerator and beam line enclosures is inside the former Tevatron ring. In order to evaluate surface and ground water activation, a geological survey (core borings) will be required to understand ground water migration rates at this site since no data presently exists. An estimate of surface and ground water activation is necessary in order to ensure compliance with regulatory requirements for surface and ground water. However, based upon losses projected by the Safety Analysis, no significant surface water of ground water activation is anticipated. The machine protection system would serve to limit the total beam loss that would also determine the level of surface water and ground water activation. The TLM system would serve a parallel, redundant role to also limit surface and ground water activation.

3.3.5.5 Radioactive surface contamination

Radioactive surface contamination happens together with the activation of accelerator and beam line components. Maintenance activities are rendered more complicated when radioactive surface contamination is present due to prescriptions for the use of personnel protective equipment including coveralls, gloves, shoe covers, and other protective measures. It is possible in megawatt-scale beam power machines to produce very significant levels of radioactive surface contamination at beam loss locations. However, as indicated in the Safety Analysis, the nominal beam power losses are expected to be approximately 0.1 W/m, about a factor of 100 below the beam power loss required to produce the onset of measurable radioactive surface contamination. Consequently, radioactive surface contamination on the accelerator and beam line components, and on the tunnel structures should be comparable to or less than levels tolerated in the existing and previous machines.

3.3.5.6 Lifetime of machine components

Based upon the level of beam loss projected by the Safety Analysis and also upon experience with existing accelerator and beam line facilities, machine components lifetimes should, in general, be on the order of many decades.

3.3.6 Fault scenarios in the superconducting Linac

An accelerator has to deliver a high-quality beam with high availability. The large number of elements in the Linac increases the likelihood of failure. In this section, ways to mitigate such failures are considered.

Failure of a beam transport element, like a cavity, solenoid or quadrupole, alters the periodicity of beam focusing, resulting in a mismatch of beam transport with the downstream sections. This, in turn, may degrade beam qualit,y and in the worst case, may cause beam losses. The implication of a failure on machine performance depends on the failure location. In some cases, a failed element results in significant beam losses. If the machine cannot be retuned to an acceptable state, it becomes necessary to replace this element before operation can continue. In some instances, a full cryomodule replacement may be required, which is a time-consuming process requiring warmup and subsequent cooldown after repair. To improve reliability, the optics should be tolerant to at least one major fault in each section. The fault tolerance of the optics diminishes as the number of failures increases. An extensive study has been performed to address this problem for the PIP-II SC Linac. Below, we discuss failure of beamline elements at critical locations and demonstrate that the optics design of the PIP-II SC Linac is sufficiently robust to compensate for failure of a cavity or a focusing magnet by retuning nearby elements. Note that in this study, one failure at a time is considered. However, it has been observed that at a sufficiently high energy (> 500 MeV), optics could tolerate failures of even a complete LB650 cryomodule..

3.3.6.1 Failure of beamline elements

Element failures can be put in two categories: temporary failures and permanent failures. Temporary failures are recoverable after applying appropriate mitigation measures. Quenching of a SC cavity and vacuum breakdown are examples of temporary failures. Such failures do not require Linac retuning and can be resolved comparatively quickly. A permanent failure occurs when one or more elements become malfunctioning and have to be withdrawn from operations. In this case, retuning of the machine, if possible, can be the most efficient way to maximize machine availability, with repairs done later when conditions allow. The most probable permanent failures are expected to be:

- Failure of a cavity tuner resulting in an inability to keep this cavity in the resonance
- Malfunctioning of the power-coupler resulting in reduced accelerating gradient or an inability to use this cavity
- Failure of a RF power supply
- Degradation of Q_0 resulting in reduced voltage
- Failure of a focusing magnet (short in a coil, quenching, non-functioning power supply, etc.).

In the following sub-sections we discuss permanent failures of accelerating cavities and focusing magnets at critical locations in the PIP-II SC Linac.

Local Compensation of Failed Elements

As will be seen in the following sections, failure of a beamline element causes longitudinal and transverse mismatches, leading to emittance growth and beam losses in the downstream part of the Linac. In order to restore the beam quality, a local compensation involving adjustments for settings in nearby elements is used. The procedure should minimize excessive oscillations of the bunch sizes. PIP-II has separate powering for each cavity and solenoid. This is greatly helpful for compensation. The constraints and assumptions for local compensation are summarized below:

- Accelerating field in cavity: fields can be varied to recover the beam energy, but the surface peak magnetic and electric fields should not exceed their design limits.
- Integral fields in quadrupoles and solenoids should not exceed their design limits.
- Synchronous phases of cavities are varied in such a way that the ratio of synchronous phase (referenced to on-crest acceleration) to longitudinal rms beam size should be greater than 3. This provides sufficient longitudinal acceptance to accommodate 3σ beam.
- A minimum number of retuned elements should be used in order to expedite retuning and to minimize overall effort.

- 100% beam transmission and minimal emittance growth at the Linac end should be achieved.

Failure of the First HWR Accelerating Cavity

The HWR is the first SC section in the PIP-II Linac. It accelerates and focuses the beam coming out of the MEBT. Each focusing period in the HWR section includes a solenoid and an HWR cavity. Failure of the first cavity in the HWR section is considered to be the most serious one due to large transverse and longitudinal beam sizes at this location. At this point the beam is non-relativistic, therefore this failure, if uncompensated, results in both phase and energy oscillations propagating downstream and growing in amplitude along the Linac. Furthermore, the space charge forces are quite large resulting in an amplification of beam losses. Figure 3.41 shows the rms longitudinal and transverse beam sizes along the Linac after failure of the first HWR cavity. Abrupt changes in the longitudinal beam profile occur due to beam losses happening at transitions between cryomodules. Total beam losses below 0.01% are observed in the SC Linac after failure of the first HWR cavity. The momentum mismatch results in a perturbation of transverse motion. However, as can be seen from Fig. 3.41, the transverse beam sizes are comparatively unperturbed due to the small energy gain in the first HWR cavity. This cavity operates at half of nominal voltage and has a large accelerating phase offset from on-crest acceleration in order to capture the beam with large longitudinal emittance.

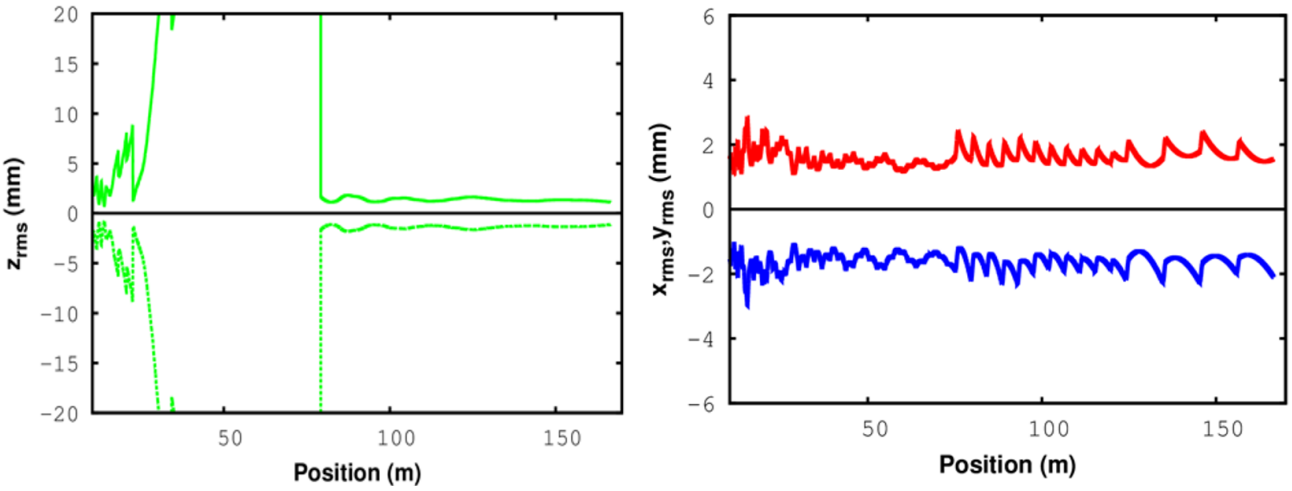

Figure 3.41: Longitudinal (left) and transverse (right) rms beam sizes along the Linac (starting at the MEBT end) after failure of the first HWR cavity (horizontal in red, negative vertical in blue).

Figure 3.42 shows normalized rms transverse and longitudinal emittances along the Linac. The abrupt change in the longitudinal emittance is caused by beam losses at the beginning of the LB650 section. In contrast, there is no significant transverse emittance growth along the Linac.

Figure 3.43 presents results of an application of local compensation used to restore the beam quality. The figure shows the rms bunch sizes and the elements used in the retuning: the last bunching cavity of the MEBT and the three HWR cavities downstream of the failed cavity. Additionally, the two subsequent HWR cavities are retuned to recover the beam energy. This prevents excessive bunch size oscillations in the downstream Linac without its retuning.

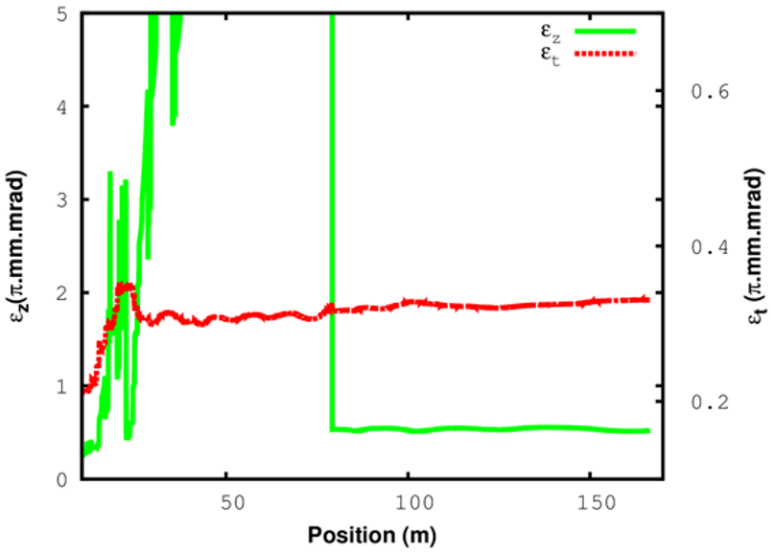

Figure 3.42: Normalized rms longitudinal (green, left scale) and transverse (red, right scale) emittances along the Linac after failure of the first HWR cavity. Note that abrupt changes in the longitudinal beam profile occur due to beam losses.

Figure 3.44 presents the bunch envelopes for the entire Linac with and without compensation. As can be seen, both the transverse and longitudinal envelopes are completely recovered, and there are no beam losses. Figure 3.45 shows the synchronous phases and the longitudinal beam size. The longitudinal acceptance is large enough to accommodate 6σ beam. The left pane in Fig. 3.46 shows the normalized rms longitudinal emittances before and after compensation. Note that the emittance after compensation is plotted on the right-hand y-axis. As expected, the compensation resulted in smaller emittances; there is no significant emittance growth in any planes. Table 3.11 presents a comparison of beam emittances at the Linac end for different cases.

Table 3.11: Final normalized rms beam emittances before and after local compensation for a failure of the first HWR cavity.

Parameter	Units	Nominal	Failure of first HWR cavity	
			No Comp.	After Comp.
ϵ_z	mm mrad	0.28	0.52	0.29
ϵ_t	mm mrad	0.25	0.33	0.25

Failure of the First Solenoid in the HWR Section

At the beginning of the Linac, the transverse beam size is relatively large, and the beam barely fits in the physical aperture. A failure of the first solenoid in the HWR section is as critical as a failure of the first HWR cavity. It results in transverse beam size oscillations with large amplitude, leading to emittance growth and beam losses. Local compensation is applied using the same approach as discussed above; the neighboring elements are retuned to achieve a smooth beam profile along the Linac. Figure 3.47 shows beam envelopes before and after applying the local compensation. The figure demonstrates that the transverse beam oscillations are minimized and the transverse beam profiles are restored. Figure 3.48 shows the corresponding normalized rms emittances before and

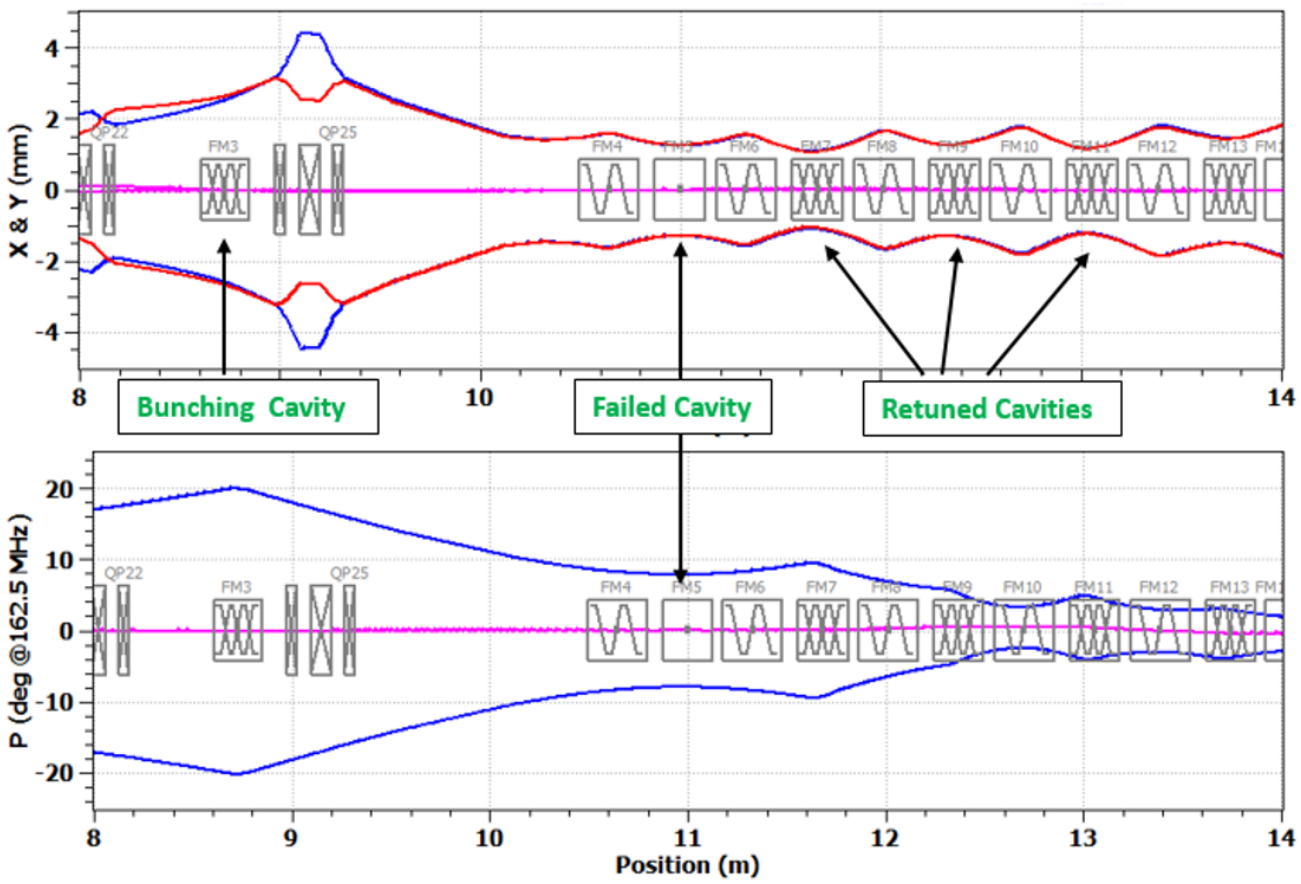

Figure 3.43: Enlarged view of beam profiles in the transverse (top) and longitudinal (bottom) planes after applying local compensation for a failure of the first HWR cavity. Elements used for retuning are pointed out by arrows.

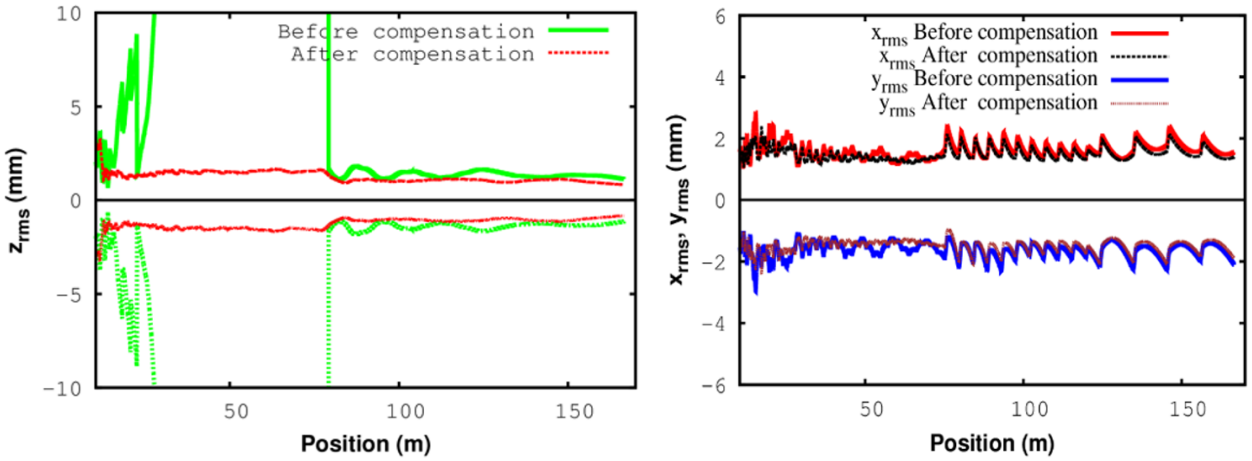

Figure 3.44: Longitudinal (left) and transverse (right) beam sizes along the Linac before and after applying local compensation for a failure of the first HWR cavity.

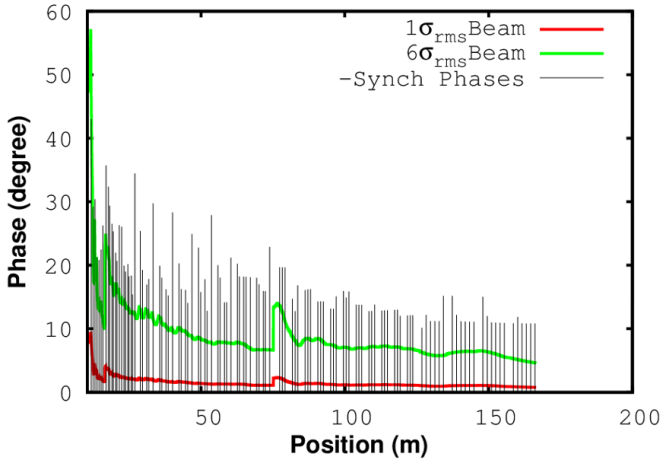

Figure 3.45: Synchronous phases with longitudinal beam size along the PIP-II SC Linac.

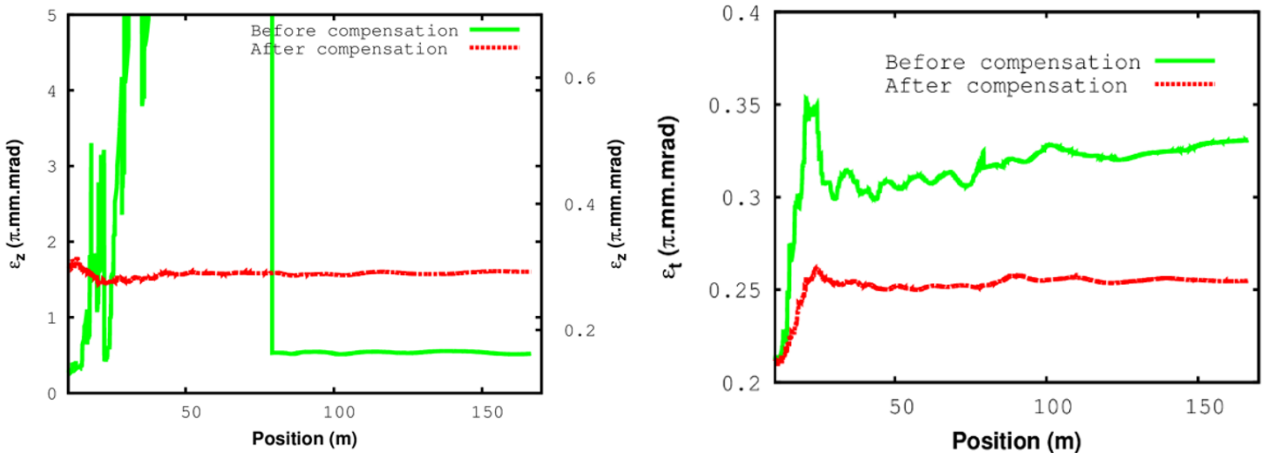

Figure 3.46: Normalized rms longitudinal (left) and transverse (right) emittances along the Linac in the presence of failure of the first HWR cavity. The picture on the left has different scales for the emitances with and whithout compensation.

after applying this compensation.

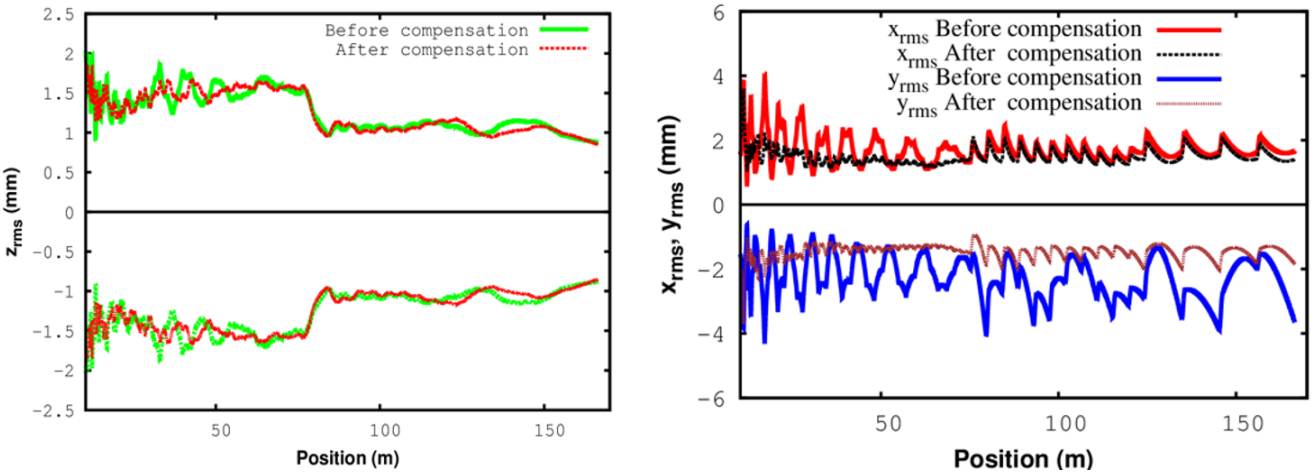

Figure 3.47: Longitudinal (left) and transverse (right) beam sizes along the Linac before and after local compensation for a failure of the first solenoid in the HWR section.

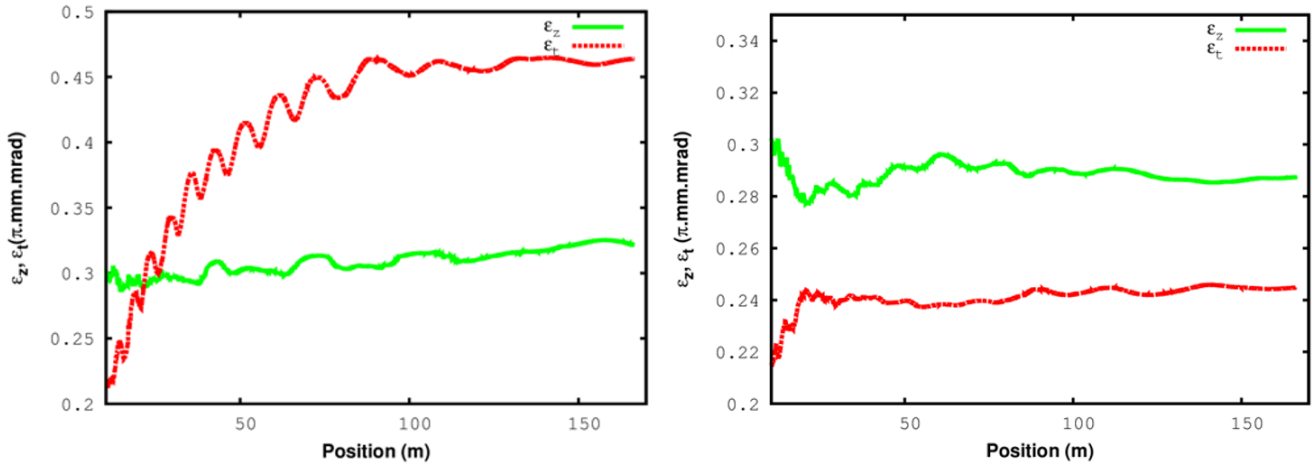

Figure 3.48: Beam emittance growth along the Linac before (left) and after (right) the local compensation for a failure of the first solenoid in the HWR section.

Failure of the Last Cavity in the HWR section

The HWR section is followed by the SSR1 section. There is a short warm section separating the HWR and SSR1 cryomodules. Beam matching is performed using nearby elements of each cryomodule to achieve a smooth beam profile around the transition. Accelerating gradients and synchronous phases in cavities are used to adjust the longitudinal beam profile, while focusing strengths of solenoids are changed to achieve matching conditions in the transverse planes. The left pane in Fig. 3.49 shows the rms longitudinal beam envelope along the Linac after a failure of the last HWR cavity. Beam oscillations are observed after the failed cavity. However, a smooth beam profile is obtained after applying local compensation. Note also from the right pane in Fig. 3.49 that longitudinal emittance is restored.

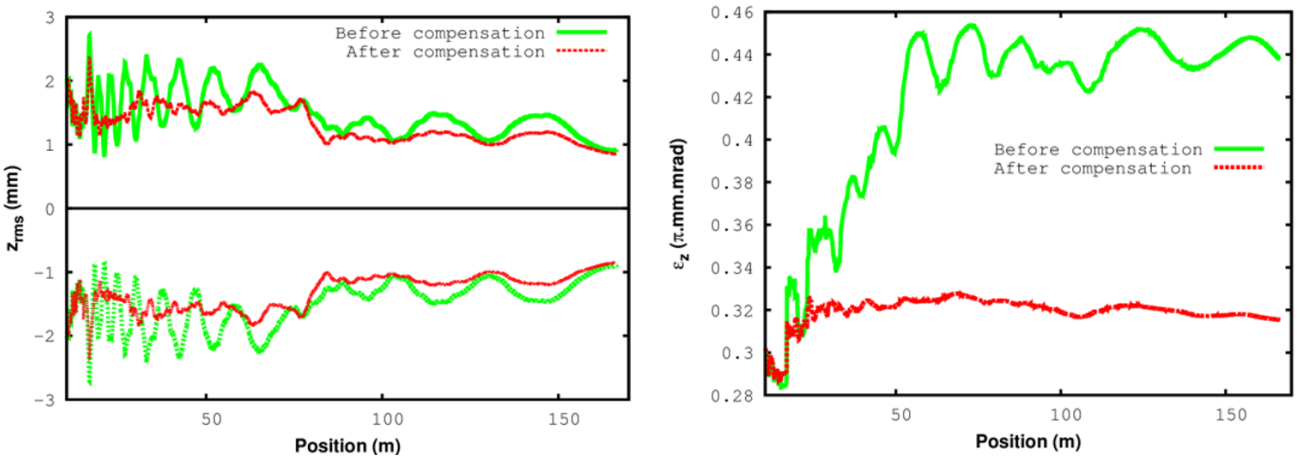

Figure 3.49: Longitudinal rms beam envelopes (left) and normalized rms emiitances (right) along the Linac before and after applying local compensation for a failure of the last HWR cavity.

Failure of the Last Solenoid in the HWR section The studies have shown that a failure of the last solenoid in the HWR section represents one of the most dangerous situations with ∼13% beam losses immediately downstream. The center-to-center distance between the last solenoid in the HWR section and the first solenoid in the SSR1 section is about 1.82 m. A failure of the last HWR solenoid increases the length of the beam transverse focusing cell to 2.51 m. This change in the length and the resulting mismatch due to the absence of focusing lead to a large beam envelope oscillation. Figure 3.50 shows the rms beam envelopes and transverse emittance before and after applying the local compensation.

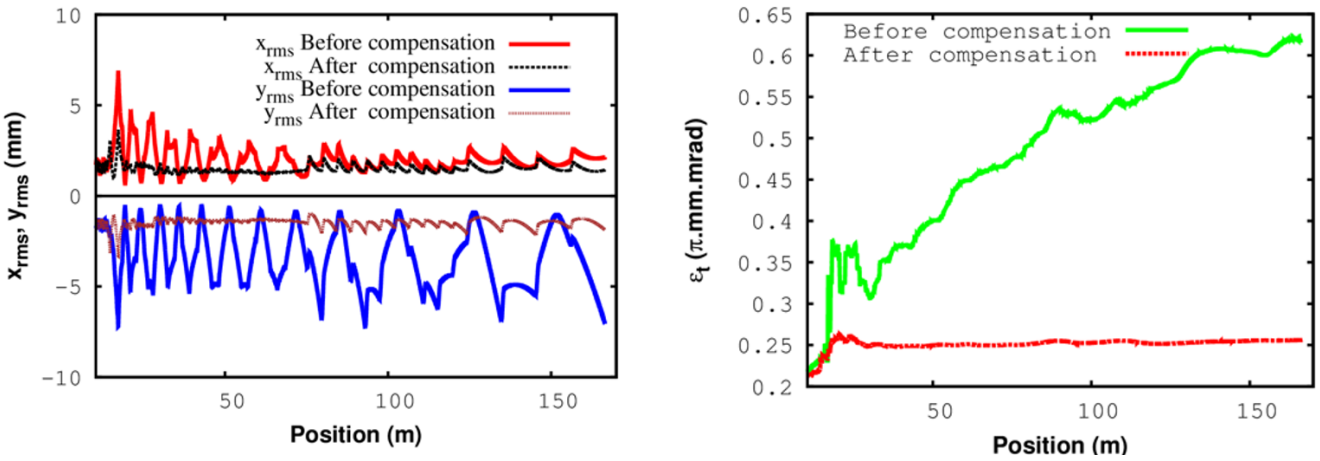

Figure 3.50: The rms transverse beam sizes (left) and normalized rms beam emittances (right) before and after applying the local compensation to failure of the last solenoids in HWR section.

Failures at Other Critical Locations As the beam energy increases, the machine performance becomes less sensitive to a single element failure. Higher beam energy reduces the impact of non-linear space charge forces as well as the focusing effect of a single element. A study was performed to analyze the performance of the Linac in the presence of failed elements at higher energy but

in critical locations. The transition from the SSR2 to the LB650 section is considered to be a vulnerable location in the Linac because of two reasons:

- Solenoidal focusing in SSR2 is replaced by focusing with quadrupole doublets in the LB section.
- A frequency jump from 325 to 650 MHz occurs at this transition.

Although a replacement of a failed normal-conducting quadrupole is much simpler and faster than for a SC solenoid, a study was performed to evaluate performance of the Linac in the presence of a failed quadrupole. In this study, we assumed that after the failure of one quadrupole in a doublet, the remaining quadrupole is also turned off. Figure 3.51 shows the normalized beam density in the vertical plane along the Linac for the case when the first quadrupole doublet in the LB section has failed. In spite of mismatch-induced oscillations, the physical aperture in the downstream sections is sufficiently large to accommodate the beam. There is still significant margin (ratio of beam aperture to maximum beam size) even for 6σ beam. Figure 3.52 shows the beam transverse envelopes and the normalized rms emittances before and after compensation.

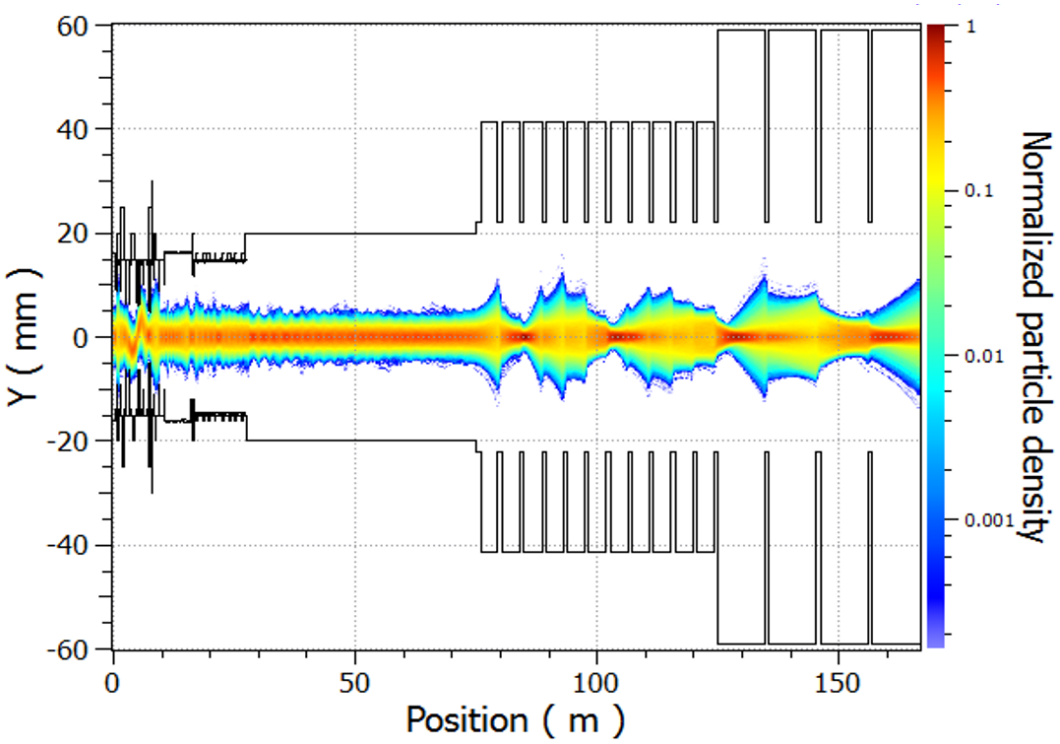

Figure 3.51: Normalized vertical particle density along the after a failure of the first quadrupole doublet at the SSR2 to LB650 transition.

A study performed to evaluate implications of a cavity failure in the LB section shows no beam losses even after a failure of the first complete LB650 cryomodule. However, the beam energy is reduced to 786.5 MeV and the final normalized rms longitudinal emittance is increased to 0.38 mm mrad.

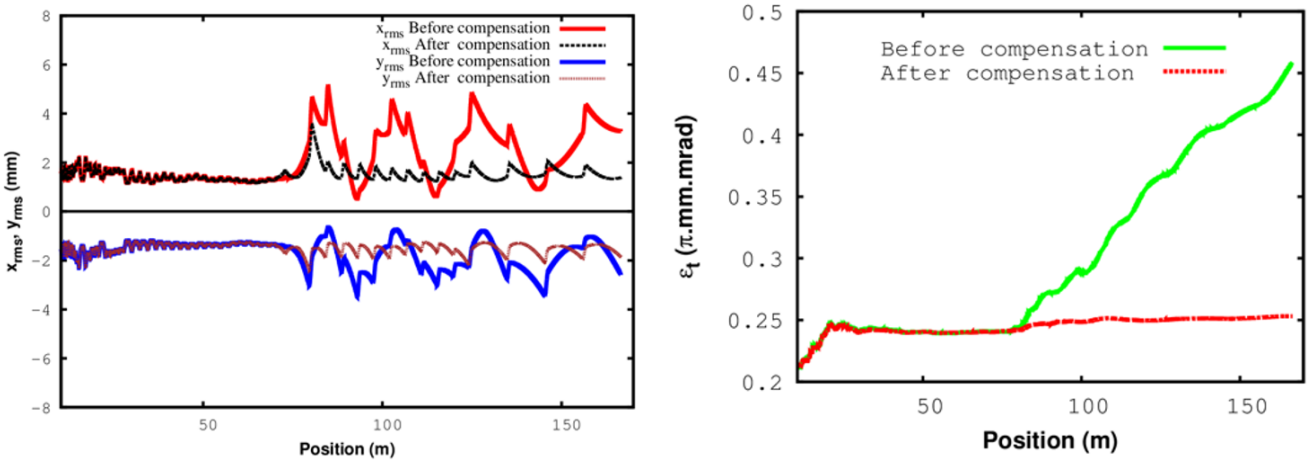

Figure 3.52: Beam transverse sizes (left) and normalized rms transverse emittances (right) before and after applying local compensation for a fault of the first quadrupole doublet at the SSR2 to LB650 transition.

Chapter 4

Accelerator Complex Upgrades

4.1 Introduction

The Accelerator Complex Upgrades include the required upgrades to the existing accelerator complex for achieving the PIP II performance requirements which includes upgrades to the beam transfer line from the superconducting Linac to the current Booster and the beam absorber line. The main performance requirement of PIP II is to deliver beam power greater than 1 MW from the Main Injector, over the energy range of 60 to 120 GeV.

To minimize the Main Injector cycle time, the Recycler Ring is used for slip stacking [45]. A total of twelve Booster batches are injected in two groups and circulated in the Recycler while the Main Injector is ramping. When the two groups of Booster batches overlap, the beam is injected into the Main Injector. This process is illustrated in Figure 4.1. The time to complete the slip stacking process in the Recycler is 13 Booster periods (ticks). The slip stacking time sets a lower limit to the energy that the Main Injector can ramp while maintaining constant beam power. With the Booster running at 15 Hz, the energy is 80 GeV and to reduce it to 60 GeV an increase in the Booster repetition rate to 20 Hz is needed resulting in a 34% reduction to the slip stacking time. With the Main Injector running at 60 GeV, the slip stacking time in the Recycler is equal to the Main Injector cycle time requiring the Recycler slip stacking RF cavities to run in CW mode.

To achieve 1.2 MW at 120 GeV in the Main Injector, 7.5×10^{13} protons per pulse need to be accelerated. This requires an upgrade of all twenty Main Injector RF stations to achieve the additional power. In order to slip stack in CW mode and at 20 Hz requires new 53 MHz RF stations in the Recycler. The Booster also requires a new injection area operating at 800 MeV with new magnets, stripping foil and absorber. To operate the Booster at 20 Hz, the capacitor banks and chokes in every cell also need to be replaced. All the Booster power supplies need to be able to operate at 20 Hz.

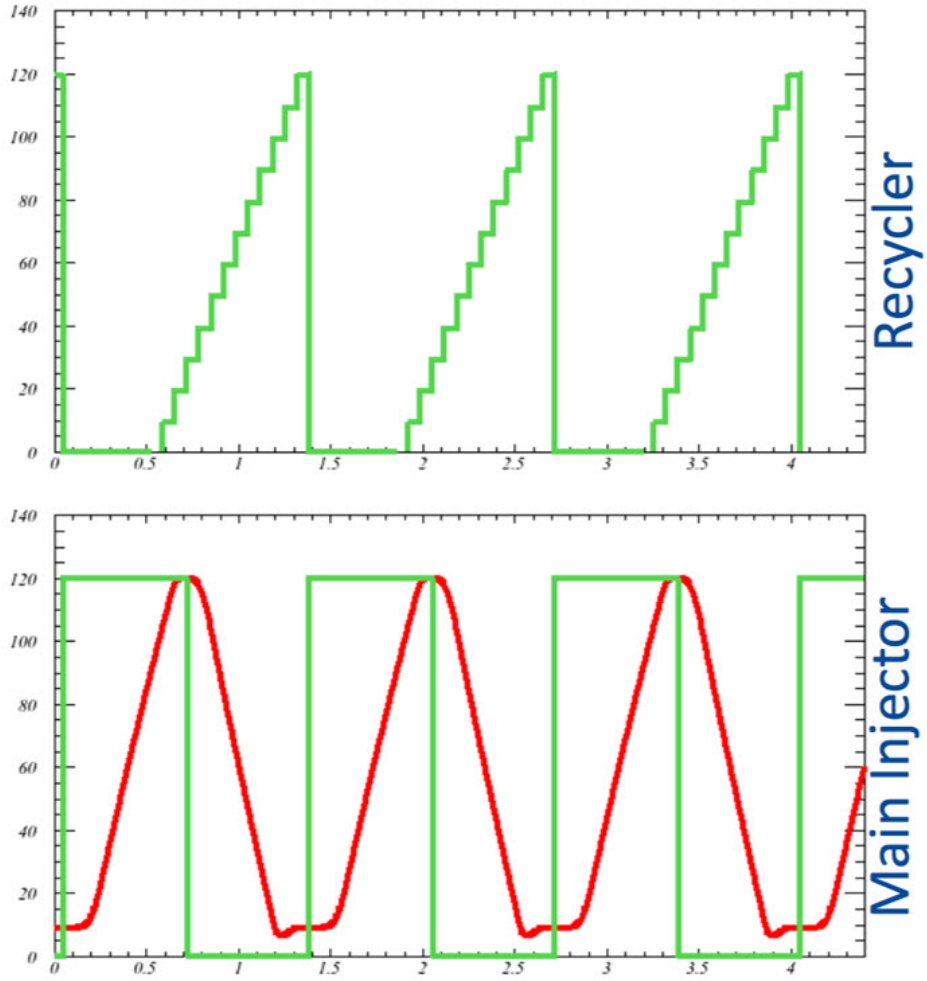

Figure 4.1: Beam in Recycler Ring (top) and in the Main Injector (bottom). The steps in the Recycler beam trace correspond to the 12 Booster injections. The red trace represents the Main Injector ramp.The units on x-axis are seconds and on the y-axis GeV

4.2 Booster injection

4.2.1 Present Booster injection

The Booster lattice contains 24 periods and can be described as a FoDooDoF lattice utilizing gradient magnets with long straight sections (5.66 meters, flange-to-flange) between the defocusing gradient magnets and a short straight section (0.5 meters) between the F and D gradient magnets. All the injection, extraction and RF systems are located in long straight sections. The horizontal beta function varies from about 6 meters in the long straight to 33 meters in the short straights while the vertical beta function varies from 20 meters in the long straights to ∼5.3 meters in the short straights. The horizontal dispersion varies between approximately 1.8 (in the long straights) and 3.6 meters (in the short straight). The optics for the full ring are shown in Figure 4.2. The optical functions of a single period starting in the middle of a short straight section and centered on the "long straight" are shown in Figure 4.3. The injection straight section is in the long straight section 01, called Long 1. The gradient magnets, ORBUMP magnets, and correctors are shown at the top of the Figure.

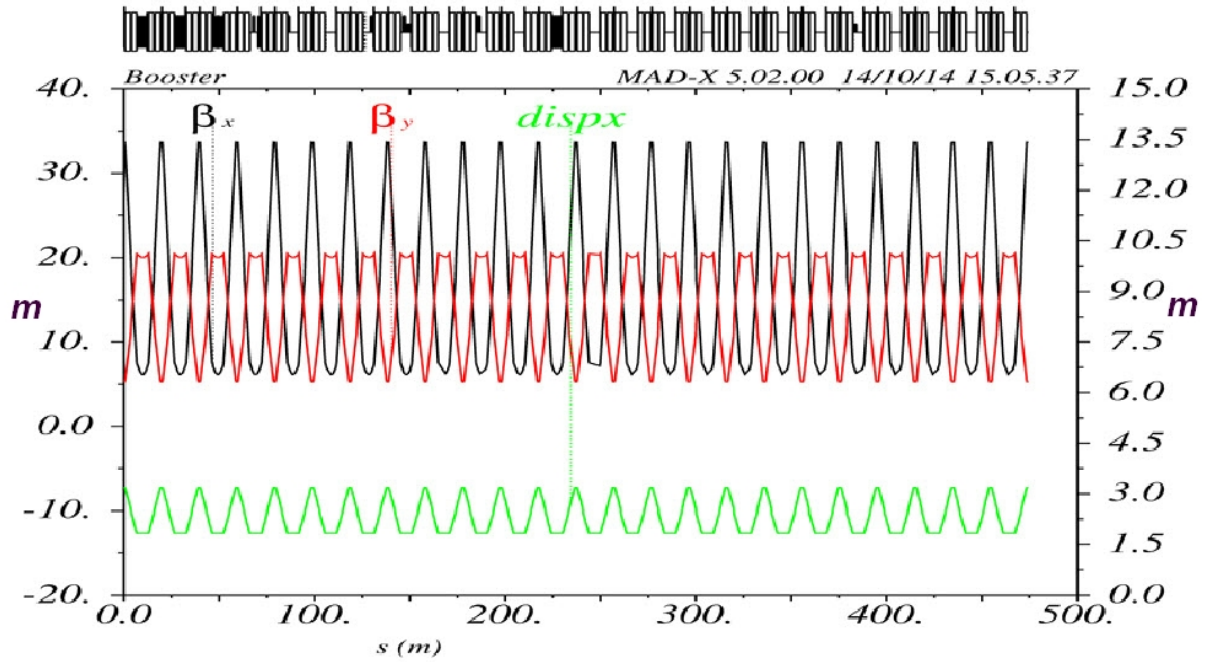

Figure 4.2: Booster lattice functions.

A new injection design using a three dipole horizontal orbit bump magnet system (ORBUMP) solution was proposed and subsequently installed in 2006 [46], [47]. Figure 4.4 shows the layout of the installed horizontal injection chicane reproduced from reference [47].

The center dipole of this insert is used to merge the incoming H^- on the closed orbit produced by the three dipoles and runs at twice the field (current) as the outer dipoles. The injection foil is located immediately after the middle ORBUMP magnet. The Booster closed orbit during injection time is moved out to ∼45mm at the foil position to match the incoming trajectory of

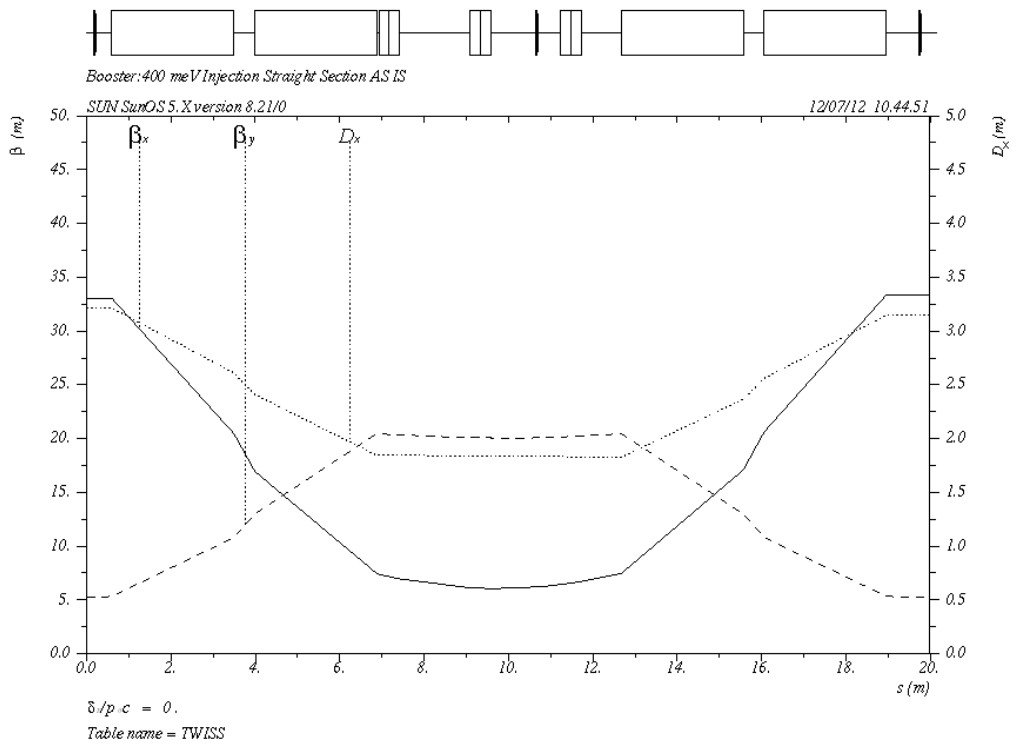

Figure 4.3: Optical functions for the existing Booster Long 1 straight section

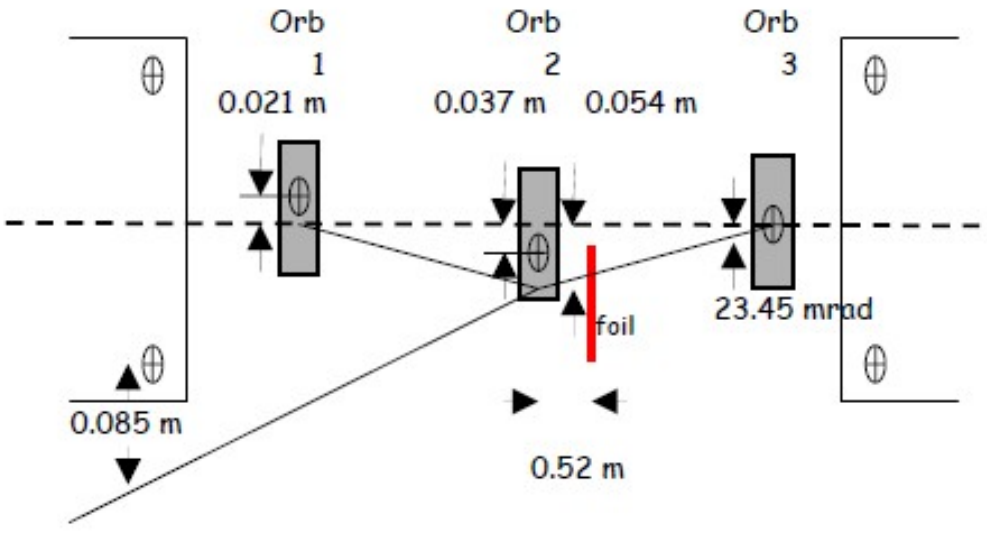

Figure 4.4: Current 400 MeV Horizontal injection insert showing the layout of the three chicane dipoles, foil and injection beam line.

the H$^-$ transport line. The field in the ORBUMP dipoles is fixed during the injection "beam on" time since injection does not implement phase space painting. All three dipoles are powered by a single resonant power supply. The current injection time is typically less than 35 μs. The current angle produced by the center dipole is approximately ~47 mr which corresponds to an integrated field of 1.5 kG-m. For an effective magnetic length of 0.5585 m, this corresponds to a peak field of about 2.7 kG, just shy of the 3 kG maximum field on the existing ORBUMP magnets. The current separation of the ORBUMP magnets is approximately 1.75 m.

To put the existing injection layout shown in Figure 4.4 in perspective, Figure 4.5 shows the plan and elevation view of the existing injection girder inside the Long 1 straight section. The insert is bordered on each end by the defocusing or "D" gradient magnets.

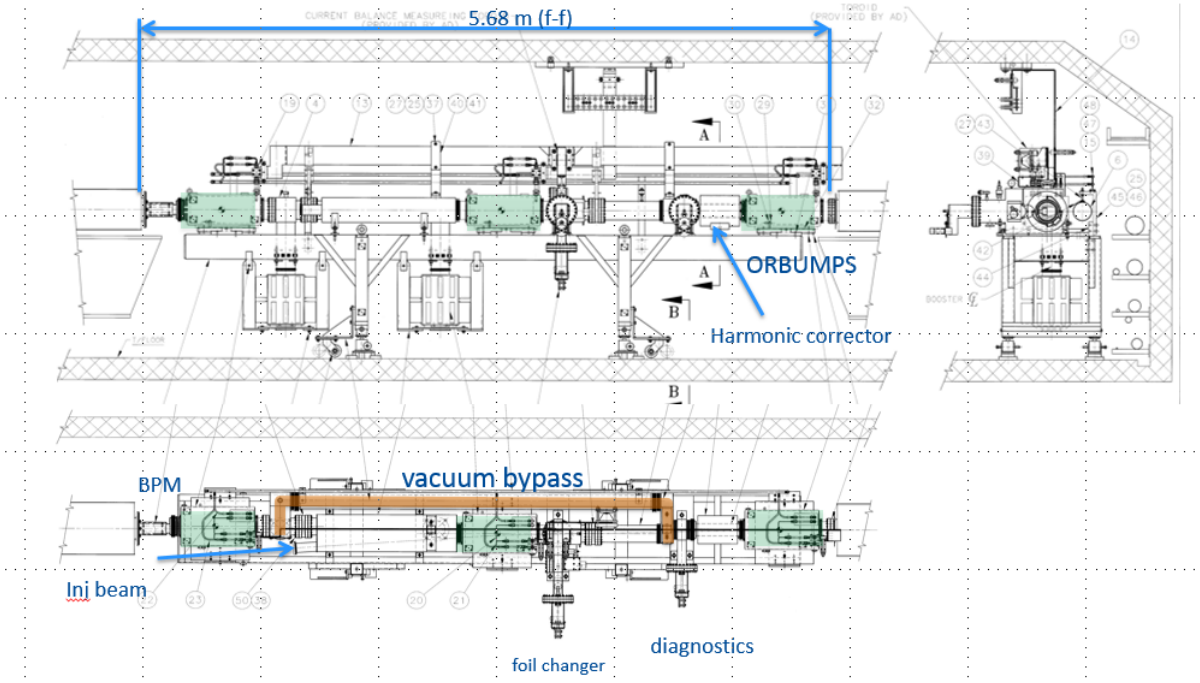

Figure 4.5: Plan (lower) and elevation (upper) mechanical layout of the existing injection straight section. Major components include the three ORBUMP magnets (green highlight), foil changer.

Also shown in Figure 4.5 are the foil changer, multipole corrector package, and the vacuum bypass for the foil changer. It will be important to keep these devices in the PIP-II era injection straight.

Referring to Figure 4.4, the injection foil is located after the center ORBUMP magnet which means that the injected ions stripped to protons by the foil and the "waste beam" (consisting of unstripped H$^-$ ions that miss the foil and partially stripped neutral ions H0) are directed into the aperture of the downstream gradient magnet. The ions that are completely stripped to protons are acted upon by the third ORBUMP magnet to place them on the circulating closed orbit. However, unstripped H- ions are deflected in the opposite direction and neutral hydrogen ions are unaffected by the last ORBUMP magnet and both of these species are lost into the aisle side of the second gradient magnet downstream of the injection straight. They produce "on-contact" residual radiation levels soon after the beam is turned off on the order 1 R/hr for the existing input beam power of ~2 kW. For PIP-II, the injected beam power is expected to be about 17 kW, which implies an increase of a factor of about ~8.5. If the foil stripping efficiency remains about the same as

the current operation, one would expect the "on-contact" residual radiation to approach 8 to 10 R/hr on contact. This is not tolerable and therefore the injection insert design must include a new "well-shielded" injection absorber in the injection straight section to intercept and contain the "waste beam". Additionally, the basic injection insert design should keep the waste beam from the aperture, which implies that the "3-bump" design of the existing straight section is not suitable as the basis for the new design. We will need to evaluate any issues with the stripped electrons and develop a plan of how to address them.

4.2.2 Preliminary design of Booster injection at 800 MeV

The injection into the Booster during the PIP-II era will be moved from the current location at "Long 1" to the "Long 11" straight section to facilitate (accommodate) injection from the SC Linac located in the Tevatron infield (Figure 4.6). As already noted in the previous section, all long straight sections have the same geometry and optics. The flange-to-flange length available for the injection insert is 5.6804 meters.

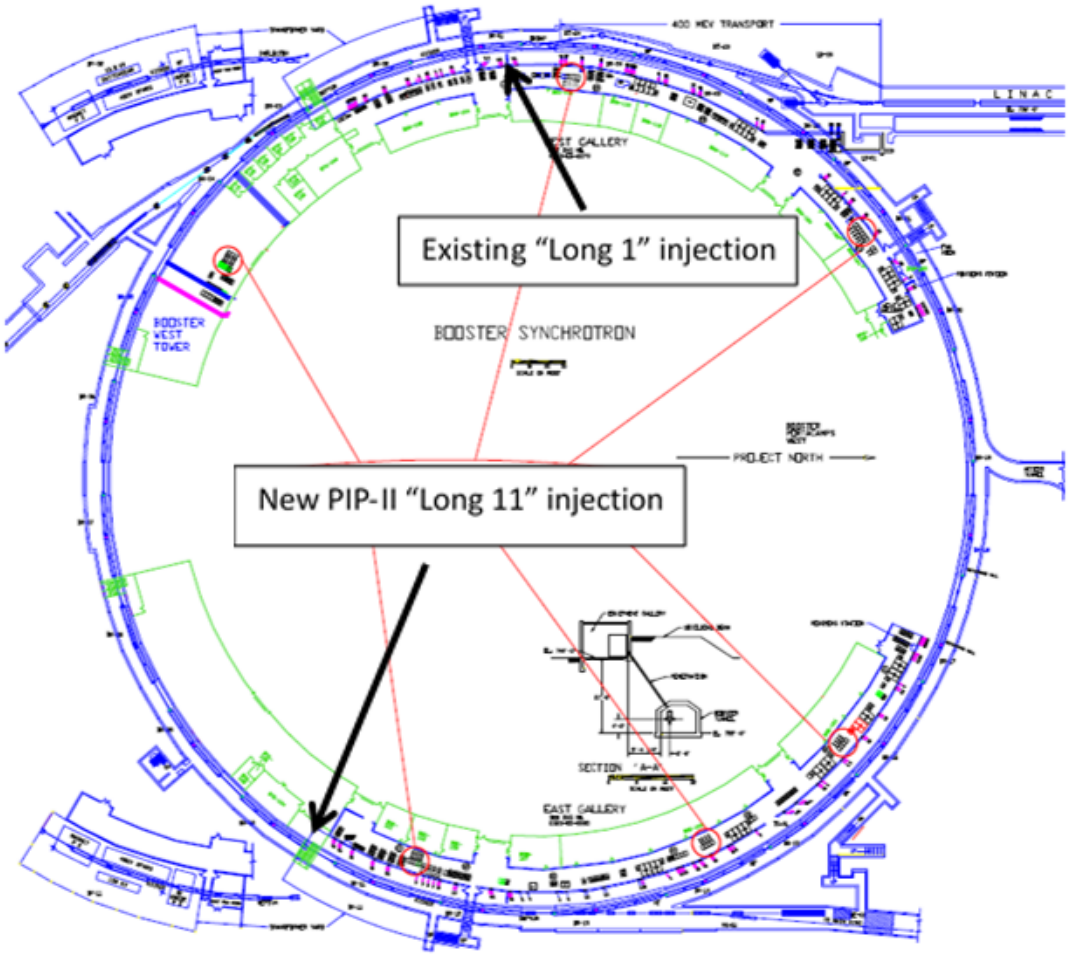

Figure 4.6: Plan view of the Booster showing the location of existing and new PIP-II injection insert.

The beam current of the SC Linac (2 mA) is more than an order of magnitude smaller than that of the present 400 MeV Linac. It will require a much longer injection time (∼300 turns over 550 us) which together with much smaller Linac emittance ($\epsilon_{n95\%} \sim 1.5$ mm-mr verses 16 mm-mr from the current 400 MeV Linac and the value specified for Booster beam) allows us to perform transverse phase space painting. During the phase space painting process, the Booster closed orbit will be moved about half of the final emittance in each plane by new dedicated horizontal and vertical phase space painting systems.

The preliminary design that will be described here utilizes a 4-bump injection chicane inside the injection straight section is shown in Figure 4.7. This design incorporates dedicated transverse painting magnet systems which is not shown in the Figure. Most importantly, a well shielded waste beam absorber is installed at the downstream end of the straight section. The major benefit to this design is to keep the waste beam (both H0 and H^- missing foil) away from the circulating beam aperture.

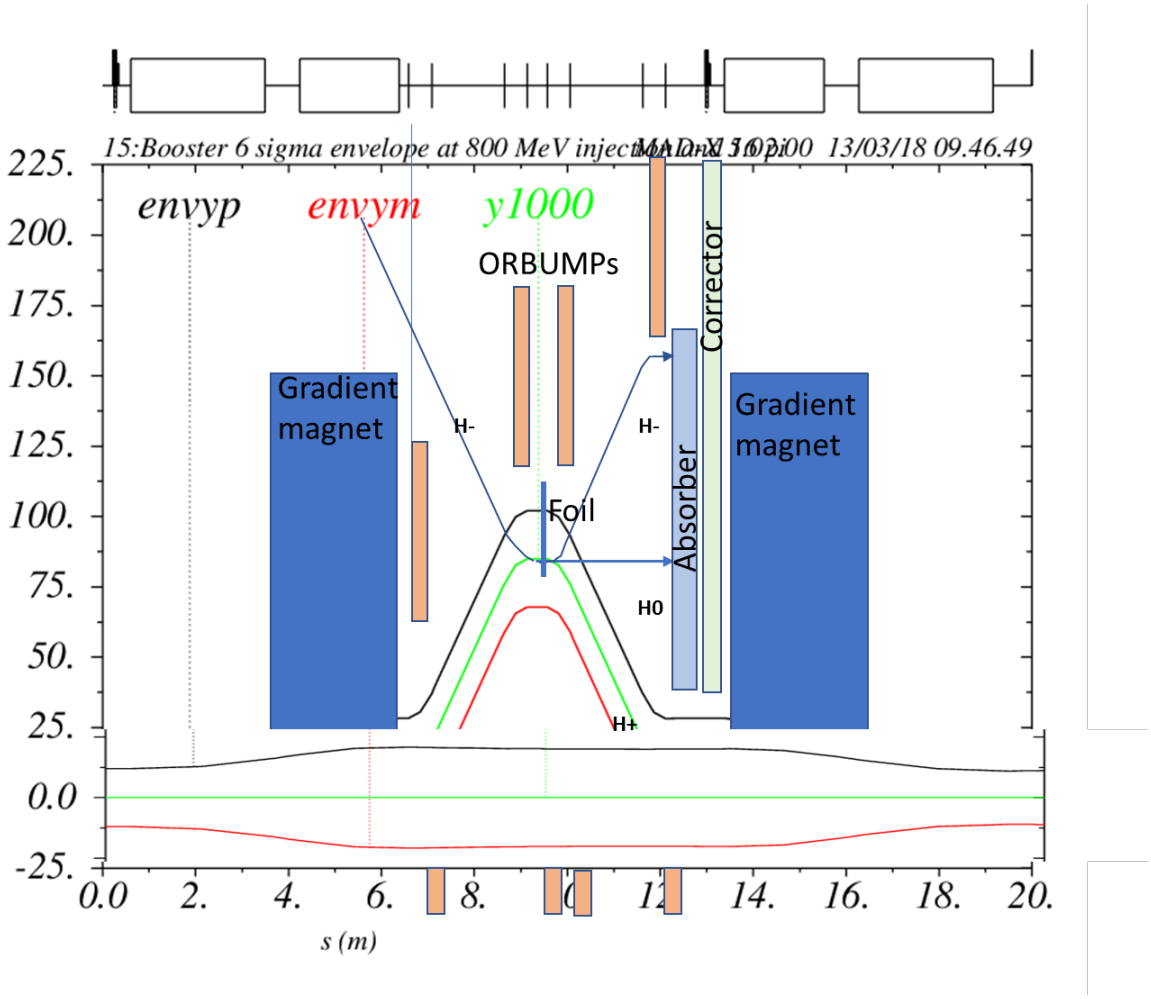

Figure 4.7: Layout of the injection straight section showing the major magnets, the injected and waste beam trajectories at the start of injection, and circulating and injected beam 6σ vertical beam envelopes.The vertical axis units are in mm.

The orientation of the injected beam is in the vertical dimension due to the transverse size of the gradient magnets on either side of the straight section that must be missed by the injected beam

(9 inches horizontal by 6.5 inches vertical half-heights).

To bring the injected beam into the straight section and accommodate the ORBUMP magnets, foil changing system, injection absorber, harmonic corrector and required vacuum components, the current length of the flange-to-flange distance between the adjacent gradient magnets must be increased by 1 meter. This is accomplished by reducing the "D" gradient magnets by a 1/2 meter and shifting the bend center outward by a 1/8 meter. The reduction in length of the gradient magnet will require a new magnet design which has the same bend angle and integrated gradient as the normal length gradient magnet. This could imply a different coil pack design depending on the method of powering the new magnets and different pole tip design to keep the integrated gradient the same as the nominal length gradient magnet. In addition, these new magnets (bend angle and harmonics) will need to track the existing gradient magnet. This magnet is scheduled to be prototyped in 2019-20. This shortened and shifted magnet was implemented in the Booster MADX lattice to determine the impact on the lattice. It was found to have minor impact on the lattice as shown in Figure 4.8. The circumference of the Booster is also preserved.

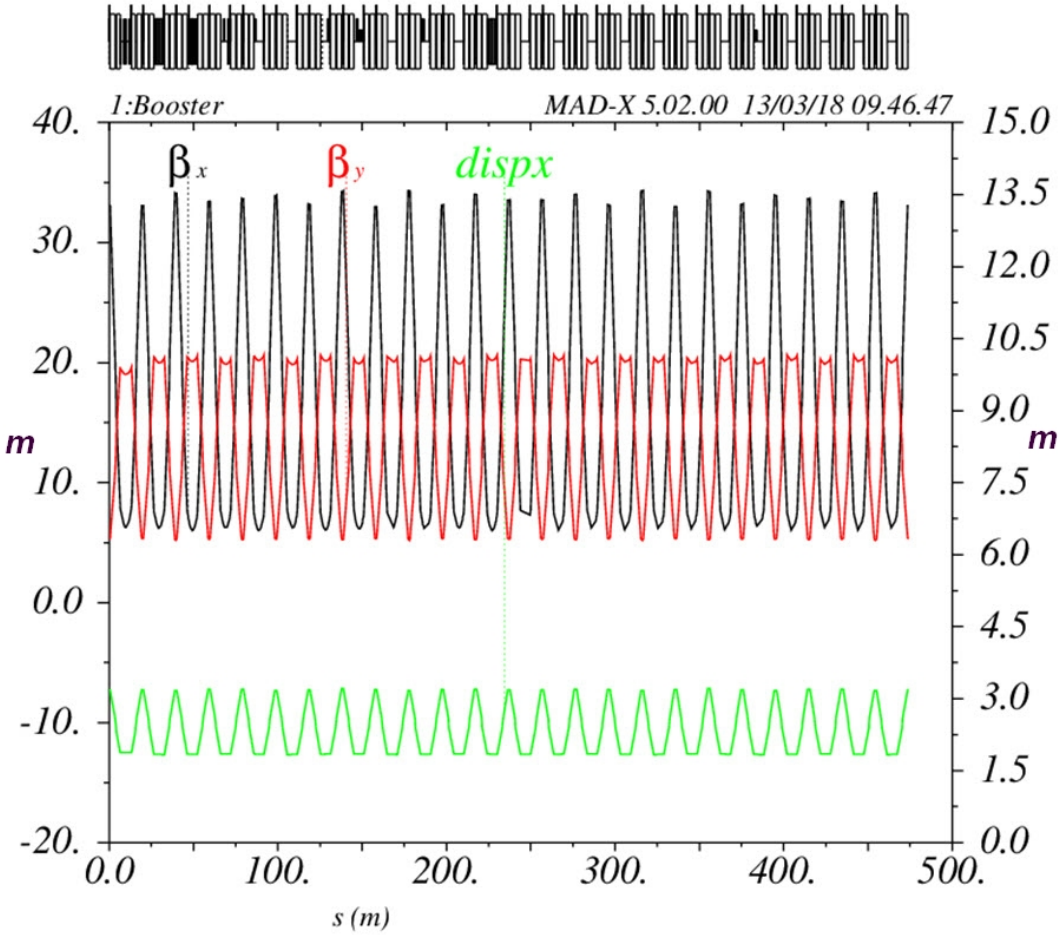

Figure 4.8: Booster ring lattice with two shorter D gradient magnets around the injection straight section.

The key to the injection girder design and the ultimate length of the straight section and the new gradient magnets is the design of the new ORBUMP magnets. The initial thought was to utilize the current design but the two main issues are 1) the increase in the required strength of the

magnet and 2) the flattop (∼600 us vs the current 45 us) length and field uniformity and quality of the field. The current ORBUMP magnets are single-turn ferrite magnets. At the peak integrated field of 1.676 kG-m (corresponding to a peak field in the gap of 3 kG) the ferrite (CDM10) is already saturating in the corners by the conductor. The preliminary straight section design which incorporates all of the major components requires an ORBUMP angle of 36 mr, which for the effective field length of 0.491 meters, calls for a field of 3.58 kG. This magnet and its power supply requires prototyping. The current concept for the magnet will be to utilize 0.2mm electrical steel which has a much larger saturation.

There will be a limit to the magnitude of the allowed magnetic field of the injection c-magnet at the end of the transport line from the Linac and the ORBUMP magnets to minimize any premature neutralization of the H^- ions due to Lorentz stripping. The lab frame lifetime of an H^- ion traveling in a magnetic field has been parameterized by Scherk. Measurements of the lifetime of 800 MeV H^- ions in magnetic field have been reported and compared with the parameterization with good agreement. Figure 4.9 shows the lab frame lifetime of 400 MeV, 800 MeV, and 1 GeV H^- ions as a function of magnetic field. From this plot, we can see that even for a 4.5 kG field, the lifetime of an 800 MeV ion is 10's of microseconds. This is compared to the time the ion actually spends in the magnetic field of the c-magnet and ORBUMP of under 10 ns and the time of flight between the c-magnet and stripping foil of under 10 ns.

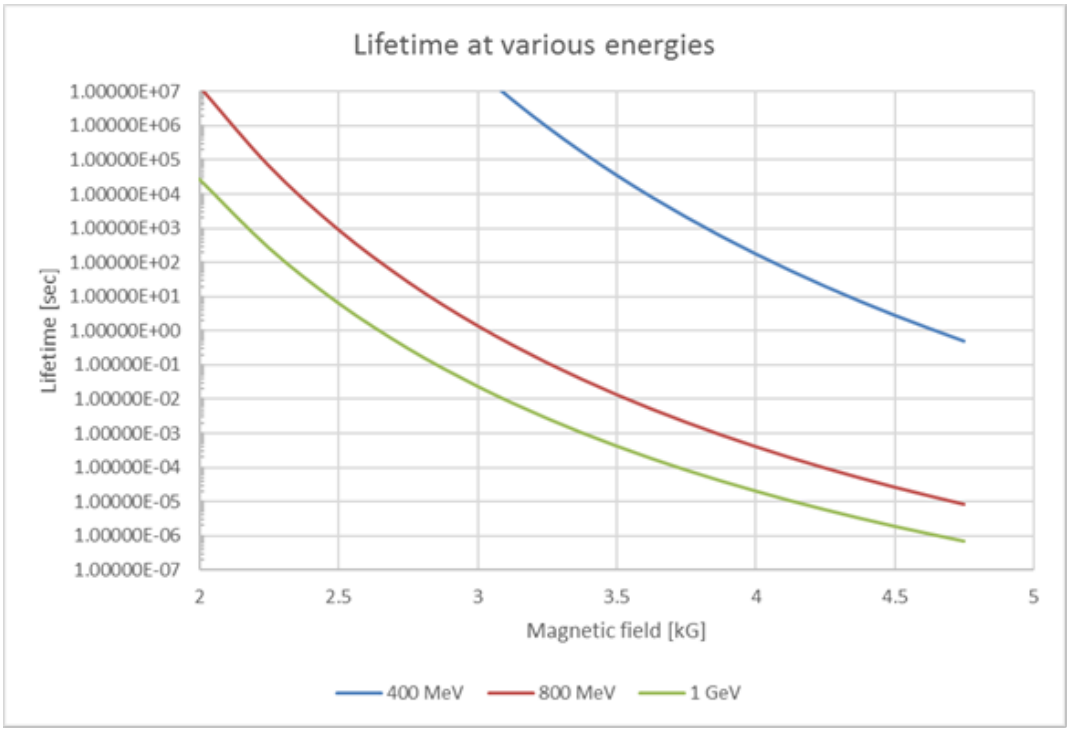

Figure 4.9: Lab frame lifetime of 400 MeV, 800 MeV, and 1 GeV H^- ions as a function of magnetic field.

The injection process starts with ramping the ORBUMP magnets to their nominal excitation which modifies the closed orbit to bring it almost in contact with the stripping foil. The painting magnets are then energized to move the closed orbit further to the position of the injected beam on the foil. All of this is done prior to the injection of the ions. Once the ions start the injection process, the excitation of the painting magnets is collapsed during the injection process. Once the

last ions are injected, the ORBUMP field is collapsed. The magnitude of the closed orbit distortion in the vertical plane due to ORBUMP is 74 mm and that of the vertical painting magnet is 11 mm implying that the injected position of the incoming H^- ions on the foil is at 85 mm above the closed orbit. Figure 4.10 shows the vertical closed orbit in the injection straight due to the ORBUMP and the vertical painting magnets.

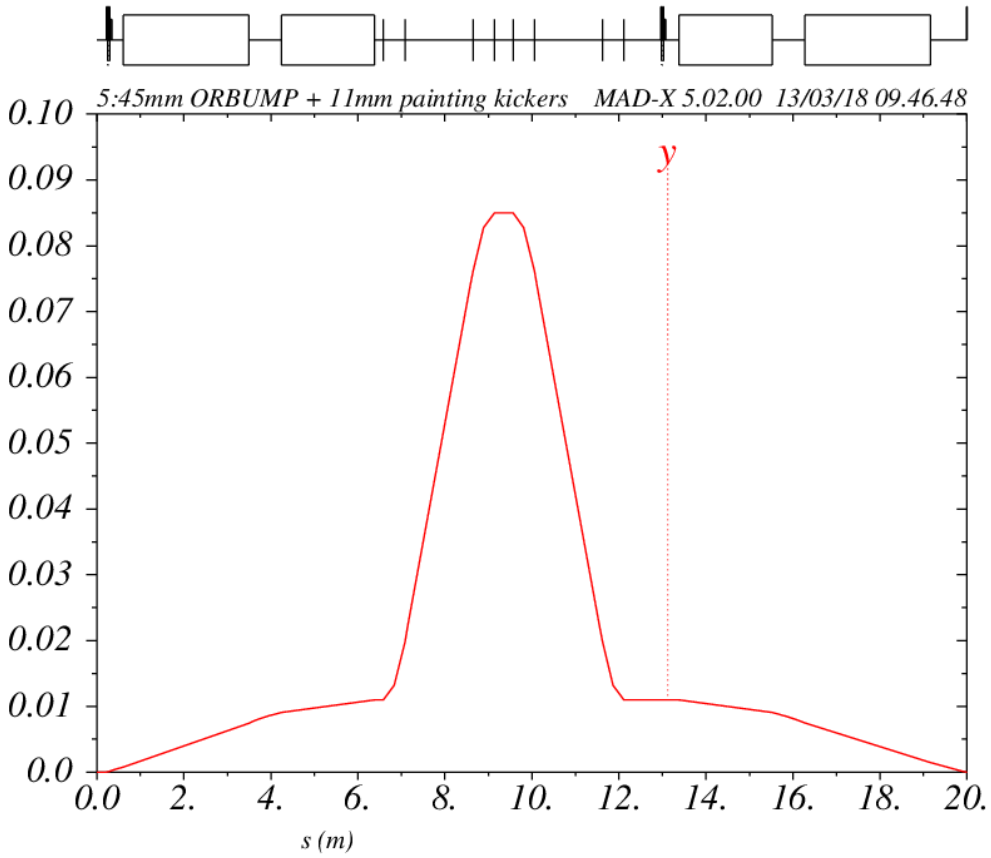

Figure 4.10: Vertical closed orbit at the start of injection due to ORBUMP and vertical painting magnets.The units on the vertical axis are in meters.

The vertical painting magnets that make up a 4-bump are located outside of the injection region, in the short straight section and the space between the F and D gradient magnets on either side of the injection straight shown in Figure 4.11.

The required angle of the first and last painting magnet is approximately 2 mr with the inner angles being < 1 mr. For an effective length of 0.2038 meters, this corresponds to a field of something shy of 500 Gauss. The engineering design of the painting magnets has not been finalized.

Horizontal painting is required to move the beam 6.1mm onto the foil based upon current simulations, about half the distance required in the vertical plane. Painting in both planes will be optimized to minimize the space-charge effects.

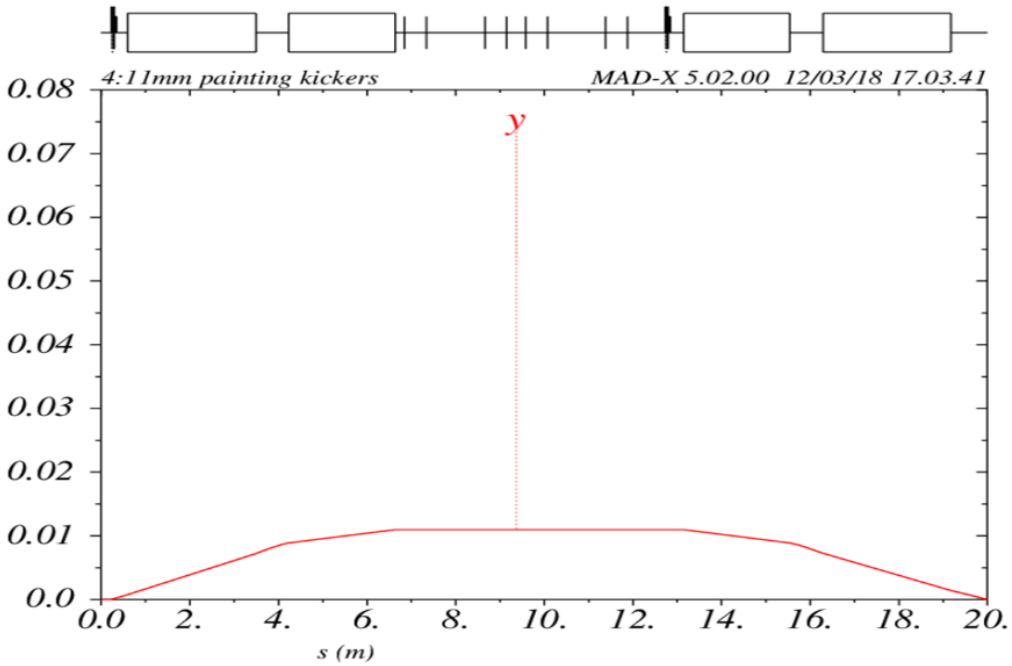

Figure 4.11: Closed orbit due to vertical painting magnets.

4.3 Resonant magnet upgrade

4.3.1 Booster magnets

The Booster gradient magnets are placed on girders and are part of a cell which consists of one defocusing D and one focusing F magnet, a choke and a capacitor bank. Two magnet girders form one period in the Booster lattice and since the Booster lattice consists of 24 periods, there are 48 total cells in the Booster Ring.

A picture of a Booster cell is shown in Figure 4.12. Each of the Booster cells forms a resonator that currently resonates at 15 Hz.

An equivalent electric model of one Booster module is shown in Figure 4.13. Power for the Booster magnets is supplied by the Gradient Magnet Power Supply (GMPS). This supply is really four programmed solid-state power supplies, each of which powers twelve resonant cells.

The Booster power supplies generate a current of the form:

$$I = I_{dc} - I_{ac}\cos(2\pi f t) \tag{4.1}$$

Both the DC and AC current components are generated simultaneously through the use of Silicon Controlled Rectifier (SCR) supplies. The system is resonant; that is, energy is exchanged between the magnets and the capacitors banks, with the power supply making up the losses. A distributed choke system is used to bypass the DC current around the capacitors and for coupling between the

different resonant modules. A schematic of the Booster Gradient Magnet Power Supply System is shown in Figure 4.14

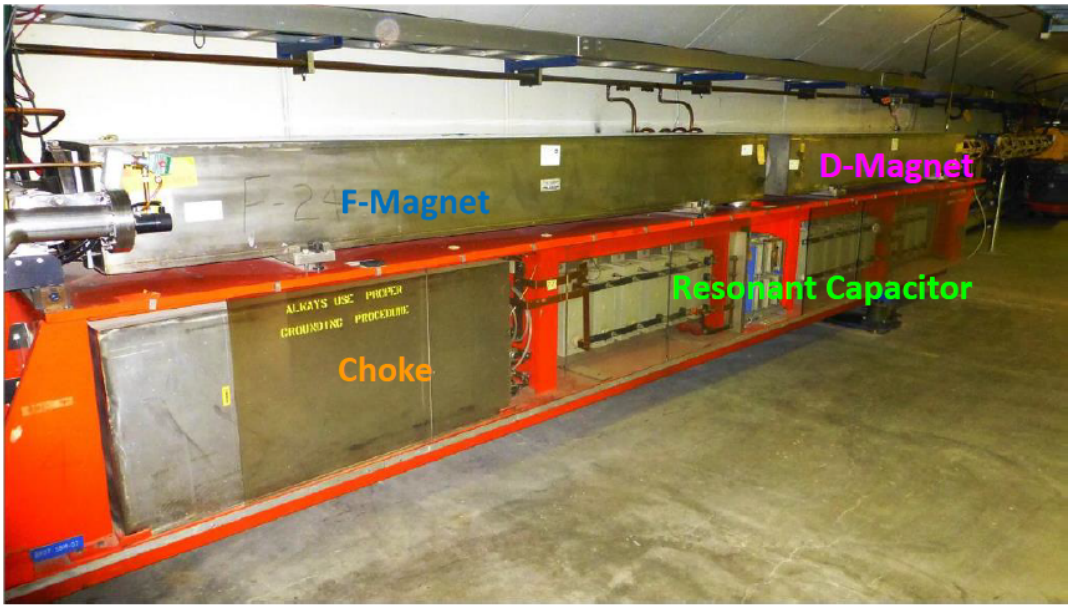

Figure 4.12: Picture of a Booster girder with the two Gradient magnets the Choke and the Capacitor Bank.

4.3.2 Booster 20 Hz magnet upgrade

In order to understand the Booster magnet operation at 20 Hz instead of 15 Hz a series of measurements were performed on both a Booster gradient magnet and a Booster choke. The results of measurements are shown in Figure 4.15. The reduced current in the right plot is the result of the larger inductance of the choke.

The measurements suggest that running the Booster magnets at 20 Hz with a current equal to the present 15 Hz will require about 3.9% more power. Capacitor voltage will increase by about 32% and the resonant capacitor at each module must decrease from 8.33 mF to 4.69 mF.

The present Booster power supply system is capable of higher voltage/Power operation. Currently only 3 out of the 4 supplies are used for operation but the 20 Hz operation will require the use of all 4 supplies.

The capacitor bank in each Booster cell is to be replaced with a new one able to operate at the higher voltages.

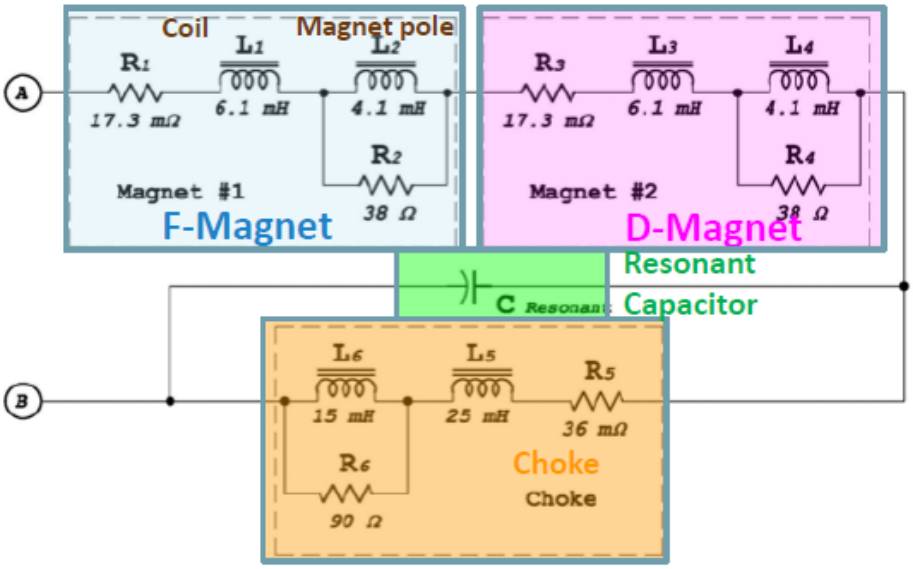

Figure 4.13: Equivalent electric circuit of a Booster module.

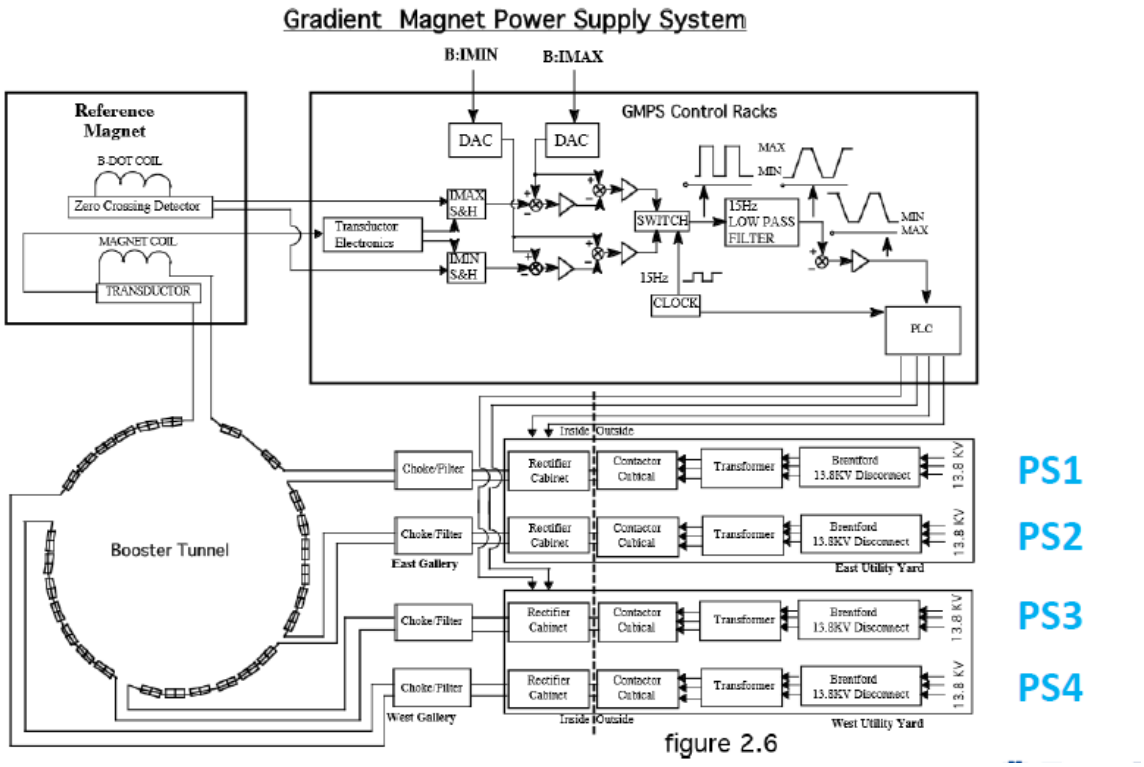

Figure 4.14: Booster Gradient Magnet Power Supply System.

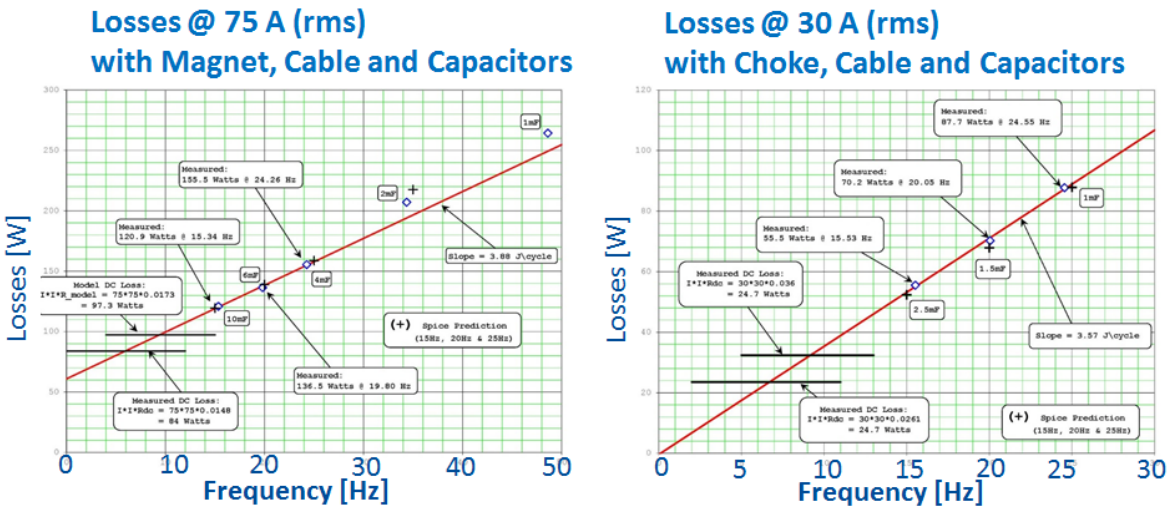

Figure 4.15: Losses vs frequency for a Booster magnet (left) and a Booster choke (right).

4.4 Booster power supply upgrade

4.4.1 Booster power supplies

All the Booster pulsed devices along with their power supplies should be able to operate at 20 Hz. A new injection girder will be required for injection from the PIP-II Linac. New orbit bump (ORBMP) magnets will be developed for the new injection girder and will require new power supplies.

The Booster extraction kickers will operate at a larger average anode current (from 15 mA at 15 Hz to 20 mA at 20 Hz). These currents are well within the allowed 2 amp maximum average anode current limit for the thyratrons. Average power into the resistive loads will rise from ∼400 watts to ∼540 watts under the same conditions but no issues are anticipated since they are already water cooled. The kicker power supplies have been modified as shown in Figures 4.16 and 4.17 and tested at 20 Hz with no issues. The Booster septa magnets were thermally tested at higher rms currents and no issues were found except at the area where the power feed-throughs enter and exit the magnet. This was addressed with the addition of external cooling plates. The septa pulsed power supplies were designed to handle higher operating voltages at 15 Hz but additional cooling will be required to operate at 20 Hz.

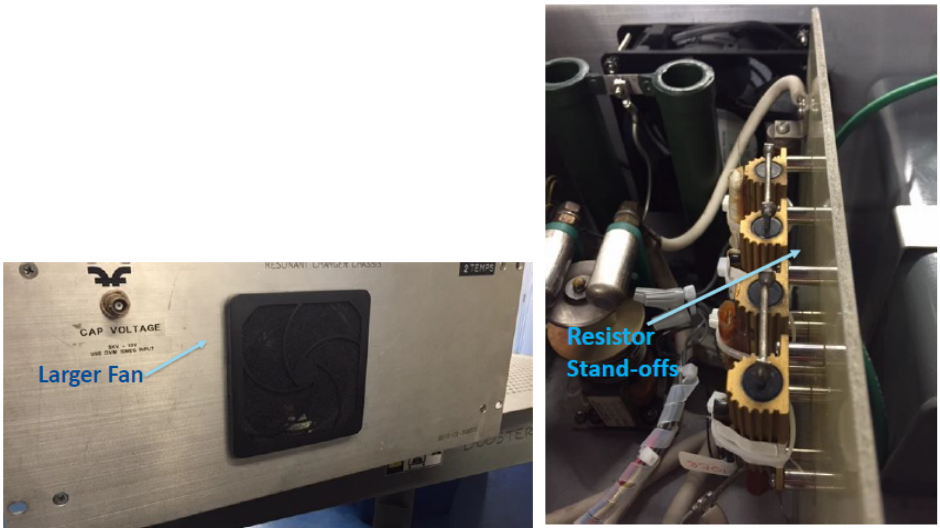

Figure 4.16: Kicker power supply chassis modifications for running at 20 Hz.

Figure 4.17: Picture of two septa magnets

4.5 Main injector RF upgrades

4.5.1 Current main injector RF

Currently the Main Injector RF system consists of twenty RF cavities powered by an Eimac Y-567B power tetrode. A picture of the current Main Injector RF cavity is shown in Figure 4.18. The cavity power amplifier (PA) with the Eimac Y-567B tube is shown in Figure 4.19. These RF cavities are used to accelerate 5.0×10^{13} protons from 8 to 120 GeV with a maximum acceleration rate of 240 GeV/sec.

For PIP-II we will need to accelerate 50% higher beam intensity with the same acceleration rate. The beam power capabilities of the current RF cavities compared with the PIP-II requirements are shown in Table 4.1. As we can see from Table 4.1 the current Main Injector RF system does not have enough power to accelerate the required PIP-II beam intensity.

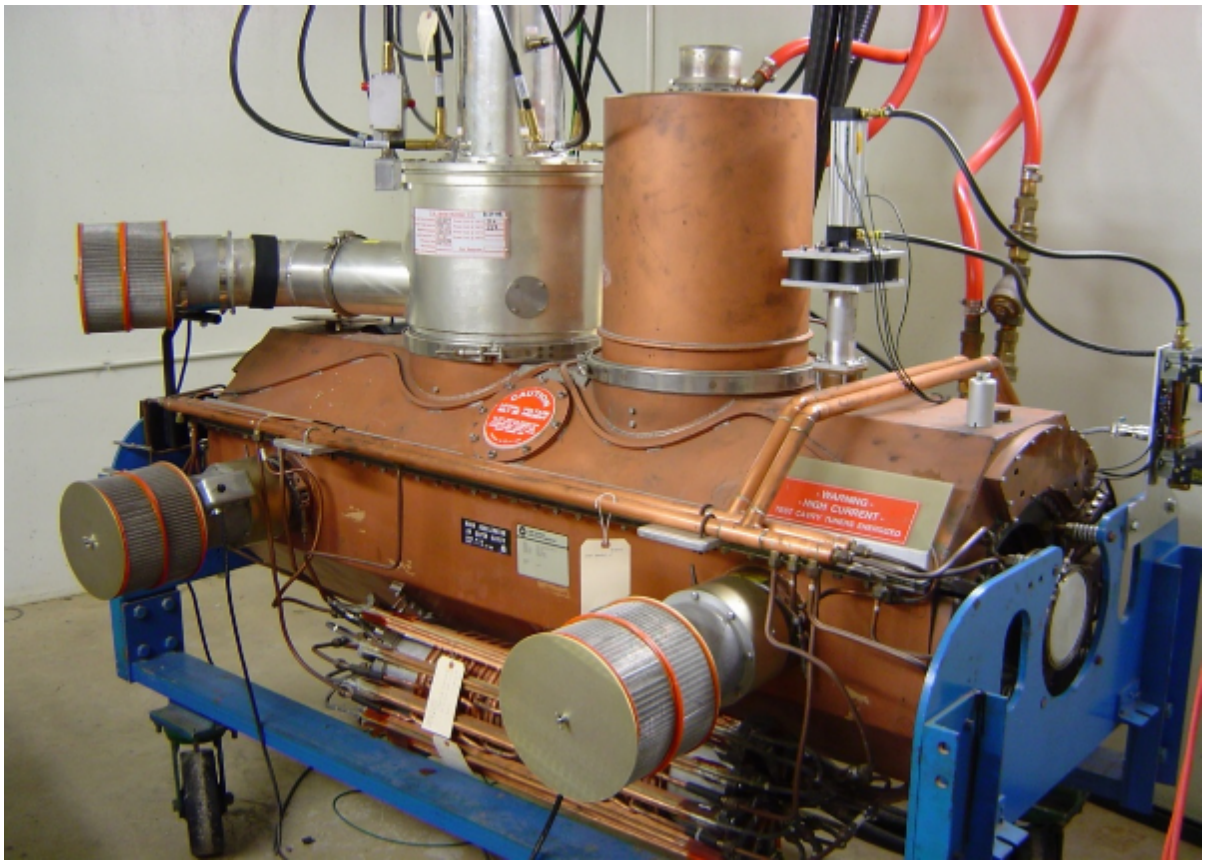

Figure 4.18: Present One Power Amplifier Main Injector Cavity.

Figure 4.19: Main Injector Power Amplifier, Eimac Y-567B Power Tetrode

Table 4.1: Power Calculations

	PIP-II	Main Injector - Present Capability
Beam Intensity	7.5×10^{13} protons	6.24×10^{13} protons
Harmonic Number	588	588
Number of Filled Buckets	504	504
Frequency	52.808-53.104 MHz	52.808-53.104 MHz
Acceleration Ramp Slope	240 GeV/s	240 GeV/s
Beam Intensity	7.5×10^{13} protons	6.24×10^{13} protons
Main Injector Ramp Rate	1.2 s	1.2 s
Beam Power at 120 GeV	1.2 MW	998.8 kW
Beam Accelerating Power	2.88 MW	2.40 MW
Number of Accelerating Cavities	20	20
Cavity R/Q	104	104
Maximum Cavity Accelerating Voltage	235 kV/cavity	235 kV/cavity
Operating Peak Voltage	210 kV/cavity	210 kV/cavity
Accelerating Voltage Required: V$\sin\phi_2$	2.66 MV	2.66 MV
Total Accelerating Voltage Available	4.7 MV	4.7 MV
Total Operating Voltage	4.2 MV	4.2 MV
Cavity Power Loss	45.11 kW/cavity	45.11 kW/cavity
Total Apparent Power	240.5 kW/cavity	204.2 kW/cavity
Robinson Stability Factor	4	4

4.5.2 MI RF upgrades

The Main Injector cavity has the capability to add a second PA and operate in a push-pull manner for increased power output. A schematic of an Main Injector cavity with two power amplifiers is shown in Figure 4.20. The modified coupling loop required to run with two PAs is shown in Figure 4.21.

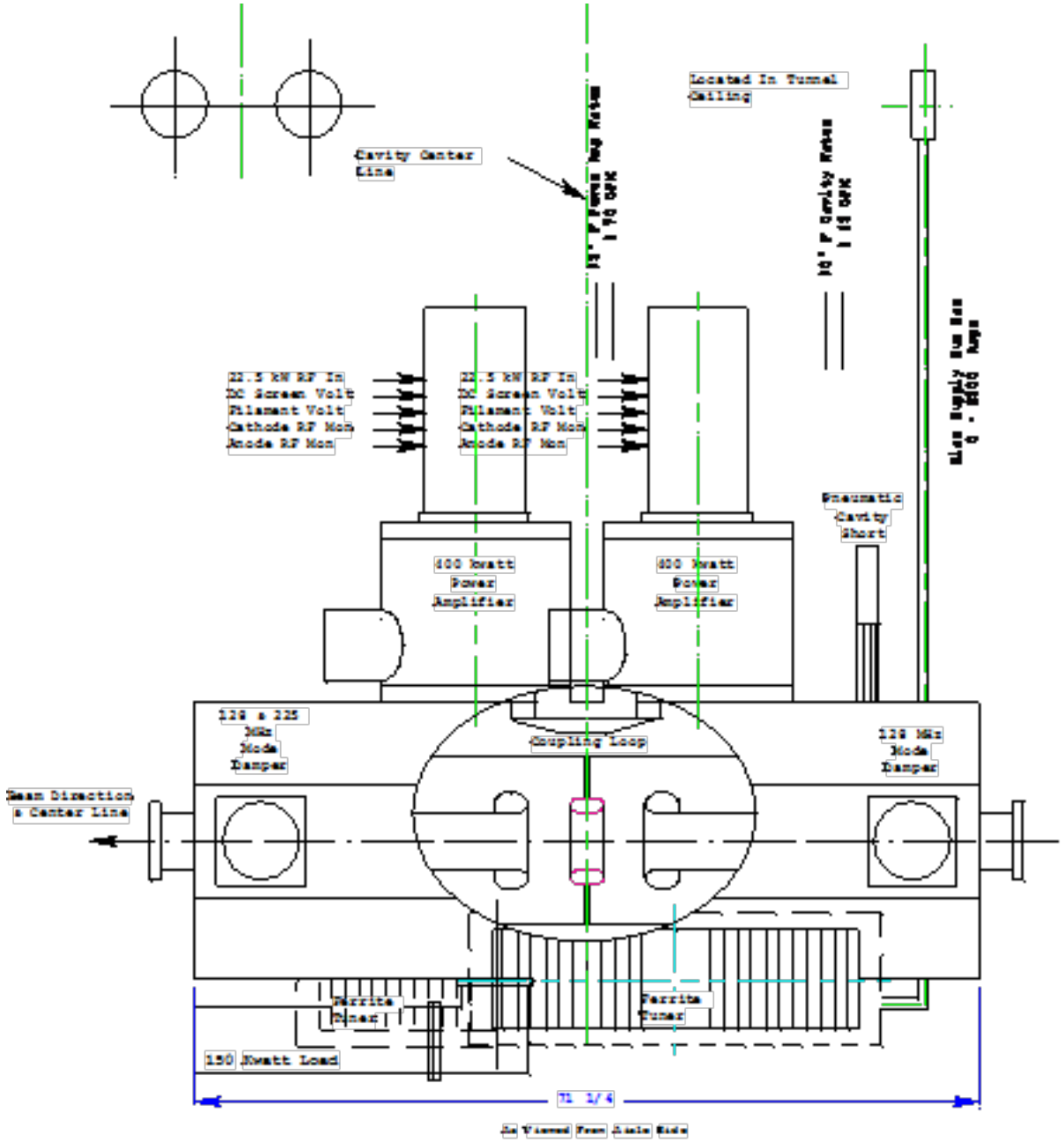

Figure 4.20: Main Injector Cavity Modified with Two Power Amplifiers

This upgrade will require major modifications to the current RF infrastructure. The addition of a PA to the cavity will require the purchase of two new 8 kW solid state amplifiers with each capable of driving the cathode of a PA at 12.5 Ω. The current one-PA 8 kW solid state drive is

Figure 4.21: Two Power Amplifier Coupling Loop

6.25 Ω and will not be reused. Biasing this power tetrode will call for another filament, grid and screen power supply. The anode side of the tube will require a new modulator that is capable of driving two Power Amplifiers but take up the same volumetric space as the old modulator, see Figure 4.22. Additionally, the low-level RF will necessitate the metering chassis being modified to have an output of both 0^0 and 180^0. The last part is to make this operational which will require the interlocking of the new system to the old.

The upgrade plan is to start with a low-level test using two power amplifiers to check for the frequency, quality factor (Q), and step up ratio of the cavity, see Figure 4.23. Once all of this is established, the cavity will be tested under low power conditions in the MI-60 test cave. If this proves to be successful, a cavity from the Main Injector tunnel will be modified and the corresponding equipment will be modified for two PA operations. The objective is to do a proof of principle with the beam before beginning mass production.

The full upgrade will consist of the modification of four cavities during a summer shutdown. The remaining eight stations would be modified during the extended Long-Baseline Neutrino Facility (LBNF) shutdown. The current status of the cavity configuration consists of an installed Mock Power Amplifier with low-level measurements being performed in this configuration.

Figure 4.22: Main Injector Modulator (left)

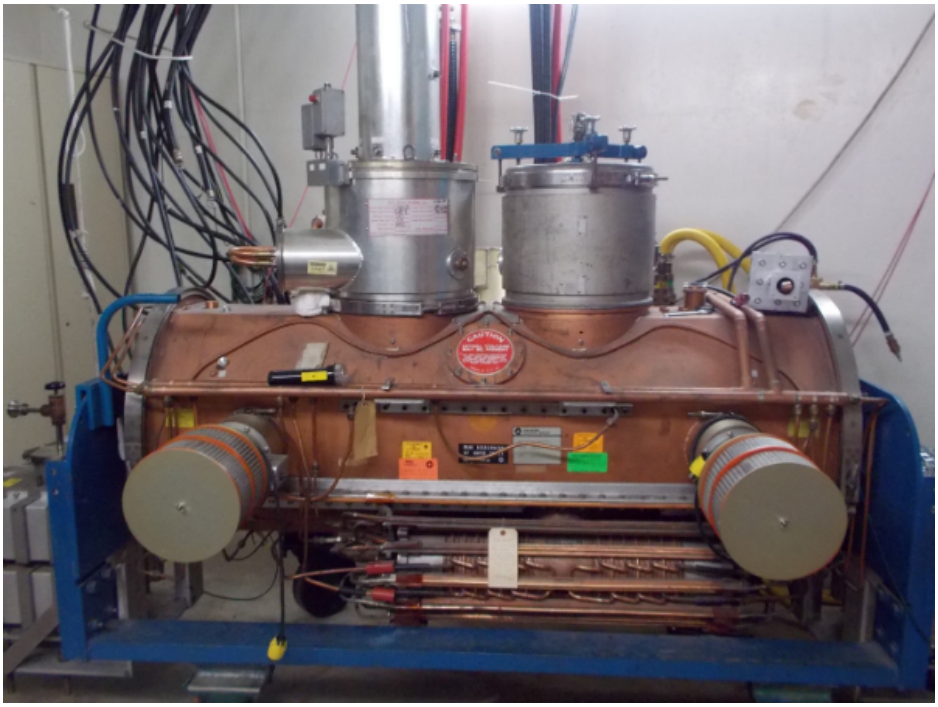

Figure 4.23: Main Injector Cavity with Mock Power Amplifier

4.6 Recylcer RF upgrades

4.6.1 Current Recylcer RF

Currently the Recycler uses three 53 MHz cavities capable of providing up to 120 KV with up to 60% duty factor. They have an R/Q 13 ohms in order to reduce the transient beam loading with water-cooled cooling hoops to dissipate the power.

For PIP-II the slip stacking frequency separation will increase to 1680 Hz from 1260 Hz and the bunches will be decelerated to 50 msec instead of 67 msec. In order to maintain the same bucket area during deceleration the required voltage will be increased to 140 KV. In addition the support of Main Injector operations down to 60 GeV will be needed which will require the RR slip stacking cavities to operate in CW, which is not possible with the current cavities.

4.6.2 Recycler RF upgrades

A new 53 MHz cavity has been designed with a $\frac{R}{Q}$ of 45. These cavities will be capable of operating at higher voltages and continuous operation. A schematic of the new cavity is shown in Figure 4.24. In the fall of 2017, a prototype cavity was fabricated, shown in Figure 4.25. The prototype Q and shunt impedance measurements agree very well with models as shown in Tables 4.2 and 4.3.

Table 4.2: Comparison of Theoretical and Experimental Q Data

Mathematica Transmission Line Model: Q = 16,283
CST Microwave Studio Model: Q = 15,860
Prototype Cavity Measurement: Q = 14,715

Table 4.3: Comparison of Theoretical and Experimental Shunt Impedance Data

Mathematica Transmission Line Model: 700.2 kΩ
CST Microwave Studio Model: 705.8 kΩ
Stretched Wire Method on Prototype Cavity: 717.5 kΩ

A perpendicularly biased tuner is being fabricated to verify the needed frequency sweep for slipping. Current plans for the tuner are to use twelve 1 cm thick TCI Ceramics AL-0400 garnets.After verifying the tuning with the prototype cavity the plan is to build a preproduction RR cavity which will be fully tested before proceeding with the fabrication of the additional two cavities.

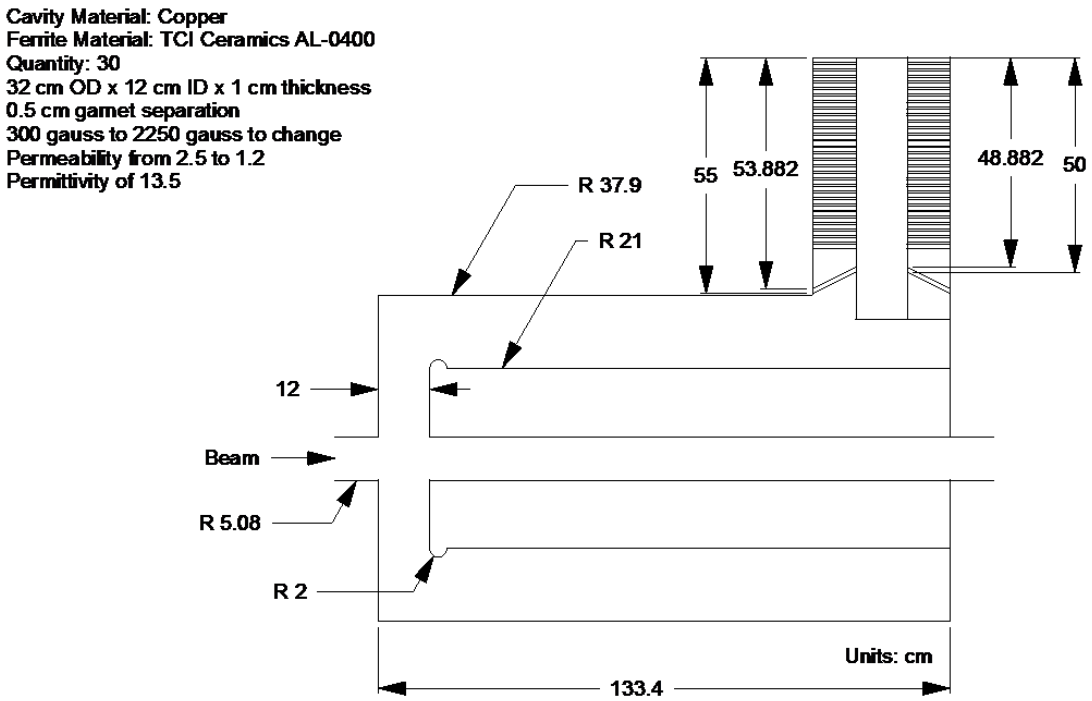

Figure 4.24: Recycler 53 MHz Cavity with a R/Q of 45

Figure 4.25: Prototype of Recycler 53 MHz Cavity with a $\frac{R}{Q}$ of 45

4.7 Transfer line and beam absorber

4.7.1 Linac-to-Booster beam transport

4.7.1.1 Particle loss and limitations on beam transport parameters

The primary loss mechanisms for 0.8 GeV transport are the H^- intrabeam stripping, Lorentz stripping, inelastic beam-gas scattering, and scraping of beam halo on the apertures. Stripping due to black-body radiation inside the room temperature beam pipe is negligible at this energy. The intrabeam stripping in the Linac results in an acceptable loss rate even in the case of CW beam. The strength of transverse focusing in the beam line is similar to the focusing strength at the Linac end. Consequently, the beam loss at the transfer line beginning is close to the beam loss at the Linac end. The particle momentum spread leads to natural debunching in the course of beam transport from the Linac to Booster. This results in a bunch length increase by more than an order of magnitude (the rms length is increased from 1.1 mm to about 14 mm), and, consequently, a reduction of intrabeam stripping inversely proportionally to the bunch length. This yields a negligible intrabeam stripping loss of about 0.1 mW/m at the transport line end for a 1% duty factor. Note that this 1% duty factor is used for the beam injection to the Booster and the major part of the line sees this beam only; while the initial part of this line is also planned to be used for beam transport to an upgrade of the Mu2e experiment requiring 100 kW beam. Consequently, a maximum beam loss of up to 5 mW/m is expected. Beam motion in a magnetic field excites an electric field in the beam frame. If this electric field is sufficiently strong, it can detach a weakly bound outer electron (Lorentz stripping) from the H^- ion. The results of experimental measurements for H^- lifetime are presented in Ref. [48] and can be approximated by the following equation:

$$\tau_E(E) = \frac{A\tau}{E} e^{B_\tau/E}$$

where $A_\tau = 2.47 \cdot 10^{-8}$ cm. Figure 4.26 shows the corresponding loss rates per meter for a 0.8 and 1 GeV H^- beams as a function of magnetic field. The magnetic field in the dipoles of the transfer line is chosen so that the loss rate would not exceed 10^{-8} m^{-1} for a beam of 1 GeV energy. This corresponds to a limit of 2.77 kG equivalent to a bending radius of 20.431 m. Keeping the same radius of curvature for the 0.8 GeV beam, one obtains a limit for the magnetic field in the dipoles of 2.39 kG with a loss rate of 3×10^{-13}.

The loss rate due to H^- scattering on residual gas molecules is proportional to their density and their ionization cross sections. The cross sections decrease proportionally to β^{-2} and therefore are weakly dependent on the beam energy for energies about or above 1 GeV. The cross section of H^- stripping for 0.8 GeV beam on residual gas is about 10^{-19} cm^2 for atomic hydrogen and 7×10^{-19} cm^2 for atomic oxygen and nitrogen and grows somewhat slower than proportional to Z for heavier atoms [49], [50]. The requirement of less than 10^{-8} m^{-1} for the partial loss rate yields a vacuum requirement of 10^{-8} Torr or better for H2 and about an order of magnitude

better for heavy molecules (hydrocarbons, water, etc.). Consequently, an application of vacuum practices developed at Fermilab for not-baked vacuum systems, which routinely achieve low 10^{-8} Torr, should be sufficient.

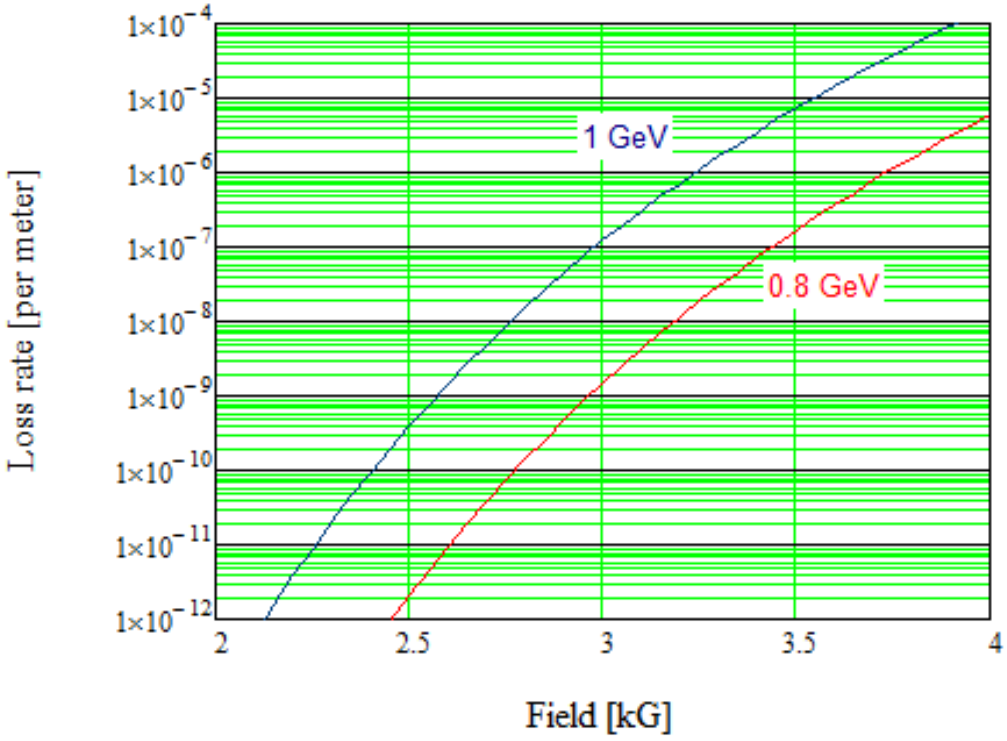

Figure 4.26: Fractional loss due to Lorentz stripping for 0.8 and 1 GeV H^- beams traveling in a dipole field.

4.7.1.2 Linac-to-Booster transfer line

The Linac-to-Booster Transfer Line transports the beam from the exit of the SC Linac to the injection girder of the Booster. Figure 4.27 shows the transport line layout. The transport line has two arcs and a straight section connecting them. In this straight section the Booster line splits into two additional lines. One goes to the Linac beam dump and the other one goes to the Mu2e experiment which in a future upgrade is expected to receive 800 MeV beam from the SC Linac.

As can be seen in Figure 4.27 the second arc crosses the Tevatron tunnel. In the vicinity of this crossing, the line has a local vertical bump bringing the line close to the Tevatron tunnel ceiling. This is done to allow a free passage for personnel and equipment along the Tevatron tunnel, which contains the operating 120 GeV transfer line. This line brings beams extracted from the Main Injector to the Fermilab Test Beam Facility and is scheduled to be still in use at the time of PIP-II operations.

The SC Linac beam is at the same elevation as the Booster beam; 726.48 ft. (221.431 m) above sea level. The Linac beam is at 1.300 m above the Linac floor. This translates to a floor elevation

of 722.215 ft. (220.131 m) above sea level. The tunnel floors for the SC Linac, Transfer Line, and Tevatron are at the same elevation. The injection into the Booster is vertical using a C-dipole magnet. At its entrance, the beam orbit is located 33.6 cm (13.23 in.) above the Booster orbit. The angle difference in the horizontal plane between the Linac direction and the Booster injection straight is around -210 degrees. This bending angle is produced by thirty-two identical 2.45 m long dipoles with a 2.406 kG field. These dipoles are connected serially and are split into two families powered by two power supplies. One power supply supports the beam transport to the beam dump, and another one supports the beam transport through the rest of the line to the Booster.

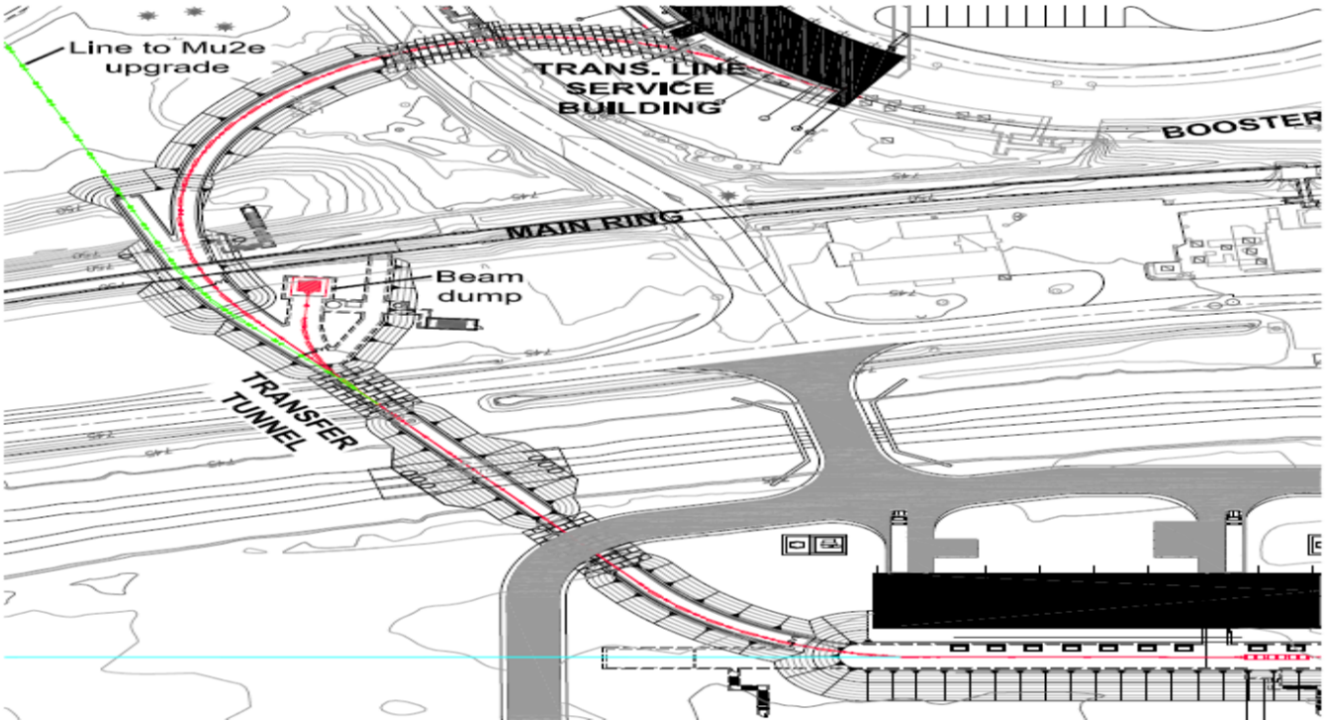

Figure 4.27: Layout of the beam transport line from the SC Linac to Booster. The Linac beam dump and future transport line to the Mu2e upgrade are also shown.

The transport line has two arcs and a straight section connecting them. The cartoon plots in Figure 4.28 to Figure 4.32 show the sections of the Linac-end, first arc, the straight section, the second arc, and the dump line, respectively. Figure 4.28 shows the first section of the transfer line which is located in the extension of the Linac tunnel. This is reserved for a future energy upgrade and includes four periods with doublet focusing and the same period length as in the HB section of the Linac. Such choices enable an installation of up to four additional HB650 cryomodules in the future, upgrading the Linac energy to about 1.2 GeV.

To simplify Linac commissioning, a small power (∼5 kW) removable beam dump will be installed downstream of the Linac at the very end of the Linac tunnel. Steering and focusing on the dump will be performed by correctors and quadrupoles at the end-of-Linac line.

The momentum spread of the Linac beam is sufficiently small therefore, RF debunching is not planned and consequently, no debunching RF cavities are presently anticipated. However, there

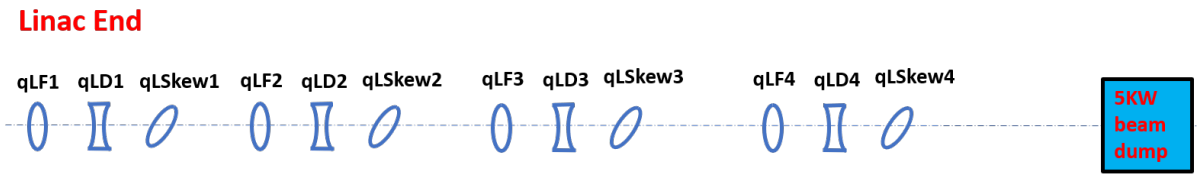

Figure 4.28: Linac end

is sufficient space for debunching cavities should they be needed in the future. A FODO lattice is used for the rest of the beam transport. The period is chosen to keep the dispersion and beta-functions comparable to their values in the SC Linac and Booster. Geometrical constraints set the cell length to about 11.8 m.

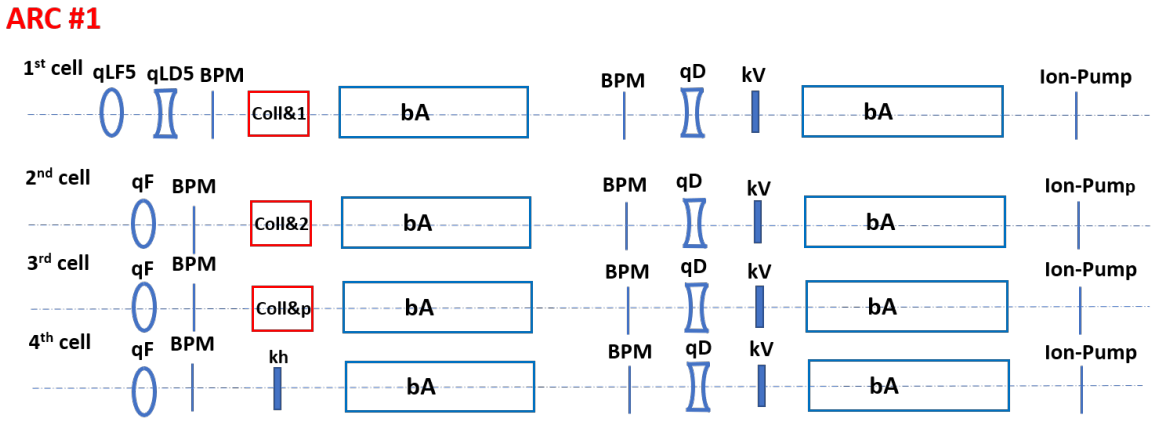

Figure 4.29: First ARC, composed of 4 FODO cells

Figure 4.29 shows the first arc, which consists of four FODO cells. Each FODO cell has 90° and 111° horizontal and vertical phase advances, respectively, in order to cancel the dispersion in both planes at the end of the arcs. The cells in the straight section and in the arcs are identical except that in the arc cells the dipoles are inserted between the quadrupoles. This choice automatically ensures that the arcs and straight sections are matched to each other, and allows all focusing (defocusing) quads to be connected serially and powered from two power supplies: one for focusing and one for defocusing. The two arcs are composed of four and twelve cells and are both achromatic. The straight section connecting them consists of eight cells. Low power adjustable collimators are installed at the beginning and at the center of the first arc. Two collimators at the beginning of the arc (each collimating on both sides for both the vertical and horizontal planes) separated by one cell remove particles having large betatron oscillations. Another collimator installed in the arc center, where the maximum dispersion is achieved, is used for momentum collimation. The length allocated for each collimator is about 1 m. Since each arc cell includes two dipoles, the packing factor of the arcs is 42%. This choice leaves sufficient space for horizontal and vertical correctors after each focusing and defocusing quadrupole, respectively, as well as for ion pumps, BPMs and other instrumentation, such as loss monitors, wall current monitors, multiwires, etc. This space can also be used for installation of debunching RF cavities and additional collimators if needed. The integrated strengths of the quadrupoles are set by the constraints on the phase advances per cell and are about 0.25 m^{-1} and -0.28 m^{-1} for the focusing and the defocusing quads, respectively . The specifications of the quads are L=0.2 m, G=0.60882 kG/cm for the focusing

quad and G=-0.69057 kG/cm at E=0.8 GeV for the defocusing quads. For the particles of E=0.8 GeV, (Bp)=4882.89348 kG.cm, β=0.841637261, γ=1.85170351, (βy)=1.55846267).

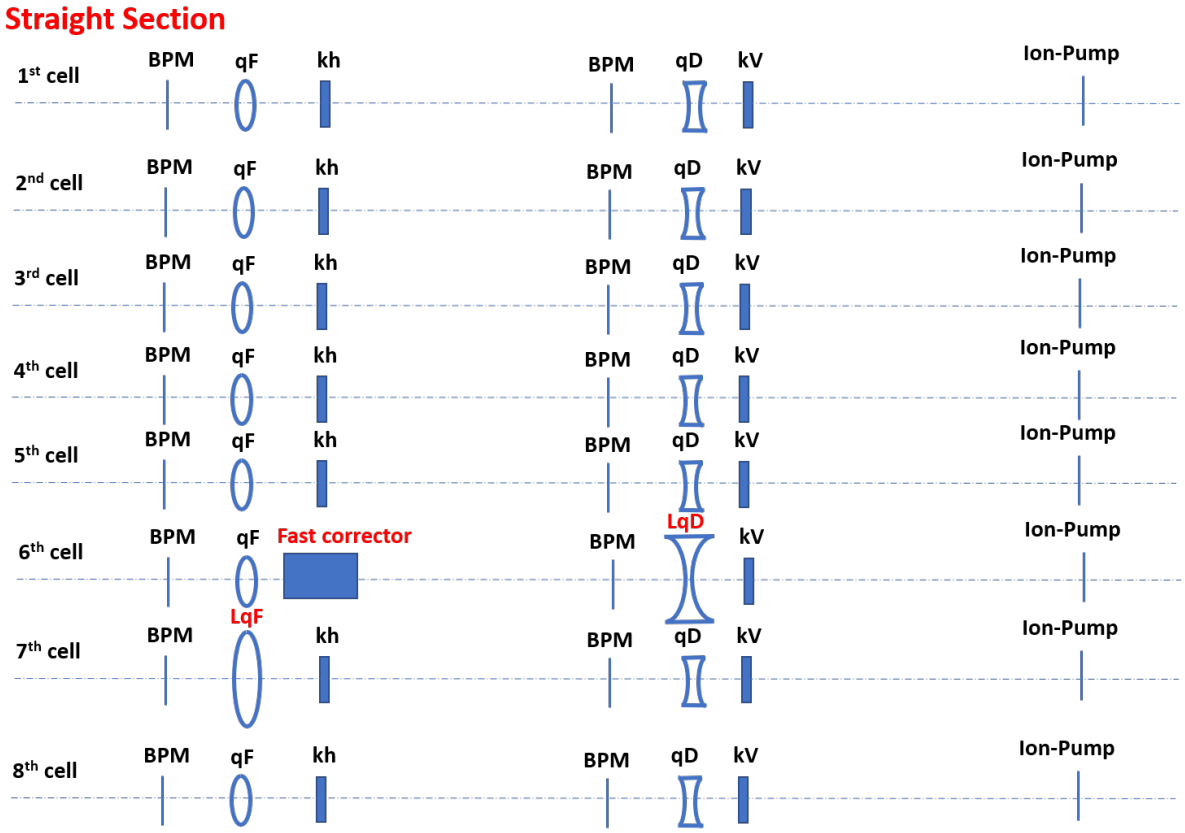

Figure 4.30: Straight section connecting ARC #1 and ARC #2

The straight section is composed of eight FODO cells, which connect the first arc and the second arc. Notice that a fast corrector is located after the focusing quad in the 6th cell which is the start of the beam switch system which switches the beam from the Booster line to the Dump line or to the line going to the future upgrade of the Mu2e experiment. The defocusing quad in the 6th cell and the focusing quad in the 7th cell are large aperture quads, with half of the magnetic field strength, but double the length (0.4 m) of the regular quads. The specifications of these magnets will be explained in the description of the dump line.

The second arc of the Transfer Line crosses the Tevatron tunnel. To create the vertical bump mentioned above, the first few dipoles of the second arc are rolled around their longitudinal axis in order to increase the beam elevation from 1.3 m to about 2.4 m at the location of the crossing. A roll of a few other dipoles before and after the crossing returns the beam to the Linac elevation. This vertical bump creates vertical dispersion and perturbs the horizontal dispersion. Therefore, in addition to bringing the line to the Linac level, rolls of these dipoles are adjusted to cancel both dispersions. Note that the choice of the phase advances was also driven by the necessity of dispersion cancellation. Note also that the dipoles have sufficiently small focusing, and therefore their rolls do not produce measurable x-y coupling.

The last straight section of the Transfer Line is downstream of the second arc and is aligned with the Booster injection straight. At its beginning, this line has the same elevation as the Booster

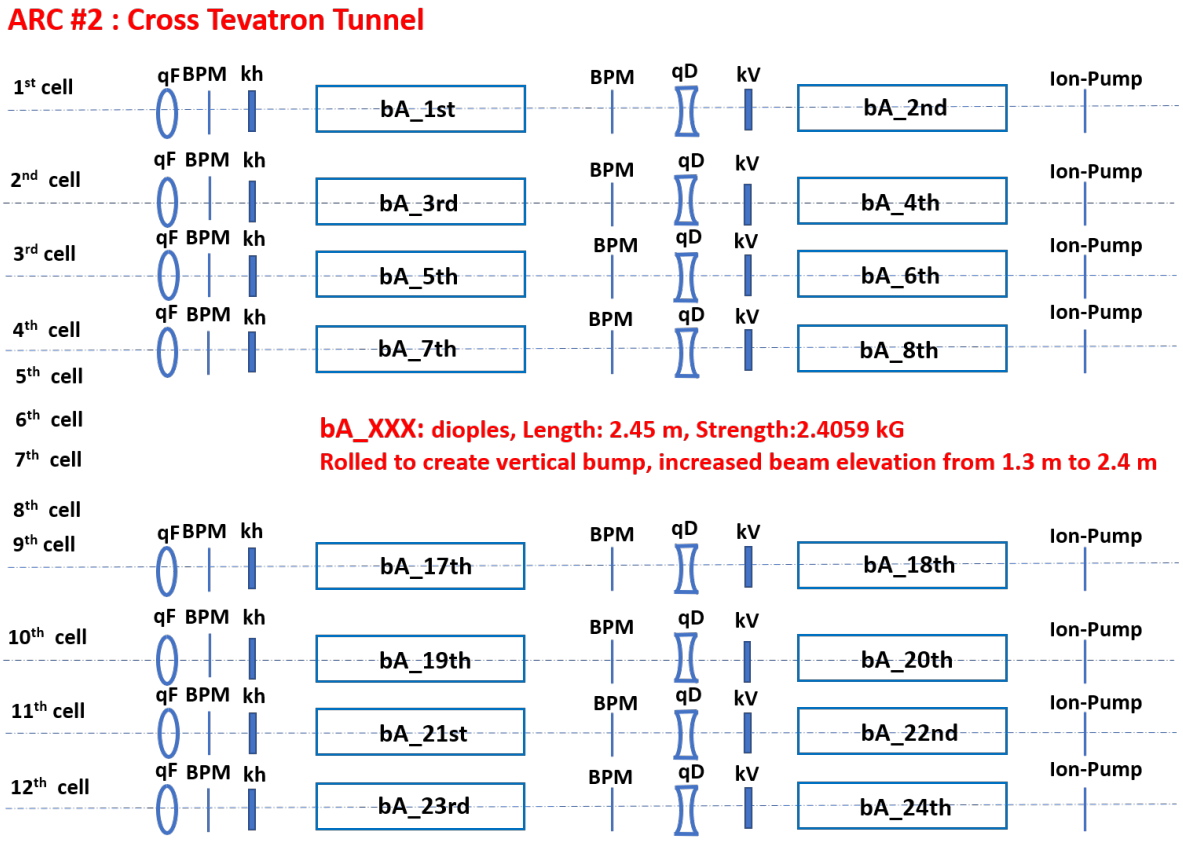

Figure 4.31: Second ARC.

and the SC Linac. The Booster injection is in the vertical plane with a C-Dipole bending the beam downward into the Booster as shown in Figure 4.32. To bring the beam to the elevation of the C-Dipole a vertical dogleg is created, using two bending dipoles with a length of 1.8 m and a magnetic field of 2.475 kG with a bending angle of 5.227 deg (0.091 rad). A triplet is placed after the second vertical dipole to match the line Twiss parameters to the values required for efficient injection into the Booster. The first magnet in the Booster ORBUMP will be acting as a dipole to bend the beam into the center of the stripping foil. The lattice fuctions of the Transfer Line are shown in Figure 4.33.

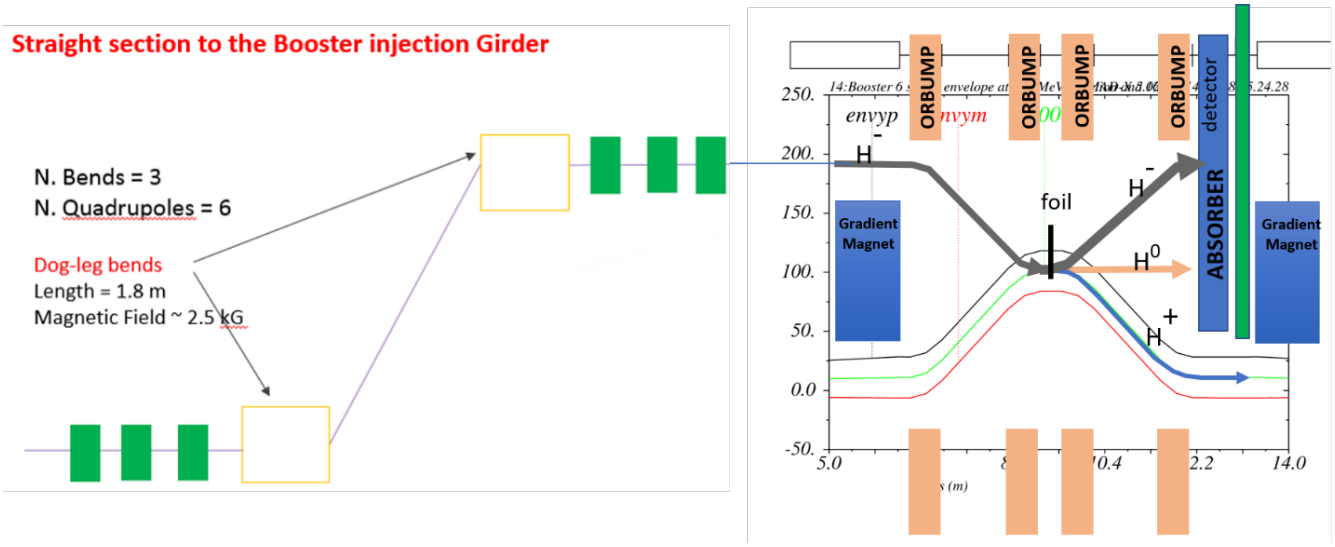

Figure 4.32: Schematic layout of the injection beam line

4.7.1.3 Beam switching system

A beam switching system is installed in the sixth and seventh cells of the straight section (located between the arcs). It consists of a fast corrector and a septum with three apertures. The system can switch the beam from the Booster line to the dump line or to the line going to the future upgrade of the Mu2e experiment. The layout of the switching system along with 10σ beam envelopes is shown in Figure 4.34.

In order to keep the field strength on the beam deflected to the dump less than 2.39 kG, the large-aperture focusing quad LqF will have double the lenght and half the gradient.

4.7.1.4 Beam dump line

The dump line consists of five dipole magnets of the same design as used in the arcs. This deflects the beam horizontally to the beam dump which is placed such that no other beam lines are at distances smaller than 10 m. Beam focusing is provided by alternate focusing and defocusing quads of the same design as used in the arcs, for a total of four. All the magnets in the dump

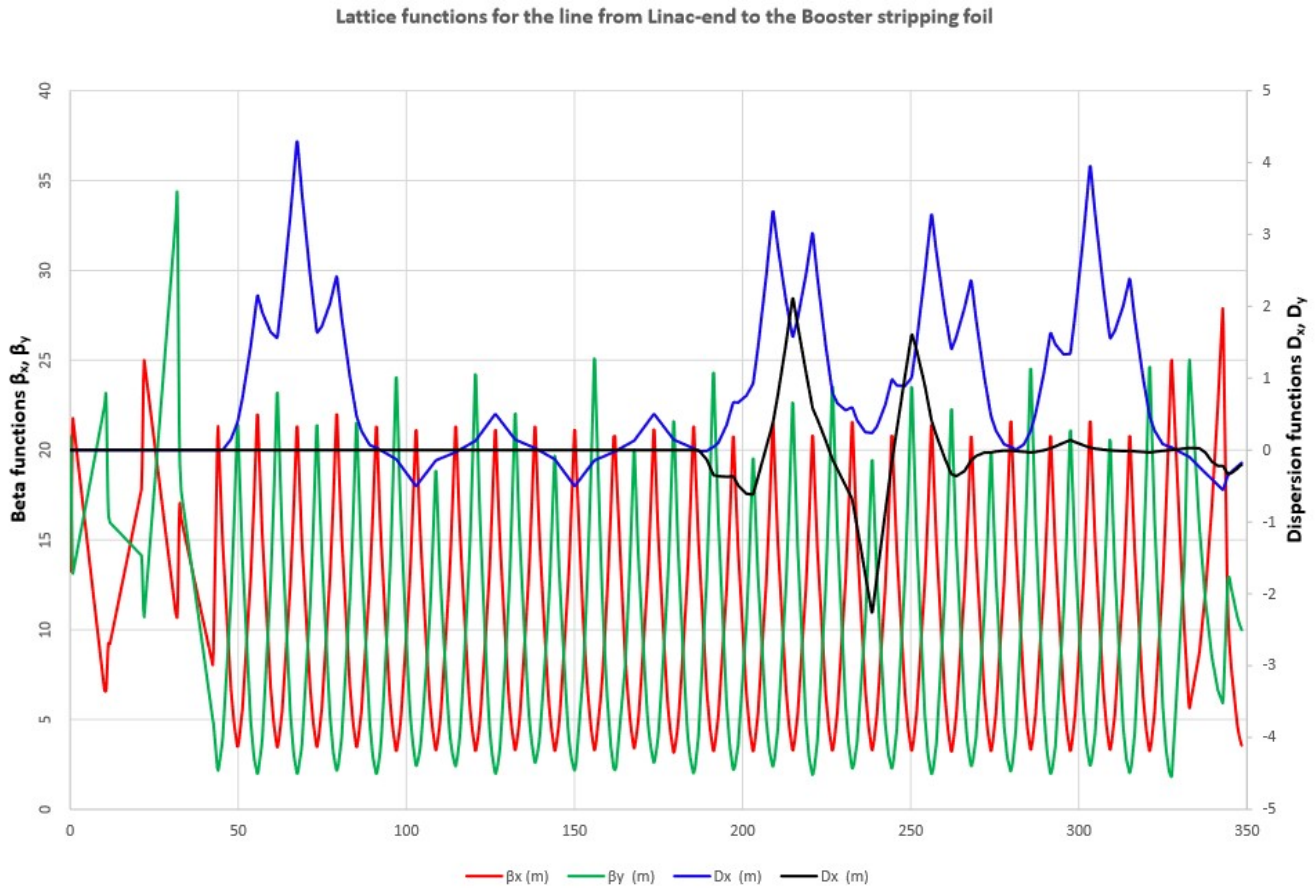

Figure 4.33: Optics of the Transfer Line from the SC Linac end to the stripping target.

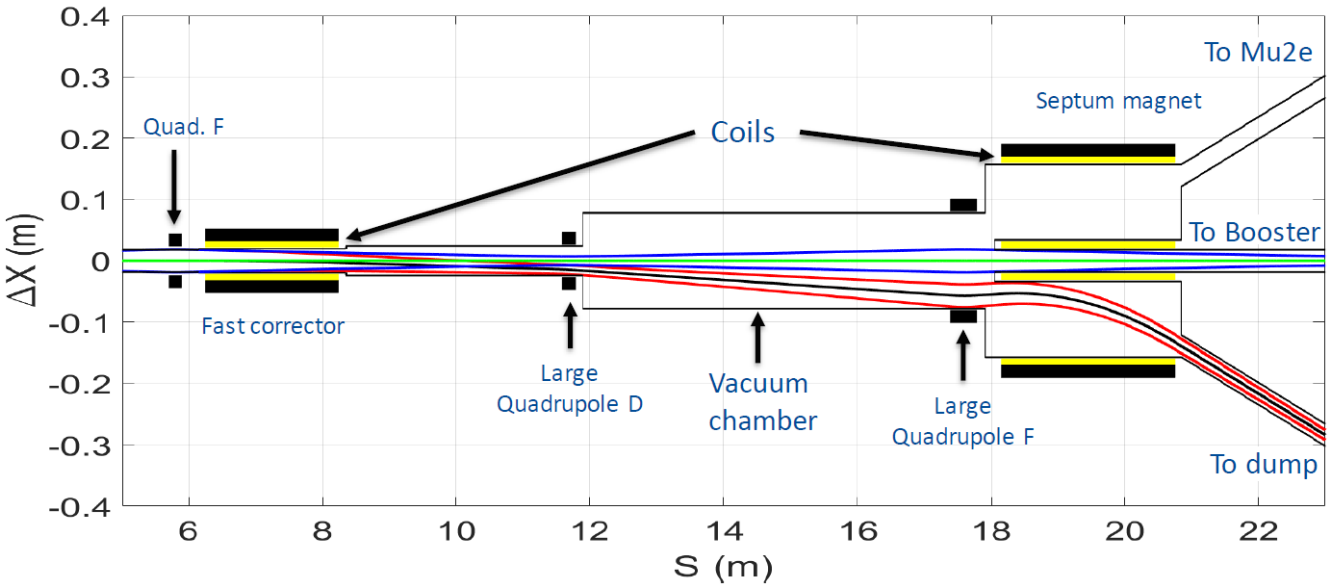

Figure 4.34: Horizontal 10σ envelopes of the beam directed to the Booster (blue) and to the dump (red). An inversion of field polarity for the fast corrector directs the beam to a symmetric trajectory leading to the Mu2e experiment.

line are powered in series with the corresponding families of the transfer line. A sweeping magnet in the long drift before the dump helps to reduce the power density on the dump entrance, see Figure 4.35. The beam dump is rated for 50 kW of 800 MeV beam.

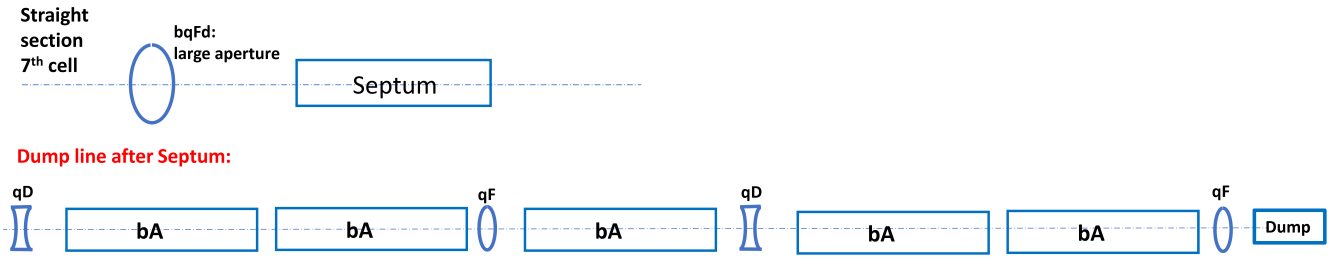

Figure 4.35: Dump line after 7th cell of straight section

Figure 4.36 shows a cartoon of the Dump line after the beam is deflected from a switch magnet (fast corrector). At the end of the dump line, the deflected angle in the x direction is -0.670752 rad (38.43 degree), the offset in the x direction is -10.99 m. A sweep magnet is located 4 m in front of the Dump. In practice, there would be 3 feet (0.9144 m) of concrete placed in front of the core of the absorber with a total drift space of 4.9144 m. The maximum bending angle of the sweeping magnet is 0.02333 rad which results in 0.115 m of the sweeping radius. The angle of the beam injected into the absorber depends on the installation of the sweeping magnet and dump.

Energy deposition simulations using the MARS code show that round beam on the core of the absorber is preferred over rectangular beam. There are four quads in the dump line after the septum. Two families of independently controlled power supplies for these quads allow adjustment

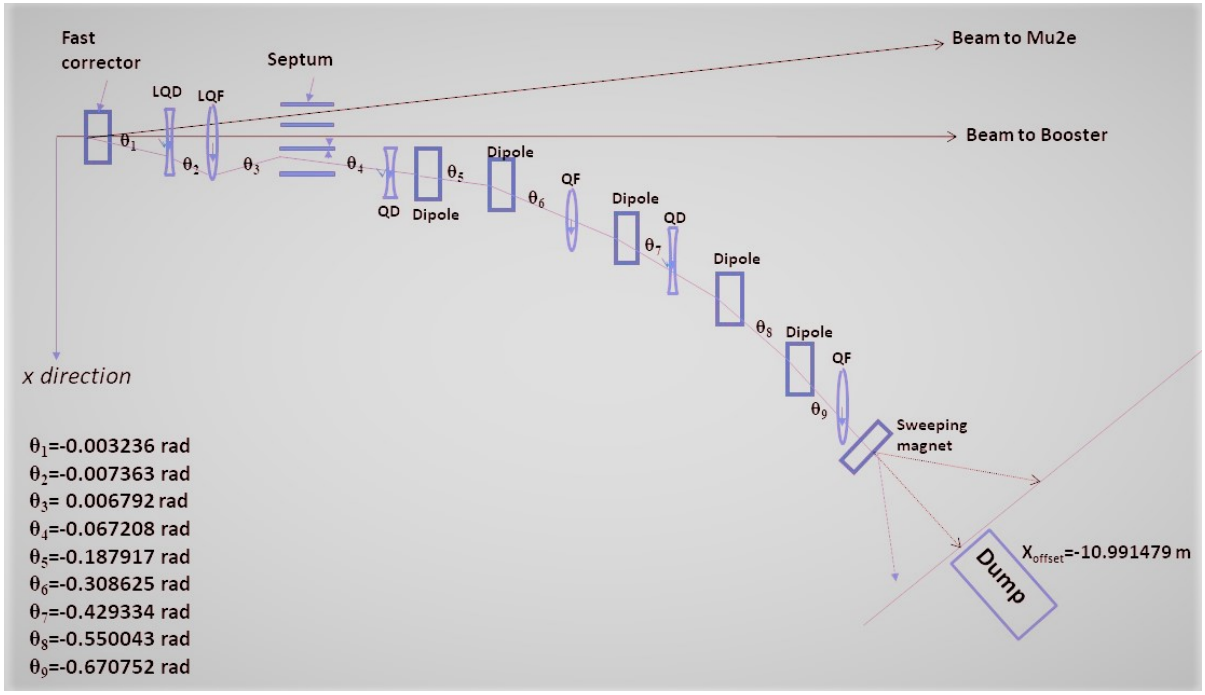

Figure 4.36: Cartoon of the Dump line

of the strengths of the quad magnets to achieve the desired beam sizes at the absorber. Figure 4.37 shows the lattice functions in the dump line after the fast corrector. The requested strength for the focusing QF is 1.877 ($1/m^{-2}$) and -1.600 ($1/m^{-2}$) for the defocusing quad QD. In this case, the beam at the core of the absorber is round and the size is 2.483 mm. Checking the aperture in the dump line, the maximum beam size is 2.918 mm at the entrance of the last focusing quad QF (βx=53.053 m) and ($\pm 5^{*}\sigma$x) is $\pm$14.59 mm, which is safe for a ϕ46mm beam pipe.

4.7.1.5 Beam dump

A permanent beam dump rated for 1 GeV beam energy and 50 kW beam power will be installed at the end of the dump line.

The dump consists of a graphite central core (R = 8 cm, L = 1 m) inside an aluminum jacket (56 cm by 56 cm). The aluminum jacket is surrounded by 14 cm thick aluminum plates and 12 cm of steel plates. The back core consists of 0.9 m aluminum. Cross sections of the beam dump are shown in Figure 4.38.

The dump is water cooled using two sets of cooling channels drilled inside the aluminum jacket. Using only one set of cooling channels, the graphite maximum temperature does not exceed 220 degrees C, so no significant oxidization is expected, see Figure 4.39.

The dump is surrounded by concrete shielding blocks, see Figure 4.40. The maximum temperature in the concrete blocks is kept below 100 degrees C to avoid any deterioration.

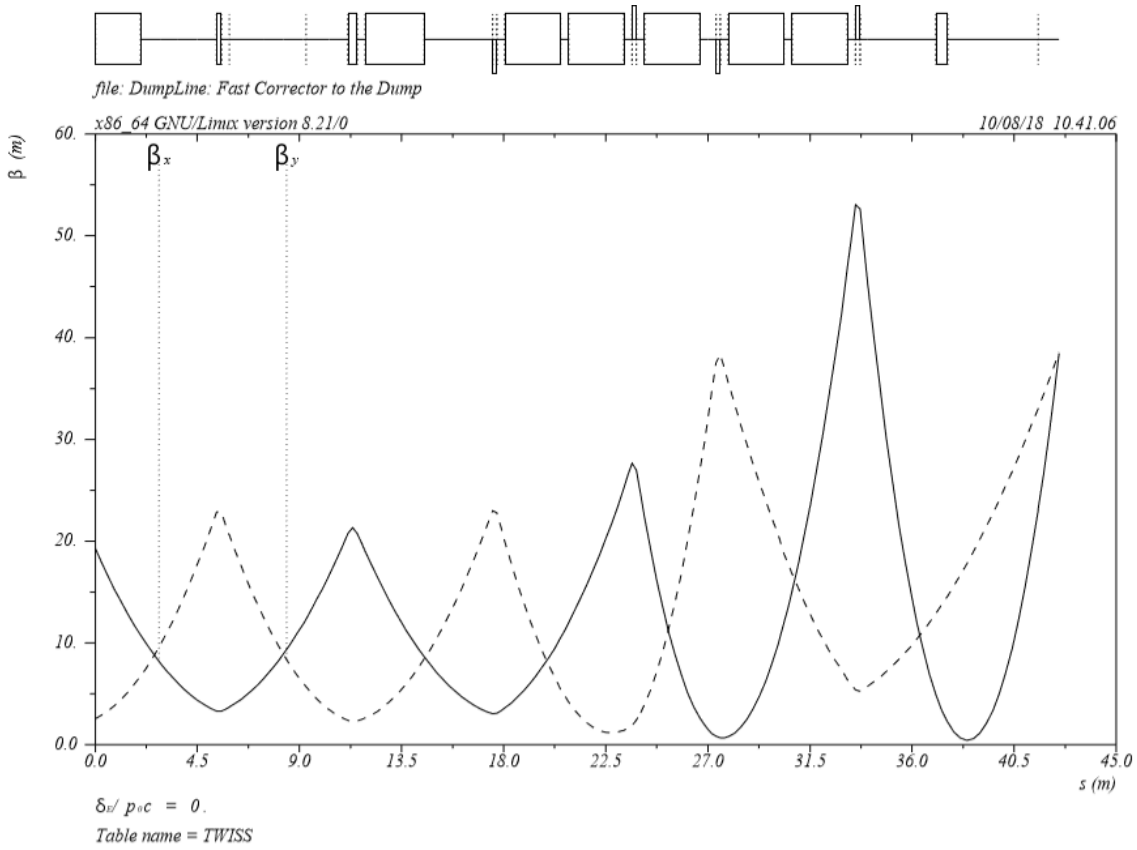

Figure 4.37: Lattice functions of the Dump line from the Fast Corrector to the core of the absorber.

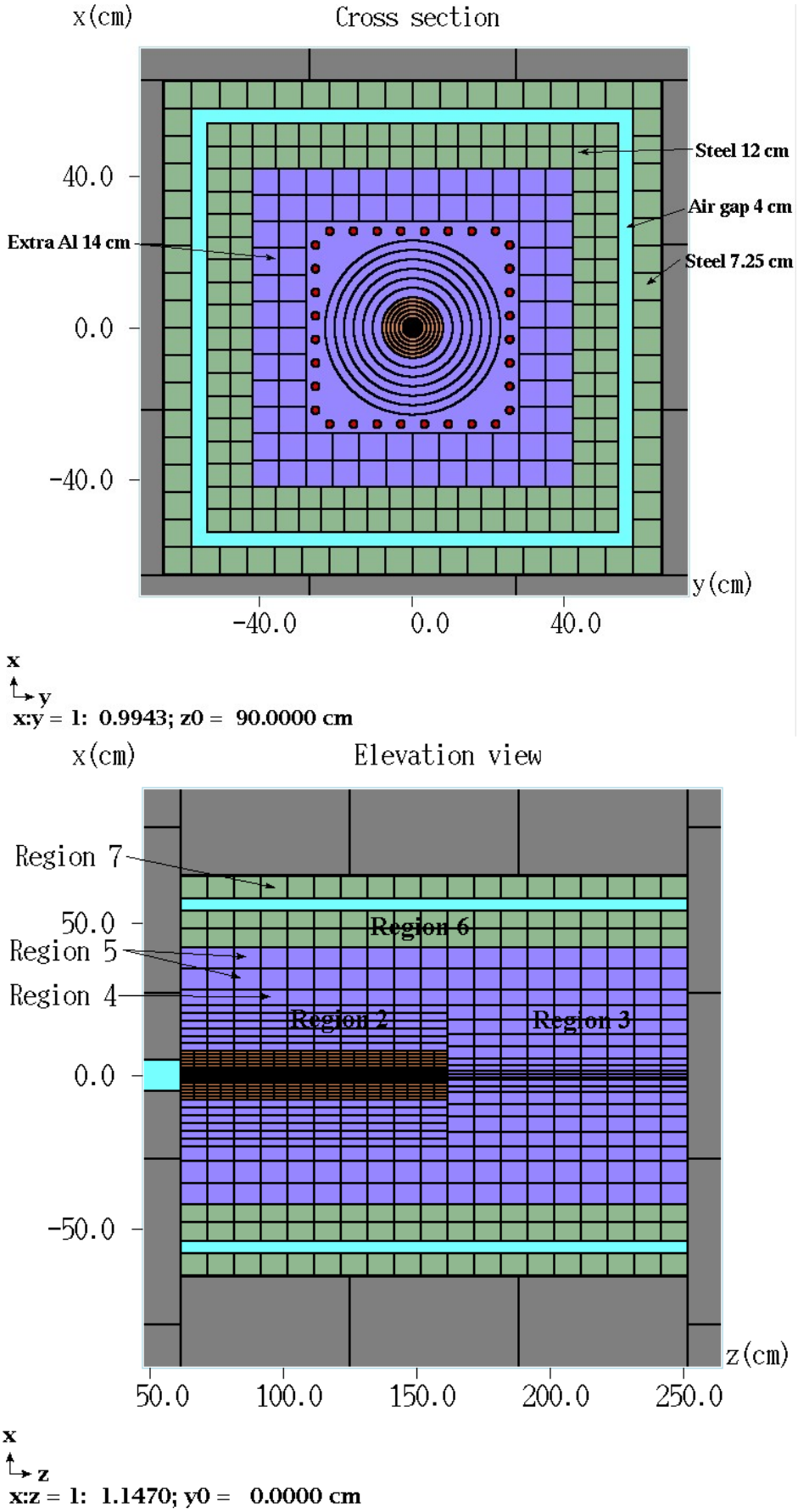

Figure 4.38: Cross sections of the beam dump.

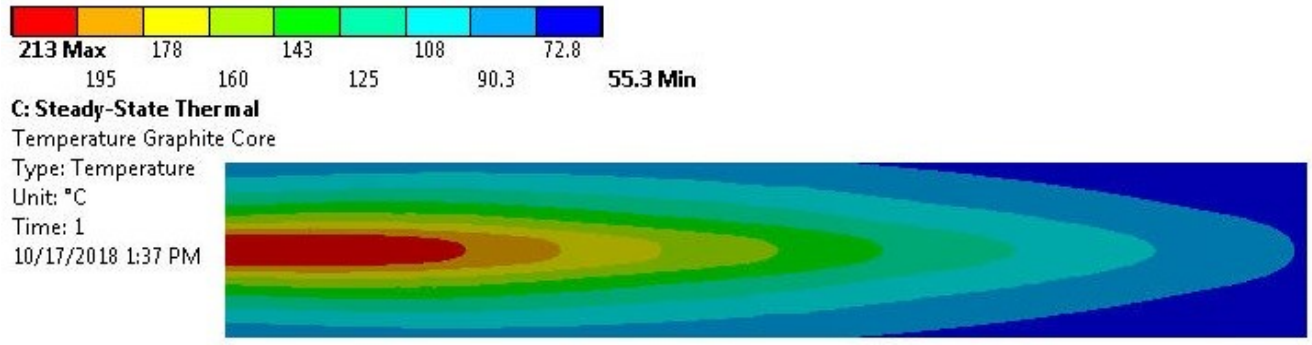

Figure 4.39: Temperature along the Graphite central core.

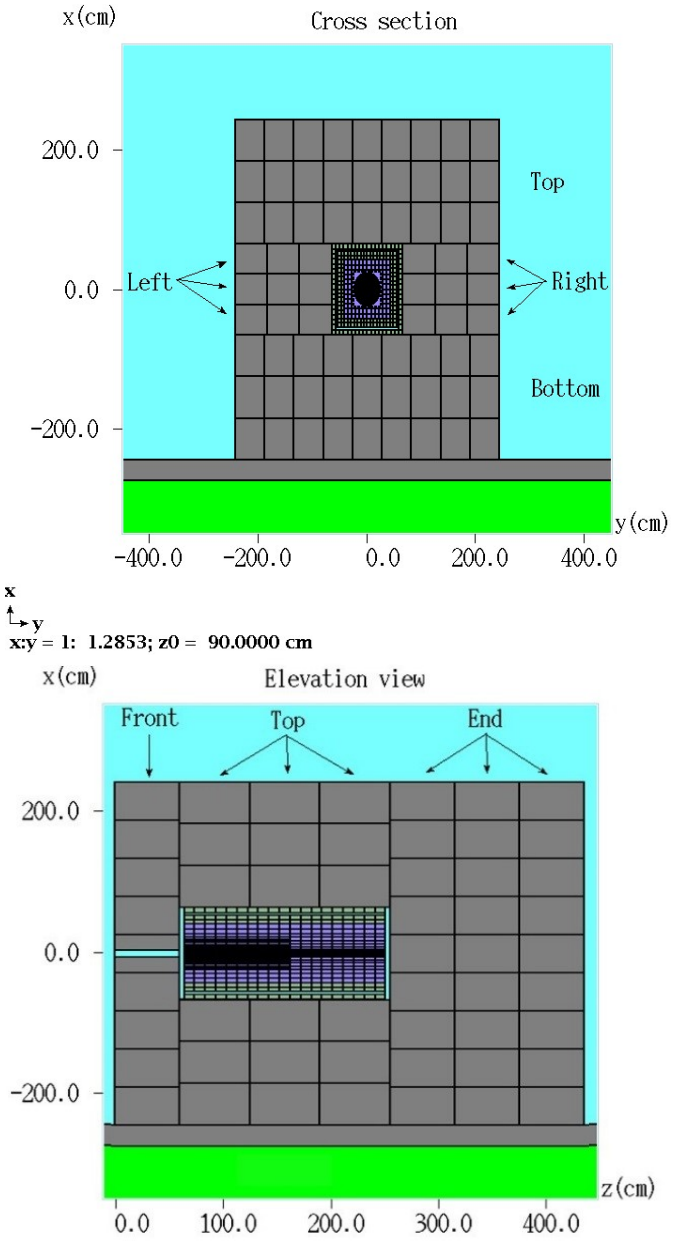

Figure 4.40: Cross sections of the beam dump including the concrete shielding blocks.

4.7.1.6 Simulation for the tolerance of dipole errors

A preliminary dipole design was performed and the magnet specifications are as follows:

- L(eff)=2.45 m
- Gap =52 mm
- Pole tip width = 135 mm
- Width = 640 mm, and height = 320 mm
- Maximum DC current 500 A.
- Max field integral = 0.7 T-m (nominal field is 2.4 kG = 0.24 T)
- Good field region = 24 mm and dB/B = 0.02%.

With this design, for B0=-0.24651 T, dB/(B=0.013%) <0.2% can be obtained in the good field region.

The simulations for the tolerance of dipole errors were done using MAD8. The dipole field errors were assigned relatively to all the dipoles in the transfer line, both randomly and systematically. Figures 4.41 through 4.44 show the orbit distortion with 10^{-4}, 2×10^{-4}, 10^{-3} of systematically assigned dipole errors and 10^{-3} of randomly assigned dipole errors.

The simulations show that 0.02% uniformity of the dipole field is a good value. The preliminary design predicts that 0.013% can be achieved. This is not a particularly stringent requirement for the production magnets. There are methods to optimize the pole tips by shaping as well as increasing the overhang (the distance from the edge of the good field region to the edge of the pole tip). Better than 10^{-4} can be achieved without any pole tip shaping.

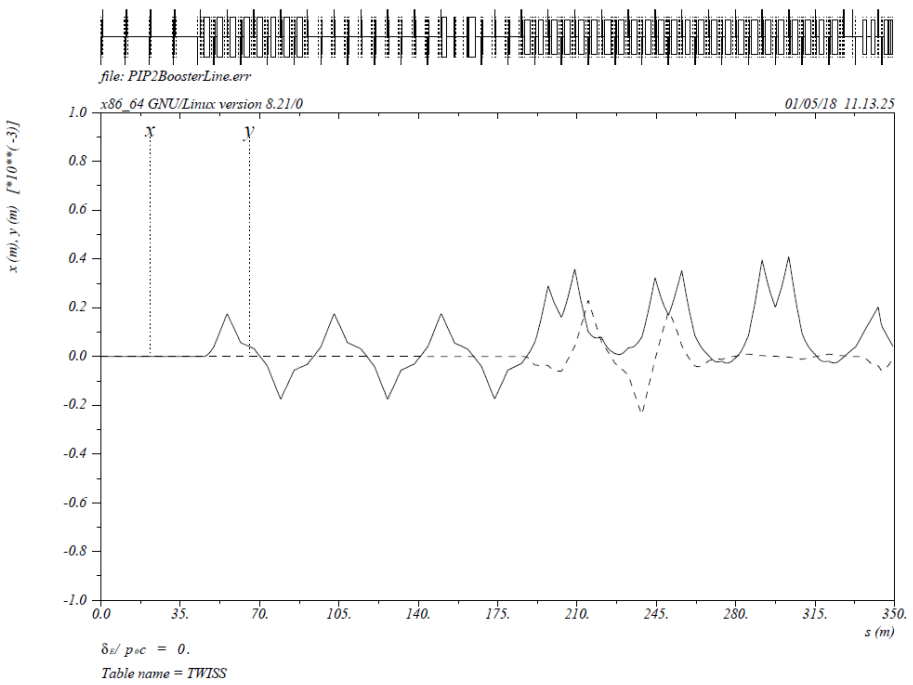

Figure 4.41: Orbit distortion in the case of 1.e-4 of systematically assigned dipole errors. The unit of the orbit x and y are in unit of mm.

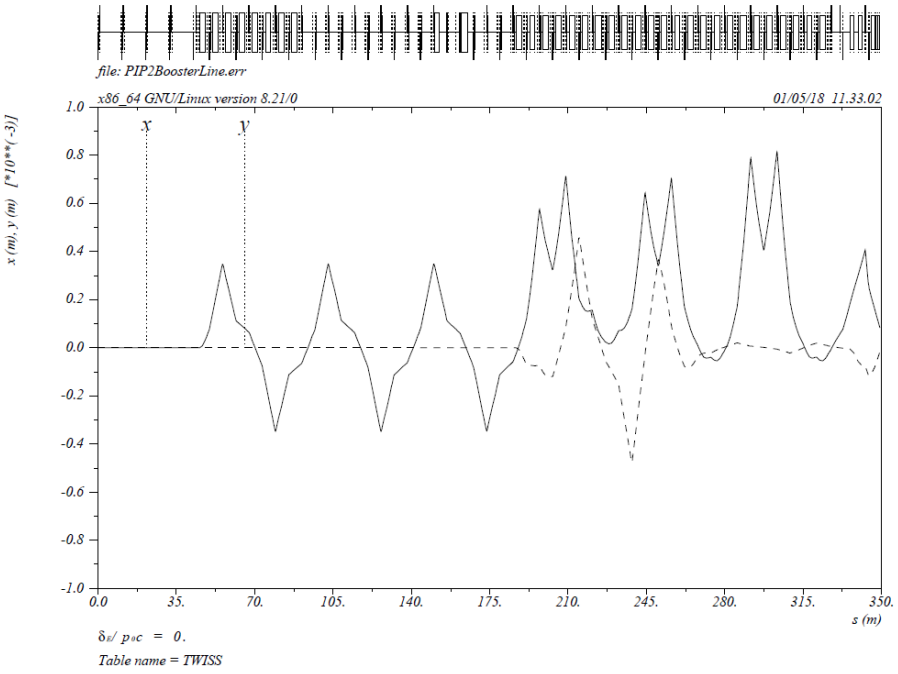

Figure 4.42: Orbit distortion in the case of 2.e-4 of systematically assigned dipole errors. The unit of the orbit x and y are in unit of mm.

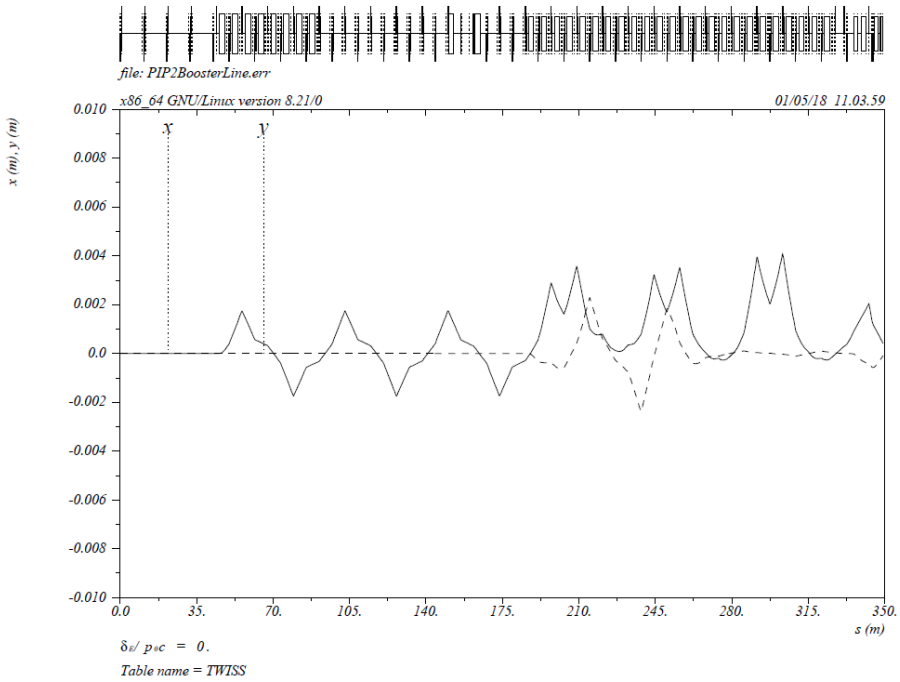

Figure 4.43: Orbit distortion in the case of 1.e-3 of systematically assigned dipole errors. The unit of the orbit x and y are in unit of m

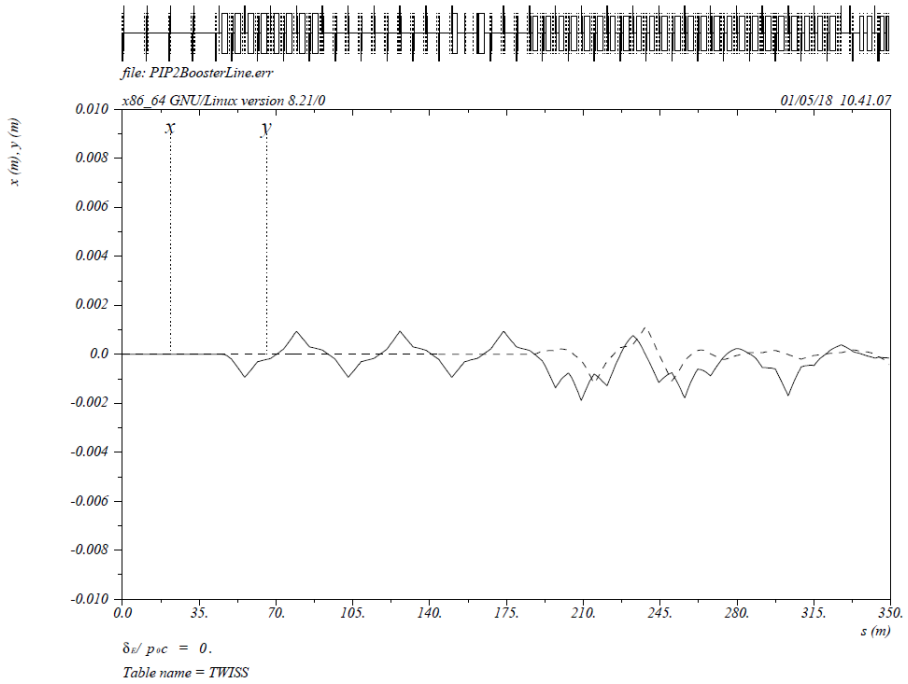

Figure 4.44: Orbit distortion in the case of 1.e-3 of randomly assigned dipole errors. The unit of the orbit x and y are in unit of m

Chapter 5

Off-Project Upgrades for 1.2 MW

Beam physicis in the existing Booster and Main Injector was discussed in the Conceptual Design Report [39]. Several upgrades to the existing accelerator complex which are needed to run at 1.2 MW are covered by an accelerator operations campaign called PIP-I+ to improve reliability and increase beam power to roughly 900 kW for the NOvA experiment in the next few years. Although PIP-I+ is not a formal project, project management, earned-value tracking, and reporting on the subprojects will be performed, and milestones can be incorporated in the PIP-II project schedule.

Increasing the number of protons per pulse from the Booster will require further measures beyond those of the completed Proton Improvement Plan (PIP) [3] to keep beam losses at acceptable levels. A new two-stage collimation system will be installed in the Booster to reduce losses, including surface losses which may otherwise require additional shielding. New Booster transverse dampers will allow lower chromaticity at injection for reduced beam loss during injection, and Booster longitudinal dampers will also help with beam loss in the Recycler and Main Injector as well as in the Booster. The Booster is one of the earliest rapid-cycling synchrotrons and until very recently was providing beam at a rather low duty factor. Detailed specifications on many devices in the Booster lattice built during the first two to three decades are not available, which makes understanding the Booster lattice a challenging task. Beam experiments will be conducted at higher beam intensities and new lattice simulations will be developed.

New Booster RF cavities, prototyped on PIP, will be constructed and installed to replace the existing 50-year-old cavities. The new cavities are designed to run at higher voltage, have larger aperture, will be more reliable, and could be used in a future rapid-cycling synchrotron to replace the existing Booster.

A γ_t-jump system will be installed in the Main Injector to allow crossing transition during acceleration more quickly, reducing beam losses. This includes designing, building, and installing 18 quadrupole magnets and associated power supplies.

The expected timescale for PIP-I+ provides Booster dampers, collimators, and beam physics improvements by 2022 and the Main-Injector γ_t-jump system by 2023. This will allow commissioning and operation of 900-kW beam well before the commissioning of PIP-II beam in the Booster and

Main Injector. The new Booster RF cavities will be installed one at a time as they are completed, so that a subset will have operated for an extended period before the shutdown for PIP-II to connect to the Booster. Thus the accelerator complex will be well prepared for commissioning with PIP-II beam and will be able to confidently operate at beam powers of 1.2 MW when running at 20 Hz.

Chapter 6

Warm Front End

6.1 System overview

6.1.1 Introduction

Figure 6.1 shows the structure of the Linac, with the Warm Front End (WFE) represented by the red boxes. The WFE accelerates the beam to 2.1 MeV and creates the desired bunch structure for injection into the SC Linac. The RFQ and the first superconducting section (HWR) operate in a CW mode. Operation with a peak current of up to 10 mA is supported by the ion source, LEBT and RFQ. The bunch-by-bunch chopper located in the MEBT removes undesired bunches leaving the beam current at up to 2 mA (averaged over a few μs) for further acceleration. There is also a "slow" chopper in the LEBT with rise and fall times of about 100 ns. It allows forming of the macro-structure of the beam timing required for machine commissioning and avoids unnecessary beam loading in normal operation. Together, the LEBT and MEBT choppers form the desired bunch structure.

Figure 6.1: The linac technology map. The optimal betas are shown for HWR, SSR1 and SSR2, while the geometric betas, β_g, are shown for the LB650 and HB650.

6.1.2 Scope

The PIP-II Warm Front End consists of two ion sources, a Low Energy Beam Transport (LEBT), a Radio Frequency Quadrupole (RFQ), and a Medium Energy Beam Transport (MEBT). The H- beam originates from a 5 mA (nominal, 15 mA max) DC ion source and is transported through the LEBT to a CW normal-conducting RFQ, where it is bunched and accelerated to 2.1 MeV. The MEBT transports and matches the beam to the first SRF cryomodule. In the MEBT, a bunch-by-bunch chopper provides the required bunch patterns, removing 60-80% of the bunches according to a pre-programmed timeline. To foresee possible upgrades, all elements of the front end are designed for beam currents of up to 10 mA. A wall, shielding the front end from radiation generated in the main Linac, is envisioned in the MEBT to allow servicing the ion sources without interrupting the Linac beam.

6.1.3 Requirements

To support beam injection into the Booster, the WFE operates at 20 Hz with a beam macro-pulse duration of 0.55 ms, resulting in a 1.1% beam duty factor. Within the beam pulse, the MEBT chopping system creates the proper bunch structure for bucket-to-bucket injection into the Booster. This corresponds to a maximum average switching frequency of 33 MHz between passing bunches and those being removed. The operational parameters for the WFE are listed in Table 6.1.

Vacuum requirements vary significantly along the WFE beam line. It ranges from mTorr levels near the ion source to $\sim 10^{-10}$ Torr where the WFE connects to the SRF Linac. Large gas loads may also be expected where the beam is dumped, in particular the MEBT absorber, leading to local vacuum bumps. Hence, the downstream end of the WFE is designed such that it is as isolated as possible from upstream from a vacuum point of view. In addition, the design, fabrication and assembly of the section closest to the first SRF cryomodule are consistent with ultra-high-vacuum/low-particulate best practices.

The choice of 30 keV for the ion source/LEBT is a compromise between considerations of beam space charge effects that may increase the transverse emittance at low energy and adiabatic bunching in the RFQ, where the longitudinal emittance is reduced with decreasing the injection energy. This choice balances the warm front end final emittance among the three degrees of freedom.

The RFQ energy of 2.1 MeV is chosen because it is below the neutron production threshold for most materials, thereby simplifying the RFQ and MEBT maintenance. At the same time, this energy is sufficiently large to mitigate space charge effects in the MEBT with currents as high as 10 mA.

Finally, the WFE is a key component of the Machine Protection System (MPS) and Personnel Protection. Its components (e.g.: LEBT chopper) allow interrupting the beam promptly when a fault is detected by the MPS. At the same time, the WFE includes beam inhibiting Critical Devices satisfying Fermilab's requirements for accesses.

Table 6.1: WFE Operational Parameters

	Requirement	Unit
Particle species	H^-	
Ion source/LEBT beam energy (kinetic)	30	KeV
Output beam energy (kinetic)	2.1	MeV
Pulse repetition rate	20	Hz
Pulse length	0.55	ms
Bunch repetition rate	162.5	MHz
Sequence of bunches (within the pulse)	Programmable	
Peak beam current at the RFQ output (i.e. before chopping)	5	mA
Average beam current output (i.e. after chopping, averaged over a few μs)	2	mA
Output rms norm. transverse emittance, $\epsilon_x = \epsilon_y$	$\leq$0.23	mm-mrad
Output rms norm. longitudinal emittance, $\epsilon_x = \epsilon_y$	$\leq$0.35(1.1)	mm-mrad (keV-ns)

6.1.4 Interfaces

The WFE is, by definition, an integrated system, which includes many different components working together to generate and provide beam to the SRF Linac. From the beam line point of view, the WFE interfaces only with the first SRF cryomodule, transitioning from 'warm' (i.e. room temperature) to 'cold' (i.e. cryogenic temperature) accelerator components. However, this transition is not technically included in the design of the WFE proper; it is part of the Half-Wave Resonator (HWR) cryomodule deliverables.

In order to operate the WFE and optimize the beam, the WFE includes various beam diagnostics, which need to be taken into account in the design of the WFE beam line. For instance, it implies providing drift spaces to accommodate the instrumentation (e.g.: current transformers, wire scanner) or, in some cases, integrating the instrumentation within the beam line components (e.g.: BPM buttons). Overall, the design of the WFE is strongly correlated to the type and frequency of the measurements specified. Concurrently, the latter is guided by the complexity of the optics lattice and beam manipulations.

Beside design considerations directly related to the beam dynamics and control of the beam properties (e.g.: beam size, emittance), the WFE drives various requirements for auxiliary equipment and services, going from vacuum pumping stations, to High-Power and Low-Level RF, to water cooling, to electrical power distribution to the building infrastructure as a whole. Furthermore, operation of the accelerator relies on support from controls and the implementation of various safety systems, which may impact the design of the WFE.

6.2 System design

6.2.1 Description of the ion sources and LEBT

6.2.1.1 Concept

The conceptual layout of the ion sources and LEBT is shown in Figure 6.2. Two ion sources in a "Y"- configuration are installed with a slow switching dipole bending magnet to maximize beam availability. Vacuum valves isolate the ion sources from the rest of the LEBT. Thus, each source can be removed for repairs, reinstalled, and conditioned without interrupting the operation of the other. The 3-solenoid LEBT (in each leg) transports the beam from the exit of the ion source to the entrance of the RFQ, matching the beam's optical functions to the ones required for low loss acceleration in the RFQ. In addition, a chopping system can form a beam with low duty factor required for commissioning and tuning of the downstream accelerator in a pulsed mode. At the same time, the chopping system interrupts the beam as part of the Machine Protection System (MPS) and prohibits beam to be accelerated in the RFQ accordingly to the safety system status. Ref. [6] presents the Functional Requirement Specifications (FRS) for the LEBT.

Achieving high reliability for the Warm Front End and its components is a task of primary importance. With that in mind, a principal goal of the LEBT design is the requirement of maintaining good vacuum in the RFQ, as well as minimizing particle bombardment of the RFQ vanes in order to reduce the frequency of sparking. As a result, a fairly long LEBT ($\tilde{2}$ m) is envisioned in order to isolate the inherently bad vacuum near the ion source exit from the good vacuum required at the RFQ entrance. In addition, the bend between the first two solenoids ensures that there is no direct line of sight between the ion sources and the RFQ (as well as the superconducting elements further downstream). This greatly reduces the bombardment of the RFQ vanes by fast neutrals and should help the overall reliability of the RFQ. Good vacuum in the LEBT also reduces the stripping of H- to protons, which can be subsequently accelerated in the RFQ and result in uncontrolled losses in the accelerator downstream.

Similarly, the need for low duty factor operation mainly arises from the desire to limit the potential for failures during tuning of the SRF cryomodules, as well as to limit irradiation of the cavities. However, because the neutralization process is not instantaneous, the optimal tune for a short pulse may noticeably differ from long pulse operation. To minimize this effect, the PIP-II LEBT provides an atypical transport scheme in which the beam is not neutralized in the downstream part of the LEBT, independently of its time structure. Figure 6.3 illustrates the geometry of the transport scheme. The vacuum is quite poor near the ion source. It results in a relatively short neutralization time and nearly full beam space charge neutralization in the neutralized section.

The transition to un-neutralized transport is achieved by combining a potential barrier (red oval on Figure 6.3), which confines neutralized particles upstream, and a clearing electric field removing compensating ions downstream of the potential barrier. The clearing electric field is obtained by applying a DC voltage to one of the chopper electrodes, which sweeps ions out of the beam path. In addition, a low vacuum pressure is maintained between the potential barrier and the RFQ to

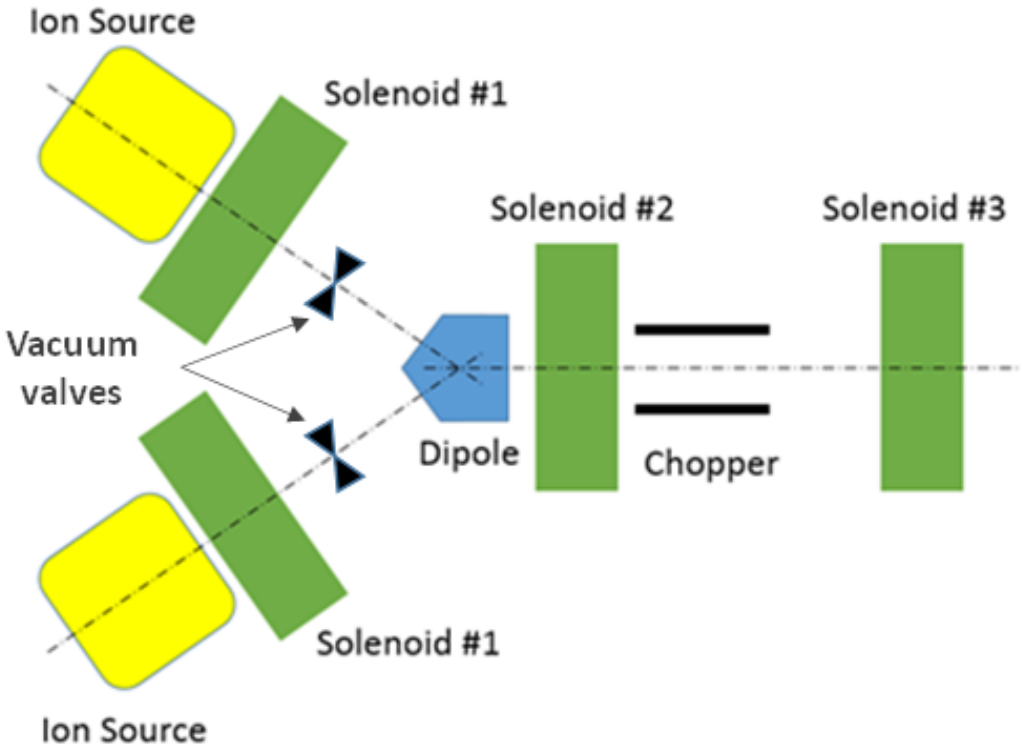

Figure 6.2: Conceptual schematic of the PIP-II LEBT with two ion sources

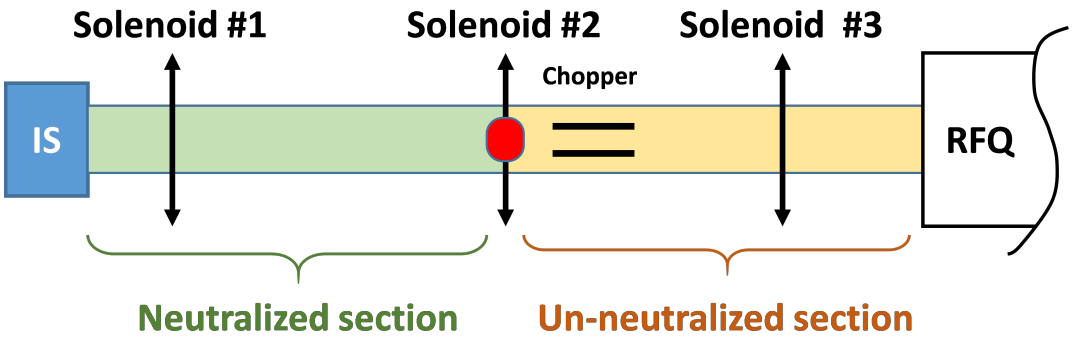

Figure 6.3: Transport scheme concept schematic

limit the rate at which neutralized particles are created. The corresponding beam optics is shown in Figure 6.4. This optics has been implemented at the PIP-II Injector Test [51], where a low emittance beam ($\epsilon\eta \leq 0.18$ mm mrad, rms) with Twiss parameters adequate for injection into the RFQ was obtained at the end of LEBT.

The location of the chopper, between solenoids #2 and #3, hence relatively far from the RFQ entrance, conforms to the principles expressed previously for achieving high reliability (i.e. good vacuum in the RFQ and low particle bombardment of the vanes). In addition, it leaves space for diagnostics both before and after solenoid #3, as well as provides room for a vacuum pump. Note that unlike many other LEBT designs, where a chopping system is located just upstream of the RFQ, the PIP-II LEBT layout provides sufficient room for a simple and robust chopper.

Finally, we would like to stress again that the design of the LEBT described above, beside the beam physics requirements, is driven by requirements of high reliability and efficiency in operation. They call for (1) good vacuum in the RFQ, (2) a simple and reliable chopper, (3) a beam transport scheme, which tuning is independent of the time structure, and (4) sufficient room for diagnostics.

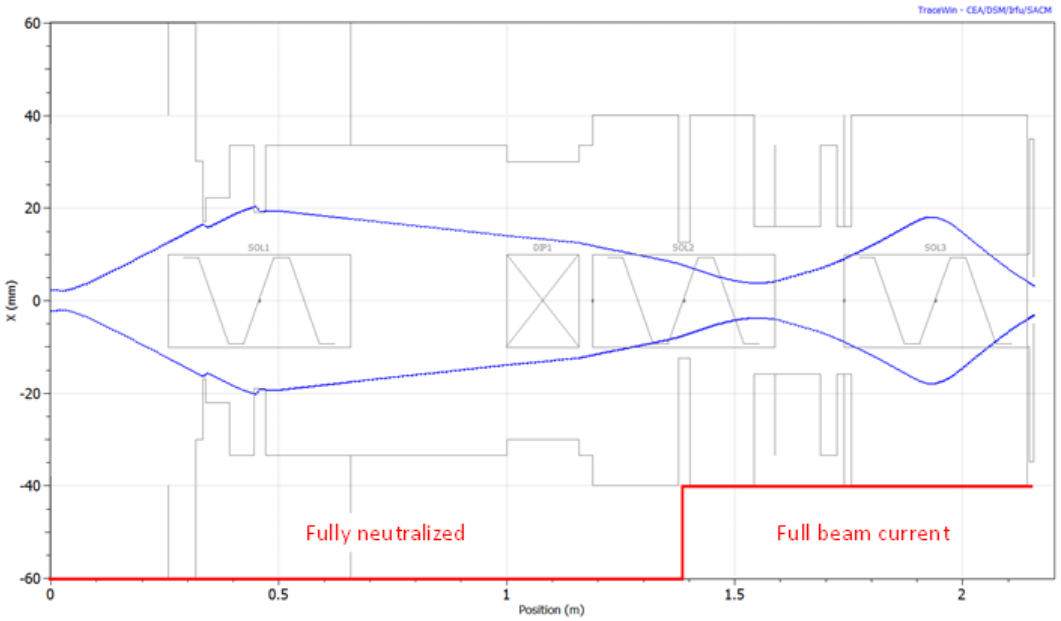

Figure 6.4: Beam horizontal envelope (2.5σ) for the partially un-neutralized LEBT optics solution simulated with TraceWin.The grey lines show aperture limitations.The red line indicates the level of neutralization (from fully neutralized to full beam current of 5 mA). Focusing is nearly symmetric which makes the vertical envelope quite close to the horizontal one. The initial distribution was derived from measurements of the ion source phase space carried out initially at LBNL [52] and later at the PIP-II Injector Test (PIP2IT).

6.2.1.2 Ion source

The ion source assembly is a DC, H^- source delivering up to 15 mA of beam current at 30 keV to the LEBT. The ion source specifications are listed in Ref. [6]. The present scenario uses the

volume cusp, filament-driven, ion source commercially available from D-Pace Inc. ([53], 6.5). This source is capable of delivering up to 15 mA with a satisfactory transverse emittance of < 0.2 μm (rms, normalized), but its mean time between maintenance is relatively short. The main reason is the source filaments, which need to be replaced every 300-500 hours. To maximize the beam uptime, two ion sources are planned to be installed (see Figure 6.2). Each source can be removed for repairs, installed back, and conditioned without interrupting the operation of the other source. To enable accessing the portion of the beam enclosure where the ion sources reside, a radiation shielding wall is installed in the MEBT.

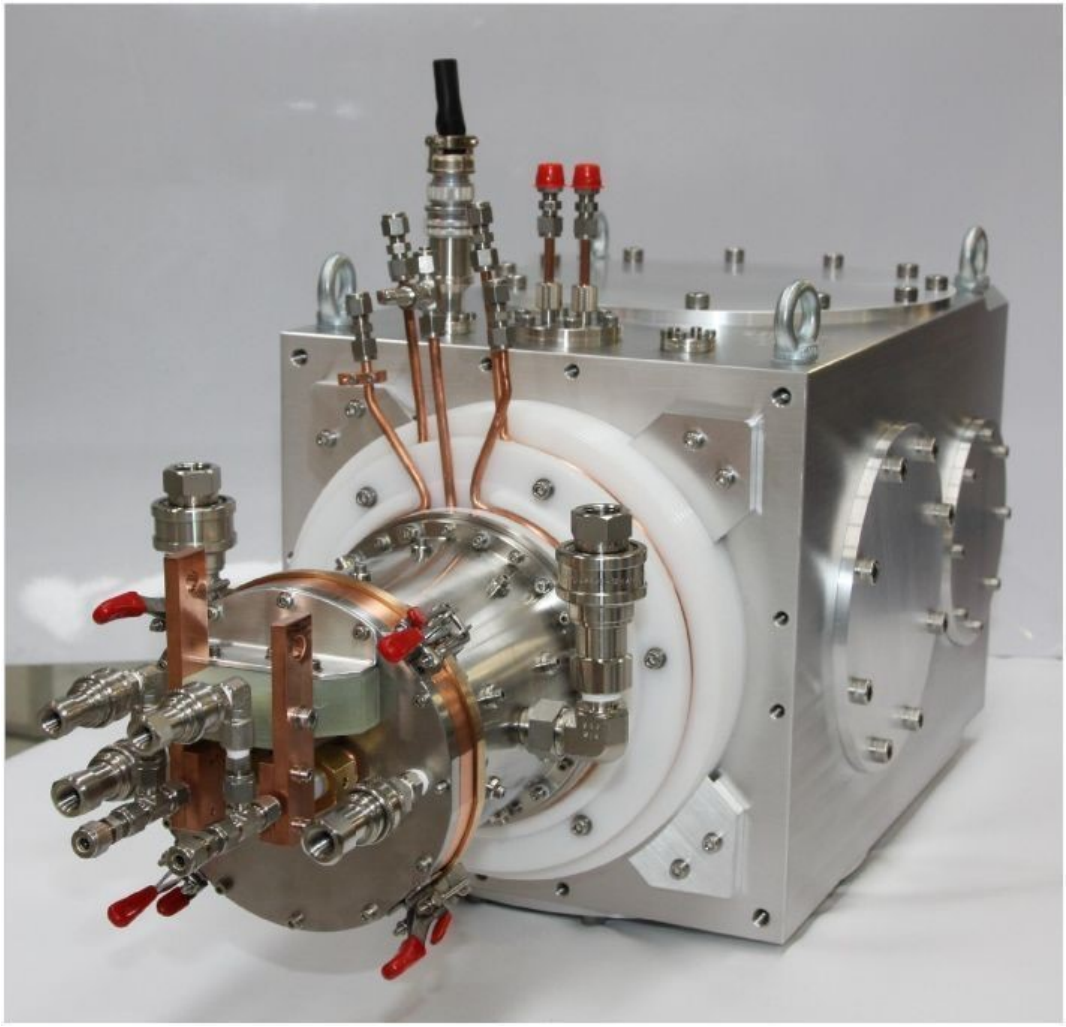

Figure 6.5: Photograph of the D-Pace ion source (foreground) with a vacuum chamber.

The ion source was purchased from D-Pace Inc. to be used in the PIP2IT. It has been in operation since 2013. While presently not stated as a requirement for PIP-II, a modulation circuit was built and mounted onto the ion source extraction electrode to provide pulsed operation. This capability brings flexibility to the commissioning of the beam line downstream and provides an additional level of protection in the Machine Protection System.

Alternatives to the D-Pace Inc. ion source may be considered. Several groups around the world have been engaged into R&D that may lead to an ion source with the proper characteristics for PIP-II and a much longer time between maintenance than is currently available.

6.2.1.3 LEBT

The LEBT transports the beam from the exit of the ion source to the RFQ entrance, creates the macro-pulse structure at 20 Hz and matches the optical functions to those of the RFQ. In addition, the LEBT forms a very low-duty factor beam during commissioning and tuning of the downstream beam line and can interrupt the beam as part of the Machine Protection System (MPS). Pulsed beam operation and fast machine protection are achieved via a chopper assembly, which consists of a kicker combined with an absorber. In addition, should the LEBT kicker fail, the beam is further disabled by turning off the ion source's extraction and bias voltages, as well as the switching dipole power supply.

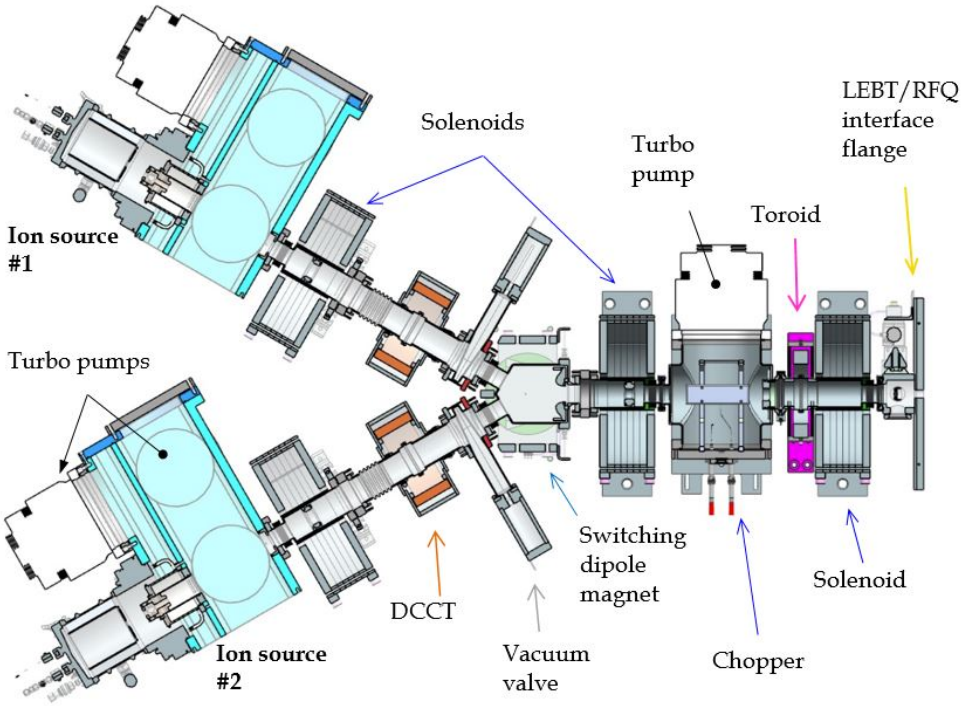

Figure 6.6: Section view of the LEBT with two ion sources..

Layout

The LEBT consists of 3 solenoids (in each leg), a slow switching dipole magnet, a chopping system, water-cooled Electrically Isolated Diaphragms (EID), an electrically-isolated, water-cooled, movable vertical electrode assembly with 3 apertures, and beam current diagnostics - DCCT after solenoid #1 and AC current transformer ("toroid") after the chopping system (Figure 6.6). An emittance scanner [54] is located at the exit of each ion source. Dipole correctors are mounted inside each solenoid allowing the beam to be steered in any direction. The edge focusing of the switching dipole is adjusted to minimize the asymmetry between horizontal and vertical focusing. As already stated in the Concept Section, the 2 m beam line length ensures that the gas migrating from the ion source to the RFQ is kept at a manageable level.

Chopping system

For accelerator front ends with beam parameters similar to PIP-II, most LEBT's employ a transport scheme that relies on almost complete neutralization of the beam to counteract the effects of space charge during transport. However, neutralization is inevitably broken in the vicinity of a chopper. In order to decrease the distance that the beam travels with full space charge and low energy, the chopping system is often located just upstream of the RFQ. Such location has several features contradicting the principles described in the Concept Section. First, absorption of the cut-out beam creates a significant gas load into the RFQ. Second, the short distance required between the last solenoid and RFQ limits the possibilities of fitting in a simple and robust chopper. It also makes it difficult to place diagnostics downstream of the chopper, for instance, to measure the beam current entering the RFQ. Following this logic, for PIP-II, the WFE's chopping system is placed between solenoids #2 and #3.

The chopping system is a simple electrostatic kicker, with the particularity that one of the electrodes is also the absorber [55]. Such a design is inherently robust against un-controlled beam losses, which can quickly become an issue even at the relatively modest maximum beam power of 300 W (DC). In addition, it removes the need for a dedicated absorber electrode downstream, thus making the overall chopping system more compact. The absorber plate is at the ground potential but electrically isolated in order to measure the primary beam current. When the beam is passing through, the design of the chopper electronics allows applying a DC voltage to the kicking plate to clear secondary ions out of the beam path.

Electrically Isolated Diaphragms (EID)

The beam line includes 3 water-cooled, Electrically Isolated Diaphragms (EIDs), two of which are located within solenoid #1 and #2 and the third is just downstream of the electrostatic kicker.

The primary function of these electrodes is to minimize uncontrolled beam losses. They are sized such that if there is some beam loss (e. g. before the optics is properly tuned, or during the rise and fall time of the kicker (EID #3)) it would most likely occur at these locations first. The EIDs are electrically isolated to allow the beam loss to be measured.

Second, the EIDs play the role of potential barriers in the transport scheme with an un-neutralized section, confining ions in sub-sections of the beam line.

Finally, they are used to measure the beam size and center the beam. This is achieved by steering the beam with upstream correctors and recording the current drawn by the electrodes. In addition, there is a scraper assembly just downstream of Solenoid #3, which is an additional movable electrically-isolated and water-cooled electrode with 3 apertures (2 round apertures and a 'D-shaped' aperture). A small round aperture is used to create a pencil beam. A larger round aperture placed concentrically with the RFQ entrance aperture protects the RFQ vanes during normal operation. The 'D-shaped' aperture is used to measure the beam current density profile by moving its edge across the beam and recording the scraper current as a function of the scraper position. This is also the largest aperture, which allows full transmission of the beam to the RFQ entrance. Finally, the scraper can be placed such as to intercept the beam completely. For the larger round aperture, the size of the opening is chosen to scrape the halo particles that otherwise would be lost in the RFQ or MEBT. Also, variation of the beam current intercepted by the scraper while moving the beam across the opening with upstream dipole correctors gives information about

the beam position and core size for both planes.

Emittance growth mitigation

To satisfy both the beam physics requirements and the design choices, a hybrid transport scheme was devised, where the beam propagates through the first 'high pressure' part of the LEBT being neutralized, but neutralization is prevented in the second part, which starts just upstream of the chopper (see Concept Section). For a beam with modest perveance, this transport solution nearly preserves the beam emittance if the transition to the un-neutralized section occurs where the beam current density profile is close to the profile corresponding to uniform distribution [56] thus minimizing non-linear effects from the beam's space charge. While the ion source may not be optimized to deliver a beam with uniform current density, because of the finite extent of the beam emitter (e.g. plasma surface) and the geometry of the extraction system, one would expect the spatial distribution of the beam to have relatively sharp edges. In addition, because of the ion source current overhead, it is possible to implement significant scraping that would result in only keeping the core of the particles' distribution, which is inherently more uniform than the tails. At the same time, the beam formation out of a plasma in a near thermal equilibrium must result in a Gaussian velocity distribution in transverse momentum at the beam emitter location.In the simplest linear optics model, that distribution is reproduced at the image plain of a focusing element (here solenoid 1) with a given magnification. Ideally this is where space charge dominated transport starts such that forces from the the beam's space charge are linear, in which case the emittance is preserved. Otherwise, the combination of non-linear space charge forces and, to much lesser extend, aberrations within solenoid 3, leads to significant emittance growth.

To illustrate this model, Figures 6.7 to 6.9 show the results from TraceWin simulations, where the initial distribution is uniform in the subspace of transverse coordinates and Gaussian in the velocity subspace. While the final Twiss parameters are nearly equal (Figure 6.7), the solenoids have different current values: in one case (red traces or dots on the plots), the beam is nearly uniform near the chopper, while it is Gaussian for the second case (blue traces or dots on the plots) (Figure 6.8). Correspondingly, the emittance growth is lower in the first case than in the second one (Figure 6.9). Note that 20% of the beam is scraped off before the first solenoid.

Measurements at PIP2IT were carried out with the transverse emittance station [57] installed close to the location of the RFQ input flange. They show a behavior similar to the simulations. Namely, starting with the same ion source tune, different solenoid current settings lead to different emittances for the same measured Twiss parameters at the end of the beam line. In addition, profile measurements carried out between solenoid #1 and #2 show that the beam distribution is indeed uniform-like or Gaussian-like depending only on the value of the solenoid #1 current. Thus, both measurements and simulations indicate that the proposed transport scheme allows one to deliver beam with the required properties to the RFQ.

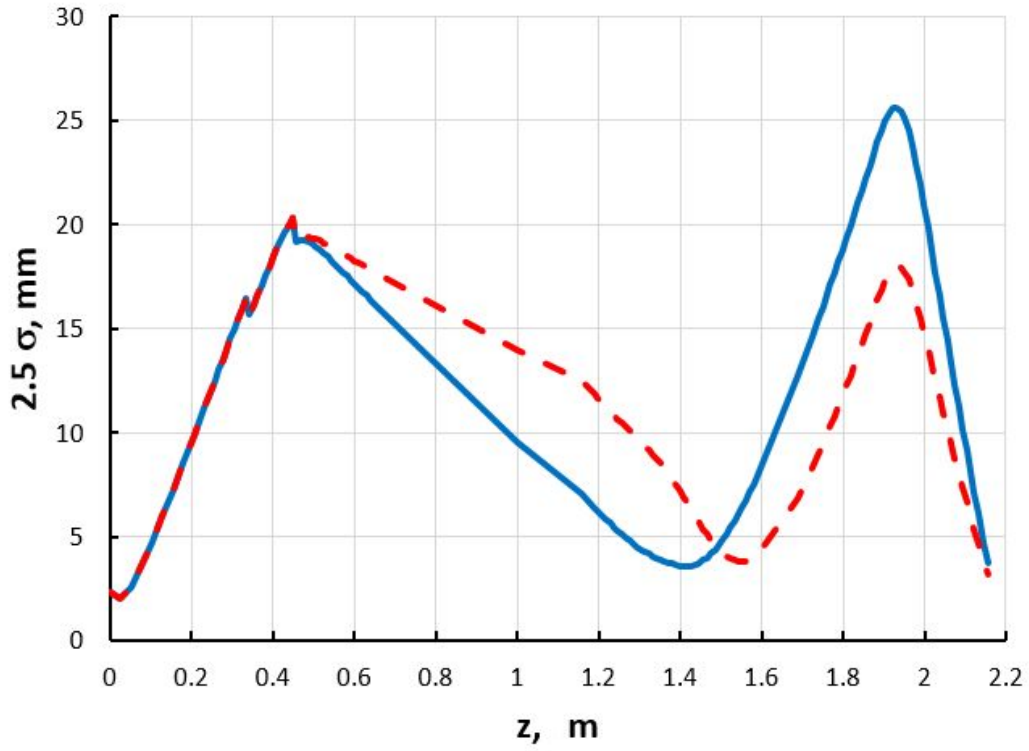

Figure 6.7: Beam envelopes (2.5) obtained with TraceWin. Currents in focusing solenoids are 154, 187 and 223.5 A (blue curve) and 143, 158 and 240 A (red dashed curve) for Solenoids #1, #2 and #3, respectively. Input distributions (uniform current density and Gaussian distribution in velocity subspace) are the same for both simulations; $I_{beam} = 5$ mA (after scraping in the first solenoid).

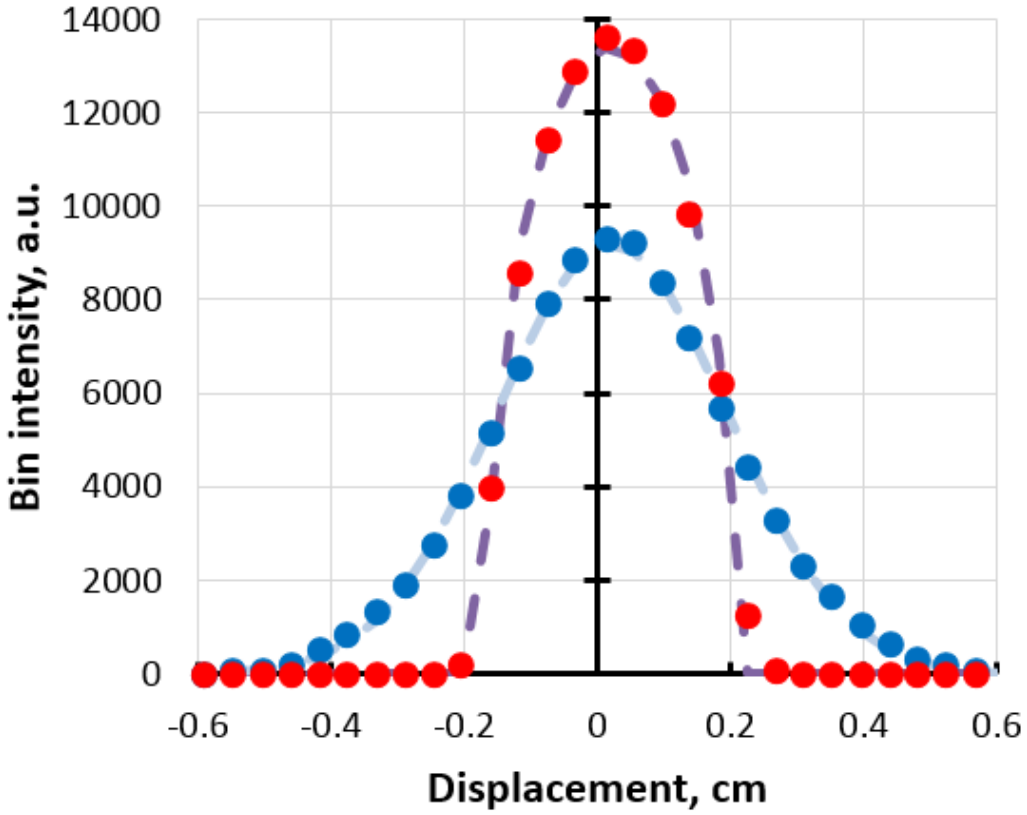

Figure 6.8: 1D beam profiles near the chopper (20 cm downstream of EID #2) corresponding simulations shown on Figure 6.7. Dashed curves are fits, assuming uniform (purple) or Gaussian (light blue) distributions.Data points mimic the results that would be measured experimentally (due to binning and the finite step size of the measuring device).

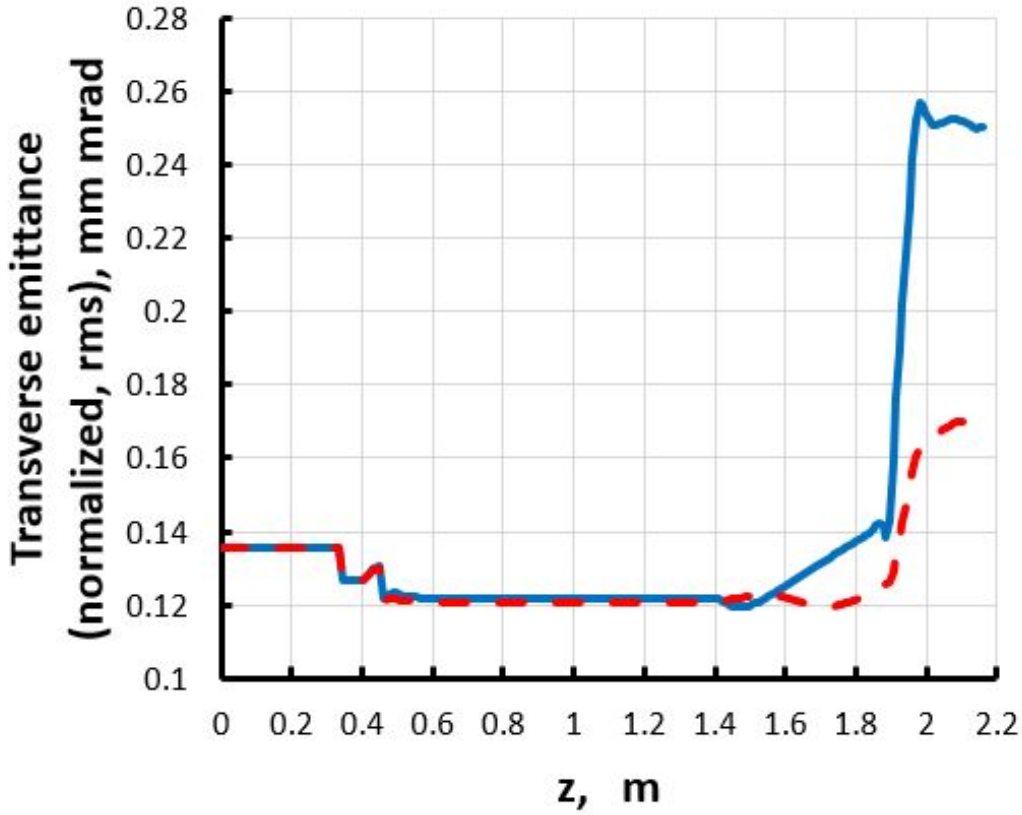

Figure 6.9: Emittance evolution along the beam line corresponding to the simulations shown in Figure 6.7.

6.2.2 Description of the radio frequency quadrupole (RFQ) structure

6.2.2.1 Concept and requirements

The 162.5 MHz RFQ accelerates the 30 keV H^- ion beam to 2.1 MeV at beam currents of up to 10 mA CW. The design requirements are presented in Table 6.2.

The original requirement of CW operation forced the design optimization to be aimed at the minimization of RF power loss in the structure since most of RF power is dissipated on the cavity walls creating a considerable thermal load. The relatively low nominal vane tip-to-vane tip voltage of 60 kV was adopted to limit the overall RF power requirement, which in turn makes thermal management of the RFQ structure easier. The RF design is based on detailed simulations including 3D electro-magnetic simulations of the entire RFQ. Mode stabilization with pi-mode rods significantly reduces the structure sensitivity to manufacturing errors. The geometry of the vane-ends (vane-to-end-plate transition) was adjusted to achieve good field flatness [58]. The field quality is also supported by 80 slug tuners compensating manufacturing errors and imperfections of simulations.

The beam dynamics design was simulated using PARMTEQ [12] and it either meets or exceeds all of the requirements in capture efficiency, transmission efficiency and emittance growth. Figure 6.10 shows a PARMTEQ simulation for a 5 mA beam, ideally matched into the RFQ. The transmission is 99.8% and output longitudinal emittance is 0.7 keV-ns. For an input transverse emittance of 0.11 mm mrad, the output transverse emittance is 0.15 mm mrad, a 35% increase but still well below the maximum specified. Additionally, error analysis (e.g. mismatch, centroid offsets, field errors...) was carried out and indicate that the design is very robust and error tolerant. Results of simulations of the transverse and longitudinal emittances as functions of the beam current (assuming a 0.11 mm-mrad rms normalized emittance at the RFQ entrance) are presented in Figure 6.11.

Table 6.2: Main parameters of the RFQ

Parameters	Value	Unit
Input energy	30	kV
Output Energy	2.1	MeV
Duty factor	100	%
Frequency	162.5	MHz
Beam current	5 (nominal); 1-10	mA
Transmission (1-10 mA)	$> 95\%$	%
Output transverse Emittance (1-10 mA)	< 0.25	mm-mrad
Output longitudinal Emittance (1-10 mA)	0.8-1.0 (0.26-0.32)	keV-nsec (mm-mrad)

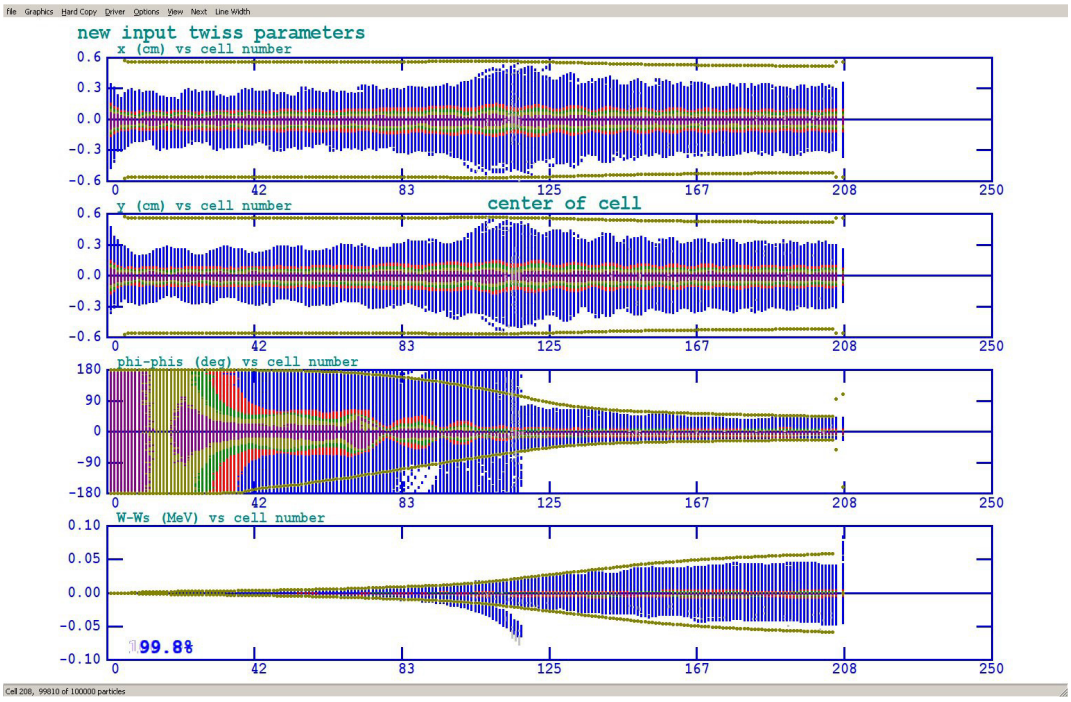

Figure 6.10: PARMTEQ simulation of a 5 mA beam using 100,000 macro-particles.

Excessive longitudinal tails can result in beam losses in the course of acceleration and can affect how small the particle population of the removed bunches could be made (i.e. limit to beam extinction). The latter is an important requirement for possible future high duty factor experiments. Figure 6.12 presents the longitudinal distribution of the particles at the exit of the RFQ (Figure 6.12a) and the integral of this distribution (Figure 6.12b) plotted against the longitudinal Courant-Snyder invariant,

$$\epsilon_s = (1 + \alpha_s^2)s^2/\beta_s + 2a_s s\Delta p/p + \beta_s(\Delta p/p)^2$$

Here β_s and α_s are the longitudinal beta- and alpha-functions, respectively, and s and Δp/p are the deviations in the longitudinal coordinate and the relative momentum from the reference particle, respectively. Note that 3.1% of the particles, located in a halo with the Courant-Snyder invariant being three times above the rms emittance , were not accounted for in the computation of s, s and the rms emittance. One can see from Figure 6.7 that about 2.5% of the particles are in the non-Gaussian tails. This stresses the necessity of accounting for longitudinal tails in the computation of particle losses during further acceleration.

6.2.2.2 RFQ design

The 162.5 MHz CW RFQ will accelerate an H^- ion beam with currents of up to 10 mA from 30 keV to 2.1 MeV (see Ref. [59] for specifications). Presently the PIP-II RFQ is assumed to be identical to the one used for PIP2IT, which was constructed and built by LBNL [60], and which design is based on the experience accumulated by the LBNL team earlier and, in particular, on the SNS RFQ [61].

The RFQ is a 4.45-m long, four-vane copper structure composed of four longitudinal modules. The nominal vane-to-vane voltage is 60 kV. A series of 32 water-cooled pi-mode rods provides transverse quadrupole mode stabilization, and a set of 80, evenly spaced, fixed slug tuners is used for the final frequency adjustment and for local field perturbation corrections. It was delivered to FNAL in 2015 and has been commissioned and operated in the PIP-II Injector Test (PIP2IT). The PIP2IT RFQ has already proven that it can operate at full CW power and can accelerate pulsed beam with 98±2% efficiency. Figures 6.13 and 6.14 present the RFQ CAD model and a photograph of it installed in the PIP2IT enclosure, respectively.

RF matching into the RFQ cavity is done with two 162.5 MHz input couplers designed and verified at FNAL [62]. A CAD illustration of the coupler is shown in Figure 6.15. These couplers were designed to transport up to 75kW of RF power with full reflection, without breakdown. They have two design features that are unique with respect to other RF cavity input couplers: the antenna is forced-air cooled (not water cooled) to avoid potential water leaks to the RFQ vacuum chamber, and the antenna is capacitively coupled to the end-wall, allowing DC biasing to reduce multipacting. The RFQ has been tested with up to 120kW of CW drive from two couplers transporting about 60 kW of power, each. A bias of about 4 kV on the antennas is required to eliminate multipacting around the couplers at any power level.

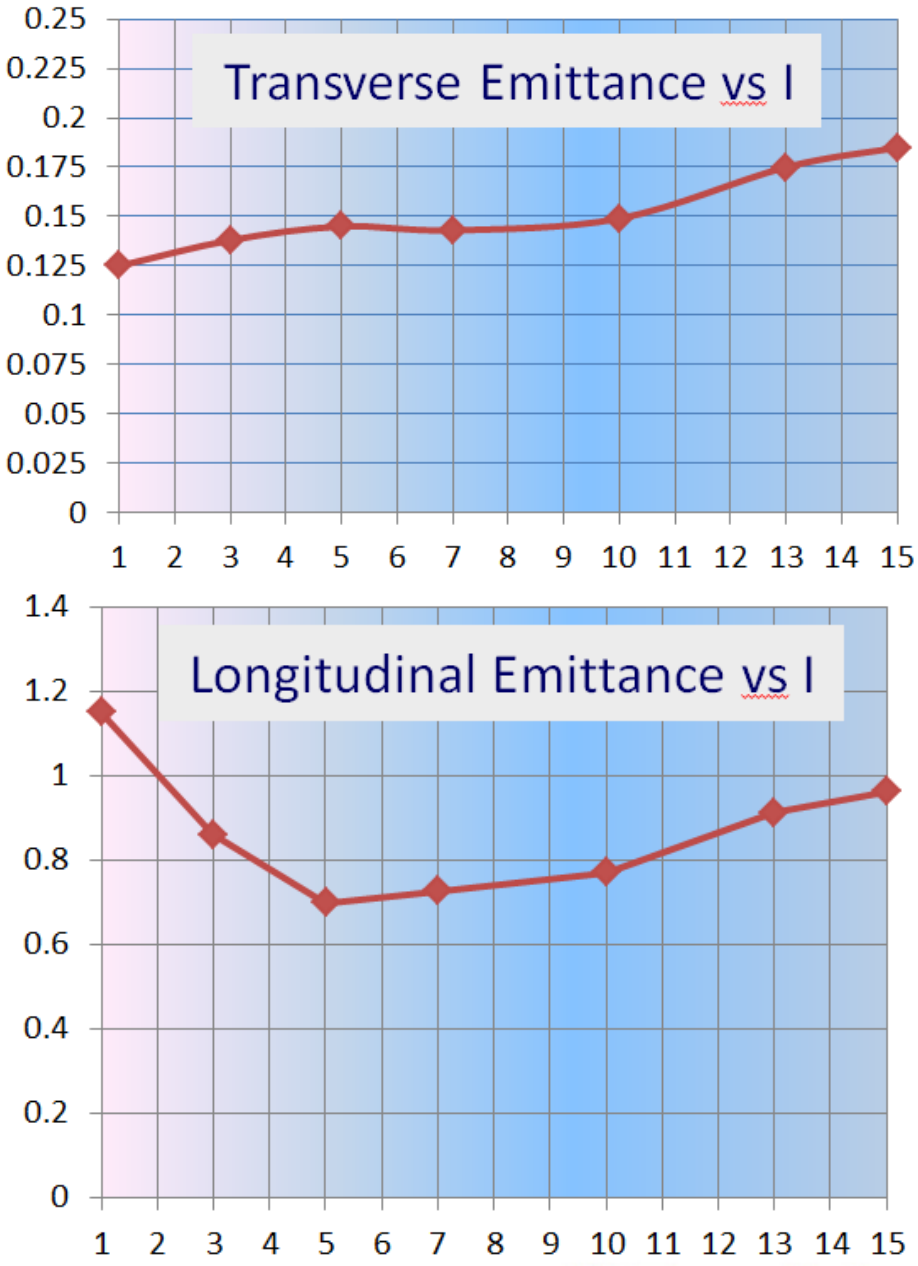

Figure 6.11: Dependence of the calculated transverse (above) and longitudinal (below) rms normalized emittances on the beam current; the transverse emittance is presented in mm·mrad and the longitudinal one in keV·ns (1 keV·ns $\approx$ 0.32 mm mrad).

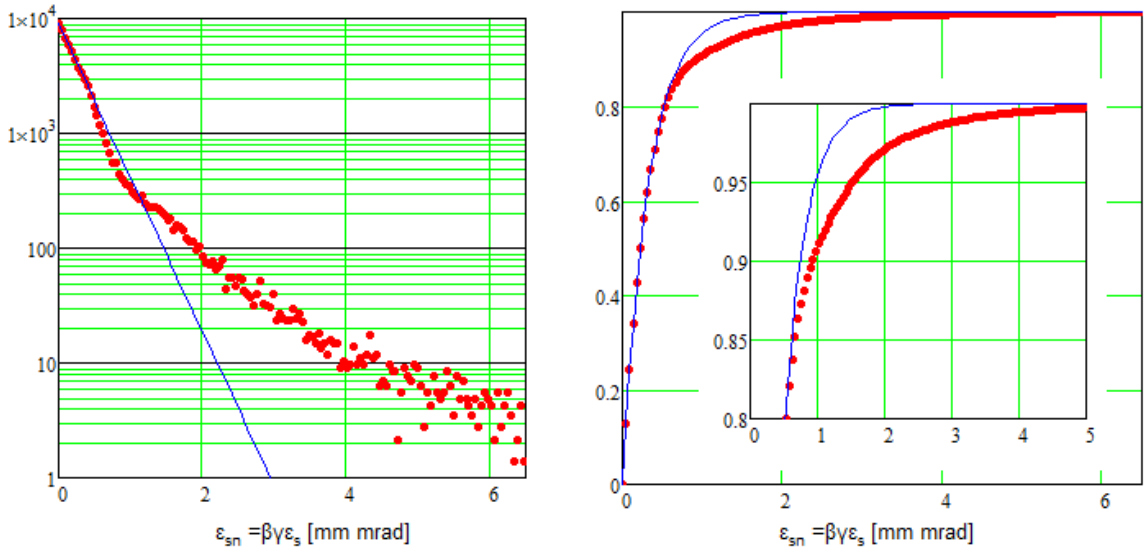

Figure 6.12: The particle longitudinal distribution (left) and its integral (right) at the end of the RFQ simulated for 5 mA beam current; β_s=1.69 m, α_s=0.087, rms normalized emittance of 0.162 mm mrad. Blue lines show the Gaussian distribution and its integral built for longitudinal rms emittance computed from the particle distribution. 100,000 particles were used in the simulations.Vertical units for the left plot: "Number of particles". Vertical units for the right plot: "Particles distribution integral (normalized)"

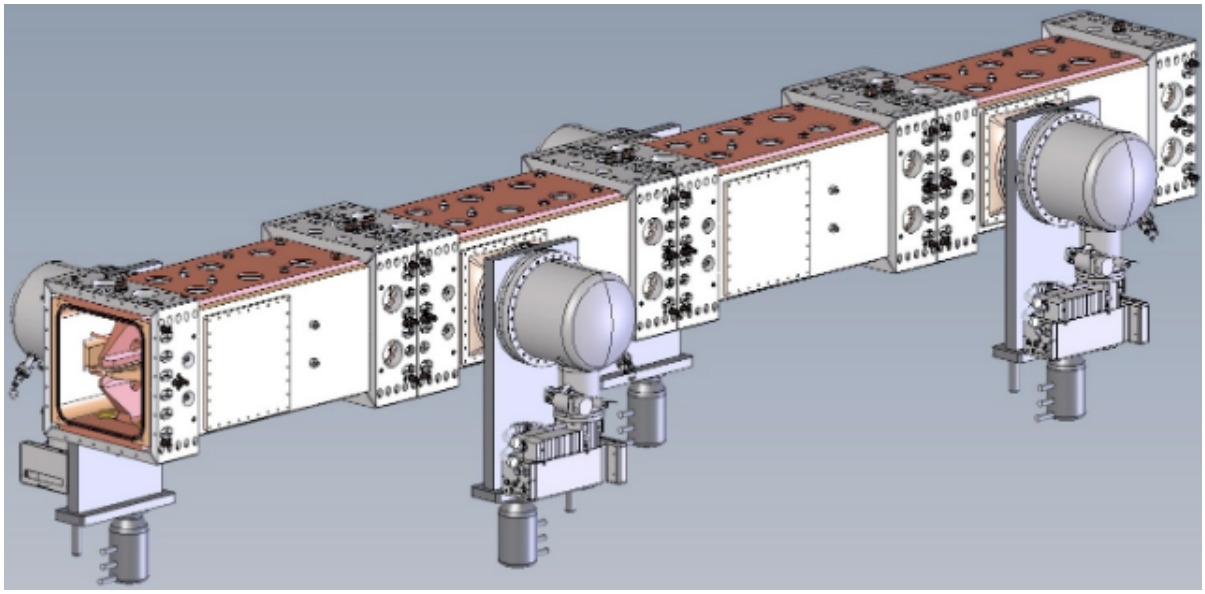

Figure 6.13: CAD model of the full four-module RFQ.

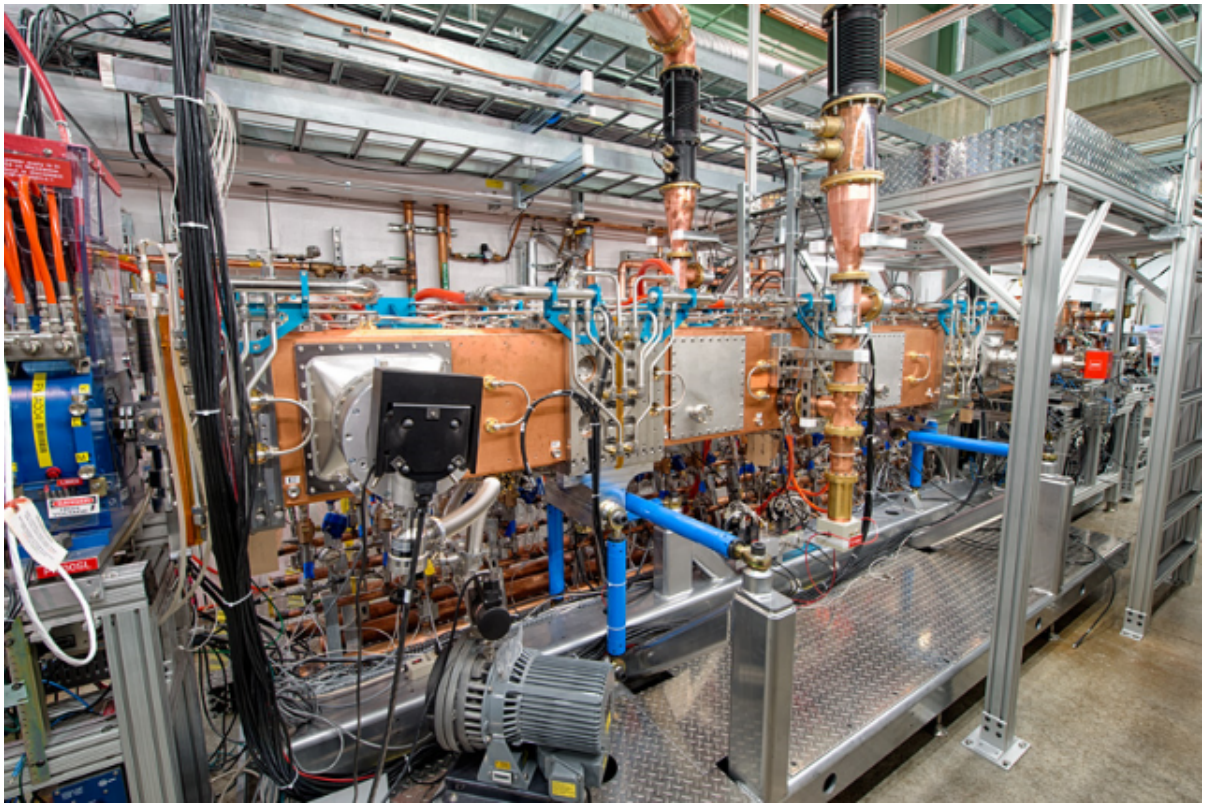

Figure 6.14: RFQ installed in PIP2IT beamline.

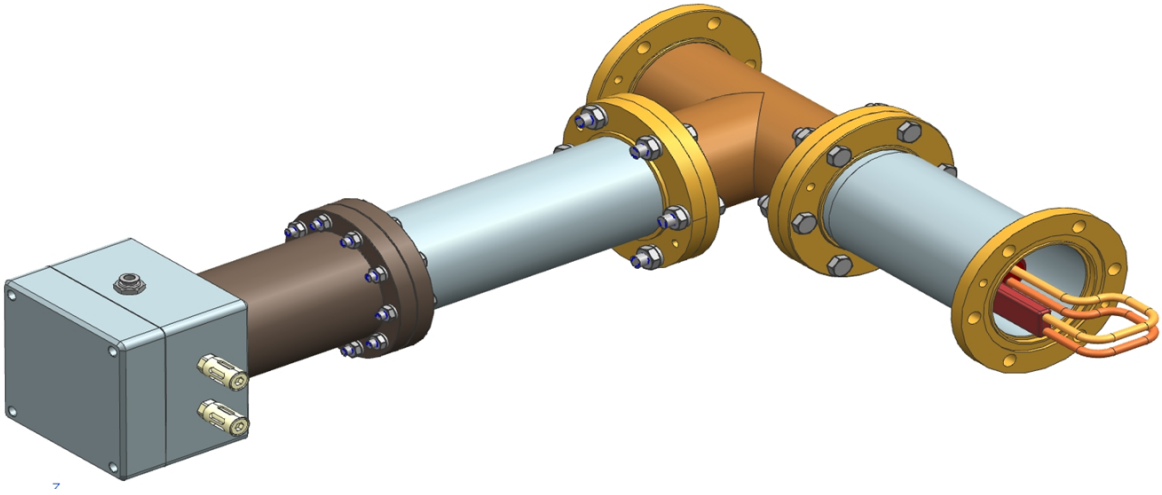

Figure 6.15: Solid model of the RFQ input RF coupler design.

RF power is provided by two, 75kW 162.5 MHz solid-state power amplifiers from Sigma Phi Inc. Each amplifier is protected from power reflected from the RFQ using 75kW circulators from Ferrite Inc. The added expense of the RF circulators is justified by the improved stability of RFQ operation. In particular, they allow the RFQ operation over a larger range of resonant frequency offsets and support pulsed operation with variable duty factors.

The resonant frequency of the RFQ is controlled thermally by adjusting the temperature difference of the water circuits, which cool the vanes and the RFQ walls. The choice of this scheme is supported by a much larger sensitivity to the temperature difference than to the average temperature of the circuits. The corresponding frequency response parameters are shown in Table 6.3. The temperature difference is achieved by redistribution of cooling water flow between these two circuits. For pulsed operation, the duration of the RF duty cycle can also be used for temperature stabilization. For CW operation, the resonant frequency must be maintained by cooling water temperature regulation only. An adaptive control system has been designed that will regulate the steady state temperature of the RFQ cooling system to better than 0.1°C. A simple block diagram description of the system is shown in Figure 6.16. The system is also designed to respond to sudden changes of thermal load due to RF power trips. The goal is a reduction of the time necessary for bringing the RFQ resonant frequency to the nominal value after a trip. Consequently, it will decrease the beam downtime.

A series of RF and thermal finite-element models of the RFQ have been developed using ANSYS®. An example of the temperature contour plots for the cavity body and vane cutback region is shown in Figure 6.17. From the RF analysis, the average linear power density was determined to be 137 W/cm with a peak heat flux on the cavity wall of only 0.7 W/cm^2. With 30° C water in the vane and wall cooling passages, the resulting temperature profile in the cavity body ranges between 32 and 37°C at full RF gradient.

Additional modeling has been carried out. This includes stress and displacement analyses, thermal analyses of the tuners, pi-mode rods and vane cutbacks, and prediction of the frequency shift of the RFQ cavity due to thermal loading and changes in the cooling water temperature.

The RF design issues [58] include mode stabilization, field flatness, radial matching, and entrance and exit terminations. Table 6.3 summarizes the RF and thermal design results.

Table 6.3: Main parameters of the PIP-II RFQ electromagnetic design

Parameter	Calculated	Measured
Center Frequency, MHz	162.493	162.445
Frequency of the dipole mode, MHz	181.99	180.52
Q0 factor	14660	13000
Total power loss at 60 kV, kW	74.6	90
Vane cooling resonant frequency parameter, kHz/°C	-16.7	-16.4
Wall cooling resonant frequency parameter, kHz/°C	13.5	13.9

Beam loss inside the RFQ may result in degradation of the RFQ performance [63]. In the course of its lifetime the PIP-II RFQ is expected to accelerate a very large charge and, consequently,

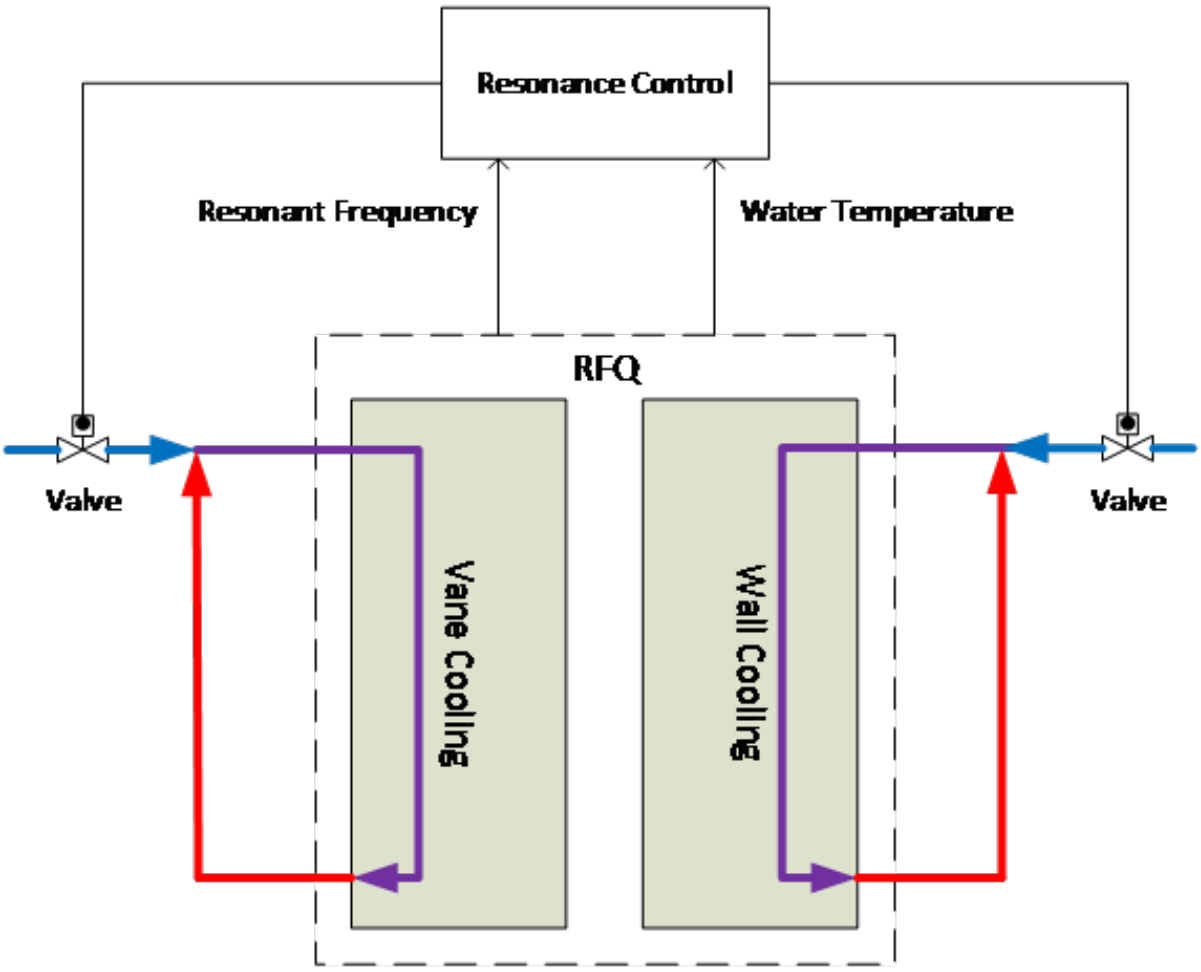

Figure 6.16: A simple block diagram showing the resonant control system of the RFQ. The system monitors the water temperature and the RFQ resonant frequency, and adjusts the flow rate of cooling water into the wall and vane cooling loops.

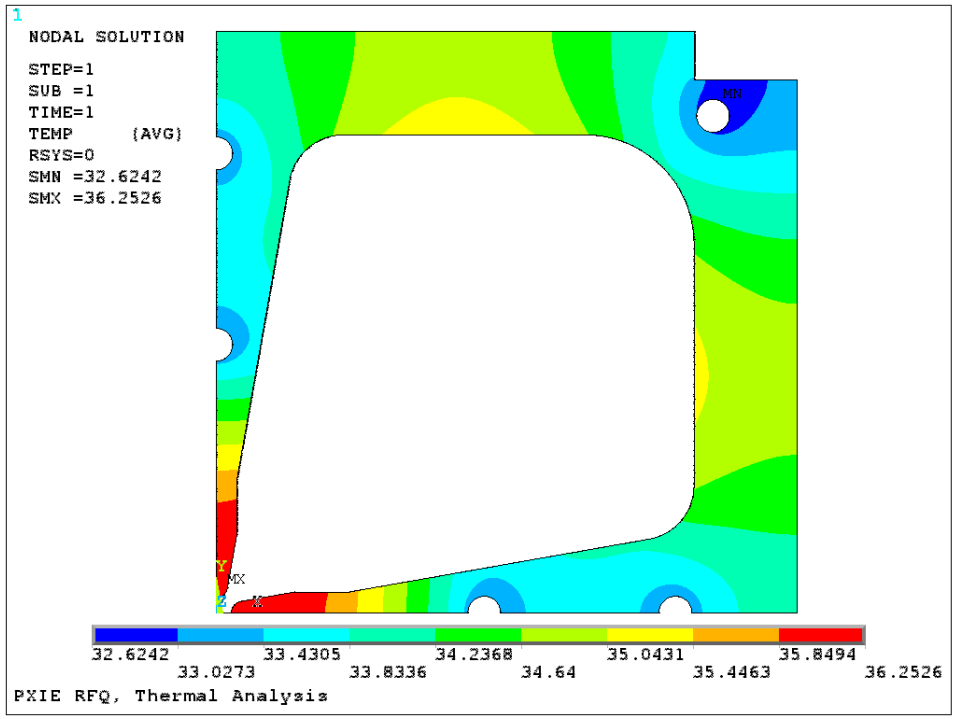

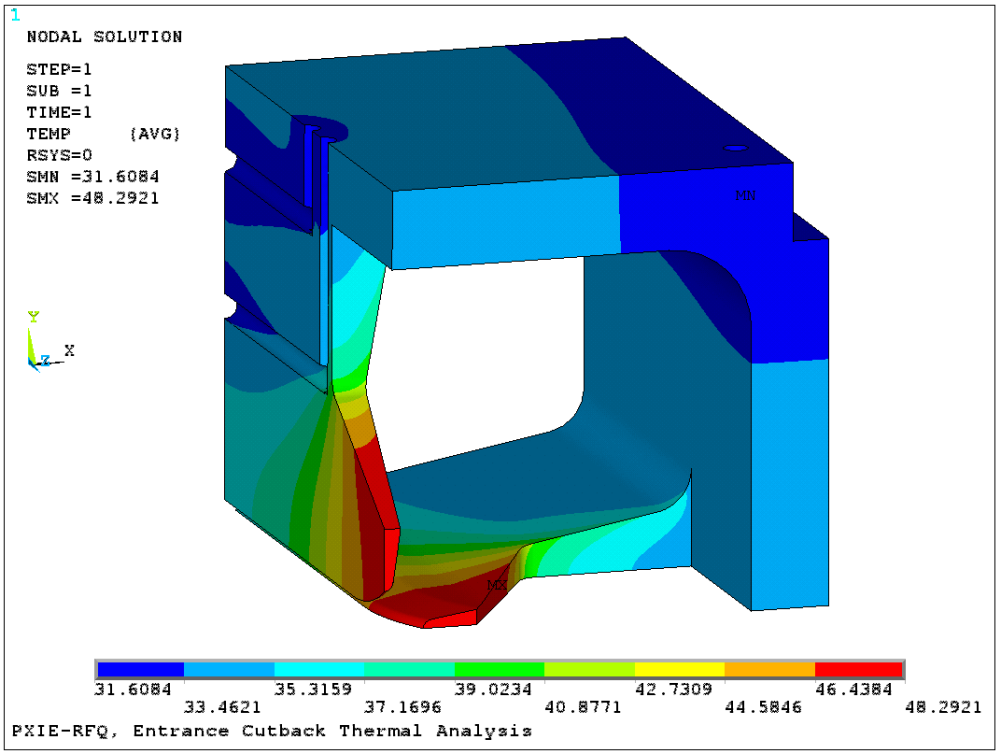

Figure 6.17: Temperature distribution in one RFQ quadrant body (above) and cut-back (below). The color scheme (degrees C) is at the bottom of each plot.

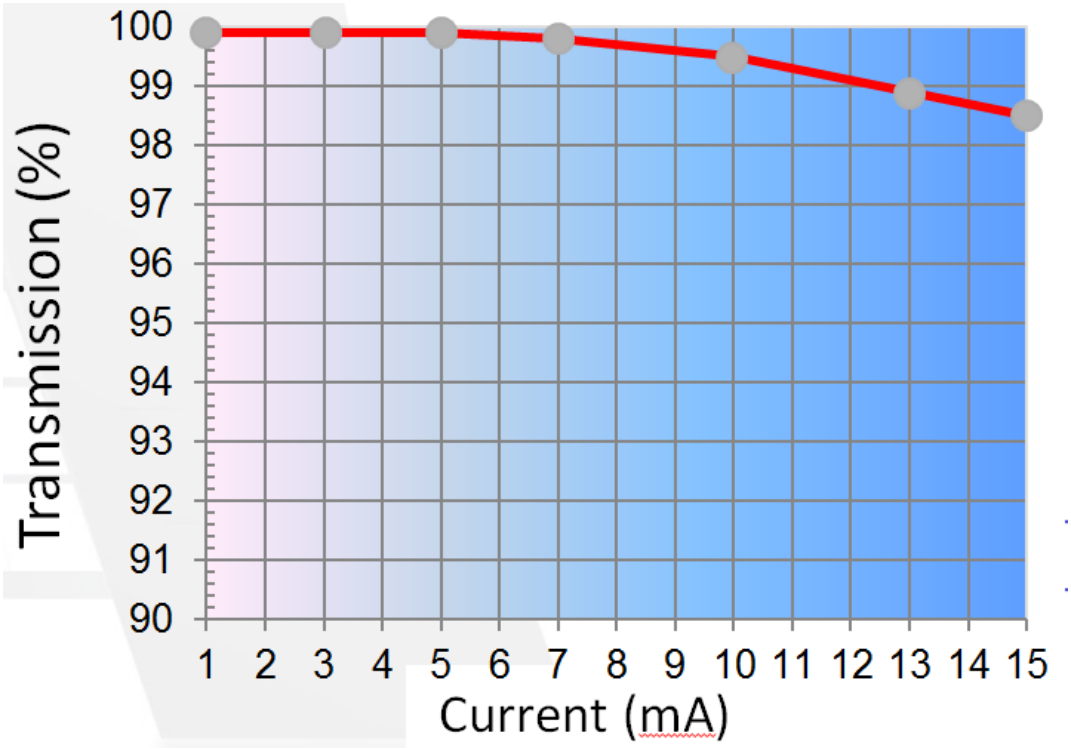

Figure 6.18: Dependence of the calculated RFQ transmission on the beam current.

minimization of the beam loss has a primary importance. Figure 6.18 presents the dependence of the computed RFQ transmission on the beam current. The design has over 98% transmission for a beam current from 1 to 15 mA. At the nominal current of 5 mA, 99.8% beam capture is achieved in this simulation.

6.2.3 Description of the MEBT

6.2.3.1 Concept

The Medium Energy Beam Transport (MEBT) transports the 2.1 MeV, 1-10 mA H^- beam between the RFQ and the HWR cryomodule with low emittance growth ($< 10\%$) and low beam losses of the passing bunches.

Typically, the main functions of an MEBT are to provide optical matching between the RFQ and the main Linac and to include tools for measuring the beam properties. The PIP-II MEBT is envisioned to have, in addition, several other distinctive features.

First, many of the PIP-II MEBT properties are determined by the bunch-by-bunch selection concept. The MEBT wideband chopping system directs unneeded 162.5 MHz bunches from the macro-pulse to an absorber according to a pre-selected pattern and transfers bunches chosen for further acceleration into the SC Linac with minimum distortions. This bunch separation is performed with two kickers separated by $\sim 180^\circ$ of betatron phase advance; the absorber is positioned

at ∼90° phase advance downstream of the second kicker. Thus, implementation of the chopping system requires significant elongation of the MEBT. On the one hand, the system itself requires 5 m of the beam line. On the other hand, the high-power density of the removed bunches onto the MEBT beam absorber makes the absorber a critical and inherently risky device. To alleviate possible catastrophic effects on the SRF cavities in case of an absorber vacuum failure, it is prudent to separate the absorber from the first cryomodule (HWR) by a beam line containing only more conservatively designed devices. The length of this region, determined by the time it takes to close a fast-acting vacuum valve in front of the HWR (10 msec) and the speed of the shock wave propagation (500 m/sec), needs to be ≥5 m. Recent experimental results at PIP2IT where a known amount of nitrogen is introduced into the vacuum chamber under various pressure loads (to simulate various vacuum leak/failure types) upstream of a Differential Pumping Insert (2.3 m upstream of a fast-acting valve) meant to significantly reduce the beam pipe's gas flow conductance, show that the amount of gas that makes it past the vacuum valve is, in the worst case tested, negligible. Thus, these results indicate that the distance of ≥5 m between the absorber and the fast-acting valve is quite conservative and may be revisited.

The second distinctive feature of this MEBT is a system of scrapers that protects both the SRF cavities and sensitive elements of the MEBT itself from errant beam. Finally, the MEBT allocates space for a wall protecting the low-energy part of the accelerator from radiation generated in the high-energy part. It should allow servicing the ion source with the PIP-II Linac still delivering beam.

The complete list of the MEBT functional requirements is presented in Ref. [64].

The resulting MEBT design is 14 m long with transverse focusing provided mainly by equidistantly placed quadrupole triplets with the exception of two doublets located immediately downstream of the RFQ. In this text, the spaces between neighboring triplets or doublets are referred to as MEBT sections. To keep the beam properly bunched, the MEBT includes four identical bunching cavities. The structure of the MEBT is presented schematically in Figure 6.19.

The period in the regular part of the beam line is 1175 mm, which leaves 650-mm long (flange-to-flange) spaces for various equipment. The first section labeled #0 in Figure 6.19 and located between doublets is shorter. It has an available space of 480 mm.

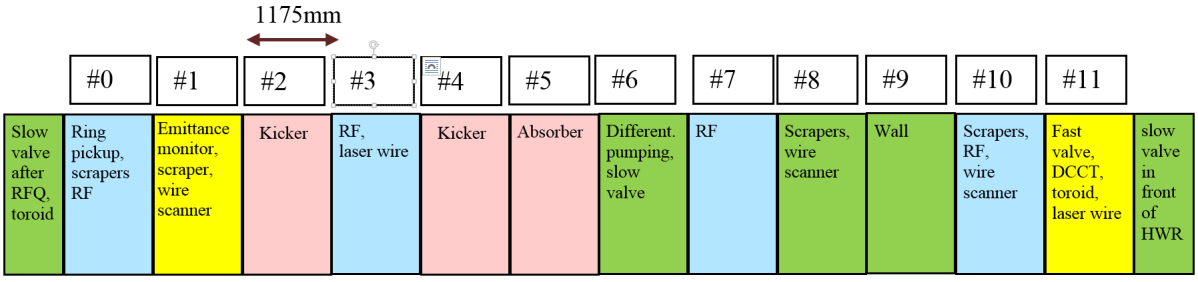

Figure 6.19: The MEBT structure. Sections are color-coded according to their main functions: green-vacuum, blue- RF, yellow- instrumentation, and pink - chopper.

6.2.3.2 Design

The H^- beam accelerated in the RFQ to 2.1 MeV enters the MEBT line, where it is chopped and matched for injection into the HWR cryomodule.

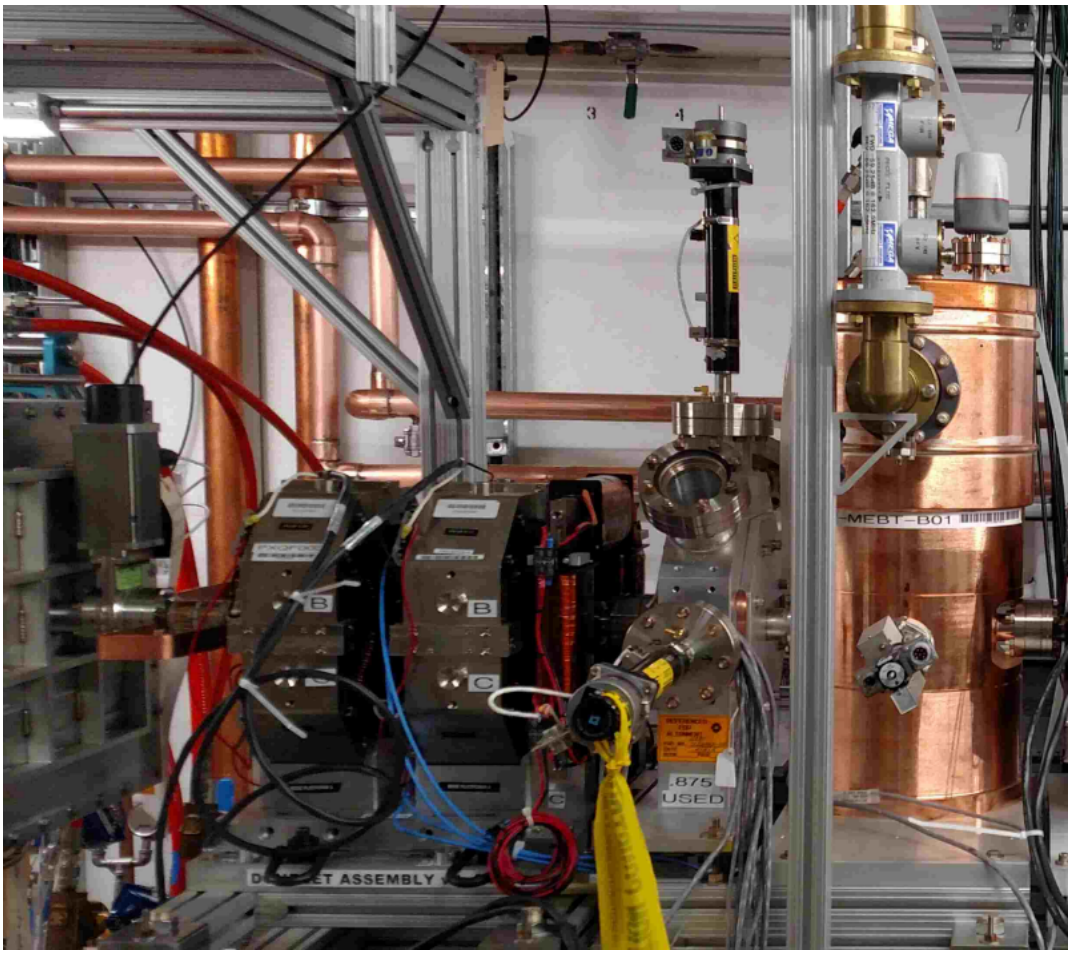

Figure 6.20: The MEBT section #0 as installed at PIP2IT. A quadrupole doublet is followed by a dipole corrector set, a scraper assembly, and a bunching cavity. A BPM is placed between the quadrupoles and is attached to the pole tips of the upstream quadrupole.

In addition to chopping and matching, the MEBT contains tools to measure the beam properties; a scraping system to protect both the SRF cavities and sensitive elements of the MEBT itself; and a vacuum system. In this chapter, the following major MEBT subsystems are discussed:

1. Transverse focusing
2. Longitudinal focusing & bunching cavities
3. Scraping

Note that the vacuum system, instrumentation, MPS, HLRF, LLRF, and controls are described in other sections of this document and are mentioned here only as they are relevant to the overall

design.

Transverse Focusing

Transverse focusing is provided primarily by equidistantly placed quadrupole triplets; the only exception is the two doublets immediately following the RFQ. Each triplet or doublet is followed by a pair of dipole correctors. The design of the central quadrupoles includes the BPMs mounted to the quad pole tips. The specifications for the quadrupoles and the correctors are listed in Ref. [65]. Figure 6.20 shows the air-cooled magnets. They were produced by BARC, India, according to these specifications, and are installed at PIP2IT.

The spaces between neighboring triplets or doublets are referred to as MEBT sections. The section separation in the regular part of the MEBT is 1175 mm, which leaves a 650-mm long (flange-to-flange) space for various equipment (only 480 mm in the section between doublets labeled #0 on Figure 6.19).

The 3σ envelopes of the transmitted bunches are presented in Figure 6.21, and the corresponding simulated emittances along the MEBT are shown in Figure 6.22.

The envelopes vary gently over the MEBT length to avoid emittance growth and are smaller only at the entrance and exit, where matching to the RFQ and the HWR occur. The notable exception is Section #8, where the vacuum chamber diameter is reduced to 10 mm over 200 mm. This insert is part of the Differential Pumping Section, which minimizes a flow of the gas released in the absorber to the SRF.

Longitudinal Focusing & Bunching Cavities

To keep the beam properly bunched and to match its longitudinal phase space into the first superconducting cryomodule, the MEBT includes four identical room-temperature bunching cavities. The cavities are specified in Ref. [66] and described in [67]. Each cavity is a quarter-wave 162.5 MHz resonator with the nominal accelerating voltage of 70 kV (at β=0.0668).

One of the main challenges for the RF design was operating at low frequency (162.5 MHz) combined with the limited space allowed; the flange-to-flange length should not exceed 35 cm. These requirements dictated the choice of a quarter-wave principal design for the bunching cavities (see Figure 6.23).

The power couplers and plunger tuners previously manufactured for the HINS [68] cross-bar CH cavity were used. This power coupler was designed to supply 75 kW of RF power, which significantly exceeds the maximum expected power of 4 kW. To compensate eventual manufacturing errors, a rotatable flange welded into a stainless-steel transition allows adjusting independently the RF coupling. An alumina ceramic window is utilized to separate the cavity vacuum from the surrounding atmosphere. The custom-made alumina ceramic window was brazed to two copper sleeves that later were brazed to the inner and outer conductors of the coupler. The motor-driven HINS tuners have a full stroke (the plunger active length) of about 42 mm, which is again more than sufficient to meet the tuning range requirement for the bunching cavities.

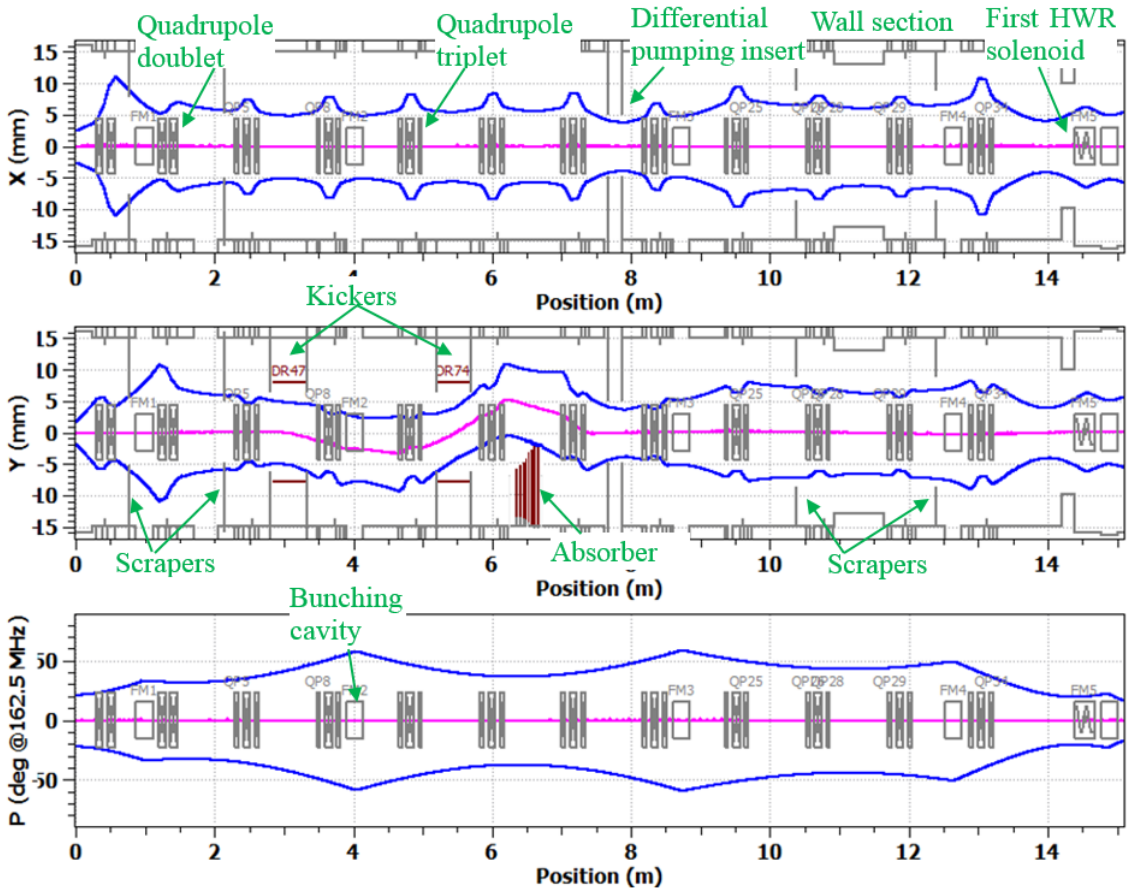

Figure 6.21: 3σ envelopes of the transmitted bunches simulated with the TraceWin code. The average beam current is 5 mA. Zero longitudinal position corresponds to the end of the RFQ vanes. The initial distribution is Gaussian in each of 6 dimensions. The initial transverse emittances are equal, 0.21 μm, and the longitudinal emittance is also 0.28 μm (both rms, normalized).

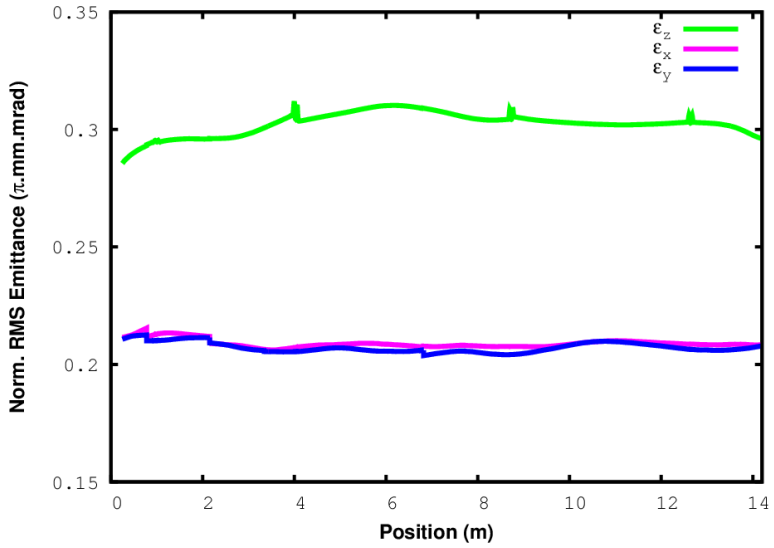

Figure 6.22: Simulated dynamics of the normalized rms beam emittance along the MEBT.

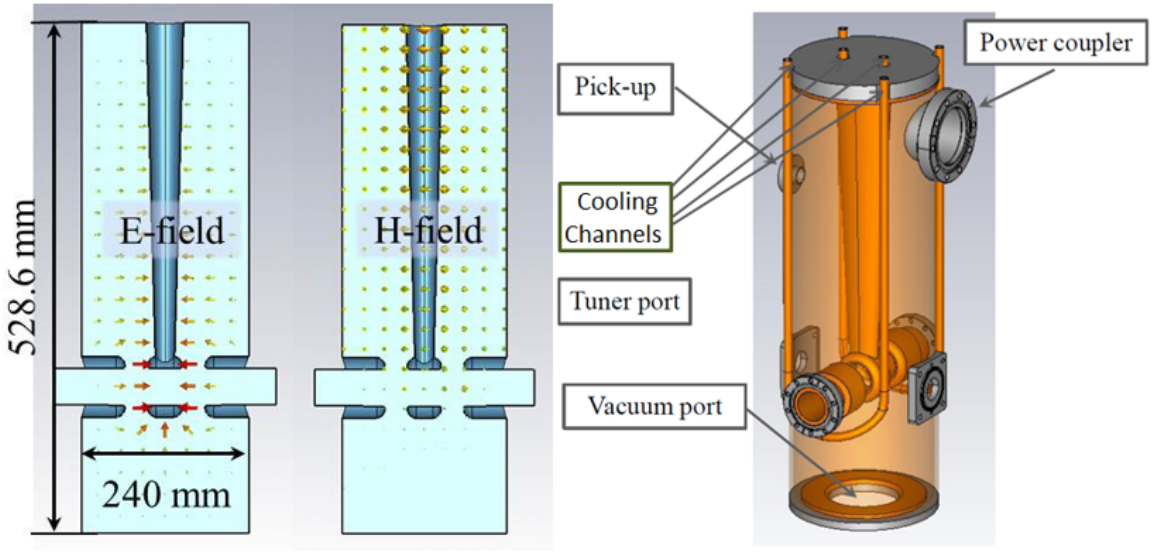

Figure 6.23: Principal RF design and the CST solid model of the bunching cavity.

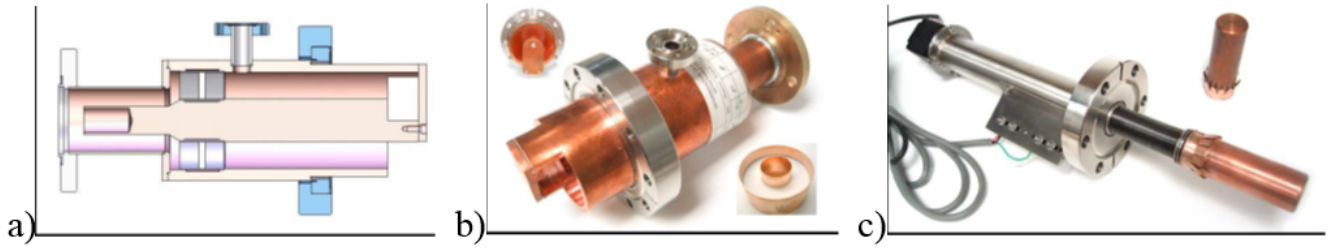

Figure 6.24: a) Principal design of the power coupler; b) Finished input power coupler; c) One of two tuners used on the buncher; Be-Cu contacts are welded to the removable copper fingers, hard stops and limit switches define the stroke, a linear actuator with captive shaft is used to operate the tuner.

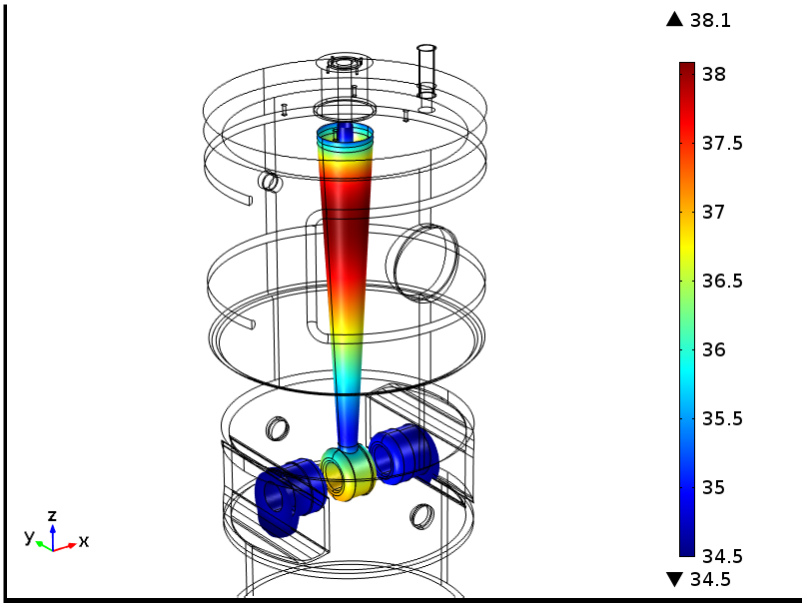

Figure 6.25: Temperature map on the stem from 3-D thermal study.

Matching simulations, preliminary thermal analyses for the power coupler and an estimate of the plunger tuning range have confirmed that the HINS parts can be used [67] (see Figure 6.24). Their usage noticeably reduced the design and manufacturing efforts.

Table 6.4: Comparison of the bunching cavities FRS with measurements

Parameter	Measurements	FRS
Frequency, MHz	162.5	162.5
Q-factor	10030	10000
Aperture diameter, mm	30	$\geq$30
Gap, mm	2·33	-
Shunt impedance, Ω	5.05×10^6	5.0×10^6
R/Q, Ω	503	500
Effective voltage, kV	70	70
Power loss in cavity wall s, kW	1.8	$\leq$2.2
Frequency tuning range, kHz	440	100
Flange-to-flange length, m	0.35	$\leq$0.35

The total power loss in the cavity walls at the effective voltage of 80 kV (nominal - 70 kV) is ~1200 W with ~850 W dissipated in the central stem. A traditional cooling approach was used for cooling the cavity body. To remove the power deposited in the central stem, a special coaxial counter-flow cooling scheme was developed [69]. The thermal study and the mock-up experiments confirmed the effectiveness of that cooling scheme (see Figure 6.25).

Four cavities have been manufactured and three are installed at PIP2IT, where they have been operated with beam. The photograph in Figure 6.26 shows the first bunching cavity with the two quadrupole doublets that form Section #0 on Figure 6.19. Prior to its installation, that cavity successfully passed high power tests. Table 6.4 presents a comparison of the functional requirements specifications (FRS) for bunching cavities and the measurement results.

Scraping System

Each of sections #0, 1, 8, and 10 in Figure 6.19 contains a set of four scrapers (Left, Right, Top, and Bottom), totaling sixteen plates. A scraper is an electrically-insulated, 75W-rated TZM rectangular plate movable across the 30-mm MEBT aperture [70]. The scrapers are used for several purposes: (1) for beam halo measurements and removal, (2) protection of downstream equipment from a beam loss caused by beam envelope and trajectory mismatches, (3) as auxiliary beam density distribution diagnostics, and (4) for formation of a pencil H^- beam for measurements downstream. The last two items only apply to the short-pulse mode of operation. The scraper sets in each of the upstream and downstream pairs are separated by a phase advance of $\sim 90^\circ$ to ensure effective removal of particles with large transverse actions.

A simulated example of the protection the scrapers provide is shown in Figure 6.27. The simulation considers that the kickers are mis-phased, so that the voltages on all kicker plates are half of the nominal value required for chopping bunches out. In this scenario a significant portion of the beam misses the absorber but is intercepted by a scraper downstream. Consequently, in high

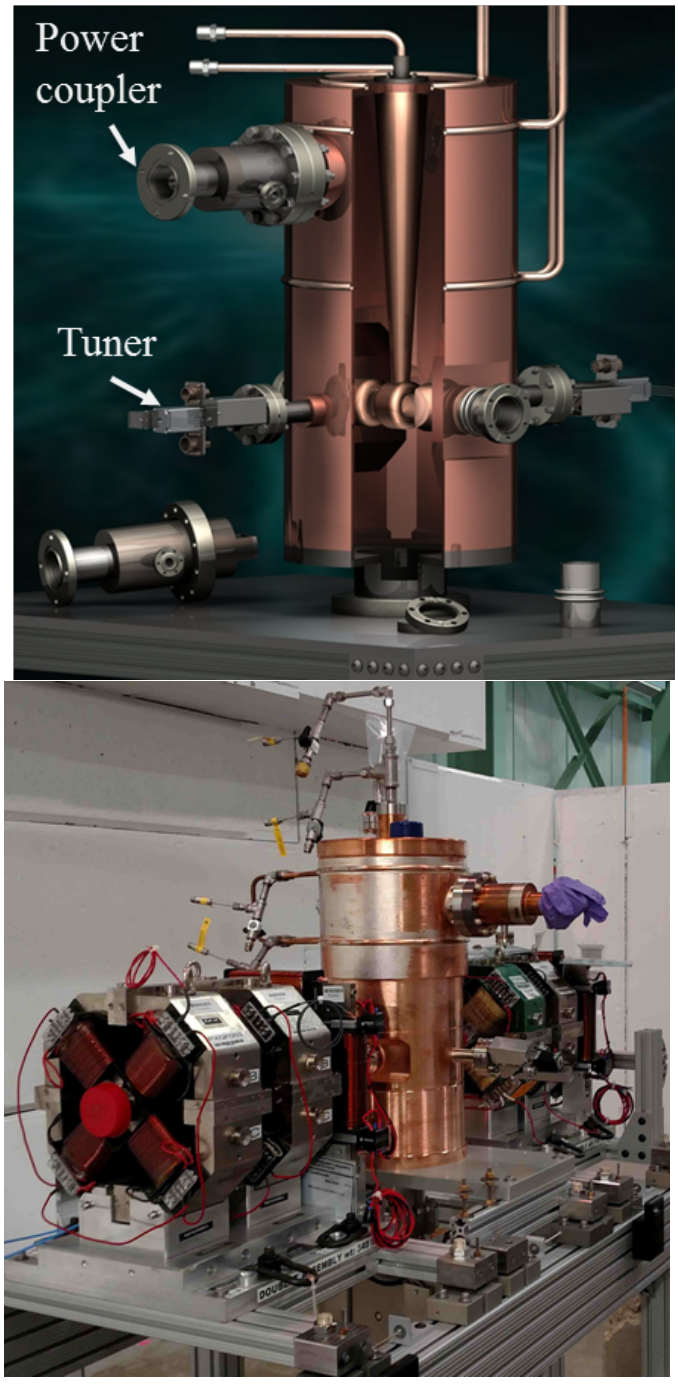

Figure 6.26: Mechanical solid model of the buncher showing the interior of the cavity and the first buncher installed in its place in the beam line of PIP2IT.

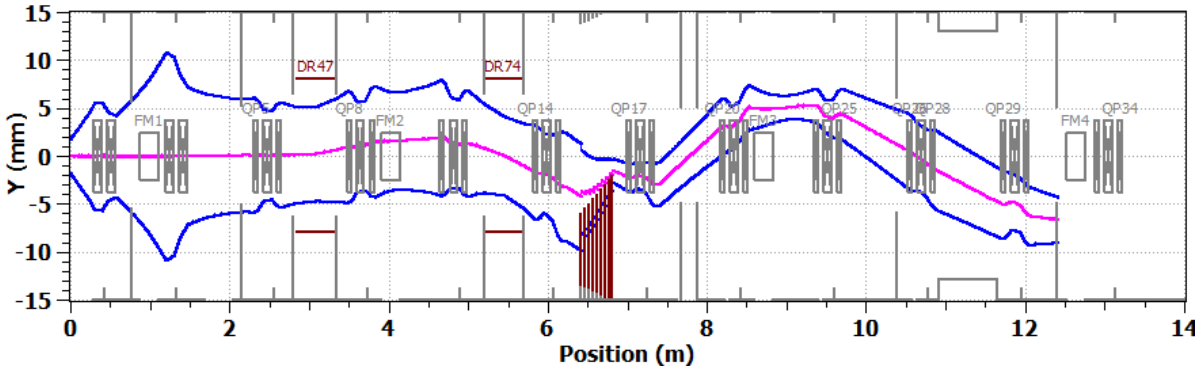

Figure 6.27: Beam Y 3σ envelope with voltages on all kicker plates equal to half of the nominal value required for chopping bunches out.

power operation this will result in a beam trip initiated by the MPS.

6.2.3.3 Description of the chopper system

The chopping system envisioned for the PIP-II MEBT consists of two identical kickers and a beam absorber. The kickers, which deflect the beam in the vertical (Y) direction, are separated by a phase advance of ∼180° (Y-direction) and synchronized, allowing the summation of their deflections. The absorber is at an additional ∼90° dvance with respect to the last kicker so that the angle introduced to a bunch by the kickers is translated at the absorber location into a 6σ separation in the vertical plane between the centers of the bunches designated for removal ("chopped-out") and for acceleration ("transmitted"). In the baseline scenario of the kicker operation, the trajectory of the transmitted bunches is such that, with the kickers off (i.e. zero voltage on the plates), using the dipole correctors, it avoids the beam absorber. To chop out bunches, the kicker plates are energized with opposite voltage polarities. This is illustrated on the second and fourth frames of Figure 6.28, which shows TraceWin simulations of the MEBT for nominal parameters. Note that the deflecting field is flipped between the first and second kicker.

Both the kickers and the absorber require state-of-the-art designs.

Kickers

Each kicker has a 50-cm long set of electrostatic plates connected by a broadband, traveling-wave structure. In average the transverse electric field of the kicking pulses propagates through the structure with a phase velocity equal to the speed of the H^- ions.(2.00 mm/ns, $\beta = 0.0668$). Specifications for the kicker can be found in Ref. [71]. The top and bottom parts of the kicker are powered from pulse generators with voltages of opposite polarity which doubles the value of the kick.

The main parameters defining the choices for the kicking scheme are the vertical emittance (∼0.2 μ n) and a reasonable voltage transition for a single kicker plate between neighboring bunches, which was chosen to be 500 V. Then, the minimum kicker gap is defined from the expected beam

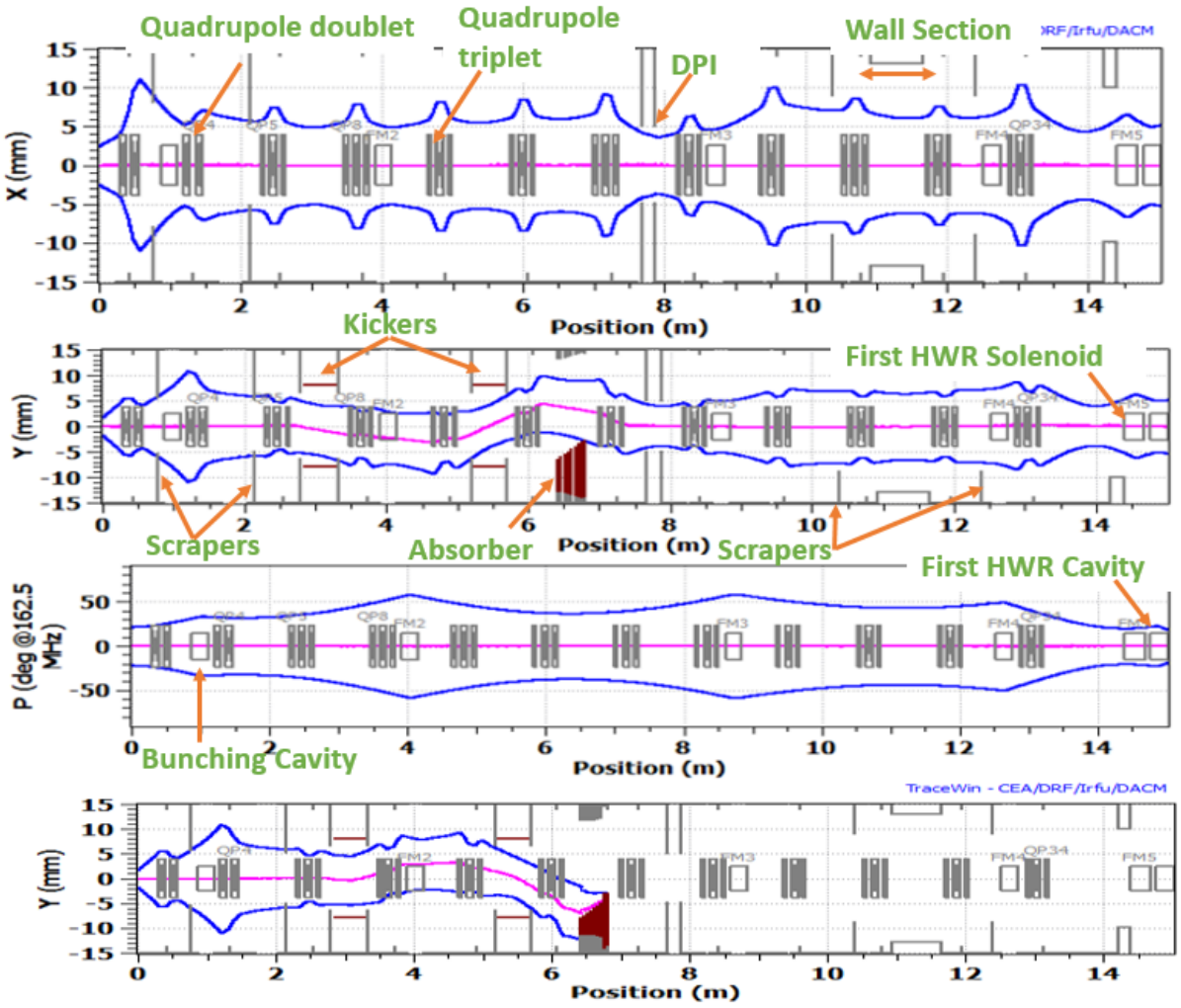

Figure 6.28: 3σ beam envelopes of the transmitted bunches for 5 mA in the horizontal (x), vertical (y) and longitudinal (p) planes, and of the chopped-out bunches (vertical plane only) simulated with TraceWin. For the 2nd frame from the top, the voltages of all kicker plates are set to zero. For the last frame, the top and bottom plates' voltages of the first kicker are +500 V and -500 V, correspondingly, and opposite for the second kicker, (-500V, +500V).

size plus some space to accommodate the trajectories of both passing and removed bunches. With an added safety factor of 20%, the kicker gap was set to 16 mm.

Based on the experience at other labs (see, for example, [72]), special attention is paid to the survival of the kickers in real operational conditions, where errors are unavoidable. First, the design of the kicking electrodes specifies being able to withstand the steady-state heating from a 20-μA CW beam loss (0.4% of the nominal 5 mA beam) and an accidental loss of 20 J (e.g.: 2 ms at 5 mA). Second, the kicker aperture - 16 mm between the two electrodes - is limited to 13 mm by electrically-isolated protection plates installed on both sides of the kicker so that in case of mismatched transport or a steering error, the beam current intercepted on these plates would trigger the MPS (Machine Protection System) to switch-off the beam.

To minimize the emittance growth, the null value of the electric field has to be uniform and constant to within $\pm$25 V along the length corresponding to 6 rms bunch lengths (1.3 ns or 26 mm). With a period of 1/162.5 s, the bunches coming out of the RFQ are separated by 123 mm, which is much larger than the gap between the kicker plates, 16 mm. Therefore, the electric field deflecting one bunch does not directly affect other bunches. Initially, two versions of the kicker were being investigated [73] and were referred to by the characteristic impedance of their traveling wave structures: 50 Ohm and 200 Ohm. Prototypes for both kickers were fabricated and tested with beam at PIP2IT. While both designs met their specifications, programmatic and funding considerations led to choosing the 200-Ohm design as the baseline for PIP-II.

The 200-Ohm traveling-wave structure is a helical winding around a grounded cylinder with plates attached to the windings (Figure 6.29).

The main idea behind this scheme is that the high impedance decreases the power requirement for the driver to the level where a state-of-the-art fast switch can be developed to drive the kicker. Since this driver is DC-coupled, the pulse can remain unipolar during each 162.5 MHz period, which in turn, reduces the requirements for the rise and fall times of the pulse (w.r.t. the 50-Ohm design). It also significantly simplifies the requirements to the dispersion of the traveling-wave structure (e.g. the non-linearity of phase response with frequency). An example of an output pulse of a prototype driver is shown in Figure 6.31. Note that because of the non-standard impedance, custom-made feedthroughs, transmission lines, and current loads had to be developed as well for this scheme.

As mentioned previously, tests with beam were successfully carried out at PIP2IT. While 2 kickers are needed to apply the proper kick to a beam with nominal parameters, the bunch structure required for bucket-to-bucket injection into Booster was realized using a single kicker and a short-pulse beam which vertical size was reduced using scrapers upstream. Figure 6.31 shows the corresponding bunch pattern as measured by a Resistive Wall Current Monitor (RWCM) located further downstream.

Absorber

The undesired bunches are directed onto an absorber that is displaced vertically from the beam line axis. To accommodate the entire beam that the RFQ can deliver, the absorber is specified in Ref. [74] for a maximum beam power of 21 kW (a 10-mA CW beam completely diverted to the absorber). The power density in the beam with a 2 mm rms radius exceeds by an order of

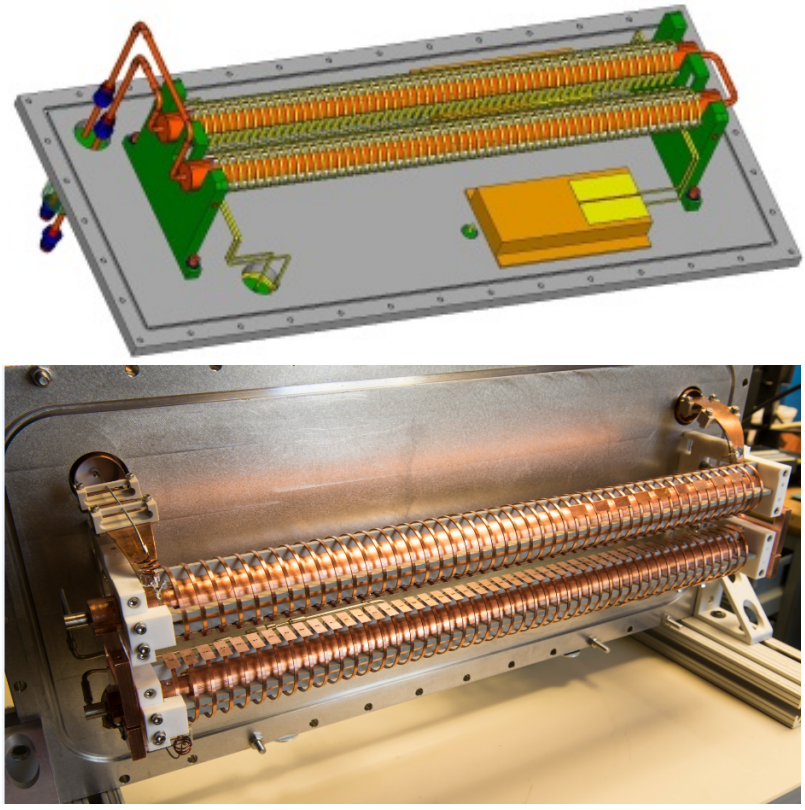

Figure 6.29: Conceptual design (left) and photograph (right) of a single-helix model of the 200-Ohm dual-helix kicker.

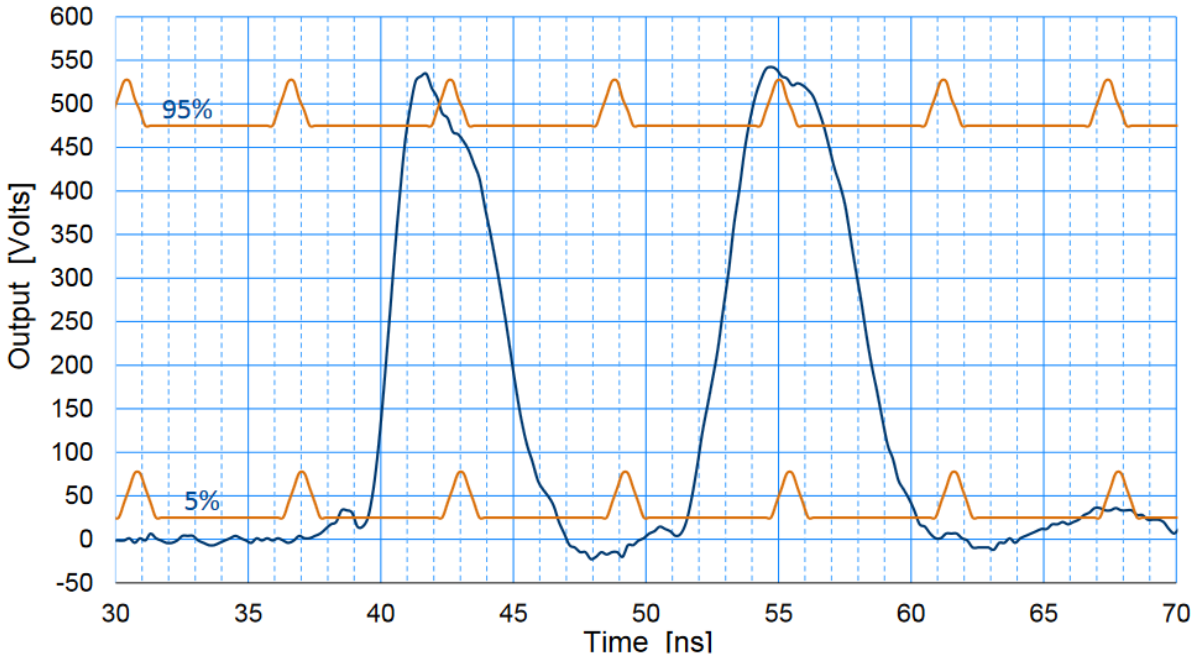

Figure 6.30: An example of an output pulse of a prototype driver being developed at Fermilab. The blue curve is the measured output voltage of the fast switch shaped to remove two bunches out of a CW sequence. The orange lines indicate the $\pm 5\%$ tolerance boundary for the voltage stability and mark the assumed position of the bunches and their 6σ length.

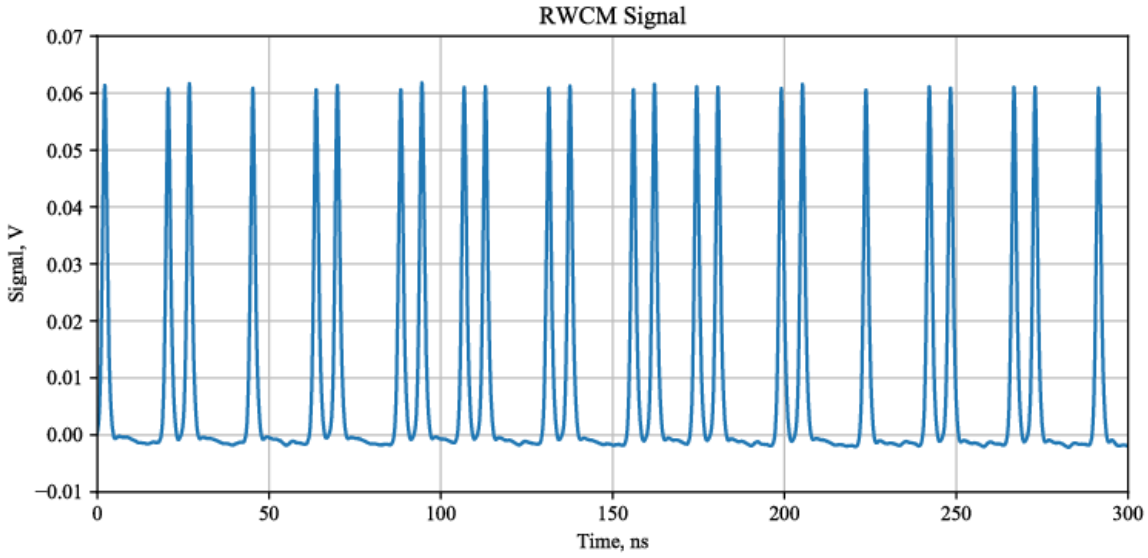

Figure 6.31: RWCM waveform showing part of the bunch pattern tailored for Booster injection created by the 200 Ohm kicker.

magnitude what is technically possible to intercept at a normal angle of incidence without melting the surface. To decrease the surface power density, the absorber is positioned at a small angle (29 mrad) with respect to the beam (Figure 6.32).

Challenges in the absorber design include spreading the energy deposition, managing surface effects (sputtering and blistering), containing secondary and reflected particles, accommodating radiation effects, maintaining vacuum quality, and survival at high temperatures with temperature-induced mechanical stresses. Presently the design choice is an absorber with an absorbing surface composed of multiple absorber blocks made of the molybdenum alloy TZM and preloaded against a water-cooled aluminum strongback [75]. In comparison with an initially considered monolithic design, this solution slightly increases the thermal conductance from the absorber surface to water channels but dramatically decreases the chance for catastrophic failure if a crack developed at the absorbing surface propagates all the way to the water channels. Power management in a $\frac{1}{4}$-size prototype of such design was successfully tested on an electron-beam test stand [75]. The prototype was also installed in the PIP2IT beam line where it was irradiated by a 735 W proton beam for 36 hours with 98% beam up time. No damage or deterioration was observed.

The beam stopped at the absorber can deliver quite a large volume of hydrogen as well as additional degassing from the receiving surface of the absorber. If not addressed, this can spoil the vacuum in the MEBT, which was actually observed with the prototype during the 735 W test just mentioned. With only one 1000 l/s turbo-pump on that assembly, the vacuum locally rose to $\sim 6\times10^{-6}$ Torr. Thus, to suppress H^- stripping and to reduce the gas load to the downstream cryomodule, the vacuum in the vicinity of the absorber should be less than or about 2×10^{-7} Torr. This vacuum requirement is supported by four turbo-pumps installed on the absorber enclosure and the differential pumping pipe installed in section #6.

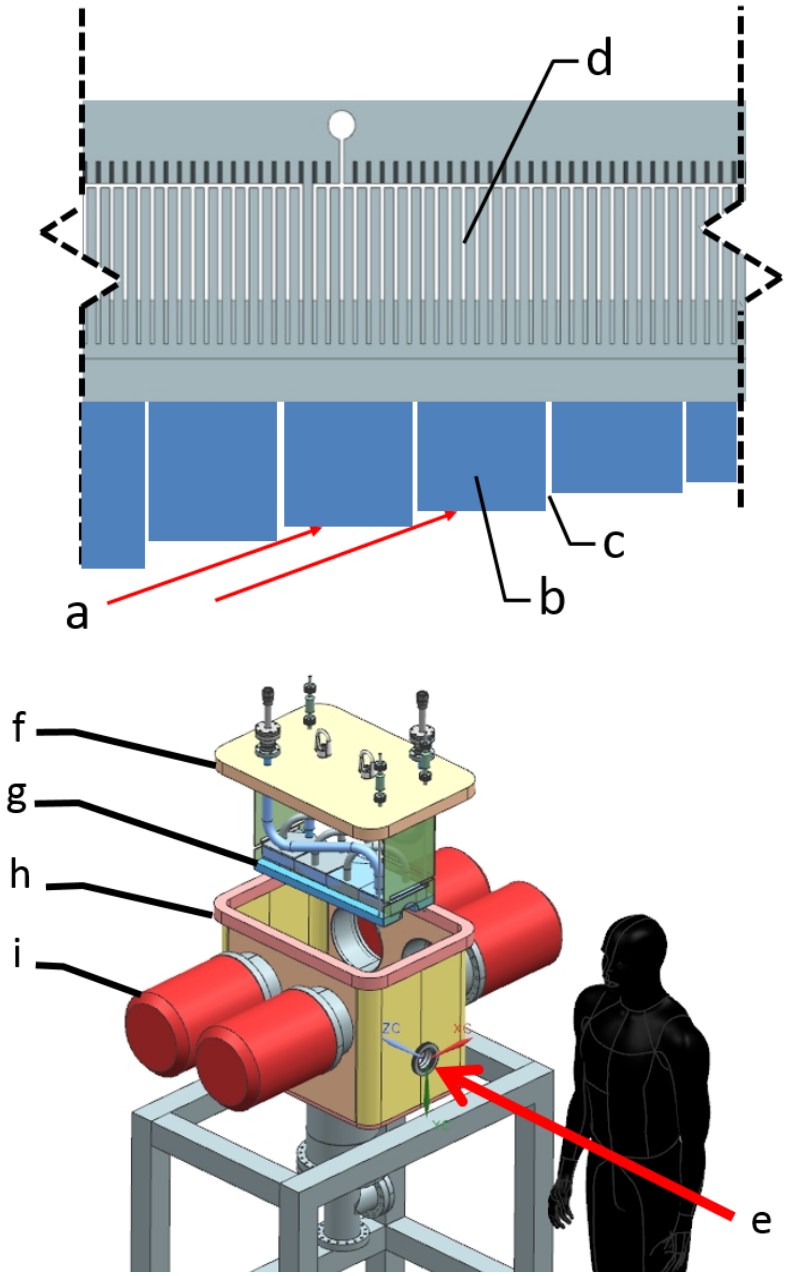

Figure 6.32: A conceptual design of the MEBT absorber. Left: a side-view cross section of the absorber showing (a) the beam incident on the surface, (b) the segmented absorber blocks, (c) the shadowing step increment (magnitude exaggerated), (d) the 300μm wide water cooling channels with 1mm pitch. Right: an exploded view of the absorber assembly showing (e) the incoming beam, (f) the flange-mounted absorber subassembly, (g) the absorber blocks, (h) the enclosure with provisions for secondary particle absorption, (i) the turbo pumps.

Chapter 7

Superconducting RF Linac

The superconducting RF Linac is composed of fully segmented cryomodule units installed in the cold Linac portion of the accelerator. This section describes the technical design of the cold section which is divided into three parts: a halfwave resonator cryomodule, spoke cryomodules and elliptical cryomodules.

Figure 7.1 shows the layout of the PIP-II Linac with the superconducting section highlighted in blue. Table 7.1 summarizes the makeup of the superconducting section and the corresponding operating energy ranges for each cryomodule type.

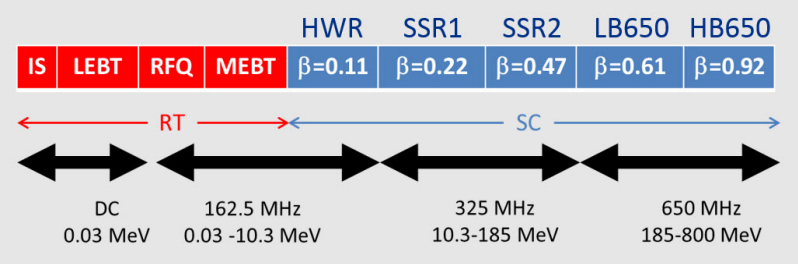

Figure 7.1: Linac technology map.

Table 7.1: Superconducting RF cavity configurations.

CM name	Number of Cryomodules	Cavities per CM	Freq. (MHz)	Cavity type	Energy range (MeV)
HWR	1	8	162.5	Half wave resonator	2.1 - 10.3
SSR1	2	8	325	Single-spoke resonator	10.3 - 35
SSR2	7	5	325	Single-spoke resonator	35 - 185
LB650	11	3	650	Elliptic 5-cell cavity	185 - 500
HB650	4	6	650	Elliptic 5-cell cavity	500 - 800

7.1 Halfwave cavities and cryomodule

The overall design of the half-wave cavity cryomodule is an evolution of the top-loaded box cryomodules used successfully for an energy upgrade of ATLAS in 2009 [76] and for an intensity upgrade of ATLAS in 2014 [77]. The HWR cryomodule is assembled in stages. First, the low-particulate clean assembly of the cavities, the RF power couplers, the RF pickup probes, the solenoids, the beamline gate valves, the vacuum manifold and the titanium strong-back support structure is carried out in a Class 100 clean room. Then, this assembly is hermetically sealed and removed from the clean room. This separates the "clean" low-particulate beamline vacuum system assembly from the "dirty" portions of the cryomodule assembly work, preserving, to the best of our ability, the cavity performance. Once out of the clean room the helium distribution system is installed and the assembly is then hung from the lid of the cryomodule. Once hung, the remainder of the cryomodule subsystems are installed such as the slow tuners, instrumentation, alignment targets, solenoid conduction cooled leads, thermal intercepts and RF transmission lines. The complete lid assembly is then lowered into the insulating vacuum vessel completing the cryomodule.

7.1.1 Cavity design

Beam dynamics optimization determined the optimal beta of $\beta_{opt} = 0.112$. The cavity design is based on recent advances in SRF technology for TEM-class structures being developed at Argonne National Laboratory (ANL). Highly optimized electromagnetic parameters which maximize the real-estate gradient while maintaining low dynamic cryogenic loads and peak surface fields were achieved using a conical shape for both the inner and outer conductors. A "donut" shaped drift tube in the center conductor has been developed to minimize the undesirable quadrupole component of the electric field presented in Figure 7.2.

The niobium cavity is integrated with the stainless steel helium vessel as shown in Figure 7.3. The regions of the cavity with appreciable surface electromagnetic fields are formed from high purity (Residual Resistance Ratio, RRR > 250) 0.125 in. $\pm$0.010 in. thick niobium sheet and consist of the cavity outer conductor, inner conductor, toroid ends, re-entrant noses, re-entrant nose doubler plates and coupling port extension tubes. Note that the re-entrant nose doubler plates are made from the same size sheet as the re-entrant noses and both parts are made from RRR > 250 niobium in order to avoid mixing of low and high purity sheets in fabrication even though the doubler plates are completely shielded from the cavity electromagnetic fields. The toroid gussets were machined from half-inch thick RRR $\sim$25 niobium plate while the beam ports (RRR > 250), coupling ports (RRR $\sim$25) and inner conductor drift tube (RRR > 250) were machined from bar stock.

The integral helium vessels surrounding the niobium cavity are fabricated using joint certified 304/304L stainless steel (SST). Niobium-to-stainless steel braze transitions [76] are utilized for joining the SST helium jacket with the niobium cavity at seven locations: two for the beam ports, one for the power coupler port and four for the toroid coupling ports. The cavity mechanical structure is designed to satisfy FNAL's safety requirements. These requirements include the niobium within the pressure boundary, prohibiting the application of any ASME U-stamp. To provide an

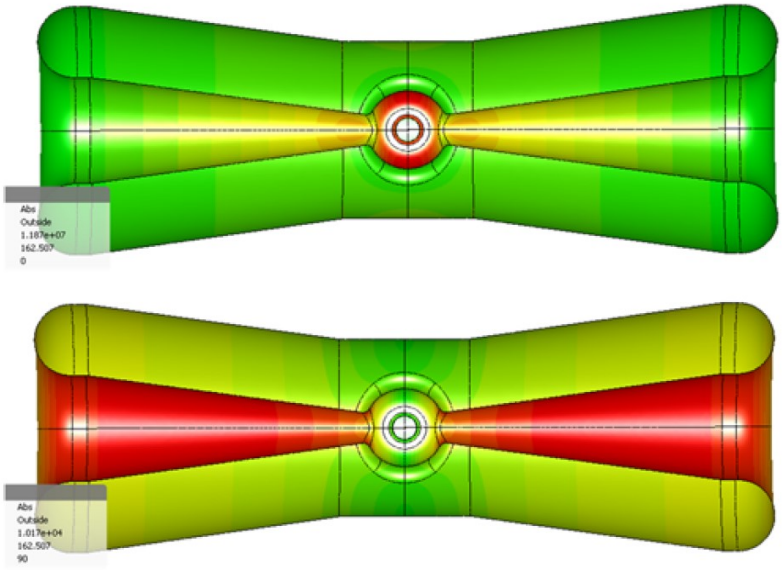

Figure 7.2: Half-wave resonator model in Microwave Studio (MWS). The picture shows electric (top) and magnetic (bottom) field distributions on the surface. Red and green colors correspond to high and low intensities, respectively.

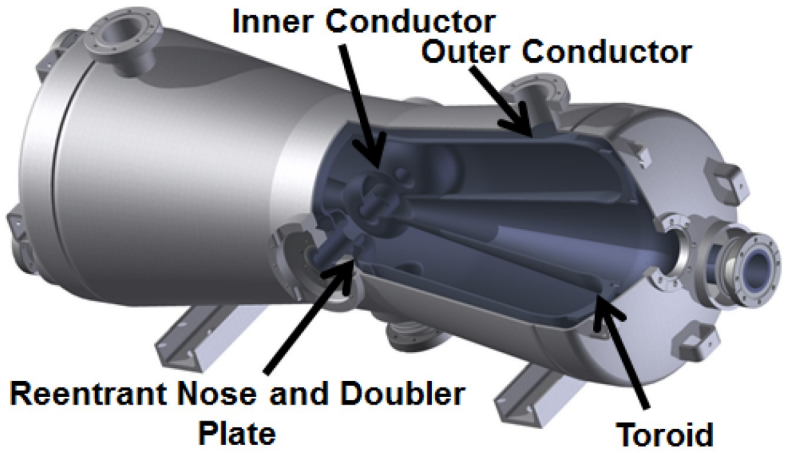

Figure 7.3: 3D cutout of a dressed HWR cavity.

equivalent level of safety in the design the analysis uses the techniques and rules set forth by the ASME boiler and pressure vessel code Section VIII, Division 2, Part 5, Design by Analysis using niobium material properties given in the code. Using this the ASME BPVC was applied to the complete niobium/SST structure to demonstrate protection against failure for a 2 bar Maximum Allowable Working Pressure (MAWP) at 293 K and a 4 bar MAWP at 2 K; we found that any analysis which passes with the 293 K material properties and 2 bar MAWP would pass at 2 K, even with the greater MAWP. This is due to the increased mechanical strength of the niobium material at low temperature. The cavity region with the smallest factor of safety, but still an acceptable one, is the area around the inner conductor drift tube. This region was reinforced by increasing the wall thickness of the solid rod used to fabricate the inner conductor drift tube. The thicker wall reinforced the area ensuring safe operation above the safety analysis requirements. Figure 7.4 shows the cavity niobium strain from a pressure load analysis. The central portion of the inner conductor is the most susceptible to plastic collapse but still exceeds the FNAL safety requirements.

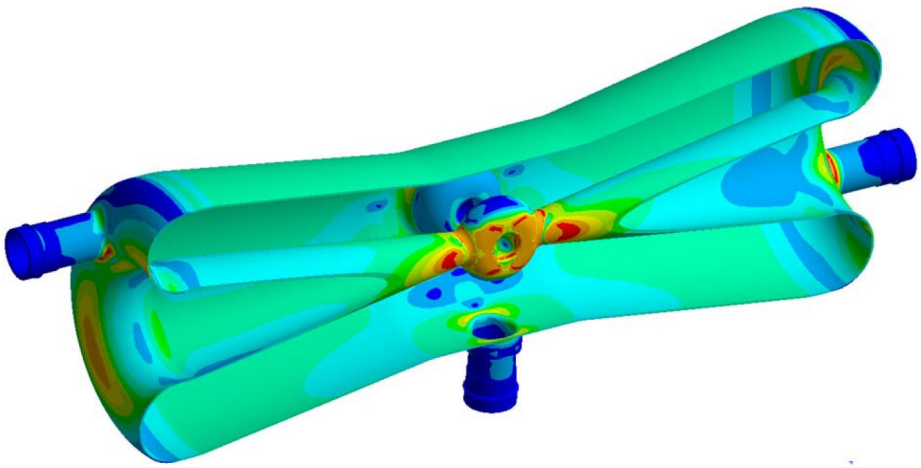

Figure 7.4: Niobium material strain from a limit-load analysis of the half-wave cavity. Areas of high strain are around the ports and in the center of the inner conductor where the beam passes. No strain values are given due to the unrealistic material properties used in a limit-load analysis.

The results of the safety analysis studies showed that no gusseting is required. Simulations of the slow tuner were performed by applying a force to the SS flanges of the helium jacket. For example, a 10 kN force results in a frequency shift of -120 kHz. In operation the slow tuners are limited by mechanical stops to this frequency range and pose no threat of plastically deforming the half-wave resonators.

The primary operational parameters for the HWR presented in Tables 2.2, 3.7 and 3.8 show parameters that are based on experience with the ATLAS energy upgrade cryomodule and its long-term operation [78], as well as recent tests of the first HWR cavities [79]. As shown in Figure 7.5, the prototype tests of the two half-wave resonators show less than 3 nΩ residual surface resistance at 48 mT, which readily supports the design parameters of the HWRs. Recent measurements of the first two HWR cavities showed Q_0's exceeding 1.7×10^{10} at the operating gradient which corresponds to a surface resistance of 2.6 nΩ. This value is slightly larger than that achieved with the 72 MHz quarter-wave cavities installed in the ATLAS heavy-ion Linac in 2014 and it is a more optimistic value for the surface resistance if one considers the 2.2 times increase in the

operating frequency. Thus, the measured Q_0's provide a margin of more than 3 times relative to a conservative value of Q_0 presented in Table 3.8. Note that the ATLAS cavities were measured in a real cryomodule while the HWR cavities were characterized in an off-line test stand. However, the experience accumulated in recent years assures us that there is no significant Q_0 increase when a cavity is installed in an Argonne cryomodule.

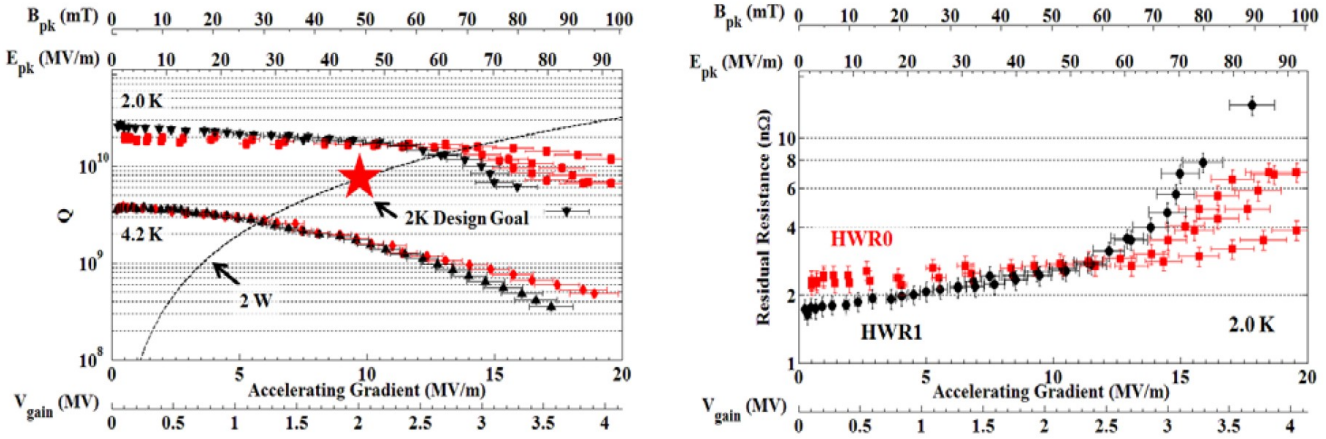

Figure 7.5: Left, the measured Q_0 vs E_{acc} for the two half-wave resonator prototypes. Right, the cavity residual resistance corresponding to the Q_0 measurements. Note that the operating voltage is 2 MV which corresponds to the peak magnetic and electric surface fields of 48 mT and 45 MV/m, respectively.

7.1.2 Cold tuning system

The first production half-wave resonator with a slow tuner installed is shown in Figure 7.6. The slow tuner is a pneumatically actuated device which compresses the cavity at the beam ports. The slow tuner is based upon multiple prototype tests conducted at both room temperature and 4 K. In addition, the safety analysis studies described in 7.1.1 showed that a df/dP equal to 8 Hz/mbar was achieved. This value was determined sufficient for operation and further design modifications to reduce df/dP have not been pursued. Design changes implemented in this unit include the elimination of the bushing/rod assemblies which can bind and gall. The test of the assembly verified the slow tuner design and the cavity frequency tuning calculations, and determined its 2 K performance. Previous testing and evaluation of the microphonic RF noise found the cavity dynamic detuning to be less than 5 Hz, thus a fast tuner is not required. The RF power margin was chosen to be sufficient to control microphonic induced RF phase noise (mainly related to helium pressure fluctuations) without a fast tuner at the nominal cavity loaded bandwidth of 66 Hz. The main parameters of the HWR are shown in Tables 2.2, 3.7 and 3.8.

7.1.3 Fundamental power coupler

A capacitive adjustable 7 kW RF coupler prototype has been designed, constructed, and successfully tested. Figure 7.7 shows the 7 kW RF coupler attached to a half-wave resonator on a 2

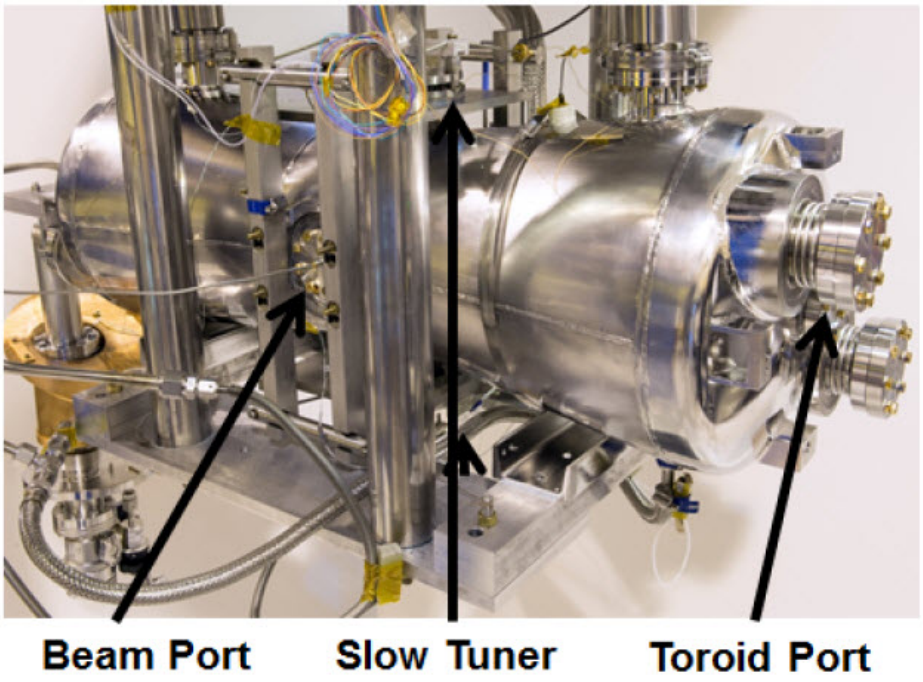

Figure 7.6: Halfwave resonator with slow tuner installed.

in. port located in the plane of the beam ports at 90° to the beam direction. Figure 7.8 shows the coupler performance with full reflection up to 7 kW which is the design goal. However, it is important to note that the coupler bellows and the cold window have previously been tested at up to 9 kW with full reflection. A 1 kV DC voltage bias is used to suppress multipacting in the entire range of operating power. The coupler antenna is at a negative potential relative to the outer conductor.

7.1.4 Focusing element

The HWR cryomodule has eight superconducting solenoids. Each solenoid has one main focusing coil in series with polarity reversing bucking coils, and four correction coils as shown in Figure 7.9. Measured fields are shown in Table 7.2.

Table 7.2: Field measured for a production solenoid

Coils	Field	Current	Note
Main coil	6 T	82.3 A	No quench/heating
X-dipole	30 T.mm	47.3 A	No quench/heating
Y-dipole	30 T.mm	48.2 A	No quench/heating

The dipole correction field was measured and compared with the main solenoid coil powered on and off. No screening effect was observed. The stray field was simulated and verified by measurement as shown in Figure 7.10. A cold test was performed which verified that the stray solenoid field does not compromise the cavity performance. A repeated intentional cavity quench while the solenoid

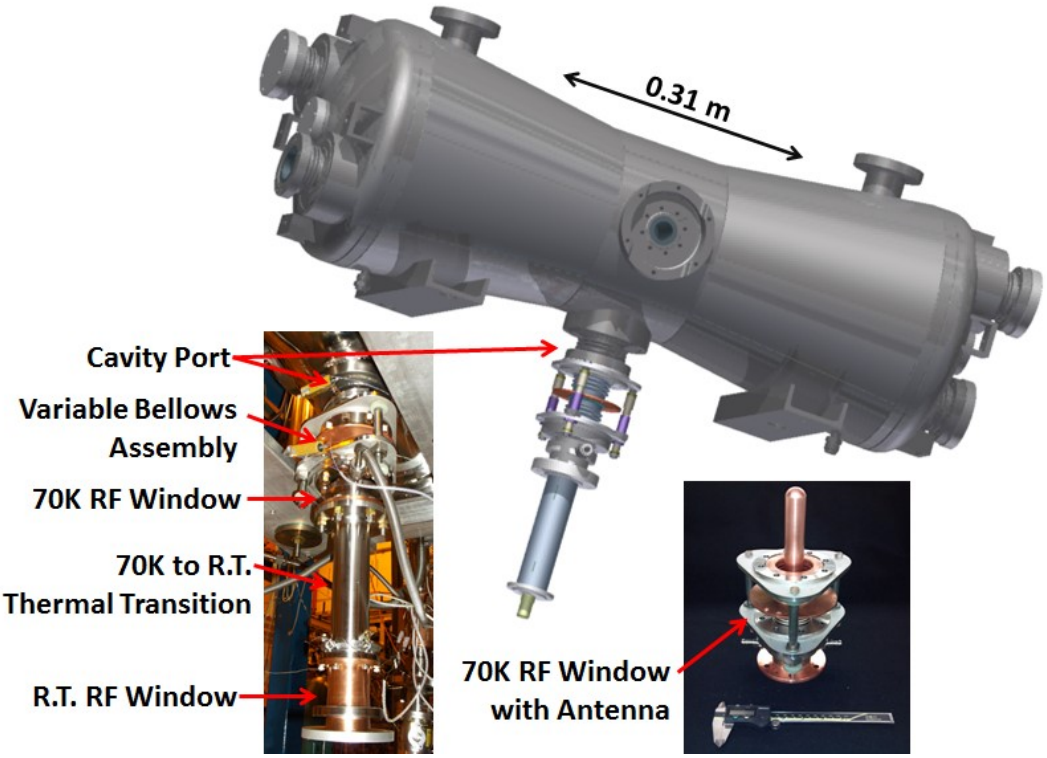

Figure 7.7: HWR cavity 3D model in INVENTOR with coupler hardware, insets. R.T. = room temperature.

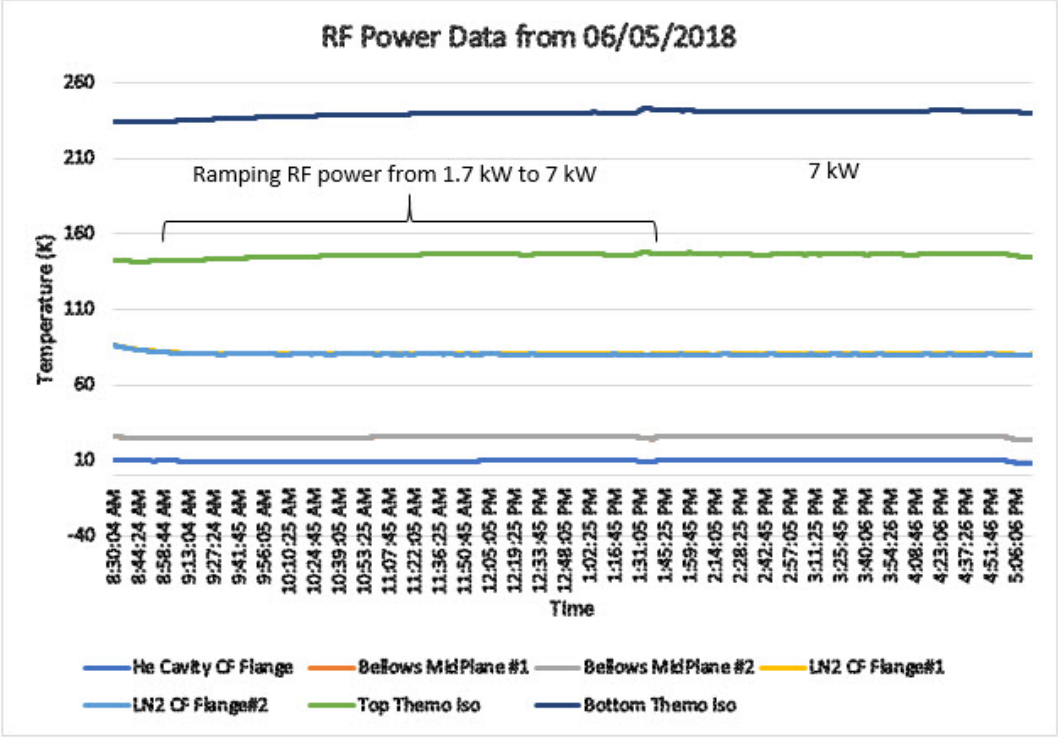

Figure 7.8: Cold testing results from running the RF coupler up to 7 kW, the design operating power level and operating conditions. During testing, no multipacting heating was observed with 1 kV bias voltage.

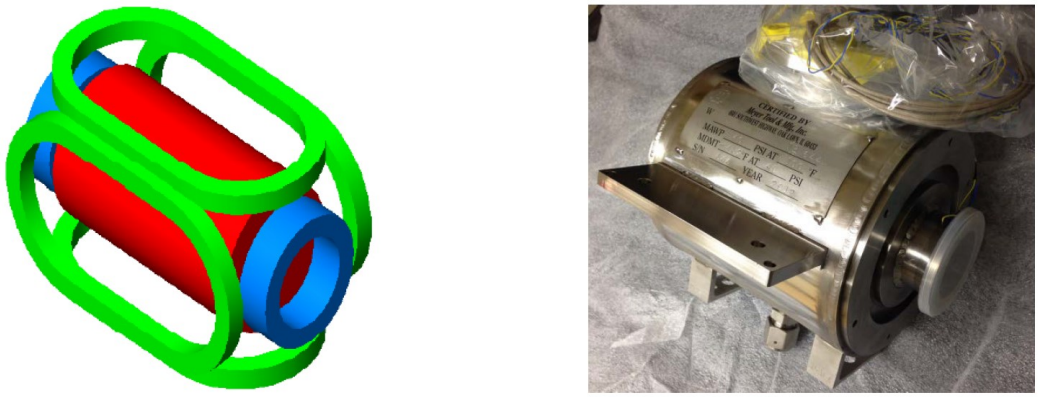

Figure 7.9: Superconducting solenoid with steering coils.

was powered at nominal current did not show any negative quality factor drop. Measured field alignment was demonstrated to be within 0.25 mm after cool down.

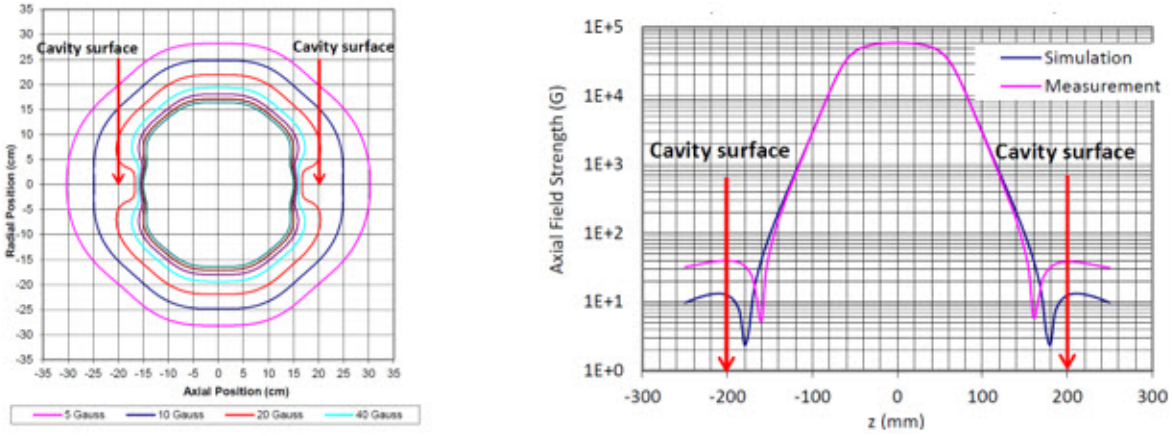

Figure 7.10: Solenoid stray field calculated (left) and measured (right).

7.1.5 Cryomodule

The HWR cryomodule vacuum vessel design balances the need to house a 6 meter long accelerator string with all of its support systems inside the limited space available for assembly while maintaining compliance with FNAL's safety standards. The vacuum vessel has two cryogenic input coolant streams: a 5 K, 3 bar gaseous helium stream and a 70 K, 20 bar gaseous helium stream. The 70 K helium stream cools the radiation shielding and the thermally intercepted penetrations running from room temperature. The 5 K helium coolant stream is split for two separate purposes in the cryomodule. One 5 K branch is used for thermal intercepting while the second branch is used for the production of 2 K helium. 2 K is achieved by heat exchanging the input 5 K helium gas with the 2.1 K exhaust gas and then J-T expanding the pre-cooled input to drop the 3 bar supply pressure to 32 mbar for 2 K liquefaction. The manifolds, heat exchanger and reservoirs that

these coolant streams occupy are all designed to comply with ASME B31.3, the process piping standard [80], and the ASME BPVC. All systems have independent safety reliefs sized for the Maximum Allowable Working Pressure (MAWP). The safety reliefs are all located outside of the cryomodule and vent to atmosphere. In this manner, the pressure systems of the cryomodule are separated from the insulating vacuum vessel. This allows us to define the cryomodule box as a vacuum vessel since it is not part of any pressure system boundary, saving considerable design and fabrication costs.

The FNAL safety requirements do not mandate following the ASME BPVC for vacuum vessels but they recommend applying the rules. Because of this the design was developed using the requirements of the 2010 release of the ASME BPVC Section VIII Division 2, Part 5, even though the code explicitly excludes devices with static pressure gradients less than 15 psi. This analysis method allowed for relatively rapid evaluation of the complex vacuum vessel design which resulted in significant time-savings relative to traditional hand-based calculations. The ASME BPVC Section VIII Division 2 gives the required procedures for analyzing the 304 SST vessel material properties (yield and ultimate strengths), strain limits, buckling load factors, cyclic loading and collapse criteria. These analysis procedures, when combined with the ASME fabrication and inspection requirements, protect against failure modes of the device: plastic collapse, local failure, buckling and cyclic loading. Our analysis followed these requirements and the results are presented below.

The vacuum vessel is evacuated to less than 10^{-6} Torr and a static pressure gradient of $\sim$14.7 psi. Rounding up gives a 15 psi MAWP which is used for all analyses. All the simulations presented here were done with ANSYS and used a model with no symmetry planes. The assembly was restrained by placing constraints equivalent to the kinematic mounting system designed for the vessel. The model was also loaded with the weight of all elements and appurtenance loads.

Several analyses are presented here. The first one is a static structural analysis of an elastic-perfectly-plastic vessel model which demonstrated the design was protected against plastic collapse and predicted the deflections due to evacuating the vessel. Figure 7.11 shows the cryomodule vessel deflections from the pressure load analysis at MAWP, which the vessel passes. Most areas display stresses well below that allowable for both membrane and bending analyses. Some local high membrane stresses are predicted, and Figure 7.12 shows the primary membrane stress results from a linear elastic analysis of the cryomodule. The contour levels in Figure 7.12 have been adjusted so that all stresses over 20 ksi are red and are indicated with labels. 20 ksi represents the allowable limit for 304 SST in the ASME BPVC at room temperature. The stress concentrations are located on the reinforcing gussets where the largest bending occurs: the weld joint between the cryomodule end-walls and sidewalls and on the four mounts on the base of the cryomodule.

Beyond demonstrating that the design protects against plastic collapse the ASME BPVC requires several other analyses to demonstrate that the design protects against local failure, buckling and cyclic loading. The local failure analysis requires that at each point in the component the sum of the primary membrane and the principal bending stresses shall not exceed 4 times the allowable stress or 80 ksi for 304 SST. This was satisfied with an elastic-material analysis at all locations. Protection against collapse from buckling must also be demonstrated for a vessel with a compressive stress field under the design loads. A bifurcation buckling analysis was performed using an elastic 304 SST material model free of geometric nonlinearities to determine the pre-stress in the vessel. The

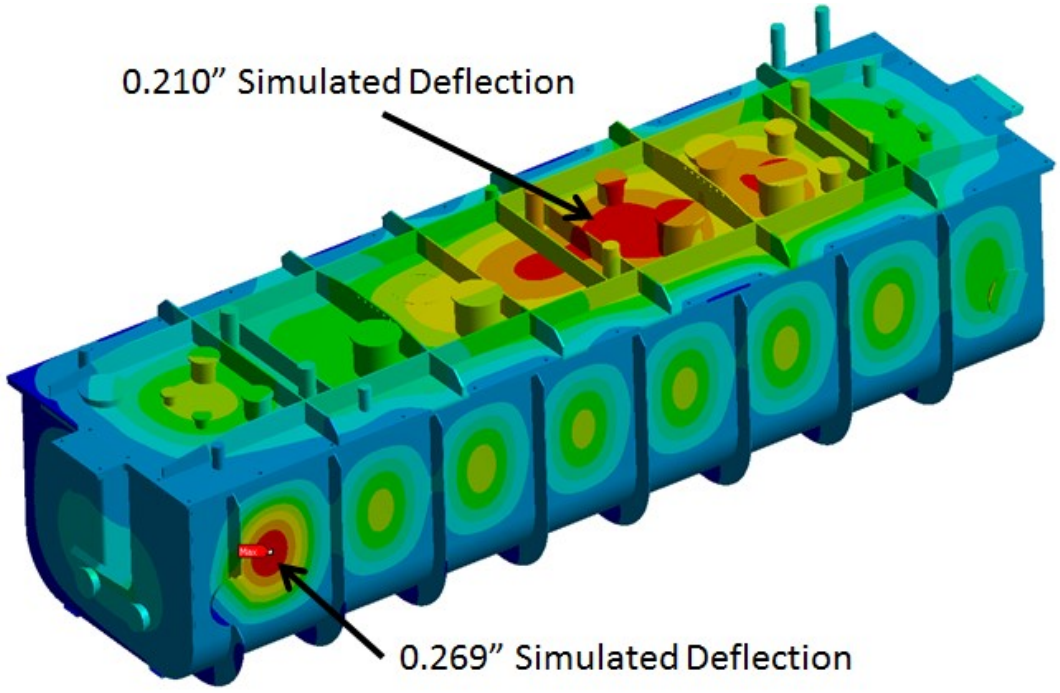

Figure 7.11: Pressure analysis at MAWP of the cryomodule vacuum vessel. The labeled area on the side of the cryomodule corresponds to the largest deflection of the vessel with a 15 psig static pressure. The measured deflection during the first pump down was 0.240 in. giving good confidence that the vessel exceeds our design expectations.

acceptance criterion is that the buckling load factor be greater than 2/cr where cr is the capacity reduction factor given in the ASME BPVC. Since the vessel contains ring stiffened cylinders under external pressure, $cr = 0.80$; and the minimum required buckling load factor is 2.5. The lowest buckling mode load factor was found to be 3.17 exceeding the minimum requirement of 2.5 predicting that the device will not buckle under the applied loads. Finally, the ASME BPVC requires that the vessel will not fail under cyclic loading. The cyclic loading analysis requires two evaluations: one to protect against high cycle fatigue and another to protect against ratcheting. Evaluation for high cycle fatigue is not required if the total number of cycles is low as defined in the code. We expect to have only 80 to 100 full and partial loading cycles over the lifetime of the vacuum vessel, which does not come close to the cycle requirement of greater than 1,000, the level where a more detailed analysis is required. Therefore, the high-cycle fatigue requirements are satisfied. Finally, a ratcheting analysis to evaluate the performance of the device when the material stresses exceed the yield was done. It demonstrated protection against ratcheting.

The half-wave cryomodule was fabricated by Meyer Tool and Manufacturing in Oak Lawn, Illinois. Meyer Tool assembled the magnetic shielding and the 70 K radiation shielding with 32 layers of MLI on the exterior and 16 layers on the interior sides as part of the fabrication contract. Figure 7.13 shows the complete vacuum vessel at Argonne. The cryomodule houses eight sets of identical components. Each set forms a focusing period and includes a resonator, a SC solenoid with four dipole coils and a Beam Position Monitor (BPM).

Beam dynamics requires the solenoids to be aligned after cooling down to within ±1 mm (0.5 mm

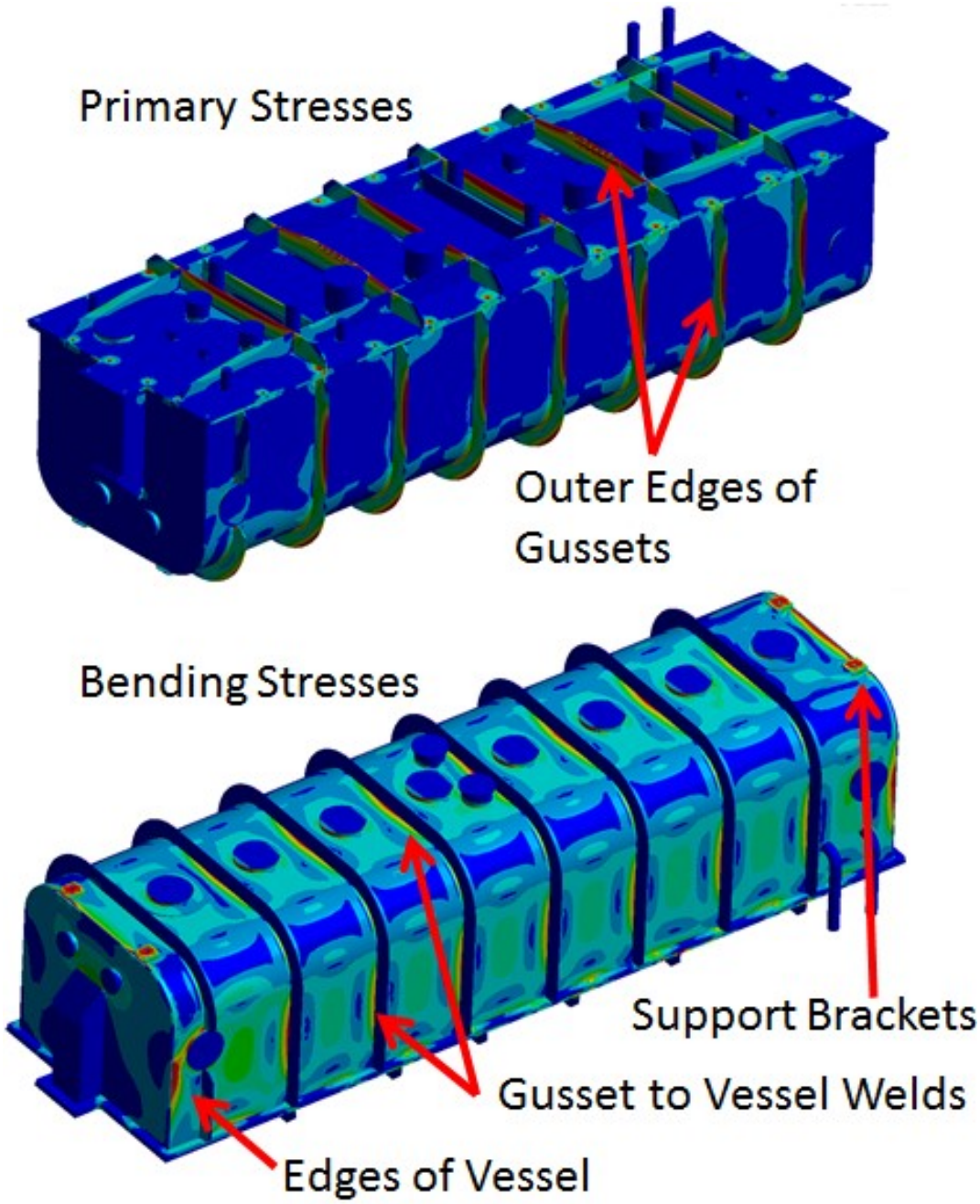

Figure 7.12: The calculated vacuum vessel membrane stresses for an elastic material model for the 304 SST vessel. Top, the primary stress derived from the calculations. Bottom, the secondary bending stress derived from the same calculations. Areas of high stress, 20 ksi for primary and 30 ksi for secondary stresses as set forth in the ASME BPVC, are specified with arrows and labels. This vessel passes the required pressure load analysis for protections against plastic collapse.

Figure 7.13: The finished vessel assembled at Argonne. The vessel is now being prepared for cryogenic testing.

Figure 7.14: The titanium strong-back hung from the lid of the half-wave resonator lid. No cavities or solenoids are mounted on the strong-back.

rms) for both transverse coordinates and within ±2 mrad (1 mrad rms) for the angle between the solenoid magnetic axis and the beam direction. The requirements for cavity coordinate positioning are the same as for the solenoids but the angular alignment can be relieved to ±4 mrad (2 mrad rms). The beamline string length is about 6 m and is supported and aligned on a cryomodule spanning titanium rail system, called the strong-back as shown in Figure 7.14. The strong-back is composed of 2 in. x 8 in. grade 2 titanium rails with interconnecting plates which hangs from the cryomodule lid. All components are mounted on top of the strong back with independent kinematic-alignment hardware.

Table 7.3 summarizes the estimated static and dynamic heat loads at each temperature level in the cryomodule assembly from all sources. The following sources were included in the calculation of the 2 K heat load: cavities, RF couplers, helium manifold, radiation from 70 K to 2 K, instrumentation, high current leads, strong-back hangers, cavity and solenoid cooldown lines, vacuum manifold, slow tuners and gate valves.

Table 7.3: HWR cryomodule heat load estimate

Temperature	Heat Load, W
2 K, static	30
2 K, dynamic	24
5 K, static	90
5 K, dynamic	24
70 K, static	198
70 K, dynamic	200

7.2 Spoke cavities and cryomodules

The beam acceleration profile splits spoke cryomodules into two main designs with beta as 0.222 for SSR1 cavities and 0.475 for SSR2 cavities.

Acceleration from 10 to 35 MeV utilizes superconducting cavities with $\beta_{opt} = 0.222$ operating at 325 MHz, referred to as Single Spoke Resonator of type 1 or SSR1, see Figure 7.15 [81].

Acceleration from 35 to 185 MeV utilizes superconducting cavities with $\beta_{opt} = 0.475$ operating at 325 MHz, referred to as Single Spoke Resonator of type 2 or SSR2. The following sections describe the technical design of the spoke cavities and cryomodules.

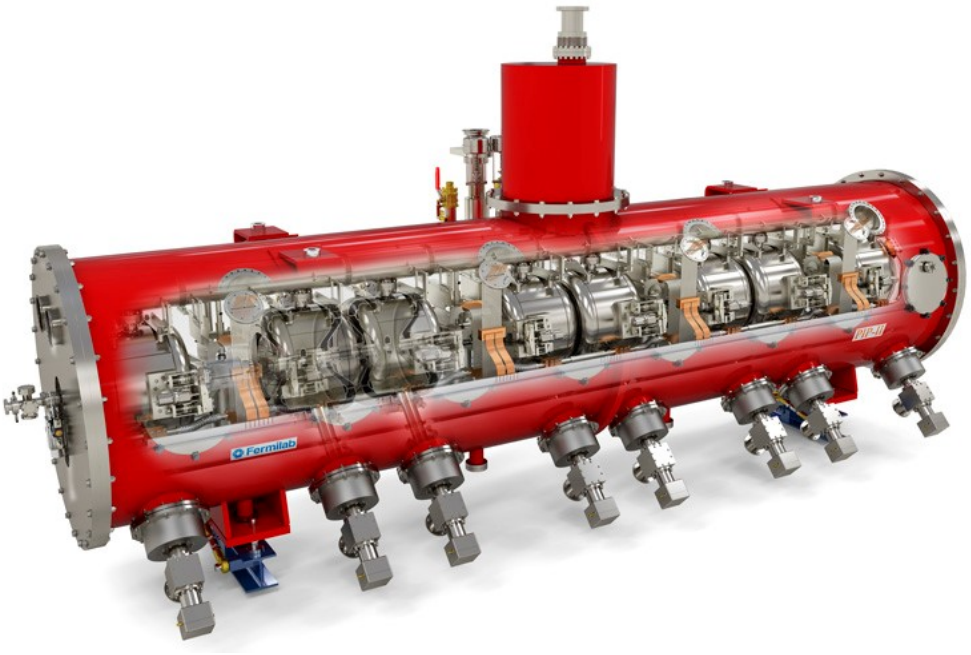

Figure 7.15: Cut-away view of SSR1 cryomodule designed for PIP-II.

7.2.1 Cavity design

7.2.1.1 Cavity RF design

7.2.1.1.1 RF design of SSR1 cavities

RF design and optimization of the SSR1 cavity was done using Microwave Studio (MWS) software. Figure 7.16 presents the main geometrical parameters used for optimization: LCAV is the cavity length, end-wall to end-wall along beam axis, LIRIS is the iris to iris length, D is the spoke base diameter, W is the spoke width, T is the inner electrode thickness, and h and v are cylindrical shell and end-wall dimensions. Beam dynamics considerations led to the choice of $\beta = 0.222$ and a 30 mm aperture diameter. Table 7.4 lists the general requirements to the electromagnetic parameters.

Minimization of the peak surface electric field (Epeak) involves W, T and Liris as main parameters, since they define the geometry in the region of high electric field, see Figure 7.17. The ratio D/Lcav and the end cup profile dimensions were optimized to achieve a low peak magnetic field, see Figure 7.18. The corresponding electric and magnetic 3D fields are shown in Figure 7.19. The plots have been generated with Comsol software.

A spoke cavity has no axial symmetry. Therefore, its quadrupole component cannot be compensated over the entire range of cavity operation. Figure 3.28 presents the dependence of the quadrupole effect on the beam velocity. Due to engineering limitations, mainly related to the RF couplers, the cavities are rolled by 45°; consequently, their quadrupole field is also rolled and is a skew-quadrupole field. The cavity skew-quadrupole fields is compensated by correction coils

Table 7.4: SSR1 electromagnetic parameters

Parameter	Value
Frequency	325 MHz
Shape	Single Spoke Resonator
β_{opt}	0.222
Effective length, $\beta_{opt}\lambda$	205 mm
Iris aperture	30 mm
Inside diameter	492 mm
Bandwidth	107 Hz
E_{peak}/E_{acc}	3.84
B_{peak}/E_{acc}	5.81 mT/(MV/m)
G	84 ohms
R/Q	242 ohms

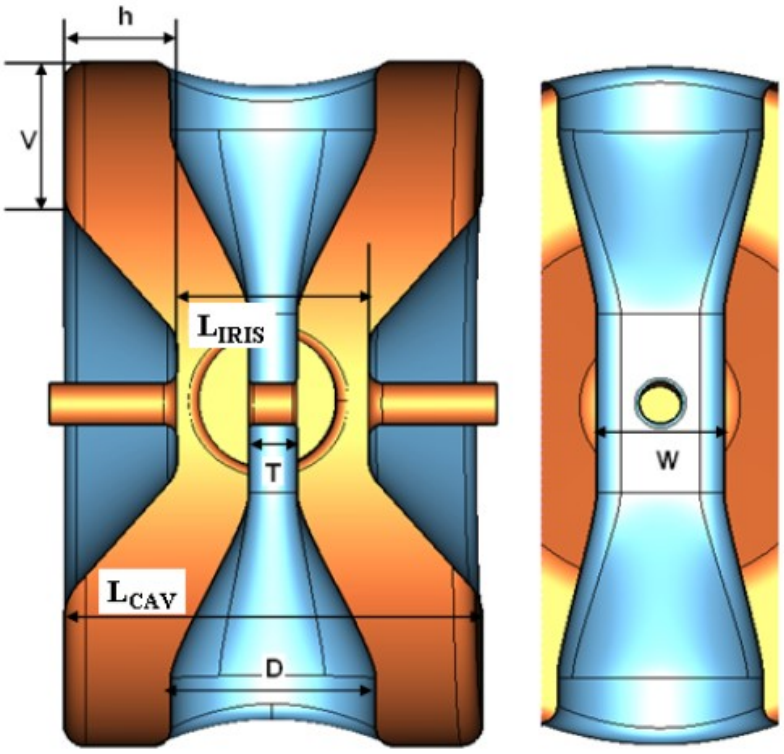

Figure 7.16: Cross section of the SSR1 with the main parameters used in the optimization process.

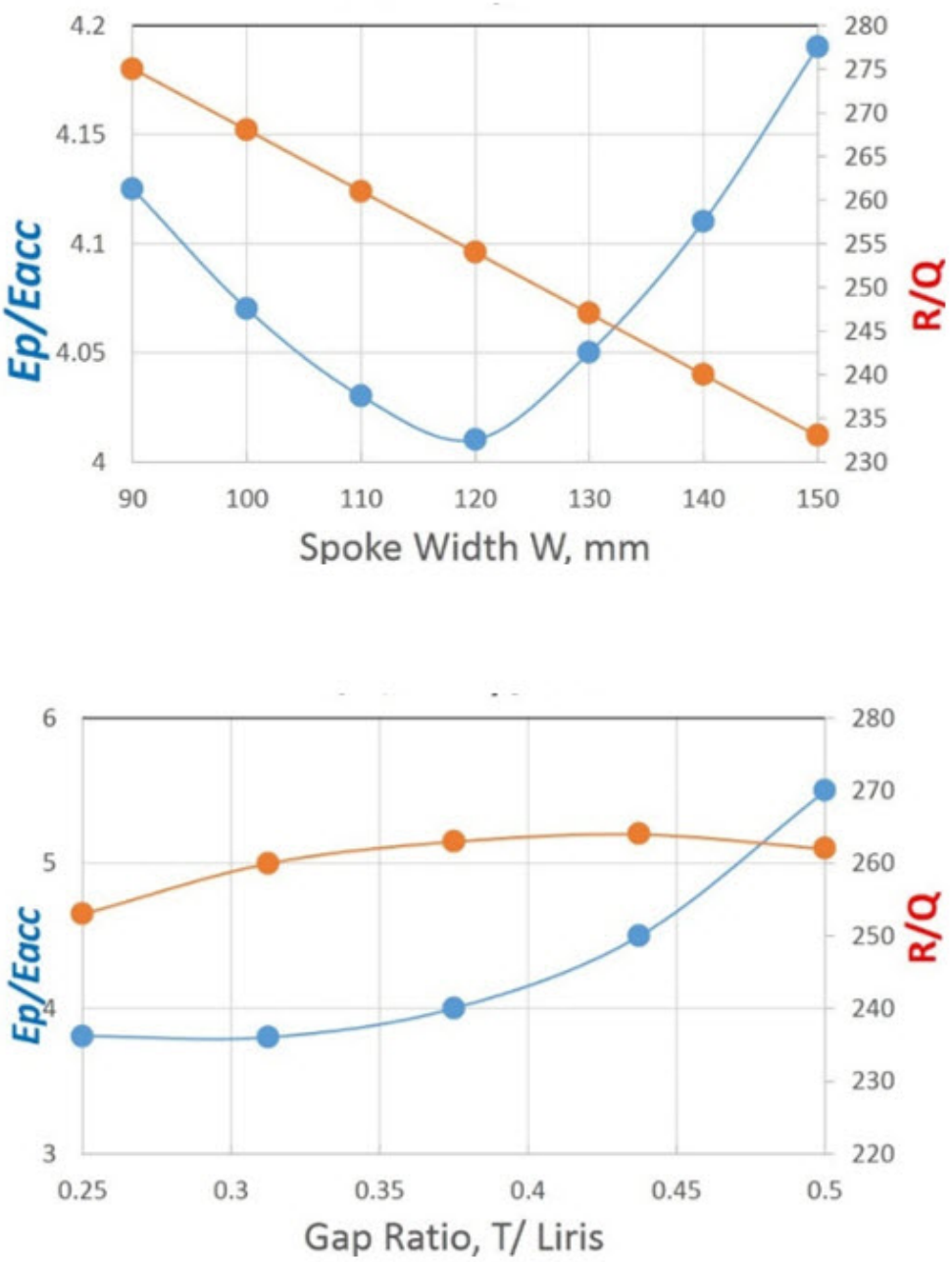

Figure 7.17: Optimization process of Epeak.

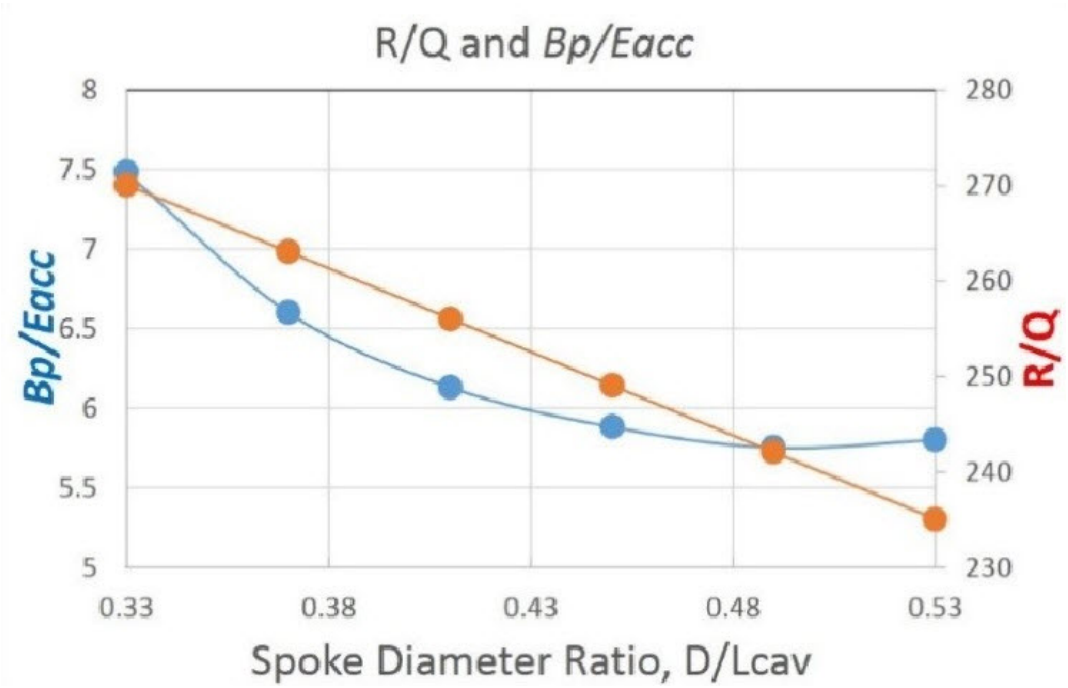

Figure 7.18: Optimization process of Bpeak.

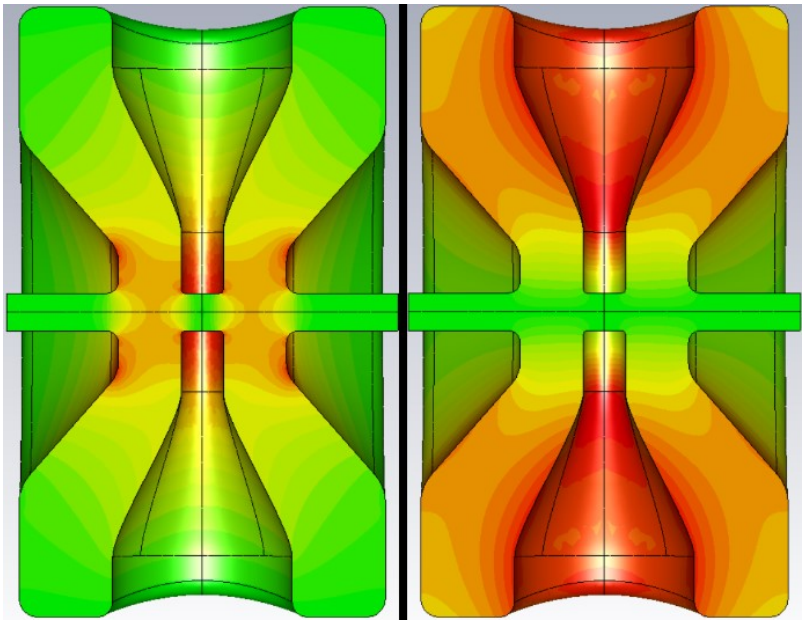

Figure 7.19: Electromagnetic fields of SSR1: (a) Electric field and (b) Magnetic field. The field strength increases as the color changes from green to yellow and to red.

located inside nearby focusing solenoids which are capable of creating dipole and skew-quadrupole fields.

Multipacting, higher order modes and transverse kick are other key concerns in the design of this type of cavity. Multipacting analysis was performed to make sure that no evidence of multipactoring activity appears in the range of the cavity operating gradients. Analysis predicts two multipactoring barriers at 4.5 MV/m and 7 MV/m. These barriers are sufficiently far from the operating gradient of 12 MV/m. These barriers were later observed in the course of vertical testing of the bare SSR1 cavities, confirming the validity of the analyses.

Higher order modes were investigated in a dedicated simulation study. Monopole, dipole, and quadruple modes were simulated and R/Q for each mode was calculated. Simulated R/Q values are sufficiently small thus enabling operation without any HOM dampers. Bead-pull measurements were carried out for all the HOM monopoles up to 2 GHz. The measured R/Q of the HOM monopoles is less than 1Ω. Simulated and measured R/Q values are in good agreement. The HOMs frequency spread on the tested cavities is within 7 MHz.

Geometrical errors in the fabrication process of a SSR1 cavity can result in a transverse kick. Fabrication experience has identified three major types of possible variations related to the alignment of both the beam pipe and spoke with respect to the beam axis. Simulation studies have been carried out implementing these variations in the simulation model. Bead-pull measurements were also conducted to measure the transverse kick in the fabricated cavities. The simulations and the measurements are in relatively good agreement. The maximum kick in the fabricated cavities is less than 154 KeV, which corresponds to a 1.12 mrad beam deflection. It is well within the 10 mrad specified for the SSR1 corrector strength.

7.2.1.1.2 RF design of SSR2 cavities

The SSR2 is a single spoke resonator operating at 325 MHz. These cavities accelerate particles from 35 MeV to 185 MeV. Figure 7.20 shows the SSR2 RF geometry in the y-z cross-section, where y is directed along the spoke and z is directed along the beam axis. Definitions for the main geometry parameters are shown in the figure, and their values are listed in Table 7.5. Electric and magnetic 3D fields have been simulated with "COMSOL multi-physics" and are plotted in Figure 7.21.

The value of $\beta_{opt} = 0.475$ has been chosen to accommodate the beam dynamics requirements and to minimize the overall number of cavities. The accelerating gradient E_{acc} is defined over the effective length $L_{eff} = \beta_{opt}\lambda$, for acceleration at β_{opt}. Here λ is the electromagnetic field wavelength at 325 MHz. Table 7.6 shows the electromagnetic parameters of the SSR2 cavity. For the given limitations of the peak fields (40 MV/m and 70 mT) the SSR2 cavity provides a maximum energy gain of 5.17 MeV.

One of the challenges of the SSR1 cavity was the strong multipacting during power ramping. Although the multipacting can be conditioned away, it may take from 4 to 48 hours. The SSR1 cavity typically took around 12 hours to condition even with the advantage of a high power coupler

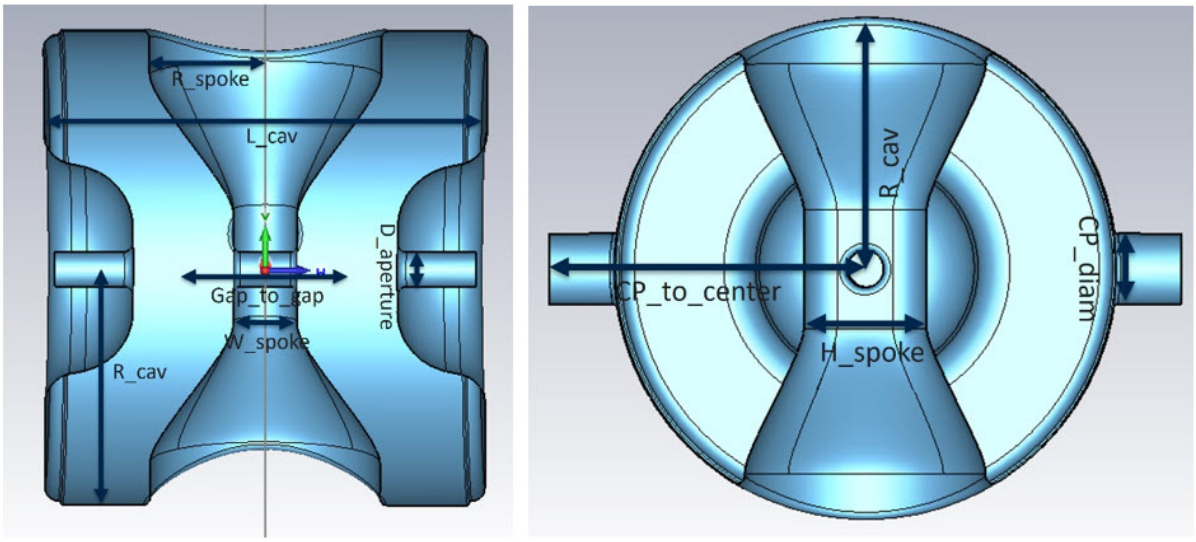

Figure 7.20: SSR2 cross-section and definition of main geometry parameters.

Table 7.5: Main parameters of SSR2 cavity geometry

Parameter	[mm]
L cav	500
R cav	271.6
R spoke	130.7
D aperture	40
Gap to gap	185.9
W spoke	72.26
R cav	271.6
CP to center	337
CP diam	76.90
H spoke	133

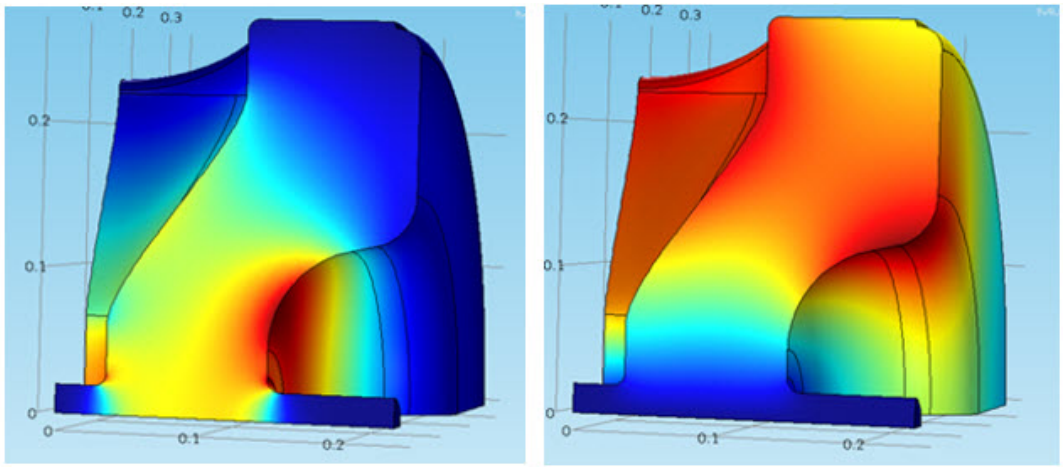

Figure 7.21: SSR2 electric (left) and magnetic (right) 3D fields computed by COMSOL.

Table 7.6: SSR2 electromagnetic parameters

Parameter	Value
Frequency	325 MHz
Shape	Single Spoke Resonator
Optimal β_{opt}	0.475
Geometrical β_g	0.402
Beam Aperture	40 mm
Effective length, $\beta_{opt}\lambda$	438 mm
E_{peak}/E_{acc}	3.38
B_{peak}/E_{acc}	5.93 mT/(MV/m)
G	115.2 ohms
R/Q	296.6 ohms

installed during RF conditioning.

The last iteration on the SSR2 electromagnetic design was focused on the reduction of multipacting, since the previous cavity design showed strong and wide multipacting barriers. The growth rate in the number of electrons is used as a figure of merit in multipacting simulations. Figure 7.22 compares the growth rates for different designs of spoke cavities: SSR1, SSR2 v1.0 (old design) and SSR2 v2.6. One can see significant reduction in multipacting for the latest design. The simulations also demonstrate multipacting levels lower than those for the SSR1 cavity, which is already built and tested, and demonstrated satisfactory multipacting performance.

According to the simulation, the most severe multipacting takes place near the transition of the cylindrical portion to the end walls. To improve the multipacting in SSR2 cavities, a step at the edge of the cavity was added on both sides as shown in Figure 7.23. This change helped reduce the growth rate in the multipacting simulation. The growth rate has been indicative of multipacting in SSR1 testing. Figure 7.22 showed the improvement from the current design (v2.6) and the previous design without the step (v1.0). For comparison, the SSR1 multipacting simulation is plotted as well.

High order modes were calculated using eigen mode analysis. Figure 7.24 is a plot of all the HOMs including monopoles, dipoles and quadrupoles. The R/Q for monopole modes was calculated as a function of particle velocity and are shown in Figure 7.25. The zero mode was calculated to be 343 MHz and its R/Q is higher than the accelerating mode R/Q at lower particle velocity. However, considering its far away from the accelerating mode of 18 MHz, it is unlikely that a resonance can be excited. Further studies with beam harmonics can further verify.

In addition to the two RF ports and two beam pipe ports, two additional ports have been added to one side to allow for further high pressure rinsing and may possibly be useful for electropolishing, see Figure 7.26. These two ports do not affect the RF parameters calculated earlier. Additional multipacting analysis is in progress to verify that multipacting has not worsened.

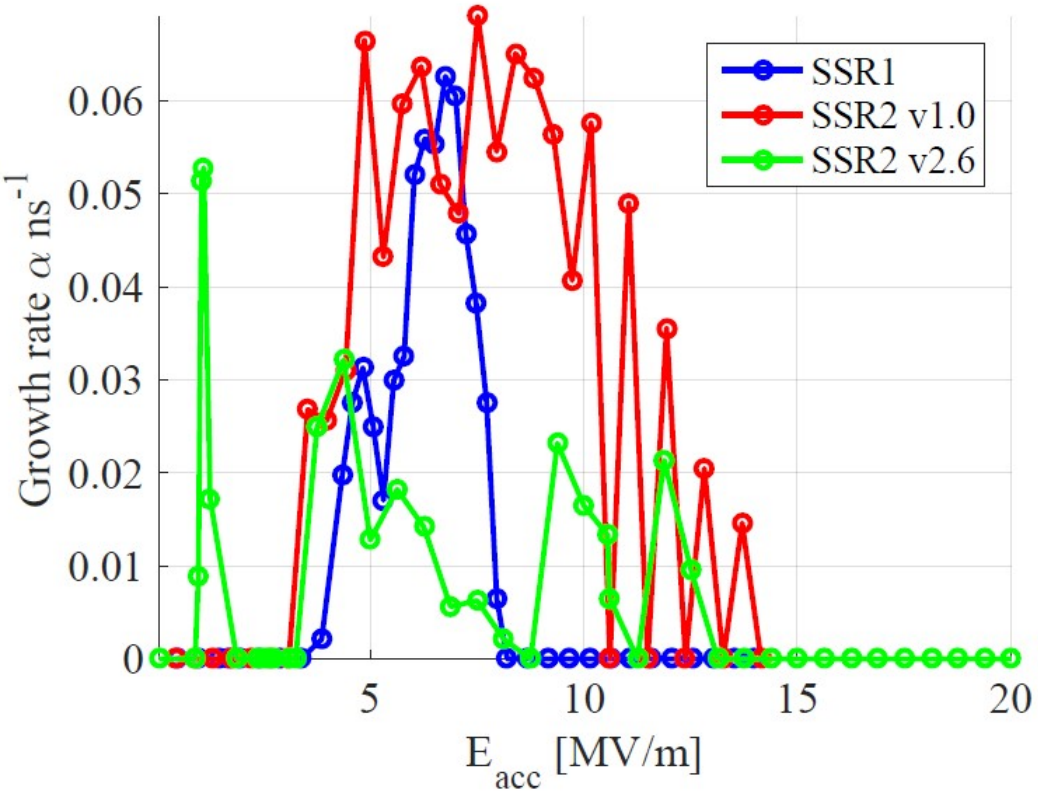

Figure 7.22: Growth rate in the number of electrons comparison from CST, SSR1 and SSR2 designs.

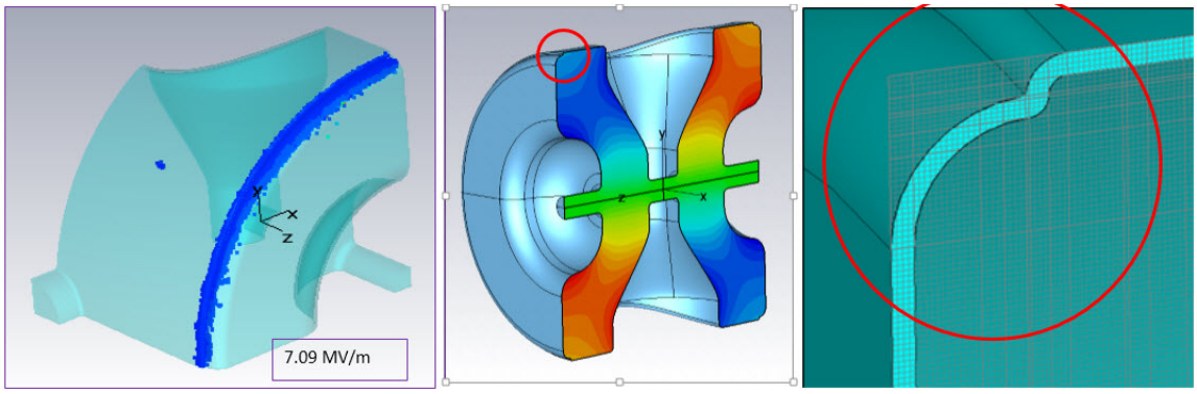

Figure 7.23: A step in cavity corner helps reduce multipacting.

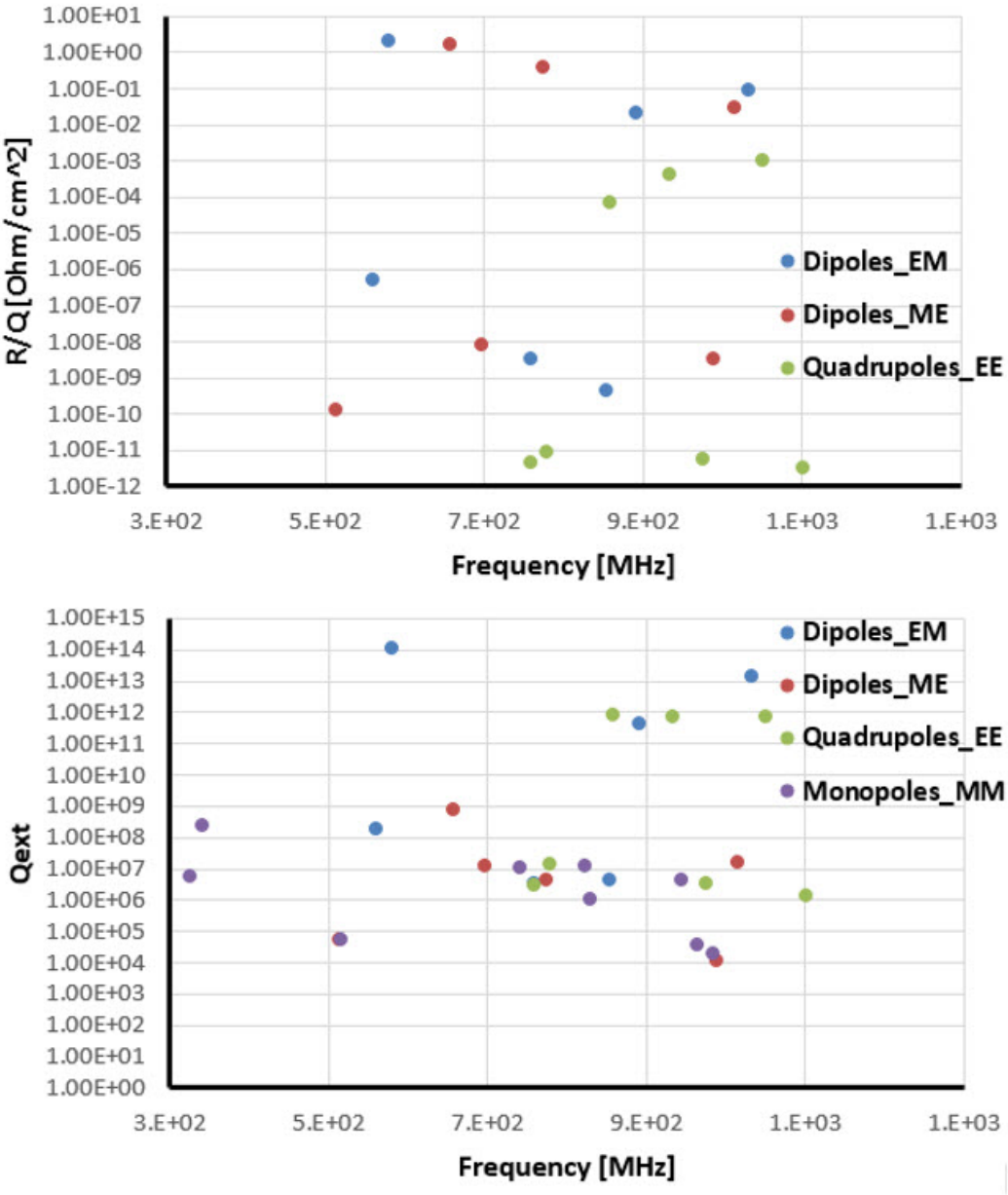

Figure 7.24: SSR2 cavity HOMs frequency, R/Q (upper) and Qext (lower).

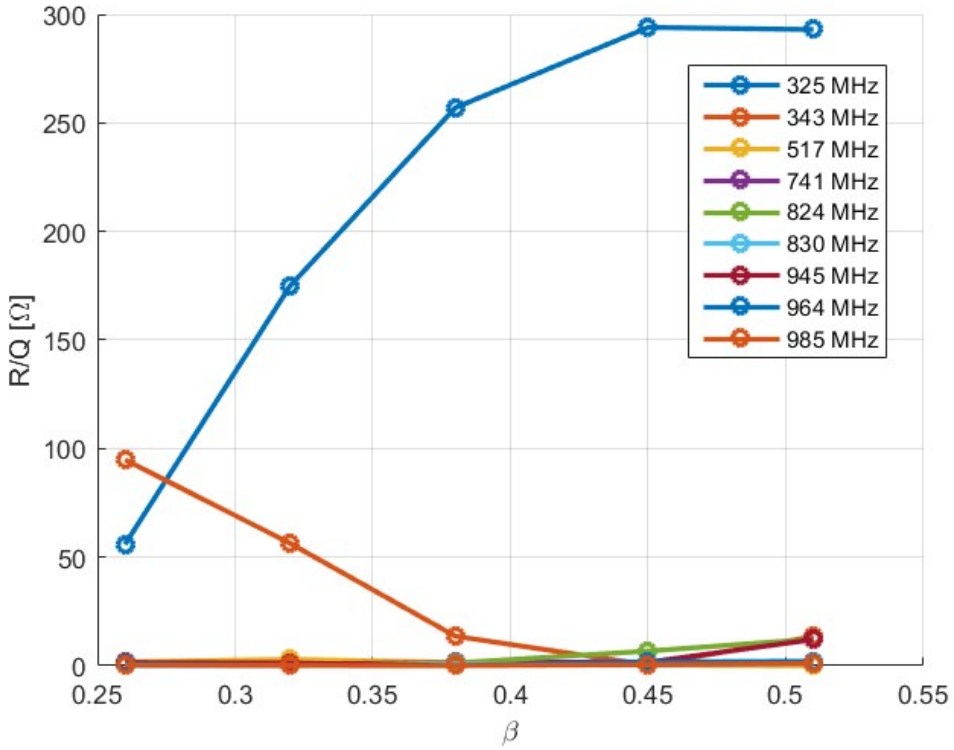

Figure 7.25: R/Q for monopole modes.

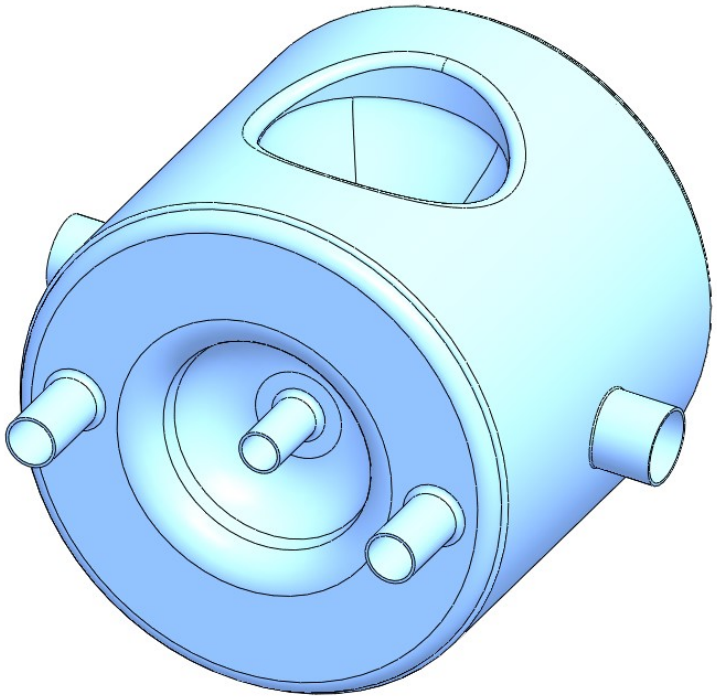

Figure 7.26: Two additional rinsing ports that can be used for electropolishing.

7.2.1.2 Structural design

7.2.1.2.1 Structural design of SSR1 cavities

In a machine like PIP-II, operating both in continuous wave (CW) and pulsed regimes, perturbations of the cavity fundamental frequency caused by the Lorentz Force Detuning (LFD) and pressure fluctuations in the liquid helium bath need to be minimized.

The SSR1 was the first superconducting spoke resonator developed at Fermilab for the High Intensity Neutrino Source (HINS) accelerator [84]. The first prototype of SSR1 cavity with a helium vessel (SSR1-01) [82], designed and manufactured for the HINS project, did not meet the PIP-II specifications. A sensitivity to helium vessel pressure of df/dP = 140 Hz/Torr, significantly exceeded the PIP-II requirement of df/dP $\leq$ 25 Hz/Torr.

A new generation of jacketed SSR1 cavities was redesigned for the PIP2IT project. The major goal of the helium vessel design was reduction of df/dP. First, the effect of different design modifications was studied. This was helpful for choosing the design path and, consequently, avoiding costly errors. The minimum value of df/dP was achieved by coupling the helium vessel with the end-wall of the resonator by a bellows of optimal diameter. The cavity tuner stiffness was accounted for in this process. This work resulted in the third generation design for the SSR1 bare cavity. The structural design of the SSR1 cavity is based on the SSR1 cavity Functional Requirement Specification [86]. The major requirements are listed in Table 7.7.

Table 7.7: SSR1 cavity requirements

Parameter	Requirement
Max leak rate (room temp)	$< 10^{-10}$ atm-cc/sec
Operating energy gain per cavity	2.05 MeV
Maximum gradient per cavity in VTS	12 MV/m
Max power dissipation per cavity at 2 K	3 W
Sensitivity to He pressure fluctuations, df/dP	$<$ 25 Hz/Torr
Field flatness	Better than 90%
Lorentz force detuning (when jacketed)	$< 5Hz/(MV/m)^2$
Multipacting	None within $\pm 10\%$ of operating gradient
Operating temperature	1.8 - 2.1 K
Operating pressure	30 ± 5 mbar differential
MAWP	2 bar (at room temperature), 4 bar (at 2K)
RF power input per cavity	12 kW (CW, operating)

7.2.1.2.2 Structural design of SSR2 cavities

The structural design of the SSR2 cavities are similar to that of the SSR1 cavities. The IIFC (Indian Institutions Fermilab Collaboration) is working on the cavity design. The design is guided

by the Functional Requirement Specifications for the SSR2 cavity [83]. Table 7.8 lists the major requirements.

Table 7.8: Requirements for the SSR2 cavity structural design

Parameter	Requirement
Maximum leak rate (room temp)	$< 10^{-10}$ atm-cc/sec
Operating gain per cavity	5.0 MeV
Maximum gradient per cavity in VTS	13 MV/m
Maximum power dissipation per cavity at 2K	11 W
Sensitivity to He pressure fluctuations df/dP	$< 25Hz/torr$
Lorentz force detuning (when jacketed)	$< 2.8Hz/(MV/m)^2$
Field flatness	Better than 90%
Operating temperature	1.8-2.1K
Operating pressure	30 ± 5 mbar differential
MAWP	2 bar (room temp), 4 bar (at 2K)
Maximum RF power input per cavity	28 kW (CW, operating)

7.2.1.3 Bare cavity

The first step in the SSR1 design was the optimization of the RF performance. This was followed by an optimization of the resonator structural integrity which was achieved by adding an adequate system of stiffeners to the outside surfaces, without any modification to the RF shape, in order to withstand the liquid helium pressure during the vertical test (2 bar; 29 psi at 4 K).

The cavity parts are formed and machined from high-purity niobium (Nb) joined by electron-beam welding. The cavity has four stainless steel flanges which attach to the helium vessel. The flanges are connected to the niobium using copper-brazed joints. The structural design of the bare SSR1 cavity is shown in Figure 7.27. The SSR2 bare cavity design is based on the SSR1 bare cavity design. The SSR2 bare cavity geometry were summarized in Table 7.5 and the dimensions were illustrated in Figure 7.20.

7.2.1.4 Jacketed cavity

From a mechanical engineering standpoint, a jacketed SRF cavity is comprised of an inner niobium vessel (an SRF cavity) surrounded by a liquid helium containment vessel made of stainless steel or titanium. The helium bath may reach pressures exceeding 15 psi (0.103 MPa) and generally has a volume greater than five cubic feet (0.142 m^3). All this leads to consider a jacketed SRF cavity as a system of pressure vessels. Based on the Department of Energy (DOE) directive 10 CFR 851, it is mandatory for safety reasons that all pressure systems designed, fabricated and tested by U.S. National Laboratories conform to ASME Codes. Consequently, jacketed SRF cavities fall within the scope of the ASME Boiler and Pressure Vessel Code.

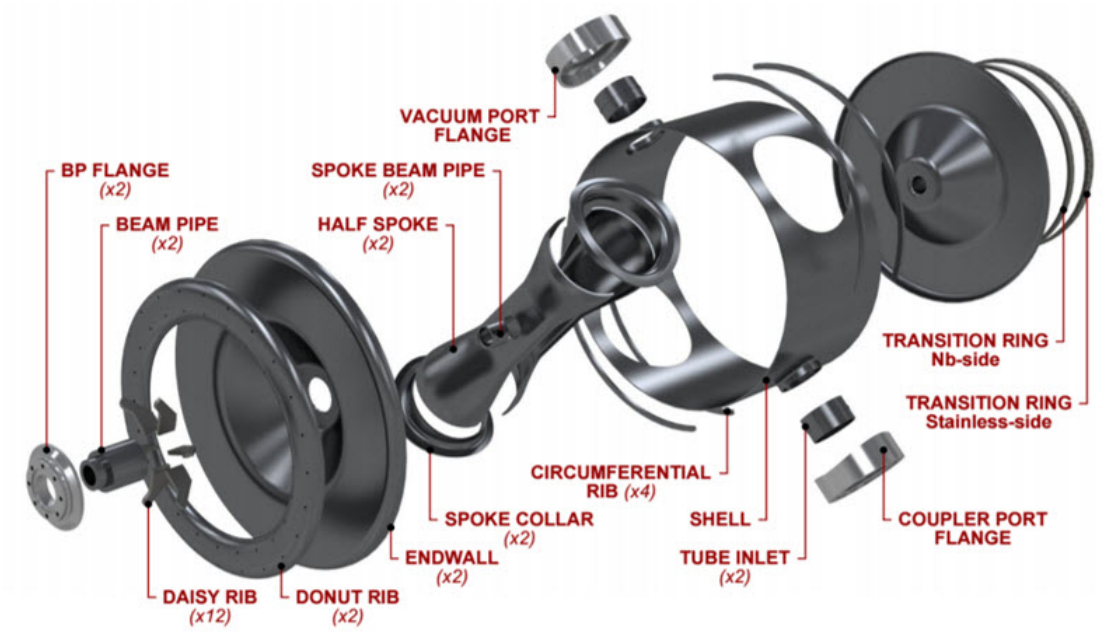

Figure 7.27: Exploded view of the bare niobium SSR1 cavity.

However, a true Code design is not currently possible due to the use of non-Code materials, the unfeasibility of Code required nondestructive examinations of welded joints and the use of unqualified procedures for welding and brazing. A set of rules have been developed by engineers at Fermi National Accelerator Laboratory [84] based on their understanding of best practices in the design, fabrication, examination, testing, and operation of jacketed SRF cavities. These guidelines comply with Code requirements wherever possible, and for non-Code features, procedures are established to produce a level of safety consistent or exceeding that of the Code design [85].

The jacketed SSR1 cavity consists of two nested cryogenic pressure vessels: the inner vessel is the superconducting SSR1 cavity, see Figure 7.27, and the outermost vessel is the helium containment (or helium) vessel, see Figure 7.28. The helium vessel is made entirely of 316L stainless steel and is assembled around the cavity by full penetration tungsten inert gas (TIG) welds.

The typical operating temperature of an SRF cavity is in the 1.8 to 2.1 K range. A bath of superfluid helium, confined by the helium vessel, surrounds the cavity exerting a pressure on both vessels. The RF volume of the cavity is pumped down to ultra-high vacuum and the entire jacketed cavity is placed in a cryostat under insulating vacuum, see Figure 7.29. The greatest risk with vessels containing superfluid helium is that an accidental loss of vacuum results in very rapid boiling of the helium, causing a consequent pressurization of the helium space. Moreover, differential pressure appears between the volumes defined by the cavity and the helium vessel during the first phases of operation before the cooldown, see Figure 7.29. A relief valve setting of 2 bar is needed to ensure the cavity is protected during initial testing and during cooldown. The jacketed SSR1 cavity has two maximum allowable working pressures (MAWP), 2 bar at 293 K when the niobium material strength is low and 4 bar at 2 K when the niobium strength is significantly higher. At low temperature, higher material strength allows the system piping to be

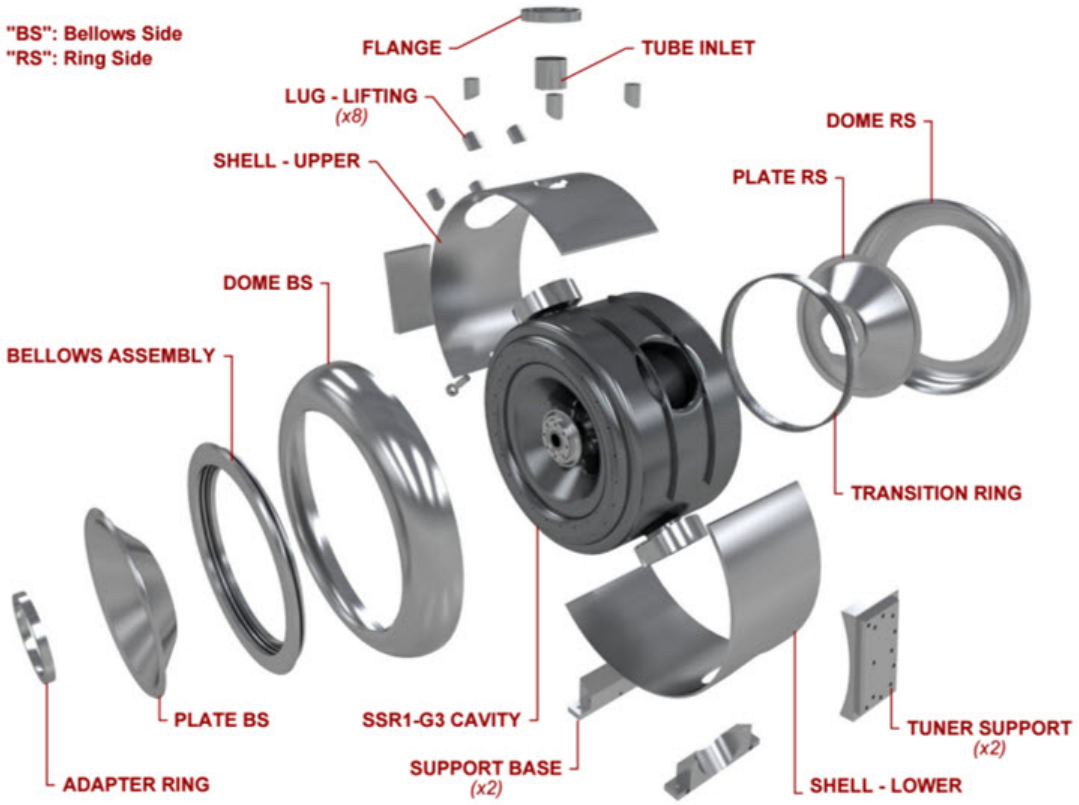

Figure 7.28: Exploded view of the stainless helium vessel surrounding the SSR1 cavity.

sized for higher short-term pressure increases. This can occur during a loss of cavity vacuum or loss of insulating vacuum when the cavity is cold.

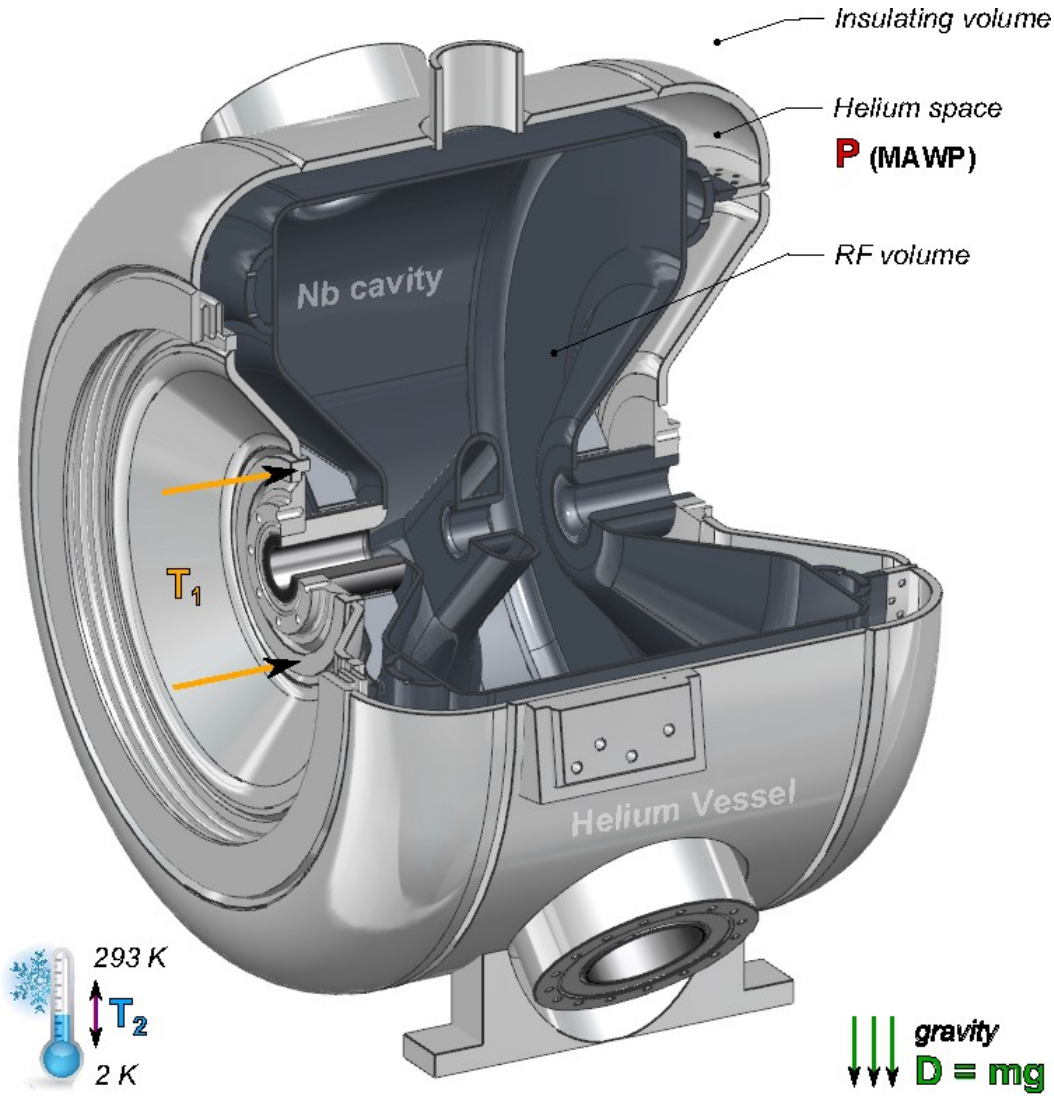

Figure 7.29: Cutaway view of jacketed SSR1 cavity with schematic loads applied. The pressure (P) is applied normal to the surfaces confining the helium space, the frequency tuning displacement (T1) is applied normal to the beam pipe (along the arrows), the gravitational force (D), and the cooldown (T2) applied to the entire system.

The geometry of the structures and loading conditions of SRF cavities, and therefore the stress distributions, are often complicated and do not lend themselves entirely to design-by-rules methods. The design-by-analysis method can be used to optimize those features in lieu the design-by-rules method. The design-by-analysis method assumes that a numerical analysis technique is used and either elastic or elastic-plastic analysis is carried out. In the case of the SSR1, ANSYS structural analysis software was used to perform the finite element analyses and to ensure protection against the four modes of failure: plastic collapse, buckling, cyclic loading and local fracture. The SSR2 cavities follow a similar jacketed design and follow the same design requirements.

7.2.1.5 Testing of SSR1 and SSR2 cavities

Presently, twelve bare SSR1 cavities have been tested at 2 K in the vertical test stand. The test results for the ten qualified bare cavities are presented in Figure 7.30. The qualified cavities were then jacketed with the helium vessel. Views of the bare and jacketed cavities are shown in Figure 7.31. After jacketing, the mechanical performance of the cavities was measured at room temperature. All cavities showed sound structural behavior and very promising performance in terms of sensitivity to He-pressure fluctuations (df/dp), see Table 7.9.

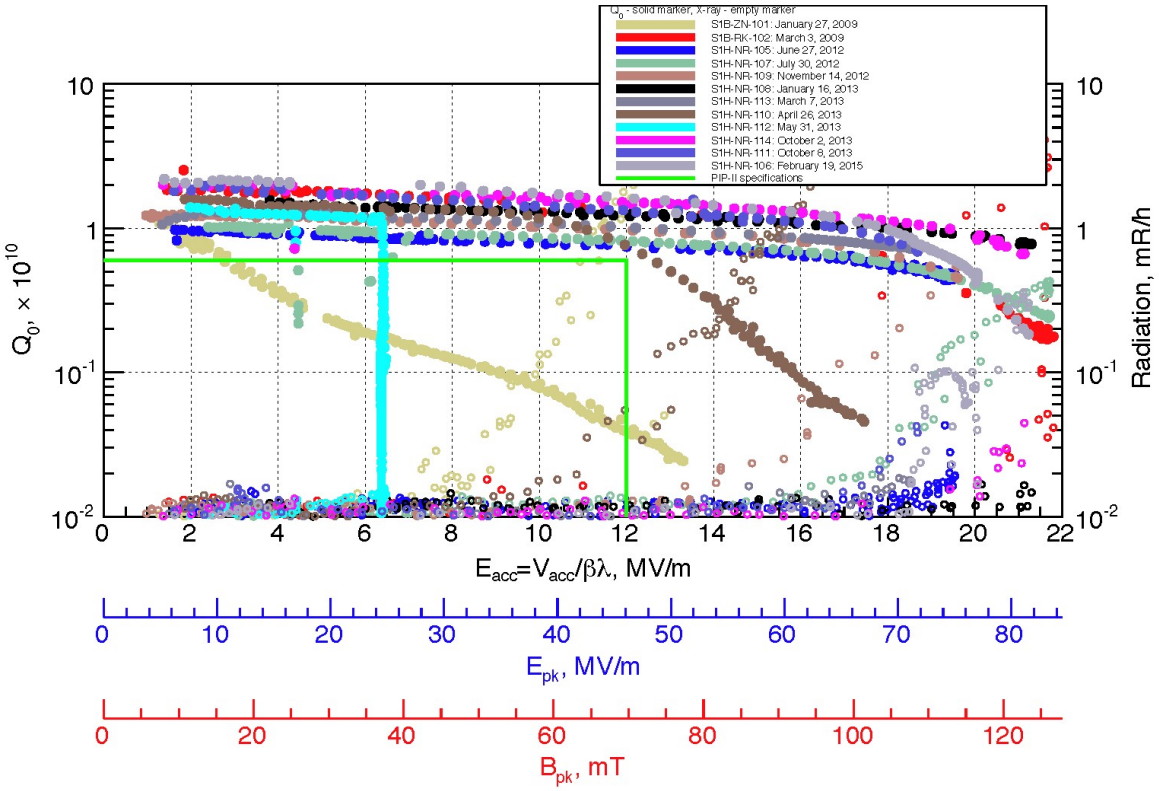

Figure 7.30: Q0 vs. acceleration gradient from the cold test of the twelve bare SSR1 cavities ($\beta = 0.222$).

The first jacketed SSR1 cavity (S1H-NR-107) was tested in the STC (Spoke Test Cryostat) [86] [87]. Figure 7.32 shows this cavity installed in the cryostat. The measured quality factor and radiation versus accelerating voltage are presented in Figure 7.33 which meet the PIP2IT specifications. Note that the quality factors for the jacketed and bare cavities are quite close. This indicates that the jacketing (welding) process has not degraded the niobium cavity performance.

After cooling down S1H-NR-107 to 2 K, df/dp was measured by varying the helium bath pressure from 18 to 43 Torr and measuring the cavity resonance frequency with a network analyzer. The measurement yielded df/dp = 4.5 Hz/Torr. This value is lower than the specification of 25 Hz/Torr for the PIP-II project, thus validating the design approach for the SSR1 helium vessel. Testing of the SSR2 cavities follow a similar approach to the SSR1 cavities. To date no SSR2 cavities have been tested.

Figure 7.31: SSR1 bare (left) and jacketed (right) cavities.

Table 7.9: Frequency sensitivity to pressure (df/dp) for the ten jacketed SSR1 cavities manufactured up-to-date. *Except S1H-NR-107 that was already measured in STC at 2K, the "df/dp fully operating cavity at 2K" for other cavities is an estimation based on calculations and experience with S1H-NR-107.

Cavity Serial	df/dp of bare cavity	df/dp of jacketed cavity	df/dp of fully operating cavity*
	[Hz/Torr]	[Hz/Torr]	[Hz/Torr]
S1H-NR-105	-560	0	0*
S1H-NR-106	-564	0	0*
S1H-NR-107	-561	8	4
S1H-NR-108	-553	-1.2	0*
S1H-NR-109	-555	5.4	2*
S1H-NR-110	-569	7.9	4*
S1H-NR-111	-526	2.7	2*
S1H-NR-112	-525	9.0	5*
S1H-NR-113	-555	6.3	3*
S1H-NR-114	-557	10	5*

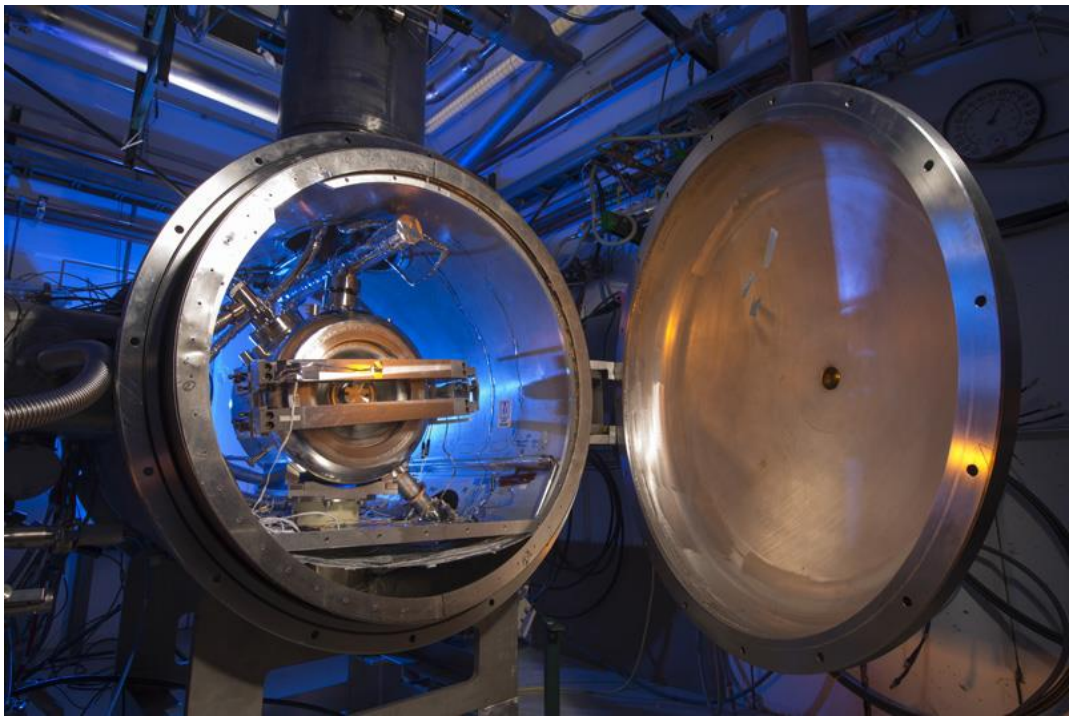

Figure 7.32: Jacketed S1H-NR-107 dressed with tuner mechanism and power coupler, installed in the STC.

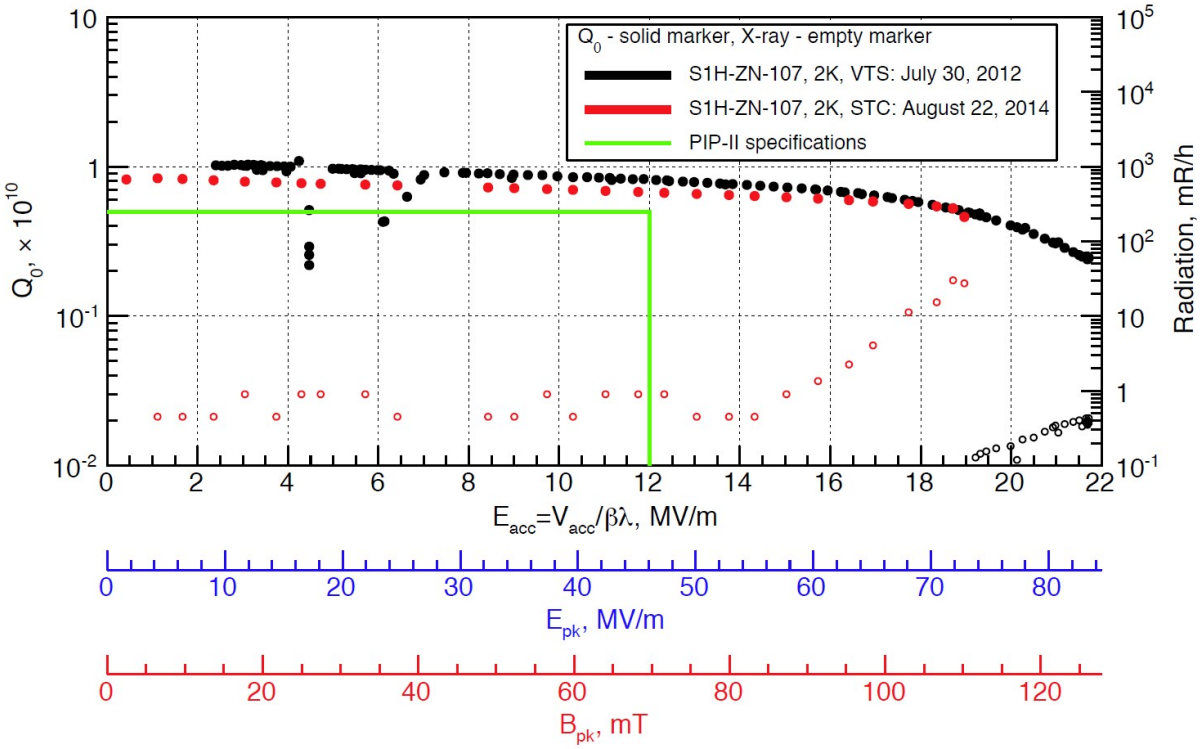

Figure 7.33: Quality factor (Q0) and radiation vs accelerating voltage (Eacc) measured for the S1H-NR-107 at STC before (black) and after (red) jacketing.

7.2.2 Cold tuning system

The cavity tuner has to compensate for its resonant frequency perturbations. In order to meet the requirements for frequency range and resolution, the tuning system integrates coarse and fine mechanisms engaged in series. The former utilizes a stepper motor with a large stroke capability and limited resolution, the latter contains piezo-electric actuators with a limited stroke but virtually infinite resolution. With the goal of maintaining the cavity at the operational frequency of 325 MHz, the tuner has to be designed to compensate uncertainties in the frequency shift due to the cooldown from 293 K to 2 K and to minimize detuning caused by microphonics and Lorentz forces. Cooldown uncertainties are estimated to be less than 200 kHz, while the amplitude of perturbations is estimated to be less than 1 kHz. These two values define respectively the requirements for the coarse and fine tuning mechanisms. In order to achieve a low sensitivity to pressure (df/dp), the stiffness of the tuner seen by the cavity flange (passive stiffness) must be greater than 30 kN/mm. Table 7.10 presents requirements for the tuning system. Each cavity has its own tuning system.

Table 7.10: SSR1 tuning system requirements

	Requirement
Coarse frequency range	200 kHz
Coarse frequency resolution	5 Hz
Coarse tuner hysteresis	$\leq$ 100 Hz
Fine frequency range	1 kHz
Fine frequency resolution	$\leq$ 0.5 Hz

The reliability of a frequency-tuning system is always of great concern. Experience suggests that the active components are prone to failures if not integrated and operated carefully. Failure of the tuning system has an immediate impact on the accelerator complex. Thus, the system shall be designed to allow for the replacement of the actuating devices in case of failure or deterioration. Maintenance operations shall be simplified, where possible, considering that the system is serviced manually through access ports in the vacuum vessel of the cryomodule.

Considering various types of tuner systems [88] and based on experience and lessons learned with the previous SSR1 tuner [89], a lever mechanism was chosen for the control of the resonant frequency in both operating conditions: CW and pulsed regime [90]. The resonant frequency is changed by adjusting the spacing between the cavity end-wall and the spoke. This is achieved by acting on the cavity sidewall, which is connected to the helium vessel by a flexible joint (bellows). Controlling this gap by elastically deforming the cavity niobium structure, the resonant frequency has to be kept within the $\pm$20 Hz from the nominal value of 325 MHz.

Figure 7.34 shows the schematic of a double lever mechanism that allows coarse and fine cavity tuning. The large scale tuning (135 kHz range) is accomplished via a stepper motor actuating through a threaded rod and traveling nut, translating rotational motion into axial motion of a double-lever mechanism, compressing and relaxing the cavity wall at one of the two beam-pipes. The fine-tuning has a tuning range of 1 kHz and is achieved with piezoelectric actuators (or piezos) acting serially with the coarse tuning mechanism. This fast tuner has to compensate for perturbations related to the helium bath pressure fluctuations, Lorentz force detuning and

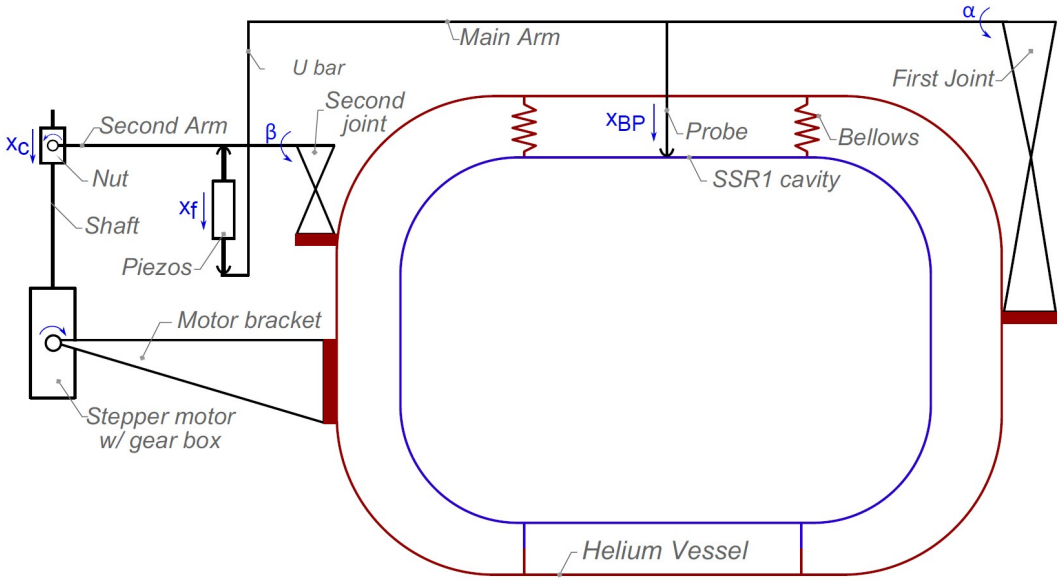

Figure 7.34: Jacketed S1H-NR-107 dressed with tuner mechanism and power coupler, installed in the Spoke Test Cryostat (STC).

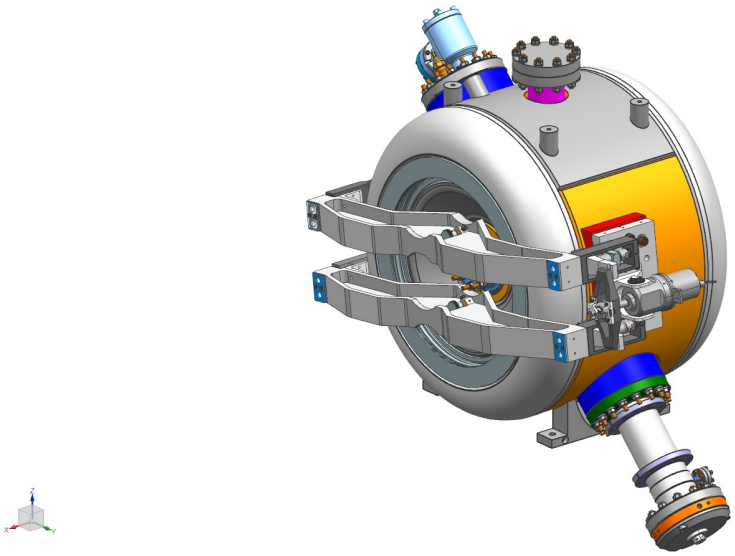

Figure 7.35: SSR1 cavity, helium vessel, tuner and coupler.

mechanical vibrations. The two main arms are hinged at one end and connected to the actuation system at the other end. The cavity is tuned by pushing on the beam pipe.

The main structural components are made of 316L stainless steel. The helium vessel is made of the same material. This has the advantage of having the same thermal contraction ratio during cooldown. Figure 7.35 shows the 3D model of the SSR1 tuner assembled on the jacketed cavity.

Figures of merit for the tuner such as tuning range, components hysteresis and the overall performance were measured during tests in the STC with the prototype tuner at low temperature. The results are presented in Figure 7.36. The tuner mechanism has excellent linearity in the entire tuning range. All specifications for stiffness, tuning ranges, tuning efficiencies, and resolutions of the active components have been met. More details can be found in Ref. [91]. This prototype tuner was also successfully used in studies of resonant control [92] for SSR1 cavities. The fast tuner was used to drive cavity characterization routines, including mechanical-to-electrical transfer functions. The design of the production tuner is in progress.

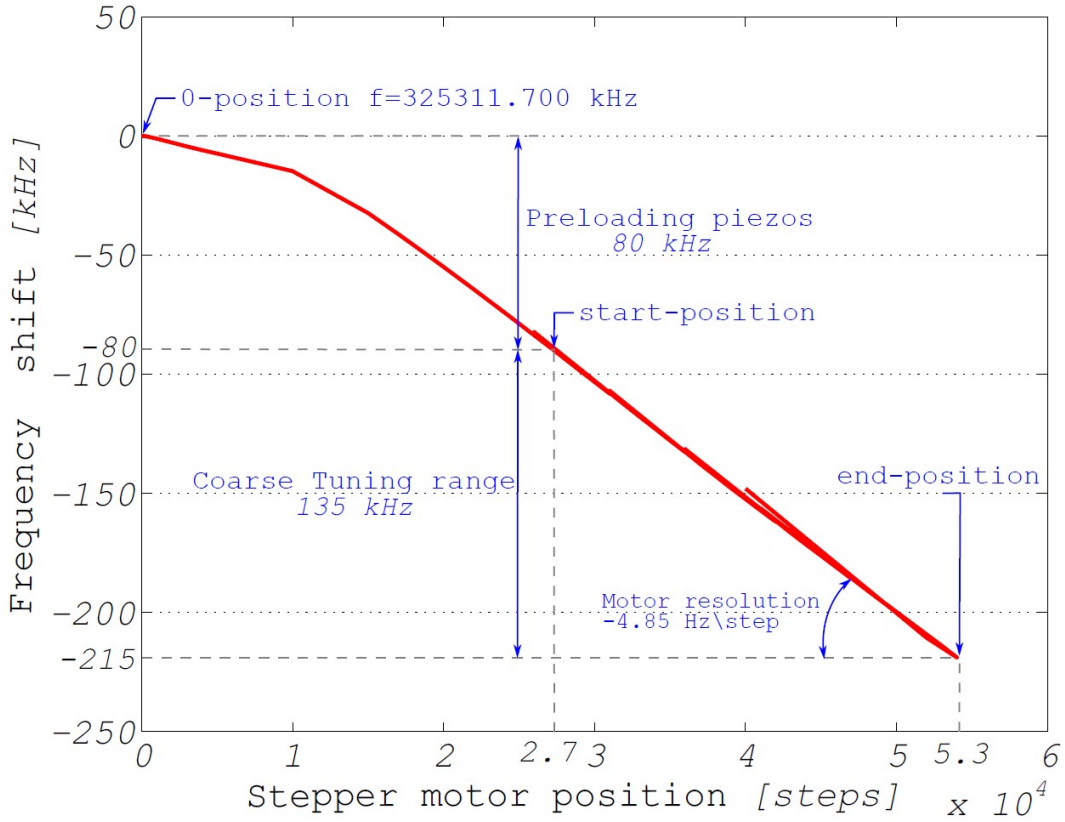

Figure 7.36: The dependence of cavity frequency on the stepper motor position.

The SSR2 tuner design is mostly identical to the SSR1 tuner. The requirements for the tuner performance are identical to the SSR1 tuner which were presented in Table 7.10.

7.2.3 Fundamental power coupler

The 325 MHz fundamental coupler has to deliver up to 5 kW CW power to the SSR1 cavities and up to 14 kW CW power to the SSR2 cavities to provide the necessary accelerating gradient for the 2 mA beam current. The coupler configuration is based on a room temperature single coaxial RF window. The outer window diameter is 2.94 in. and the antenna diameter is 0.5 in. These sizes correspond to a 105 ohm coaxial impedance, approximately a factor of two higher than the traditional geometry. This relatively high impedance reduces the losses in the outer conductor which is directly connected to the superconducting cavity (losses are inversely proportional to the impedance). This allows the use of a pure stainless outer conductor without a copper coating, keeping the dynamic cryogenic loading at an acceptable level with increased multipactor threshold. A coupler without a copper coating is more reliable and less expensive. The outer conductor has a thermal intercept at 5 K and 50 K. The coupler antenna is also air cooled. The air side of the coupler includes bellows sections to compensate for thermal contraction during cool down and warm up. The multipactor is suppressed by the high voltage bias which can be up to 5 kV. To protect the RF source against high voltage bias, the coupler is connected to the RF source through a DC block. This device blocks DC current and voltage but is transparent to the 325 MHz power.

Prototypes of the coupler with the DC block were successfully tested up to 30 kW in full reflection mode with different reflected phases. These tests exceeded the PIP-II power requirement of 2 mA and allows the possibility of upgrading to higher current in the future.

Multipactor is suppressed completely by high voltage bias and the couplers do not require conditioning if the high voltage bias was applied from the beginning. Configuration of the 325 MHz coupler and the DC block are presented in Figures 7.37 and 7.38.

Each coupler is qualified on a high power test stand before being installed on the superconducting cavity. Couplers are qualified in pairs connected through a room temperature coupling cavity under vacuum. The qualification power level exceeds (∼2 times) the operating power level in the accelerator. It provides assurance of the reliable operation of the coupler with the superconducting cavity in the accelerator. Figure 7.39 shows the test stand scheme and Figure 7.40 shows a picture of two couplers installed for qualification.

7.2.4 Focusing element

There are four magnet packages in the cryomodule. Each contains a focusing solenoid (lens) and four corrector coils, all operating in a helium bath at 2 K. The general design requirements for the lenses in the SSR1 cryomodule are based on Ref. [93] and summarized below:

- Each lens must contain four additional coils whose fields can be combined into two dipole correctors (x & y) and a skew-quadrupole;
- The clear aperture in the lens must not be less than 30 mm;

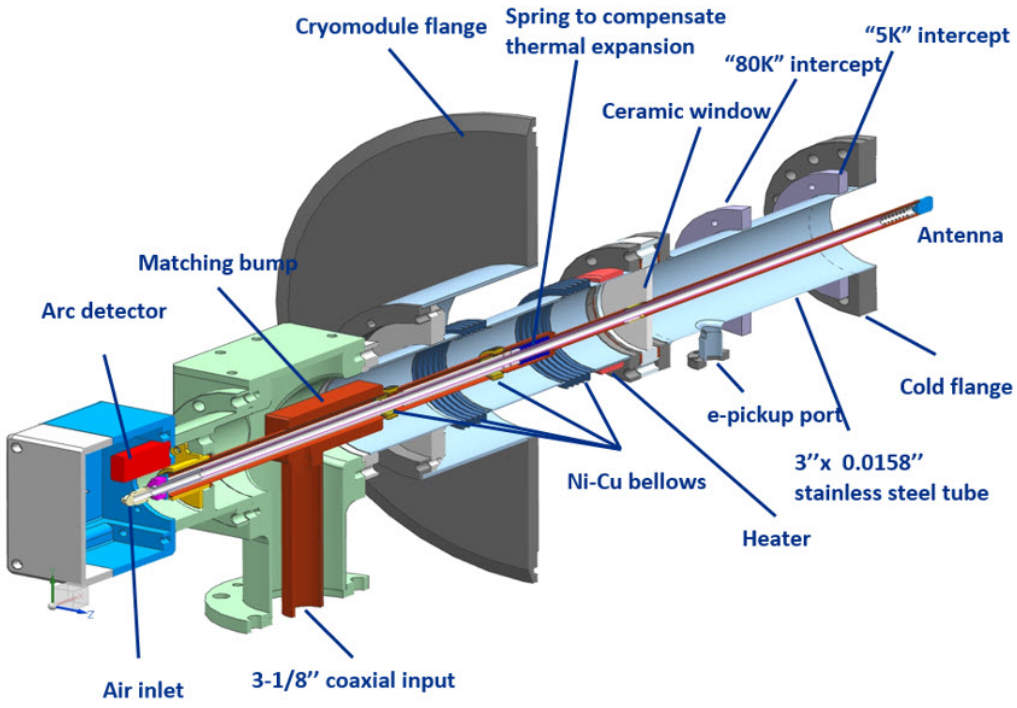

Figure 7.37: Configuration of the 325 MHz coupler.

- The uncertainty in the location of the effective magnetic axis in the focusing solenoid of the lens relative to reference points on the outer surface of the device must be better than 0.1 mm rms.

- A liquid helium vessel must be used for cooling the windings down to 2 K;

- The lenses must be quench-protected; the energy deposited in the lenses after quenching must be as low as reasonably achievable;

- The liquid helium vessel must meet the requirements of the Fermilab's ES&H manual chapters for pressure vessels;

- The design of the LHe vessel must ensure a reliable and reproducible mechanical connection to the alignment fixture of the cryomodule;

- The maximum magnetic field generated by the lenses in the cryomodule in the area near the surface of the SSR1 superconducting cavities must not exceed the level that would result in more than a two-fold reduction of the intrinsic quality factor after a quench event at any point on the surface of the cavity.

The SSR1 magnet assembly was designed and built. The results of the magnetic measurements as well as the main functional requirements of the magnet strength are presented in Table 7.11 and Table 7.12.

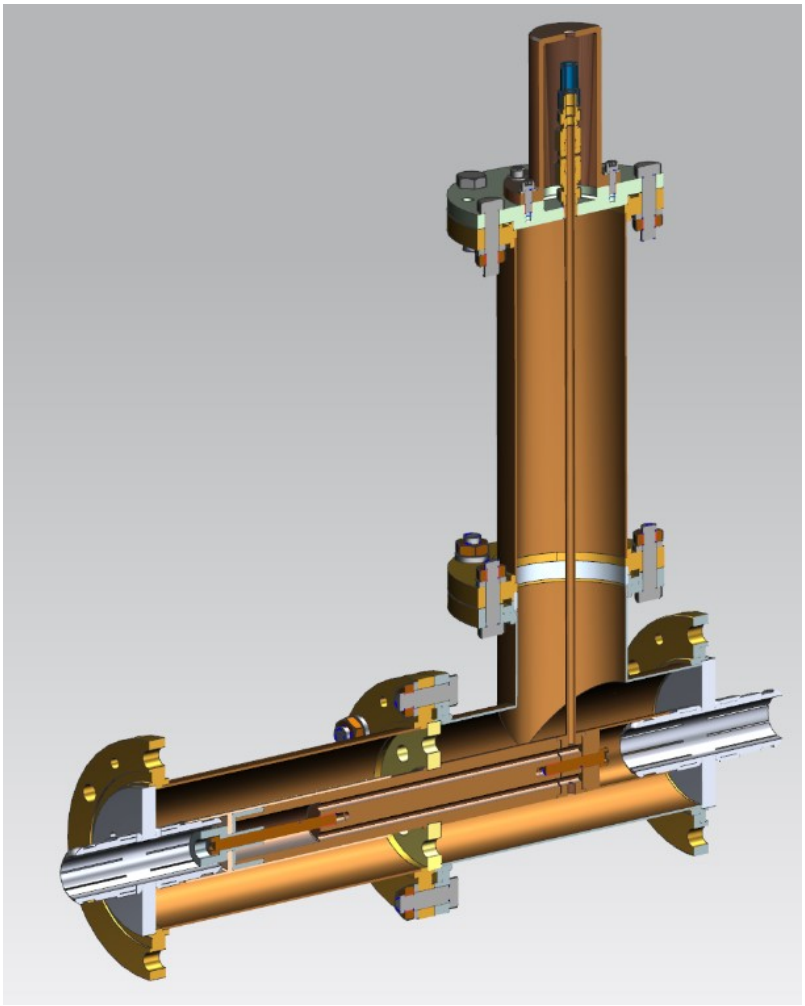

Figure 7.38: Cut away view of the 325 MHz DC block. The DC block is short-circuited for DC current and voltage and transparent to 325 MHz RF power.

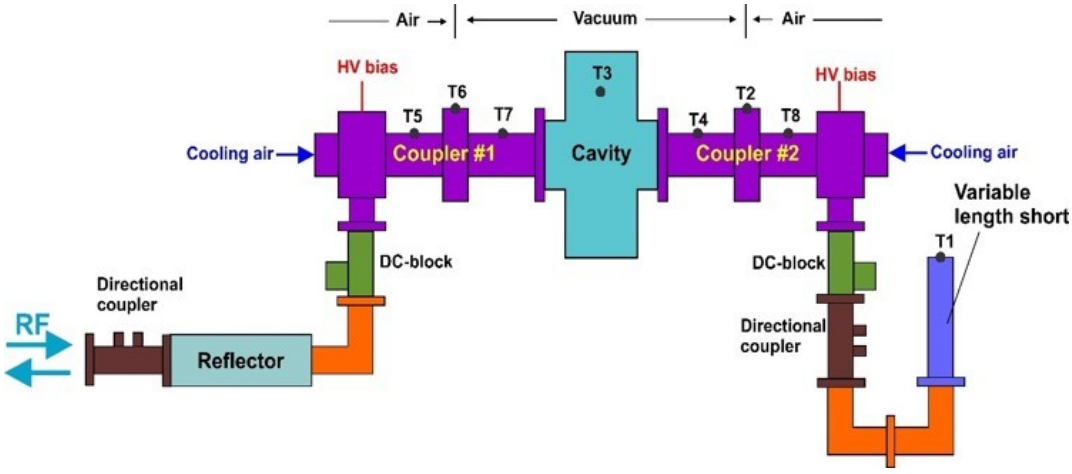

Figure 7.39: 325 MHz coupler test stand scheme.

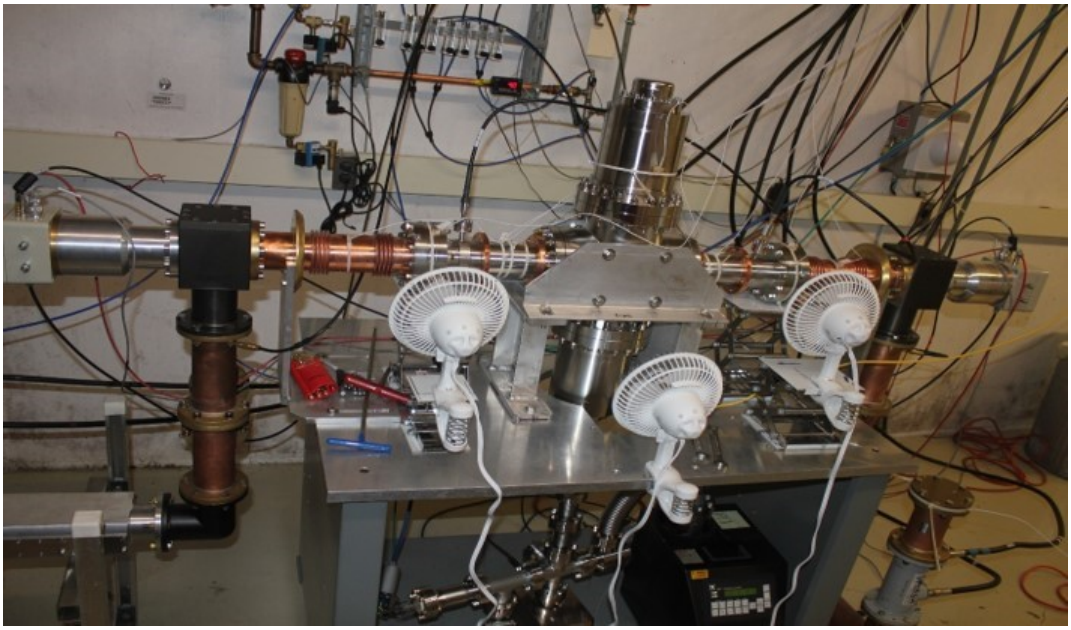

Figure 7.40: Two 325 MHz couplers installed to a high power test stand for qualification.

Table 7.11: Main parameters of the SSR1 magnet assembly solenoid

Solenoid	
Maximum current	65.2 A
Maximum focusing strength, $\int B^2 dL$	4 $T^2 m$
Maximum field integral, $\int BdL$	0.763 Tm
Field in the center at maximum current	6.82 T
Effective length, $\int BdL/B_0$	11.19 cm

Table 7.12: Main parameters of the SSR1 magnet assembly dipole

Dipole corrector	
Maximum current	32.5 A
Maximum field integral, $\int BdL$	2.5 mTM
Beampipe aperture	30 mm

As stated above, each focusing element package contains five coils: the main solenoid, and four corrector coils. The conduction cooled current lead design must support 100 A in the solenoid leads and 50 A in the corrector leads. Their design is based on the design of similar leads installed in the LHC at CERN. Thermal intercepts at 70 K and at 5 K help to reduce the heat load to 2 K, nonetheless, these current leads represent a significant source of heat at the low temperature end. There is one lead assembly for each magnetic element.

The Linac lattice, especially the low-beta section, provides limited space along the beamline for beam diagnostics either inside individual cryomodules or between adjacent modules. In order to conserve axial space along the beamline a button-type beam position monitor (BPM) was chosen for installation in the SSR cryomodules [94]. For a non-relativistic beam they also generate larger signal than strip-line BPMs. A total of four BPMs are installed in the cryomodule, one near each magnetic package. These devices are compact and lend themselves well to incorporation into the solenoid magnet package as shown in Figure 7.41. The bellows at either end of the beam tube allow independent alignment of each magnet package.

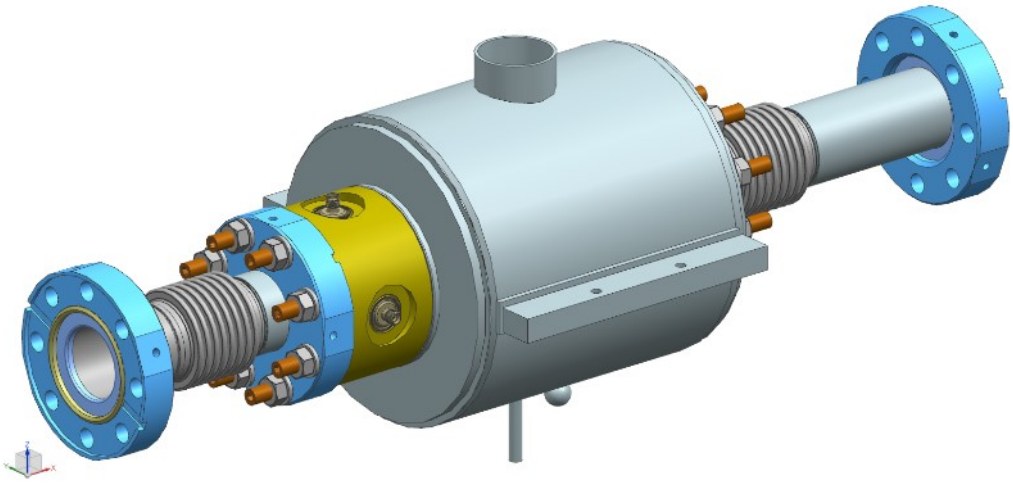

Figure 7.41: Solenoid and BPM assembly.

Focusing in the SSR2 cryomodules is provided by solenoids and is axially symmetric. However, spoke resonators have a central electrode which is perpendicular to the particle motion. It breaks the axial symmetry of the system and the symmetry of the transverse electric and magnetic fields and results in non-axially symmetric focusing of the cavity. The transverse electric and magnetic fields of an SSR2 cavity are shown in Figure 7.42. Together they create a quadrupole component of the cavity defocusing, see Figure 3.28. This focusing asymmetry is compensated by skew-quadrupoles located in the magnet assemblies, which are built similarly to the SSR1 magnet assemblies.

There are three magnet packages in the SSR2 cryomodule. As in the SSR1 cryomodule, each package contains a focusing solenoid (lens) and four corrector coils all operating in a helium bath at 2 K. The general design requirements for the lenses in the SSR2 cryomodule are based on Ref. [95]. The main parameters of the magnet assemblies are presented in Tables 7.13 and 7.12 [96].

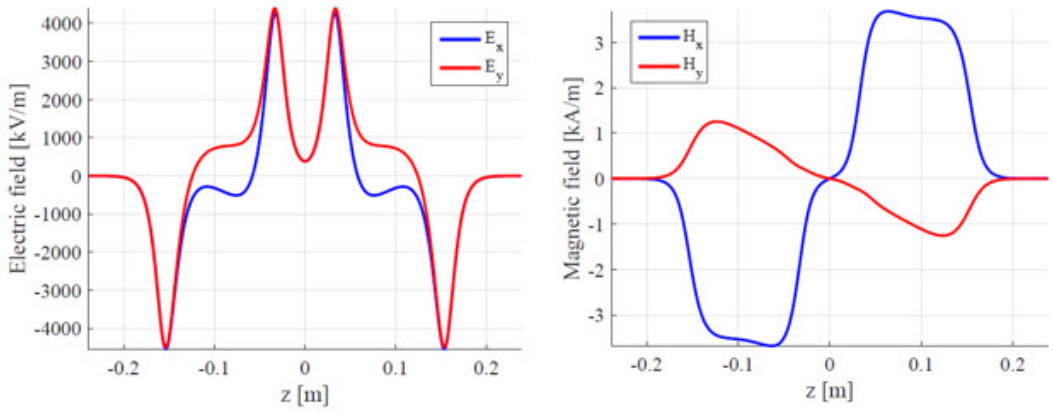

Figure 7.42: SSR2 transverse electric (left) and magnetic (right) fields, calculated at r=10 mm.

Table 7.13: Main parameters of the SSR2 magnet assembly solenoid

Solenoid	
Maximum focusing strength, $\int B^2 dL$	5 $T^2 m$
Maximum current	74.97 A
Maximum field integral, $\int B dL$	0.978 Tm
Field in the center at maximum current	6.024 T

Table 7.14: Main parameters of the SSR2 magnet assembly dipole corrector

Dipole corrector	
Maximum field integral, $\int B dL$	5 mTm
Maximum current	37.3 A
Beampipe aperture	40 mm

The design of the button-type beam position monitor (BPM) represents a scaled (from 30 to 40 mm) version of the SSR1 button BPM design. The current leads and RF coupler of the SSR2 cryomodules are identical to the corresponding items of the SSR1 cryomodules.

7.2.5 Cryomodule

7.2.5.1 String assembly

The cavity string assembly of the SSR1 cryomodule, which constitutes the beamline volume, contains eight superconducting SSR1 cavities with their RF couplers and four solenoids. The sequence of elements in a cryomodule is: C-S-C-C-S-C-C-S-C-C-S-C, where C denotes a cavity and S a solenoid. Figures 7.43 and 7.44 show views of the string assembly. Horizontal and vertical dipole correctors are located inside each solenoid. A four-electrode beam position monitor (BPM) is attached to each solenoid.

The connections along the beamline are made using aluminum diamond seals and stainless steel flanged joints and bellows. At each end, the beamline is terminated with ultrahigh-vacuum (UHV) gate valves through which the beamline is pumped down. The planned pumping system for the cryomodule consists of two turbo pumps with a pumping speed of 300 l/s and an ultimate pressure of 1×10^{-8} Torr at the pump inlet. The UHV is supported by ion pumps. The cavity string is assembled in a class 10 cleanroom to minimize particle contamination in the beamline. The contamination is known to cause field emission and degrade cryomodule performance. Limiting the number of beamline components and sub-assemblies from the initial stages of design simplifies the installation procedure and promotes a cleaner assembly. A vacuum level of 5×10^{-5} or lower is achievable by pumping only through the beamline [97]. The pressure threshold of 5×10^{-5} Torr was chosen to avoid negative effects such as increased field emission [98] and residual resistance due to condensed gases [99]. This level of vacuum must be reached in less than 12 hours to minimize the down-time associated with thermal cycles for the cryomodule.

7.2.5.2 Coldmass assembly

Each cryomodule has a single thermal shield cooled with helium gas, nominally at 45-80 K. It is currently envisioned to be aluminum with cooling channels on both sides. Two 15-layer blankets of multilayer insulation, between the vacuum vessel and thermal shield, reduces the radiation heat load to the 80 K shield from the room temperature vacuum vessel to approximately 1.5 W/m^2. A 5 K circuit intercepts heat on the RF couplers and current leads, but there is no plan to install a full 5 K thermal shield.

All cavities and solenoids are mounted on individual support posts, which are in turn mounted to a full-length room temperature strongback located between the vacuum vessel and thermal shield. This enables the entire cavity string to be assembled and aligned as a unit then inserted into the vacuum vessel during final assembly. Presently, the strongback is aluminum, but stainless steel is

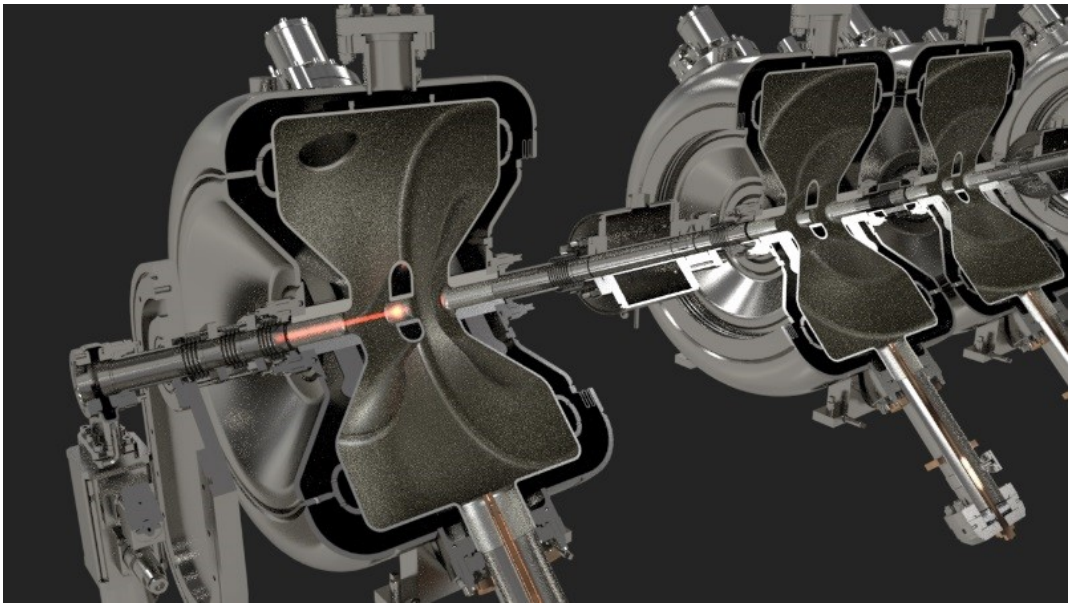

Figure 7.43: View on SSR1 cavity string assembly.

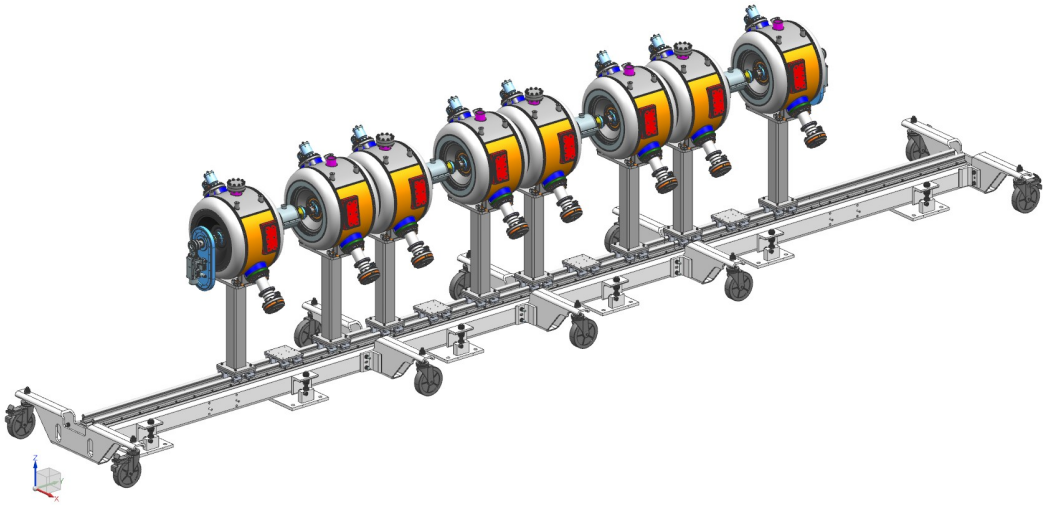

Figure 7.44: SSR1 cavity string assembly.

an option. Maintaining the strongback at room temperature helps to minimize axial movement of the cold elements during cooldown, reducing displacement of couplers, current leads, and other internal piping components. The support posts are similar to supports utilized in the SSC collider dipole magnets, and the ILC and XFEL 1.3 GHz cavity cryomodules. The main structural element is a glass and epoxy composite tube. The tube ends and the intermediate thermal intercepts are all assembled using a shrink-fit technique in which the composite tube is sandwiched between an outer metal ring and an inner metal disk [100]. All of the cavities and solenoids are mounted to the support posts using adjustable positioning mechanisms. Figure 7.45 shows a view of the cold-mass assembly.

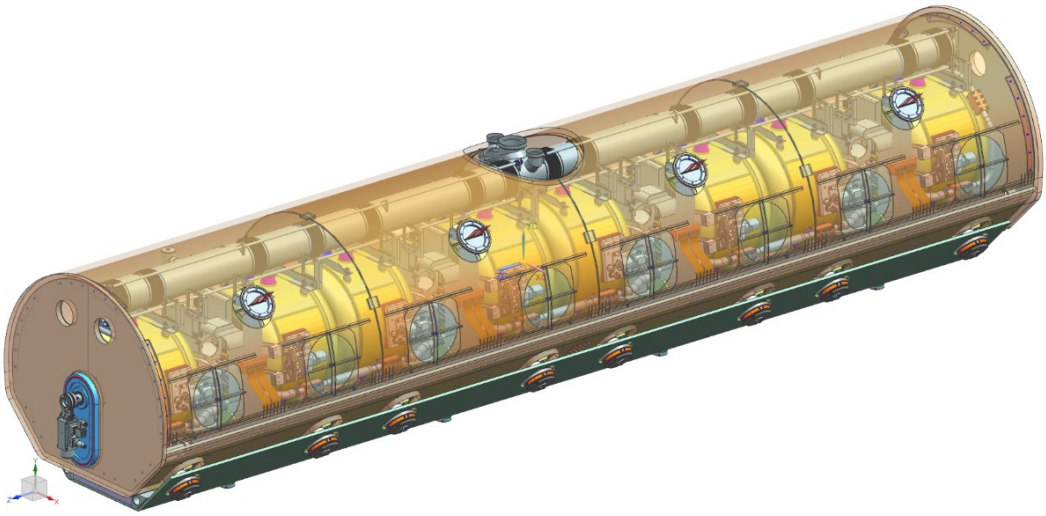

Figure 7.45: SSR1 cold-mass assembly.

Alignment of cavities and solenoids is accomplished using optical targets installed on the internal assemblies translated to fiducials installed on the vacuum vessel. Changes in alignment due to shipping and handling or during cooldown and operation is monitored using a series of wire targets on each cavity and solenoid, viewed through optical windows in either end of the cryomodule assembly. The requirements on the alignment of cavities and magnet assemblies for the SSR1 are presented in Table 7.15.

Table 7.15: Requirements on alignment of SSR1 cavities and magnet assemblies

	Cavities	Magnet assemblies
Rms transverse position, mm	1	0.5
Rms angular alignment, mrad	5	0.5

7.2.5.3 Cryomodule integration

The SSR1 and SSR2 vacuum vessels contain all the cryomodule components in their as-installed positions. It has a secure anchorage to the tunnel floor, thermally insulates all cryogenic compo-

nents thus minimizing heat loads to 80 K, 4.5 K, and 2 K, and maintains the insulating vacuum. The vessel is 1.219 m (48 inches) in diameter. A view of the SSR1 is presented in Figure 7.46.

Just inside the vacuum vessel, nearly in contact with the inner wall, is a magnetic shield that shields the cavities from the earth's magnetic field. Tests show that a 1.5 mm thick mu-metal shield at room temperature reduces the residual field inside the cryostat to less than 10 μT. It is likely that separate magnetic shields will also be installed around individual magnetic elements to further reduce trapped fields in the superconducting cavities.

The intent is to have all external connections to the cryogenic, RF and instrumentation systems made at removable junctions at the cryomodule itself. The only connection to the beamline is the beam pipe, which is terminated by "particle free" valves at both ends. The major goals of the design are minimization of mean time between failures and time required for repairs. The latter is achieved by allowing in-situ repair of some internal systems like cavity tuners.

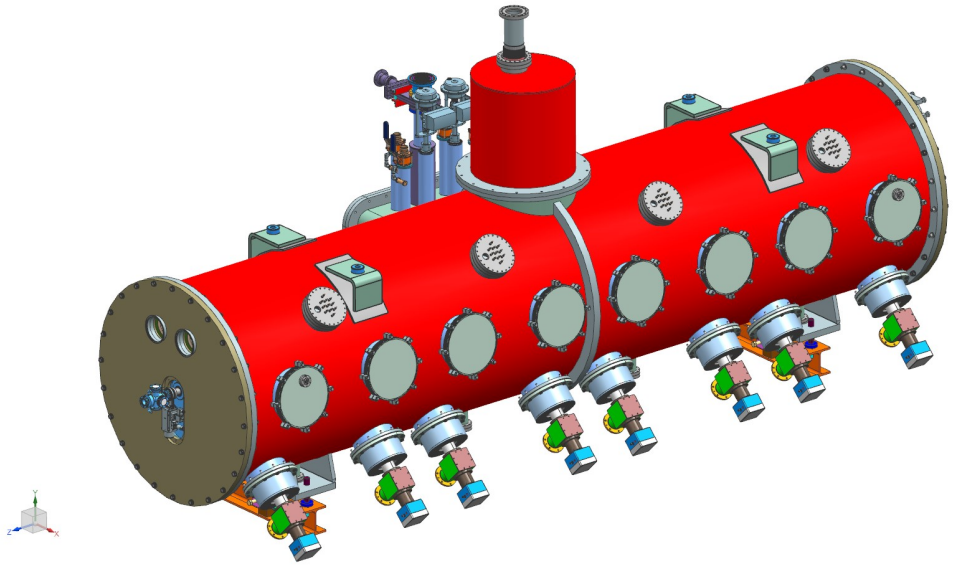

Figure 7.46: SSR1 cryomodule assembly.

Table 7.16 and Table 7.17 summarize the estimated static and dynamic heat loads at each temperature level in the SSR1 and SSR2 cryomodule assembly from all sources, respectively.

7.3 Elliptical cavities and cryomodules

Acceleration from 185 MeV to 800 MeV is provided by two families of 5-cell elliptical cavities operating at 650 MHz and designed for $\beta_G = 0.61$ and $\beta_G = 0.92$ designated the LB650 and the HB650 cryomodules, respectively.

Table 7.16: SSR1 cryomodule heat load estimates.

	Per Unit (W)			# of Units	Total (W)		
	35-50 K	5 K	2 K	-	35-50 K	5 K	2 K
RF coupler, static	6.20	0.80	0.07	8	49.6	6.4	5.6
RF coupler, dynamic	1.30	0.70	*	8	10.4	5.6	*
Cavity, dynamic	-	-	1.60	8	-	-	12.8
Support post	1.90	0.90	0.10	12	22.8	10.8	1.2
Beam line	0.20	0.60	0.020	2	0.4	1.2	0
Thermal shield	72.20	-	1.30	1	72.2	-	1.3
View ports	0.20	-	0.70	4	0.8	-	2.8
Relief line	1.10	-	0.50	1	1.1	-	0.5
Current leads, static	4.50	6.50	2.70	4	18.0	26.0	10.8
Current leads, dynamic	10.40	0.70	0.50	4	41.6	2.8	2.0
Valves and Instrumentation	11.10	3.20	0.70	-	11.1	3.2	0.7
Total static	-	-	-	-	**176.0**	**47.6**	**22.9**
Total dynamic	-	-	-	-	**52.0**	**8.4**	**14.8**
Total static + dynamic	-	-	-	-	**227.8**	**55.8**	**37.7**
* Input coupler dynamic heat load is embedded in the cavity dynamic heat load value							

Table 7.17: SSR2 cryomodule heat load estimates.

	Per Unit (W)			# of Units	Total (W)		
	35-50 K	5 K	2 K	-	35-50 K	5 K	2 K
RF coupler, static	6.20	0.80	0.70	5	31.0	4.0	3.5
RF coupler, dynamic	5.36	2.82	*	5	26.8	14.1	*
Cavity, dynamic	-	-	8.40	5	-	-	42
Support post	1.90	0.90	0.10	8	15.2	7.2	0.8
Beam line	0.20	0.60	0.02	2	0.4	1.2	0
Thermal shield	69.8	-	1.20	1	69.8	-	1.2
View ports	0.20	-	0.70	4	0.8	-	2.8
Relief line	1.10	-	0.50	1	1.1	-	0.5
Current leads, static	4.50	6.50	2.70	3	13.5	19.5	8.1
Current leads, dynamic	10.40	0.70	0.50	3	31.2	2.1	1.5
Valves and Instrumentation	9.90	2.70	0.60	-	9.9	2.7	0.6
Total static	-	-	-	-	**141.6**	**34.5**	**17.2**
Total dynamic	-	-	-	-	**58.0**	**16.2**	**43.5**
Total static + dynamic	-	-	-	-	**199.6**	**50.7**	**60.7**
* Input coupler dynamic heat load is embedded in the cavity dynamic heat load value							

7.3.1 Cavity design

7.3.1.1 LB650 cavity design

The 650 MHz cavities require sufficient wall thickness to minimize sagging caused by the overall weight. Note that stiffening rings are used for both the ILC and 650 MHz cavities to increase the rigidity of cavities. Limiting the maximum cavity sag to $120\mu m$ (the same as in the ILC) results in a 4 mm wall thickness. A small cavity wall slope gives more freedom in decreasing the field enhancement factors. However, the slope is also constrained by surface processing and mechanical stability requirements. The chosen slope of about 2° results in an acceptable value for the field enhancement. The physical description of the cavity shapes is presented in Figure 7.47 and Table 7.18. All dimensions are shown at a temperature of 2 K.

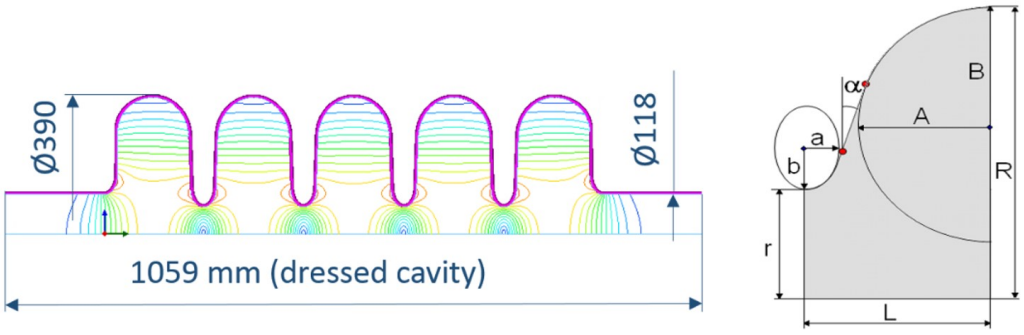

Figure 7.47: Layout of LB650 MHz cavities.

Table 7.18: Dimensions of the LB650 MHz cavities (cold). *See Figure 7.47 for definitions of dimensions.

Dimension*	LB650	
	Regular cell	End cell
r, mm	44	59
R, mm	194.9	196.05
L, mm	70.4	69.9
A, mm	54.2	54.2
B, mm	54.2	54.2
a, mm	13.7	13.7
b, mm	24.3	24.3
α,°	2	2
Equator flat, mm	0	0
Iris flat, mm	0	0

7.3.1.2 HB650 cavity design

The 650 MHz high beta cavity design is similar to the LB650 cavity but at a much more advanced stage. Figure 7.48 shows the layout of the cavity RF design with the parameters listed in Table 7.19. Four 5-cell bare cavities were fabricated with $\beta_G = 0.9$, which is very similar to the $\beta_G = 0.92$ design.

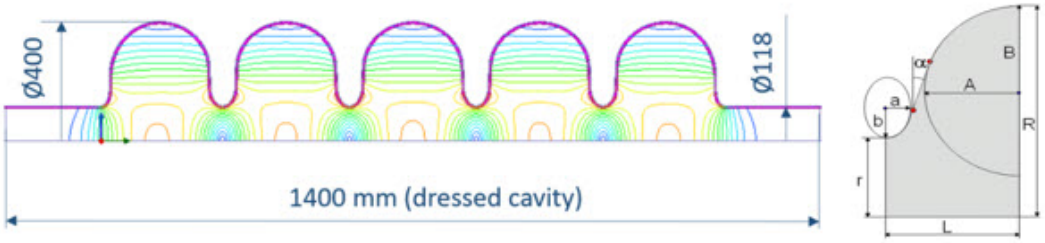

Figure 7.48: Layout of HB650 MHz cavities.

Table 7.19: Dimensions of the HB650 MHz cavities (cold). *See Figure 7.48 for definitions of dimensions.

Dimension*	HB650	
	Regular cell	End cell
r, mm	59	59
R, mm	200.1	200.1
L, mm	106.1	97.6
A, mm	85	84
B, mm	78	90
a, mm	20	13
b, mm	33	28
α,°	1.9	1.9
Equator flat, mm	0	0
Iris flat, mm	0	0

Multipacting simulations have indicated barrier could exist within 10.5 to 17 MV/m as indicated in the simulation, see Figure 7.49. While some barriers have been seen in this region during testing, they were not prohibitive to testing and the statistics are not enough to give definitive statements about the final cavity multipacting.

A series of qualification tests indicated a Q0 at 3×10^{10} at 20 MV/m is achievable for bare cavities. The baseline processing includes 120 μm electropolishing, a hydrogen bake out for three hours at 800°C in a UHV furnace, N-doping with a 2/6 recipe (2 mTorr nitrogen soaking for six minutes at 800°C at the completion of the hydrogen bake out) and a final 5 μm light electropolishing. Figure 7.50 shows the performance of several tests of the four prototype cavities. Since some cavities indicated lower performance, an R&D program using a single cell has been undertaken to explore ways to improve both cavity Q0 and yield.

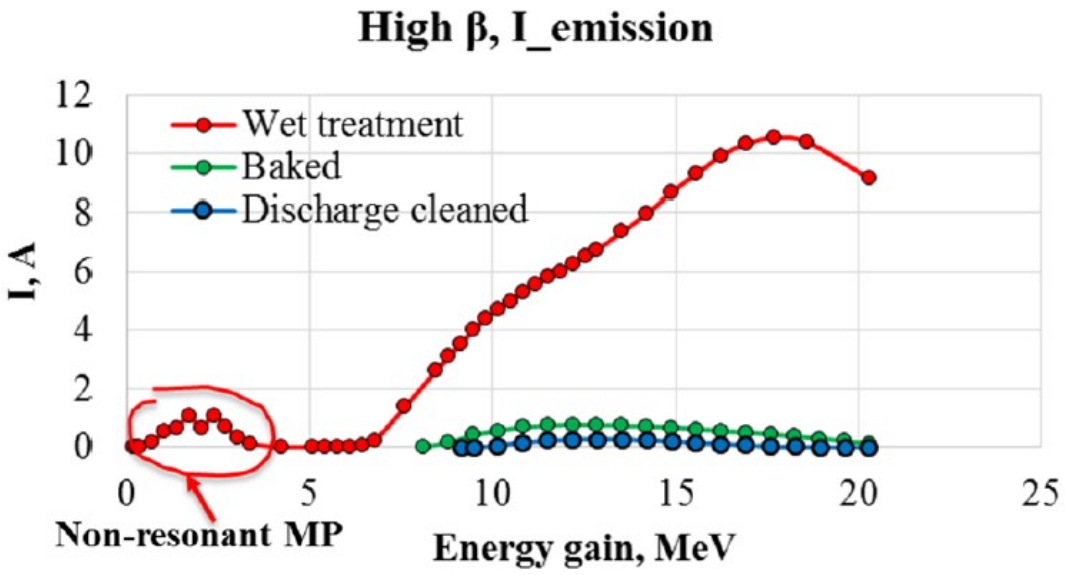

Figure 7.49: Multipacting simulation for a 650 MHz center cell.

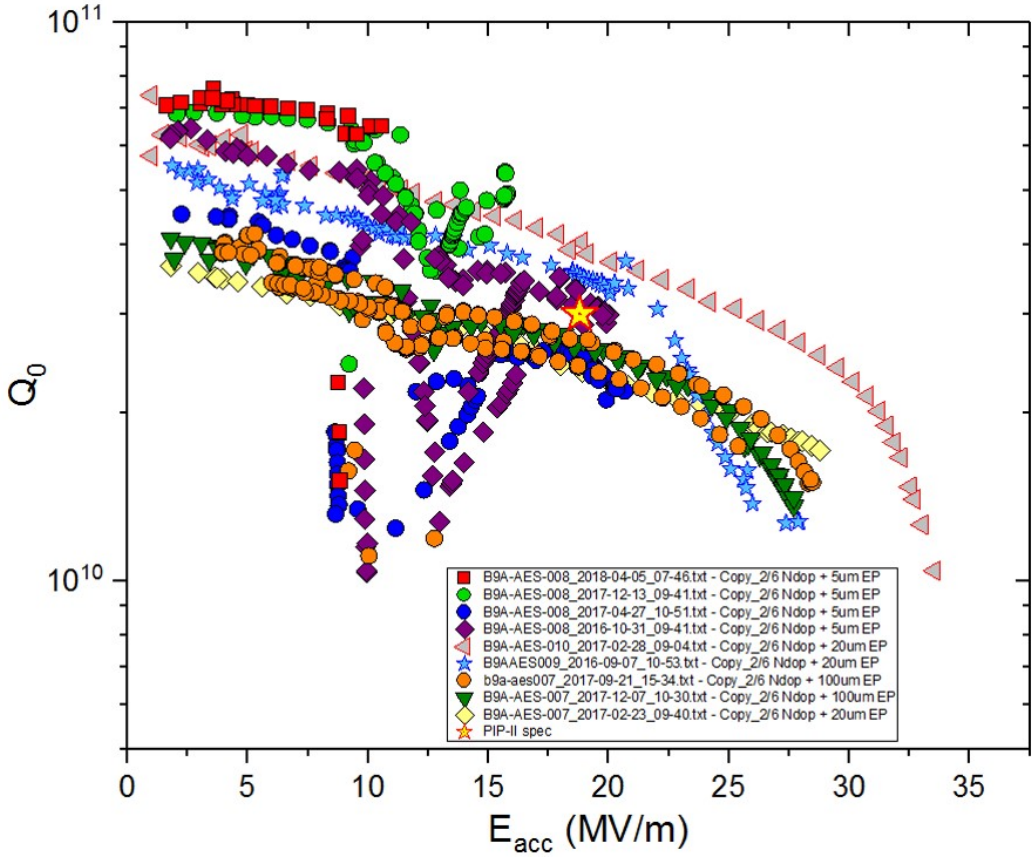

Figure 7.50: Accumulated 5-cell vertical test performance.

Figure 7.51 shows that the latest processing of a single-cell cavity is successful in achieving 4×10^{10} at 20 MV/m after electropolishing and 120°C baking. The improvement is attributed to better process control during electropolishing and modified low temperature baking. The science of the improvement is still being investigated.

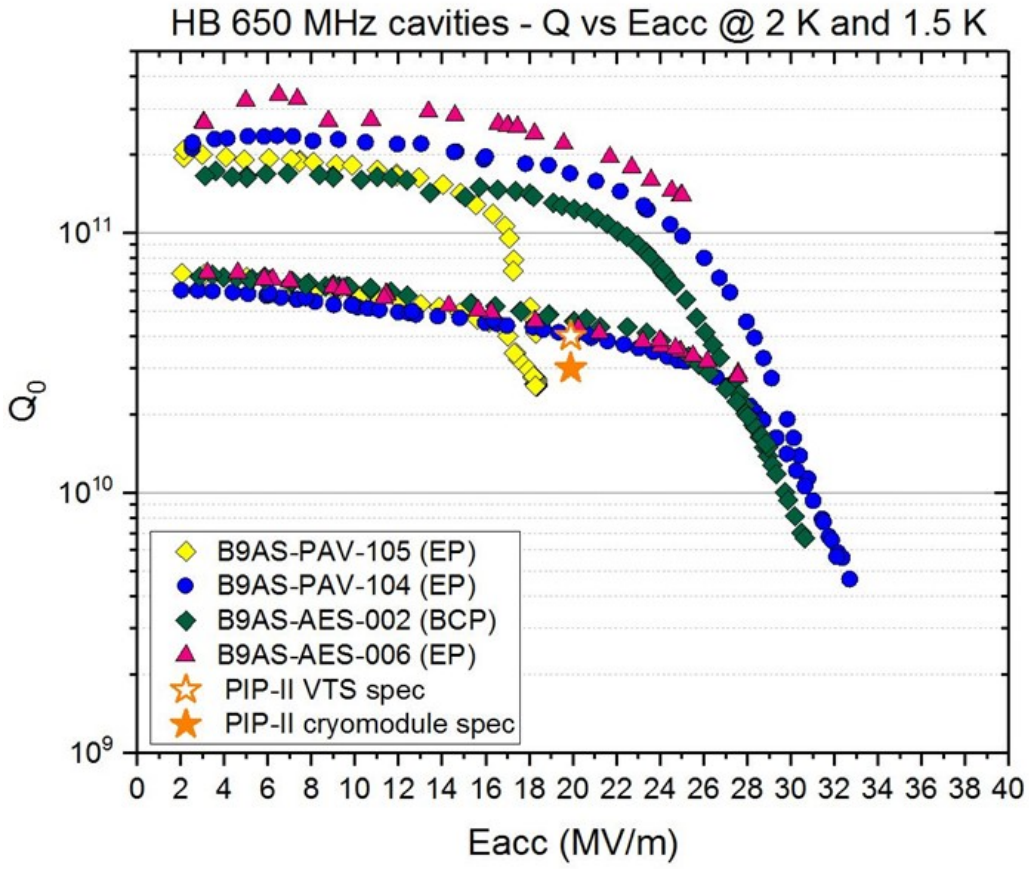

Figure 7.51: VTS test results from B9AS-PAV-104 and B9AS-AES-106 after 75°C/120°C baking and 40 μm EP reset, respectively. Lower and upper set of curves represent 2 K and 1.5 K measurements, respectively. B9AS-PAV-105 after EP and B9AS-AES-002 after BCP are illustrated for comparison.

The dressed cavity design follows a similar design of the LCLS-II 1.3 GHz dressed cavity utilizing titanium bellows at the tuner end. However, for the HB650, the diameter of the bellows is reduced at the end to allow for similar pressure loading to the bellows as shown in Figure 7.52.

A 5-cell cavity B9A-AES010 has been chosen as the prototype cavity to be dressed with the helium vessel. The dressing procedure has been prepared and a mock-up test was successful as shown in Figure 7.53.

7.3.2 Cold tuning system

The SRF cavity cold tuning system has to fulfill several tasks: (1) to protect the cavity during CM assembly and operation, (2) to tune the cavity to the operational frequency after cool-down to 2 K,

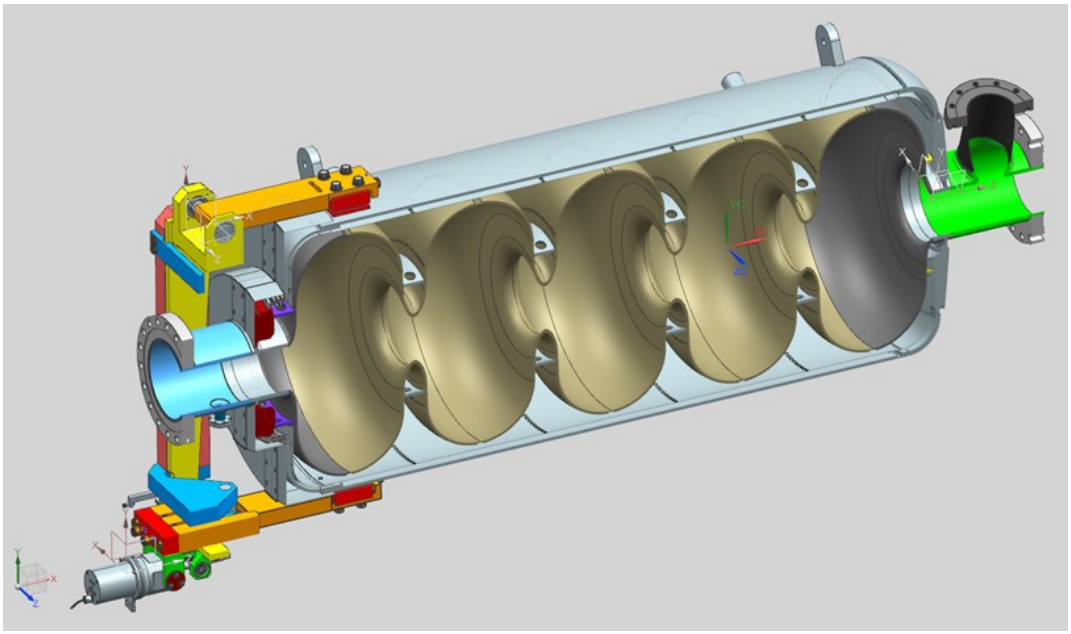

Figure 7.52: High-beta dressed cavity cross section.

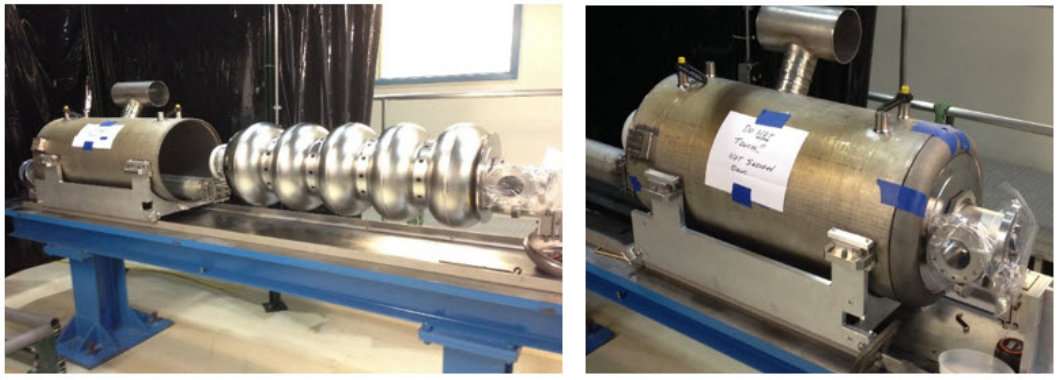

Figure 7.53: HB650 helium vessel welding procedure prepared with a successful mock-up test.

(3) to compensate for the cavity frequency detuning caused by Lorentz forces and microphonics and (4) to detune off resonance if the cavity is malfunctioning. An identical cold tuning system (tuner) serves both types of 650 MHz cavities (LB and HB). The tuner is designed to compensate for the spread in the warm cavity tuning during production and uncertainties in the cavity frequency shift due to cooldown from 293 K to 2 K and to minimize detuning caused by microphonics and Lorentz forces (LFD). Production and cooldown uncertainties are estimated to be less than 200 kHz and are managed by the slow (coarse) tuner. Dynamic cavity detuning (microphonics and LFD) are anticipated to be less than 1 kHz and are compensated by the fast (fine) tuner. The 650 MHz cavity tuner specifications are presented in Table 7.20.

Table 7.20: Tuner requirements for LB and HB cavities

	LB650-HB650
Coarse tuner frequency range, kHz	200
Coarse tuner frequency resolution, Hz	1-2
Coarse tuner hysteresis, Hz	≤ 100
Fine tuner frequency range, Hz	1000
Fine tuner frequency resolution, Hz	0.5
Tuner-dressed cavity system stiffness	> 40 kN/mm

To meet the requirements for frequency range and resolution, the tuning system integrates coarse and fine mechanisms engaged in series. The design of the 650 cold tuning system is similar to the LCLS-II 1.3 GHz [101] tuner system with appropriate scaling to fit to the 650 MHz cavity dimensions [102]. The kinematics model and the 3-D model of the tuner are shown in Figures 7.54 and 7.55. The coarse tuner is a double lever tuner (with a 20:1 ratio), that utilizes an electromechanical actuator to translate the rotation of the stepper motor to linear motion. The tuner works in the "cavity-push" direction by compressing the cavity. The fine tuner consists of a two piezo-stack that is installed between the coarse tuner's levers (top and bottom), close to the cavity end flange. This means that the piezo stroke is translated directly to the cavity, not through flexible and/or bearing connections. This configuration delivers better piezo-tuner resolution and decreased group delay of the fast tuner. Safety rods are placed between the cavity end flange and the main lever of the tuner. These safety rods protect the cavity from non-elastic deformation during the cavity/helium vessel system leak check. The tuner is anchored to the helium vessel with two strong horizontal arms. These arms have adjustment capabilities to accommodate differences of up to several millimeters in the length of the 5-cell elliptical cavities after final tuning. To decrease the cost and the weight of the tuner frame and to simplify the assembly of the tuner on the cavities, it was designed in several parts that are connected by welding or through the use of screws. Set-screws, special washers and lock-tight were used to prevent loosening of the assembly screws during warmup and cool-down cycles.

Ball connections were chosen for the connections between the top and bottom encapsulated piezo-stack and the main lever. This prevents the build-up of shearing forces on the piezo-stack during tuner operation which is detrimental to piezo lifetime. Two adjustment screws, one in each main arm, help to uniformly preload the piezo-stacks during assembly.

The 650 MHz cavity has a half-bandwidth of 30 Hz and the cavity's resonance needs to be controlled to the level of 20 Hz (peak). Detuning of the 650 MHz cavity by Lorentz forces is large and strongly

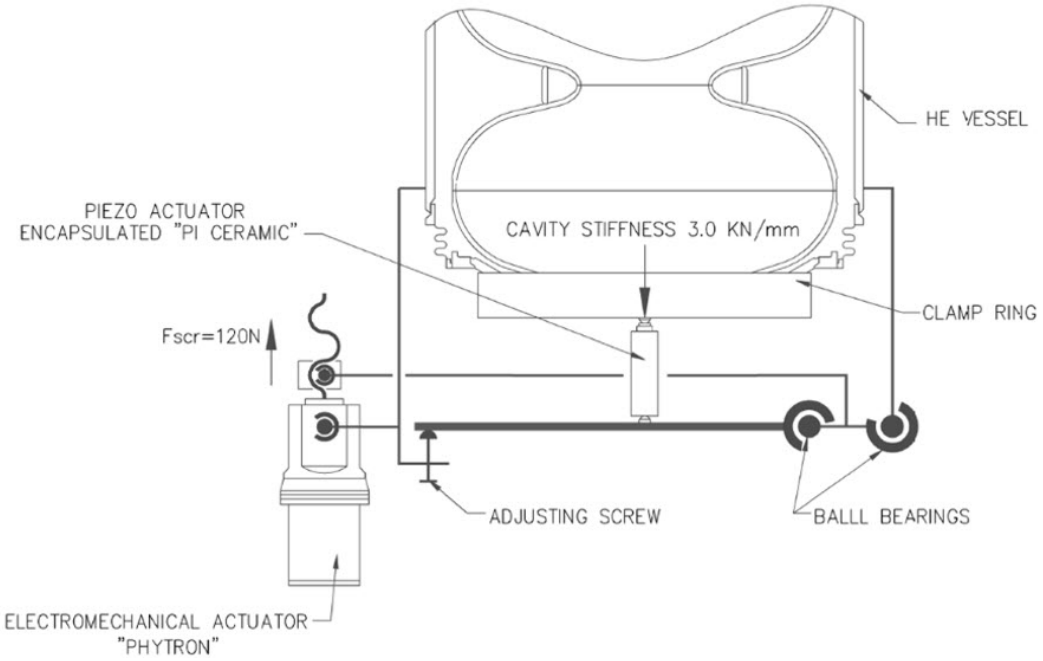

Figure 7.54: Tuner kinematic model.

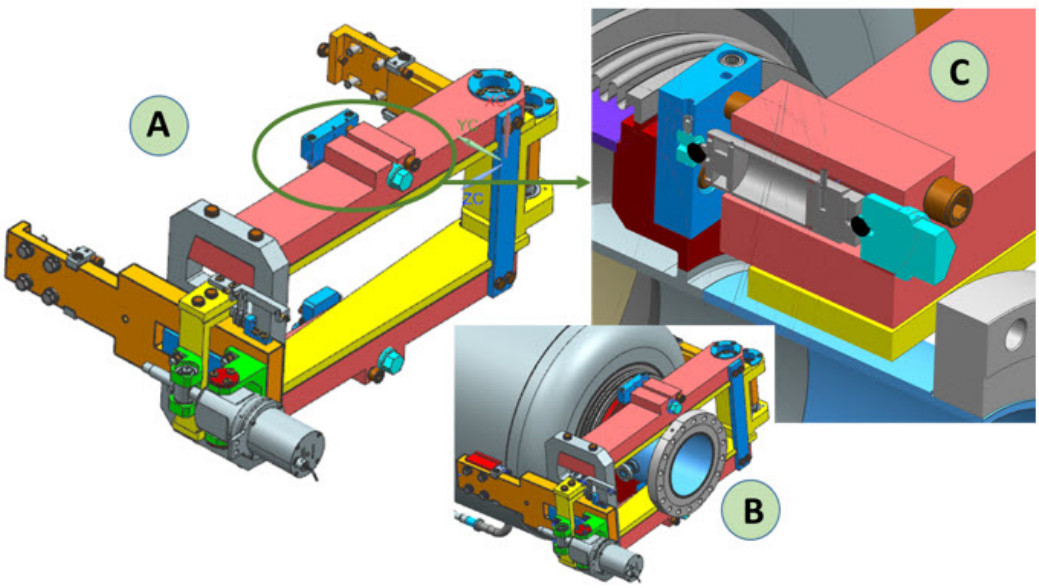

Figure 7.55: (A and B) 3-D model of the modified tuner. (C) piezo-actuator inserted into main tuner arm and interfaced cavity through Nb-Ti ring.

dependent on the stiffness of the cavity's tuner [103]. Tuner stiffness is one of the key parameters that was addressed during the tuner design.

ANSYS simulation was used to conduct optimization studies by varying the dimensions of the different components of the tuner. The calculated stiffness of the slow tuner frame with the electromechanical actuator is on the order of 140 kN/mm, see insert A in Figure 7.55. The calculated stiffness of the dressed cavity/tuner system which includes the piezo-capsules with a stiffness of about 100 kN/m [6] and the Nb-Ti cavity-tuner transition ring, see insert C in Figure 7.55 and Figure 7.57, decreased to the level of 42 kN/mm. Results of the tests of the first 650 MHz tuner assembled on the test stand is shown in Table 7.21 with a mock-up of the 650 MHz cavity shown in Figure 7.57.

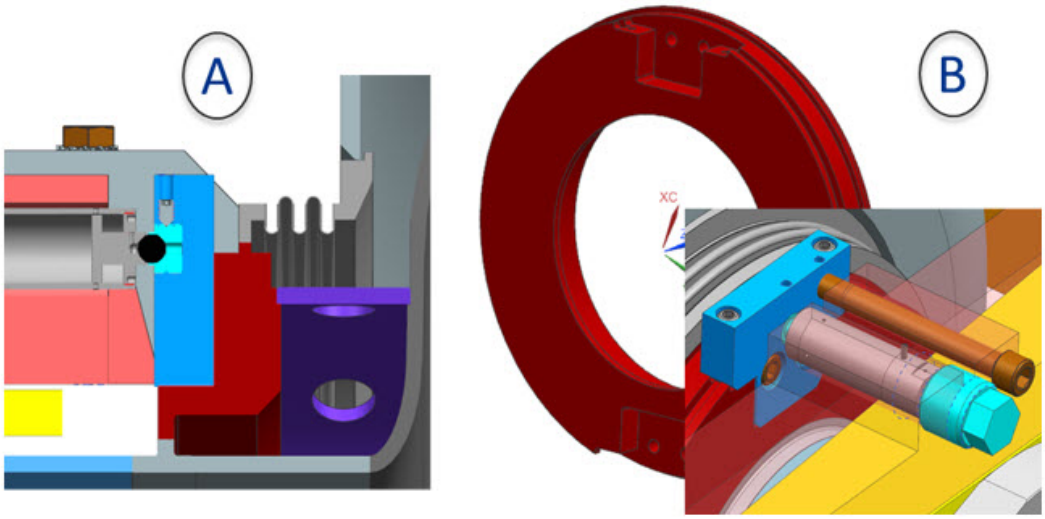

Figure 7.56: (A) Cross-section of the tuner/cavity interface system. (B) The Nb/Ti interface ring, shown in red, is welded to the cavity beam-pipe. The piezo-capsule - to - Nb/Ti ring interface component, shown in blue, holds the ceramic ball and has threads which connects to the safety bracket.

Table 7.21: Tuner parameters (measured warm, installed on the cavity mock-up)

Coarse tuner frequency range, mm/kHz	1.5 mm/300 kHz
Coarse tuner frequency resolution, Hz/step	1 Hz/step
Fine tuner stroke warm, μm	32 μm
Expected fine tuner frequency range at 10 K	1.2 kHz
Estimated tuner/dressed cavity system stiffness	$\sim$ 40 kN/mm

The electromechanical actuator is the active element of the slow/coarse tuner. The electromechanical actuator translates the rotation of the stepper motor to linear motion of the tuner arms. The tuner is equipped with a Phytron actuator (LVA 52-LCLS II-UHVC-X1) designed for the FNAL ILCTA SRF project [104], see Figure 7.58. More than three hundred Phytron actuators have been built and successfully installed into LCLS-II cryomodules. The Phytron actuator consists of:

- Stepper motor LVA 52 UHVC

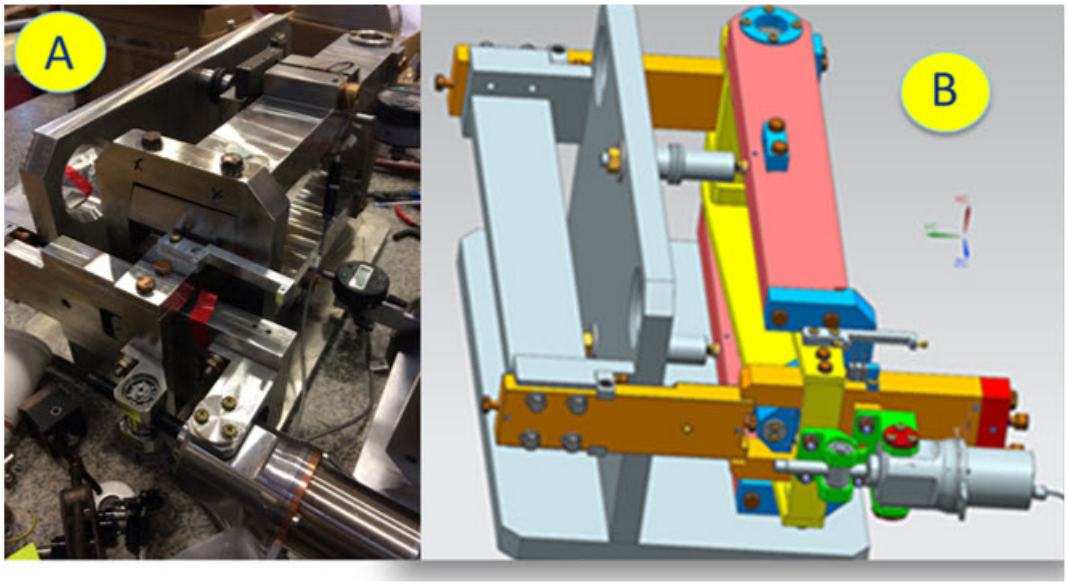

Figure 7.57: (A) photo of 650 MHz tuner assembly on the test stand (cavity mock-up). (B) 3-D model of the tuner installed on the test stand.

- Planetary gear (1:50 ratio)
- M12X1 spindle made from titanium
- Traveling nut made from stainless steel and radiation hardened plastic material TECASIN-1041

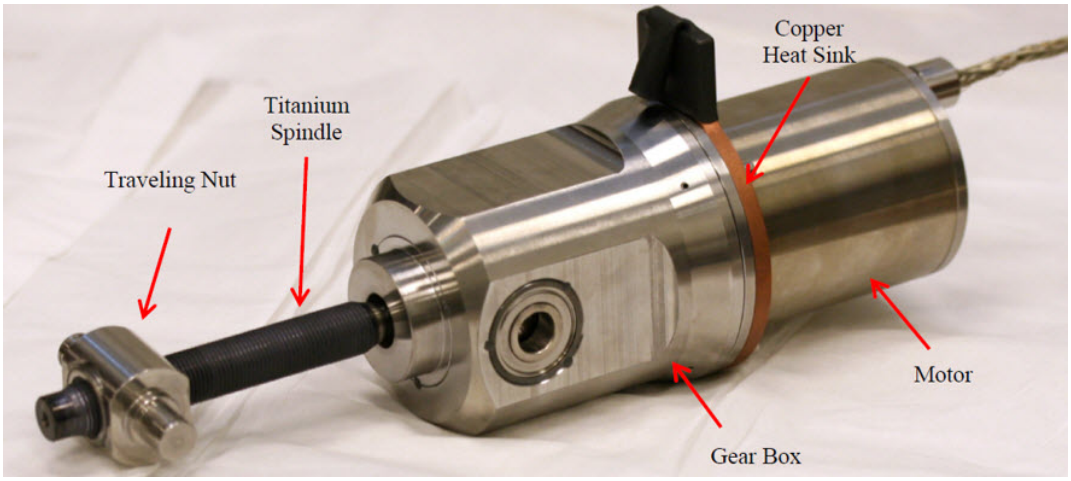

Figure 7.58: Phytron electromechanical actuator (LVA 52-LCLSII-UHVC-X1).

The actuator is specified for extended life operation inside the insulating vacuum at cryogenic temperatures (1000 spindle rotations over a 20 plus year lifetime). The actuator was designed for a 1300 N maximum force between the motor body and the traveling nut. The actuator was successfully tested up to 10,000 spindle rotations (or 10× the lifetime of the PIP-II Linac) without any performance degradation [105] [106]. The Phytron actuator was also subjected to radiation using a gamma source of up to 5×10^8 rad. No degradation of the actuator's performance has

been observed.

The piezo actuator P-844K075 used in the 650 MHz tuner is an encapsulated piezo-capsule designed and built by Physik Instrumente (PI) [107] per FNAL specifications, see Figure 7.59. The encapsulation is made from 316L stainless steel. Inside are two 10×18 mm PICMA piezo-stacks butted together. During normal operation the tuner uses all four piezo-stacks (two on the top and two on the bottom of the piezo capsule). Lowering the piezo's operational voltage significantly increases the actuator lifetime. In the case where three (from a total of four) piezo-stacks fail, the piezo-tuner is still be able to deliver the specified cavity elongation which significantly increases the reliability of the fast (fine) tuner. The piezo is preloaded to 800 N inside it's encapsulation at cryogenic temperature. The technique (patented by PI) for piezo-stack encapsulation minimizes the shearing forces and, as a result, increase the lifetime of the piezo tuner. More than six hundred piezo-actuators have been built and installed into LCLS-II cryomodules. In the framework of the LCLS-II project, a comprehensive program has been conducted to test the piezo-actuator's lifetime. Piezo-actuators irradiated by gamma sources of up to 5×10^8 rad have shown no damage to the actuator [101].

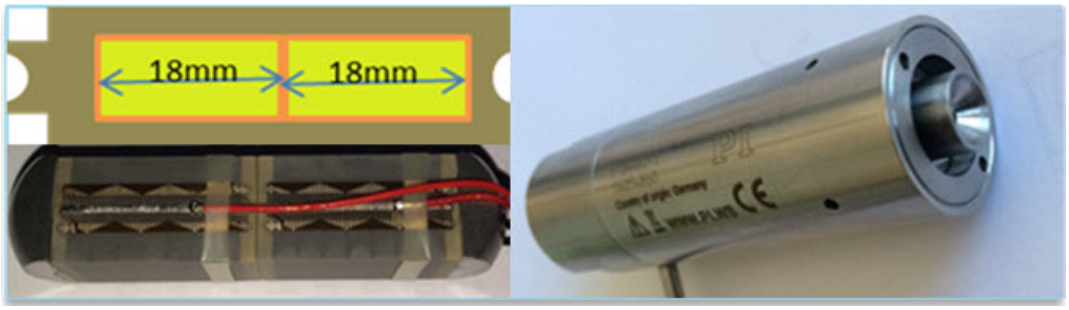

Figure 7.59: PI piezo actuator P-844K075.

FNAL has also conducted an accelerated piezo longevity test of the piezo-actuators operating inside an insulated vacuum environment at cryogenic temperatures. The P-844K075 piezo-actuators accumulated 2×10^{10} pulses without any degradation of the performance and without any overheating "run-away" events [105].

7.3.3 Fundamental power coupler

The 650 MHz couplers are a common design for both low beta and high beta 650 MHz cavities. The 650 MHz fundamental power coupler is designed to deliver RF power of up to 45 kW CW to the Low Beta (LB) and the High Beta (HB) elliptical superconducting cavities. The base configuration of the 650 MHz coupler uses a single coaxial room temperature RF window. Because of the higher power and frequency and, as result, the higher losses for the 650 MHz coupler, the approach of using a pure (uncoated) stainless steel outer conductor is not feasible. Typically, a thin copper coating on the stainless steel conductor is used to reduce the losses and to keep the thermal conductivity acceptably low. The requirements for copper coating used in SRF technology are rather difficult to achieve. Taking into account that the copper coating procedure is complicated and still not well established for SRF applications, a new approach was used for the 650 MHz

coupler design. Instead of using a copper coating, the electromagnetic shields are made of solid copper instead. The configuration of the vacuum part of a coupler is presented in Figure 7.60.

Table 7.22: Parameters of 650 MHz main couplers

Operating frequency	650 MHz
Power rating, P_{max}	120 kW
Output diameter	3 in.
Antenna diameter	0.5 in., copper
Antenna cooling	Air
Window	Single, Al_2O_3, 4 in. x 6 mm
Input	Rectangular waveguide
Multipactor suppression	HV bias
Cryo-load, 2K, 0 kW/100 kW	0.15 W / 0.60 W
Cryo-load, 5K, 0 kW/100 kW	0.6 W / 1.0 W
Cryo-load, 70K, 0 kW/100 kW	3.3 W / 6.5 W

Three copper shields isolate the stainless-steel walls from the electromagnetic field and thus reduce the RF losses. There are gaps between the shields which eliminate the heat flow from shield to shield. The gap sizes are small enough to avoid multipactor at any RF power. This approach has several advantages:

- Solid copper is more reliable since no chips or flakes are generated during the application process as is sometimes the case in copper coated couplers. A single flake can completely damage a superconducting cavity. This is the main reason for the use of electromagnetic shields instead of using a copper coating.

- All static heat flow from room temperature to cryogenic temperature goes through pure non-coated stainless steel. The thermal conductivity of stainless steel is much less than copper coated stainless steel. As a result, the static cryogenic loading of the new coupler is less than the conventional design.

Practically all of the RF current propagates through the electromagnetic shields. Solid copper has a higher RRR than coated copper which helps reduce the total RF losses. Because of the shield configuration, the majority of the RF losses are taken at the 50 K intercept, reducing the portion going to 5 K and 2 K. As a result, the total cryogenic properties of the new coupler is approximately 2.5 times better than the conventional coupler. The new design includes screens, an iris and a disk, which protect the ceramics against charged particles coming from the cavity. The iris also reduces the thermal radiation from the room temperature parts of the coupler. As a backup to the new coupler, the copper coated coupler was designed as well. The difference between the couplers is only at the vacuum outer conductors with other parts being interchangeable. Cut views of the couplers are presented in Figures 7.61 and 7.62. Figure 7.63 shows a photo of the vacuum housings of the new and backup couplers. The non-vacuum sections of the couplers include a bellows section to compensate for thermal contraction during cool down and warm up. The couplers have waveguide inputs which allows for application of high voltage bias to suppress multipactor. The antennas are

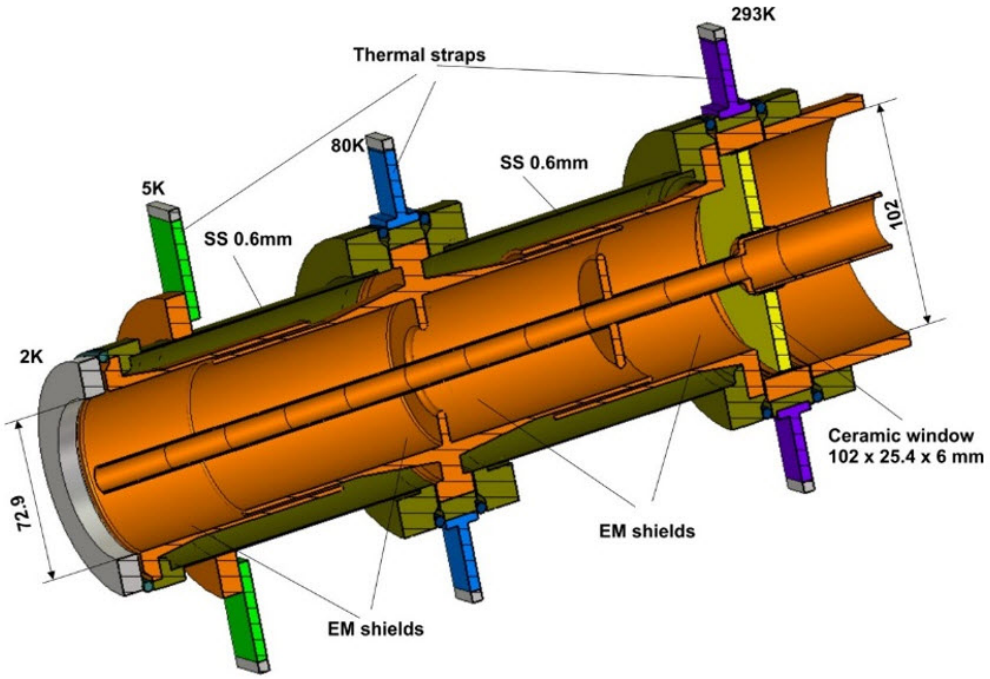

Figure 7.60: Vacuum portion of the 650 MHz coupler.

also air cooled. Before installation on the cavities, each coupler is qualified on a room temperature test stand at power levels exceeding the operating level.

7.3.4 Cryomodule

7.3.4.1 String assembly

7.3.4.1.1 LB650 string assembly

The cavity string design for each LB650 cryomodule is based on the similar designs for SSR1 and SSR2 as well as LCLS-II. The cavity string is supported on a room temperature strongback located inside the vacuum vessel. Each cavity is supported by two composite support posts. The attachment to the supports allows axial motion during cooldown to prevent excessive loading on the supports with one end fixed. The fixed end is located closer to the input coupler, thus minimizing coupler motion during cooldown. Figure 7.64 shows the LB650 string assembly dimensions.

7.3.4.1.2 HB650 string assembly

Overall the HB650 string assembly is similar to SSR1 and SRR2 as well as the LCLS-II string assembly. Couplers are attached to vertical qualified cavities with leak checks being skipped to re-

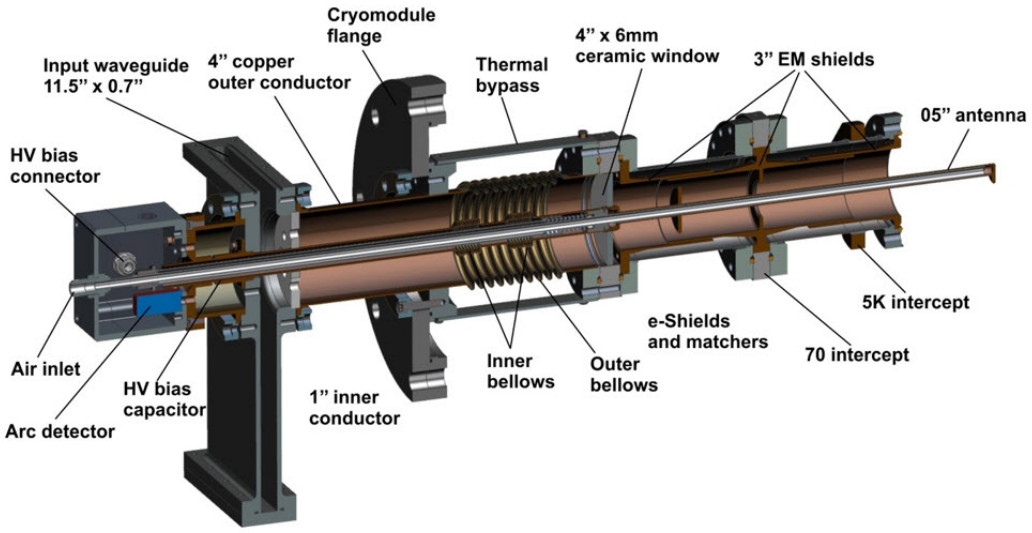

Figure 7.61: Cut view of the 650 MHz coupler with electromagnetic shields (no copper coating).

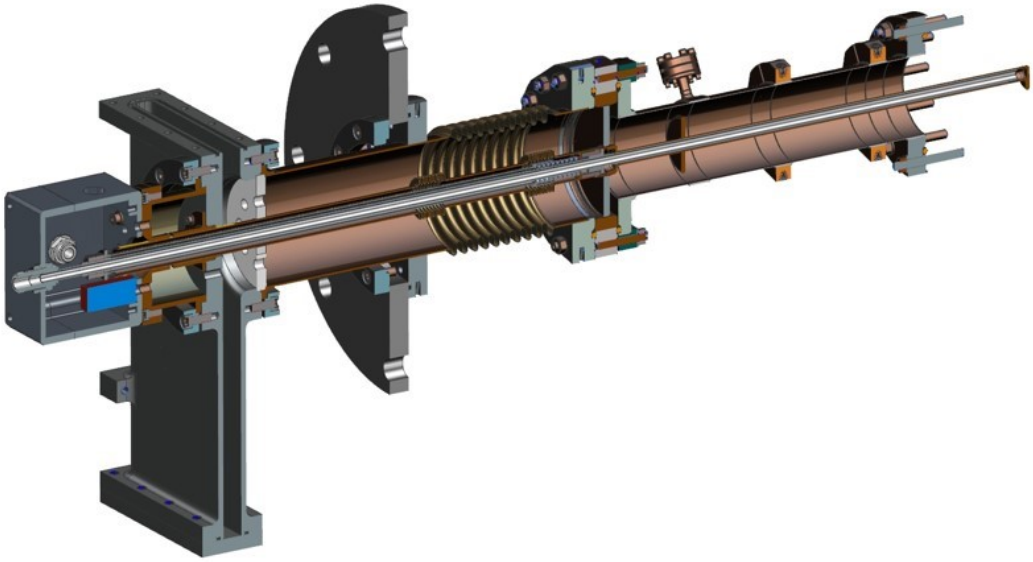

Figure 7.62: Cut view of the 650 MHz coupler with copper coating.

Figure 7.63: Vacuum parts of couplers with electromagnetic shields. No copper coating on left and with copper coating on right.

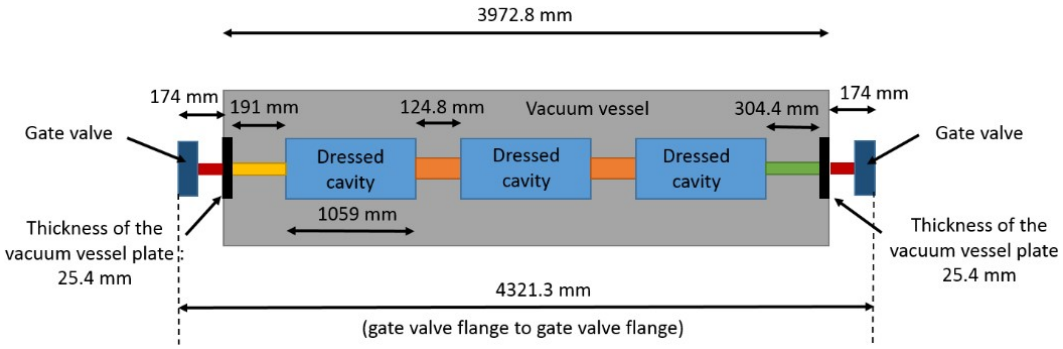

Figure 7.64: Low-beta 650 MHz cryomodule configuration.

duce particulate movement. Cavities are joined with the inter-cavity bellows placed on supporting Lolli-pops. Figure 7.65 shows the HB650 string assembly dimensions.

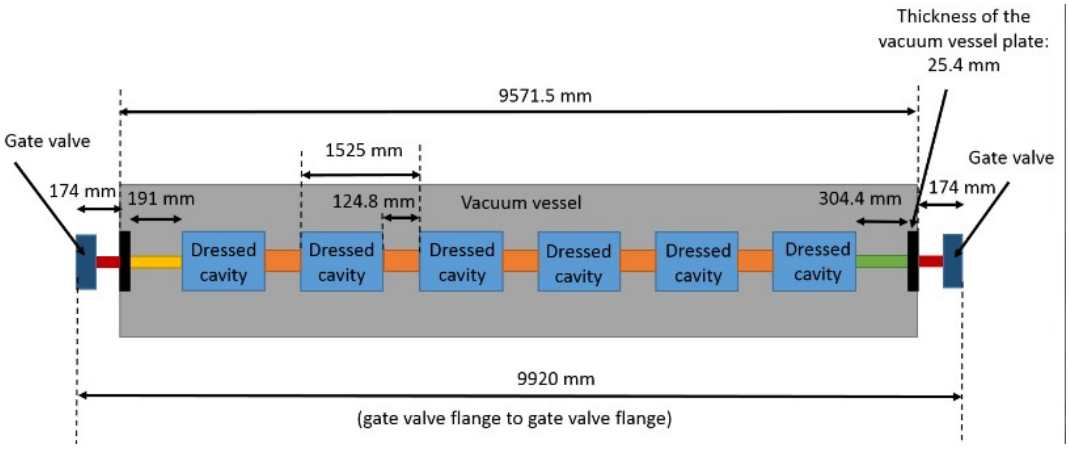

Figure 7.65: High-beta 650 MHz cryomodule configuration.

Figures 7.66 and 7.67 illustrate the cavity string assembly for the high-beta cryomodule with the warm strongback, support posts, 2-phase pipe, and cryogenic piping. Figure 7.70 shows the complete cryomodule assembly.

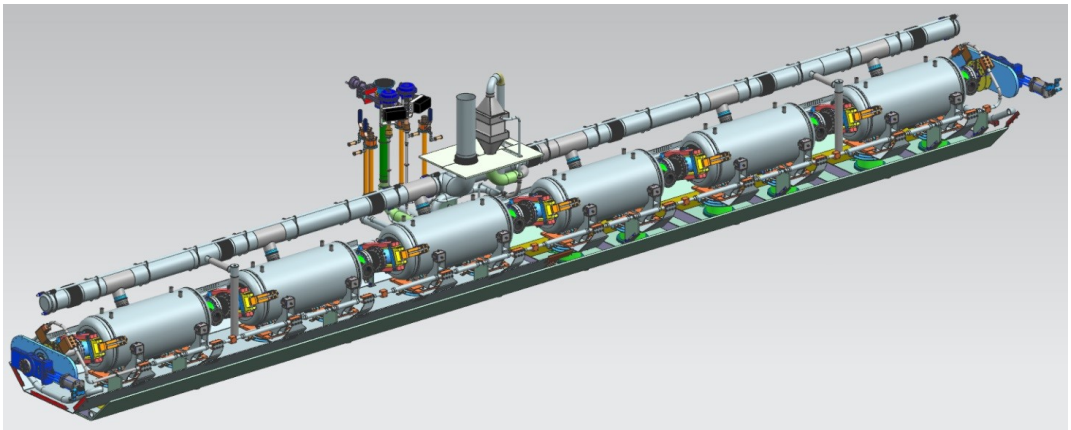

Figure 7.66: High-beta 650 MHz cavity string assembly.

7.3.4.2 Coldmass assembly

Once the string assembly is qualified and rolled out of the cleanroom, it is lifted onto the lifting tooling. While on the lifting tooling, the cool down line is welded to the cavities followed by attachment of the cavity heaters and instrumentation. Helium vessel multilayer insulation is then wrapped prior to the magnetic shield assembly. Tuners are then attached to each cavity once the magnetic shields are in place. The design pressure of the cool down line is 20 barg and the two phase pipe connection is 2.05 barg at room temperature and 4.1 barg at 2 K.

The 650 MHz cryomodule design is similar to the SSR1 cryomodule design. A strong back support sits at room temperature to allow alignment locking with high impedance G-10 posts supporting

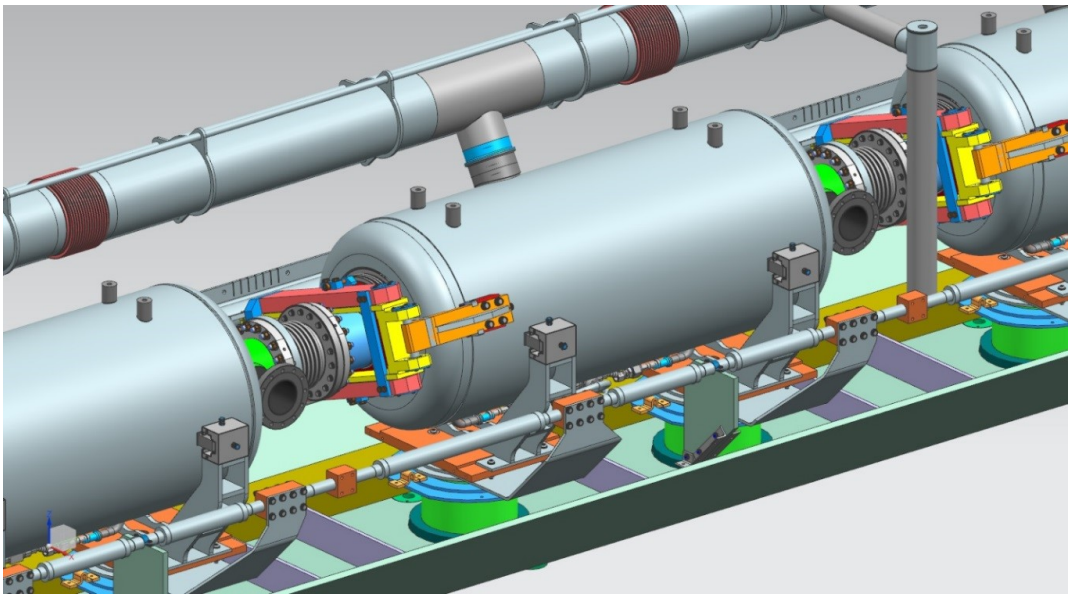

Figure 7.67: High-beta 650 MHz cavity string detail.

the cold mass on the strong back. Since the 650 MHz cavities are longer in length compared to the SSR cavities, there are two support posts for each cavity. The cavity support structure between the helium vessel and the support posts are similar to the XFEL/LCLS-II design except that the orientation is reversed with the cavities supported from the bottom instead of the top.

As shown in Figure 7.68, four lugs are welded on each cavity similar to the LCLS-II cavities. Compared to LCLS-II, there is no invar rod inside the coldmass, the alignment is exclusively performed using C-clamps, see Figure 7.69. Using several sets of screws and springs, the location of each cavity can be controlled throughout the alignment process. An anchoring plate between the support post and the lugs is still in the design phase. If the alignment precision using the C-clamps are not sufficient, additional adjustment can be introduced.

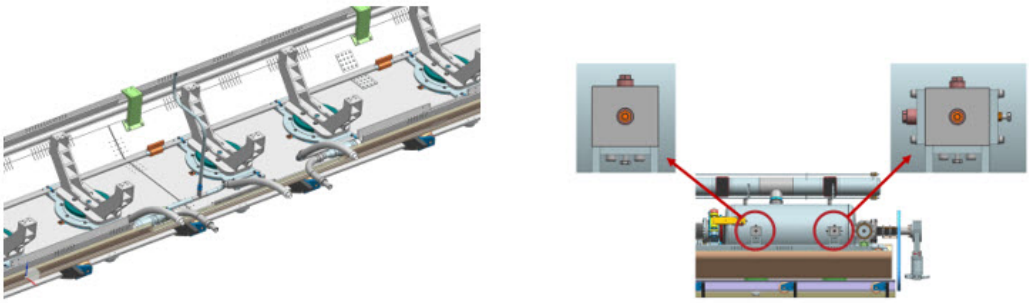

Figure 7.68: Support lugs for 650 MHz cavities.

7.3.4.3 Cryomodule integration

Figure 7.70 shows the complete high beta 650 MHz cryomodule assembly. Table 7.23 and Table 7.24 summarize the estimated static and dynamic heat loads at each temperature level for the LB650

Figure 7.69: Cavity c-clamp support similar to LCLS-II cryomodules.

and HB650 cryomodule assembly from all sources, respectively.

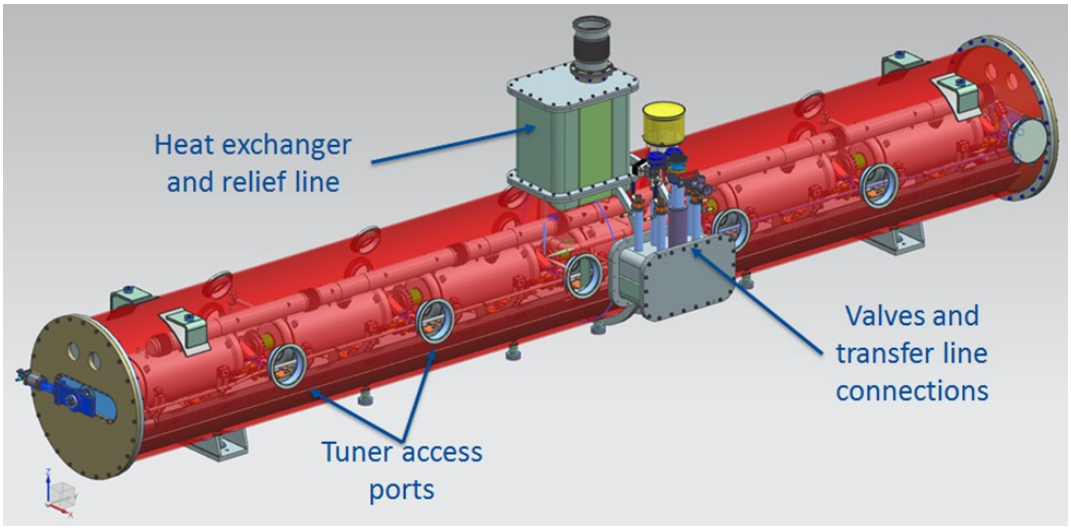

Figure 7.70: High-beta 650 MHz cryomodule assembly.

Table 7.23: LB650 cryomodule heat load estimates.

	Per Unit (W)			# of Units	Total (W)		
	35-50 K	5 K	2 K	-	35-50 K	5 K	2 K
RF coupler, static	3.30	0.60	0.15	3	9.9	1.8	0.5
RF coupler, dynamic	4.34	0.65	*	3	13.0	2.0	*
Cavity, dynamic	-	-	15.9	3	-	-	47.7
Support post	1.90	0.90	0.07	6	11.4	5.4	0.4
Beam line	0.14	0.74	0.02	2	0.3	1.5	0.0
Thermal shield	62.50	-	1.10	1	62.5	-	1.1
View ports	0.20	-	0.70	4	0.8	-	2.8
Relief line	1.10	-	0.50	1	1.1	-	0.5
Valves and Instrumentation	7.90	1.81	0.50	-	7.9	1.8	0.5
Total static	-	-	-	-	**93.9**	**10.5**	**5.8**
Total dynamic	-	-	-	-	**13.0**	**1.8**	**47.7**
Total static + dynamic	-	-	-	-	**106.9**	**12.3**	**53.5**
* Input coupler dynamic heat load is embedded in the cavity dynamic heat load value							

Table 7.24: HB650 cryomodule heat load estimates.

	Per Unit (W)			# of Units	Total (W)		
	35-50 K	5 K	2 K	-	35-50 K	5 K	2 K
RF coupler, static	3.00	1.10	0.1	6	18.0	6.6	0.6
RF coupler, dynamic	0.70	0.40	*	6	4.2	2.4	*
Cavity, dynamic	-	-	20.8	6	-	-	124.8
Support post	1.90	0.90	0.07	12	22.5	10.6	0.8
Beam line	0.14	0.74	0.02	2	0.3	1.5	0.0
Thermal shield	124.50	-	2.20	1	124.5	-	2.2
View ports	0.20	-	0.70	4	0.9	-	2.8
Relief line	1.10	-	0.50	1	1.1	-	0.5
Valves and Instrumentation	8.60	2.00	0.60	-	8.6	2.0	0.6
Total static	-	-	-	-	**175.9**	**20.7**	**7.5**
Total dynamci	-	-	-	-	**4.2**	**2.4**	**124.8**
Total static + dynamic	-	-	-	-	**180.1**	**23.1**	**132.3**
* Input coupler dynamic heat load is embedded in the cavity dynamic heat load value							

Chapter 8

Radio Frequency Systems

8.1 Overview

The Radio Frequency (RF) system in the PIP-II Linac consists of the Master Oscillator and Precision Phase Reference System, Low Level RF (LLRF) control system, the RF Protection Interlocks (RFPI), the RF Power Amplifiers (RFPA), the RF distribution between the RFPA and the cavity input coupler, and the cavity resonant frequency tuner control.

There are 121 cavities requiring RF power and control in the Linac, and each one has one dedicated power amplifier and LLRF control system with the exception of the RFQ which has two RFPAs and a special controller to drive it. Table 8.1 shows the power requirements and base frequency operation for the Linac power systems. The power levels in the table were calculated based on the greatest power demand from the specific cavity type assuming up to 2 mA of peak beam acceleration with at least 30% overhead for distribution losses and RF dynamics envelopes. All RF systems are capable of operating CW during beam operations.

Table 8.1: Parameters of RF amplifiers

	Frequency (MHz)	Number of RF cavities	Number of RF amplifiers per cavity	RF amplifier power (kW)
RFQ	162.5	1	2	75
MEBT bunching cavities	162.5	4	1	3
First HWR cavity	162.5	1	1	3
Other HWR cavities	162.5	7	1	7
SSR1	325	16	1	7
SSR2	325	35	1	20
LB650	650	33	1	40
HB650	650	24	1	70

Due to the rapid advancements in high efficiency Laterally Diffused MOS (LDMOS) technology in UHF band, the cost per watt of solid-state amplifiers at sub-GHz frequencies has dropped significantly. The solid state RF power amplifiers (SSRFPA) have many advantage such as simple start up procedure (no warm up time for the filament), long life time, low voltage power supplies, and low power, internal circulators. This makes them cost competitive with vacuum devices and allows for considerable flexibility as to CW or pulsed operation. They also can be more cost effective to maintain, due to their modular design. The SSRFPA can deliver the partial output power to the RF accelerator even though a few of its power modules are down, and a single, faulty, intermediate power RF amplifier module can be replaced instead of an entire klystron or tube. All the RF amplifiers for PIP-II are assumed to be solid-state.

The RF accelerating cavities in the PIP-II Linac have certain common attributes in their RF drive systems. Each cavity has a dedicated RF control and instrument system capable of regulating the cavity field amplitude and beam synchronous phase. Each cavity has a dedicated resonance frequency control system. Each cavity has a dedicated solid-state power amplifier (the RFQ has two). Each power amplifier has a dedicated output circulator to protect the RF source from reflected power from the cavity.

8.2 Warm front-end RF systems

The warm front end RF systems are an exception to the RF systems for the rest of the SRF Linac, primarily because the quality factor of the cavities is an order of magnitude lower. Since the cavity couplers are tuned close to critical coupling and there is no risk of quench, the RF protection interlock design is simplified. In this case the fast interlocks rely on the reflected power signals, which are more sensitive to cavity and coupler breakdown than they are in SRF systems.

The RFQ has two RF input ports and is driven by two, 75 kW, CW, solid state amplifiers. The output of each amplifier drives a 6-1/8 in. coaxial hardline RF distribution, capable of withstanding the full CW RF power. This distribution includes a 75 kW, CW, 162.5 MHz circulator, directional coupler, and a 6-1/8 in. to 3-1/8 in. adapter for each RFQ input coupler. The LLRF system maintains the amplitude and phase balance between the two RFQ inputs for the best match into the load.

The RFQ resonance frequency control system varies the cooling water temperature of the RFQ. The RFQ has independent, water temperature control for the vane cooling channels and the wall cooling channels. The resonant frequency is most sensitive to the difference in temperature between the vane and the wall cooling channels. The resonance control system monitors the water temperatures and RF power to optimize the system recovery from RF trips. Recovery times vary from less than a minute, from a series of fast trips, to just under 30 minutes from a cold start.

The buncher cavities are driven by 3 kW, CW, 162.5 MHz, solid state amplifiers. The output of these amplifiers drives a 1-5/8 in. flexible, coaxial RF distribution that connects to the cavity input coupler. This distribution includes a 7 kW, CW, 162.5 MHz circulator and directional coupler just upstream of the input coupler. Resonance control is performed with a stepper motor connected to

a mechanical plunger that varies the cavity volume. There is no feedback system associated with the buncher cavity resonant control, because there is significant overhead in available RF power if the cavity goes slightly out of tune.

8.3 SRF systems

The SRF RF systems comprise the majority of the RF systems for the Linac. Since the cavities are driven highly overcoupled due to the high beam loading factor, the load seen by the RF at the cavity couplers is almost fully reflective without beam current. This puts extra stress on the RF distribution and circulators, and it complicates the RF protection system. Figure 8.1 shows the layout of the SRF RF systems including the Linac master oscillator and phase reference system. This diagram illustrates the compartments of the SRF RF systems design according to the cavity resonant frequencies of 162.5 MHz, 325 MHz, and 650 MHz.

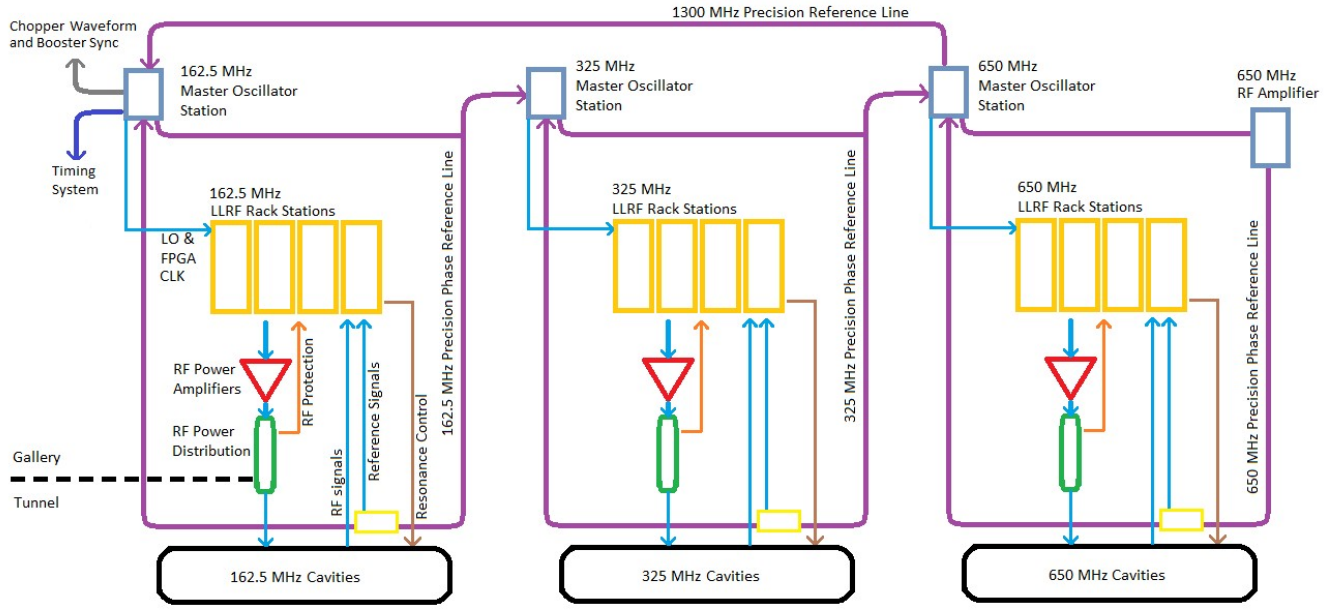

Figure 8.1: Block diagram of the PIP-II SRF RF system.

8.3.1 SRF low level RF

The Low Level RF system encompasses the programming and regulation of the cavity field amplitude and phase as required by the longitudinal beam dynamics in the machine. It also controls or interfaces to ancillary equipment that is involved in the generation of RF. Hardware and software modules include a Cavity Field Controller, a Resonance Frequency Controller, a Master Oscillator, a Phase Reference Line, a LO distribution, a Transfer Synchronization to Booster, a Beam Chopper Waveform Generator, and the interface to interlocks, timing systems, Machine Protection and

the control system. Figure 8.2 shows the typical interfaces of a LLRF control rack system to the external accelerator systems. Items in red are part of the LLRF scope.

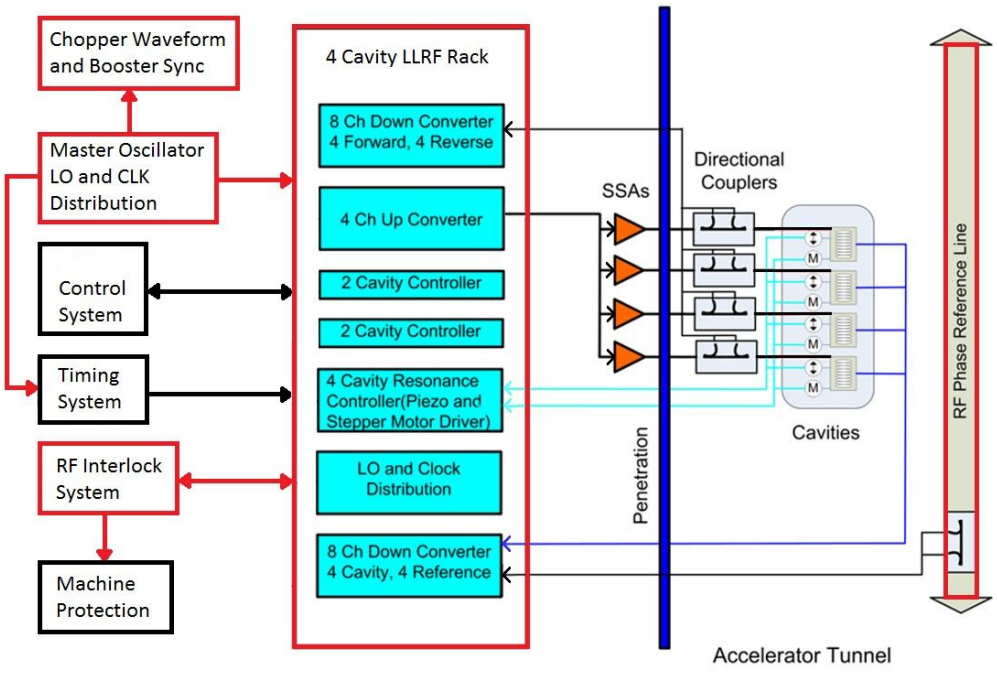

Figure 8.2: LLRF interface to accelerator systems (Four cavity LLRF control rack system shown).

8.3.1.1 Low level RF regulation strategy

The requirements for the Linac beam energy stabilization are determined by the Booster RF bucket height and requirements related to the static longitudinal painting in the course of multi-turn beam injection. The latter requires a Linac beam energy stability of 0.01% rms. The LLRF feedback controller should be capable of regulating this level over a time period of less than one second. For time periods greater than one second an adaptive feed-forward algorithm corrects for drift in the cavity phase and amplitude calibrations. This is accomplished by utilizing beam-based diagnostics along the Linac and in the Booster as well as RF diagnostics to provide feed-forward corrections and slow adjustments to LLRF calibrations.

The beam current, cavity field gradients, and worst-case microphonics determine the loaded cavity Qs, bandwidths and RF power requirements. Precision corrections of the microphonic disturbances through Resonance Frequency Control are required for gradient regulation without exceeding the available RF power overhead. The total RF power specifications are based on cavity specifications with 2 mA of CW beam current and 20 Hz peak amplitude microphonics. Power loss through the HWR and SSR RF distribution is assumed to be 10% and power loss through the 650 MHz distribution is assumed to be 6%. The final power specification includes a 25% overhead on top of the distribution loss that will allow for RF control margin.

8.3.1.2 Master oscillator and precision phase reference system

The Master Oscillator and Precision Phase Reference System starts at the Linac front-end with the LLRF 162.5 MHz Master Oscillator Station. A simplified diagram of the system is shown in Figure 8.3. Contained in the LLRF 162.5 MHz Master Oscillator Station is a low noise 162.5 MHz RF source (inside a temperature controller chassis) that provides a source for RF reference signals, local oscillator signals for up and down converters, and clock signals for FPGA controllers. The 162.5 MHz RF source is also driven into a closed loop phase averaging reference line that runs alongside the accelerating structure in the tunnel. In the tunnel, the reference line is tapped to provide precision phase reference signals to cables that run alongside the cavity probe cables, providing first order cable temperature compensation. The LLRF 162.5 MHz Master Oscillator Station provides signals for the main timing system, instrumentation, beam chopper controller, and Booster injection synchronization.

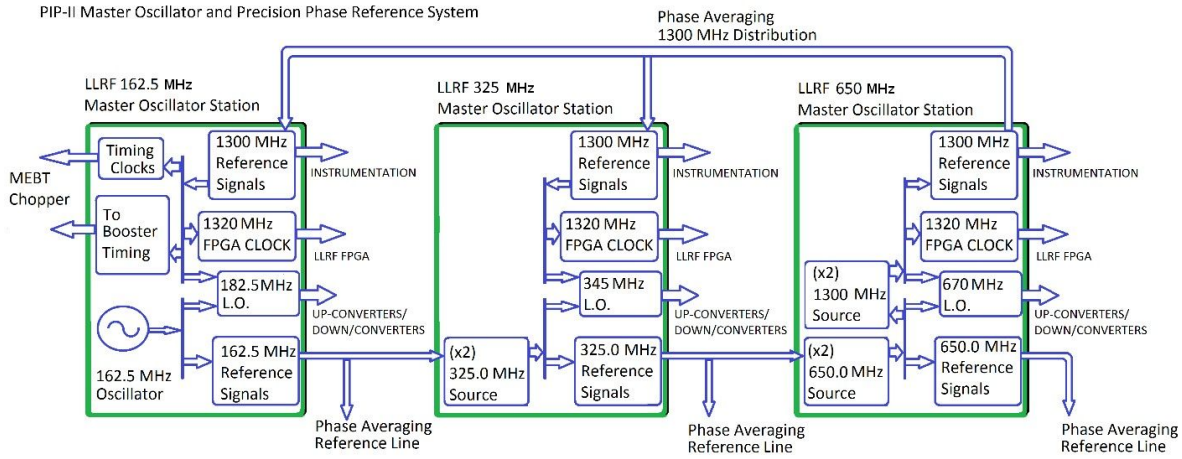

Figure 8.3: Master oscillator and precision phase reference system.

The 162.5 MHz phase reference line provides a signal to the LLRF 325 MHz Master Oscillator Station located at the beginning of the 325 MHz section of the Linac. The 325 MHz oscillator station tightly tracks the 162.5 MHz phase reference and generates local oscillator signals and FPGA clock signals in the same fashion as is done in the LLRF 162.5 MHz Master Oscillator Station. A 325 MHz phase averaging reference line is setup in the same fashion as the 162.5 MHz reference scheme. This chain of frequency multiplication is repeated for the 650 MHz sector. A 1300 MHz reference signal is generated in the LLRF 650 MHz Master Oscillator Station and travels back down the Linac to provide phase stable signals for LO signal generation, FPGA clock generation, and reference signals for other accelerator systems such as instrumentation. The three master oscillator stations shown in Figure 8.3 are located in a low vibration area at the beginning of each frequency section in the gallery.

8.3.1.3 Four cavity LLRF control rack

The LLRF system is organized in a group of up to four cavities serviced by one rack of electronics. The group of four cavities allows for an economy of scale in the hardware design while keeping cable runs as short as possible. Figure 8.4 details the rear panel connections and wiring layout. The rack hardware includes the LO, FPGA clock, and phase reference distribution chassis' which are used to distribute RF signals throughout a LLRF Rack Station. A diagram of the four cavity control system architecture is shown in Figure 8.5. A LLRF Rack Station consists of multiple four-cavity control racks and typically controls 12 to 16 cavities. A description of each module is described in the following sections.

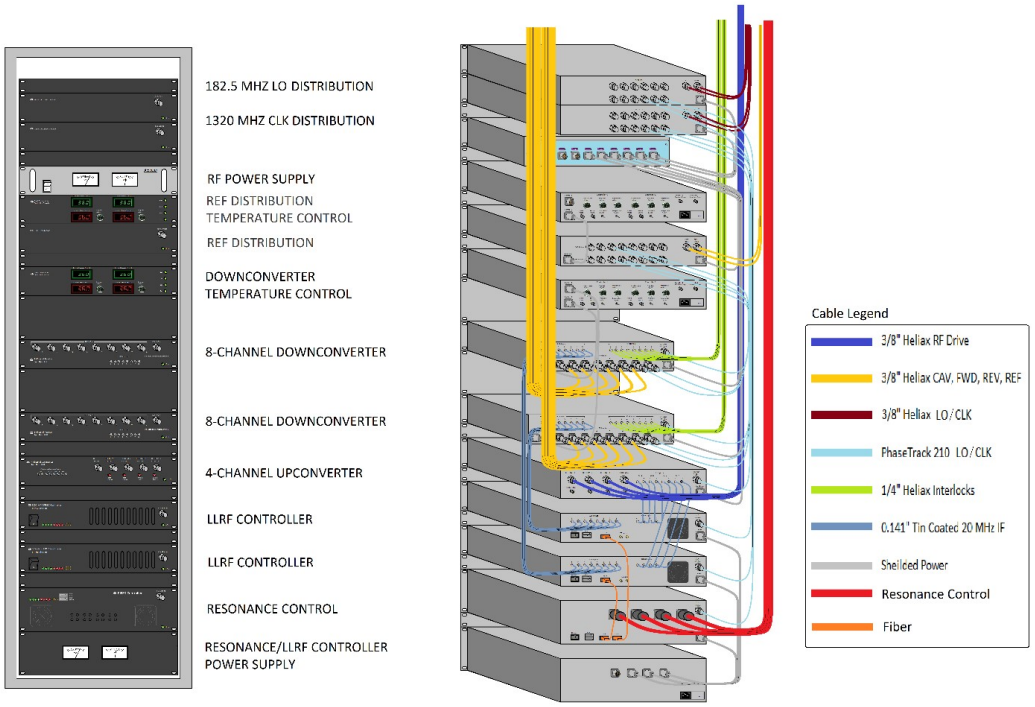

Figure 8.4: LLRF four cavity control rack configuration.

The 8-Channel Down-Converter is used to translate the RF signals at the various frequencies across the accelerator to a common intermediate frequency (IF) of 20 MHz. In order to achieve the regulation requirements, the proposed down-converter has low-noise (-162 dBc), low jitter (1.8 fs, 1-100 Hz), high channel isolation (greater than 90dB), phase stability to within 0.005 degrees below 1 Hz, and amplitude stability of 0.005% below 1 Hz. The down converter includes temperature regulation to maintain the tight phase and amplitude regulation requirements.

The 20 MHz IF out of the down-converter is digitized by a high-speed Analog to Digital Converter (ADC) in the FPGA LLRF Controller Chassis. The ADC's must have a sample rate greater than 94 MS/s, and goals of achieving -155 dBc noise power density and less than 200 ns of signal latency. There are several ADCs on the market that achieve these specifications; the present choice is the AD9653 from Analog Devices. The digitizer board has 8 channels of ADC's that are sent to the Field Programmable Gate Arrays (FPGA).

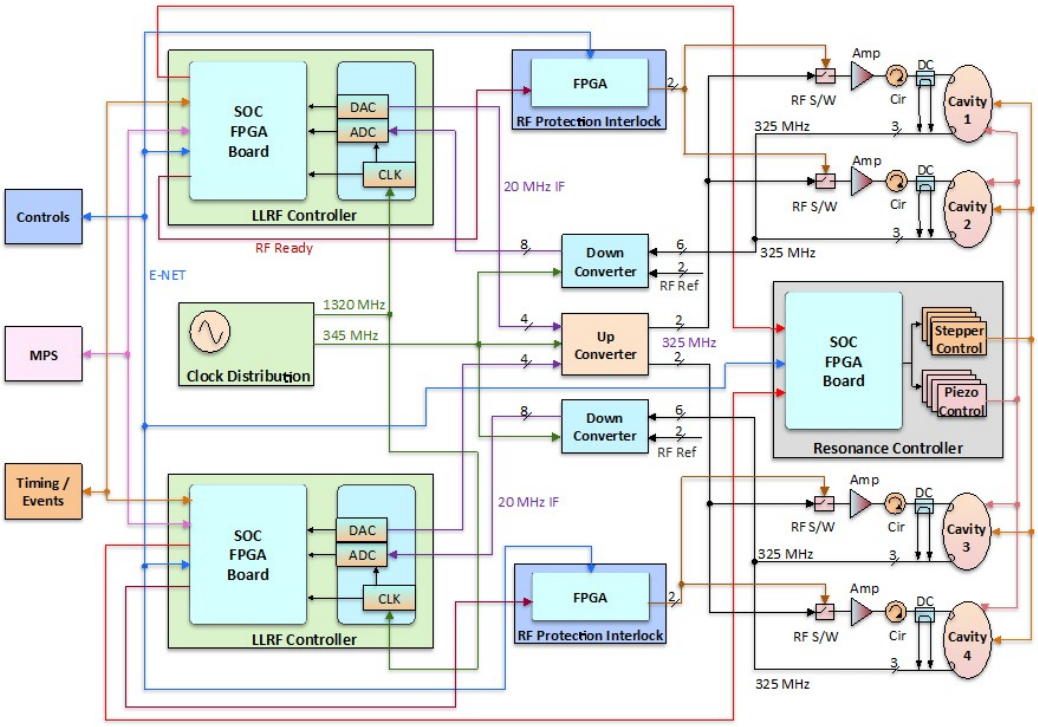

Figure 8.5: LLRF for a four cavity control system architecture. Note that this system is showing an RF frequency of 325 MHz, with a corresponding LO of 345 MHz. The 162.5 MHz and the 650 MHz systems have an LO of 182.5 MHz and 670 MHz, respectively.

The FPGA processes the digitized signals for both read-back and for closed loop feed-back to the input to the controller. The controller has a closed loop bandwidth of 30 kHz and is designed to support both CW and pulsed operation. Each controller has the ability to run in a self-excited loop where the drive frequency tracks the cavity, and in a generator driven mode where the output is at a fixed frequency. CW operation typically requires startup in a self-excited loop with a transition to a generator driven loop to align with the beam phase. A diagram of the FPGA controller is shown in Figure 8.6. The FPGA is capable of controlling two cavities independently.

The outputs of the FPGA controller are converted to I and Q components at 20 MHz IF and sent to two DAC's. The DAC outputs are sent to a 4-Channel upconverter module, which converts the 20 MHz I and Q signals to the desired RF frequency to drive the RF amplifiers (162.5, 325, or 650 MHz). The proposed prototype upconverter maintains <0.5% non-linearity up to full output (12 dBm), has low noise (-142 dBm), low crosstalk between channels (>88 dB), and a RF switch at the output with better than 60 dB isolation. The RF switch is controlled by RF interlocks.

8.3.2 Resonance control

The high value of cavity loaded quality factor and narrow bandwidth lead to a high sensitivity to microphonics. It is important to minimize cavity detuning, so that the LLRF system can regulate the cavity field without running out of available RF power. Microphonics reduction can

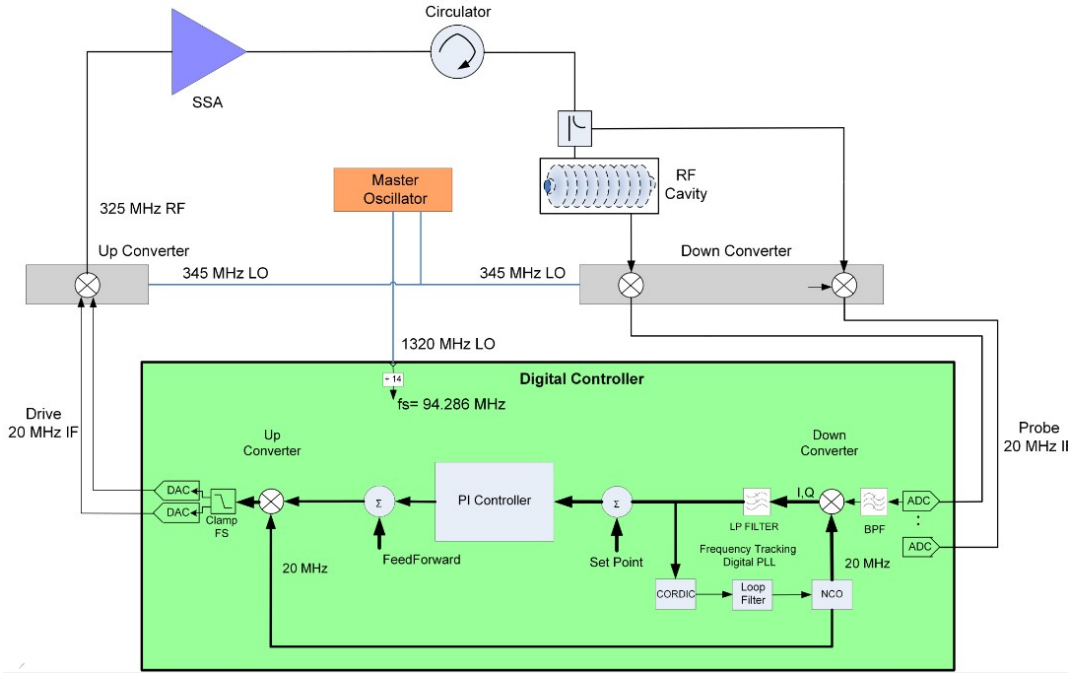

Figure 8.6: Conceptual diagram of the LLRF control system at 325 MHz.

be performed with both passive (design to reduce vibration coupling to cryomodules), and active processes. This section describes the active processes that will be utilized in PIP-II.

As shown in Figure 8.5, the LLRF system produces a drive signal for the SRF cavity tuners. The resonance control active compensation system utilizes the piezo actuator for tuner control, due to its faster response time over the motor control. The resonance control SOC FPGA calculates the cavity bandwidth and detuning offset. The detuning offset is digitally filtered with parallel, bandpass filters that allow the system to focus on specific resonances within the microphonics bandwidth. Testing of the SSR1 dressed cavity revealed dominant resonances at 20 Hz and 200 Hz. A DC filter was used to stabilize the cavity against pressure drifts.

While the baseline design is for CW operation of all RF systems, there is an opportunity to significantly reduce energy cost through supporting lower duty factor RF mode operation when there is no need for CW beam. Modulation of the RF gradient allows for a lower average cryogenic load as well as a lower RF power requirement but comes at the cost of the need for Lorentz force detuning (LFD) compensation. A graded approach starting with CW RF, followed by gradient modulation producing sinusoidal Lorentz force, and then extending towards short pulsed RF provides a success driven path in LFD compensation. Current engineering efforts include a robust, state-of-art, adaptive feed-forward system that utilizes highly accurate calibrations of the cavity response and RF distribution and show strong progress towards the required compensation goals.

8.3.3 RF interlocks

The primary objective of the Radio Frequency Protection Interlock (RFPI) system is to protect devices connected to RF energy sources (Solid State Amplifier) from damage due to RF power when the device is not in a state to handle it. The RFPI system monitors signals associated with the SSA-coupler-cavity system and controls the drive of low level RF to the power amplifier with a fast RF switch. For secondary protection, it can also disable the bias to the solid state amplifier.

The second objective is to provide a status to the accelerator machine protection system (MPS) to disable beam when the RF component cannot accept RF power. The third objective is to provide diagnostic information (waveforms and status bits) to the controls system in real-time during high power operation of each SSA-Coupler-Cavity being monitored.

Quench detection is carried out in the LLRF system. The forward power, reflected power and transmitted power are used to detect a cavity quench. The algorithm using these signals is implemented in an FPGA based on previous work developed at DESY and LBNL. The LLRF provides the RFPI a signal when the quench is detected, so that it can disable the fast RF switch and inform the MPS.

The system architecture of RFPI is VME64X based, where a MVME8100 processor acts as a crate controller and carrier VME64X boards together with mezzanine boards are used to process analog and digital signals. The carrier boards are arranged from left to right, where the left-most carrier board acts a system controller as shown in Figure 8.7. All other boards send their status to the system controller who OR's these signals and generates the required trips. These trips are independent of any VME bus activity.

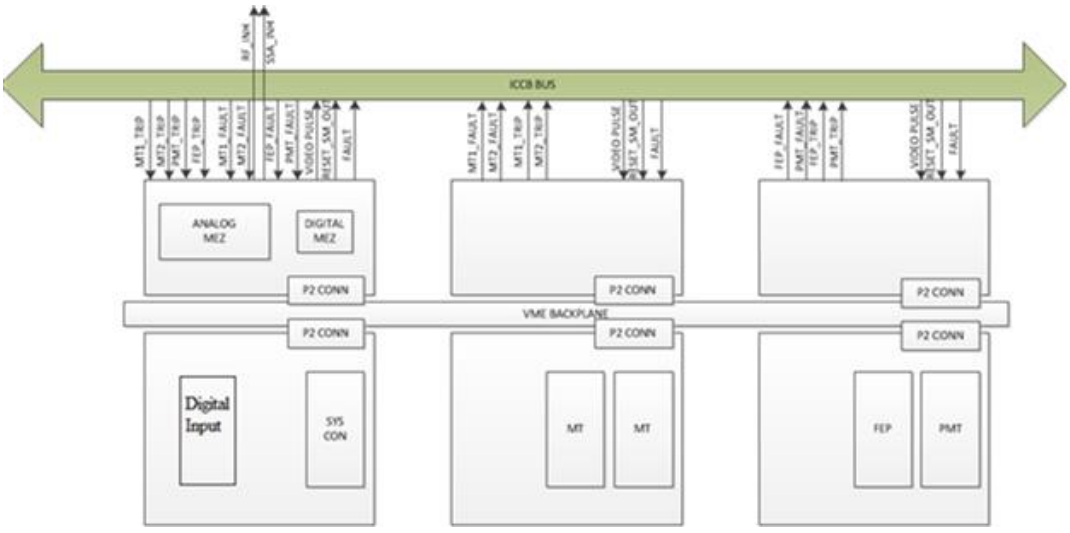

Figure 8.7: RFPI system architecture.

8.3.4 SRF power and distribution

The RF distribution for SRF cavities has many common features over the different frequencies and power levels. Each amplifier is protected by a circulator that is specified to withstand the full, CW available power from the amplifiers in the forward and reflected directions. The circulators are also specified to withstand short pulses of high reflected power that can arise from a sudden loss of drive power to a heavily overcoupled SRF cavity. The RF transmission medium is also specified to handle the full, CW available power from the amplifiers. The RF distribution includes a directional coupler that is compatible with the transmission medium residing just upstream of the cavity input coupler.

8.3.4.1 HWR RF power and distribution

The Half-Wave Resonator (HWR) cryomodule first cavity requires only a 3 kW, CW RF power amplifier at 162.5 MHz. This is satisfied by one of the warm front end buncher cavity amplifiers. The rest of the cavities are driven by 7 kW, CW power amplifiers. The frequency and power level of these amplifiers are within the range of the international, commercial power amplifier industry's capabilities and are procured according to specification.

The HWR distribution transmission is based on 1-5/8 in. coaxial, foam or air dielectric cable. This cable can handle the full power of the amplifiers while allowing ease of installation through penetrations. The circulators are also within the range of the domestic, commercial RF power industry's capabilities and are specified with enough headroom to handle operation at CW with full reflected power and withstand the high reflected power pulse caused by sudden interruption of RF drive power.

8.3.4.2 SSR1 RF power and distribution

The SSR1 cryomodule cavities require 7 kW, CW RF power amplifiers at 325 MHz. These amplifiers were designed and are being constructed by DAE colleagues in the IIFC collaboration according to mutually agreed upon specifications between DAE and FNAL. The design of these power amplifiers leverages the new, LDMOS transistor technology. The RF output power capabilities of these transistors is an order of magnitude greater than the transistors made with previous processes. This improves the efficiency of the amplifier in both size and power, because fewer amplifier modules are required with fewer, high power combiners. LDMOS based 1 kW power amplifier module at 325 MHz is the basic building block. Figure 8.8 shows the layout of the SSR1 power amplifier consisting of:

- Power combiner and power splitter
- Eight, 1 kW PA modules
- Compact DC bias supplies

- Water cooling system

The SSR1 distribution transmission is based on 1-5/8 in. hardline cable. The flexible 1-5/8 in. cable does not have the necessary power handling headroom at the higher frequency compared to the HWR system. These circulators are also within the range of the domestic, commercial RF power industry's capabilities and are specified with enough headroom to handle operation at CW with full reflected power and withstand the high reflected power pulse caused by sudden interruption of RF drive power.

8.3.4.3 SSR2 RF power and distribution

The SSR2 cryomodule cavities require 20 kW, CW RF power amplifiers at 325 MHz. These amplifiers which are designed and developed by DAE colleagues will also be based on LDMOS transistor technology. The design of these amplifiers is based on scaling the quantity of 1 kW power amplifier modules in the SSR1 amplifiers.

The SSR2 distribution transmission is based on 3-1/8 in. hardline. These circulators are also within the range of the domestic, commercial RF power industry's capabilities and are specified with enough headroom to handle operation at CW with full reflected power and withstand the high reflected power pulse caused by sudden interruption of RF drive power.

8.3.4.4 LB650 RF power and distribution

The LB650 cryomodule cavities require 40 kW, CW RF power amplifiers at 650 MHz. These amplifiers were designed and are being constructed by DAE colleagues in the IIFC collaboration according to mutually agreed upon specifications between DAE and FNAL. As shown in Figure 8.9, the design comprises two, 20 kW amplifier units that have their outputs combined in phase to form the full 40 kW output. The design of these amplifier units also leverages the new, LDMOS transistor technology. Figure 8.10 shows the layout of the 650 MHz, 20 kW power amplifier unit. This unit is comprised of forty-eight, 500 W amplifier modules that are combined in one combiner for the final output.

The LB650 distribution transmission is based on 6-1/8 in. hardline. These circulators are also within the range of the domestic, commercial RF power industry's capabilities and are specified with enough headroom to handle operation at CW with full reflected power and withstand the high reflected power pulse caused by sudden interruption of RF drive power. After the 6-1/8 in. directional coupler, there is a coax to WR1150 waveguide transition that matches into the cavity input coupler warm end.

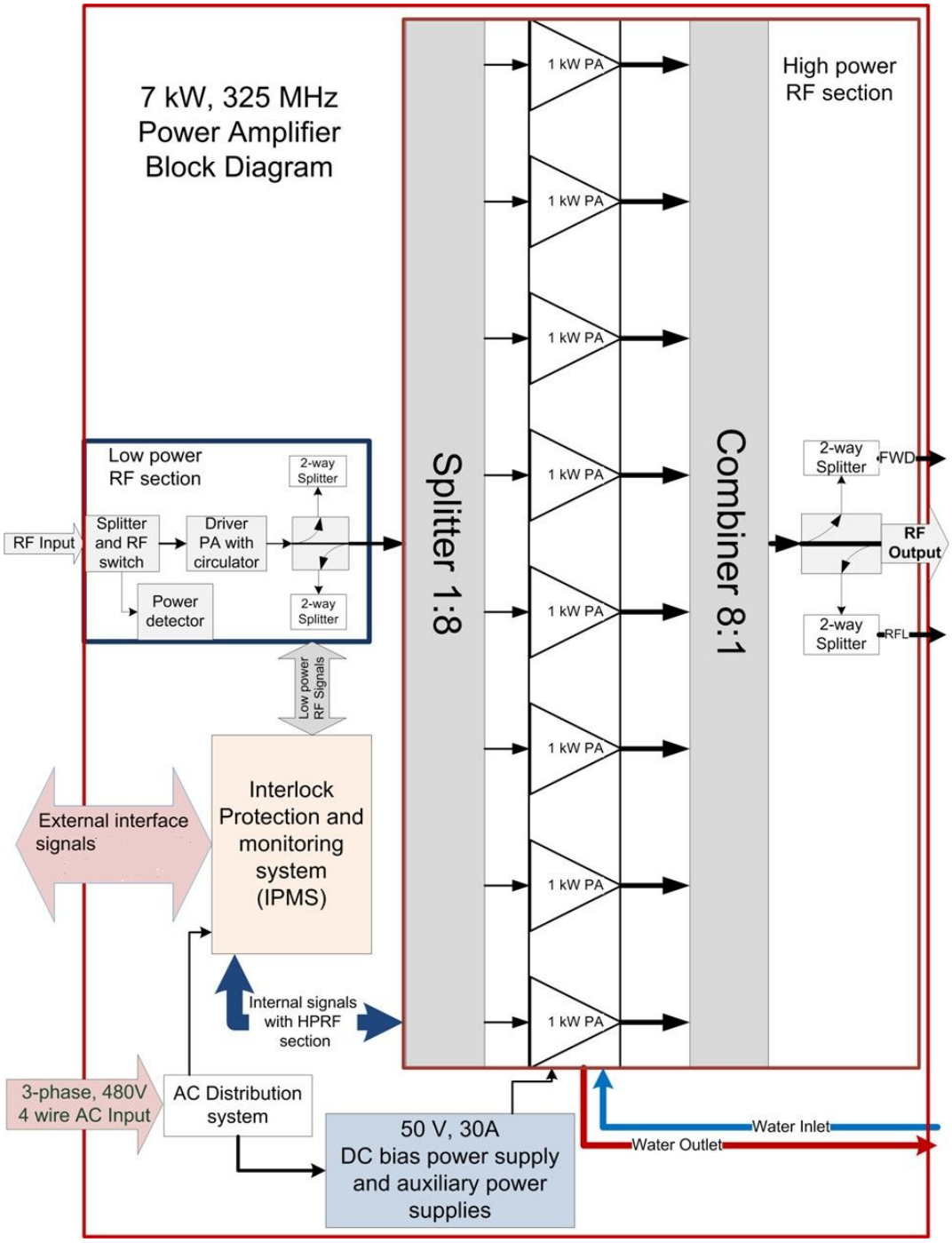

Figure 8.8: Block diagram of 7 kW, 325 MHz amplifier.

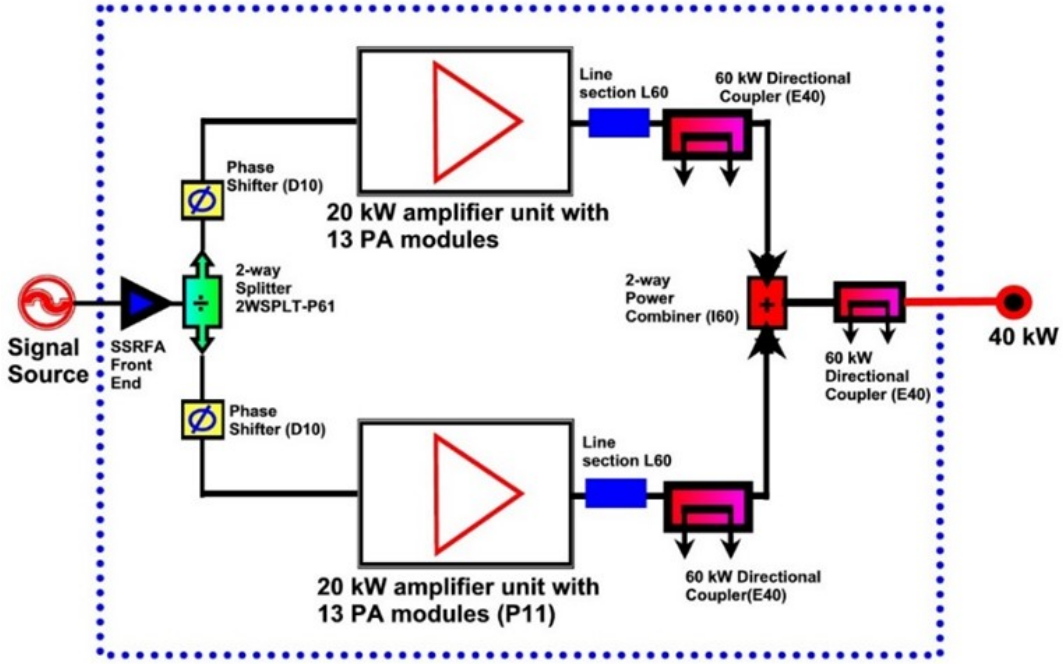

Figure 8.9: LB650 40 kW RF power amplifier layout.

8.3.4.5 HB650 RF power and distribution

The HB650 cryomodule cavities require 70 kW, CW RF power amplifiers at 650 MHz. These amplifiers are being design by DAE colleagues and the design comprises four, 20 kW amplifier units from the LB650 design that have their outputs combined in phase to form the full 70 kW output.

The HB650 distribution transmission is be based on 6-1/8 in. hardline. These circulators are also within the range of the domestic, commercial RF power industry's capabilities and are be specified with enough headroom to handle operation at CW with full reflected power and withstand the high reflected power pulse caused by sudden interruption of RF drive power. After the 6-1/8 in. directional coupler, there is a coax to WR1150 waveguide transition that matches into the cavity input coupler warm end.

8.4 Booster injection synchronization

Booster injection synchronization is accomplished using the block diagram shown in Figure 8.11. The 162.5 Master Oscillator Station generates a 162.5 MHz reference for the beam pattern generator, which controls the beam pattern and synchronization between the Linac and the Booster. At the front end of the Linac, the arbitrary waveform generator produces the waveform necessary to create the beam pattern for injection to the Booster and other operational modes using a pair of 200 ohm kickers. To align the beam at the end of the Linac to the Booster, the waveform

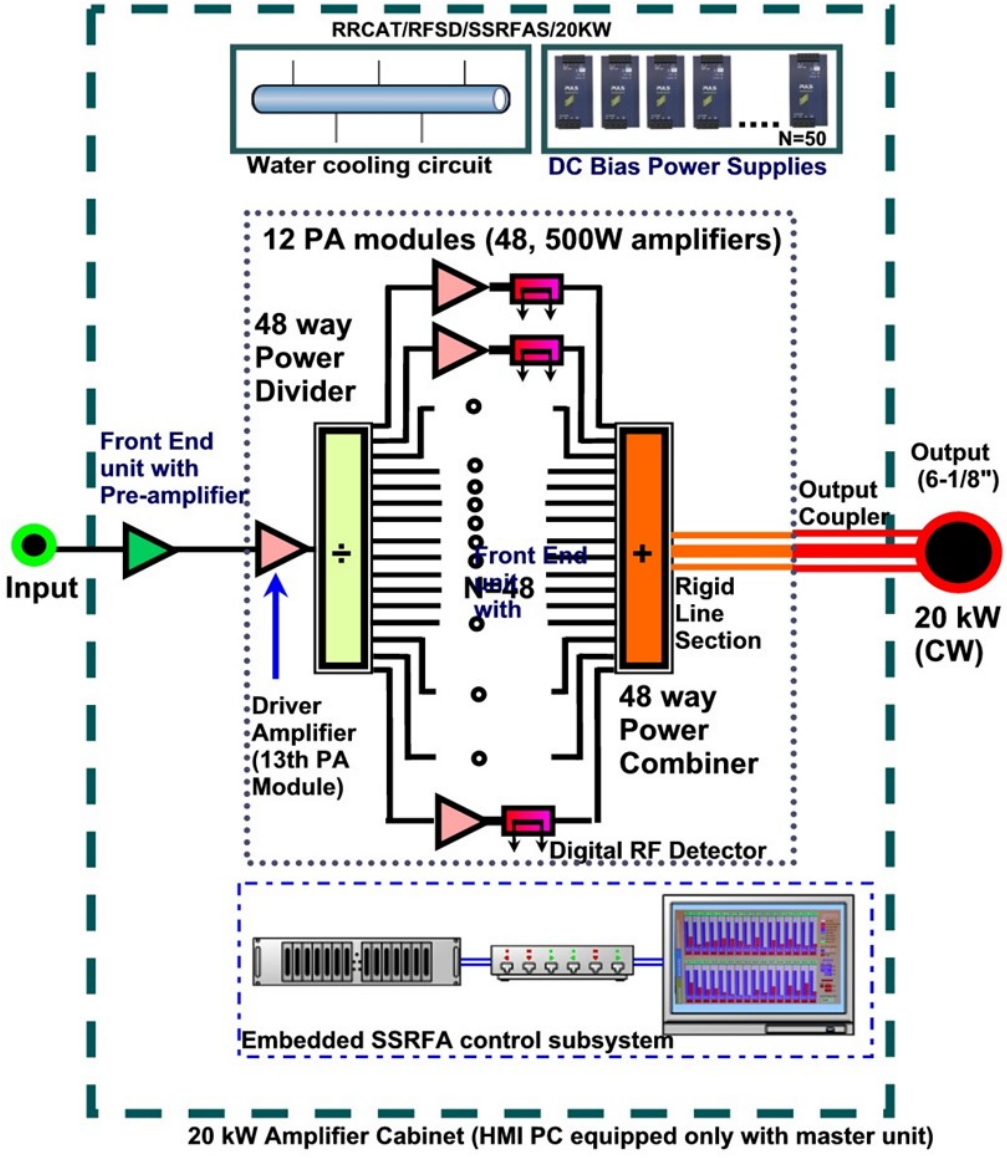

Figure 8.10: 650 MHz, 20 kW amplifier module diagram.

generator also creates a Booster RF reference signal for the Booster RF system to lock to during beam injections.

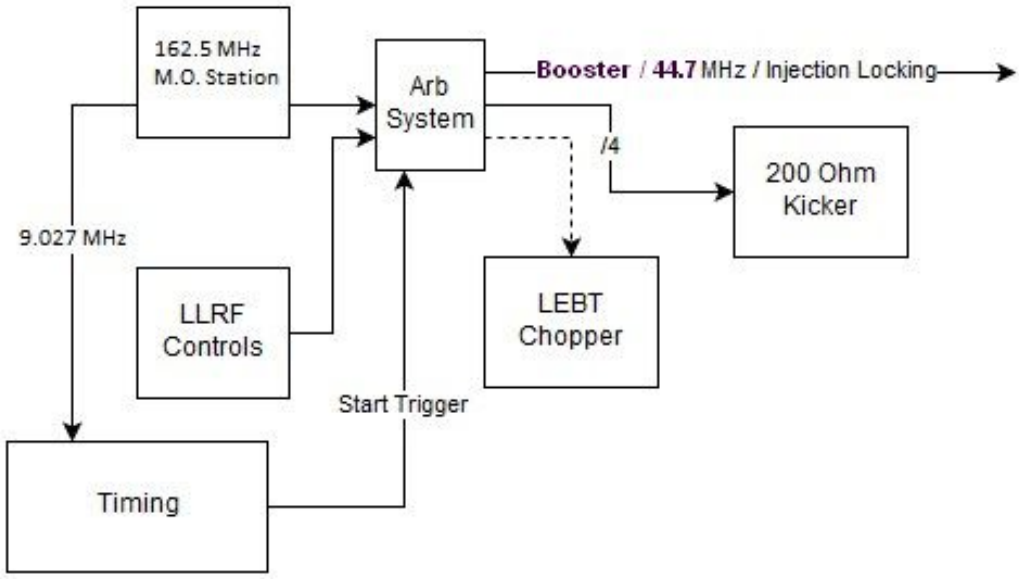

Figure 8.11: Booster injection synchronization scheme.

Chapter 9

Beam Instrumentation

9.1 System overview

Various beam instrumentation and diagnostics systems are necessary to characterize and monitor the beam parameters and the performance in all PIP-II sub-accelerators. For startup and initial beam commissioning we need to provide, at a minimum, beam instruments in order to observe:

- Beam intensity
- Beam position / orbit
- Beam loss
- Transverse beam profiles
- Beam phase / timing

Beside these core beam instrumentation systems, additional beam diagnostics will be needed. These instruments will be used to characterize such beam parameters as the beam emittance, transverse beam halo, bunch-by-bunch chopping efficiency and advanced beam emittance measures.

When possible, the beam instrumentation and diagnostics systems must be able to operate over a wide bandwidth from few-microsecond-long pulses for machine commissioning and tuning to long operational pulses. In addition, these systems must be compatible with CW beam operation. Table 9.1 presents an estimate of quantities of different beam instrumentation systems by location for the Linac and the 800 MeV beam transport line. In the table the SC Linac also includes the Linac extension capable to include 4 additional HB650 cryomodules.

In addition to diagnostic measurement, the high beam intensity / power and the presence of superconducting technologies require a reliable, fail safe machine protection system (MPS) to

Table 9.1: Estimate of beam instrumentation in the Linac and 800 MeV transfer line.
† one per focusing element (solenoid, quad, doublet, triplet), CM = cryo-module,
* = laser wire

Location	Beam current	Transverse position /phase†	Transverse profiles	Beam loss	Transverse emittance	Bunch extinction
LEBT	3	N/A	-	-	2	-
MEBT	3	12	4+1*	TBD	1	1
SC Linac	5	59	10*	2 per CM	-	-
Transport line	3	57	5	1 per FE	1*	-

prevent quenches in cryogenic elements or damage due to an uncontrolled loss of the high-power beam. The MPS system will rely on timely information from beam loss monitors (BLM) and beam intensity monitors such as toroids and dedicated ring pickups.

9.2 System design

9.2.1 Beam position monitor system

Beam orbit monitoring is the most fundamental measurement and powerful diagnostics tool in an accelerator. PIP-II requires a large number of new warm and cold beam position monitors (BPM) for the Linac and 800 MeV transfer beam line. Both the warm and cold BPMs must be capable of measuring all 3 coordinates: horizontal and vertical position and beam phase relative to the RF, as well as a relative measure of the beam intensity. The beam line design includes a single four-button BPM located near each beam focusing element (solenoid, quad, doublet, triplet). The geometry of all BPMs will be similar with their aperture slowly increasing with acceleration. The styles of BPMs are presented in Table 9.2.

Table 9.2: Styles of PIP-II BPMs.

Location	Quantity	Aperture [mm]	Operating temperature	Location (quantity)
MEBT	12	28.5	warm	MEBT
HWR & SSR1	16	36	cold	HWR, SSR1
SSR2	21	43	cold	SSR2
SC Linac	20	45	warm	LB650 (11), HB650(4), Linac extension (5)
Transport line	56	45	warm	Arc 1(19), Arc 2(33), beam dump (4)
Beam split	1	160	warm	In front of transfer line Lambertson

The signal duration is approximately proportional to the BPM aperture and shortens with beam acceleration as shown in Fig. 9.1 for the HWR style BPM [108].

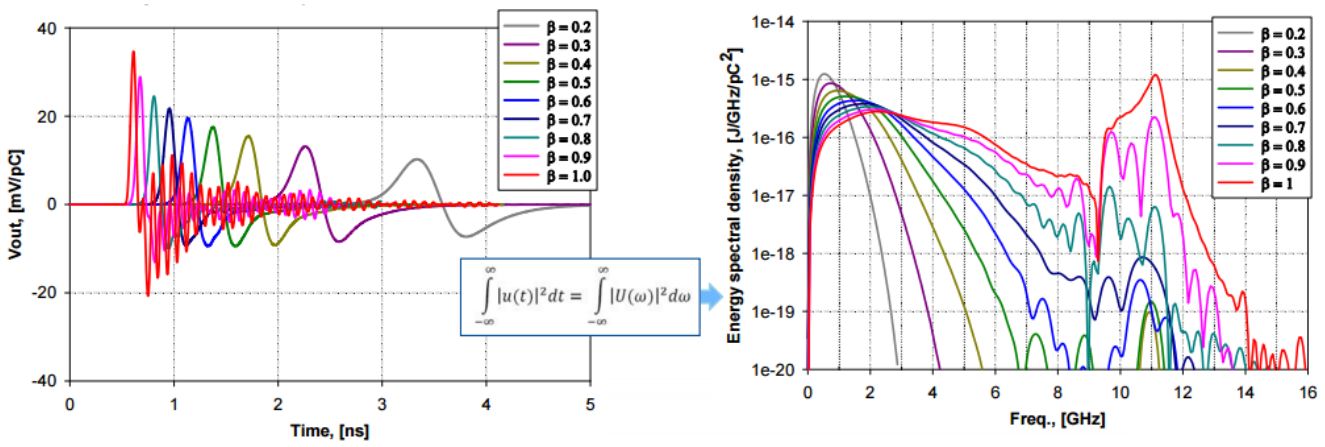

Figure 9.1: Numerical simulations of BPM signals produced by a bunch moving with different velocities: (left) time domain signals, (right) corresponding spectra; rms length is 4 mm.

9.2.1.1 BPM measurement modes

There are two modes that need to be supported by the BPM measurements for PIP-II commissioning and operation. The first mode is assigned for the pulsed beam at a single trajectory. It is applicable to all BPMs upstream of the MEBT chopper and to all other BPMs when the MEBT chopper is off. The second mode is assigned for pulsed beam split into two trajectories. This occurs only for the four BPMs located in the MEBT chopper region and only when the chopper is operational. In this case the chopper kicker splits the beam into two streams propagating downstream and oscillating relative to each other at the betatron frequency. Table 9.3 presents the resolution requirements for the BPM system for these two beam modes for beam pulses with duration at least 10 μs.

Table 9.3: BPM measurement requirements for one- and two-trajectory modes.

	One-trajectory Mode	Two-trajectory Mode
Transverse position, μm	10	100
Phase, degrees of 162.5 MHz	0.05	NA
Relative intensity, %	1	2

9.2.1.2 Warm MEBT BPM pickups

The MEBT includes 12 warm BPMs, one for each focusing element. Each BPM is mounted to a quadrupole of a MEBT quad doublet or triplet (focusing element). For a low energy beam, button-type pickups provide a good compromise between amplitude and time responses. Prototype four-button BPMs have been designed and installed for testing in the MEBT of PIP-II Injector Test beamline. The left pane of Fig. 9.2 shows the BPM view, and the right pane shows the BPM mounted to the iron of a MEBT focusing quadrupole magnet. The total BPM length is 3 in. Its maximum diameter is 2.7 in. and a beam aperture 1.12 in. The BPM is composed of non-magnetic

stainless steel and utilizes 20 mm diameter button pickups. The design is similar to the FRIB BPM design [109].

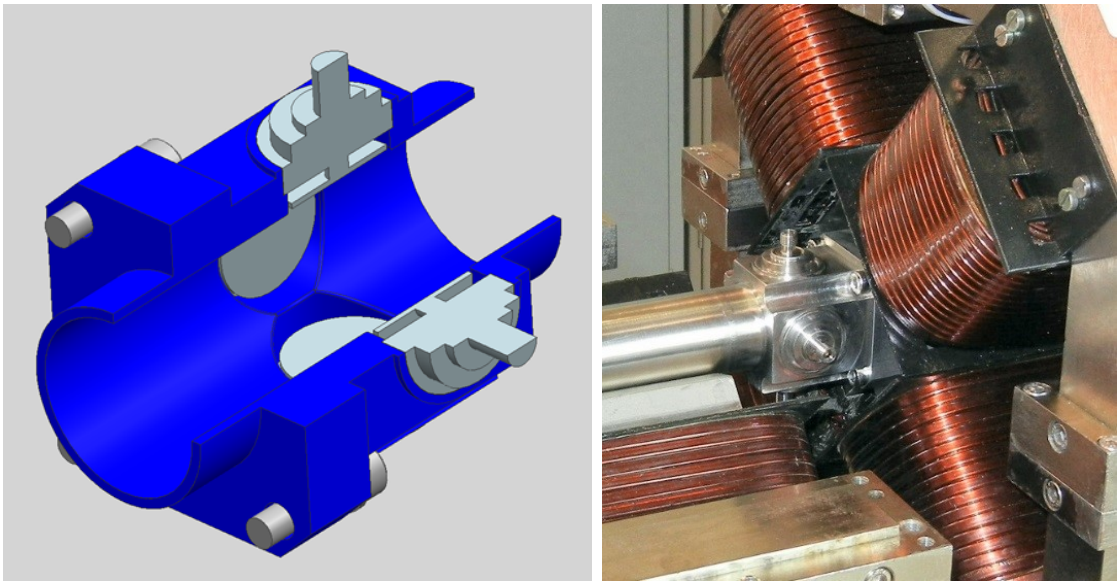

Figure 9.2: Section view of a prototype MEBT BPM (left) and prototype BPM mounted to a MEBT quadrupole (right).

9.2.1.3 Warm Linac and transfer line pickups

After HWR, SSR1 and SSR2, focusing elements for the rest of the Linac will reside in warm sections between the eleven LB650 and the four HB650 cryomodules. Each focusing element will have a four-button BPM of the SC Linac style. These BPMs will be mounted to the iron of one of the focusing element quadrupoles, in a design similar to the MEBT BPMs. This quadrupole magnet design will also be utilized in the 800 MeV transfer line, which will also include a BPM for each focusing element.

9.2.1.4 Cold BPM pickups

The Linac HWR, SSR1 and SSR2 cryo-modules will contain 37 cold BPM pickups which will be located inside the HWR, SSR1 and SSR2 cryo-modules and attached to each solenoid (focusing element). Their design must meet UHV, cryogenic and clean room requirements. The left pane of Fig. 9.3 shows a view of BPM pickup design and the right pane shows an assembled prototype BPM to be used in the SSR1 cryomodule.

Beam instrumentation within a cryogenic environment needs extra care to meet ultra-high vacuum, cryogenic, and clean room requirements simultaneously. Therefore, it is limited to beam orbit monitoring with button BPM pickups due to its simple mechanical design and good reliability.

The signal performance of the button-style BPM for H^- beams has been simulated [108]. For a

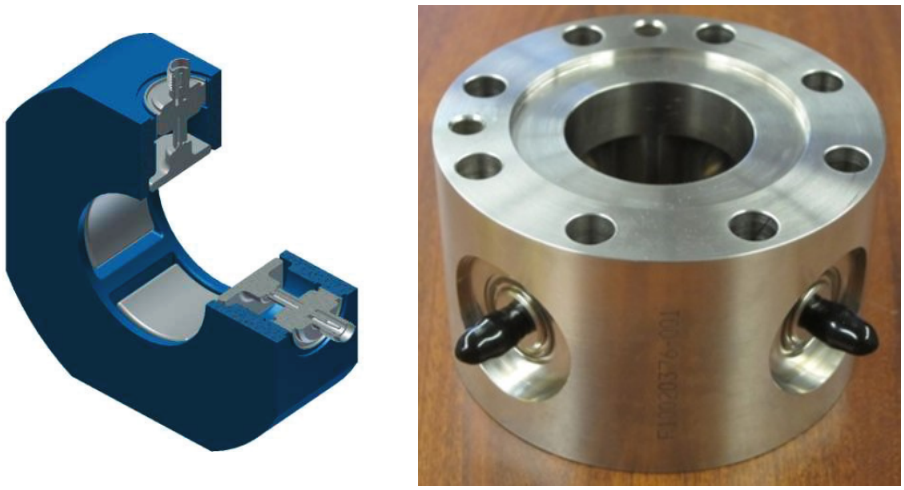

Figure 9.3: Section view of prototype cold BPM (left) and a prototype SSR1 cold BPM assembly (right).

low-energy beam the button-type pickups yield a good compromise between amplitude and time responses. Figure 9.4 shows the time and frequency domain responses of a button BPM for a low-energy beam with $\beta = 0.2$ which corresponds to the end of the first SSR1 cryomodule. The calculations were performed with CST Studio particle wake-field solver. For 5 mA RFQ current, the bunch charge is 30.8 pC, which, in accordance with Fig. 9.4, corresponds to a peak voltage on each BPM electrode of about 0.25 V. As shown in Fig. 9.1, the voltage grows approximately linearly with an increase of beam velocity β, and the pulse duration decreases approximately inversely proportional to β. Here we take into account that the bunch length is shorter than the duration of a single particle signal in the course of entire acceleration.

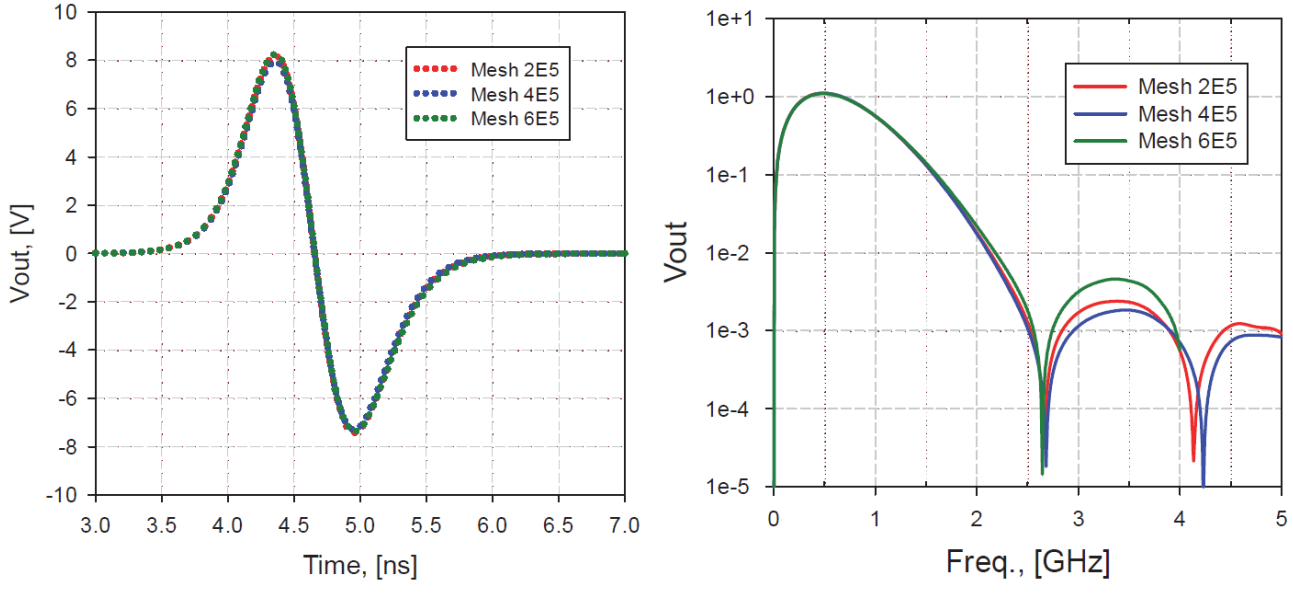

Figure 9.4: BPM output voltage in time (left) and frequency (right) domains versus mesh size (CST Studio, 4 mm rms, $\beta = 0.15$, 1 nC bunch).

9.2.1.5 BPM data acquisition

The standard BPM readout electronics for PIP-II will measure position, intensity, and phase using direct digital down-conversion by measuring the amplitude of the 1^{st} beam harmonic (162.5 MHz) for each electrode. In addition, the BPM readout will also take measurements at the 3^{rd} harmonic in an attempt to make a relative bunch length measurement [110]. This 1^{st} and 3^{rd} harmonic acquisition system will be tested at the PIP-II Injector Test accelerator. A simplified block diagram of the readout electronics is shown in Fig. 9.5.

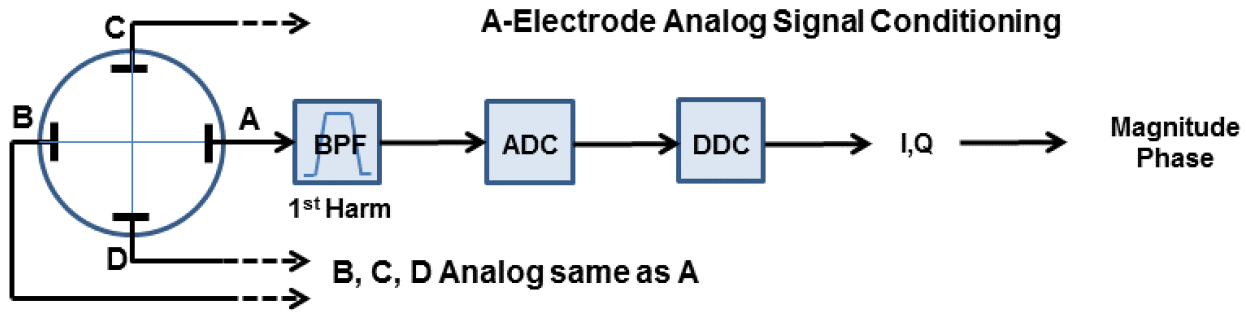

Figure 9.5: Block diagram for BPM electronics. The third harmonics part is similar and is not shown.

Figure 9.6 presents benchtop stretched wire measurements of a prototype MEBT BPM and a prototype cryo-module BPM. The stretched-wire measurements show non-linear distortions in the position measurements due to finite button pickup size. A 2D polynomial fit to the difference over sum in each plane will be used to correct nonlinearities in position and intensity responses of the button pickups. In addition, the calculated position correction will include a compensation for beam velocity which also affects the measurement.

As seen in Figs. 9.1 and 9.2, the 1^{st} harmonic gives adequate signal for a low-energy beam. However, if the signal strength will be found inadequate at higher beam energies, we will then change the readout electronics to operate at the 2^{nd} harmonic.

In the MEBT chopper region, the BPM system needs to measure simultaneously two different beam paths. This will require the BPM system to have sufficiently high bandwidth to make bunch-by-bunch transverse position measurements. The proposed BPM electronics will not allow high-bandwidth bunch-by-bunch measurements because of the 1^{st} harmonic bandpass filter. To acquire bunch-by-bunch information, high bandwidth oscilloscopes will be used to directly sample the button which will provide reasonable signal integration and transverse position resolution. Although oscilloscopes have high-bandwidth signal acquisition, they are relatively slow in signal processing. Therefore, the MEBT chopper bunch-by-bunch measurements will not acquire measurements for every PIP-II beam pulse.

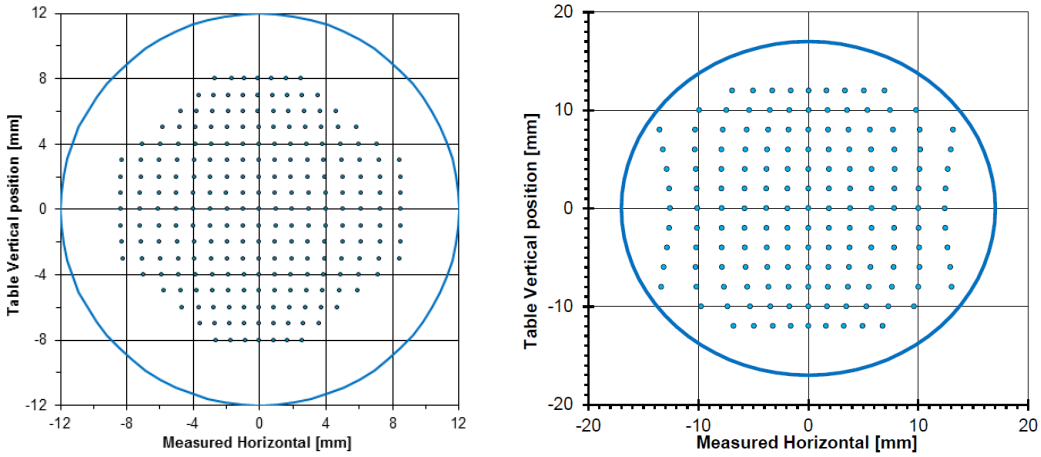

Figure 9.6: Benchtop stretched wire mapping of a prototype MEBT BPM (left) and a prototype cryomodule BPM (right).

9.2.1.6 Beam-based Linac energy stabilization

High quality injection into the Booster requires relative energy stability better than 10^{-4} rms. This places a requirement that the BPM system measure the Linac beam energy for every beam pulse. The beam energy is measured by BPMs located in the first arc of the transport line. The accuracy of the system is determined by the BPM accuracy and is expected to be $\sim 10^{-5}$ with $\sim$10 µs sampling time. This energy measurement will be used to support operation of the beam-based energy stabilization system. A high accuracy absolute energy measurement is not required.

9.2.2 Beam current monitor system

Protection of the PIP-II superconducting Linac will require high-precision measurements of pulsed and, in the future, CW beam currents as well as an accurate measure of beam current loss computed from the difference of beam currents at different locations. Such measurements are an important input to the MPS system. The beam current will be measured by a combination of different beam current instruments. The primary instruments will include DCCTs and beam toroids. In addition, a relative measure of beam current will be made by the BPM system as well as dedicated ring pickups.

The primary measure of absolute beam current will be via DCCTs and beam toroids. Standard beam toroids have the advantage of being less expensive than DCCTs and having a wide bandwidth to measure pulsed beam but are AC coupled and so cannot measure CW beam. DCCTs can measure CW beam but cannot measure short beam pulses and are generally more expensive. PIP-II will employ both types of instruments to adequately cover the proposed range of PIP-II beam timing structures. PIP-II will also utilize the BPM system to give a relative measure of the beam intensity.

In addition, several dedicated ring pickups will be employed in the PIP-II Linac to give an indepen-

dent measure of the relative beam current. The ring pickup is similar to a single button BPM and will utilize rectifying electronics to generate a measure of the PIP-II beam pulse. Figure 9.7 shows a view of the ring pickup to be tested in the PIP-II Injector Test accelerator and the response of the rectifying electronics to a 20 μs test beam signal.

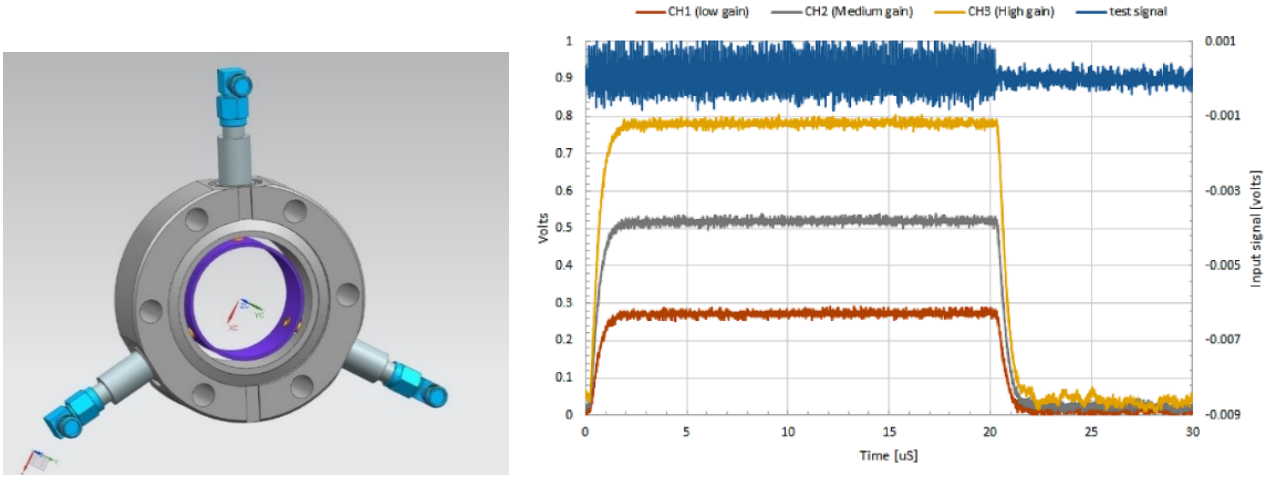

Figure 9.7: Drawing of a prototype ring pickup (left) and response of the ring pickup rectifying electronics to a simulated 20 μs 162.5 MHz test signal (right).

Both the BPM intensity and the ring pickup intensity, as well as absolute current from the beam toroids, can be utilized by the differential beam current monitor system to detect fast beam loss for the machine protection system. A similar differential beam current monitor system has been employed by the SNS accelerator [111].

9.2.3 Beam loss monitor system

Beam loss monitoring is an important tool for beam tuning as well as a critical part of machine protection. The PIP-II beam loss monitoring system will also help to prevent excessive activation of materials.

PIP-II will utilize three types of Beam Loss Monitor (BLM) devices through the Linac and the Linac-to-Booster transport line. The primary BLM devices will be ionization chambers. Ionization chambers have a relatively good response time ($\sim$ few μs), are simple in design and are resistant to radiation damage. The other two BLM devices will be fast Photomultiplier Tube (PMT) based detectors and neutron detectors. Both the ionization chamber detectors and PMT detectors are sensitive to charged particles, however the scintillator-based PMT detectors have a faster response time ($\sim$10 ns), adjustable gain and are sensitive to lower-energy gamma rays. The BLM detectors will be evenly distributed along the Linac and 800 MeV transport line with ionization detectors located near focusing elements between the cryo-modules and neutron detectors located near the middle of cryo-modules. The PMT-based detectors will mostly be distributed at the low-energy end of the Linac ($\sim$<100 MeV) and at key locations that require fast beam loss measurements. The beam loss monitoring system will also include a number of movable BLM detectors to be used to study specific beam loss issues as they occur during commissioning and beam tuning. In

addition, a fourth type of beam loss monitor will be used, the total loss monitor. Such monitors better characterize the total beam loss but without detailed information on its location.

9.2.3.1 Beam loss monitor signal processing

Since several types of BLMs will be utilized in PIP-II, the signal processing will vary depending on the particular application of the given monitor. Fast PMT based signals for machine protection will be processed to provide both a Fast Shutdown Signal to the MPS as well as integrated to provide a tuning signal. The time scales for these signals are a few microseconds with cable delays included. Ionization type loss monitor signals will be digitized at a sampling rate of 125/250 MHz and various thresholds for losses will be established according to the damage potential and diagnostic protection requirements. Figure 9.8 shows a typical block diagram of a VME-based signal processing scheme for a PMT-based beam loss monitor.

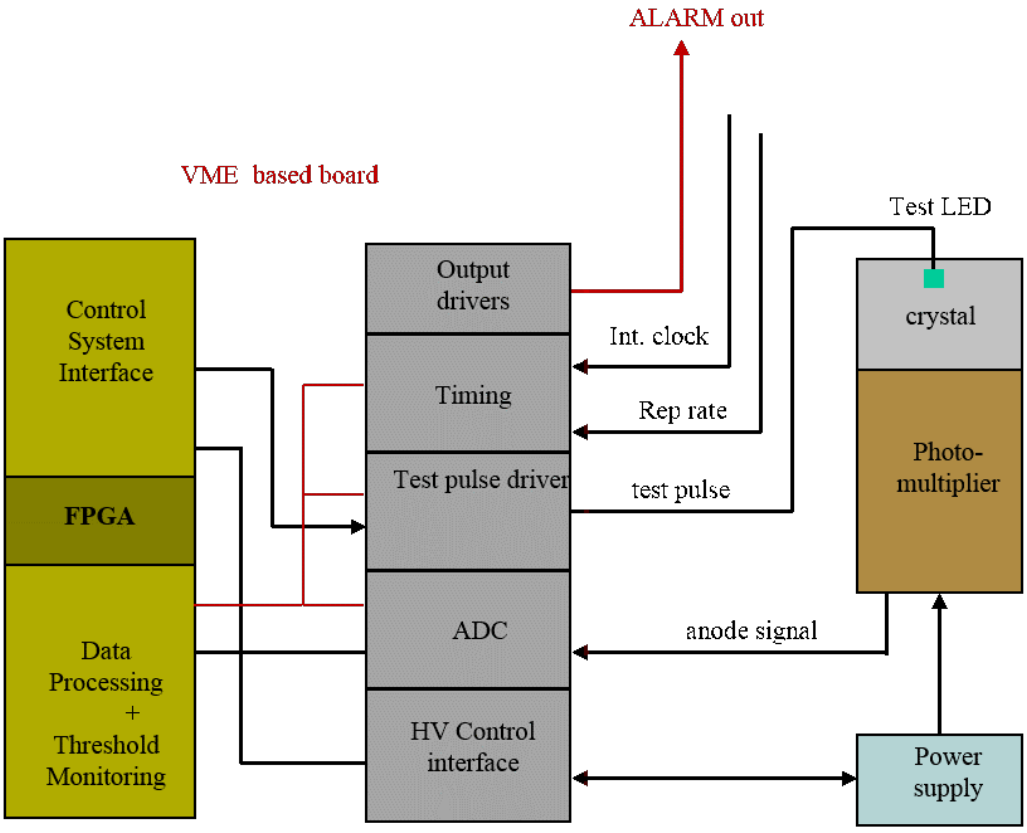

Figure 9.8: Example of PMT-based beam loss monitor electronics.

9.2.4 Beam profile monitor system

We are considering two types of transverse wire profiling methods for PIP-II. The first method would use photo-disassociation of H^- by laser radiation, and the second method would be a

traditional wire scanner. Because of the minimal interaction with the beam, the laser-based profile monitor is our primary choice near the superconducting cryomodules. However, traditional wire scanners are a proven technology in accelerators and they will be considered as a backup choice for certain areas of the Linac. Wire scanners will be the primary choice in the 800 MeV transfer line. Table 9.4 shows the preliminary requirements for beam transverse profile measurements. In addition to these two primary choices for transverse profiles we will utilize transverse scrapers in the LEBT and MEBT to produce beam profile measurements.

Table 9.4: Requirements for beam transverse profile measurements.

Parameter	Value
Spatial resolution	< 0.1 mm
Signal dynamic range	> 103
Spatial range	± 15 mm

9.2.4.1 Laser-based transverse profile measurements

PIP-II will utilize transverse laser profile monitors throughout the Linac near the SC cryomodules. Laser-based transverse profile measurements of H^- beam have been demonstrated by different groups [112, 113]. SNS at Oak Ridge National Lab has implemented laser-based profile measurements as part of its operation [114]. Traditionally, the technique of photo-disassociation ($H^- + \gamma \rightarrow H^0 + e^-$) is accomplished with high peak power lasers and signal detection through the collection of electrons. However, SNS has demonstrated a longitudinal profile measurement in their MEBT utilizing a low peak power laser with electron collection. A low peak power laser produces far fewer photo-disassociations and, hence, a smaller signal.

For PIP-II we will construct a transverse H^- beam profiling instrument utilizing a low peak power, high rep-rate fiber laser with optical fiber transport to the accelerator and synchronous signal detection. The system will detect this small signal through narrow-band synchronous detection of a modulated laser pulse train. Figure 9.9 shows a diagram of the proposed laser profile monitor [115]. This system utilizes a high rep-rate, picosecond, mode-locked laser (MLL) that is locked to the accelerator LLRF. The laser pulse train amplitude is modulated by a variable RF signal that is asynchronous to the accelerator RF. The laser pulse train is then transported to the beamline via optical fiber and scanned across the beam. Signal detection can be measured either by observing the modulated intensity of H- beam at downstream BPM(s) with the synchronous lock-in detection or by collecting electrons by magnetically deflecting them into a Faraday cup. Where bunch lengths are not too short, longitudinal profile scans can be measured by changing MLL phase relative to the LLRF. Initial studies show that longitudinal profiles are probably only feasible in the MEBT. Laser-based longitudinal measurements have been demonstrated in the SNS MEBT [116]. A prototype version of the laser profile monitor is being tested at the PIP-II Injector Test accelerator.

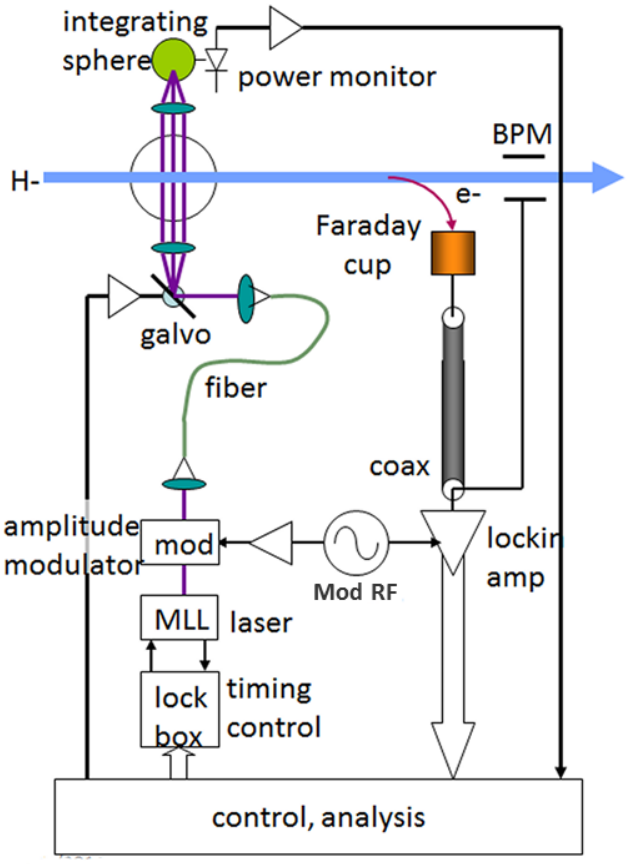

Figure 9.9: Proposed transverse and longitudinal beam profile system. Drawing courtesy of R. Wilcox, LBNL [115].

9.2.4.2 Wire scanner transverse profile measurements

Wire scanner systems are a traditional method used for beam transverse profile measurements. They have the advantage of being a straightforward and well-understood technique. They have the disadvantage of being invasive, causing beam loss, and requiring multiple beam pulse to reconstruct a profile. Excessive beam loss and potential wire damage will limit wire scanner operation for PIP-II to short beam pulses ($\sim$10 µs). We will utilize wire scanners as the primary profile measurement method in the MEBT and the 800 MeV transport line. It is unadvisable to use such systems in close vicinity to SC cryomodules due to spattering of wire material by the beam and possible micro-particle formation due to blistering. A prototype wire scanner is being tested in the PIP-II Injector Test accelerator.

9.2.5 Other beam instrumentation

9.2.5.1 Transverse emittance monitors

Transverse emittance measurements are a highly useful and versatile tool for the tuning and operation of an accelerator. There are various techniques that can be used to determine the transverse emittance. PIP-II will employ two types of emittance measurements for transverse phase-space: (1) Allison-type emittance scanners and (2) laser-based emittance scanners.

In addition to these phase-space measurement techniques, PIP-II will also make rms emittance measurements utilizing focusing (quadrupole or solenoid) scans and transverse profile monitors. These rms measurements will occur at locations that can provide a necessary combination of focusing elements and profile monitors.

Allison-Type Emittance Scanners

An emittance scanner for intense low-energy ion beams, based on sweeping electric fields, was proposed in 1983 [117]. This type of emittance scanner has been typically classified as an Allison-type transverse emittance scanner. Typically, such scanners have been utilized for ion source and LEBT beam emittance measurements [118]. A functional representation of an Allison scanner illustrating the two slit design with electric field deflecting plates is shown in Fig. 9.10. The angular scan is performed with voltage change on the deflecting plates, and the coordinate scan is performed with mechanical displacement of the monitor with a step motor. PIP-II will utilize two Allison scanners: one for the LEBT and one for the MEBT.

A water-cooled Allison scanner has been built and tested at the LEBT of PIP2IT for measuring ion source emittance [119]. The scanner has been operated extensively for both pulsed and DC 30 keV H^- beam up to beam current of 10 mA. Figure 9.11 shows a set of phase space measurements taken in the PIP-II Injector Test LEBT with this Allison scanner. This figure illustrates the capability of the Allison emittance scanner.

Laser-Based Emittance Scanners

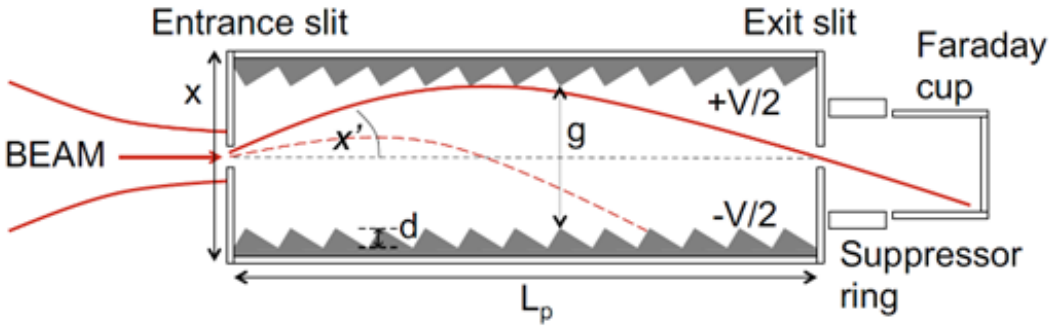

Figure 9.10: Pictorial representation of an Allison-type scanner with an illustration of the bending properties of the electric deflecting plates.

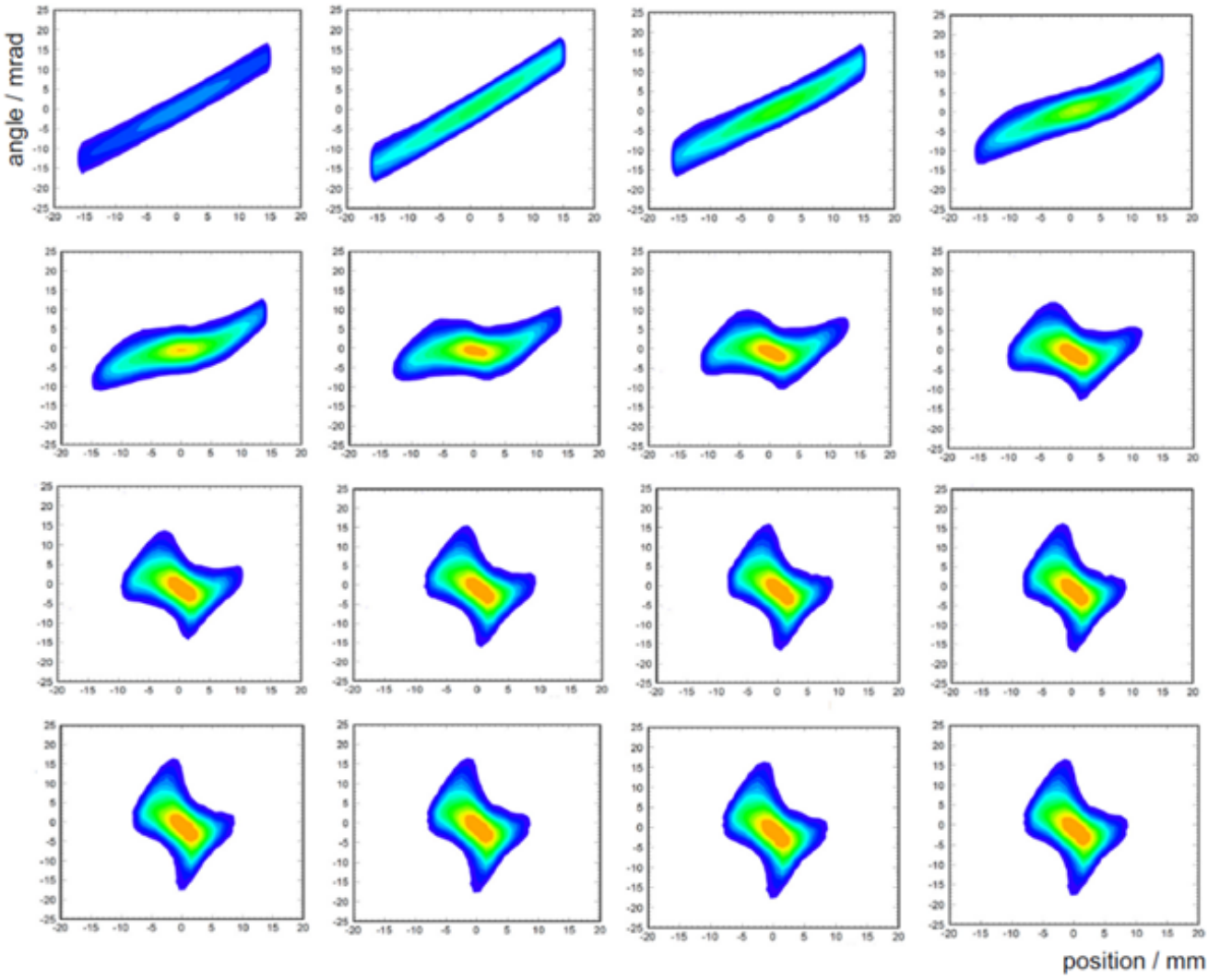

Figure 9.11: An example of evolution of the transverse phase space on time after pulse beginning taken in the LEBT of the PIP-II Injector Test accelerator for a 2 ms pulsed, 5 mA H^- beam with 0.125 ms time steps. The evolution is happening due to beam space charge neutralization.

Measurements of transverse phase space and emittance at the end of the PIP-II Linac will be performed with a laser-based emittance scanner. A functional diagram of a laser-based emittance scanner is shown in Fig. 9.12. A laser-based scanner has the advantage of minimal beam interaction, enabling it to make measurements for both pulsed and CW beam. A similar, but not identical, technique has been implemented at both the SNS and LINAC4 accelerators [120, 121].

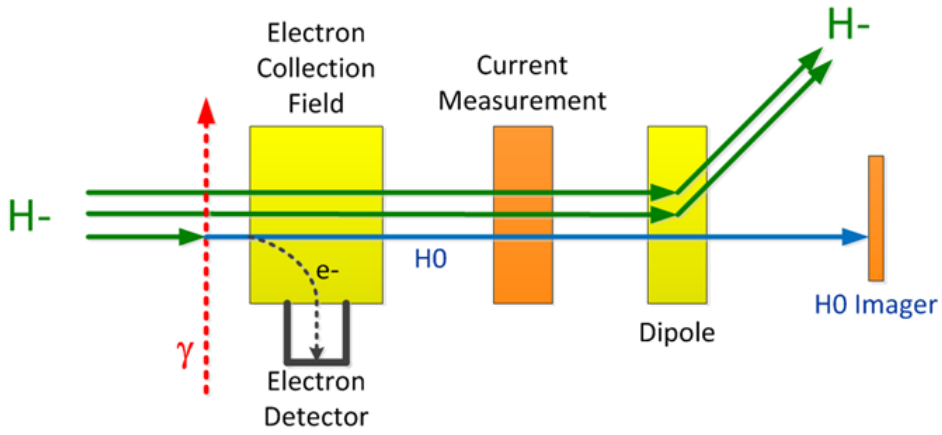

Figure 9.12: Functional diagram of a laser-based transverse emittance monitor.

9.2.5.2 Chopper extinction measurements

The PIP-II MEBT chopper will be able to arbitrarily remove individual bunches from the beam. The chopping efficiency of bunch removal needs to be verified to a level of better than one part in 10^{-4}. PIP-II will utilize a high-bandwidth resistive wall current monitor (RWCM) to measure the integrated field produced by individual beam bunches. Integration of the RWCM signal will be accomplished using a fast oscilloscope. This technique is similar to the Fermilab sampled bunch display systems used to measure longitudinal particle distribution of individual bunches in the Tevatron and Main Injector accelerators [122]. Figure 9.13 shows a block diagram of the proposed MEBT bunch extinction system.

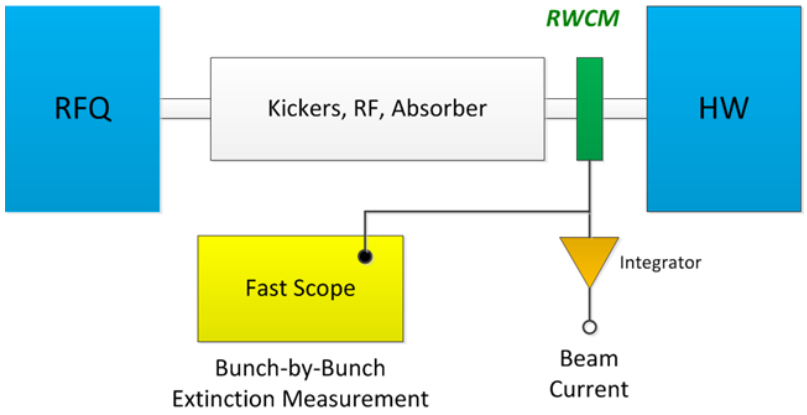

Figure 9.13: Block diagram of the PIP-II MEBT extinction measurement system.

9.2.5.3 Beam halo measurements

For any superconducting accelerator, measurement and control of the longitudinal and transverse beam halo is important. Typically, beam halo measurements are defined to be at the intensity level of 10^{-4} to 10^{-6} of the core beam [123]. This places a large dynamic range requirement for any halo measurement system.

For transverse beam halo measurements and control in the MEBT, PIP-II will primarily utilize electrically isolated scrapers. Such scrapers, with current readout, have been tested in the PIP-II Injector Test accelerator. Wire scanners will also be used to measure transverse beam halo but in order to protect the superconducting Linac, wire scanners will be limited to operation in the MEBT and the 800 MeV transport line. Also, the LEBT and MEBT emittance scanners will be utilized to make transverse tails and halo measurement.

In addition, the laser-based profile monitors also can measure transverse tails of bunch charge distribution. However, their sensitivity to tails is limited by scattered light with initial estimates of no better than $\sim 10^{-3}$. We are also investigating the use of diamond detectors for halo measurements. Prototype diamond detectors are being tested at PIP2IT.

Measurement of longitudinal bunch tails and halo is more difficult because of the very short bunch structure in the Linac. PIP-II will utilize laser-based profiling in the MEBT to measure bunch tails but the dynamic range is limited by scattered light of the laser pulse.

Chapter 10

Magnets and Power Supplies

10.1 Introduction

Power supply systems are needed to power both superconducting magnets located within the HWR, SSR1 and SSR2 cryomodules, warm magnets for the 650 MHz high beta and low beta cryomodules as well as the Linac to Booster Transfer line magnets. In addition, the power supply systems also provide for quench protection of all superconducting magnets. This also includes the warm magnets from the 650 MHz high beta and low beta quads and correction dipoles (which are partner deliverables) and all the transfer line magnets. The requirements for the magnets and power supplies are listed in Table 10.1.

10.2 System design

10.2.1 PIP2IT cryogenic magnet supplies

There are a total of twelve 80 amp switcher supplies, sixteen 10 amp switcher supplies, sixteen 50 amp switchers and eight QPMs along with the associated cables between power supplies and magnets which are part of the PIP2IT system. A prototype QPM has been constructed and testing is underway using a warm load. This system was also tested with a cold SSR1 solenoid at the VTS facility. Test results show that the system meets or exceeds the specifications. Investigations are underway to upgrade the common 65 amp switchers to 80 amps. New components have been identified and are in the process of retrofitted a 65 amp switcher for tests. Once testing is complete all the parts needed for operating the PIP2IT cryogenic magnets will be procured. Once installed and operational the power supply system will be tested to insure that its performance meets the requirements of the project. Control and readbacks of the power supplies will be performed through the QPM.

Table 10.1: Requirements for magnets

Section	Count	Effect. length [m]	Field integral (2a)	Gap or aperture region	Good field	Uniformity, $\Delta B/Bor$ $\Delta G/G$	Oper. temp.
HWR solenoids	8	-	2 T2m	33 mm	-	-	cold
HWR 2-plane dip. correctors	8	-	±2.5 mT·m	33 mm	-	-	cold
SSR1 solenoids	8	-	4 T2m	30 mm	-	-	cold
SSR1 2-plane dip. correctors	8	-	±2.5 mT·m	30 mm	-	-	cold
SSR2 solenoids	21	-	5 T2m	40 mm	-	-	cold
SSR2 2-plane dip. correctors	21	-	±5.0 mT·m	40 mm	-	-	cold
SC C quads	40	0.2	3 T	52 mm	∅24 mm	0.1%	warm
SC Linac 2-plane dip. correctors	20	∼0.1	±10.0 mT·m	52 mm	∅24 mm	1%	warm
SC Linac skew-quads	4	∼0.1	1 T	52 mm	∅24 mm	0.3%	warm
Transport line regular quads	49	0.2	2 T	52 mm	∅24 mm	0.1%	warm
Transport line large bore quads	2	0.4	2 T	80	150x10 mm^2	0.1%	warm
End of Booster line quads	6	0.2	3T	52 mm	∅24 mm	0.1%	warm
Tr. line one-plane dip. correctors	56	∼0.1	±10.0 mT·m	52 mm	∅24 mm	1%	warm
Transport line dipoles	37	2.45	0.7 T·m	52 mm	∅24 mm	0.02%	warm
End transport line dipoles	2	1.8	0.52 T·m	52 mm	∅24 mm	0.02%	warm
C-dipole of Booster inj.	1	1.8	0.69 T·m	52 mm	∅24 mm	0.05%	warm
Fast dipole switch	1	2	17 mT·m	45 mm	∅24 mm	1%	warm
3-way septum magnet	1	2.6	0.43 T·m	34x34 mm^2	∅30 mm	0.2%	warm
Beam dump sweep magnet	1	0.5	0.05 T·m	52 mm	∅24 mm	1%	warm

10.2.2 SSR cryogenic magnet supplies

Once PIP2IT is complete the HWR and SSR1 systems will be used at CMTF to test SSR2 cryomodules. Once testing is complete these systems will be relocated to the PIP-II Linac gallery for use in the PIP-II Linac. A second SSR1 cryomodule will be installed requiring four new QPMs, four additional 80 amp switchers and sixteen additional 50 amp switchers. The seven SSR2 cryomodules will require twenty-one of the 80 amp switchers, eighty-four of the 50 amp switchers and twenty-one new QPMs. Control of the power supplies will be performed through the QPMs.

10.2.3 650 MHz section warm magnets and supplies

The low beta and high beta 650 MHz sections include warm quadrupoles and dipole correctors situated between cryomodules. A total of forty-four quads (including four skew quads, ten of these are in the Linac extension which allows for additional cryomodules to boost the Linac energy to 1 GeV) and twenty two-plane dipole corrector magnets. The magnets will be provided by our International Partners. During the Preliminary Design Review process FNAL the specification for the maximum current was increased from 15 amps up to 100 amps. Since our colleagues had earlier proposed a 110 amp design it is expected that a new PDR can begin soon . A final Design Report is due in March of 2019 at which time we will have a prototype set of magnets. Each quadrupole will be individually powered using a commercial power supply with a FNAL built regulator. The expected maximum current is 100 amps. The correction magnets will be powered by a FNAL designed ± 12 amp switcher power supply system. All these magnets will be controlled via the integrated control system.

10.2.4 Transfer line magnets and supplies

10.2.4.1 Dipoles

The Transfer Line dipoles will be provided by an outside vendor who will provide a final magnet design and a prototype magnet. There will be a total of thirty-seven dipoles and two vertical end of transport line dipoles (for injection into Booster). One of the main constraints for the design is that the magnetic field must be such as to not result in sufficient stripping of the H- ions that will result in beam loss and residual radiation in the enclosure. This limits the maximum magnetic field of the dipoles to 2.4 kG. FNAL has completed a preliminary design which meets this specification. There will be three strings of eight magnets in the arcs, one string of five magnets in the abort line, one string of six magnets (arc1), two individually powered dipoles in arc1 that will act as critical devices (part of the electrical safety system) and two strings of one shorter dipole for the vertical Booster Injection dog leg. The expected current for 800 MeV is 420 amps. The power supply system is currently in the preliminary design stage and will consist of a commercially available SCR supply with a FNAL built regulator that will regulate to 100 parts per million.

10.2.4.2 Quadrupoles

Similar to the dipoles, the Transfer Line regular quadrupoles will be provided by an outside vendor who will provide a final magnet design for FNAL approval as well as a prototype magnet for evaluation. There will be forty-nine regular quads, two large aperture quads (for the beam dump) and six end of line quads. A preliminary design of the quadrupoles has been completed with three options evaluated and a cost estimate based on these designs. The transfer line quads will be powered in sixteen separate strings of varying lengths with the maximum expected current of 100 amps. This consists of a focusing and defocusing string for both arc 1 and arc 2, a focusing and defocusing string for the abort line, two independently powered arc 2 quads (for fine tuning), one focusing and one defocusing large aperture quad in the abort line and the six Booster Injection quads. The power supply system is currently in the preliminary design stage and will be composed of an appropriately sized commercial switcher power supply with FNAL built regulators which regulate the current to a level of 300 parts per million.

10.2.4.3 Correctors

There are fifty-six one-plane corrector magnets in the transfer line. These magnets will be provided by an outside vendor who will provide a final design to FNAL for review and approval. The maximum expected current for these magnets is +/- 12 amps and powered by the FNAL switcher power supplies.

10.2.4.4 Specialty magnets

There are four specialty magnets which will be designed and built by FNAL. These consist of a fast switch magnet (which moves beam between the beam dump and the Booster injection line), a 3-way septum magnet (the two field regions deflect beam to the beam dump and to the Mu2e beam line and the field free region is the beam to Booster), a beam dump sweep magnet (which spreads the aborted beam in a circle of radius 5 cm so that beam is not always hitting the same spot on the beam dump) and a C-magnet (for Booster injection). These magnets and their associated power supplies are in various stages of development. Preliminary designs for the three-way septum and fast sweep magnet have been completed. A similar though longer version of the three-way septum can be used for the Booster Injection C-magnet. The fast sweep magnet is powered by a IGBT style power supply which provides 411 amps of current to the magnet. This power supply is currently in the design phase. The three-way septum magnet is composed of three short magnets each of which have the field region aligned with the extracted beam. The power supply delivers approximately 1200 amps and is a commercial SCR supply with a FNAL built regulator. The Booster injection C-magnet operates at 1200 amps and requires a similar power supply. The following is a list of the magnets and power supplies:

Table 10.2: List of the magnets and power supplies

System	# of Power Supplies	# of magnets supplied
HWR(PIP2IT)	8-65 amp switchers 16-10 amp switchers 4 QPMs 1-5 kW bulk supply	0
HWR(PIPII)	8-80 amp switchers	0
SSR1(PIP2IT)	4-65 amp switchers 16-40 amp switchers 4 QPMs 1-5 kW bulk supply	
SSR1 #1(PIPII)	4-80 amp switchers 16-50 amp switchers	0
SSR1 #2	4-80 amp switchers 16-50 amp switchers 4 QPMs 1-5 kW bulk supply	
SSR2	21-80 amp switchers 84-50 amp switchers 7 QPMs 6-5 kW bulks	0
650 MHz Warm Magnets	44-750 W commercial power supplies 40-10 amp switchers 1-10 kW bulk supply	44 quads 20 two-plane corrector packages
BTL Dipoles	5-75 kW commercial supplies	37
BTL end of line dipoles	2-10 kW commercial supplies	2
BTL regular quads	6-10 kW commercial supplies	49
Large aperture quads	2-1 kW commercial supplies	2
End of Line Quads	6-1 kW commercial supplies	6
Correction dipoles	56-10 amp switchers 2-10 kW bulk supplies	56
3 way septum magnet	1-30 kW commercial supply 3	
Fast switch magnet	1 FNAL design/built IGBT supply	1 (A0 abort magnet)
Sweep magnet	2-80 amp switchers (?) 1- 5 kW bulk	1
Booster injection C-magnet	1-135 kW commercial power supply	

10.3 Production and assembly

10.3.1 Production plan

The plan for the magnets is to produce a requisition which will have the vendor provide first a final design which must be approved by FNAL, then provide a prototype magnet for evaluation at FNAL and if the prototype tests show the design meets our requirements then the vendor will provide all the production magnets. FNAL will perform acceptance tests on all incoming magnets as well as full magnetic tests on selected magnets. For QPMs the plan is to order components based on our parts list from the tested prototype system, assemble all boards at FNAL and test the boards in our prototype system.

10.3.2 Verification and testing

For the QPMs and FNAL switcher supplies, test procedures have been established and will be followed. Commercial power supplies will be inspected and tested to verify they meet the requirements. Upon receiving magnets, each magnet will be inspected to insure that it has the correct electrical properties (resistance, inductance), that any water cooling paths allow for the proper flow and that the magnet is effectively isolated from ground (hipotting). Each magnet is then magnetically tested to insure that it meets the field requirements.

Chapter 11

Integrated Control System

11.1 Controls

The control system is responsible for control, monitoring, and operation of the PIP-II accelerator as well as the existing complex. It provides a core infrastructure to interface all hardware and software required to operate the accelerator. The controls scope includes selected hardware systems, the low-level interface to all hardware, computing and network infrastructure, and general service and application software.

11.2 Requirements

The scale of the control system is expected to be similar to that of the complex when the Tevatron was operating. The system should support up to several million device properties. Timing signals must be provided to control beamline equipment and provide time stamping so that diagnostic data from the PIP-II linac can be properly correlated with that from the existing complex. Services for alarms, data archiving, and machine configuration save and restore should be common for the entire complex. The control system should contribute less than 2% to operational unavailability. Access to the control system should be limited to authorized users. Common code frameworks and management systems should be provided for each level of the system.

11.3 Architecture

The PIP-II control system will be based on the well established EPICS toolkit and integrated with the control system for the main accelerator complex. Currently that uses a custom system known as ACNET [124]. As shown in Fig. 11.1, ACNET is a three-tiered system with front-end, central

service, and application layers. Front-end computers directly communicate with hardware over a variety of field buses. Central service computers provide general services such as a database, alarms, archiving, application management, as well as more specialized services. Communication to the front-end system uses a connectionless protocol also known as ACNET.

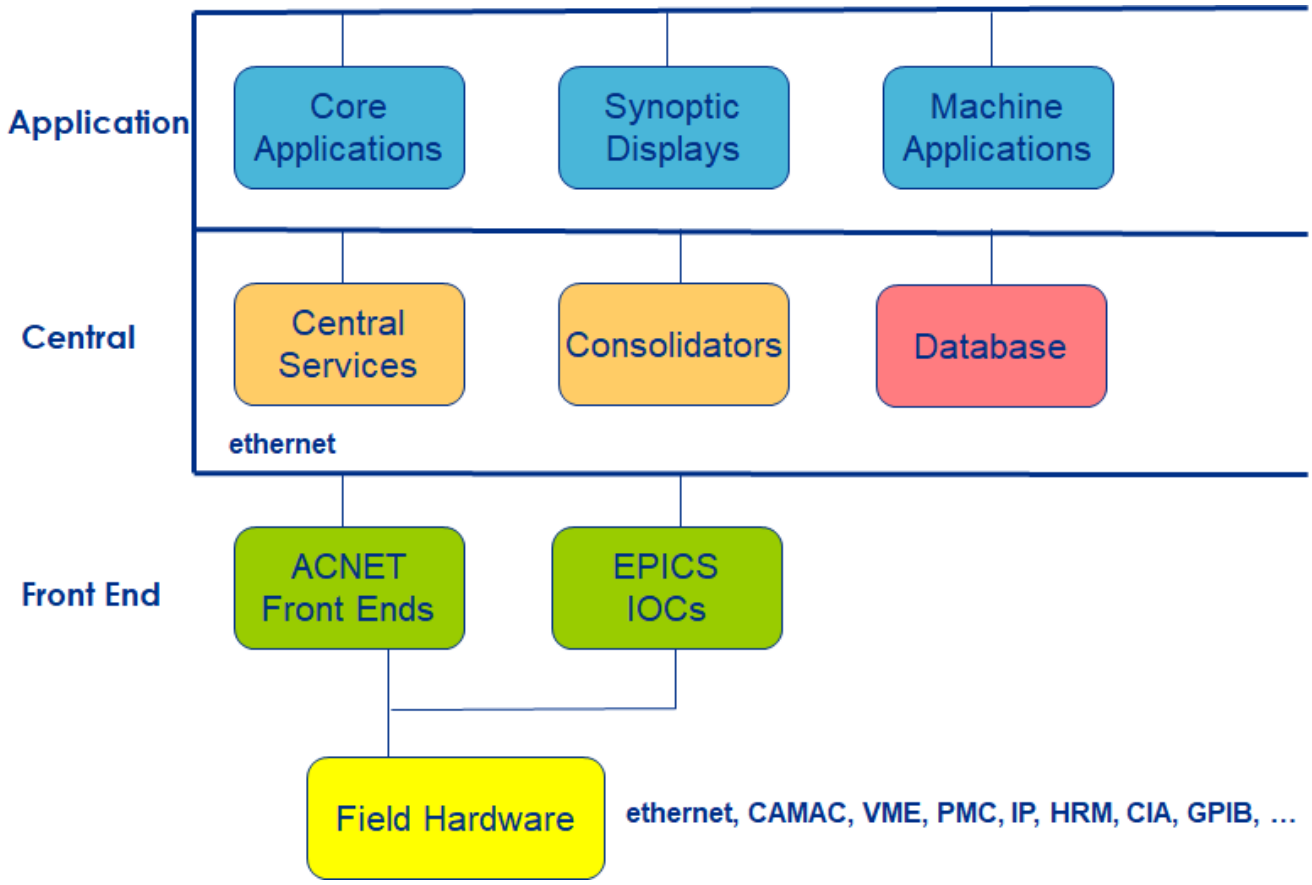

Figure 11.1: The ACNET control system

The system is very modular supporting a variety of hardware and software frameworks. It is highly desirable to have a single control system for the entire complex. This simplifies development and operation and reduces long term maintenance costs. The plan is to begin by integrating EPICS IOCs into the current control system taking advantage of its modular nature and three-tier model where communication passes through an intermediate consolidator process. This process will be modified to support both ACNET and EPICS communication protocols. A similar ACNET-EPICS integration has been done at past test facilities at Fermilab [125]. This will allow beginning PIP-II development early with a modest investment in a new infrastructure. In parallel to PIP-II development a project will be established to update the non-PIP-II portion of the control system. There is a substantial amount of aging hardware and software that will need to be replaced prior to PIP-II operations. As this is done more modern solutions for hardware and core software systems that are more directly compatible with EPICS will be adopted. Due to the large scale of the system, likely funding constraints, and the need to continue operating the main complex for most of the time leading up to PIP-II, this will be a gradual evolution.

11.4 Network infrastructure

The network for the PIP-II control system will be centered around a core router in the linac gallery connected to the central controls switch in the main computer room. There will be switches distributed along the gallery for connection of local devices. Separate VLANs will be provided for controls devices, video, VOIP, waveform data acquisition, and safety systems. The controls network is isolated from the general lab network by a firewall. Read-only access to the control system is available to authenticated users via gateway processes.

11.5 Computing infrastructure

Centrally located servers provide front-ends for ethernet connected hardware, central services such as data archiving and alarms and other processes required for machine operation, a central database, and console computers. Central file servers host all files needed by the control system. These run the Fermilab Scientific Linux operating system. A central database stores configuration and other data needed by applications and save/restore data. The current Sybase database will be migrated to PostgreSQL before PIP-II operations begin.

11.6 Front-end systems

Front end systems connect field hardware to the control system providing a common interface for everything in the control system. Front-ends developed for PIP-II will use the EPICS IOC framework. These will run on different platforms depending on the requirements and nature of the field hardware. Systems requiring hard real-time response will run on VME (or successor) based processors using a real-time operating system. Examples of such systems include beam diagnostic instrumentation. For ethernet connected field equipment where hard real-time response is not required conventional PCs running Linux will be used. Examples are front-ends for PLC based hardware such as vacuum and LCW cooling systems.

11.7 Central services

Central services include data archiving, alarms, data request consolidation, and calculational processes.

Each front-end is responsible for scanning its devices for alarm conditions. A central alarm server receives alarm messages from the front-ends and distributes them to active alarm viewing applications.

The data archiving system employs a parallel system of logging nodes each with an independent database. Data in a local logger wraps around when a size limit is reached. Central backup and archive loggers preserve a rate limited sample of the data indefinitely. For PIP-II this system will be upgraded with a higher performance, EPICS compatible archiving technology so that fewer logger nodes are required.

The current ACNET system allows collection and correlation of data on a pulse by pulse basis. Collection of multiple pulses in a single data packet is possible in some cases. However with the higher pulse rate and larger amount of data to be collected at PIP-II an updated and more standardized system for pulsed data acquisition will need to be created.

The current archiving system is limited when recording a high rate of waveform or other array data. For PIP-II to ensure optimal machine performance it will be desirable to record a substantial amount of such data from RF and beam instrumentation systems. A new system optimized for logging high rates of waveform data will be created modeled after instrument data acquisition systems used at light sources. This will involve long term storage and cataloguing of data as well as its acquisition and recording.

11.8 Applications

Applications provide the primary user interface to the control system. There are some general applications as well as applications that deal with very specific functions of the accelerator. In the current control system these are written in one of two frameworks. The first is based on the C++ language and X-windows graphics. The second is based on the Java language and graphics. All applications may be launched from a dedicated console framework. Also some web-based applications have been created, but there is not currently a standard framework for these. For PIP-II new console and application frameworks will be created using modern programming languages and user interface technologies. Web-based technologies will play a larger role.

General applications include a Parameter Page, plotting applications, Synoptic Display, archive and alarms viewers, device and front-end information viewers, a Sequencer, and an interface to the save/restore system. The Parameter Page presents tables of devices that can be viewed and manipulated by an operator. Plotting utilities allow convenient plotting of any device. Archive viewers allow full access to all archived data. The Synoptic Display is a framework where graphical displays may be created using a drag and drop builder without writing additional code. The Sequencer executes predefined sets of commands to perform complicated functions such as beam turn on and intensity ramp up. An editor is provided so that sequences may be created without traditional programming. For PIP-II, new versions of these core applications will be created. For some of these, previously developed EPICS-based solutions may be adopted.

11.9 Timing system

The current control system makes use of a 2-tiered timing system for the accelerators. The present top level is a 10 MHz based clock system (TCLK) that provides basic system co-ordination and data acquisition timing. The second level clock systems are specific to each accelerator and synchronous to beam in that machine (MIBS, RRBS, PCLK, NML-CLK & HINS_CLK). The beam sync clocks have base frequencies that are derived from the machine's RF to provide bunch level timing for devices such as intensity monitors, BPMs and kickers. Relevant clock events are reflected from one level of clock system to the other as needed to support operations and data acquisition. There is an additional system called MDAT that provides various machine data to the complex. Among MDAT's data are frames for individual machine states (MI, Recycler, BSSB and Switchyard), MI bus related data (programmed and measured currents and momenta) along with various intensity monitor readings.

A new upper level timing system (ACLK) will be developed that is expected to provide a major enhancement over the TCLK and MDAT links presently used in the main complex. A simple prototype has been developed based on a 1 Gbps data link that adds a data payload and cycle stamp to each clock event transmission. The latter will allow reliable correlation of data across different front-ends. A critical requirement of the new system will be its ability to be synchronous with the existing TCLK, as legacy systems around the complex that can only listen to TCLK (and MDAT) will need to be supported for the foreseeable future.

It is expected that the ACLK design will serve as the basis for a new Linac beam synchronous clock based on requirements for the SC linac with reflected ACLK events, cycle stamps and data payloads as needed. This clock in relation to ACLK will function in an analogous fashion to the existing PCLK at PIP2IT to TCLK today.

Chapter 12

Machine Protection System

12.1 Introduction

The Machine Protection System (MPS) for PIP-II is intended to protect the Linac and its components from direct beam-induced damage and excessive radiation damage from component activation. This MPS will be integrated into the entire Fermilab complex MPS so as to protect both equipment in PIP-II as well as associated downstream machines. Integration is key to the proper design of an MPS for a high-power accelerator as it necessarily spans virtually every subsystem, requiring knowledge of the relative "health" of all aspects of the machine itself and downstream destinations so as to ensure safe and reliable delivery of beam.

The main goal of the MPS is to inhibit the beam in case of excessive beam loss, equipment failures, or upon operator request in order to protect the machines from beam-induced damage. In achieving that objective, the system will include the following features:

- Manage beam intensity and permit limits of MPS-designated devices,
- Provide post-mortem data to the control system upon detected loss of an MPS permit,
- Provide a comprehensive overview of the machine state and readiness status to subsystems and the broader complex,
- Provide a global synchronization trigger for beam-related system fault analysis,
- Provide Linac beam status to the accelerator complex control system,
- Provide high availability and fail-safe operation where possible,
- Manage and display MPS-related alarms.

The MPS is not a personnel safety system, however, it is required to operate in a fail-safe manner and will include the personnel safety system as an input. The design will take into account the redundant implementation of critical MPS components, where possible, to reduce the probability of costly damage and corresponding downtime.

The MPS for PIP-II is based on the general design philosophies and best practices of existing and already-planned ones at similar facilities around the world [126].

12.2 Design

The PIP-II MPS will be comprised of a logic system that takes in signals from various sub-systems as inputs (system triggers) and drives permits to beam-enabling devices, removing these permits when an input signal generates a fault condition. These devices interacting with the MPS will be divided into primary and secondary categories based on how critical they are to mitigating beam damage. Primary devices are main actuators for beam and should guarantee that, when they function properly, no significant damage can be caused by the beam even if protection through secondary devices fail. The MPS will be initially designed to support pulsed beam operation with an eye to the potential for continuous wave operation in the future. To the extent possible, anticipation of CW operation will be factored into the design.

Both categories include sensing and beam-inhibiting devices. The primary beam-inhibiting devices are located at the Ion Source, in the Low Energy Beam transport (LEBT) section, and in the Beam Tranfer Line (BTL) at the output of the PIP-II Linac. They will include the LEBT chopper, the LEBT dipole, the Ion Source modulator, the Ion Source bias power supply, and devices directing beam to the abort line.

Dedicated instrumentation and diagnostics specifically developed for MPS use are included as primary inputs. Foremost is a differential beam transmission system which compares beam current at various locations along the linac as well as permit signals from downstream beam destinations indicating readiness to receive beam from the PIP-II linac.

The secondary beam inhibiting devices are those devices whose malfunctioning will not create dramatic damage; either because the effects can be detected and mitigated by the primary devices, or because the inclusion of the devices into the MPS is for the protection of the device itself (e.g. insertion devices). These secondary devices further decrease the probability of damage and possible irradiation of components. The list of secondary sensing devices includes the system providing the beam request sequence from the accelerator complex, status signals from the Linac subsystems, e.g., RF amplifiers, magnet power supplies, quench detection system, cryogenic system, LCW, the control system etc. In addition, these also include malfunctioning subsystems which can affect the beam delivery (e.g. RF amplifier) thereby dropping the Linac beam permit. Devices and systems that are beam losses indicators (like radiation monitors, current signals induced on scrapers by the beam), vacuum gauges, valves and positions of insertion devices will also be capable to inhibit the beam. Examples of beam-inhibiting secondary devices are the MEBT chopper, switching magnets, separators, and beam stops that can prevent the beam entering an alarmed area. General protocols

of interaction between the secondary devices and MPS together with details of specific levels and timings are prescribed in the necessary requirements documents.

The PIP-II MPS is based in large part on experience gained from commissioning and operating the Spallation Neutron Source (SNS) at Oak Ridge Laboratory along with that of the Fermilab Accelerator Science & Technology facility (FAST) superconducting linac as well as with experience already gleaned from the PIP-II Injector Test facility (PIP2IT) [127, 128, 129, 130]. SNS is a logical choice given that it is a 1-GeV linear accelerator capable of accelerating both H^- ions and protons employing both normal and superconducting RF sections. The FAST linac has accelerated electrons up to 300 MeV and its MPS is a basis for other MPS development at Fermilab including PIP2IT. PIP2IT has played a valuable role for operation of an MPS and also as a test bed for enhancements necessary for PIP-II operation.

The SNS peak current specifications are of order twenty times higher than the PIP-II peak beam current specification and its warm to superconducting RF transition occurs at 187 MeV as opposed to 2.1 MeV for PIP-II. Above 200 MeV, the PIP-II MPS hardware design and placement can be modeled after the SNS system. The PIP-II MPS system will not need response times as stringent as the SNS because of lower peak currents. The challenge for the PIP-II MPS comes from the protection of low energy cryomodules (2.1 MeV - 150 MeV) where the radiation created by beam losses has difficulty penetrating the cryomodule and beam pipe.

12.3 Protection of the Warm Front End

Detection of beam losses in the PIP-II warm front end is performed mainly by secondary devices, in particular by the scraping system. Complicated trajectories, which vary from bunch to bunch, and the changing beam structure along the beam line, make it impractical to designate a small set of devices to be primarily responsible for the beam loss detection. On the other hand, lower beam power density, negligible residual radiation, lower sensitivity of the warm elements to beam losses and their lower cost to replace, decreases the potential for critical beam-induced damage. The robustness of the warm front end should be achieved by the redundancy in secondary devices which protect the warm front end.

12.4 Configuration

The MPS will be the collection of all subsystems involved in the monitoring and safe delivery of beam to the dumps or designated user and not limited to any particular subsystem or diagnostic device. It has connections to several external devices and sub-systems. Figure 12.1 shows a conceptual overview diagram of the MPS. The top layer (1) comprises signal providers such as beam loss monitors, beam position monitors, magnet power supplies etc. Systems at this level send alarms or status information to the MPS logic subsystems (permit system) which issues a permit based on the comprehensive overview of all inputs and requests. Only simple digital signals

(e.g. on-off, OK-alarm) are transmitted. All devices or subsystems that are determined to be pertinent to protecting the machine or necessary for machine configuration are included. The Logic layer (2) of the MPS will be FPGA based, fully programmable to handle complex logic tasks. The overarching logic will be designed to ensure safe operating conditions by monitoring operational input, chopper performance, the status of critical devices and by imposing limits on the beam power. The final layer of the system shows the main actuators (3). This will comprise all points where the MPS logic may act on the operation of the machine to prevent beam from being produced or transported.

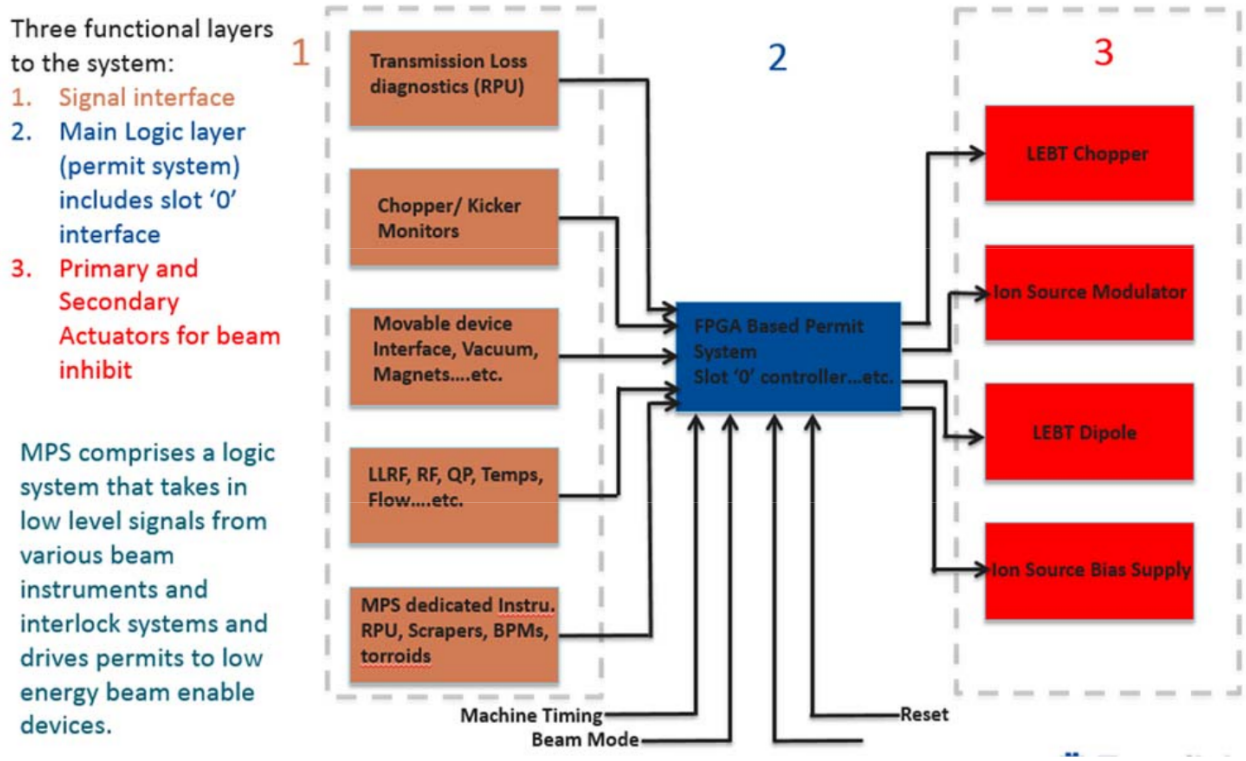

Figure 12.1: MPS conceptual layout.

The comprehensive overview of the entire machine will be obtained by monitoring of all relevant inputs from machine diagnostics and critical systems affecting safe operation.

PIP-II will accelerate to full energy and supply beam to downstream areas if an MPS permit is issued. The distribution of the beam between users is defined by the time sequence in the MEBT chopper and by bending magnet(s) according to usersâĂŹ requests summed in the Beam Switch Sum Box (BSSB). Removing a request by a user inhibits the beam to this user but generally allows running the Linac beam to other users.

In a case of observing of an un-requested beam or a failure requiring a fast and reliable termination of the beam, the user drops the permit, interrupting the entire Linac beam. The entire protection system interfaces with the accelerator control system and machine timing system for configuration management, timing and post mortem analysis as shown in Fig. 12.2.

The operational modes, operational logic, reaction time and complexity of inputs will differ based

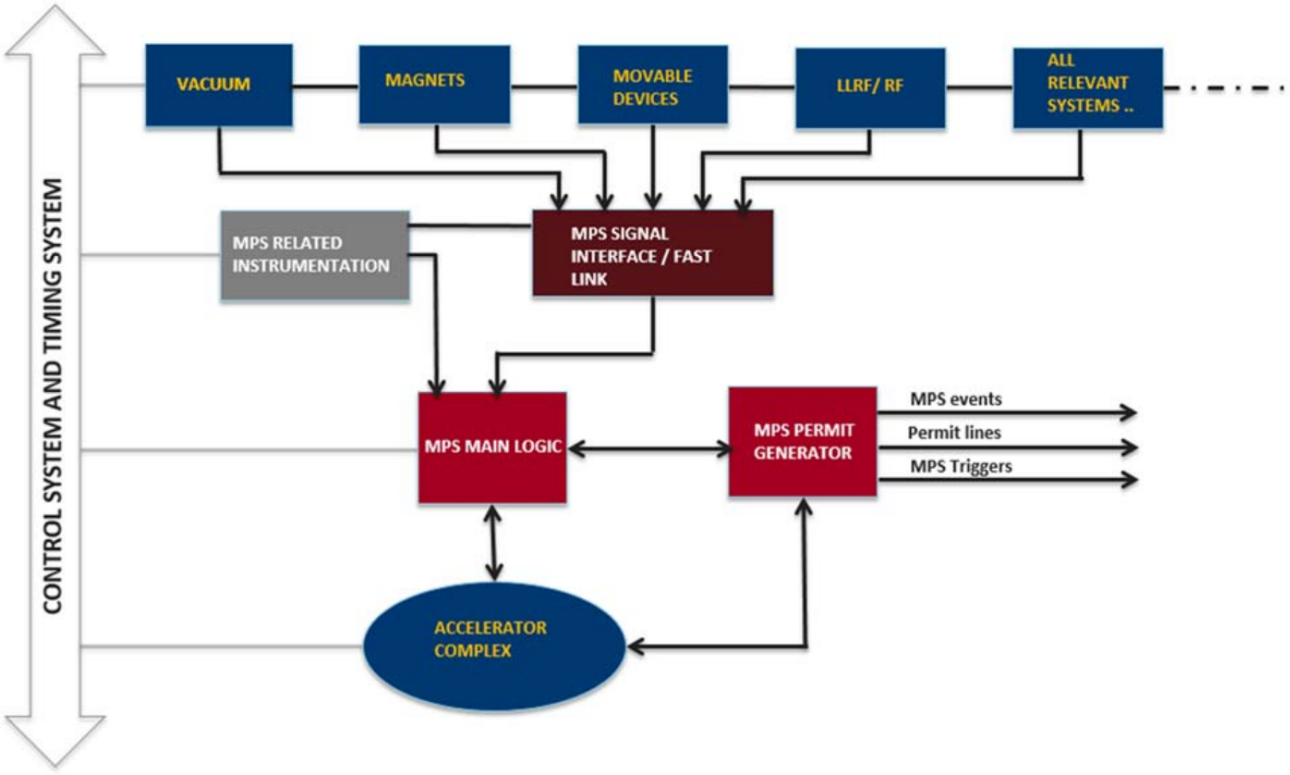

Figure 12.2: Conceptual MPS layout integrated with control system.

on the machine configuration and damage potential at various stages of the accelerator complex.

12.5 Specifications for primary systems

Preliminary specifications for the MPS are summarized in Table 12.1.

Table 12.1: Preliminary high-level MPS specifications.

Parameter	Value	Units
Average beam current	2	mA
Peak beam energy	800	MeV
Pulse width	0.54	ms
Pulse frequency	20	Hz
Duty factor	1.1	%
MPS response time	10	μs
Acceptable differential beam current	< 500	μA/μs

A drop of the beam permit will inhibit the Linac beam at the entrance of the RFQ within 10 μs after the PIP-II MPS receives the signal. Specific times scales relevant to interfacing to the global accelerator complex will be based on mitigating damage potentials at downstream machine location, specific hardware limitation, and signal time-of-flight issues. A separate interface document shall describe interaction between the PIP-II MPS and the remainder of the Fermilab accelerator complex, including these time requirements and protocols.

In the PIP-II Linac the primary systems for comparing beam current losses (Transmission Loss System) will identify the beam losses expressed as a difference between readings at specified locations and shall drop the beam permit if it detects a beam loss > 500 μA averaged over 1 μs sliding time window, and > 5 μA averaged over one power line period (1/60 s) for operation in the CW regime. The primary system will also drop the permit if it detects a large deviation of the measured beam pattern from the expected one. This deviation is deemed large when the average current measured in a 30 μs sliding time window exceeds the expected value by more than 20% of the beam current or 20 μA, whichever is larger. The MPS will inhibit beam in a single step or with a two-step process designed to limit downtime. Beam inhibits by the LEBT chopper will occur within 10 μs after a system drops its beam permit. This time is measured as the difference between the permit being removed at the failure location and the disappearance of the beam at the entrance of the RFQ.

Alternatively, if the average beam current measured by designated primary system devices does not drop below measurable level within 15 μs of the fall of the beam permit, the Ion Source modulator, LEBT dipole and the Ion Source bias power supply will be turned off in a fail-safe manner. MPS will be capable of initiating both steps at once in cases considered as potentially severe such as bad vacuum or failed subsystems. Scenarios with only one step is envisioned primarily to inhibit the beam in response to RF sparking, where recovery is typically fast and the beam can be restored automatically.

The MPS latching scheme will be capable of differentiating between the fault inputs. It will either latch the status of all failed system inputs on a fall of the permit and do not restart beam until an operator command to reset the permit and resume beam operations, or, for some pre-set fault inputs, resume operation automatically after a given time.

12.6 R&D

Protecting the superconducting cavities from low energy protons losses where the particle energies are too low to produce significant detectable radiation will be a major part of the developmental work needed to effectively inject beam without quenching these cavities. To achieve this, an R&D program to evaluate means for measuring these losses with sufficient sensitivity and develop an effective feedback for machine protection will be undertaken as part of future PIP2IT beam tests with the first two (HWR and SSR1) cryomodules installed as the test bed. Developing an effective algorithm to monitor the beam position as a feedback to machine protection will be of interest for both PIP2IT and PIP-II. The following goals as a result of designing, constructing and operating the PIP2IT MPS have either already been achieved or are planned:

- Understand and verify acceptable loss rates in the room temperature sections,
- Develop a strategy to monitor chopped beam from the MEBT,
- Estimate the particle shielding effects of superconducting cavities and cryomodules,
- Develop effective algorithms for the FPGA based logic system,
- Demonstrate effective integration with controls/instrumentation and all subsystems,
- Understand dark current effects as it relates to protection issues.

12.7 Dedicated instrumentation

Several diagnostic instruments will be dedicated to provide MPS-related functions and will be integral to MPS ability to determine errant beam events. These devices will be outside of the scope of normal diagnostic operation related to machine tuning and calibration. In particular, these are foreseen to be ring pickups (see Chapter 9) and MEBT kicker protection electrodes and scrapers. Several ring pickups will be dedicated to monitor the LEBT chopper performance, monitor beam intensity, and provide transmission loss information to the MPS.

In addition, electronics designed to monitor both MEBT kicker electrodes and machine scraper currents will provide fast comparative analysis of beam-induced current signals from these devices. It is planned to provide both digital and analog integration methods for monitoring excessive beam

loss of these devices. Figure 12.3 is a schematic diagram of the integration process that will be implemented. The integration criterion will be based on the characteristic time constant required to prevent damage to a given device. Ideally the total interruption time interval will limit the beam power to which the given device can be exposed below its damage potential limits.

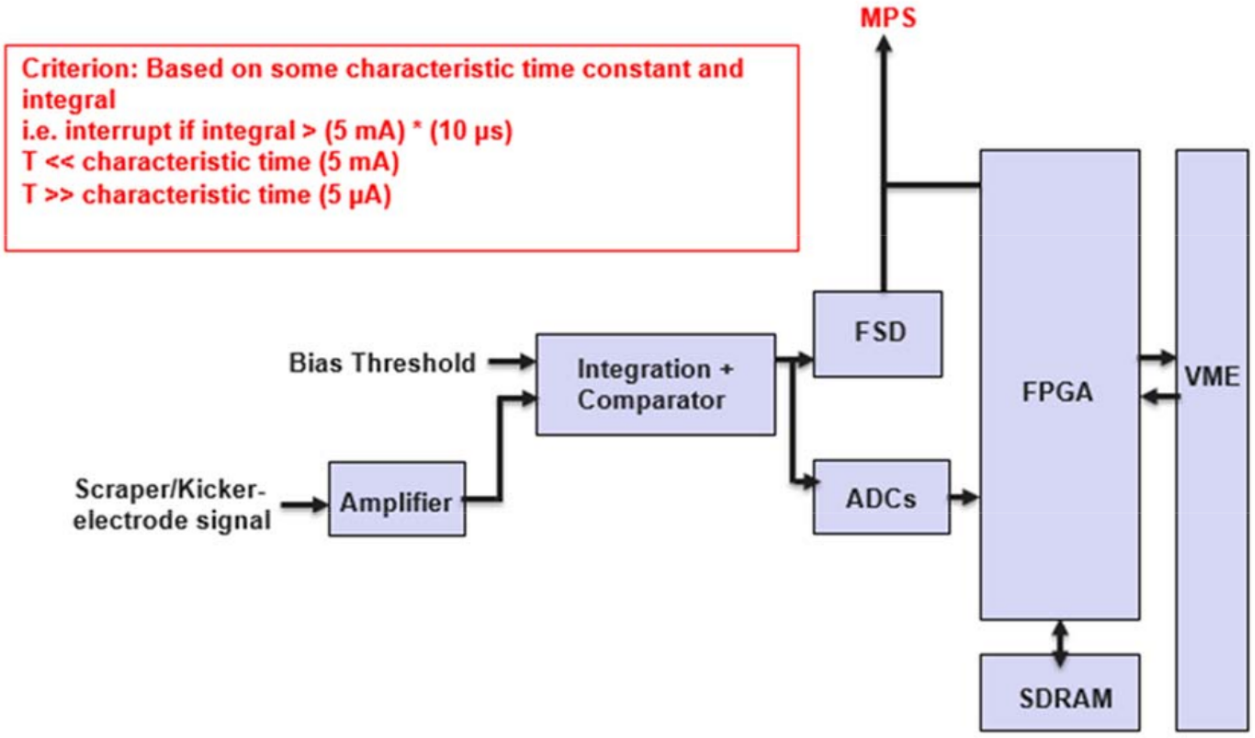

Figure 12.3: Schematic diagram of signal processing.

The PIP-II Linac is being designed to accelerate up to 2 mA average beam current. Initially the machine will provide 800 MeV high-intensity beams for the Fermilab neutrino program and should be capable of working in a pulsed (0.54 ms, 20 Hz) mode for injection into the Booster. That corresponds to 1.1% duty factor and an average beam current of 22 μA. The future mode of PIP-II operation is to deliver a quasi-CW beam simultaneously to multiple users (e.g. muon experiments). A quasi-CW beam implies that the beam current is constant when averaged over one period with duration of few microseconds, where the bunch sequence inside one period is set by requirements coming from experiments and, from the accelerator points of view, the bunch sequence is arbitrary (i.e. cannot be determined at the design stage, and can be changed at any time in the course of machine operation). This planned upgrade to CW operation implies that the total beam current and damage potential will be greater than in any present HEP Hadron Linac.

Chapter 13

Cryogenics

The PIP-II cryogenic system shown in Figure 13.1 consists of two major subsystems: the superfluid helium cryogenic plant and the cryogenic distribution system. The cryogenic plant provides the required cooling capacity at three nominal temperature levels: 35-40 K for the high temperature thermal shields and intercepts, designated as HTTS; 4.5 K for the low temperature intercepts, designated as LTTS; and 2 K for the SRF cavities and magnets within each cryomodule. The cryogenic distribution systems encompasses the various cryogenic and warm gas connections between the cryogenic plant and the cryomodules. Table 13.1 summarizes the cryogenic nominal operating temperature and pressure ranges for each circuit. The cryogenic system provides sufficient cooling at the appropriate temperature levels to enable operation of the SRF cavities and other cryogenic components within their respective operational conditions.

Table 13.1: Cryogenic system circuit operating temperature and pressure ranges, where ΔP is the pressure drop in the the HTTS line.

Circuit	P (MPa)	T (K)
4.5K CM Supply	$0.22 \leq P \leq 0.4$	≤ 4.5
2K CM Return	$2.7 \times 10^{-3} \leq P \leq 3.1 \times 10^{-3}$	≤ 3.8
LTTS Return	$P_{Supply} - 0.003$	≤ 9
HTTS Supply	$0.3 \leq P \leq 1.8$	$35 - 40$
HTTS Return	$P_{Supply} - 0.028$	≤ 80

The cryogenic system is expected to operate for twenty years, with an estimated continuous operation of two to five years without a scheduled shutdown. The expected availability of the cryogenic plant is 98%, which defines the availability of the entire system.

Availability refers to the fraction of time that the cryogenic system is able to provide the cooling required. PIP-II cannot deliver beam if the cryogenic system is not functioning. Therefore, the cryogenic system must have a very high availability. If properly designed, availabilities greater than 98% can be achieved. A number of features in the proposed cryogenic system design are chosen to achieve the 98% availability, including a back-up control power supply and a backup compressed instrument air system. Backup power is used to power the control system and other

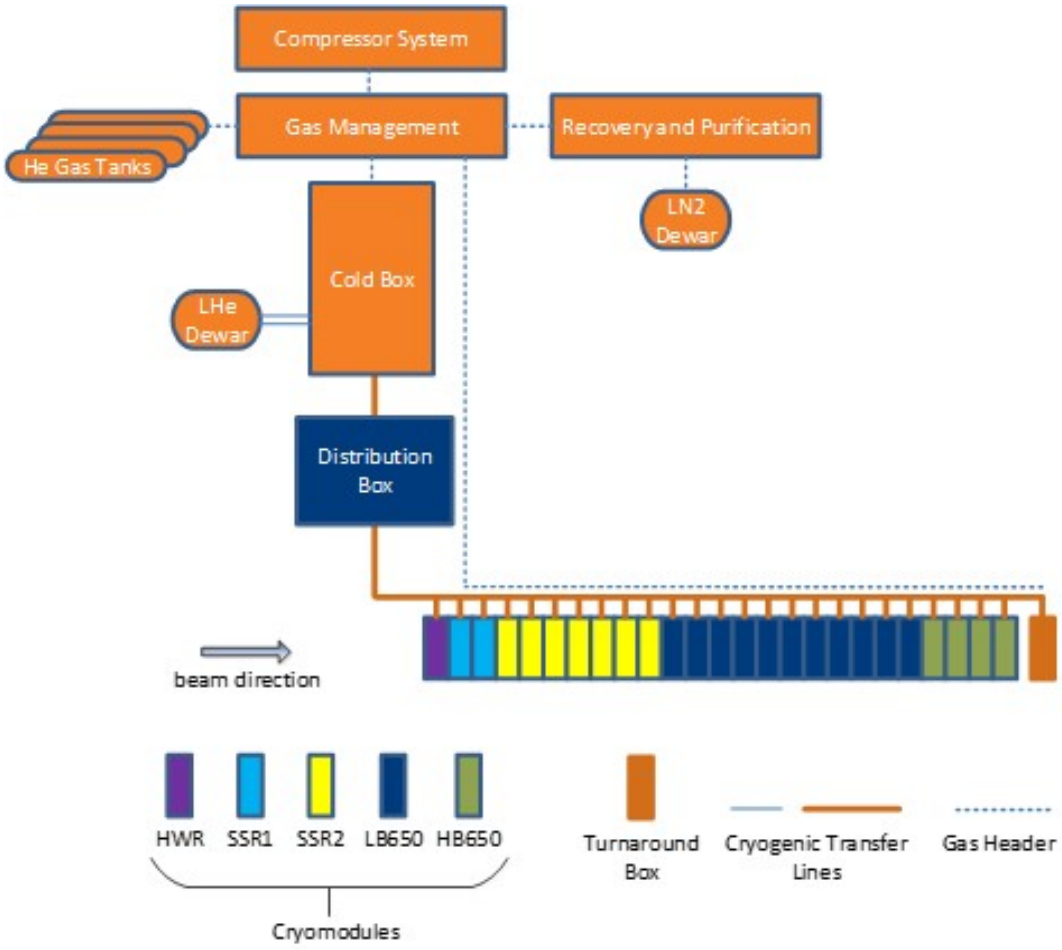

Figure 13.1: Simplified Layout of the PIP-II Cryogenic System.

critical systems during power outages. Given the large amount of power required to run the helium compressors it is not possible to power them with a backup power supply. Therefore, in the rare event of a site power outage, the cryogenic system shuts down.

13.1 Cryogenic plant

The detailed specifications for the cryogenic plant were developed jointly by Fermilab and DAE (India) as a part of the ongoing IIFC collaborative efforts. The cryogenic plant will be procured by DAE from qualified companies and supplied as an in-kind contribution to Fermilab.

The cryogenic vendor is responsible for the detailed cryogenic plant refrigeration cycle design, however the general configuration and components can be estimated based on similar cryogenic systems. Figure 13.2 shows a simplified schematic of the major components of the cryogenic plant. It can be broken into four primary systems: coldbox, warm compressor system, recovery and purification and bulk storage.

The overall layout of the cryogenic plant facility is shown in Figure 13.3. The coldbox room houses the coldbox and the liquid helium Dewar and the compressor room houses the warm compressor system, gas purification and recovery system. Outside of the building are seven 114 m^3 gas helium storage tanks and one vertical 3000 gallon liquid nitrogen Dewar.

The major interfaces of the cryogenic plant include those between the coldbox and warm compressor system, cryogenic distribution system and liquid helium Dewar. The coldbox is connected to the warm compressor system by a maximum of four warm helium lines; a high pressure delivery (HP), a medium pressure return (MP), a low pressure return (LP) and a sub-atmospheric return (SP). The physical interface between the coldbox and the cryogenic distribution system consists of a transfer line incorporating the six process lines. The transfer line contains a vacuum barrier to separate the insulating vacuum of the transfer line from that of the cold box.

The liquid helium Dewar, apart from providing a liquid helium buffer during regular operation, is used during the acceptance of the cryogenic plant and as another means of storing bulk helium during shutdowns. The physical interface between the coldbox and the transfer lines leading up to the liquid helium Dewar utilize bayonet couplings.

13.1.1 Safety factors for cryogenic plant capacities

The required capacity of the cryogenic plant is based on a detailed analysis of all the heat load contributions and applying appropriate safety factors. Safety factors that represent the uncertainty of the predicted cryogenic heat loads for each component must be defined to minimize the risk of undersizing the required cryogenic plant capacity. Undersizing can lead to operational issues and costly upgrades. Conversely, applying too large of a safety factor can lead to oversizing the cryogenic plant, leading to its own operational issues, inefficiencies and an overall costly system.

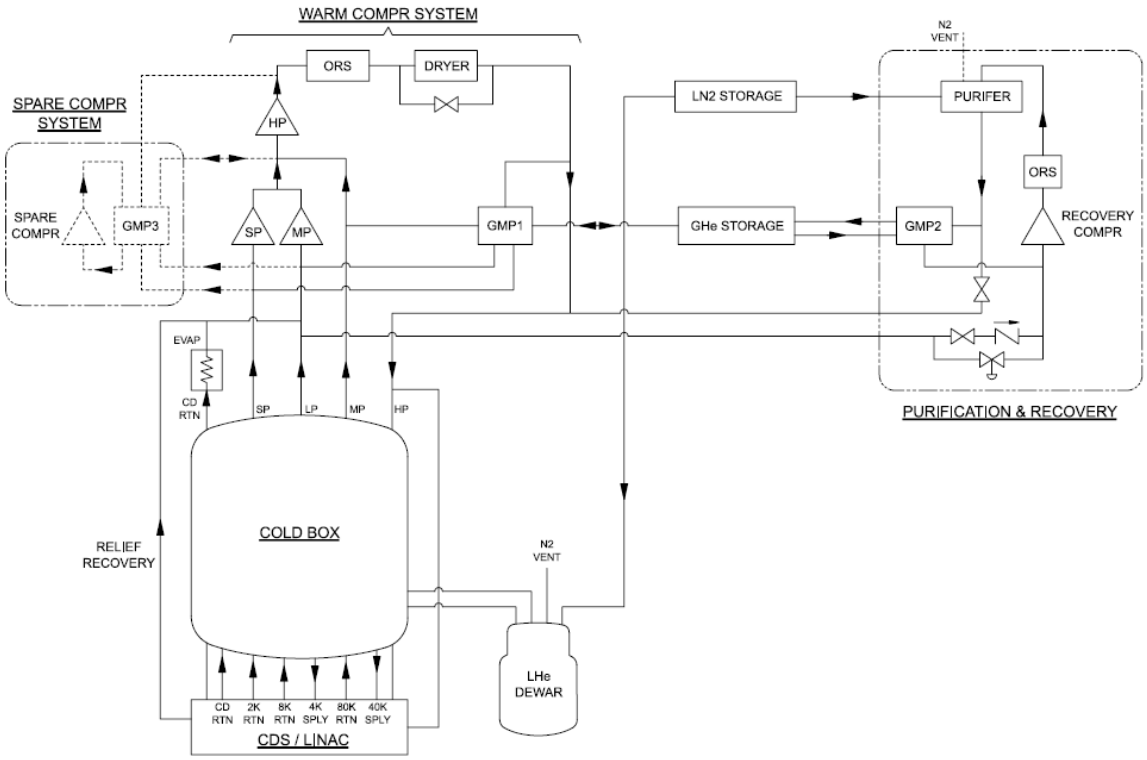

Figure 13.2: Simplified schematic of the integrated cryogenic plant system.

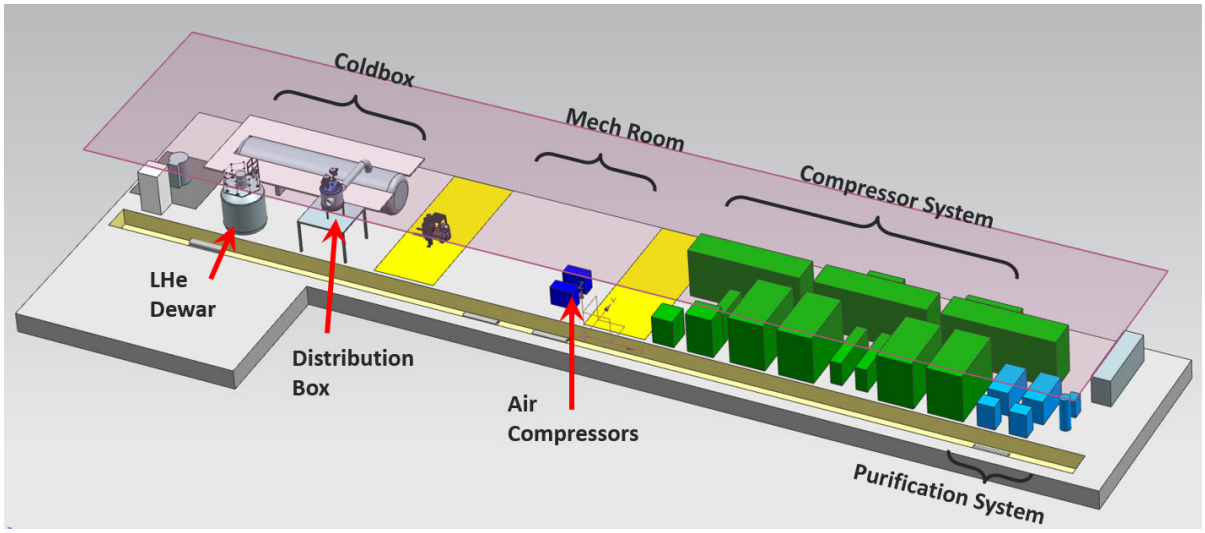

Figure 13.3: Overall layout of the cryogenic plant facility.

To avoid mis-sizing the cryogenic plant capacity, the safety factors and their application needs to be clearly and explicitly defined at the preliminary design stage and prior to the cryogenic plant contract. The PIP-II project uses the following formula for calculating the required plant capacity:

$$Q_C = F_O(F_S Q_S + F_D Q_D) \tag{13.1}$$

where

- Q_C is the required plant capacity
- Q_S is the predicted static heat load
- Q_D is the predicted dynamic heat load
- F_O is the operational safety factor
- F_S is the static heat load safety factor
- F_D is the dynamic heat load safety factor

The operational safety factor (F_O) is used to provide a capacity buffer to reliably operate the plant through system transients and potential performance degradation between maintenance periods. Therefore, the operational safety factor improves the availability and reliability of the cryogenic system. The static (F_S) and dynamic (F_D) safety factors represent the uncertainty in the static and dynamic heat load predictions, respectively. Table 13.2 lists the PIP-II cryogenic plant safety factors at each temperature level. The dynamic heat load safety factor is set to 1.15, representing the uncertainty and deviation in cavity performance achieved to date.

Table 13.2: Cryogenic plant safety factors at each temperature level.

Temperature (K)	F_O	F_D	F_S
2, 5 and 40	1.1	1.15	1.3

A summary of the predicted heat loads from the cryomodules and cryogenic distribution system to each temperature level are listed in Tables 13.3 and 13.4, respectively. The detailed analysis of the dynamic and static heat loads of each cryomodule is described in Chapter 7 and for the cryogenic distribution system later in this Chapter. These predictions are based on the preliminary cryomodule and cryogenic distribution systems designs and the expected performance. The dynamic loads of the cavities represent the average performance achieved to-date. The safety factors may be adjusted as the project advances and as additional design and performance data becomes available. Both the heat load analysis and the proposed plant sizing have been peer reviewed by external experts, see ED0008200 - PIP-II Heat Load Analysis.

The capacity of the cryoplant depends on the process return temperature, pressures and mass flow. To accurately specify these parameters, a thermodynamic model of the entire cryogenic system was developed. The model includes the heat load to the cryogenic distribution system and cryomodules,

Table 13.3: Cryomodule heat load at 800 MeV.

	2 K [W]	5 K [W]	40 K [W]
CM Dynamic	1419	407	1081
CM Static	274	684	3156
Total Nominal	**1693**	**1091**	**4237**
Total with SF	**2187**	**1493**	**5880**

Table 13.4: Cryogenic distribution system heat loads.

	2 K Return [W]	5 K Supply and Return [W]	40 K Supply and Return [W]
Total Nominal	250	134	1971
Total with SF	**358**	**192**	**2819**

the JT heat exchanger effectiveness (0.85) and the JT expansion process to determine the percent flash and ultimately the 2 K return flow rate.

Contamination in the helium gas can lead to capacity degradation due to reductions in turbine efficiencies and heat exchanger effectiveness. Therefore, the cryogenic plant facility includes an active contamination monitoring system, a full flow purification system internal to the coldbox and a smaller purification/recovery system for initial clean-up. In addition, PIP-II will leverage Fermilab's well-established operational procedures and best practices to avoid contamination issues.

13.1.2 Warm compressor system

The warm compressor system design is the responsibility of the cryogenic plant vendor, but certain design features can be anticipated based on compressor systems from similar cryogenic plants. The warm compressor system is expected to utilize oil flooded screw compressors configured in three stages. The coldbox's sub-atmospheric pressure (SP) return is compressed by the SP compressor directly to the medium pressure (MP) level. In parallel, the low pressure (LP) return gas is compressed by the LP compressor to the MP level. The MP coldbox return gas is combined with the SP and LP compressor MP discharge, before being compressed to the high pressure (HP) level by the final HP compressor stage.

The compressor oil temperature is maintained with oil to water heat exchangers using industrial water for cooling. The helium discharge temperature is reduced using an aftercooler heat exchanger before entering the oil removal system. The oil removal system sequentially removes bulk oil, oil mist, oil vapor, water vapor and particulates before the flow enters the high pressure gas header supplied back to the coldbox. The oil removal system consists of three stages of oil coalescers, a charcoal adsorber, a dryer and a final particulate filter.

The gas management system controls the SP, LP, MP and HP pressures and the loading and unloading of helium to and from the pure gaseous helium storage. The warm compressor system pressure stages are regulated by the gas management system to optimize operating efficiency through each operating mode.

13.1.3 Recovery and purification system

In addition to the primary coldbox compressor system, a separate recovery and purification compressor system is integrated into the overall cryogenic plant. The recovery and purification system allows operators to clean the system prior to initial start-up, decontaminate during shutdown periods and decontaminate bulk helium gas supplies prior to entering the active system. In addition, the system allows recovery of helium gas during unplanned power outages and short maintenance periods when a full system warm-up is not desired or if the total gaseous helium inventory of the system is larger than the available gas helium storage capacity.

A gas management panel for the recovery/purifier compressor system is used to regulate the recovery compressor suction and discharge independently of the primary gas management system of the coldbox compressor system and allows for purification of individual gas helium storage tanks and bulk helium gas supplies. The recovery compressor system is interconnected with the coldbox primary HP supply and LP return. Combined with the primary gas management system the entire system can be scrubbed and purified.

13.1.4 Coldbox

A simplified schematic illustrating the primary components within the coldbox is shown in Figure 13.4. The HP compressor discharge gas stream enters the coldbox at 10-20 K above room temperature due to the preceding heat of compression. The HP flow enters a series of heat exchangers, where it is counter-flow cooled by the returning MP, LP and SP streams below 80 K, before entering an inline adsorber for removing contamination. The HP stream is then further cooled by passing through additional heat exchangers and turbine expander branches that produce refrigeration by expanding a portion of the HP stream into the MP or LP return streams. At ∼35 K to 40 K, one part of the HP stream is used for the Linac HTTS supply. The HTTS return enters at the ∼80K point where it is heat exchanged with incoming HP helium. At ∼20 K, the HP stream enters another charcoal adsorber to remove neon and hydrogen contamination. The HP stream is then further cooled by additional counter flow heat exchangers with cold return gas from the Linac and/or additional turbine expansion branches. The HP stream undergoes a final expansion through an inline turbine to ∼5 K. Downstream, the helium is typically subcooled to 4.5 K by a helium subcooler bath.

The 4.5 K supercritical helium is then sent to the 4.5 K Linac supply for cryomodule cavity and LTTS cooling or to the liquid helium Dewar for capacity regulation and/or storage. The LTTS return is fed into the ∼8 K point of the LP stream of the coldbox to heat exchange with the HP stream. The SP return gas from the 2 K load enters the coldbox at ∼3.8 K and is compressed by

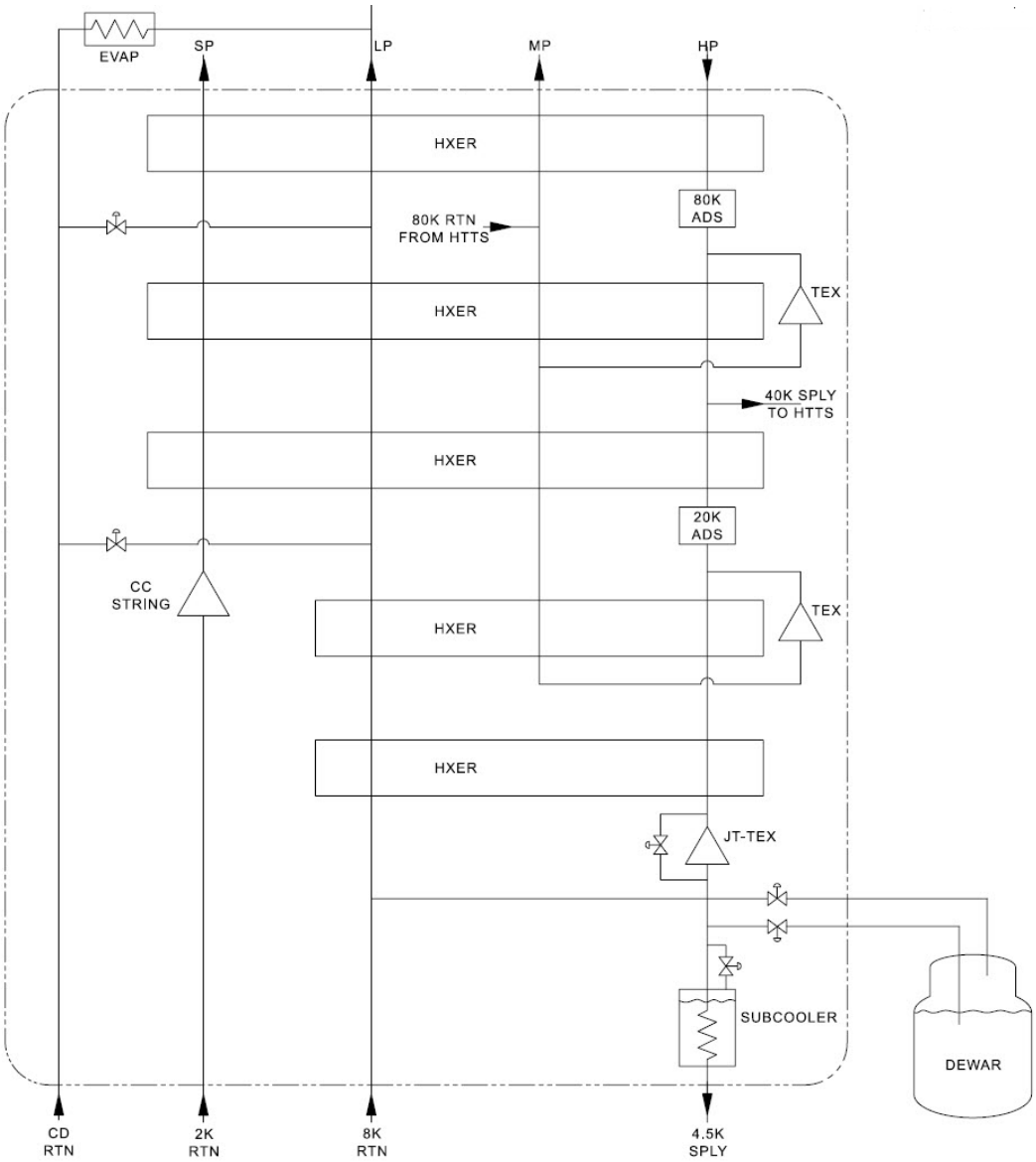

Figure 13.4: Simplified schematic of coldbox showing primary features.

a string of three cold compressors from ∼30 mbar to 300 to 500 mbar and heat exchanged with the HP supply stream. The MP, LP and SP streams all exit the coldbox at approximately room temperature and flow back to the warm compressor system where the gas is recompressed to HP discharge pressure and fed back to the coldbox, thus closing the loop.

13.1.5 Mixed compression cycle

The cryogenic plant supplies 4.5 K helium at 3 bara to the cryomodules. The 4.5 K helium heat exchanges with the 2 K return gas by utilizing JT-heat exchangers located within each individual cryomodule. The subcooled helium undergoes JT-expansion into the 2 K bath. This approach minimizes the isothermal heat load to 2 K and limits the possibility of two-phase flow in the cryogenic distribution system.

To achieve a saturation temperature of 2 K, the liquid helium bath surrounding the cavities must be maintained at a pressure of ∼30.7 mbar by continuous pumping of the helium boil-off and returning it to the cryogenic plant to recover the refrigeration. In plants of this size, there are two options for such a pumping system; a string of five cold compressors or a string of three cold compressors backed by a warm vacuum compressor. The mixed compression cycle has the major advantage of being capable of operating efficiently over a wide range of capacities [131]. Since, the PIP-II Linac has a wide range of operating heat loads from 2 K static, to full dynamic heat load, the cryogenic plant utilizes the mixed compression cycle.

In addition to normal turndown of the plant capacity through the mixed compression cycle method, a mass flow compensation scheme of heaters and/or an LP to SP bypass is utilized to provide make-up flow in case of sudden transient changes in load. This mass flow compensation scheme gives the refrigerator time to adapt and keep the cold compressors within their operating field. The cryomodule bath pressure of 31 mbar is regulated within ±1 mbar by the cold compressors and by means of 2 K return control valves in each cryomodule bayonet can. The mixed compression cycle was also recently chosen by XFEL (DESY) and the European Spallation Source (ESS) in Lund [132],[133],[134],[135].

13.1.6 Bulk helium storage

The total required gas helium storage capacity is based on the estimated cryogenic system process volumes and associated helium density in each circuit during normal operations. The entire inventory of the PIP-II Linac and cryogenic system can be stored in either liquid form in the liquid helium Dewar or gaseous form in the ten gas helium storage tanks. A summary of the required helium storage capacity is presented in Table 13.5. It is assumed that during normal operation, 15% liquid volume will be maintained in the liquid helium Dewar and 2 bara of equivalent buffer pressure will be maintained in a reduced set of gas helium storage tanks. The large liquid storage capacity combined with the helium recovery compressor, provides the flexibility of storing the entire Linac capacity into the liquid helium Dewar and recovery of the boil-off into the gas helium storage tanks during maintenance periods.

Table 13.5: Summary of helium inventory volumes and storage capacity.

	Volume (m^3)	Level (%)	Pressure (bara)	Temperature (K)	Mass (kg)
GHe Buffer	1140	-	2	300	371
WCS	20	-	18	300	22
CP	3.46	-	-	-	216
LHe Storage	20	15%	1.2	sat. liq.	375
Linac	9.57	-	-	-	1286
CDS	37	-	1.3	4.5	317
TOTAL	-	-	-	-	**2586**

	Volume	Level	Pressure	Temperature	Mass
GHe Storage (10 tanks)	1026	-	16.2	300	2701
Full LHe Dewar	20	90%	-	-	2250

13.2 Distribution system

The PIP-II cryogenic distribution system consists of the equipment required to feed and return the cold helium from the cryogenic plant via vacuum insulated piping to the SRF Linac cryomodules. Figure 13.5 shows the scope of the cryogneic distribution system (excluding cryomodules). The cryogenic distribution system is divided into three main sections: a connection to the cryogenic plant (via a short transfer line and distribution box), a distribution box to Linac distribution line and cryomodule bayonet boxes.

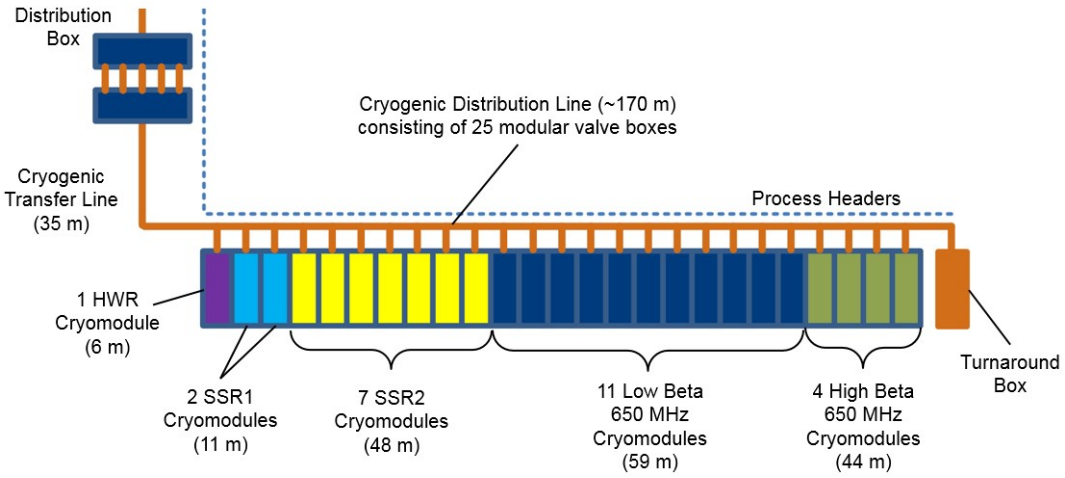

Figure 13.5: Cryogenic distribution system.

Key features of the cryogenic distribution system include:

- All cryogenic supply and return lines are installed within one common, vacuum-jacketed cryogenic transfer line, the diameter of which is primarily driven by the 2 K sub-atmospheric

helium return line.

- The cryogenic distribution system transfer line consists of six circuits as listed below:
  - 2 K sub-atmospheric helium return
  - 4.5 K helium supply
  - Low temperature thermal shield (LTTS) return
  - High temperature thermal shield (HTTS) supply
  - High temperature thermal shield (HTTS) return
  - Warm up and cool down (WUCD) return
- Transfer line circuit operating parameters are listed in Table 13.6.
- The cryogenic distribution system has a WUCD return line to recover refrigeration during cool down of the cryogenic distribution system and cryomodules by returning gas to the cryogenic plant.
- Note: a 4 K heat exchanger and JT valve is located in each cryomodule and not located within the cryogenic distribution system.
- The 4.5 K helium supply is divided into two streams inside the cryomodules, one of which is directed to the heat exchanger and subsequent JT valve, while the other is directed to the Low Temperature Shield (LTTS). This LTTS return line enters the cryogenic distribution system at a temperature of about 9 K in normal operation.
- Each cryomodule is connected to the cryogenic transfer line via vacuum insulated bayonet connections also called u-tubes (one for each cryomodule circuit). This provides for maximum segmentation of the Linac.
- The cryogenic distribution system transfer line utilizes twenty-five inline bayonet cans (one for each cryomodule) and a turnaround box at the end. In parallel, there is a warm helium vent header.
- The system allows for individual cool down and warm up of a cryomodule, while keeping the rest of the system at cryogenic temperatures. The cool down warm up time is limited by the temperature rate constraint fo 10 K/hr for the HTTS. Therefore cool down or warm up is anticipated to take approximately 24 hours from room temperature to operating temperature.
- The estimated transfer line circuit sizes are listed in Table 13.7.

Table 13.6: Cryogenic distribution system transfer line circuit parameters

Circuit	Nominal Temperature K	Operating Pressure bar	Estimated Pressure Drop kPa
4.5 K Supply	4.5	2.2 to 4.0	25
LTTS Return	9	2.2 to 4.0	3
HTTS Supply	40	3 to 18	5
HTTS Return	80	3 to 18	7
Cooldown Return	10 to 300	3 to 18	-

Table 13.7: Estimated Transfer Line Circuit Nominal Pipe Sizes

Line description	Line size (in.)
4.5 K Supply	2
2 K Return	10
LTTS Return	2
HTTS Supply	2
HTTS Return	2
Cooldown Return	3

13.2.1 Connection to cryogenic plant

The cryogenic distribution system connects to the cryogenic plant via a short multi-circuit transfer line which in turn connects to a distribution box. The distribution box provides isolation between the cryogenic plant and the rest of the cryogenic distribution system via a combination of bayonet connections (u-tubes) and multiple valves in series. The distribution box also includes relief valves for protecting the process circuits of the cryogenic distribution system.

13.2.2 Interconnect transfer line

A multi-circuit transfer line, approximately 40 m (130 ft) in length, extends from the distribution box located in the cryogenic plant building to the Linac tunnel to supply cryogens between the cryogenic plant and cryomodules. The transfer line exits the cryogenic plant building from the top of the cryogenic plant and extends outdoors towards the Linac complex high bay located above the Linac. It then vertically enters a penetration to an alcove in the Linac, upstream of the halfwave resonator cryomodule where it connects with the Linac tunnel distribution line. Running along the transfer line are additional process piping such as a low pressure return header, a relief vent header, a high-pressure supply header and compressed instrument air lines.

13.2.3 Cryomodule bayonet boxes

In the Linac tunnel, the interconnect transfer line connects to the Linac tunnel distribution line through an alcove upstream of the halfwave resonator cryomodule. In this Linac section, the cryogenic distribution system consists of transfer line sections with individual bayonet cans for each cryomodule running the length of the SRF Linac. The cryomodules are connected in parallel to the cryogenic distribution system with each cryomodule having its own insulating vacuum separate from the cryogenic distribution system. Each cryomodule is connected to its corresponding bayonet box via vacuum insulated u-tubes, one for each cryogenic process circuit. Note, the cooldown return circuit flow path is routed within the cryogenic distribution system bayonet cans and not within each individual cryomodule and therefore does not require its own independent u-tube. At the end of the cryogenic distribution system, there is a turnaround box for returning cryogenic flows to the cryogenic plant. The function of the turnaround box is for flow control during various modes of operation and to allow independent cooldown and operation of the cryogenic distribution system transfer line and consists of three cryogenic control valves and a phase separator which allow turn around flow for each supply circuit. The turnaround box also includes relief valves for protecting the process circuits of the cryogenic distribution system. In addition, running alongside the Linac tunnel distribution line are warm helium discharge, suction and vent headers. The bayonet boxes connect the cryogenic distribution system to the cryomodules as shown in Figure 13.6.

The bayonet boxes and Linac tunnel distribution line provide the following functions and features:

- Each circuit within a bayonet box includes a cryogenic valve to isolate each process line from a given cryomodule.
- Positive isolation of each process circuit to a cryomodule by removal of individual u-tubes.
- Independent cooldown and warmup of each cryomodule.
- A turnaround box is located at the end for turnaround flow control.

13.3 Integrated cryogenic control system

High level reliability and availability of the cryogenic system is achieved through automation of the cryogenic operations using an integrated cryogenic control system. The system is controlled by a programmable logic controller (PLC) based system that communicates to the ACNET based human machine interface (HMI) through a Gateway OPC. The detailed accelerator control architecture is presented in Figure 13.7. The cryogenic plant PLCs and cryogenic distribution system PLCs directly communicate to each other through Ethernet. The ACNET based system allows the operators to control, data log, trend and configure alarms for the entire cryogenic system. This model has been successfully employed at Fermilab for decades, during the historic operation of the Tevatron cryogenic system and current operation of the various cryogenic test facilities.

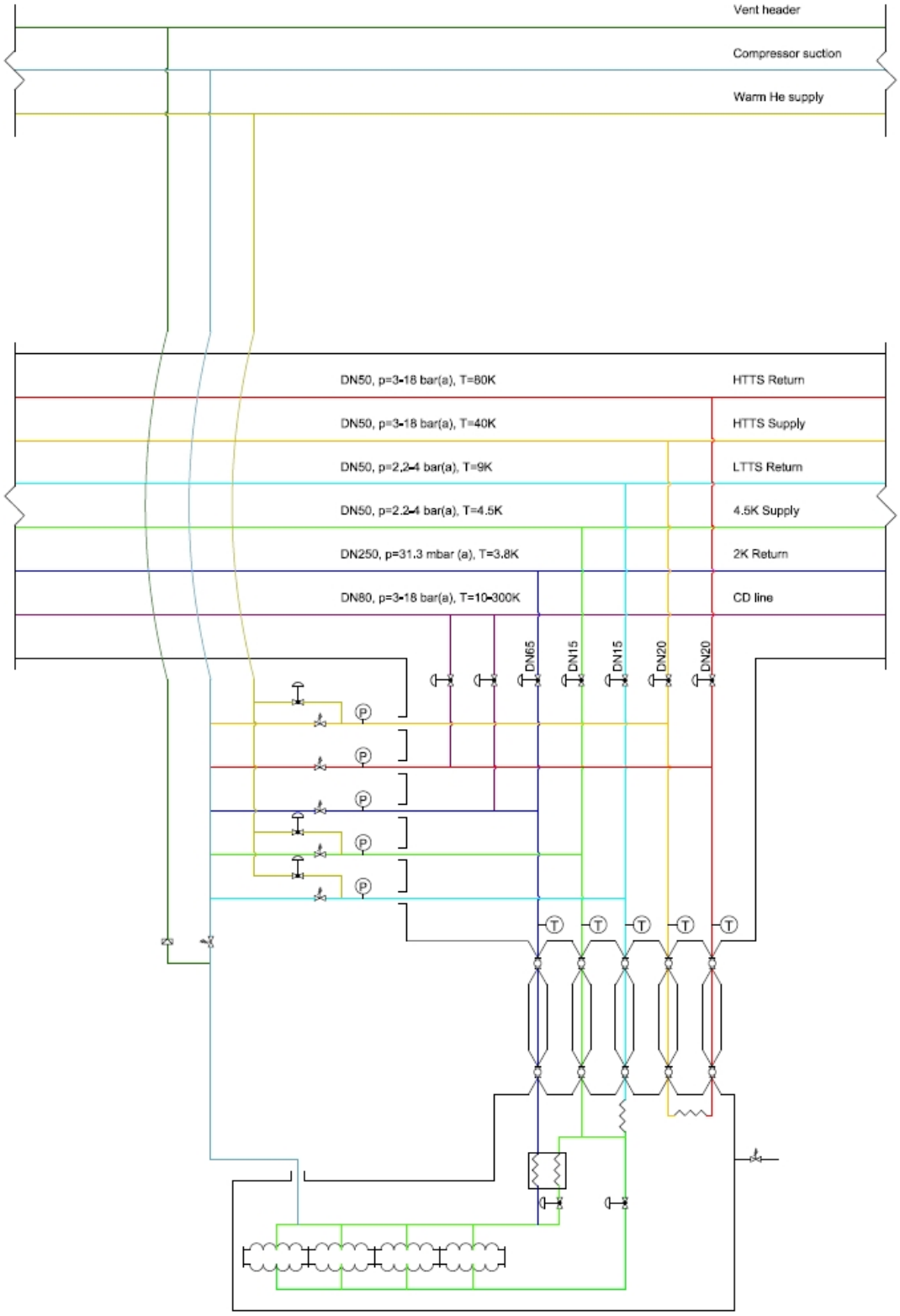

Figure 13.6: Process diagram of the cryogenic distribution system connection to a cryomodule.

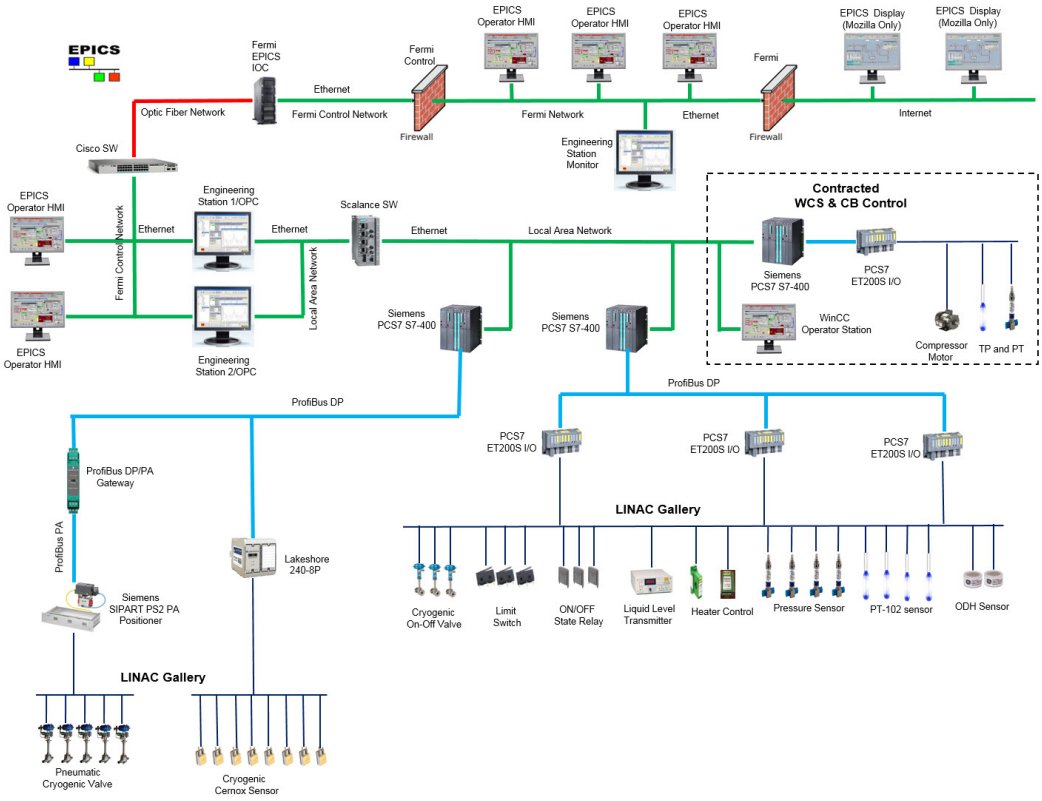

Figure 13.7: Preliminary distributive control system for the PIP-II cryogenic system.

Chapter 14

Vacuum Systems

14.1 Accelerator vacuum systems

The PIP-II vacuum system includes all of the vacuum environments which the beam passes through on the way from the ion source to the Booster. The vacuum system includes three regions: (1) the frontend (ion source, LEBT, RFQ, MEBT), (2) Main Linac which includes all cryomodules, and (3) the beamline from the Linac to the Booster. There are vacuum gate-valves capable to isolate each section for commissioning or operation. The vacuum system design is focused on the requirement of a low particulate vacuum that is sufficient but practical and cost efficient to ensure reliable performance of the cryomodules. The vacuum system also includes the insulation vacuum of cryomodules, which is absolutely essential for their operation. Requirements for the insulation vacuum systems are covered in the Functional Requirement Specifications and Interface Documents for the cryomodules [136], [137], [137], [138], [139], [140].

The PIP-II vacuum system faces significant technical challenges, including a large hydrogen flux from the H- ion source (500 mTorr-l/s) and large outgassing from the MEBT absorber ($\sim$1 mTorr-l/s at 10 mA ion source current). Therefore, pumps with high effective pumping speed have to be used within available space, which is quite tight in many places. Turbo pumps have been chosen for the ion source, RFQ and the MEBT beam absorber. Ion pumps are used for distributed pumping among the beamline where applicable.

The greatest challenge is probably the risk minimization for performance degradation of SC cryomodules due to excessive gas load and migration of micro-particles. Therefore, it is important to apply low particulate vacuum practices in vicinity of cryomodules and, in particular, upstream and downstream vicinities of the SC Linac. The roughing/venting ports are arranged so that to minimize particle migration towards cryomodules. The flow rate of roughing/venting is regulated to reduce the risk of particle migration in the course of pumping/venting. Differential pumping scheme is arranged at the vicinity of cryomodules to minimize the hydrogen gas flux towards them.

As usual, the gate valves are included in the interlock system to minimize consequences in the case

of vacuum incidents. Data logging will be implemented for operation and analysis.

14.2 Functional requirements

The requirements for PIP-II vacuum vary depending on the characteristics of the specific regions. A summary of the residual pressure for various regions is shown in Table 14.1. The vacuum requirements can be classified in three levels: 1) Ultra High Vacuum (UHV) and Low Particulate Practice for Main Linac; 2) UHV and Low Particulate Practice for the transition regions located upstream and downstream of the SC Linac; 3) High Vacuum for the region from Ion source to the MEBT absorber and the beam transfer line to Booster. All components shall be vacuum certified accordingly before being installed in the beamline.

14.3 Vacuum sections

Ion Source - The ion source is continuously supplied with hydrogen gas in order to produce H- ions. Inside the plasma chamber a hydrogen pressure is about 3×10^{-2} Torr, while the pressure downstream of ion source should be better than 10^{-6} Torr in order to avoid excessive beam loss due to H- stripping. The pumping system and internal structures of the ion source and the vacuum box are designed to achieve this large pressure gradient within several inches. Classified as a High Vacuum (HV) region.

LEBT - The low energy beam transfer line provides beam focusing, beam analysis and proper beam parameters prior to entering the RFQ. A pressure of 10^{-6} Torr is required in this $\sim$2 m long region. To prevent an unacceptable amount of doubly stripped protons in the LEBT which will be accelerated by the RFQ, the LEBT is interlocked if pressure is higher than 10^{-5} Torr. Classified as a HV region.

RFQ - The RFQ accelerates the H- beam to 2.1 Mev. It requires 10^{-7} Torr vacuum for normal operation. Classified as a HV region.

MEBT - The medium energy beam transfer line prepares the H- beam time structure prior to entering the HWR (the first cryomodule) by removing (chopping) undesired bunches. Typically, 50 - 80% of the H^- beam is chopped out and directed to the absorber. Sputtering and hydrogen production (due to incoming H^- flux) at the absorber are expected in normal operation. From the ion source to the MEBT absorber, only a regular high vacuum is achievable with reasonable cost. This is classified as a HV region. The region from downstream of MEBT absorber to the HWR is the transitional area bridging the regular high vacuum environment to the ultrahigh vacuum and low particulate environment in the cryomodules. This is critical for normal operation of the cryomodules. The UHV and low particulate requirement is applied to the design, cleaning and installation in this region. This is classified as a UHV and Low Particulate region. A fast acting gate valve is installed upstream of cryomodule, in order to protect CM from contamination due to

Table 14.1: Beam vacuum requirements.

	Ion Source	LEBT	RFQ	MEBT	MEBT-DS	CMs	Warm Units*	Trans Section	BTL
Pressure (torr)	10^{-2} to 10^{-6}	10^{-7}	10^{-7}	10^{-7}	10^{-10}	10^{-10}	10^{-10}	10^{-10} to 10^{-8}	10^{-8}
Leak check sensitivity (mbar-l/s)	2×10^{-9}	2×10^{-9}	2×10^{-9}	2×10^{-9}	2×10^{-10}	2×10^{-10}	2×10^{-10}	2×10^{-10}	2×10^{-9}
Pumping	Turbo pump, Ion pump				Ion pump	Cryo	Getter	Ion pump	
Vacuum seals joints	metal gasket or elastomer; CF† or KF‡					CF only: metal gasket only			metal gasket
Parts cleaning	UHV procedures								
Gauging	Ion gauge					CC△ gauge		Ion gauge	
Low particulate practice	no	no	no	no	yes	yes	yes	yes	no
Controllers	Equipped with RS485 to communicate with control system via a PLC								

*Transition Section is defined as the vacuum space between the CM's and BTL

†Conflat flange (metal gasket flange)

‡Elastomeric o-ring flange

△Cold cathode

vacuum failure.

Cryomodule Beam Vacuum - The cryomodules operate at 2K. The internal surfaces provide sufficient cryo-pumping effect so that the residual gas pressure is lower than 10^{-10} Torr, mainly driven by the operational temperature. The challenge for this region is to achieve low enough pressure (10^{-7} Torr) at room temperature before cooling down. All areas between cryomodules, including the Warm Units (1100 mm inserts) between 650 MHz cryomodules (see Figure 14.1) are also classified as UHV and Low particulate as well. Gas flow control, proper filtration and cold trap shall be applied for pumping down and venting up. Cold Cathode (CC) gauges shall be used to minimize the heat load from gauging. This is classified as an UHV and Low Particulate region.

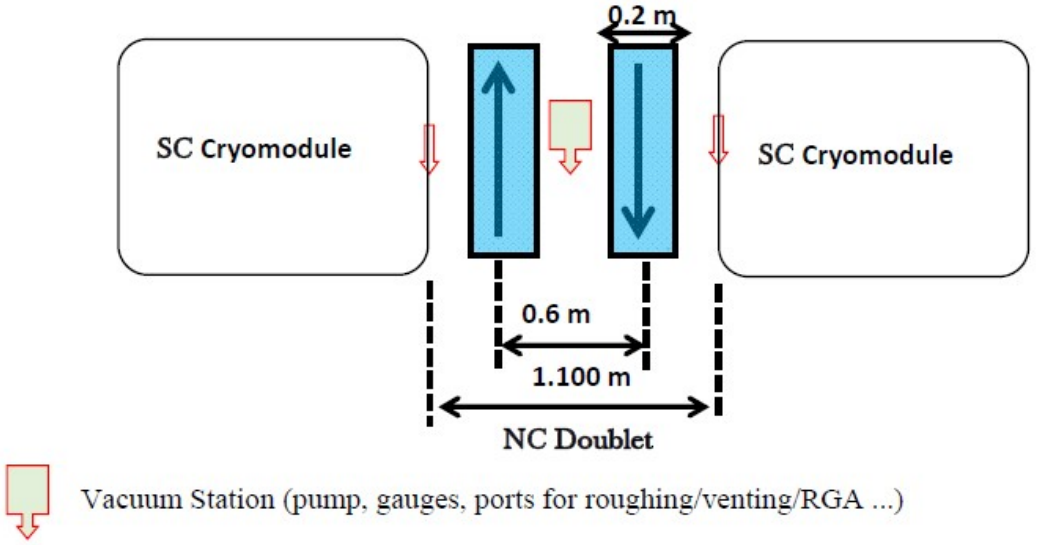

Figure 14.1: Warm inserts between 650 MHz cryomodules.

CM Insulating Vacuum - The pressure shall be 10^{-5} Torr prior to cooldown. This system is pumped with turbo and roughing pumps. The pressure shall be maintained at 10^{-6} Torr or better when cold. CC gauges shall be used. Pumps used in this system should not be used for the UHV system because of contamination. Classified as HV region.

Linac-to-Booster transfer line - The beamline consists of magnets and beam instrumentation at room temperature. It connects the SC Linac and Booster. In order to maintain a high quality vacuum in the cryomodules at the Linac end, the UHV and low particulate requirement shall be applied in its differential pumping section for transition to the regular beam transport line. It requires cleaning of beam pipes and clean installation of this region and is classified as a UHV and Low Particulate region. A fast action gate valve is installed at the Linac end to protect the cryomodules from contamination due to vacuum failure.

14.4 Components

Materials - Materials chosen for vacuum components must not only have a low outgassing rate with no contamination in general, but also must be resistant to radiation and corrosion, and have low magnetic permeability, particulate generation, etc. in the specific environment. Plating or coating is not allowed in areas that require low particulate vacuum. Vacuum personnel shall be informed and/or involved in all material related decisions.

Beam pipe - All beam pipes in an UHV region must be electropolished and hydrogen degassed, an in-situ bakeout may be required. 316L stainless steel must be used in areas sensitive to corrosion, magnetic field and/or high radiation.

Flanges - CF flanges (70° preferred) are required in UHV and preferred in HV.

Gauges - Inverted magnetron cold cathode gauges (CC's), thermocouple gauges (TC's), ion gauges (IG's), convection gauges (PG's), capacitance manometers, and residual gas analyzers (RGA's) are required.

Hardware - In the low particulate vacuum regions, standard unplated ConFlat® copper gaskets should be used with the ConFlat® flanges. They should be ordered individually wrapped and already UHV cleaned. Bolts and studs shall be made of domestic 316L unplated stainless steel. Nuts should be 651 silicon bronze. Silicon bronze studs should be used for blind holes. Nuts, bolts, and studs shall be ultrasonically cleaned prior to installation.

Valves - Manual and pneumatic gate valves are installed along the beamline for protection and commissioning purposes. All-metal valves are required in UHV regions. Some gate valves, including the fast action valves, are interlocked as part of machine protection.

Cleaning - All vacuum parts for PIP-II shall be cleaned as UHV, even the parts for HV regions, and bagged properly (ADDP-ME-000145, procedure for particle free vacuum components) for parts used in regions which require low particulate vacuum.

Certification

All devices that are part of the beamline vacuum shall be certified by vacuum personnel, prior to being installed in the beamline. The certification must verify that the specific device meets the vacuum requirement. The specific procedures and criteria will be defined accordingly.

Assembly and Installation

The procedures for assembly and installation are specific to each region.

Roughing and Venting

Since there is a risk of particle migration towards a CM, the valves that isolate the CM from its vicinity shall remain closed during the period of roughing down and venting up in the adjacent

regions. Turbo cart equipped with flow restriction (50 mbar-l/s) and proper filtration shall be used for such activities, until pressure is below 1 Torr. The locations of pumping/venting ports should be chosen so that the risk of particle migration towards CM minimized.

14.5 Basic low particulate requirements

- All processes and procedures shall be performed per released written procedures [141].
- All processes, procedures and facilities used to install or maintain such hardware shall be validated by testing before being approved for use on the PIP-II "low particulate" hardware.
- All "low particulate" vacuum components shall have the final stages of cleaning performed in ISO Class 4 (FED-STD Class 10) environments per ISO 14644, in the operational state, considered size 0.5 μm (352 particles/m^3).
- All interconnections of "low particulate" vacuum components shall take place in an ISO Class 5 Cleanroom (FED-STD Class 10) or Clean Zone per ISO 14644-1, in the operational state, for 0.5 - 5.0 μm particles.
- Integration, service, or maintenance operations on the Cryomodule beamline vacuum (for example, removing beamline transport spools, connecting the beamline between two Cryomodules, or connecting the beamline between a Cryomodule and a transitional warm beamline section, etc.) shall take place in ISO Class 4 Clean Zones per ISO 14644, rest state, for 0.3 micron particles, 0.5 micron particles and 1.0 micron particles.
- All test equipment used to validate "low particulate" components, processes, procedures, and facilities shall be properly calibrated, with valid calibration at the time of their use.
- All personnel entering the Clean Rooms or Zones while "low particulate" hardware is exposed must be trained as cleanroom users.
- Implementation of low particulate technology in an "as low as reasonably achievable" approach can be justified by the cost of determining the true risk imposed by excessive relaxation of requirements. This approach is adopted for the PIP-II project.

Chapter 15

Test Stands

Test stands located at Fermilab are utilized for verification testing of the various dressed cavities and assembled cryomodules required for the PIP-II project. Although these test stands already exist as part of Fermilab's Superconducting Radio Frequency (SRF) test infrastructure, modifications of the test infrastructure are required to facilitate testing of the PIP-II specific components. Three test stands, located at separate test facilities on the Fermilab complex, are used to test the PIP-II components (STC, HTS-2 and PIP2IT).

15.1 Spoke test cryostat (STC)

The PIP-II project requires the construction of a superconducting Linac, part of which requires cryomodules with elliptical cavities operating at 325 MHz and 650 MHz. As part of the development and construction of these cryomodules, the cavities undergo comprehensive system-level cold RF power testing in the horizontal configuration with tuners, couplers and helium vessels attached, as in the cryomodules themselves. The Spoke Test Cryostat (STC), located in the MDB test facility, is an SRF cavity test stand used for design verification studies and initial qualification testing of 325 MHz cavities, specifically for the SSR1 and SSR2 cryomodules at 4 K and 2 K, see Figures 15.1 and 15.2.

At present, there is no facility at Fermilab that can support the testing of the 650 MHz cavities for the HB650 and LB650 cryomodules. A new horizontal test cryostat (HTS-2) for testing of 650 MHz cavities has been designed and is being fabricated as part of the Indian Institutes-Fermilab Collaboration (IIFC). However, delivery and initial commissioning/operation of this cryostat at Fermilab is not expected to occur in time for it to be able to be used to qualify cavities for the first prototype 650 MHz cryomodule, let alone perform earlier design verification testing. Therefore, the existing STC horizontal test cryostat currently being used for testing 325 MHz spoke cavities will be modified to also accommodate testing of 650 MHz cavities for PIP-II. The STC facility already includes cryogenic systems and controls; low level RF controls; data acquisition systems and data logging; and vacuum systems for cavities/couplers, which do not require any modifications

Figure 15.1: Existing STC test cryostat.

to accommodate the 650 MHz testing. Modification of the STC cryostat involves lengthening the cryostat, magnetic and thermal shields, to accommodate the longer 650 MHz cavities; modifying the internal support structure to accommodate the size, shape and increased weight of the 650 MHz cavities; and development of appropriate tooling and fixtures to allow insertion/removal of the cavities, see Figure 15.3. Additionally, a new RF distribution line from the existing 650 MHz IOT RF source to the STC cryostat cave will also be designed and installed. These modifications shall not preclude use of the cryostat for testing of 325 MHz cavities. The STC infrastructure modifications to accommodate testing of 650 MHz cavities are underway and expected to be completed in early 2019.

15.2 Horizontal test stand 2 (HTS-2)

The PIP-II project requires elliptical cavities operating at a frequency of 650 MHz. In order to test these cavities, a new horizontal test stand, called HTS-2, is being designed and implemented at Fermilab at the MDB test facility, see Figures 15.4 and 15.5. The design and fabrication of the HTS-2 cryostat is a joint effort between Fermilab and the RRCAT laboratory in India, as part of the Indian Institutes and Fermilab Collaboration (IIFC) for PIP-II. The HTS-2 cryostat will be able to accommodate up to two 650 MHz (or 1.3 GHz) cavities at a time, dramatically increasing test throughput. HTS-2 will operate at 2 K, and employ a full suite of RF, cryogenic, and data acquisition systems for cavity characterization. The main operating mode for HTS-2 will be the CW testing of two 650 MHz cavities up to gradients of approximately 25 MV/m at temperatures from 1.7 to 2.0 K. The cavities will not be powered simultaneously. The HTS-2 cryostat is expected

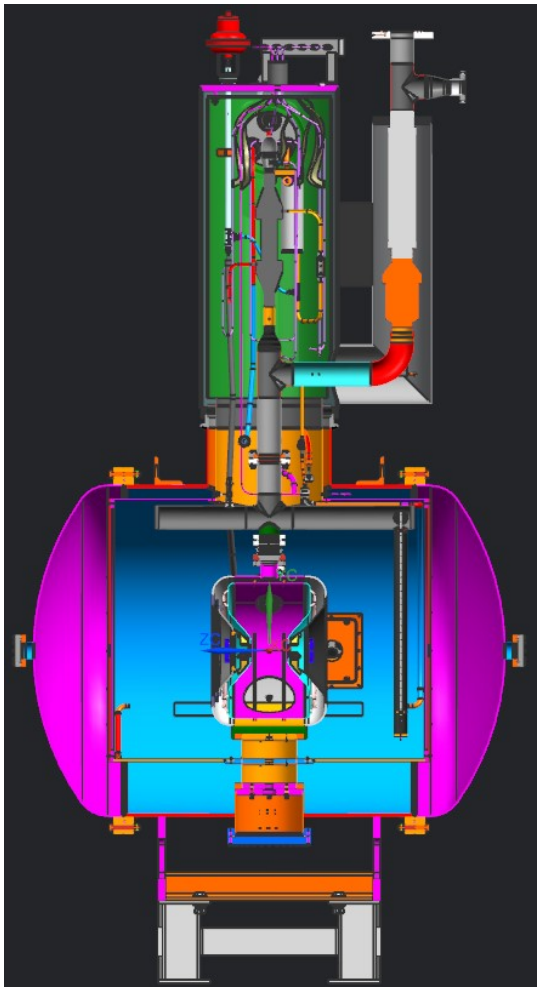

Figure 15.2: Cut-away of STC cryostat.

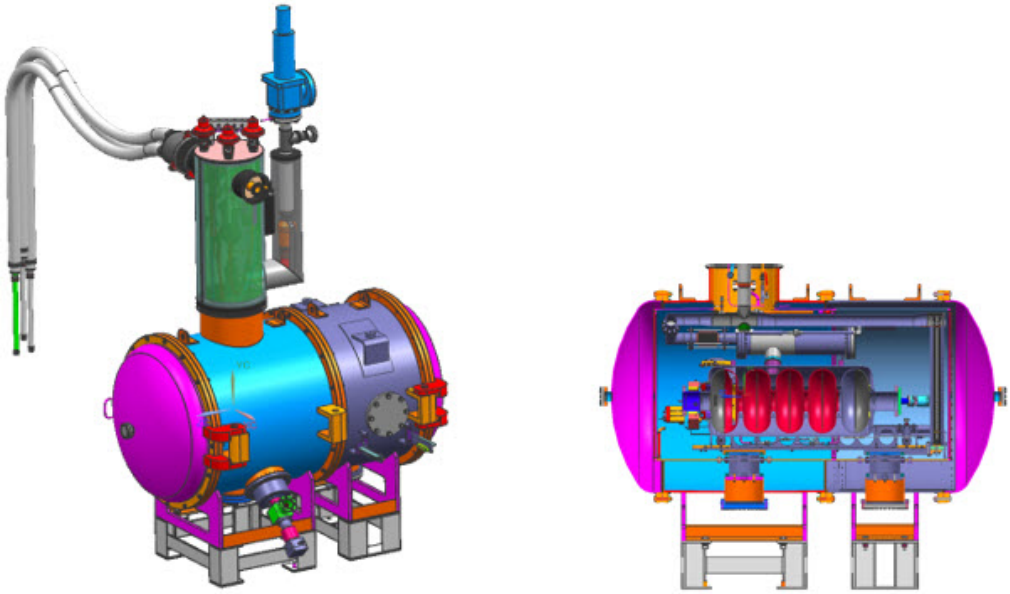

Figure 15.3: STC cryostat modified with extension to accommodate 650 MHz cavity testing.

to arrive at Fermilab in 2020 and will be put in storage, unless it is determined that it is needed to supplement STC 650 MHz cavity testing.

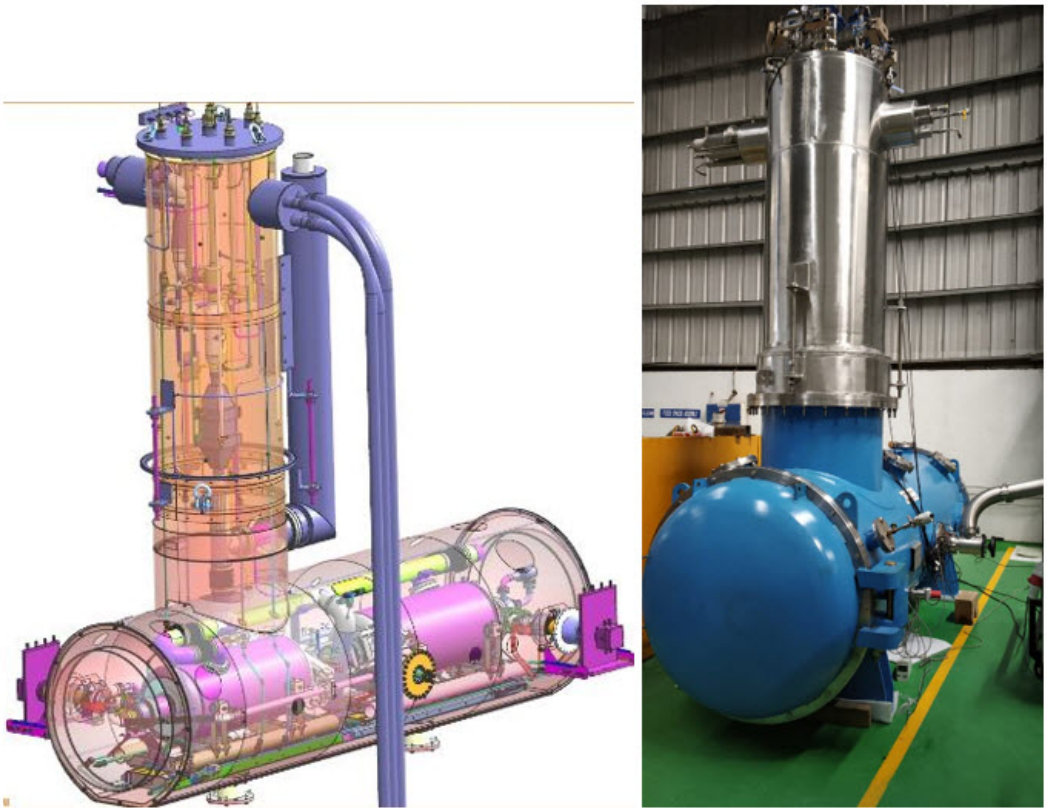

Figure 15.4: 3-D model and photograph of the HTS-2 cryostat.

15.3 PIP-II injector test (PIP2IT)

The PIP-II cryomodules will be tested at the PIP-II Injector Test (PIP2IT) test stand located inside Fermilab's Cryomodule Test Facility (CMTF) building, see Figure 15.6. CMTF is a research and development facility for accelerator science and technology, in particular, the testing and validating of superconducting radio frequency (SRF) components. CMTF provides the necessary test bed to measure and characterize the performance of SRF cavities in a cryomodule with and without beam. CMTF was designed to be a flexible test facility, configurable in different ways to meet the needs of current as well as future projects at Fermilab and abroad. The facility consists of a 15,000 sq. ft. high-bay with a 20-ton overhead crane, two test stands (CMTS1 and PIP2IT), a test area for RF components and electrical systems, a cleanroom area for particle-free preparation of SRF components and a control room/office area. The CMTF facility also houses a large state-of-the-art cryogenic plant capable of providing 500 W of cooling capacity at 2 K, that can provide simultaneous cold operation of the two independent test stands, consisting of a shielded concrete test cave and the associated infrastructure to characterize the cryomodules with RF power at cryogenic temperatures. The CMTS1 test stand is currently being used to test 1.3 and 3.9 GHz cryomodules for the LCLS-II project being built at the Stanford Linear Accelerator (SLAC).

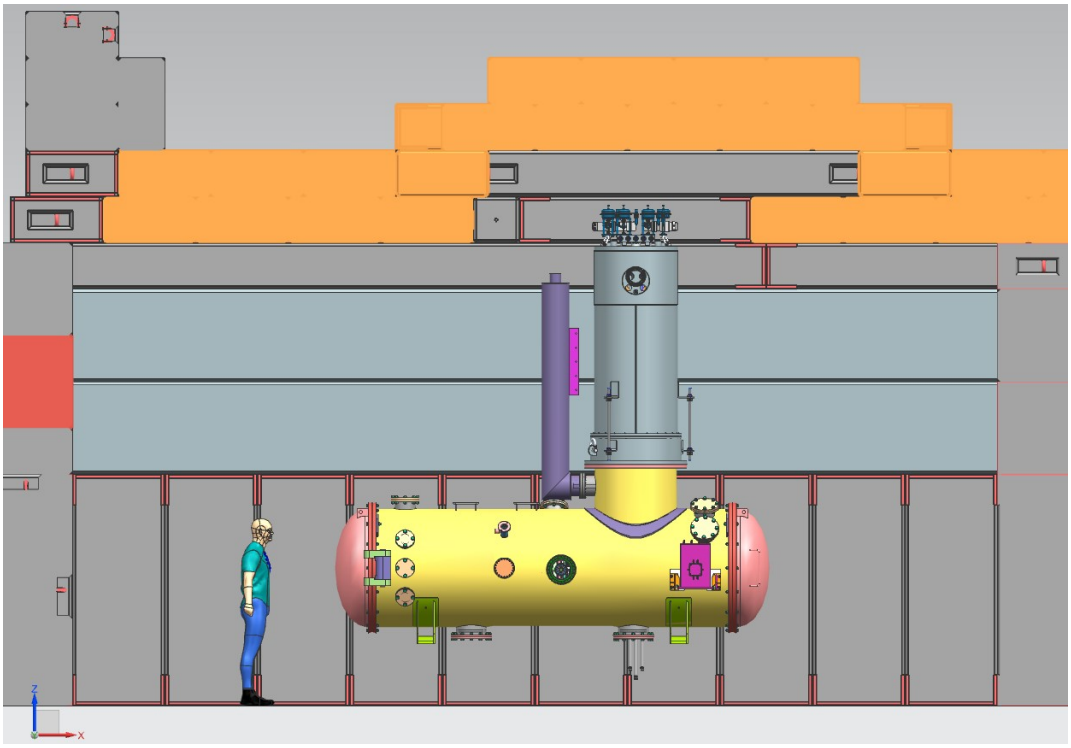

Figure 15.5: HTS-2 test stand.

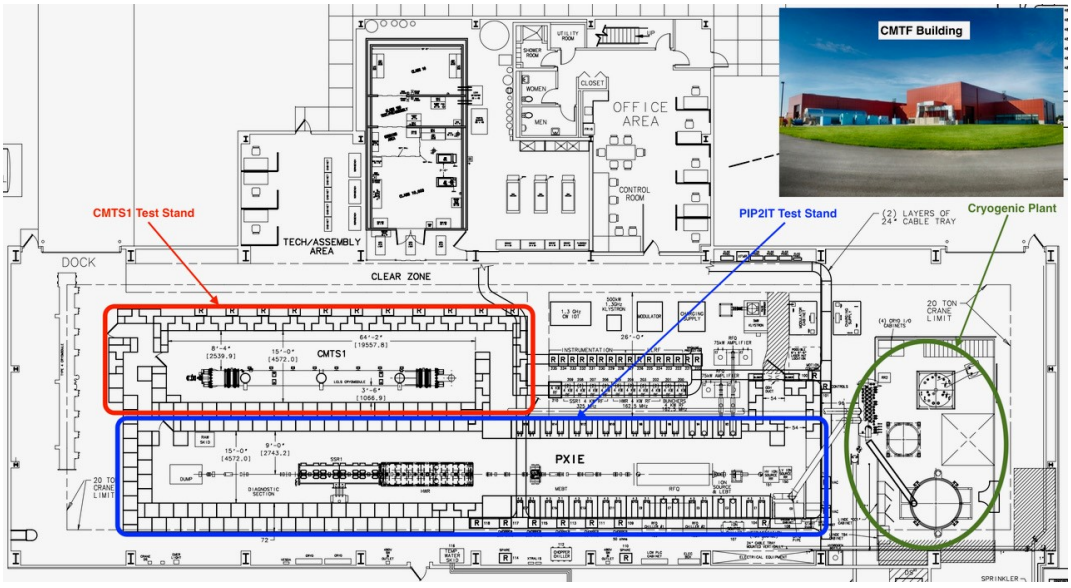

Figure 15.6: CMTF building layout.

The second test stand at CMTF contains the PIP-II Injector Test (PIP2IT). PIP2IT is a test cave where a nearly full-scale test of the front-end of the PIP-II accelerator is being constructed and tested with beam, see Figure 15.7. This test includes the warm front end (WFE) and the first two cryomodules of the PIP-II accelerator, the half wave cryomodule (HWR) and the first single spoke cryomodule (SSR1). Following the completion of the PIP-II injector test, the PIP2IT cave will be converted into a cryomodule test stand for cold RF testing of the remaining SSR cryomodules (SSR1 and SSR2) and the 650 MHz cryomodules (LB650 and HB650), without beam.

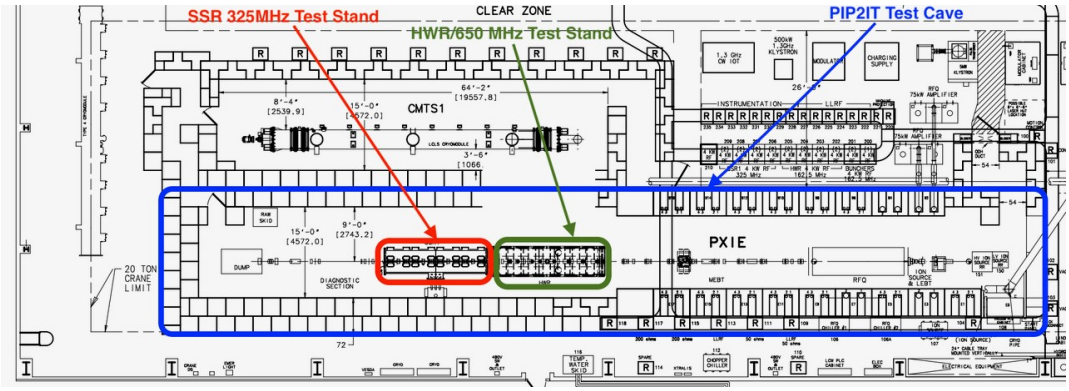

Figure 15.7: PIP2IT test stand in CMTF.

A total of 25 cryomodules of five different varieties will be built for PIP-II at various laboratories around the world and all of them are planned to be acceptance tested at PIP2IT.

The type and number of cryomodules is listed below:

- (1) Half Wave Resonator (HWR)
- (2) Single Spoke Resonator - type 1 (SSR1)
- (7) Single Spoke Resonator - type 2 (SSR2)
- (11) Low Beta 650 MHz (LB650)
- (4) High Beta 650 MHz (HB650)

In order to test the various styles of cryomodules, modifications to the PIP2IT infrastructure are required. This includes installation of RF power amplifiers, modifications to the controls, instrumentation, mechanical, electrical, safety and cryogenic distribution systems. The most significant infrastructure modification at PIP2IT is the installation of the cryogenic transfer line.

15.3.1 Cryogenic transfer line

PIP2IT will be an integrated system test for the PIP-II front end and will include two cryomodules, a half-wave resonator (HWR) and a single spoke resonator (SSR1). The PIP2IT cryogenic transfer line services these cryomodules.

The CMTF facility includes a helium refrigerator sized to supply both PIP2IT and CMTS1. A dedicated transfer line will run from the existing distribution box into the PIP2IT enclosure, see Figure 15.8.

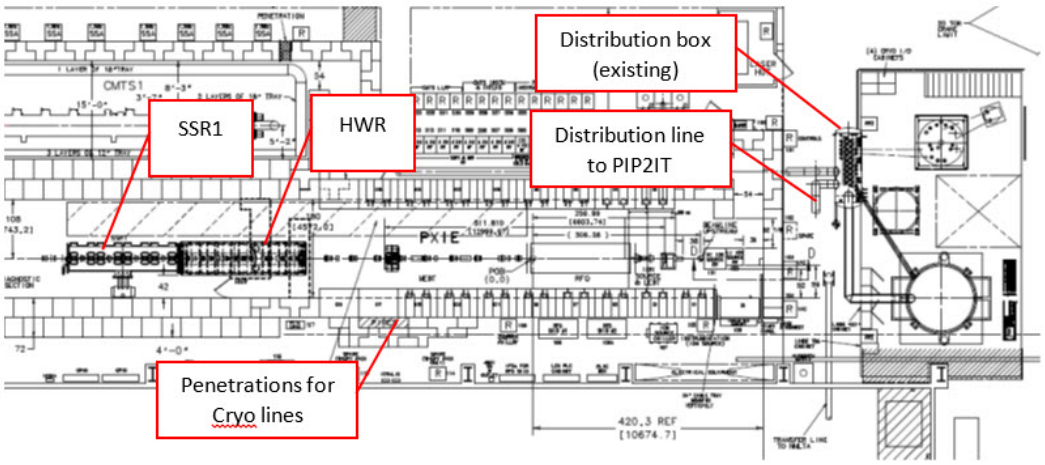

Figure 15.8: PIP2IT within CMTF.

The scope of the cryogenic transfer line includes all the hardware and controls required to cool the PIP2IT cryomodules, including:

- Existing shared cryogenic infrastructure (e.g. plant, distribution box, controls, etc.)
- New cryogenic infrastructure dedicated to PIP2IT (e.g. transfer line, suction headers, relief piping, etc.), see Figure 15.9

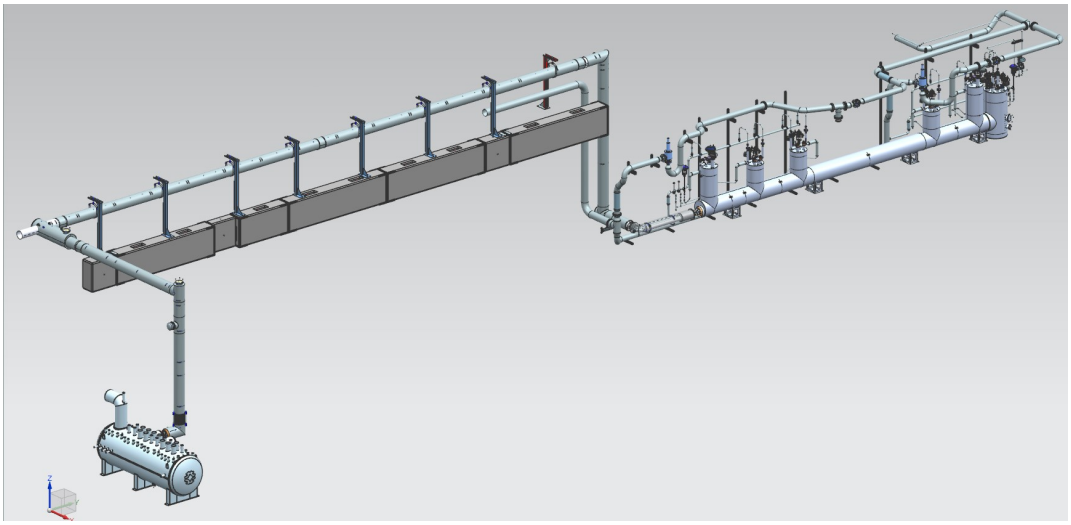

Figure 15.9: Cryogenic infrastructure at PIP2IT.

15.3.2 Operational modes

It is anticipated that the PIP2IT cryomodules will be received and commissioned at different points in time. To allow for flexibility in commissioning and operation, the design of the cryogenic transfer line shall support the following operations modes to allow for independent operation of each cryomodule.

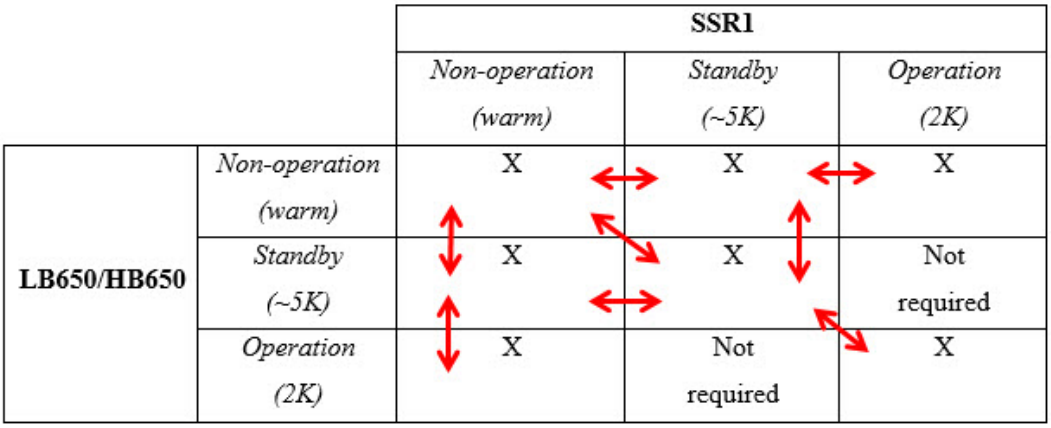

Figure 15.10: Cryogenic operational modes and mode transitions.

The design of the cryogenic transfer line shall permit transitions between modes as indicated by red arrows in Figure 15.10.

Equivalently, these requirements are expressed in the following list:

Steady State Modes

- SSR1 operation at 2 K while LB650/HB650 operation at 2 K
- SSR1 operation at 2 K while LB650/HB650 warm at 300 K
- SSR1 standby at 5 K while LB650/HB650 warm at 300 K
- SSR1 standby at 5 K while LB650/HB650 standby at 5 K
- SSR1 warm at 300 K while LB650/HB650 operation at 2 K
- SSR1 warm at 300 K while LB650/HB650 standby at 5 K
- SSR1 warm at 300 K while LB650/HB650 warm at 300 K

Mode Transitions (Transient States)

- SSR1 cool down from 300 K to 5 K while LB650/HB650 warm at 300 K
- SSR1 pump down from 5 K to 2 K while LB650/HB650 warm at 300 K

- SSR1 standby at ∼5 K ±1 K while LB650/HB650 cool down from 300 K to 5 K
- SSR1 pump down from 5 K to 2 K while LB650/HB650 pump down from 5 K to 2 K
- SSR1 warm at 300 K while LB650/HB650 warm at 300 K
- SSR1 warm at 300 K while LB650/HB650 cool down from 300 K to 5 K
- SSR1 warm at 300 K while LB650/HB650 pump down from 5 K to 2 K
- SSR1 cool down from 300 K to 5 K while LB650/HB650 standby at ∼5 K ±1 K

Note: the reciprocal warm-up transitions are also required

Standby modes are defined by one or more cryomodules at cold conditions, but not in the superfluid (2 K) regime. Cavity temperature while in standby mode is ideally 5 K. In cases where one PIP2IT cryomodule is in standby mode while the other warms up or cools down, transient cavity temperatures of the cryomodule staying in standby mode shall be maintained <50 K.

15.3.3 Relationship with CMTS1

It is anticipated that CMTS1 will undergo frequent cool down/warm up cycles. The PIP2IT cryogenic transfer line shall be designed such that PIP2IT can be stably maintained in non-operational or standby modes as defined in Figure 15.10 during CMTS1 warmup or cooldowns. During CMTS1 transitions while a PIP2IT cryomodule is in standby mode, temperatures at PIP2IT cavities shall be held at 5 ± 1 K.

The PIP2IT cryogenic transfer line shall be capable of mode transitions as defined in Figure 15.10 during periods where CMTS1 is in a stable warm or stable cold (5 K) condition.

It is not required that the PIP2IT cryogenic transfer line be capable of any mode transition simultaneously with a CMTS1 mode transition.

15.3.4 System capabilities

The cryogenic transfer line shall supply helium to PIP2IT with the parameters shown in Table 15.1.

In addition the cryogenic transfer line will satisfy the following requirements:

- During stable operation at 2 K, pressure stability of the 2 K circuit shall be $\leq$ 0.1 mbar RMS. Note: this requirement is driven by the SSR1.
- There are no MAXIMUM warm-up or cooldown rates for either cryomodule.

Table 15.1: Cryogneic transfer line capabilities. ‡Capacity requirements for the cryogenic transfer line apply at the transfer line/cryomodule interface. This is the maximum heat load from the cryomodules that the cryogenic transfer line must be able to remove. Values are chosen to provide 50% margin in the delivered cooling capacity relative to cryomodule heat loads specified in the cryomodule FRS documents. Note that this allocation to PIP2IT still represents less than half of the CMTF cryo plant capacity.

Circuit	Operating Temperature	Min. Capacity of Cryo TL‡
2 K cavity circuit	2.0 K	150 W
5 K shield circuit	5 K	240 W
45-80 K Outer shield circuit	45-80 K Adjustable within this range	750 W @ 70 K

- The cryogenic transfer line shall ensure that the MINIMUM cooldown rate of cavities through the Q-disease regime (90-175 K) is > 20 K/hr.
- The cryogenic transfer line shall ensure that the MINIMUM cooldown rate of cavities through the superconducting transition (9.2 K) is > 2 K/min.
- The cryogenic transfer line shall be designed such that warmup or cooldown of one cryomodule can be accomplished in ≤ 3 calendar days.
- Rate calculations presented in the PIP2IT cryogenic transfer line TRS should be based on the real cold mass values.

15.3.5 HWR and 1st SSR1 testing

The HWR cryomodule and the SSR1 cryomodule will be cold-tested with beam as part of the PIP2IT front-end test as depicted in Figure 15.11. Installation of the PIP2IT cryogenic transfer line is currently in progress which will be followed by installation and cooldown of these two cryomodules in 2019. Cold testing of these cryomodules with beam is planned to be completed in 2020. A 3-D model of this phase of PIP2IT is shown in Figure 15.11.

15.3.6 SSR and 650 MHz cryomodule testing

Once the PIP-II injector test testing is complete, PIP2IT will be converted to a test stand to test the remaining PIP-II cryomodules. The SSR1 cryomodule will be removed and its slot location will become a test stand for the remaining SSR1 and SSR2 cryomodules. This conversion will require minimal modifications, as the SSR1 and SSR2 cryomodules are similar in size and have the same cryogenic connections.

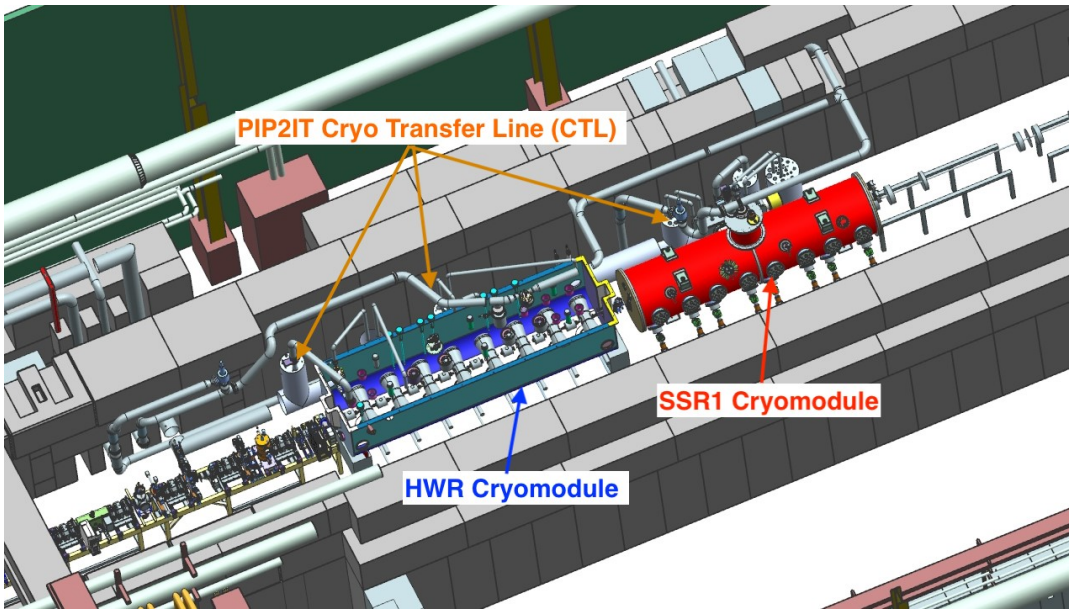

Figure 15.11: 3D model of HWR, SSR1, and CTL in PIP2IT.

The HWR cryomodule will also be removed and its slot location will become a test stand to test the LB650 and HB650 cryomodules. Because these cryomodules are significantly longer than the HWR and have different cryogenic connections, substantial infrastructure modifications will be required. The major modifications include:

- Removing a portion of the MEBT to accommodate the longer physical length and allow for enough space between the SSR and 650 cryomodules for testing
- Installation of new RF amplifiers and associated RF distribution
- Design and installation of a secondary cryogenic transfer line

A 3-D model showing the modified PIP2IT test stand with an SSR2 and HB650 cryomodule along with the secondary cryogenic transfer line is shown in Figure 15.12.

The current plan for testing cryomdodules assumes there are minimal (if any) testing constraints between the 650 MHz and SSR tests stands. The cryogenic connections will be done via u-tubes, allowing each cryomodule to be connected/disconnected independently from the cryogenic system. Also, only the roof blocks directly over the cryomodule will be removed during a cryomodule switchover, leaving the other test stand protected. Finally, written procedures will be reviewed and approved and all involved personnel will be trained on these procedures to safely install/remove cryomodules for testing. These procedures will be modeled after the existing procedures currently in use for testing of LCLS-II cryomodules in the neighboring CMTS1 test stand, which has a very similar configuration.

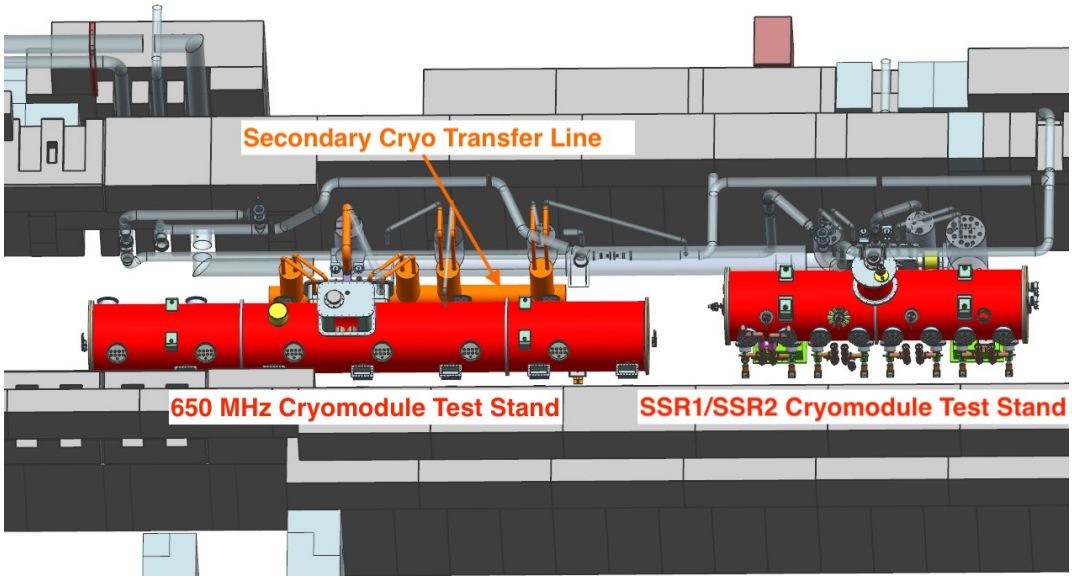

Figure 15.12: PIP2IT converted to a cryomodule test stand for SSR and 650 cryomodules.

Chapter 16

Safety Systems

16.1 Introduction

Safety Systems provide for personnel protection of known hazards within beamline enclosures and cryogenic buildings. The hazards the Safety Systems provide protection from are listed below:

- Oxygen Deficiently Hazard
- Exposed magnet buss and connections
- Laser Class 3b and 4
- Radiation exposure and limiting Beam loss

The following sections detail the specific safety systems and how they mitigate the specific hazards.

16.2 Oxygen deficiency safety system

The Oxygen Deficiency Hazard Safety System (ODH SS) is used to warn personnel when an area's oxygen level drops below 19.5% or rises above 21.5%. ODH SS's are installed in areas based upon an ODH Analysis, which are completed and reviewed prior to ODH hardware installation. The ODH SS follows FESHM Chapter 4240 "Oxygen Deficiency Hazards (ODH)". Currently both ODH safety system installations appear to be straight forward and consistent with previous installations at Fermilab.

Superconducting RF cavity installations at Fermilab require cryogens for proper operation. In areas where cryogens are used oxygen displacement is a possibility due to possible cryogenic gas leakage. Oxygen level monitoring cells are installed within these cryogenic areas. Their locations

are based upon an ODH Analysis completed by the Cryogenic Department. These areas are similar to other enclosures on site with similar ODH equipment and quantities of cryogens which allow for a good understanding of what classification to expect prior to the final ODH Analysis. Depending upon the type of cryogens used oxygen cells are installed at different elevations in these areas. Typically, nitrogen cryogenic gas use requires low mounted (near floor level) cells as nitrogen is heavier than air while helium cryogenic gas use requires high mounted (usually near ceiling) cells as helium is lighter than air. Audio and visual warning devices are installed within the area to warn personnel if the oxygen level drops below 19.5% or above 21.5%. ODH alarms may also provide signals to turn on exhaust and intake air ventilation to purge the area with fresh air if the oxygen level drops below 19.5%. Alarms for levels above 21.5% do not turn on exhaust and intake ventilation, only audio and visual alarms. Level readings above 21.5% would normally indicate an oxygen cell out of calibration.

16.3 Electrical safety system

The Electrical Safety System (ESS) provides personnel protection from inadvertent contact with supply exposed connections or buss of high voltage or high current magnet power supplies. ESS installations shall follow Fermilab Environmental Safety and Health Manual (FESHM) Chapter 9140 "Protection Against Exposed Electrical Buss".

The ESS provides a safety system "permit" signal to all magnet power supplies who's buss and or magnet connections are exposed which is commonly found in beamline enclosures at Fermilab. This ESS permit becomes part of the magnet power supply's "interlock circuit". Without the ESS permit the magnet power supply cannot be energized. In some cases, the ESS also permits high power RF amplifiers powering RF cavities within an enclosure. All ESS permits for beamline enclosures and small test caves or enclosures originate from the enclosure ESS. All safety system interlocked power supplies have their AC input power removed before keys are issued to enter the beamline enclosure.

The ESS monitors all access doors and emergency exits of an enclosure using redundant monitoring switches, normally one mechanical and one magnetic. Keys to access an enclosure are monitored by the ESS. When access keys are not being used for access into an enclosure they are returned to their interlocked key tree position. Enclosure access keys are monitored in the key tree using redundant switches, to verify their key tree position to the ESS. Search and secure boxes (reset boxes) are located at all access and exit locations. Equipment alcoves and enclosure areas that are not easily seen may also have search and secure boxes to force the search and secure personnel to these areas. Enclosure search and secure personnel must go through and reset each search and secure box in a predefined sequence using the reset key. While search and secure personnel are moving through the enclosure resetting the search and secure boxes they also verify that all "crash switches" are enabled. Once an enclosure is searched and secured and keys are returned to the key tree, the enclosure audio warning sounds for a predetermined length of time. When the audio warning message is complete the enclosure ESS permits are complete.

The enclosure ESS output permit signals (redundant A & B signals) are sent to a "Safety System

Interface Unit" (SSIU) as it's input. The SSIU takes the ESS output permits and fans it out to provide eleven separate magnet power supply ESS permits. Each fan out permit signal is two normally open relay contacts (A & B permit) in series to provide a permit contact to the magnet power supplies or other devices needing an ESS permit. The enclosure ESS output A & B permits are also used as inputs to the Critical Device Controller (CDC) for the RSIS of that beamline area. Below shown in Figure 16.1 is a logic diagram showing an enclosure ESS being used to provide ESS permits.

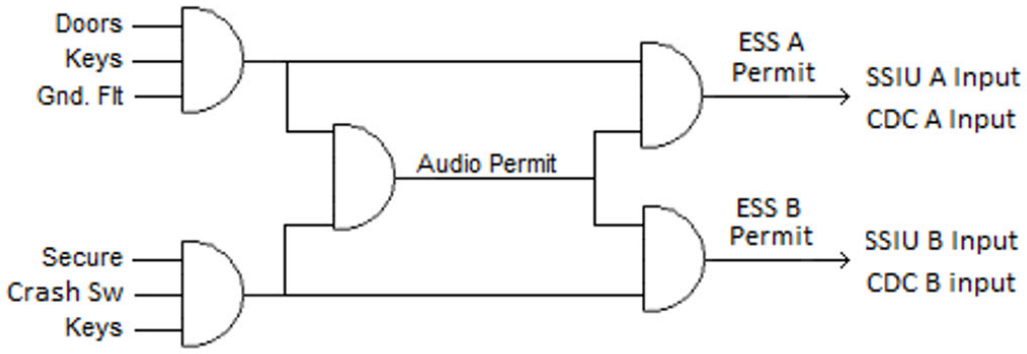

Figure 16.1: Electrical safety system logic tree.

16.4 Laser safety system

Laser Safety Systems (LSS) interlock enclosures operating lasers of class 3b and 4. A LSS disables the laser when its laser enclosure is opened. Requirements for LSS installations shall follow FESHM Chapter 4260 "Lasers".

Most LSS installations at Fermilab monitor a laser lab and or a laser table / box with removable access panels that are interlocked. All laser labs laser tables / boxes with removable panels must be light tight. Laser installations are usually secured by interlocking the laser lab and or table. Some laser installations at Fermilab have one to three laser tables that do not have interlocked removable panels. In installations like this, only the laser lab is interlocked to the lasers. When a laser table / box has removable panel covers, the panels also are interlocked. When the interlocked table panel covers are removed (possible laser exposure) the laser lab itself must be secured to provide the laser permit. Tuning a laser is done by trained laser operators wearing the proper PPE for the laser they will tune. Shown below in Figure 16.2 is a typical LSS logic diagram for a laser Lab that has a laser table with removable panel covers.

16.5 Radiation safety interlock system

The Radiation Safety Interlock System (RSIS) is installed to prevent personnel exposure from high radiation levels. RSIS installations shall follow Fermilab Radiological Control Manual (FRCM)

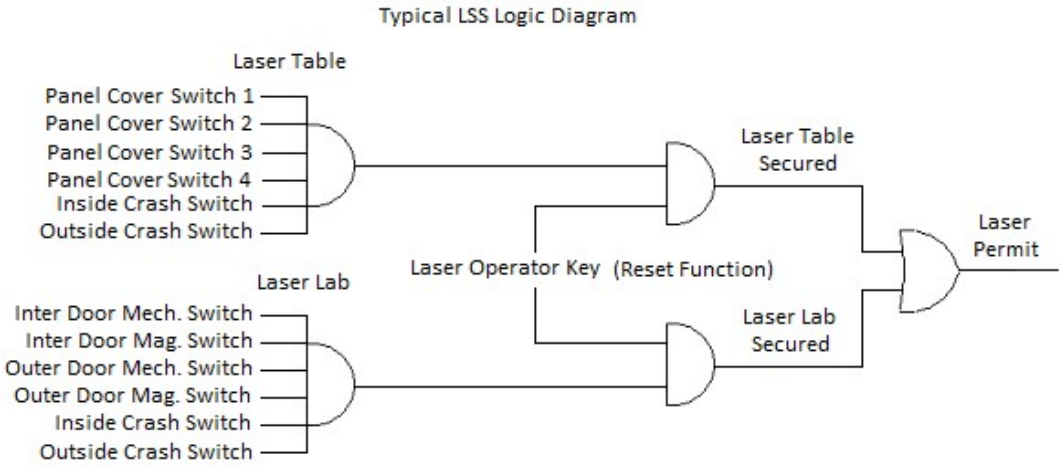

Figure 16.2: Typical LSS logic diagram.

Chapter 10 "Radiation Safety Interlock Systems" guidelines. RSIS installations include interlocking of radiation enclosure, radiation monitoring, and activation / deactivation of critical devices.

RSIS installations can involve one or more enclosures and radiation monitors. All RSIS enclosures designs incorporate passive radiation shielding for radiation protection outside of the enclosure. RSIS installations are used for radiation protection of particle beamline areas and small test enclosures incorporating radiation generating devices.

Radiation monitoring devices are also part of the RSIS which consist of Area Monitors and Total Loss Monitors (TLM). The Area Monitors are designed, fabricated and calibrated by the Instrumentation Team of the ESH&Q's Radiation Physics Engineering (RPE) Department. TLM's are designed, fabricated and calibrated by the Interlock Group of the ESH&Q's RPE department. An RSIS can have one or more interlocked radiation monitoring devices. Should individual components on these systems become obsolete or unavailable after all spare parts have been exhausted, there is a design change process in place to address it which has been used in the past.

These radiation monitoring devices interface to the RSIS using a Radiation Monitor Interface Board. Radiation Monitor Boards can be installed in a Rad Monitor Chassis. This chassis sums multiple Radiation Monitor Interface Boards to provide redundant inputs to the CDC. A Radiation Monitor Interface card monitors the radiation levels from a monitoring device along with "ID" and "Fail Safe" signals. The radiation trip point for a given radiation monitor is determined by the Radiation Safety Officer (RSO) of that area. The Radiation Monitor Interface Card is programmed configured to this trip point by Interlock Group Technicians and then tested to ensure the trip point is set properly.

Small testing enclosures are used for various testing functions. These small enclosures can be used for radiation testing of various materials, using a self-contained radiation generating device. RF cavity testing where the RF cavity itself generates x-rays. The RF amplifier driving the RF cavity is the device the RSIS allows to be activated and deactivates if the enclosure ESS is not secured, or a radiation monitor exceeding its trip point. The RSIS in this case provides two separate permits to the RF System. Two separate permit methods are required as the RF cavity can produce more

than 1000 mrem/hr. at one foot. Figure 16.3 shows a typical RSIS logic diagram for a small enclosure with one RF Cavity as the radiation generating device.

Beamline RSIS installations use a Critical Device Controller (CDC). The CDC is a Fermilab designed and fabricated rack mount chassis. This chassis sums enclosure ESS, radiation monitor and other required device permits for radiation safety of a beamline. The summation of these redundant inputs provides the A & B permits to the beam line critical devices. Beamlines are required to have two separate critical devices or one critical device with a failure mode device, as a back-up. Beamline RSIS installations normally have two separate critical devices. These critical devices are monitored (redundantly) by the CDC. If a critical device fails to deactivate when the CDC disables their permit, the CDC disables its failure mode device. A RSIS having two separate critical devices and a failure mode device exceeds the critical device requirements in Chapter 10 of the FRCM. Figure 16.4 shows a typical CDC logic diagram for a beamline area having multiple beamline enclosures.

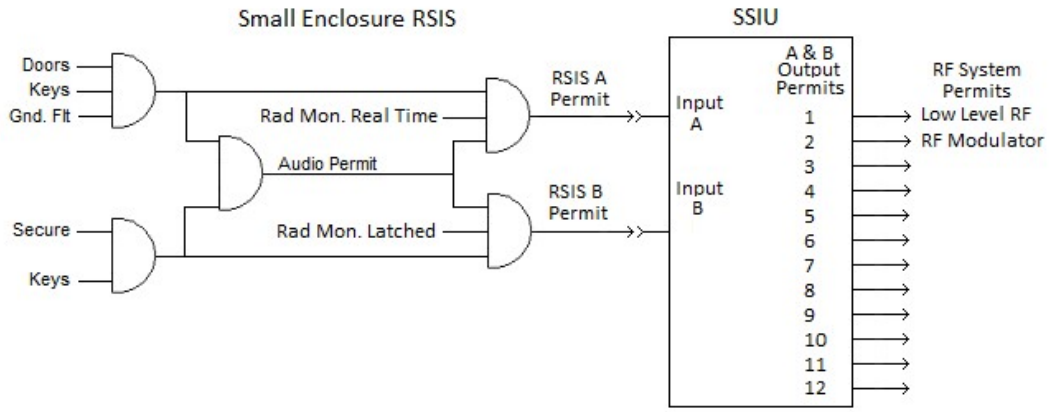

Figure 16.3: Typical RSIS logic diagram.

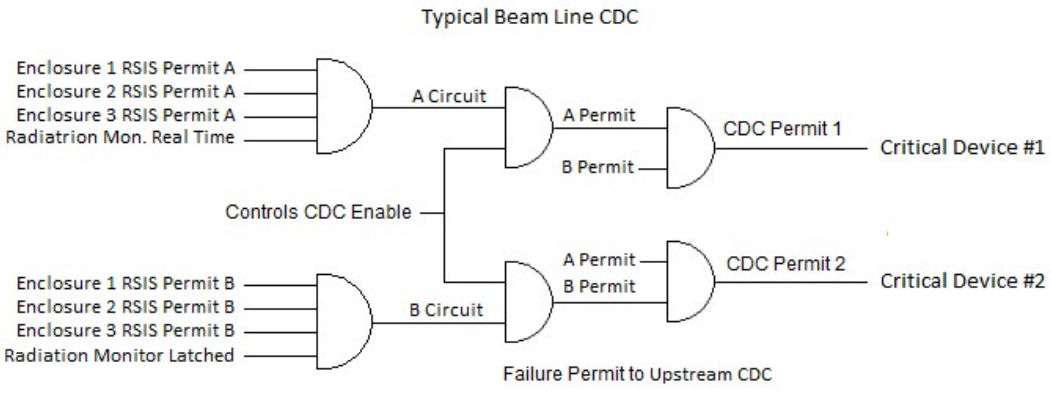

Figure 16.4: Typical beamline CDS logic diagram.

16.6 Safety system design

The following sections describe the designs of the PIP-II safety system including designs for the Cryoplant Building and Linac Enclosure ODH SSs, and designs of the ESSs and RSISs for the MEBT, Linac, BTL, and BAL.

16.6.1 Oxygen deficiency hazard safety system design

The final ODH analysis for the Cryogenic Plant Cold Box Station, Warm Compressor Station Rooms and Linac enclosures were not available during the initial ODH SS design. The current design is based upon the PIP-II construction drawings and previous similar installations. Minor changes may be needed when the analysis is completed and approved. The design of the ODH SS calls for two Siemens S7-300 safety rated PLCs. One PLC is located within the Cryo Control Room of the Cryoplant Building and the second is centrally located in the Linac Gallery. A dedicated relay rack is required for each of these ODH safety systems.

16.6.1.1 ODH SS desgin cryoplant building

The Cold Box Station Room design has three oxygen monitor cells, two sirens and four strobe lights. Cables needed for the oxygen cell, sirens and strobes are run to the Control Room of the Cold Box Station room where the ODH SS PLC is installed. The ODH Monitoring System when in alarm provides an alarm signal to the exhaust and intake ODH ventilation equipment.

The Warm Compressor Station room design has five oxygen monitor cells, two siren amplifiers (high dB) and six strobe lights. Cables needed for the oxygen cell, sirens and strobes are run to the Control Room of the Cold Box Station building where the ODH SS PLC is installed. The ODH Monitoring SS provides an alarm signal to the exhaust and intake ODH ventilation equipment.

16.6.1.2 ODH SS design Linac enclosure

Helium is the only cryogen used in the Linac Enclosure. The Linac Enclosure design has eight oxygen monitor cells, six sirens, and 12 strobe lights. Cables needed for the oxygen cell, sirens and strobes are run to a central point of the Linac gallery due to the length of the Linac enclosure. The Linac enclosure is nearly 700 feet in length. Having the ODH SS located in a relay rack centered in the Linac Gallery would reduce cable lengths to devices located within the enclosure. An air barrier door separating the Linac and Beam Transfer Line (BTL) enclosures is installed as part of the PIP-II construction contract. This air barrier door separating the Linac and BTL enclosures can possibly also serve as the radiological boundary separating the enclosures. At this time, it is not known if oxygen monitor cells will be needed in the Linac Gallery, verifying the ODH 0 Classification. The ODH SS when in alarm provides an alarm signal to exhaust and intake ODH

ventilation equipment.

16.6.2 Electrical safety system design

All PIP-II ESSs use standard Fermilab safety system hardware and assemblies. A Rack Mount Safety System (RMSS) interlocks the components for each ESS installation. The RMSS Interlock is used for all reset boxes. ESS enclosures requiring more than four reset box locations also include the RMSS Section Board for reset box cable terminations. Enclosure access doors/ gates use the âĂIJFlashing Sign / Control Access assembly providing controlled access into the secured enclosures. Power for all safety system assemblies is provided by an Acopian 24 V DC power supply and all safety system power supply installations include an Interlock Group built UPS. All enclosure access and emergency exit doors/gates are monitored by one mechanical and one magnetic switch with an audio warning system for each ESS enclosure.

16.6.2.1 Linac ESS design

The Linac ESS consists of two separate ESS areas. The first area is the MEBT Enclosure and the second the Linac Enclosure. The Ion Source area includes the LEBT and RFQ, which is not a safety system interlocked area. Both the MEBT RMSS and Linac RMSS chassis are located in the Safety System Relay Rack in the Control Room of the Linac Gallery. The safety system relay rack (SSRR) has a 24 VDC safety system power supply and UPS providing power for the MEBT and the Linac ESS and RSIS installations. The SSRR in the control room also has an âĂIJEnd RackâĂİ attached to one side for external wiring of the ESS and CDC chassis.

The MEBT enclosure (begins at the downstream end of the RFQ) access keys are located in a remote key-tree located in the Linac Gallery Control Room. The MEBT key-tree has nine enter keys and one reset key. Based upon the existing PIP2IT installation, ESS permits to magnet power supplies are not needed as no magnet buss connections are exposed.

The Linac Enclosure enter and reset keys are located in the Main Control Room. There are 22 enter keys and two reset Keys for the Linac enclosure. RF loads in the Linac enclosure have the capability of generating greater than 1000 mrem/hr. at one foot. The safety system is required to turn off each of the RF Systems (radiation generating devices) in two separate methods at this level of radiation. The Linac ESS provides a total of 232 permit signals for the LinacâĂŹs 116 RF systems. One of the redundant ESS permit signals disables the low-level RF for each of the RF systems. A second ESS permit signal disables the 162.5 MHz RF amplifiers by disabling (removes AC power) the DC power supply of the amplifier. The ESS permit signal disables the DC bias supply (removes AC power) of each of the 325 MHz and 650 MHz RF amplifiers. To provide the necessary ESS permit signals for the RF systems, twenty-two (22) SSIUs are used. The SSIUs are installed throughout the Linac Gallery to help keep the individual ESS permit cables as short as possible.

16.6.2.2 Beam transfer line and beam absorber line ESS design

The first ESS will be installed for the BTL Enclosure and the second ESS will be installed for the BAL Enclosure. Both RMSS chassis for each of these ESSs are installed in the same safety system relay rack (SSRR) located at the downstream end of the Linac Gallery. This SSRR has an end-rack for wiring terminations and for housing a 24 V power supply with a UPS which provides safety system power for both ESS areas. Magnet power supplies for the BTL and BAL enclosures are located at the downstream end of the Linac Gallery. These magnet power supplies may be required to be interlocked, but this requirement has not been determined presently. The SSRR has space to install an SSIU chassis for the magnet power supplies that may require ESS permits.

Enter keys and reset keys for the BTL enclosure reside in a key-tree located in the Main Control Room. There are 22 enter keys and two reset keys. The BTL enclosure intersects the Main Ring tunnel and provides a personnel access bypass path around the BAL enclosure. The reconstruction of the Main Ring tunnel between the F3 and F4 service buildings requires the replacement of the safety system trunk line cables. The gates and fence sections separating the BTL and Main Ring enclosures are part of the Interlock Group responsibilities. A third fence and gate section separate the BTL and BTA enclosures from the Booster enclosure. The position of these three gates are determined by the radiation shielding analysis of the enclosures. The civil construction of the BTL enclosure into the Booster tunnel adds a new Booster emergency exit to the Booster. The BTL ESS includes the necessary safety System hardware for this new exit.

Enter and reset keys for the BAL enclosure reside in a key-tree located in the Main Control Room. The BAL key-tree has 10 enter keys and two reset keys. The PIP-II civil construction project provides the BAL gates and fence sections separating the BAL and BTL enclosures.

16.6.3 Linac enclosure LSS design

Laser Safety System requirements for the Linac laser beam profiling system is not known currently. Estimates for material and labor costs are based upon past LSS installations. The PIP2-IT area will include the first laser beam profiling system used at Fermilab and the LSS design requirements will be developed from the experience gained from this installation.

16.6.4 Radiation safety interlock design

Three RSIS are anticipated for PIP-II. One RSIS combines the MEBT and Linac enclosures with interlocked critical devices, a second RSIS combines the BTL and BAL enclosures with interlocked critical devices, and the third RSIS interlocks critical devices for the Booster.

16.6.4.1 MEBT and Linac enclosure RSIS design

The Linac RSIS has two separate ESS enclosure areas. The first area is the MEBT enclosure, and the second is the Linac enclosure. This CDC is identified as the Linac CDC. Critical devices for the Linac CDC include the ion source 30-degree bend magnet and the ion source high voltage power supply. No failure mode device is identified. The Linac CDC is located in the Safety System Relay Rack of the Control Room in the Linac Gallery. CDC Inputs required to permit the CDC are identified as the MEBT Enclosure ESS, Linac Enclosure ESS, Radiation Monitors (two TLM installations are estimated), and the CDC Failure signal from the BTL CDC. Figure 16.5 shows the proposed PIP-II beamline enclosure boundaries.

16.6.4.2 Beam transfer line and beam absorber line enclosure RSIS design

The BTL and BAL CDC are in the Safety System relay rack of the Linac Gallery. This CDC is identified as the BTL CDC. Critical devices for the BTL CDC are identified with Critical Device one as the magnet power supply powering the first bend magnet in the Linac enclosure bending the beam to the BTL Enclosure. Critical Device two is the magnet power supply powering the second bend magnet in the Linac enclosure bending the beam to the BTL Enclosure. Each of these critical devices include their own 480V AC contactor that is controlled by the CDC. Inputs required to permit the CDC include the BTL and BAL Enclosures ESSs, Radiation Monitors (three TLM installations are estimated), and the CDC Failure signal from the Booster CDC.

16.6.4.3 Booster enclosure RSIS design

The existing Booster CDC will be relocated to the Safety System relay rack in the Linac Gallery. Critical devices for the Booster CDC consist of two 480 V AC contactors. Each contactor provides power to a 45 KW magnet power supply. Each of these magnet power supplies powers a string of eight dipole magnets bending BTL beam to the Booster Enclosure. CDC Inputs required to permit the CDC include the Booster ESS, Booster Radiation Monitors (includes area monitors and TLMs), 8 GeV ESS, and Booster Logic module.

16.7 Safety considerations

Design of safety systems follows the "PIP-II Integrated Environment, Safety and Health Management Plan" (pip2-doc-141).

Consideration of emergency egress must be given serious thought. A continuous beamline tunnel that is broken into two or more ESS areas or connected to an existing ESS area, emergency egress must be part of the design. The Beam Transfer Line tunnel will connect to the Booster tunnel and cross through the Tevatron F-sector tunnel section. At this time the safety system interfaces

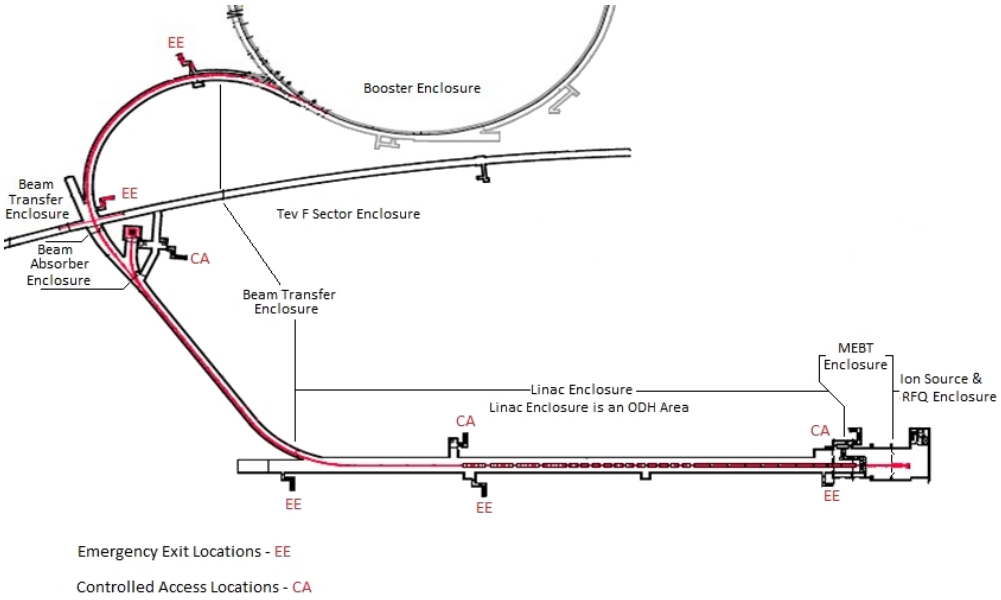

Figure 16.5: PIP-II Beamline Enclosure Boundaries.

between these enclosures is well understood. Access into an ESS area requires the use of an Enter key for that ESS enclosure. If an adjacent enclosure is an emergency egress passage a "break-out" panel must be installed in the gate separating the two enclosures. Pulling out the break-out panel allows one to reach through the gate and open the gate, breaking the ESS secure of that enclosure to allow emergency egress. The placement of Safety System reset (search & secure) boxes within a beamline enclosure must be installed with ease of accessibility in mind for the search and secure team. Placement of controlled access boxes on each side of a door or gate needs to be thought of for ease of use for access personnel.

Chapter 17

Conventional Facilities

17.1 Introduction

17.1.1 Overview

The PIP-II Conventional Facilities will provide space and infrastructure to support the installation, commissioning and operation of the equipment for the PIP-II accelerator components as well as the staff required to operate and maintain the facility. The Conventional Facilities portion of the project includes the management, planning, design and construction of new structures, buildings and utilities as well as modifications to existing structures required to install and operate the PIP-II accelerator.

The PIP-II conventional facilities scope includes the elements of work normally included in conventional construction such as earthwork, utilities, structural concrete, structural steel, architectural cladding, finishes, roofing, plumbing, process piping, heating ventilation and air conditioning (HVAC), fire protection, fire detection, lighting and electrical. This also includes the work required to extend the utilities to the project site, excavation associated with the below grade cast-in-place concrete enclosures, creation of a shielding berm and site restoration.

17.1.2 Siting

The location of the PIP-II facility is driven primarily by the physics requirement for close proximity to the existing Booster accelerator and access to existing infrastructure. The location in the Main Ring infield, adjacent to the Footprint area of the Fermilab campus, allows direct access to existing electrical, water, and cryogenic infrastructure currently located in the vicinity. The Main Ring infield location is also well suited to extensions of chilled water service from the existing Central Utility Building (CUB). In addition, the Main Ring infield location provides space for future expansion opportunities.

Figure 17.1: Aerial view looking south

The siting of PIP-II facility was chosen to minimize the impact to existing known wetlands within the Main Ring (Tevatron) infield as well as conform to the 2015 Fermilab Campus Master Plan which has designated the area east of Wilson Hall as the Superconducting Linac Complex.

17.1.3 Work package summary

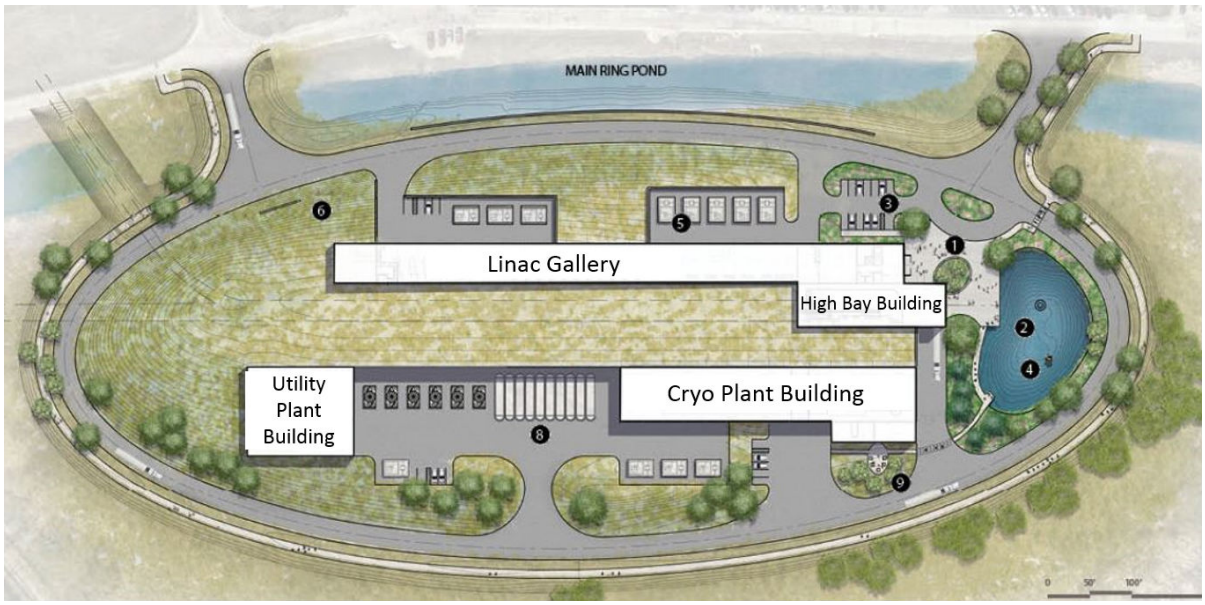

Figure 17.2: Site Plan

The PIP-II Conventional Facilities will be constructed in five (5) work packages as listed below and described in more detail in the following sections.

- Site Preparation
- Crygenic Plant Building
- Utility Plant Building
- Linac Complex
- Booster Connection

17.1.4 Design requirements

The design of the PIP-II Conventional Facilities will be completed in accordance with recognized engineering practices and design standards and will comply with the applicable portions of the U.S. Department of Energy and the State of Illinois codes, orders and regulations as incorporated into

contract No. DE-AC02-07CH11359 between the U.S. Department of Energy and Fermi Research Alliance, LLC.

Fermilab has adopted the Necessary and Sufficient Process (NSP) for determining the Work Smart Set (WSS) of Standards which are used to determine the appropriate environment, safety and health standards used to ensure the safe and environmentally responsible operations of the Laboratory. Where no edition or "latest edition" is noted on the Work Smart Set, it is assumed that the edition in effect at the time of the acceptance of this Project Plan will be used.

17.2 Site preparation

The Site Preparation scope includes the work to prepare the project site by installing erosion control measures, clearing existing vegetation, extending existing utility infrastructure to the project site, reworking the existing AZero pond, extending the existing road network and restoring the site after construction.

17.3 Cryogenics plant building

Figure 17.3: Cryo Plant Building Rendering

The PIP-II Cryogenics Plant Building (CPB) will provide space and infrastructure to support the installation, commissioning and operation of the cryogenics equipment for the PIP-II accelerator components. The Cryogenics Plant Building will be located adjacent to the Linac Complex to minimize the lengths of the cryogenic distribution system. The design of the Cryogenics Plant Building will be developed based on the 2015 Fermilab Campus Master Plan including the desire that "New buildings and structures should be designed to be fresh, inviting, innovative, dynamic and forward-looking."

The Cryogenics Plant Building scope includes the elements of work normally included in conventional construction such as earthwork, utilities, structural concrete, structural steel, architec-

tural cladding, finishes, roofing, plumbing, process piping, heating ventilation and air conditioning (HVAC), fire protection, fire detection, lighting and electrical.

17.3.1 Structural systems performance requirements

The structural systems for the Cryogenics Plant Building are expected to be constructed utilizing conventional methods similar to systems utilized at Fermilab over the past 40+ years.

Shallow building foundations will be constructed of cast-in-place concrete. The above grade portion of the building will be a braced steel frame sized to accommodate overhead bridge cranes.

The structural systems for the Warm Compressor Station of the Cryogenics Plant Building will require vibration isolation in order to avoid impacting the operation of the linac. Machine and compressor foundations will be isolated from the adjacent construction to minimize vibration transmission.

The flatness and levelness of the new floor slabs built as part of the conventional facilities will be designed for normal construction tolerances and a ASTM E1155 floor flatness value of F(F) 25 and a floor levelness F(L) of 20.

The design will include an overhead bridge crane with a capacity of 25 U.S. tons (50,000 pounds) with 27-foot hook height for the Cold Box Station;

The design will include an overhead bridge crane with a capacity of 15 U.S. tons (30,000 pounds) with 27-foot hook height for the Warm Compressor Station.

17.3.2 Mechanical systems performance requirements

The mechanical systems and building automation systems controls for the Cryogenics Plant Building will be designed based on Fermilab standards.

The Heating, Ventilation and Air Conditioning (HVAC) systems will conform to ASHRAE 90.1, ASHRAE 62, applicable NFPA requirements and applicable sections of the Fermilab Engineering Standards Manual.

Ventilation outside air will be supplied to the spaces in accordance with the requirements of ASHRAE 62.1.

All plumbing work to be designed in accordance with Illinois Plumbing Code and Standard Specifications for Water & Sewer Main Construction in Illinois.

Outdoor design conditions will be based on the 2017 ASHRAE Fundamentals Handbook, data for Aurora, Illinois.

Mechanical system and HVAC parameters will be as follows (black squares indicate what is required):

Table 17.1: Mechanical System and HVAC Parameters

Mechanical System and HVAC Parameters	Cold Box Station	Warm Compressor Station	Coordination Center	Mechanical& Electrical Room
HVAC	HVAC	Heating/Ventilating	HVAC	Heating/Ventilating
TEMPERATURES (cooling)	78F(5F)	ambient +10F	78F	ambient +10F
TEMPERATURES (heating)	68F(5F)			
HUMIDITY	55%RH max, no minimum	none	55%RH max, no minimum	none
ODH VENTILATION	■	■		
PRESSURIZATION		■		
CHILLED WATER	■			
PROCESS WATER (ICW)		■		

The ODH (Oxygen Deficiency Hazard) system will be designed in accordance with Fermilab policies and guidelines.

Sustainable goals will be in accordance with the DOE HPSB (High Performance Sustainability Building) checklist. Mechanical system-related sustainability elements such as condensate reuse, water meter, gas meter, energy efficient products, and water efficient fixtures will be included. Other elements such as waste heat recovery and alternative water will be explored and included if life cycle cost effective (see PIP-II-doc-184 for details).

17.3.3 Electrical systems performance requirements

The electrical systems for the Cryogenics Plant Building will be designed based on Fermilab standards and in accordance with applicable codes, regulations and ordinances.

Two (2) electrical systems will power the Cryogenics Plant Building. One (1) system will power the loads for the technical equipment and the other will power the building loads. Primary 13.8 kV electrical power from the existing sitewide electrical system will be extended to the Cryogenics Plant Building. The power extension will include the construction of concrete encased duct banks, installation of 750 kcmil/15 kV primary conductor and related equipment.

The building power transformers will be located away from the building on a concrete pad with oil containment. Two (2) 13.8 kV-4160 Volt transformer will be installed to serve the cryogenic compressors. One (1) 1500 KVA 13.8 kV-277Y/480 Volt power transformers are to be installed, one 1500 KVA power transformer will power the cold box and building power loads. These transformers have been sized based on stakeholder requirements with an adequate safety factor.

The electrical system will provide 25 kVA Uninterruptible Power Supply (UPS) for cryogenics

controls systems, oxygen deficiency hazard (ODH) controls.

A 250-kVA standby diesel generator will be installed on a concrete pad adjacent to the transformers. The generator fuel tank will have a double wall construction with leak detection. An automatic transfer switch is provided to switch loads to the generator upon normal power failure. This generator will feed UPS backup, ODH ventilation equipment, sump pumps and life safety equipment.

17.3.4 Design

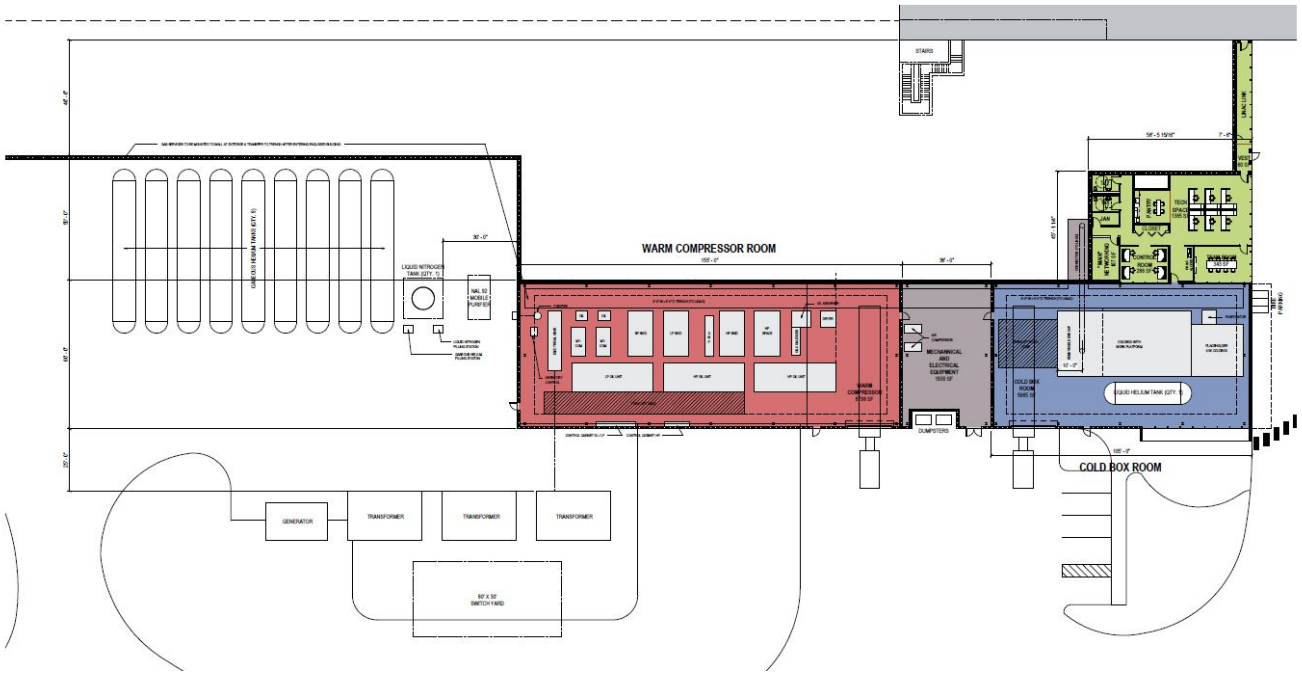

Figure 17.4: Cryo Plant Building Plan. Warm Compressor Room is shown in red, the Cold Box Room in blue and the Coordination Center in green.

The Cryogenics Plant Building will provide space and infrastructure to support the installation, commissioning and operation of the cryogenics equipment for the PIP-II accelerator components.The Cryogenics Plant Building contains three (3) primary spaces as described below:

Cold Box Station

The Cold Box Station will contain the equipment to install, operate and maintain the cold box. This includes the following criteria:

- Approximate Building Size: 15 m x 40 m (50 feet x 131 feet);
- Overhead crane with a capacity of 15 U.S. tons (30,000 pounds);

- Overhead door 5 m x 5 m (17 feet x 17 feet);
- Maximum floor loading: 20,000 kg/square meter (4,096 pounds/square foot);
- Space for five (5) 10,000-liter (2,641 gallons) dewars;
- 565 liters/minute (150 gallons per minute) of chilled water allowance;
- Coordination Center to house 4-8 people;
- Control Room to accommodate equipment, monitors and related control equipment;
- Control Room and Coordination Center should have an isolated HVAC system that can pressurize the room to reduce the oxygen deficiency hazard of the space;

Warm Compressor Station

The Warm Compressor Station will contain the equipment to install, operate and maintain the compressor and related equipment to support the Cold Box Station. This includes the following criteria:

- Space for two (2) compressors and associated equipment plus space for one (1) future compressor and associated equipment;
- Space for two (2) Mycom compressors and associated equipment;
- Approximate Building Size: 20 m x 30 m (66 feet x 100 feet);
- Overhead crane with a capacity of 25 U.S. tons (50,000 pounds);
- Overhead door 5 m x 5 m (17 feet x 17 feet);
- Maximum floor loading: 20,000 kg/square meter (4,096 pounds/square foot);
- The cooling medium for the cryogenics compressors can be industrial cooling water (ICW) if it meets PIP-II quality requirements. A review of the previous tests of the ICW indicate that the water is generally acceptable, but will require additional filtration to meet the solids requirements.

Exterior Space

The exterior space for the Cryogenics Plant Building will provide for access to the Cold Box Station and Warm Compressor Station. This includes the following criteria:

- Space for eight (8) 113,000-liter (30,000 gallon) gaseous helium storage tanks and related piping;

- Space for one (1) 41,000-liter (11,000 gallon) liquid helium storage tank and related piping;
- Space for one (1) 34,000-liter (9,000 gallon) liquid nitrogen dewar and related piping;
- Space for one (1) truck mounted mobile purifier;
- Space for tanker truck for servicing the storage tanks/dewar;
- Parking for 8-10 vehicles;
- Loading dock access to both the Warm Compressor Station and the Cold Box Station;
- Underground utility tunnel (approximate size: 5' deep x 8' wide) that connects the Cryogenics Plant to the Linac Complex.

17.4 Utility plant building

The PIP-II Utility Plant Building (UPB) will provide space and infrastructure to support the installation, commissioning and operation of the process water equipment for the PIP-II accelerator components. The Utility Plant Building will be located in a separate structure adjacent to the Linac Complex to minimize the lengths of the utility infrastructure distribution between the buildings while providing a physical separation to minimize vibration from the mechanical equipment.

The Utility Plant Building scope includes the elements of work normally included in conventional construction such as earthwork, utilities, structural concrete, structural steel, architectural cladding, finishes, roofing, plumbing, process piping, heating ventilation and air conditioning (HVAC), fire protection, fire detection, lighting and electrical.

17.4.1 Structural systems performance requirements

The structural systems are expected to be constructed utilizing conventional methods similar to systems utilized at Fermilab over the past 40+ years.

Shallow building foundations will be constructed of cast-in-place concrete. The above grade portion of the building will be a braced steel frame sized to accommodate overhead bridge cranes.

The structural systems for the Utility Plant Building will require vibration isolation in order to avoid impacting the operation of the Linac. Machine foundations will be isolated from the adjacent construction to minimize vibration transmission.

The flatness and levelness of the new floor slabs built as part of the conventional facilities will be

designed for normal construction tolerances and a ASTM E1155 floor flatness value of F(F) 25 and a floor levelness F(L) of 20.

17.4.2 Mechanical systems performance requirements

The mechanical systems and building automation systems controls will be designed based on Fermilab standards.

The Heating, Ventilation and Air Conditioning (HVAC) systems will conform to ASHRAE 90.1, ASHRAE 62, applicable NFPA requirements and applicable sections of the Fermilab Engineering Standards Manual.

Ventilation outside air will be supplied to the spaces in accordance with the requirements of ASHRAE 62.1.

All plumbing work to be designed in accordance with Illinois Plumbing Code and Standard Specifications for Water & Sewer Main Construction in Illinois.

Outdoor design conditions will be based on the 2017 ASHRAE Fundamentals Handbook, data for Aurora, Illinois.

Mechanical system and HVAC parameters will be as follows:

Table 17.2: Mechanical system and HVAC parameter

Mechanical System and Parameters	Mechanical Equipment Space	Control Room	Electronics Room
HVAC	Heating/Ventilating	HVAC	HVAC
TEMPERATURES (coolings)	ambient +10F	78F (+/- 5F)	78F (+/- 5F)
TEMPERATURES (heating)			
HUMIDITY	none	55%RH max, no minimum	55%RH max, no minimum

The following site utilities will be extended to or routed from the Utility Plant Building:

The ODH (Oxygen Deficiency Hazard) system will be designed in accordance with Fermilab policies and guidelines.

Sustainable goals will be in accordance with the DOE HPSB (High Performance Sustainability Building) checklist. Mechanical system-related sustainability elements such as condensate reuse, water meter, gas meter, energy efficient products, and water efficient fixtures will be included. Other elements such as waste heat recovery and alternative water will be explored and included if life cycle cost effective (see PIP-II-doc-184 for details).

Table 17.3: Site Utilities

Utility Pressure	(psig) 1
DOMESTIC WATER	<40
CHILLED WATER SUPPLY	∼120
CHILLED WATER RETURN	
SANITARY SEWER	NA
ICW for Process Cooling Water	∼75-80
ICW for fire protection	∼75-80

17.4.3 Electrical systems performance requirements

The electrical systems will be designed based on Fermilab standards and in accordance with applicable codes, regulations and ordinances.

Primary 13.8 kV electrical power from the existing sitewide electrical system will be extended to the Utility Plant Building. The power extension will include the construction of concrete encased duct banks, installation of 750 kcmil/15 kV primary conductor and related equipment.

The building power transformers will be located away from the building on a concrete pad with oil containment. These transformers have been sized based on stakeholder requirements with an adequate safety factor.

17.4.4 Design

The Utility Plant Building will provide space and infrastructure to support the installation, commissioning and operation of the cryogenics equipment for the PIP-II accelerator components. The Utility Plant Building contains three (3) primary spaces as described below:

Mechanical Equipment Space - This space will house the mechanical equipment required to support PIP-II operations and includes the following requirements:

- Building Size: 22 m x 46 m (60 feet x 125 feet);
- Overhead door 4.9 m x 4.9 m (16 feet x 16 feet);
- Space for plate and frame heat exchangers and associated equipment;
- Space for cooling tower and LCW pumps;
- Space for LCW filters and de-oxygenator equipment;
- Space for cooling tower water treatment and filtration equipment;

- Space for LCW make-up water system;
- Space for holding tanks and tank/sump for cooling tower system
- Loading Dock for semi-trailer;

Control Room - This space will contain the equipment to operate and monitor the Utility Plant Building. This includes the following:

- Control Room to house 1-2 people in normal operations;
- Training space for 4-6 people;
- Control Room to accommodate equipment, monitors and related control equipment;
- Control Room will be acoustically isolated from Mechanical Equipment Space;
- Space for control equipment and variable frequency drive in semi-conditioned space;
- Toilet;

Exterior Space - This space will provide space for mechanical equipment. This includes the following requirements:

- Space for cooling towers and related piping;
- Space for the air cooled chillers, buffer tank and related piping;
- Parking for 3-6 vehicles;

Construction

The Utility Plant Building is expected to be constructed utilizing conventional methods similar to systems utilized at Fermilab over the past 40+ years. The below grade portion will be constructed of a cast-in-place concrete foundations and slabs-on-grade. The above grade portion of the building will be a braced steel frame with pre-finished metal siding with steel and glass windows. The roof of the Utility Plant Building will be a built-up roof system that complies with Fermilab standards.

17.5 Linac complex

The PIP-II Linac Complex (LC) will provide space and infrastructure to support the installation, commissioning and operation of the equipment for the PIP-II accelerator components. The Linac Complex will be located in the existing Main Ring infield.

Figure 17.5: Linac Gallery Rendering

The Linac Complex scope includes the elements of work normally included in conventional construction such as earthwork, utilities, structural concrete, structural steel, architectural cladding, finishes, roofing, plumbing, process piping, heating ventilation and air conditioning (HVAC), fire protection, fire detection, lighting and electrical. The Linac Complex contains the following components:

17.5.1 High bay building

The High Bay Building (HBB) will be located at the upstream end of the Linac Tunnel (LT) and Linac Gallery (LG) and serves as the major equipment and personnel access to the Linac Complex. The HBB includes a high bay service building with a loading dock and related services to accommodate the installation and servicing of beamline components. This includes space for unloading, staging and assembling beamline components. The at-grade loading dock will include an overhead bridge crane for moving equipment from grade to the below grade portion of the building. The above grade portion of the High Bay Building will be designed to accommodate visitor tours as part of the Fermilab outreach program.

The below-grade portion of the High Bay Building would be sized to accommodate the low energy portion of the PIP-II beamline components that do not require radiation shielding as well as space for staging and preparing beamline components for installation. The below-grade portion will also contain the support equipment and infrastructure required to operate the adjacent beamline components.

17.5.2 Linac tunnel

The below grade Linac Tunnel (LT) will house the superconducting accelerator components and is sized to accommodate the length of a 0.8 GeV Linac which includes modest space to accommodate a possible future upgrade of the Linac energy. The Linac Tunnel will provide space for the Linac hardware, penetrations for utilities (power, water, cryogens) and cabling, as well as for equipment

installation and maintenance. The Linac Tunnel will also accommodate the logistics of installation, repair and removal of beamline components and related support equipment.

17.5.3 Linac gallery

The Linac Gallery (LG) will house the equipment needed to operate the Accelerator components in the adjacent, below grade Linac Tunnel. The gallery will be constructed parallel to the below-grade Linac Tunnel and will provide penetrations for utilities, controls, cooling water, cryogens and related operational services.

17.5.4 Beam transfer line

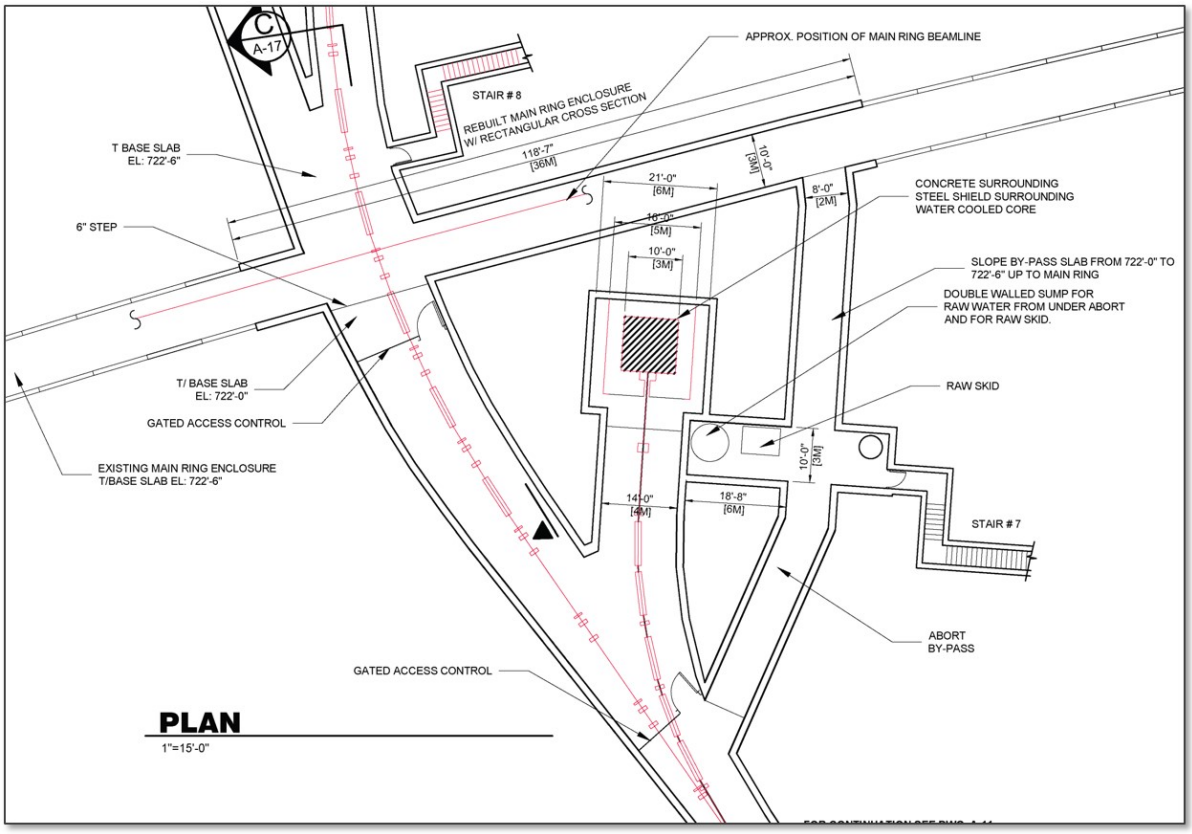

Figure 17.6: Plan at Beam Absorber

The below grade Beam Transfer Line (BTL) will house the beamline components required to bring the proton beam from the downstream end of the Linac Tunnel to the Booster Connection. This included the tunnel section from the downstream end of the Linac Tunnel and the Beam Absorber area. This work will be constructed east of the existing Main Ring enclosure.

17.5.5 Structural systems performance requirements

The structural systems are expected to be constructed utilizing conventional methods similar to systems utilized at Fermilab over the past 40+ years. Shallow building foundations will be constructed of cast-in-place concrete. The above grade portion of the building will be a braced steel frame sized to accommodate overhead bridge cranes.

The flatness and levelness of the new floor slabs built as part of the conventional facilities will be designed for normal construction tolerances and a ASTM E1155 floor flatness value of F(F) 25 and a floor levelness F(L) of 20.

The design of the High Bay Building will include an overhead bridge crane with a capacity of 20 U.S. tons (40,000 pounds) with 27-foot hook height. The Linac Tunnel and Beam Transfer Line will be designed to accommodate up to 5.6 m (18.5 feet) of earth shielding.

The below grade portion of the High Bay Building, the Linac Tunnel and the Beam Transfer Line will include embedded unistrut anchors at 3m (10 feet) spacing. The anchors on the wall closest to the beamline components will end 0.3m (1 foot) from the floor. The anchors opposite the beamline components will end 2m (6.5 feet) from the floor. The anchors will be continuous across the ceiling of the Linac Tunnel and Beam Transfer Line enclosures.

17.5.6 Mechanical systems performance requirements

The mechanical systems and building automation systems controls will be designed based on Fermilab standards.

The Heating, Ventilation and Air Conditioning (HVAC) systems will conform to ASHRAE 90.1, ASHRAE 62, applicable NFPA requirements and applicable sections of the Fermilab Engineering Standards Manual.

Ventilation outside air will be supplied to the spaces in accordance with the requirements of ASHRAE 62.1.

All plumbing work to be designed in accordance with Illinois Plumbing Code and Standard Specifications for Water & Sewer Main Construction in Illinois.

Outdoor design conditions will be based on the 2017 ASHRAE Fundamentals Handbook, data for Aurora, Illinois. Mechanical system and HVAC parameters will be as follows:

The ODH (Oxygen Deficiency Hazard) system will be designed in accordance with Fermilab policies and guidelines. The Linac Tunnel will be ventilated with neutral, dehumidified air as required by code. The underground air flow will include the provision for Oxygen Deficiency Hazard (ODH) ventilation. The conventional facilities will provide the mechanical equipment and ductwork for ODH ventilation while the controls, sensors, programming and commissioning will be accomplished

Table 17.4: High Bay Building

Mechanical System and Parameters	Mechanical Equipment Space	Control Room/ Tech Area	Upper High Bay	Lower High Bay
HVAC	Heating/ Ventilating	HVAC	Heating/ Ventilating	Heating/ Ventilating
TEMPERATURES (cooling)	ambient +1-Fl	78F (+/- 5F)	78F (+/- 5F)	78F (+/- 5F)
TEMPERATURES (heating)	68F(+/-5F)	68F(+/-5F)		
HUMIDITY	none	55% max, no minimum	55% max, no minimum	55% max, no minimum
ODH VENTILATION	■	■	■	■
PRESSURIZATION		■		
CHILLED WATER				
PROCESS WATER (ICW)	■			

Table 17.5: Linac Tunnel

Mechanical System and Parameters	Linac TUnnel
HVAC	Ventilation & dehumidification
TEMPERATURES (cooling)	no cooling, expected 70-75 F
TEMPERATURES (heating)	68F minimum
HUMIDITY	60%RH max; no minimum
ODH VENTILATION	■
PRESSURIZATION	■
CHILLED WATER	
PROCESS WATER (ICW)	

Table 17.6: Linac Gallery

Mechanical System and Parameters	Linac Gallery
HVAC	HVAC
TEMPERATURES (cooling)	no cooling, expected 70-75 F
TEMPERATURES (heating)	68F minimum
HUMIDITY	55%RH max; no minimum
ODH VENTILATION	
PRESSURIZATION	■
CHILLED WATER	■
PROCESS WATER (ICW)	

Table 17.7: Beam Transfer Line

Mechanical System and Parameters	Beam Transfer Line	Beam Dump Area
HVAC	Ventilation & dehumidification	none
TEMPERATURES (cooling)	no cooling control	no cooling control
TEMPERATURES (heating)	68F(+/-5F)	68F(+/-5F)
HUMIDITY	55%RH max, no minimum	none
ODH VENTILATION		
PRESSURIZATION		
CHILLED WATER		
PROCESS WATER (ICW)		

as part of the equipment installation.

Conventional Facilities (WBS 121.6) will provide and install the ODH equipment, including louvers, fans, ductwork and verification of operation. The Cryogenics subproject will provide and install the sensors, control wiring, control panels, displays, related equipment and testing of the completed system.

All penetrations between the Linac Tunnel and Linac Gallery (waveguides, coaxial cables, conduits, piping) will be sealed to reduce the extent possible air movement between the spaces.

Sustainable goals will be in accordance with the DOE HPSB (High Performance Sustainability Building) checklist. Mechanical system-related sustainability elements such as condensate reuse, water meter, gas meter, energy efficient products, and water efficient fixtures will be included. Other elements such as waste heat recovery and alternative water will be explored and included if life cycle cost effective (see PIP-II-doc-184 for details).

17.5.7 Electrical systems performance requirements

The electrical systems will be designed based on Fermilab standards and in accordance with applicable codes, regulations and ordinances.

Two (2) electrical systems will power the Linac Complex. One (1) system will power the loads for the technical equipment and the other will power the building loads. Primary 13.8 kV electrical power from the existing sitewide electrical system will be extended to the Linac Complex. The power extension will include the construction of concrete encased duct banks, installation of 750 kcmil/15 kV primary conductor and related equipment.

The building power transformers will be located away from the building on a concrete pad with oil containment. These transformers have been sized based on stakeholder requirements with an adequate safety factor.

The electrical system will provide 25 kVA Uninterruptible Power Supply (UPS) for controls systems

and oxygen deficiency hazard (ODH) controls.

A 250-kVA standby diesel generator will be installed on a concrete pad adjacent to the transformers. The generator fuel tank will have a double wall construction with leak detection. An automatic transfer switch is provided to switch loads to the generator upon normal power failure. This generator will feed UPS backup, ODH ventilation equipment, sump pumps and life safety equipment.

17.5.8 Special requirements

The design of Linac Complex will include the following radiological design requirements with the goal of achieving unlimited occupancy for all service buildings, shielding berms, parking lots, control rooms and associated areas.

- Passive shielding of 5.6m (18.5 feet) earth equivalent at new tunnel sections;
- Exit passages and corridors will incorporate shielding labyrinths to contained in to reduce exposure to as low as reasonable achievable (ALARA) levels per FESHM Section 1100;
- Dedicated sump at Beam Absorber Area to allow for future monitoring prior to discharge;
- All sump discharges from the Linac Tunnel and Beam Transfer Line will be directed to cooling ponds or ICW return ditches;
- Exhaust fans in the Beam Absorber Area will discharge directly to the exterior without passage through the tunnel sections.
- Radioactive Water (RAW) systems will be utilized for the programmatic equipment in the Beam Absorber area of the Beam Transfer Line. The RAW system, based on existing Fermilab system designs, will be double isolated from surface water and will reject the heat to the LCW system. The design, procurement and installation of the RAW systems are included in the accelerator portion of the project

17.5.9 Design

The Linac Complex will provide space and infrastructure to support the installation, commissioning and operation of the cryogenics equipment for the PIP-II accelerator components. The Linac Complex contains the following spaces:

High Bay Building

The High Bay Building will be located at the upstream end of the Linac Tunnel (LT) and Linac Gallery (LG) and serves as the major equipment and personnel access to the Linac Complex. The

High Bay Building contains three (3) primary spaces as described below:

Upper High Bay

This space, located at grade, will provide the loading dock and primary access point for the adjacent Linac Tunnel. This includes the following requirements:

- Building Size: 18 m x 64 m (50 feet x 175 feet);
- Overhead door 4.9 m x 4.9 m (16 feet x 16 feet);
- Loading dock/staging area of 18 m x 18 m (50 feet x 50 feet) to accommodate a semi-trailer;
- 20-ton capacity overhead bridge crane with coverage for Upper High Bay and Lower High Bay;
- Accommodation for visitor's tours;
- Access to below grade Lower High Bay;
- Access to Support Bay;
- Lower High Bay - This space, located below grade, will contain the equipment to install, assemble, operate the PIP-II accelerator components. This includes the following:
- Space to assemble, install and operate the PIP-II Injector Test (PIP2IT) room temperature accelerator components;
- Space to assemble, install and operate the process water systems to support the PIP2IT room temperature accelerator components;
- Space to assemble, install and operate the Half Wave Resonator (HWR) accelerator component and related equipment;
- The HWR will require 0.9 m (3 foot) thick concrete shielding;
- Space to install and operate the electronics racks, power supplies and related equipment for the room temperature accelerator components;
- Space for Laser Room with the following requirements:
  - The Laser Room will need to be light tight and house a 1.2 m x 2.4 m (4 feet x 8 feet) laser table;
  - The size of the room is 3.6 m x 4.6 m (12 feet x 15 feet) to allow for equipment storage and access around the table;

  - A light tight vestibule sized at 1.2 m x 1.5 m (4 feet x 5 feet) will allow access;
  - Interlocks will be required;
  - A 1.8 m wide x 2.4 m high (6 feet wide x 8 feet) set of double doors to allow for the installation of the laser table;
  - Environmental control in the laser room is important. A stable temperature (+/- 3 degrees F) is required;
  - The primary location of the Laser Room should be near the room temperature PIP2IT components.
  - It can be located at grade in the LG or at the LT level. If it is located beneath the loading dock, vibrations should be considered;
  - The routing of the 2-inch diameter laser pipe will need to be coordinated with radiation shielding

- A 0.9 m (3 foot) thick removable shield block wall will separate the Lower High Bay from the adjacent LT. The overhead crane described in the Upper High Bay portion of the requirements document will be used to install these blocks;
- An ODH barrier will separate the Lower High Bay from the adjacent Linac Tunnel;
- Support Bay - This space, located at grade, will contain the support spaces for the installation, assembly and operation of the PIP-II Linac. This includes the following:
- Control Room to house 3-4 people during normal operations;
- Control Room to accommodate equipment, monitors and related control equipment;
- Control Room will be acoustically isolated;
- Training/collaboration space for 8-12 people;
- Conference Room to accommodate 10-12 people;
- Space for twelve (12) electronics racks. Typical rack size is 1 m x 1.2 m (3 feet x 4 feet) by 42 "U" high;
- Mechanical equipment space;
- Electrical equipment space;
- Receiving Area to accommodate equipment deliveries for the Linac Gallery including the following requirements:

  - Approximately 7.6 m x 18 m (25 feet x 50 feet);
  - 3 m x 3 m (10 feet x 10 feet) overhead door;
  - One (1) ton hoist on monorail track;
- Vestibule space to accommodate:
  - Access control safeguards;
  - Fire Alarm Control Panel;
  - Space for educational posters/display;
  - Orientation space for tour groups of up to 10 people;
- Coded compliant toilets;
- Janitor's closet with slop sink and storage space for cleaning supplies;
- Shower/changing/locker facilities;
- Code compliant stairs to Lower High Bay level;
- Elevator access to Lower High Bay level;
- The Support Bay will be separated from the adjacent Upper High Bay and Lower High Bay with an ODH barrier;

Linac Tunnel

The Linac Tunnel will be located at the downstream end of the below grade portion of the High Bay Building. The requirements for the primary spaces as described below:

- Tunnel Size: 7 m wide x 4.1 m tall (21.83 feet x 13.5 feet);
- Length: Sized to accommodate the following cryogenic accelerator components:
  - One (1) - Half Wave Resonator (HWR);
  - Two (2) - Single Spoke Resonator 1 (SSR1);
  - Seven (7) - Single Spoke Resonator 2 (SSR2);
  - Eleven (11) - Low Beta 650 (LB650) cryomodules;
  - Four (4) - High Beta 650 (HB650) cryomodules;

  - Optional Length: If cost effective, the length of the Linac Tunnel will be designed to accommodate space for up to two (2) additional HB650 cryomodules;

- The downstream end of the Linac Tunnel will incorporate a 12-meter-long (40 feet) space for future extension of the Linac Tunnel. This space will include a removable hatch to allow for accelerator component installation with a mobile crane. Once complete, the space will be filled with removable shielding;

- Code compliant stairs to Linac Gallery;

- Code compliant exit stairs;

- Access to elevator at downstream end of the Linac Tunnel that connects to the Linac Gallery above;

- The Linac Tunnel will be separated from the adjacent Beam Transport Line enclosure with an ODH barrier;

Linac Gallery

The Linac Gallery will be near at parallel to the Linac Tunnel and upstream of the High Bay Building. The Linac Gallery contains three (3) primary spaces as described below:

Linac Equipment Space - This space, located at grade, will provide the infrastructure to house the equipment needed to operate the accelerator components in the adjacent Linac Tunnel. This includes the following requirements:

- Base Size: 13.7 m x 153 m (45 feet x 500 feet) to accommodate support equipment for the following accelerator components:
  - One (1) - Half Wave Resonator (HWR);
  - Two (2) - Single Spoke Resonator 1 (SSR1);
  - Seven (7) - Single Spoke Resonator 2 (SSR2);
  - Eleven (11) - Low Beta 650 (LB650) cryomodules;
  - Four (4) - High Beta 650 (HB650) cryomodules;
- Alternate: 18 m x 38 m (50 feet x 125 feet) space for the support equipment for up to two (2) additional cryomodules in the Linac Tunnel;
- Access to below grade Linac Tunnel;
- Elevator access to below grade Linac Tunnel;

- Access to High Bay Building;

Beam Transfer Line Power Supply Space - This space, located at grade, will house the powers supplies, monitoring racks and related equipment to operate the accelerator equipment in the Beam Transfer Line. This includes the following requirements:

- Size: 18 m x 7.6 m (50 feet x 25 feet);
- Penetrations to below grade Beam Transfer Line enclosure;
- Support space - This space, located above grade, will contain the equipment and infrastructure to support operation of the building. This includes the following:
- Space to house mechanical infrastructure including HVAC units, ductwork and related equipment;
- Space to house the electrical infrastructure including incoming electrical services, transfer switches

Beam Transfer Line

The Beam Transfer Line will be located at the downstream end of the below grade portion of the Linac Tunnel and upstream of the Booster Connection work scope. The Beam Transfer Line consists of two (2) primary spaces as described below:

Tunnel Section - This below grade space will be house the conventional magnets and related equipment to transport the beam from the end of the Linac Tunnel. This includes the following:

- Tunnel Size: 3 m wide x 2.4 m tall (10 feet x 8 feet);
- Interlock and oxygen deficiency hazard (ODH) isolation from adjacent Linac Tunnel;
- Capable of accommodating 5.6 m (18.5 feet) of earth shielding;
- Code compliant exit stairs;
- Beam Absorber Area - This below grade space will house the beam absorber and related equipment including the following:
- Tunnel Size to Beam Dump Enclosure: 4 m wide x 2.4 m tall (14 feet x 8 feet);
- Beam Absorber Enclosure: 6 m wide x 6 m long x 6 m tall (21 feet x 21 feet x 21 feet);
- Beam Absorber Support Room: 6 m long x 3 m wide x 2.4 m tall (18.75 feet x 10 feet x 8 feet) sized to house a double-walled sump pit, radioactive water skid and related equipment;
- The Beam Absorber area will require gated access from the tunnel sections to prevent dead

end corridors;

- Capable of accommodating 5.6 m (18.5 feet) of earth shielding;
- Code compliant exit stairs;
- The Beam Absorber area will be designed to accommodate the installation of the beam dump which will be 3 m x 3 m x 3 m (10 feet x 10 feet x 10 feet) of stacked steel surrounded by 2 m (6.6 feet) of concrete shield blocks.

17.6 Booster connection

The PIP-II Booster Connection will provide space and infrastructure to support the installation, commissioning and operation of the equipment for the PIP-II accelerator components. The Booster Connection will be located in the between the Beam Transfer Line portion of the PIP-II Linac Complex and the existing Booster Connection.

The Booster Connection scope includes the elements of work normally included in conventional construction such as earthwork, utilities, structural concrete, structural steel, architectural cladding, finishes, roofing, plumbing, process piping, heating ventilation and air conditioning (HVAC), fire protection, fire detection, lighting and electrical. The Booster Connection contains the following components:

17.6.1 Main ring crossing

The below-grade Main Ring Crossing area is defined as the portion of the Booster Connection work that intersects with the existing Main Ring enclosure. This portion will house the room temperature beamline components and related equipment that is required to transport the beam.

17.6.2 Booster tie-In

The Booster Tie-In includes the below grade Tunnel Enclosure will house the beamline components required to bring the proton beam from the downstream end of the Main Ring Crossing area to the existing Booster enclosure. This component also includes the demolition of the existing Booster Tower Southeast building and associated work.

17.6.3 Structural systems performance requirements

The structural systems are expected to be constructed utilizing conventional methods similar to systems utilized at Fermilab over the past 40+ years.

The flatness and levelness of the new floor slabs built as part of the conventional facilities will be designed for normal construction tolerances and a ASTM E1155 floor flatness value of F(F) 25 and a floor levelness F(L) of 20.

The Linac Tunnel and Beam Transfer Line will be designed to accommodate up to 5.6 m (18.5 feet) of earth shielding.

The below grade portion of the Booster Connection will include embedded unistrut anchors at 3m (10 feet) spacing. The anchors on the wall closest to the beamline components will end 0.3m (1 foot) from the floor. The anchors opposite the beamline components will end 2m (6.5 feet) from the floor. The anchors will be continuous across the ceiling of the tunnel enclosures.

17.6.4 Mechanical systems performance requirements

The mechanical systems and building automation systems controls will be designed based on Fermilab standards.

The Heating, Ventilation and Air Conditioning (HVAC) systems will conform to ASHRAE 90.1, ASHRAE 62, applicable NFPA requirements and applicable sections of the Fermilab Engineering Standards Manual.

Ventilation outside air will be supplied to the spaces in accordance with the requirements of ASHRAE 62.1.

All plumbing work to be designed in accordance with Illinois Plumbing Code and Standard Specifications for Water & Sewer Main Construction in Illinois.

Outdoor design conditions will be based on the 2017 ASHRAE Fundamentals Handbook, data for Aurora, Illinois.

Mechanical system and HVAC parameters will be as follows:

All penetrations between the Booster Connection and Linac Gallery portion of the Linac Complex (cables, conduits, piping) will be sealed to reduce the extent possible air movement between the spaces.

Sustainable goals will be in accordance with the DOE HPSB (High Performance Sustainability Building) checklist. Mechanical system-related sustainability elements such as condensate reuse, water meter, gas meter, energy efficient products, and water efficient fixtures will be included.

Table 17.8: Mechanical system and HVAC Parameters

Mechanical system and Parameters	Beam Transfer Line	Beam Dump Area
HVAC	Ventilation & dehumidification	none
TEMPERATURES (cooling)	no cooling control	no cooling control
TEMPERATURES (heating)	68F (+/-5F)	68F (+/-5F)
HUMIDITY	55%RH max, no minimum	none
ODH VENTILATION		
PRESSURIZATION		
CHILLED WATER		
PROCESS WATER (ICW)		

Other elements such as waste heat recovery and alternative water will be explored and included if life cycle cost effective (see PIP-II-doc-184 for details).

17.6.5 Electrical systems performance requirements

The electrical systems will be designed based on Fermilab standards and in accordance with applicable codes, regulations and ordinances.

The electrical power for the Booster Connection will be fed from the Linac Gallery portion of the Linac Complex.

17.6.6 Special requirements

The design of Booster Connection will include the following radiological design requirements with the goal of achieving unlimited occupancy for all service buildings, shielding berms, parking lots, control rooms and associated areas.

- Passive shielding of 5.6m (18.5 feet) earth equivalent at new tunnel sections; item âĂć Exit passages and corridors will incorporate shielding labyrinths to contained in to reduce exposure to as low as reasonable achievable (ALARA) levels per FESHM Section 1100;

- All sump discharges from the Booster Connection will be directed to cooling ponds or ICW return ditches;

17.6.7 Design

The Booster Connection will provide space and infrastructure to support the installation, commissioning and operation of the cryogenics equipment for the PIP-II accelerator components. The

Booster Connection contains the following spaces:

17.6.7.1 Main ring crossing

The below-grade Main Ring Crossing area is defined as the portion of the Booster Connection work that intersects with the existing Main Ring enclosure. This portion will house the room temperature beamline components and related equipment that is required to transport the beam and well as accommodate future expansion. This includes the following requirements:

- Tunnel Size: 3 m wide x 3.7 m tall (10 feet x 12 feet);
- Length: 36.4 m (119.6 feet);
- The Pip will cross the existing Main Ring/Tevatron tunnel and the height will increase to accommodate the PIP-II beamline components crossing over the top of the existing 120 Gev beamline;
- The area will include a 12-meter-long (40 feet) long by 2.4 m high (8 feet) extension to allow for a future beamline to serve the Muon Campus;

17.6.7.2 Booster tie-In

The Booster Tie-In will be located at the downstream end of the Main Ring Crossing and adjacent to the existing Booster enclosure. This below grade space will be house the conventional magnets and related equipment to transport the beam. The floor of the Booster Connection enclosure will match the elevation of the Beam Transfer Line component of the Linac Complex to facilitate the installation of beamline components.

The Booster Connection enclosure will be installed beneath the existing Booster Tower East parking lot to allow for the PIP-II beam to intercept the existing Booster beamline at the existing Long 11 straight section, which results in minimal displacements of the existing Booster tunnel equipment and reduces the interference with existing support services.

The installation of the Booster Connection enclosure will require a demolition of the existing Booster Tower East building to excavate and install the cast-in-place concrete connection to the existing Booster enclosure.

The Booster Tower Southeast parking lot will be replaced with a shielding berm similar in style and construction to that constructed when the Main Injector 8 GeV line was installed at Booster Tower Southwest. Vehicular access to existing electrical equipment in the northeast corner of the parking lot will be provided for maintenance of the electrical equipment.

Additional requirements include the following:

- Tunnel Size: 3 m wide x 2.4 m tall (10 feet x 8 feet);
- Capable of accommodating 5.6 m (18.5 feet) of earth shielding;
- Code compliant exit stairs;
- Demolition of the existing Booster Tower Southeast building and replacement with a shielding berm;
- Space and infrastructure to house the beamline power supply for the new PIP-II booster injection girder. This space could be within the existing Booster Gallery or housed in new construction adjacent to the existing Booster Gallery.

Chapter 18

Environment, Safety and Health

18.1 Overview

Fermilab is committed to supporting its research and operations by protecting the health and safety of staff, the community and the environment. The laboratories Safety and Health Program is in compliance with applicable standards and Local, State and Federal legal requirements through Fermilab's Work Smart Set of Standards and the contract between Fermilab Research Alliance and the Department of Energy.

The program strives for the prevention of injury or illness and continual improvement in safety and health management and performance. To the maximum extent practicable, all hazards shall be eliminated, substituted or minimized through engineering or administrative controls. Where engineering or administrative controls are not feasible, personal protective equipment (PPE) shall be utilized.

The Environment, Safety and Health (ES&H) Management System is designed to work hand in hand with the Emergency Management System to protect the public, the worker and the environment; ensure compliance with the Contract; and to improve Fermilab's ability to meet or exceed customer expectations, thereby executing the scientific mission. Fermilab uses a set of elements to plan, direct, control, coordinate, assure and improve how ES&H policies, objectives, processes and procedures are established, implemented, monitored and achieved.

The Fermilab facilities are further subject to the requirements of the Department of Energy (DOE) Accelerator Safety Order (ASO), DOE O 420.2C [1], Safety of Accelerator Facilities. These requirements are promulgated through the Fermilab Director's Policy Manual [2], the Fermilab Environ-

[1] DOE O 420.2C, Safety of Accelerator Facilities, July 21, 2011. The current web link is: `https://www.directives.doe.gov/directives-documents/400-series/0420.2-BOrder-c`

[2] Fermilab Director's Policy Manual. The current web link is: `http://www.fnal.gov/directorate/Policy_Manual.html`

ment, Safety, and Health Manual [3] (FESHM) and the laboratory's Radiological Control Manual [4] (FRCM).

18.2 Preliminary hazard analysis report (PHAR)

One of the key elements of an effective ESH program is the hazard identification process. Hazard identification produces a list of hazards present within a facility allowing these hazards to be screened, and those of concern, managed through a suitable set of controls.

The PIP-II project completed a Preliminary Hazard Analysis Report (PHAR) to assure that identified hazards are mitigated early in the evolution of the design. The focus of the report is on process hazards rather than activity hazards that are typically covered in a job hazard analysis. The PHAR has been completed to identify the hazards anticipated to be encountered during the project's construction and operational phases.

The PHAR then looks at the consequences of the hazard to establish a pre-mitigation risk category. Proposed mitigations are applied to hazards of concern to mitigate risks and then establishes a post-mitigation risk category.

As the PIP-II design matures, the PHAR is updated to ensure that all hazards have been properly identified and controlled through design and safety management system programs. In addition, some sections of the PHAR are used to meet the safety requirements defined in DOE Order 420.2C. Tables 18.1, 18.2, 18.3 and 18.4 summarize these hazards. The sections following the tables describe the hazards in more detail and the design and operational controls used to mitigate these hazards. The results of these evaluations confirm that the potential risks from construction, operations and maintenance are acceptable.

18.2.1 Construction hazards (PIP-II PHA-1)

Fermilab has a mature construction safety program with recent experience constructing the Utility Upgrade Project, G-2 and Mu2e experimental areas and the Short Baseline Near Detector building. Lessons learned from the laboratory's Lessons Learned Database and the DOE OPEXShare database are reviewed to influence the project design. Formal project and internal project reviews are utilized to capture best practices and lessons learned. The Safety by Design process provides a means to capture lessons learned and track integration into the project. Analysis of activities associated with the construction of the PIP-II Project have not identified any new or unusual hazards.

The project will use the laboratories existing Work Planning and Control process along with a Construction Project Safety and Health Plan to communicate these policies and procedures as

[3] Fermilab ES&H Manual. The current web link is: `http://esh.fnal.gov/xms/ESHQ-Manuals/FESHM`

[4] Fermilab Radiological Control Manual. The current web link is: `http://esh.fnal.gov/xms/ESHQ-Manuals/FRCM`

Table 18.1: Preliminary Hazard Analysis Identifier and Hazards List 1

Hazard ID: PIP-II linac- PHA-1	**Hazard ID: PIP-II - PHA-2**
Construction Hazards	**Natural Phenomena Hazards**
Site Clearing	Seismic
Excavation	Flooding
Vertical-Horizontal Conveyance Systems	Wind
Confined space	Lighting
Heavy Equipment	Tornado
Work at Elevations (steel erection, roofing)	
Material Handling (rigging)	
Utility interfaces (electrical, chilled water, ICW, natural gas)	
Slips-trips-falls	
Weather related conditions	
Scaffolding	
Transition to Operations	
Radiation Generating Devices	
Hazard ID: PIP-II - PHA-3	**Hazard ID: PIP-II - PHA-4**
Environmental Hazards	**Waste Hazards**
Construction impacts	Construction Phase
Storm water discharge (construction and operations)	Facility maintenance
Operations impacts	Industrial
Soil and groundwater activation-contamination	Hazardous
Tritium contamination	Radiological
Air activation	
Cooling water activation (HVAC and Machine)	
Oils-chemical leaks or spills	
Discharge-emission points	
(atmospheric-ground)	

Table 18.2: Preliminary Hazard Analysis Identifier and Hazards List 2.

Hazard ID: PIP-II - PHA-5	**Hazard ID: PIP-II - PHA-6**
Fire Hazards	**Electrical Hazards**
Facility Occupancy Classification	Facility
Construction Materials	Experimental
Storage	Job built Equipment
Flammable-combustible liquids	Low Voltage-High Current
Flammable gasses	High Voltage-High Power
Egress-access	Maintenance
Electrical	Arc flash
Lighting	Electrical shock
Welding-cutting-brazing work	Cable tray overloading-mixed utilities
Smoking	Exposed 110v
	Stored energy (capacitors and inductors)
Hazard ID: PIP-II - PHA-7	**Hazard ID: PIP-II - PHA-8**
Noise-Vibration-Thermal-Mechanical Hazards	**Cryogenic-Oxygen Deficiency Hazards**
Construction Tools	Thermal
Machine Shop Tools	Cryogenic distribution systems
Industrial Vehicles	Pressure
Drilling, Cutting, Grinding	Handling and Storage
Pressure-Vacuum Vessels and Lines	Liquid argon-nitrogen spill-leak
High Temp Equipment (Bakeouts)	Use of inert gases (nitrogen, helium)
	Specialty gases accelerator operation

Table 18.3: Preliminary Hazard Analysis Identifier and Hazards List 3.

Hazard ID: PIP-II - PHA-9	**Hazard ID: PIP-II - PHA-10**
Confined Space Hazards	**Chemical-Hazardous Material Inventory**
Sumps	Toxic
Utility Chases	Compressed gas
	Combustibles
	Explosives
	Flammable gases
	Lead (shielding)
	Cryogenic
Hazard ID: PIP-II - PHA-11	**Hazard ID: PIP-II - PHA-12**
Accelerator-Beamline Hazards	**Ionizing Radiation Exposure, inside of the accelerator or beamline enclosure**
Vacuum-Pressure	
Cooling water	
Compressed gas	Prompt radiation
Electrical	Residual (activated components)
Heavy equipment handling	Airborne contamination
High magnetic shields	
Shielding	
Mechanical (moving shutters, valves and actuators)	

Table 18.4: Preliminary Hazard Analysis Identifier and Hazards List 4.

Hazard ID: PIP-II - PHA-13	**Hazard ID: PIP-II - PHA-14**
Ionizing Radiation Hazards, outside of the accelerator or beamline enclosure	**Lasers and other Non-Ionizing Radiation Hazards**
Prompt Radiation	Alignment Laser
Tritium production	Testing and Calibration
Radioactive contamination	Magnetic Fields
Activation (equipment)	Calibration and Testing
Radioactive material (dispersible use, storage, surface contamination)	
Airborne Radionuclides	
Radiation Generating Devices used for nondestructive measurement purposes, including soil compaction	
Hazard ID: PIP-II - PHA-15	
Material Handling Hazards	
Overhead cranes-hoists	
Fork trucks	
Manual material handling	
Delivery area distribution	
Manual movement of materials	
Hoisting and rigging	
Lead	
Oils, solvents, acids	
Cryogens	
Compressed gases	

required by DOE Order 413.3b. The typical installation and construction hazards anticipated for the PIP-II Project include the following:

- Site Clearing
- Excavation
- Vertical/Horizontal Conveyance Systems
- Confined space
- Heavy Equipment Operations
- Work at Elevations (steel erection, roofing)
- Material Handling (rigging)
- Utility interfaces (electrical, chilled water, ICW, natural gas)
- Slips/trips/falls
- Weather related conditions
- Scaffolding
- Transition to Operations
- Radiation Generating Devices.

To reduce risks from construction hazards, sub-contractors working on the Fermilab site will complete the Sub-Contractor Orientation training program where all contractors working on site in an unescorted capacity are trained in site specific hazards and policies. The course has a two year requalification interval. The training course covers Fermilab's ES&H policy and the expectations concerning sub-contractors; emergency phone numbers, alarms and actions; general safety information and requirements. When required, sub-contractors take additional courses for General Employee Radiation Training or Radiation Worker Training and Radiation Worker Practical Factors.

Fermilab will use engineered and approved excavation and fall protection systems. Heavy equipment will utilize required safety controls. Fermilab's construction safety oversight program includes periodic evaluation of the construction site and construction activities, hazard analysis for all subcontractor activities, and frequent ES&H communications at the subcontractor's daily tool box meetings.

A portion of the construction work that crosses the Main Ring enclosure and where the beam transport line connects to the Booster enclosure will involve work with low level radioactive materials. Radiation surveys will be performed, radiological work permits issued, and personnel trained

in radiological work procedures. Fermilab has a long history of performing construction in and around existing accelerator enclosures. The potential level of exposure to workers is not expected to be significant.

18.2.2 Natural phenomena hazards (PIP-II PHA-2)

The PIP-II design will be governed by DOE-STD-1020-2016, Natural Phenomena Hazard Analysis and Design Criteria for Department of Energy Facilities and the International Building Code 2018 (IBC 2018). DOE-STD-1020-2016 provides criteria and guidance for meeting the natural phenomena hazard requirements of DOE Order 420.1C, Chg. 2, Facility Safety. The IBC specifies design criteria for wind loading, snow loading, and seismic events.

PIP-II also was determined to be a low hazard Performance Category 1 facility as per DOE STD-1021-93. PIP-II areas will contain small quantities of activated, radioactive, and hazardous chemical materials. Should a Natural Phenomenon Hazard cause significant damage, the impact will be mission related and will not pose a hazard to the public or the environment.

18.2.3 Environmental hazards (PIP-II PHA-3)

Environmental hazards from PIP-II include the potential for releasing chemicals and radioactive materials surrounding the beamline, absorber, soil, groundwater, surface water, air, or sanitary sewer system which if not controlled could exceed regulatory limits. Materials removed from the beamline enclosures will be surveyed for residual radioactivity or contamination, labeled, and appropriately disposed of in accordance with the FRCM.

Fermilab maintains an Environmental Management System equivalent to ISO 14001 consisting of programs for protecting the environment, assuring compliance with applicable environmental regulations and standards and avoiding adverse environmental impacts through an effort of continual improvement. These programs are documented in the 8000 and 11000 series of chapters in the FESHM.

18.2.4 Waste hazards (PIP-II PHA-4)

Waste related hazards from PIP-II include the potential for releasing waste materials (oils, solvents, chemicals and radioactive material) to the environment, injury of personnel, and a possible reactive or explosive event. Typical initiators will be transportation accidents, incompatible materials, insufficient packaging/labeling, failure of the packaging, and a natural phenomenon.

During construction of the PIP-II conventional facilities, typical construction waste, such as excavated spoils, cement, metals, and wood will be generated. The conventional construction project will manage this waste and the materials will be properly recycled or disposed of in accordance with

local, state, and federal regulatory requirements. The ESH&Q Section Hazard Control Technology Team along with the campus-wide recycling program will drive recycling efforts to minimize waste disposal.

During the installation and operation of PIP-II it is anticipated that minimal quantities of hazardous materials will be used. Such materials include paints, epoxies, solvents, oils and lead in the form of shielding. There are no current or anticipated activities at PIP-II that would expose workers to levels of contaminants (dust, mists or fumes) above regulatory limits.

The ESH&Q Section Industrial Hygiene Group and Hazard Control Technology Team provides program management and guidance to Fermilab employees who are subject to waste-related hazards. Their staff assists with identifying workplace hazards, assists with identifying controls, and monitors implementation to keep employee exposures below the ACGIH Threshold Limit Values (TLVs). Industrial hygiene hazards will be evaluated, identified, and mitigated as part of the work planning and control hazard assessment process.

18.2.5 Fire hazards (PIP-II PHA-5)

The probability of a fire at PIP-II is very low, similar to that of present laboratory operations. Accelerator and beamline components are primarily fabricated out of nonflammable materials and combustible materials are kept to a minimum during all phases of the project. Operational experience at Fermilab and at accelerators throughout the DOE complex has demonstrated that most fires in accelerator facilities are electrically initiated, typically by component failure.

Fire hazards have been evaluated and are being addressed in compliance with DOE Order 420.1C (Facility Safety), Chapter II and DOE-STD-1066, Fire Protection Design Criteria. The intent of these documents is to meet a Highly Protected Risk level of fire protection and National Fire Protection Association (NFPA) Standard 520. A Fire Protection/Life Safety Analysis for the PIP-II project was completed by Jensen Hughes, Inc. based on the preliminary project facility designs. Comments and recommendations from this report are being incorporated into the final facility designs.

The combustible loads and the use of flammable and/or reactive materials in the PIP-II facility are controlled in accordance with the International Building Code (IBC) building occupancy classification. Certain ancillary buildings outside the main structure may be classified as higher hazard areas ("H" occupancy), including the gas cylinder and chemical storage rooms because they hold more concentrated quantities of flammable or combustible materials. The "control area" concept used by IBC and NFPA 45 will be followed in hazardous chemical use and storage areas to provide the greatest amount of flexibility and control of materials by allowing inventory thresholds per control area. The PIP-II will be equipped with fire detection systems and alarm systems that will monitor water flow in the sprinkler system and supervise the sprinkler valves and the installed detection systems.

Audible/visual alarm notification devices will alert building occupants. Manual pull stations for the fire alarms will be installed at all building exits. In accordance with NFPA 90A, the air

handling systems will have photoelectric smoke detectors. Area smoke detectors, type to be determined, will be provided in areas where there is highly sensitive electronic equipment. Combination audible/visual alarm notification devices will be set up throughout the underground enclosures and service buildings to alert occupants. All Fire Alarm signals will report through a centralized system. Fermilab will utilize the Fire Incident Reporting Utility System (FIRUS). Fire alarm and supervisory signals will be transmitted to the internal and external emergency responders via the campus fire alarm radio reporting system.

While designed-in fire protection systems afford an excellent level of protection, additional strategies such as operational controls including combustible materials minimization programs, adequately fused power supplies, fire safety inspections, and Operational Readiness Reviews will be utilized to further reduce fire hazards within the facility.

18.2.6 Electrical hazards (PIP-II PHA-6)

Like existing accelerators and beam transfer lines at Fermilab, PIP-II will have significant facility-related systems and subsystems that produce or utilize high voltage, high current, or high levels of stored energy, all of which can present electrical hazards to personnel. Electrical hazards include electric shock and arc flash from exposed conductors, defective and substandard equipment, lack of training, or improper procedures.

Fermilab has a well-established electrical safety program that incorporates deenergizing equipment, isolation barriers, personal protective equipment, and training. The corner stone of the program is the implementation of Lockout / Tagout (LOTO) in accordance with FESHM Chapter 2100, Fermilab Energy Control Program (Lockout/Tagout).

Design, installation, and operation of electrical equipment will be in compliance with the National Electrical code (NFPA 70), applicable parts of Title 29 Code of Federal Regulations, Parts 1910 and 1926, NFPA 70E and Fermilab electrical safety policies documented in the FESHM 9000 series chapters. Equipment procured from outside vendors or international in-kind partners will be either certified by a nationally recognized testing laboratory (NRTL), conform to international standards previously evaluated and deemed equivalent to US standards, or inspected and accepted in accordance with Fermilab's electrical equipment inspection policies outlined in FESHM 9110, Electrical Utilization Equipment Safety.

Entry into the accelerator enclosures requires the mitigation of electrical hazards through either the LOTO of power sources or use of electrical isolation barriers. PIP-II will employ a group written Lock Out Tag Out system to de-energize any exposed buss in the enclosure before access. The system will be similar to those used in other accelerator and beamline areas in operation at Fermilab. Power sources feeding electrical equipment in the beamline enclosures with exposed conductors are also interlocked to the enclosure Electrical Safety System as a defense in depth control to further reduce the risk of exposure to electrical hazards. Appropriate levels of electrical safety, LOTO and Arc Flash training are provided to all personnel who work on or near potential electrical hazards.

18.2.7 Noise, vibration, thermal, and mechanical hazards (PIP-II PHA-7)

Hazards from noise and vibration include overexposure of personnel to American Conference of Governmental Industrial Hygienists (ACGIH) and OSHA noise limits and permanent hearing loss, also known as Permanent Threshold Shift (PTS). The vibration of equipment can contribute to the noise levels, along with potential damage to or interference with sensitive equipment.

PIP-II will incorporate a wide variety of equipment that will produce a wide-range of noise and vibration. Support equipment, such as pumps, motors, fans, machine shops, and general HVAC all contribute to point source and overall ambient noise levels. While noise will typically be below the ACGIH and OSHA 8-hour time weighted average, certain areas with mechanical equipment could exceed that criterion and will require periodic monitoring, posting, and the use of PPE. Ambient background noise is a greater concern from the standpoint of users' comfort, stress level, and fatigue.

The beamline facilities use a wide variety of noisy equipment. Pumps, fans, and machine shop devices, among others, are possible sources of noise levels that might exceed the Fermilab noise action levels. FESHM Chapter 4140, Hearing Conservation, contains requirements for reducing noise and protecting personnel who may be exposed to excessive noise levels. Warning signs are posted where hazardous noise levels may arise, and hearing protection devices are readily available. Methodologies to reduce noise and vibration will be incorporated into the PIP-II design. These techniques include using low noise/vibration producing equipment, especially for fans in the HVAC equipment, isolating the noise producing equipment by segregating or enclosing it, and using sound deadening materials on the walls and ceilings of areas.

18.2.8 Cryogenic and oxygen deficiency hazards (PIP-II PHA-8)

The PIP-II project will use large volumes of liquid nitrogen and helium to cool the superconducting Linac. Cryogenic hazards will include the potential for oxygen deficient atmospheres due to catastrophic failure of the cryogenic systems, thermal (cold burn) hazards from cryogenic components, and pressure hazards. Initiators could include the failure or rupture of cryogenic systems from overpressure, failure of insulating vacuum jackets, mechanical damage or failure, deficient maintenance, or improper procedures.

The extreme low temperatures of cryogenic liquids and gases have a significant adverse effect on the human body, as well as on inanimate objects. These effects range from destroying human tissue to altering the physical characteristics and properties of materials, such as size, strength and flexibility of metals and other materials.

Although cryogens are used extensively at Fermilab, there are strict limitations on quantities that may be used within a facility. Uses beyond defined limits require an Oxygen Deficiency Hazard (ODH) analyses and the use of ventilation, oxygen deficiency monitoring, or other controls.

Cryogenic systems are subject to the formal project review process, which includes independent

reviews by a subpanel of the Cryogenic Safety Subcommittee in accordance with FESHM Chapter 5032, Cryogenic System Review. The members of this panel have relevant knowledge in applicable subject matter areas. They review the system safety documentation, ODH analysis documentation, and the equipment before new systems are permitted to begin the cool down process.

All piping systems and storage systems will be designed and installed to comply with applicable FESHM 5000 series chapters, ASME and American National Standards Institute (ANSI) standards.

Fermilab has developed and successfully deployed ODH monitoring systems throughout the laboratory in support of its current cryogenic operations. The systems are designed to provide both local and remote alarms when atmospheres contain less than 19.5% oxygen by volume.

Fermilab has a mature training program to address cryogenic safety hazards. Key program elements include ODH Training, pressurized gas safety and general cryogenic safety.

18.2.9 Confined space hazards (PIP-II PHA-9)

Hazards from confined spaces could result in death or injury due to asphyxiation, compressive asphyxiation, smoke inhalation, or impact with mechanical systems. Initiators would include failure of the cryogenic systems releasing liquid, the release of gas, fire, or failure of mechanical systems.

Two types of confined spaces would potentially be created in the construction of the PIP-II facility. The first is the space associated with the facility's support/maintenance and typically include sump pits and HVAC plenums that will only be accessed by trained maintenance or vendor personnel. Scientific staff will not have access to these spaces. The second category is those confined spaces created by elevator pits and sanitary lift stations.

The Fermilab campus confined space program is outlined in FESHM Chapter 4230, Confined Spaces. PIP-II facilities will be incorporated into this program. The emphasis at the PIP-II preliminary design phase will be to ensure the minimum number of confined spaces are created. This is accomplished by clear articulation of the definition of confined spaces to facility designers to assure that adequate egress is designed in to them, mechanical spaces are adequately sized, and, wherever possible, a confined space not be created. During facility operations, the existing campus confined space program, along with appropriate labeling of confined spaces, work planning and control, and entry permits will be used to control access to these spaces.

18.2.10 Chemicals and hazardous materials (PIP-II PHA-10)

The PIP-II facility anticipates a minimal use of chemical and hazardous materials, based on the construction and operations of similar facilities at Fermilab. Materials such as paints, epoxies, solvents, oils, and lead shielding may be used during the construction and operations of the facility.

Exposure to these materials could result in injury, or exposures that exceed regulatory limits. Initiators could be experimental operations, transfer of material, failure of packaging, improper marking/labeling, reactive or explosive event, improper selection of or lack of, personal protective equipment (PPE), or a natural phenomenon.

Fermilab maintains an inventory of hazardous chemicals in compliance with the requirements imposed by 10 CFR 851 and DOE Orders. In addition to the inventory of chemicals at the facility, copies of the respective manufacturer's Safety Data Sheets (SDSs) are maintained. Reviews of the conventional safety aspects of the facilities show that use of these chemicals does not warrant special controls other than appropriate signs, procedures, appropriate use of personal protective equipment, and hazard communication training.

The industrial hygiene program, detailed in the FESHM 4000 series chapters, addresses potential hazards to workers using such materials. The program identifies how to evaluate workplace hazards when planning work and the controls necessary to eliminate or mitigate these hazards to an acceptable level.

Specific procedures are also in place for the safe handling, storing, transporting, inspecting and disposing of hazardous materials. These are contained in the FESHM 8000 and 10000 series chapters, Environmental Protection and Material Handling and Transportation, which describes the standards necessary to comply with the Code of Federal Regulations, Occupational Safety and Health Standards, Hazard Communication, Title 29 CFR, Part 1910.1200.

18.2.11 Accelerator/beamline hazards (PIP-II PHA-11)

Hazards from the PIP-II accelerator and beamline include vacuum/pressure, cooling water systems, compressed gases, electrical and magnetic fields, cryogenics, radiation, mechanical components (moving shutters, valves and actuators), material handling, access and egress, falls, and walking and working surfaces.

The accelerator and beamlines will have medium and high-voltage electrical equipment and associated power supplies. High-power equipment includes radio frequency (RF), vacuum pumps, vacuum gauges, detectors, and beam position monitors.

Access and egress from the tunnel will be through fire protected stairwells. The Radiation Safety Interlock Systems will ensure personnel will not enter the interlocked areas.

Conventional beamline hazards are mitigated by following the requirements outlined in the FESHM and FRCM.

18.2.12 Ionizing radiation exposure hazards, inside accelerator enclosures (PIP-II PHA-12)

Potential hazards from ionizing radiation include prompt radiation produced during machine operation, induced activity in machine components, and radioactive material (use, storage). Typical initiators of radiation exposure will include operating machines, maintenance work, and using radioactive materials. Accidental exposure, though very unlikely, could possibly result from failure of interlocks or other protective systems, inadequate design or control of shielding, or an inadequate procedure.

The PIP-II facility design will incorporate the requirements specified in 10 CFR 835, Occupational Radiation Protection Program, and the accelerator-specific safety requirements in DOE Order 420.2C, Safety of Accelerator Facilities. Access to radiation areas inside the beamline enclosure area, during machine operations, will be rigorously controlled via a Radiation Safety Interlock System (RSIS) as defined in FRCM Chapter 10.

Radiofrequency accelerating structures within the Linac enclosure may generate electromagnetic fields of sufficient amplitude to generate dark-current electrons of sufficient energy to produce x-rays. The RSIS will disable all RF power to these structures when personnel are on access thus mitigating the x-ray hazard.

The potential for radiation exposure when the beamline is not running is low since radiation levels from induced radioactivity are anticipated to be very low. Dose to workers will be monitored using a combination of personal dosimeters, area dosimeters, real time radiation monitors, and hand-held radiation survey instruments. Fermilab's dosimetry program is accredited by the DOE Laboratory Accreditation Program (DOELAP) for measuring personal exposures.

Fermilab has an administrative dose goal of 1.5 rem, well below the Federal limit of 5 rem. The Fermilab ALERT System has been established to ensure the administrative goal is not inadvertently exceeded. Any individual who meets or exceeds 350 mrem in a calendar quarter is assigned to the ALERT list.

Although cooldown periods are not anticipated for any of the PIP-II enclosures, airborne contamination in enclosures will also be monitored and as needed, administrative access controls put in place to avoid personnel exposure during beamline access.

18.2.13 Ionizing radiation exposure hazards, outside beamline enclosures (PIP-II PHA-13)

Potential hazards from ionizing radiation outside of the beamline enclosure include possible dose to employees or the public due to prompt radiation, radioactivated material, radioactivated air release, surface water, groundwater and soil activation.

During the Conceptual Design phase, a beam loss of 10 W/m was used to determine that 18.5 feet

earth equivalent shielding would result in an effective dose outside the shielding of < 0.05 mrem/hr. A total loss monitor (TLM) could be installed inside the beamline enclosure and interlocked to the Radiation Safety Interlock System to monitor for excessive beam losses.

Various components along the PIP-II beamline enclosure could contribute radiation dose to the public at the site boundary. PIP-II beamline is designed with sufficient shielding, 18.5 feet earth equivalent, so that the maximal annual effective dose, from all the PIP-II beamline operations, to a member of the public, is less than 1 mrem. Radiation monitoring systems will be installed and interlocked to the beamline to minimize radiation from beam losses.

Although PIP-II beam will be transmitted cleanly, airborne radioactive products such as ^{15}O, ^{13}N, ^{11}C, and ^{41}Ar, will be generated from beam losses along the beamline and beam intentionally absorbed in the beam absorber at the end of the Linac enclosure. Any air activation that might occur due to incidental losses is expected to be minimal.

When beam losses interact with water molecules, tritiated water is produced. The majority of potentially activated water is collected in drains around the enclosure and discharged to the site-wide Industrial Cooling Water system, which contains the tritiated water to the Fermilab site. While PIP-II beam losses are anticipated to be minimal, surface waters, groundwater and soil activation will be monitored through the Fermilab environmental monitoring program.

The radiological shielding assessment for the PIP-II enclosures will begin during the enclosure final design phase. During the final design phase, the PIP-II Project will develop a preliminary shielding assessment that is reviewed by the Fermilab Radiation Safety Subcommittee Shielding Assessment Review Panel (SARP). The assessment is reviewed for methodology, completeness and compliance with the FRCM. Once all technical issues have been resolved, the SARP chair will recommend approval of the final shielding assessment to the Senior Radiation Safety Officer.

18.2.14 Non-ionizing radiation hazards (PIP-II PHA-14)

Hazardous levels of RF electromagnetic energy will be generated by the RF power sources for the PIP-II Facility. This energy is not normally radiated and is normally confined within waveguide, coaxial transmission lines, and the accelerating structures. Specific LOTO and configuration control procedures are in place to establish safe conditions for personnel working on or around these systems. Antennae will be installed in the controls racks for each RF system to monitor for leakage and automatically shut off the appropriate RF system. Periodic surveys will be performed by the Fermilab ESH&Q Section's staff to confirm that the RF fields are confined within the vacuum enclosure and are negligible in occupied areas compared to the safety levels set by the industry standards Institute of Electrical and Electronics Engineers (IEEE) Standard C95.1 and the ACGIH TLVs.

Class 3b and Class 4, near-infrared, UV, and visible lasers will be used in the PIP-II Facility for purposes such as beam diagnostics, beam instrumentation, and dedicated studies. Production and delivery of these beams both outside and inside the beamline enclosure are required to be completely contained to transport pipes or designated enclosures for the Class 3b and Class 4 lasers,

thus creating a Laser Controlled Area (LCA) in accordance with FESHM chapter 4260. Establishing the LCA prevents areas surrounding the LCA from exceeding the Maximum Permissible Exposure (MPE) as set by the Laser Safety Officer (LSO).

18.2.15 Material handling hazards (PIP-II PHA-15)

The PIP-II will require a significant amount of manual and mechanical material handling during the construction, installation and operations phases. The consequences of these hazards include serious injury or death to equipment operators and bystanders, damage to equipment and structures, and interruption of the program. Additional material handling hazards from forklift and tow cart operations include injury to the operator or personnel in the area and contact with equipment or structures. Cranes and hoists will be used during fabrication, testing, removal, and installation of equipment. The error precursors associated with this type of work include irregular shaped loads, awkward load attachments, limited space, obscured sight lines, and poor communication. The material or equipment being moved is typically one of a kind, potentially of high dollar or programmatic value, and may not have dedicated lifting points or an obvious center of gravity.

Lessons learned from across the DOE Complex and OSHA have been evaluated and incorporated into the Fermilab material handling programs documented in the FESHM 10000 series chapters. FESHM Chapter 10100 outlines the requirements for Special and Planned Engineered Lifts. Special lifts are when the load requires exceptional care in handling because of size, shape, close-tolerance installation, high susceptibility to damage, value, impact to operations, or other unusual factors. Planned Engineered Lifts are when a lift is in excess of the crane's rated load. The laboratory limits personnel who have access to mechanical material handling equipment such as cranes and forklifts to those who have successfully completed the laboratory's training programs and demonstrate competence in operating this equipment.

18.3 NEPA compliance

In compliance with the National Environmental Protection Act (NEPA) and in accordance with DOE Policy 451.1, the PIP-II project performed an evaluation of its potential environmental impacts during construction and operation of the project. An Environmental Assessment (EA) has been prepared to evaluate the potential environmental impacts and the safety and health hazards identified during the design, construction, and operating phases of PIP-II. The EA analyzed the potential environmental consequences of the facility and compared them to the consequences of a "No Action Alternative." The assessment included detailed analysis of all potential environmental, safety, and health hazards associated with construction and operation of the facility. The public release draft EA was completed in October 2018 and posted for public comments. A "Finding of No Significant Impact" (FONSI) was issued by the DOE Fermi Site Office on January 25, 2019.

18.4 Code compliance

Codes and consensus standards are developed to protect the public health, safety, and welfare. Codes and standards function as requirements for engineers and designers of buildings and equipment. The PIP-II Project has implemented a Systems Engineering Management Plan (SEMP) which provides requirements applicable to all PIP-II project engineering tasks, performed by or for the PIP-II Project as defined and organized in the PIP-II Work Breakdown Structure (WBS). The plan provides a methodology for the management of the requirements for all engineering tasks. The SEMP identifies the high-level requirements, how the global project requirements are developed, and how cost account managers (CAMs) develop functional requirements for their respective deliverables.

Each CAM develops Functional Requirements Specifications (FRS) for their deliverables. The FRS ties back to the Global Requirements Document and drives the downstream technical designs. The FRS flow down includes Technical Requirements Specifications which identify the key codes, standards, and best practices to be followed during the design process.

18.4.1 Code

The PIP-II project will rely on significant contributions from International Partners. In many cases, an International Partner will contribute equipment for installation at Fermilab that is built per one of the International Standards or Directives. Fermilab has established a process, detailed in FESHM Chapter 2110, to establish code equivalency between U.S. and International engineering design codes and standards. This process enables the Laboratory to accept in kind contributions from International partners or purchase equipment designed per International standards while assuring an equivalent or greater level of safety.

Table 18.5 lists the equivalency studies performed and approved for use at Fermilab between National Consensus Codes and International Codes. See FESHM 2110 - *Ensuring Equivalent Safety Performance When Using International Codes and Standards* for additional information on the equivalency study process

Table 18.5: Approved equivalency studies.

Study	Component Type	National Consensus Code	International Code
1	Pressure Vessels	ASME BPVC VIII	EN13445
2	Process Piping	ASME B31.3	EN13480
3	Pressure Relief Devices	ASME BPVC VIII	EN4126
4	Structure	IBC/ASCE7, AISC360, ADM1	Eurocode EN1990, EN1991, EN1993, and EN1998
5	Electrical Equipment for Measurement, Control and Laboratory use	UL61010	IEC 61010

As necessary, the laboratory code equivalency process will be followed to establish equivalency to other international codes and standards. The current list of completed code equivalencies can be found in the ESH&Q Section Document Database document No. 3303 (`https://esh-docdbcert.fnal.gov/cgi-bin/cert/ShowDocument?docid=3303`).

18.5 Safety by design

Safety by Design (SbD) is a process to integrate hazard identification and risk assessment early in the design process to eliminate or minimize risks throughout the life cycle of the system being designed. The process encourages engineers and designers to control risks to workers and the environment to an acceptable level "at the source" or as early as possible in the life cycle of the equipment.

SbD is a shift in approach for on-the-job safety. It involves evaluating potential risks associated with processes, equipment and structures. It takes into consideration the product life cycle phases from design through disposal and increases the cost-effectiveness of enhancements to occupational safety and health.

The SbD model, Figure 18.1 graphically shows that safety implementation is easiest during the concept and design phases when the implementation is a forethought. After the design phase, safety implementation becomes a retrofit with increasing costs for implementation.

Moving safety implementation upstream in the design process helps to controls risks early in the design process. Several benefits include:

- Prevent or reduce occupationally related injuries, illnesses, and fatalities
- Fewer delays due to accidents or unwanted outcomes
- Increase productivity
- Reduce operating costs
- Improved communications between engineers with interfaces between systems
- Improved specifications and interface documents
- Reduce retrofitting to correct design shortcomings

The SbD process has been integrated into the PIP-II project. The process involves each system designer identifying and documenting the hazards at each life cycle stage of their deliverable in the SbD Hazard Assessment spreadsheet. The risks from each hazard are assessed in accordance with the Fermilab Quality Assurance Manual Chapter 12030. Mitigations are identified to reduce risks. Project documentation is updated to include the identified mitigations into the design.

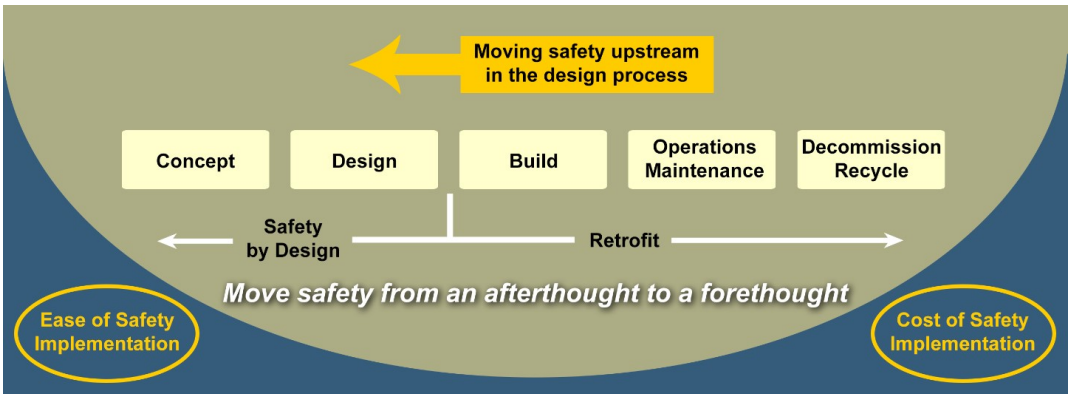

Figure 18.1: Safety by Design Model adapted from "Safety Through Design," Wayne Christensen, NSC Press, 1999.

Implementation progress is tracked within the SbD spreadsheet.

Chapter 19

Quality Management

19.1 Introduction

19.1.1 Quality assurance

The Proton Improvement Plan-II (PIP-II) Project has a defined Preliminary Quality Assurance (QA) Plan that describes the quality requirements for the systems that constitute the project. A graded approach has been designed to impose levels of control commensurate with consequences of failure or occurrence of an adverse event. The PIP-II Preliminary QA Plan aligns with the Fermilab Quality Assurance Manual (QAM) which is governed by the Fermilab Quality Assurance Program document. Subsequent Preliminary Quality Control Plans shall be established during the preliminary design phase.

19.1.2 Systems engineering

PIP-II has a defined approach to managing the overall systems engineering process in the Project. The systems engineering approach ensures that at completion, the PIP-II Project meets technical requirements outlined in the Project Mission Need Statement, as well as safety, quality, and integration which are addressed and controlled throughout the project lifecycle.

This approach is defined in the PIP-II Systems Engineering Management Plan (SEMP) [142]. This plan governs the engineering aspects of the design, fabrication, construction, technical support of a procurement process, acceptance and testing, and installation of the PIP-II Project in accordance with Project documents, Fermilab Environment, Safety, and Health Manual (FESHM), Fermilab Radiological Control Manual (FRCM), and the QAM.

19.2 Roles and responsibilities

- The PIP-II Project Director is responsible for achieving performance goals.
- The Technical Integration Office is responsible for the management of the SEMP implementation throughout the Project.
- The System Managers (SMs)/L2 Managers (L2Ms) are the design authorities and responsible for the delivery of their systems, and for actively managing interfaces with interconnected system.
- All PIP-II Project engineering participants are responsible for executing the requirements highlighted in the SEMP under the coordination of each SM/L2M.
- The PIP-II QA Manager is responsible for ensuring that the Quality Plan is established and maintained in accordance with requirements.
- All PIP-II Project SMs/L2Ms are responsible for ensuring that deliverables meet all the requirements established in the QA Plan.
- The PIP-II QA Manager collaborates with the PIP-II Project Management Office, PIP-II Technical Integration Office, and the SMs/L2Ms to ensure adherence to the PIP-II Review Plan.

19.3 Quality management in the design and design review process

PIP-II has a defined Project Review Plan [143] that establishes expectations of design and planning content and maturity at each review phase. This plan defines roles and responsibilities for design reviews from planning to execution, including post-review actions. All PIP-II Project components, systems, and installation activities are subject to the PIP-II Review process.

Quality Assurance is an integral part of the design of the PIP-II Project. The primary objectives of the QA Plan and the SEMP are to ensure the components of the project meet the design specifications and operate within the parameters mandated by the requirements. Quality and reliability is designed into the specifications and requirements. Global project requirements, system configuration, functional and technical requirements are defined and controlled. Functional and System interface requirements are defined, verified, and controlled to ensure adequacy of designs. Designs and requirements shall be documented, controlled, and managed in Teamcenter.

The PIP-II Project team recognizes the importance of identifying and properly managing issues and nonconformances during each design phase. Lessons Learned are reviewed and incorporated

into the design as applicable. The SMs/L2Ms are responsible for ensuring action items from previous reviews are effectively addressed.

19.4 Design acceptance and verification criteria

The SMs/L2Ms as the design authorities shall document that designs conform to design requirements as per established design acceptance criteria. Design acceptance and verification criteria are defined early in the design cycle and focus on design features impacting safety, performance, and reliability of a particular component or subsystem.

19.5 Quality control planning

SMs/L2Ms are responsible for defining the incoming inspection and acceptance criteria for items (software, hardware, components, equipment) procured and services received for their respective systems and subsystems. The incoming inspection and acceptance criteria shall be documented and reflect all quality-related requirements associated with a procurement or receipt of the material or service. The expectation is that vendors and Partners have an acceptable process for incoming inspections and acceptance testing. The roles and responsibilities for ensuring all requirements are met shall also be identified. This information shall be stored in the PIP-II DocDB.

SMs/L2Ms are responsible for defining in-process inspection testing and verification activities within their respective systems and subsystems. The inspection testing and verification requirements shall be defined within in-process documentation such as Travelers and Manufacturing Inspection Plans. The expectation is that vendors and Partners have an acceptable process for in-process inspection testing and verification activities. The roles and responsibilities for ensuring all requirements are met shall also be identified.

A Nonconformance (NC) shall be generated for any aspect of incoming inspection, in-process inspection/testing, verification activities or acceptance testing that do not meet requirements. Corrective actions shall be identified and documented and formally accepted to resolve any NCR.

19.6 Assessment and oversight

PIP-II Project members will perform formal or informal assessments to confirm the effective implementation of the PIP-II QA Plan which includes the implementation of the PIP-II SEMP and the PIP-II Review Plan. The ultimate goal of the assessment activities is to identify opportunities for improvement to assure the highest level of quality and reliability is reflected within PIP-II processes and systems.

The PIP-II Project shall ensure vendors/suppliers and Partners have acceptable quality programs/processes in place that will ensure items and services will consistently meet PIP-II expectations and requirements. Vendor/Supplier and Partner Oversight plans will be established which will facilitate assurance activities and communication.

19.7 Documents and records

All engineering documents will be managed and controlled in Siemens Teamcenter. Project management documents will be managed and controlled in DocDB. General documents will be managed in the PIP-II Project's Fermipoint site. Travelers will be created and controlled in the Vector database. Vendor/supplier/partner nonconformance reports (NCRs) will be captured and managed via iTrack.

Chapter 20

Integration and Installation

20.1 Organization and coordination of the installation effort

Integration and installation activities inherently have a large number of stakeholders. In order to perform work in an efficient and highly-parallel manner, good coordination and communication is required at all levels. The planned organization structure is shown graphically in Figure 20.1. Stakeholder groups are listed below, along with their respective roles and responsibilities.

Project Oversight and Support

The project office will exercise overall oversight of the installation effort. Technical integration, systems engineering, and ESHQ project representatives will have direct involvement in installation. Roles and responsibilities residing in the project office include:

- Managing the Installation Readiness Review process, through which deliverables are accepted for installation
- Providing overarching and on-the-floor safety support
- Providing overarching and on-the-floor quality support
- Highest court of appeal for technical, resource, or priority issues during installation

High-level Installation and Commissioning Coordination

Managers, or their direct delegates, from each L3 with installation or commissioning scope will jointly provide high level installation oversight and support. Their responsibilities include:

- Planning and oversight of the overall installation sequences

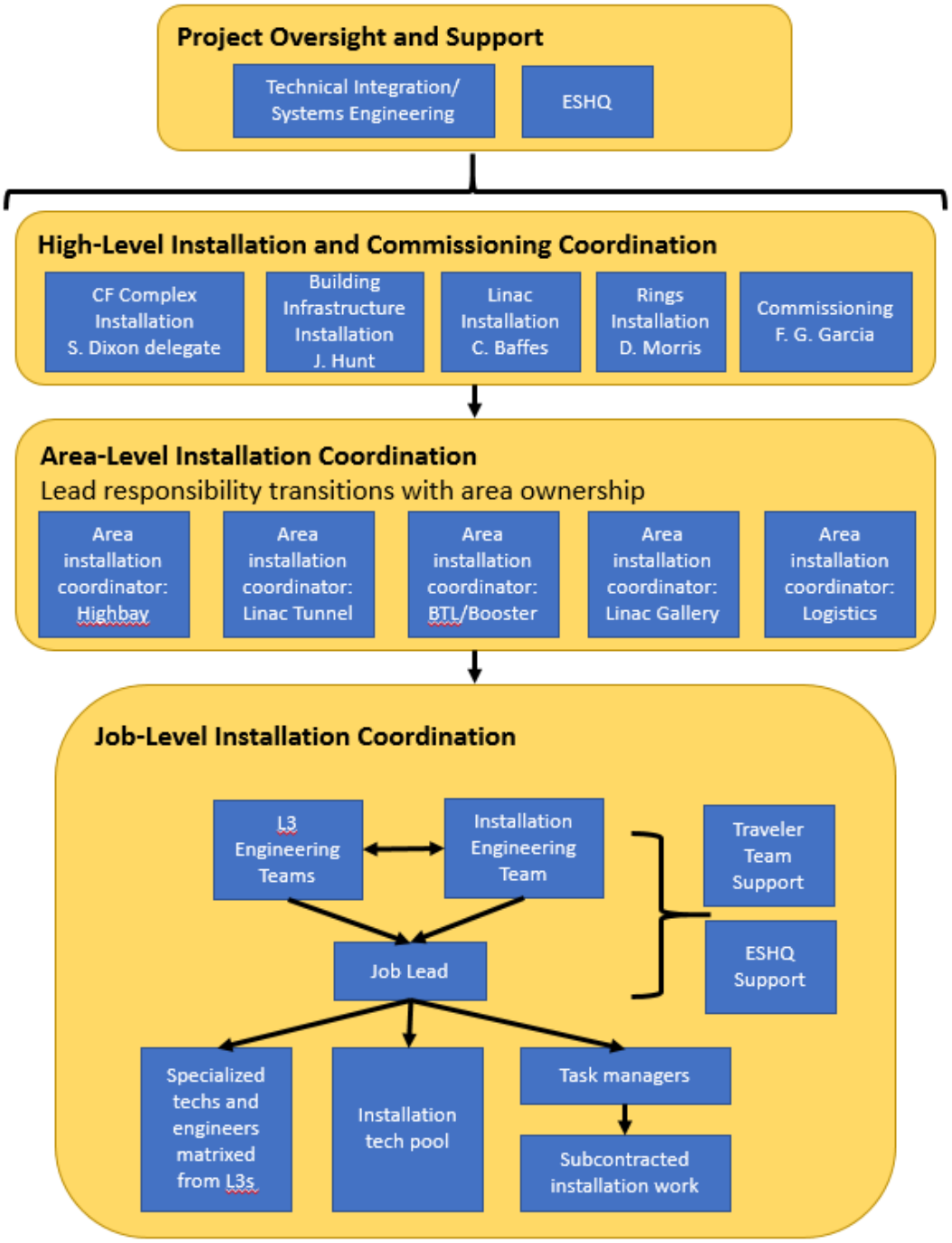

Figure 20.1: Installation Organization Structure

- Cost and schedule reporting
- Schedule tracking of major deliverables, adjustment of plans as required
- Allocation of resources where conflicts or competing priorities exist
- Definition of priorities
- Coordinate ARRs and handoff from installation activities to commissioning activities

Area-level installation coordination

Each area of the PIP-II footprint will have an area installation coordinator, whose job is to plan and ensure the efficient execution of installation activities in that area. This area-level installation coordinator will be matrixed from the L3 performing the bulk of the work at any one point in time. For example, the area installation coordinator for the gallery would be part of the CF team until beneficial occupancy. Then responsibility would pass to a member of the Building Infrastructure team. As technical installation begins to overtake utilities installation, the area coordinator responsibility would then transition to a member of the Linac Installation team. Responsibilities of the area installation coordinator include:

- Managing the installation sequence in the area on a day-by-day basis
  - E.g. coordinating delivery of large pieces of equipment
  - E.g. defining and enforcing stay-out zones to transport equipment
  - E.g. coordinating power outage schedules
  - E.g. ensuring part of the building can be cleared for a system pressure test
  - E.g. facilitating Operations Readiness Clearances (ORCs) for subsystem-level tests
- Walking the floor to identify and resolve issues
- Assigning priority and resources to individual installation jobs

Job-level installation coordination

Each individual job will be planned and managed by the appropriate system technical experts. As a general rule, it is envisioned that installation activities will be charged to an installation task code. However, the individuals defining and performing the detailed work will be matrixed as needed from the L3(s) that own the system that is being installed.

The installation elements will provide a general electrical/mechanical technician pool, and will also have generalist engineers dedicated to installation tasks.

In order to coordinate and perform a specific job, the participating groups would have roles and responsibilities as follows:

L3 and/or Installation engineering teams

- Develop installation plans, procedures, and travelers
- Assign a "job lead" single point-of-contact to execute the work

Job Lead

- Could be an engineer or an experienced technician
- Lead the team performing the work
- Follow and close out the job documentation (e.g. traveler) as required
- In cases of subcontracted tasks, the FNAL "Task Manager" could also be the "Job Lead"

ESHQ support

In this phase of the work, on-the-floor support from ESHQ will be needed to perform the following:

- Review and approve Hazard Analyses, Test Permits, etc.
- Find and address safety issues
- Address quality issues as they arise
- Ensure adherence to documentation requirements

Traveler team support

Installation work will be cataloged and tracked with travelers, administered in the Vector system by the APS-TD process engineering group. Responsibilities of this team include

- In cooperation with technical experts, develop installation travelers for PIP-II installation tasks
- Administer and organize PIP-II travelers

20.1.1 Documentation

Each installation job will be planned by the appropriate technical experts. System installation documentation will be prepared, reviewed and stored. In order to have uniformity in how this is

accomplished, the following practices will be followed:

Technical documentation

Along with physical deliverables, L3s delivering hardware for installation will also be preparing technical documentation. These could include installation drawings, installation procedures, interface control documents, and EPDMs. These documents will be stored in Teamcenter.

Travelers

Travelers will be used to document completion of recurring installation tasks. The travelers will be developed by subsystem experts, supported by the APS-TD process engineering group. For a given job, travelers document high-level completeness, data and verification. For a very simple job, the traveler itself may be sufficient documentation. For more complex jobs, the travelers may reference detailed drawings, procedures, or e-log entries.

Hazard Analyses

Where required by the FESHM or where judged to be prudent, installation jobs will have written Hazard Analyses. These will be treated in greater detail in the Safety Considerations section of this chapter. But in brief, hazard analyses will be:

- Written by the Job Lead
- Reviewed by (at a minimum) a safety professional
- Read and signed off by each job participant

20.2 Installation

Installation activities are broken up into several major installation segments as listed below. Installation within each segment begins once conventional construction is completed for the given segment. The construction phase formally ends with the granting of beneficial occupancy for the given area allowing installation teams full access.

- Installation in the Linac High Bay
- Installation in the Linac Tunnel
- Installation in the Linac Gallery
- Beam Transfer Line Installation

Once beneficial occupancy is granted the majority of the initial work is performed by the Building

Infrastructure team. This includes the basic infrastructure utilities which allow the main machine components and associated hardware to be installed and connected. This work generally consists of the following:

- Alignment network creation
- Fluids distribution installation
- Electrical distribution installation
- Cable tray network installation
- Control rack installation

20.2.1 Installation in the Linac High Bay

The Linac High Bay installation consists of three phases as listed below:

- PIP2IT Removal Phase
- Warm Front End Installation Phase
- HWR Installation Phase

The PIP2IT removal phase consists of disassembly and relocation of PIP2IT to PIP-II. This work includes disassembly of the LEBT, RFQ, MEBT beamlines and removal of the HWR cryomodule and associated support equipment.

As the highbay installation work conducted by the Building Infrastructure team nears completion, the area-level installation coordinator role passes from Building Infrastructure to Linac Installation. Linac Installation then executes the Warm Front End installation, including:

- Reassembly of ion sources, including new 2nd ion source not present at PIP2IT
- Installation of RFQ and connection of supporting equipment
- Installation of non-low-particulate section of MEBT
- Installation of low-particulate section of MEBT adjacent to HWR
- Installation of free-standing systems (e.g. RFQ amplifiers)
- RF distribution (including 6.125 in. coax hard line to RFQ)

The installation of the HWR occurs after the installation of the Cryogenic Distribution System.

As such, its schedule is largely decoupled from the Warm Front End and other systems in the high bay. HWR installation work includes:

- Rigging of the HWR into position
- Low-particulate connection to MEBT
- Connection of accelerator support systems (e.g. fluids, vacuum, cryo etc.)
- Population of associated racks
- Cable pull and connections
- RF distribution
- HWR checkout and warm testing may then begin

20.2.2 Installation in the Linac tunnel

As the tunnel installation work conducted by the Building Infrastructure team nears completion, the area-level installation coordinator role passes from Building Infrastructure to Linac Installation. Linac Installation then begins "outfitting", preparation of the tunnel to receive cryomodules. This phase focuses on work that must precede cryomodule installation, or that would be difficult or impossible to do with cryomodules in place. This work includes:

- Cryo Distribution System installation
- Cryo warm piping installation
- Laser transport system installation
- Installation of stands for cryomodules
- Hanging of rigid coax against tunnel ceiling
- Rough survey to locate stands and other components
- Safety systems installation

As cryomodules become available, they are installed in fully-outfitted locations in the tunnel. Cryomodules are transported down the Linac aisle using a dolly-based cryomodule mover. In order to perform work efficiently, cryomodule installation is planned in "blocks" of identical cryomodules. When a block of cryomodules becomes available, they are installed together. The planned blocks are as follows:

- SSR1 block installation (2 cryomodules)
- SSR2 block A (3 cryomodules)
- SSR2 block B (4 cryomodules)
- LB650 block A (5 cryomodules)
- LB650 block B (6 cryomodules)
- HB650 block (4 cryomodules)

Note that the blocks are listed here in beam order, not necessarily in installation order. Installation order will be tailored to the final delivery schedule, with installation of the final block to begin before the delivery of the final, critical-path cryomodule. Likewise, the number of cryomodules in each block will be tailored depending on the final delivery schedule.

For each cryomodule block, installation work includes:

- Interface to stand and alignment
- Cryo U-tube and relief piping field fitting
- Connection of RF distribution
- Installation of adjacent warm unit and instrumentation
- Beamline connection (low-particulate, mass flow control, portable cleanroom)
- Insulating vacuum system connection
- Cable termination and connection

Some principals that will guide the cryomodule installation are as follows:

- Warm unit installation will occur after cryomodules on both sides have been installed. This will provide greater clearance for the manipulation of the delicate cryomodules
- Cryomodules will be installed in a linear order (e.g. downstream to upstream) whenever possible. This will minimize the number of cryomodules that need to be installed with low clearance between other cryomodules. The cryomodule mover will accommodate low-clearance installation, which is inevitable in some cases due to cryomodule delivery order.
- Where flexibility exists, cryomodule installation will start at the downstream end of the tunnel to keep the aisle relatively unobstructed between the major access at the highbay and the majority of the tunnel footprint.

20.2.3 Installation in the Linac gallery

As the gallery installation work conducted by the Building Infrastructure team nears completion, the area-level installation coordinator role passes from Building Infrastructure to Linac Installation. Linac Installation then begins technical installation, which includes:

- Cable pulls within the gallery
- Cable pulls from gallery to tunnel
- Cable terminations
- Population of racks
- Installation of stand-alone RF and power supply equipment
- Installation of RF distribution, including circulators
- LCW hosing from manifolds to point of use

20.2.4 Beam transfer line installation

Prior to the start of excavation for the Beam Transfer Line and Beam Absorber Line tunnel construction, the portion of the Main Ring/Tevatron tunnel that will intersect with the Beam Transfer Line tunnel needs to be prepared by removing and securing identified components as listed below.

- Remove Tevatron magnets and transport to Railhead
- Remove Tevatron Quench Bypass System cabling
- Remove for re-installation the Main Ring Magnets used for delivering Switchyard beam
- Remove for re-installation the Main Ring beam pipe
- Remove for re-installation the Main Ring magnet stands
- Remove for re-installation the Main Ring Low Conductivity Water headers
- Remove for re-installation the Main Ring dipole and quadrupole bus
- Secure existing conventional conduits and lighting that are currently affixed to sections of the tunnel that will be removed

- Secure cables and cable trays that are currently affixed to sections of the tunnel that will be removed

As the Building Infrastructure Phase nears completion the area level installation coordinator role passes from Building Infrastructure to Transfer Line Installation for technical installation of Beam Transfer Line and Beam Absorber Line components. This phase includes:

- Alignment stake-out of tunnel components
- Installation of 50 kW absorber
- Installation of component stands
- Installation of magnets
- Installation of collimators
- Installation of beam instrumentation
- Installation of vacuum components
- Alignment
- Cable pulls from support buildings to tunnel
- Termination of cables
- Connection of cooled equipment to Low Conductivity Water distribution
- Re-installation of Main Ring components moved during CF Phase (8.3.2)

20.2.5 Installation support

20.2.5.1 Cryomodule stands

Cryomodule stands will be implemented as 6-strut kinematic mounts with turnbuckle-style adjustments. This approach confers several advantages:

- Stand is statically determinant and amenable to analysis
- Adjustment can be quasi-orthogonal, with low cross-coupling between degrees of freedom
- Stand can be configured to stroke the cryomodules along the beam axis during installation to facilitate vacuum installation in tight spaces.

The stands are designed to be adapted to SSR1, SSR2, LB650 and HB650 cryomodules with only minor changes to setup and configuration to accommodate the different cryomodule sizes. The HB650 cryomodule, the largest and heaviest, is the driving load case. Note that the HWR stand will exist at PIP2IT and be moved over to PIP-II.

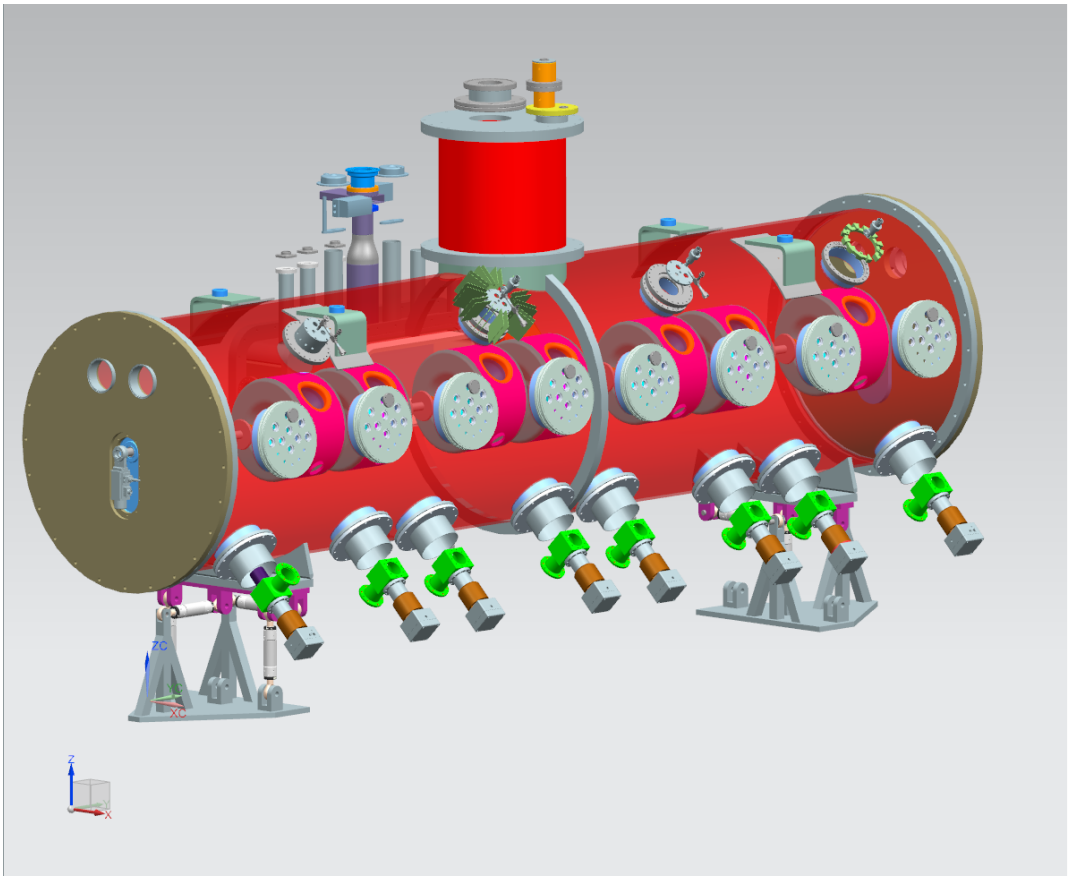

Figure 20.2: Cryomodule stand shown with SSR1

The stand is implemented in a classic "3-2-1" arrangement,

- 3 vertical adjusters react gravity load and control vertical position, pitch and roll
- 2 transverse adjusters (left/right) control transverse postion and yaw
- 1 longitudinal adjuster (upstream/downstream) controls longitudinal position

20.2.5.2 Cryomodule mover

The cryomodule mover will be a two-dolly system. One dolly will support each end of the cryomodule from underneath. Swivel casters will allow for the transition from longitudinal motion down the aisle to transverse motion into position in the cryomodule string. The cryomodule/dolly system will be towed by a powered tug.

The design borrows heavily from the SNS cryomodule mover, shown below.

Figure 20.3: SNS Cryomodule Mover

20.3 Checkout phases

20.3.1 Subsystem-level checkout

Physical installation dovetails with checkout. Checkouts begin at the subsystem level and propagate upwards to higher levels of assembly. Required checkout procedures, tests and verification plans will be established and documented as part of the subsystem design. Where special hazards exist (e.g. high power levels), subsystem-level ORC's will be conducted to verify readiness for tests. Progress of checkouts will be tracked via the traveler system. Examples of subsystem-level checkouts include:

- Verification of connections and signals
- Verification of subsystem-level controls and interlocks
- Vacuum system performance and protection tests
- Calibration activities

- Motion checks of movable devices
- RF power on loads in the gallery
- Power testing of magnet strings
- Safety systems testing

20.3.2 System-level warm checkout

As the major subsystems are brought online, system level checkouts become possible. Examples of warm system-level checkouts include:

- Verification of control and interlock interfaces across subsystems
- Exercise of cavity tuning
- Warm RF conditioning of cavities
- Testing of machine protection systems

20.3.3 Warm front end checkout phase

Warm Front End systems are expected to be fully installed before the remainder of the Linac. As such, the WFE will be the first system through the checkout process. This includes connectivity, power and functional testing, but without any beam. Warm front end checkout will be split into two parts that mirror the commissioning plan - Ion Source/LEBT checkout and RFQ/MEBT checkout. Handoff to commissioning occurs at the completion of the following ORCs:

- ORC for IS/LEBT operation
- ORC for RFQ/MEBT operation

An Accelerator Readiness Review (ARR) will be required for commissioning to begin. The Commissioning WBS element drives the ARR process.

20.3.4 Superconducting Linac checkout phase

As checkout work propagates from subsystem level to higher levels, the following high-level ORCs will need to be passed:

- ORCs for RF to warm cavities
- ORC for Cryo Distribution System Cooldown
- ORC for Linac Cooldown
- ORC(s) for RF to cold cavities

Major sub-phases include:

Superconducting Linac Cooldown

After the cryomodule string, CDS, and warm checkout work are complete, the cooldown of the cryomodule string may begin. Because each cryomodule type will have its own nuances, the cooldown will proceed in blocks of identical cryomodule types. Once a block has achieved a stable temperature, cooldown will proceed to the next block. The proposed blocking is as follows:

- HWR cryomodule (1 module)
- SSR1 cryomodules (2 modules)
- SSR2 #1-#3 (3 modules)
- SSR2 #4-#7 (4 modules)
- LB650 #1-#5 (5 modules)
- LB650 #6-#11 (6 modules)
- HB650 cryomodules (4 modules)

System-level cold checkout

Once the system has achieved stable 4 K condition, cold checkout may begin. This work includes:

- Confirm system integrity at temperature (for example, are there cold helium leaks?)
- Vacuum system performance verification
- Move cavities onto resonance
- Cold RF conditioning
- Transition to 2 K
- Final integrated systems checkouts

Where checkout work will require areas to be interlocked (e.g. cold RF conditioning), work may be performed on second shift, allowing work requiring personnel access to be performed on first shift.

At the conclusion of this work, the Linac is declared "ready to try for beam" and a hand-off to commissioning begins.

20.3.5 Beam transfer line checkout phase

Work to be completed in this phase begins with checkouts that begin at sub-system level and proceed to higher levels of assembly. Required checkout procedures, tests and verification plans will be established and documented as part of the subsystem design. Where specialized hazards exist subsystem level ORC's will be conducted to verify for testing. Progress of checkouts will be tracked via the traveler system. Examples of subsystem level checkouts include:

- Verification of connections and signal paths
- Verification of subsystem level controls and interlocks
- Vacuum system performance and protection tests
- Calibration activities
- Motion control checks of movable devices
- Power testing and polarity checks for magnet strings
- Safety system testing
- Tunnel clean-up
- Walk-throughs, inspections and traveler close-outs Following completion of these steps the Beam Transfer Line and Beam Absorber Line systems will be handed over to the commissioning WBS element who will manage the Accelerator Readiness Review. Transfer Line Installation L3 will provide input documentation (e.g. closed travelers) and support for the ARR.

20.4 Hand-off to beam commissioning

Beam Commissioning of the machine will occur in phases. The installation efforts will be structured to facilitate parallel installation work in downstream sections while upstream sections are being commissioned. This approach also affords a mechanism to accommodate the delivery of critical-

path or late components in the downstream sections of the machine.

Chapter 21

Commissioning

This section of the document outlines the provisional beam commissioning strategy and steps for the PIP-II Linac up to and including injection into the Booster. In terms of project schedule, it starts when the first machine installation campaign and hardware check-out are complete with all permits approved and ends when 700 MeV H^- ions (threshold KPP) are successfully injected into the Booster.

21.1 Commissioning strategy

A basic requirement in the design of the PIP-II Linac is the capability to build and commission the Linac without any interference with the operating Fermilab accelerators. Hence, the connection to the Booster, modifications therein and its re-commissioning must all be done during a dedicated shut-down period. Figure 21.1 shows the location of the new 800 MeV Linac in relationship with the existing 400 MeV Linac.

Figure 21.1: Location of the new 800 MeV Linac in relationship with the existing 400 MeV Linac.

While several independent installation and commissioning phases are planned for the Linac, it is expected that technical check-out and some beam commissioning activities will occur in parallel with installation activities. Naturally, beam commissioning activities will only be conducted if the configuration of the machine and the ancillary systems comply with ES&H regulations and the proper permission to safely do so is granted by the authorities.

The overall strategy follows these steps: upon completion of the installation of a section of the machine, the sub-systems within will undergo an Operations Readiness Clearance (ORC) review that permits them to be powered. In turn, this will allow the technical check-out of that section to start. Beam commissioning begins once all subsystems in the corresponding section have demonstrated achieving their nominal parameters. Depending on schedule, exceptions can be made for the ultimate gradient that some SRF cavities may reach assuming that beam commissioning can

still be successfully carried out and that cryomodule re-conditioning or replacement can be performed later. It is worthwhile to mention that beam commissioning in parallel with installation will proceed as long as the installation activities occur sufficiently far in the downstream part of the accelerator to avoid beam-induced radiation exposure and other hazards associated with operating the accelerator to any personnel. If necessary, temporary shield walls will be built beyond the movable beam dump used for commissioning so that installation activities can proceed concurrently downstream in the same tunnel. Proper interlocking and access procedures will be enforced accordingly to Fermilab's Radiological Control Manual (FRCM). This was the strategy used for building and commissioning the SNS Linac [144] and it is also the strategy adopted by ESS [145].

21.2 Commissioning stages

Presently, the Linac beam commissioning is envisioned to be divided into four major phases:

1. The warm front end: Ion Source, LEBT, RFQ, and MEBT
2. Several stages of installation and commissioning of the SC Linac and beam line to a straight dump
3. Transport line to the main Linac dump
4. Booster injection

A schematic of the PIP-II configuration is shown in Fig. 21.2.

Figure 21.2: Schematic of the PIP-II configuration.

It is foreseen that each phase will be composed of multiple steps. The granularity of these steps will depend on both the installation and commissioning paces to completion. For instance, if the cryogenics transfer lines for the HWR and SSR1 cryomodules are installed and confirmed to be working in conformance with the technical specifications then one can envision Phase 2 to be conducted in multiple steps: beam commissioning sending beam through a subset of spoke resonator cryomodules, followed by the elliptical section before initiating SCL beam commissioning after the installation and verification of all the components of the rest of the superconducting section. A method to coordinate accesses and work priority in each section of the machine remains to be developed.

Commissioning, tuning and operation will require machine flexibility and therefore a range of working modes are planned. Table 21.1 shows the proposed beam modes of the PIP-II Linac.

Table 21.1: Beam operation modes of the PIP-II linac.

Mode	Beam parameters			Main Usage
	Current [mA]	Pulse length [s]	Repetition rate [Hz]	
Pilot mode	≤ 2	≤ 10	≤ 1	Initial check Establish beam through the machine
Diagnostic mode	≤ 2	≤ 10	≤ 20	Invasive meas., LLRF setting
Low power mode	≤ 2	≤ 100	≤ 20	LLRF setting, beam loss
High power mode	2	≤ 550	≤ 1	Beam loss
Operational	2	550	≤ 20	Operation (Objective KPP)

21.2.1 Warm front end

Installation of the warm front end (WFE), composed of the Ion Source, LEBT, RFQ, and MEBT will start immediately after receiving occupational readiness of the high-bay area. The MEBT will be assembled fully except for the last section that needs to be installed simultaneously with the HWR cryomodule. At this stage, the beam will be delivered to the MEBT absorber and to an insertable beam stop/Faraday Cup capable to withstand the beam with parameters corresponding to the Booster injection. These parameters need to be demonstrated before proceeding to the next stages of commissioning. Also, this stage needs to demonstrate the main mode for commissioning of the Linac (Diagnostic mode), when the bunch population is nominal, the average pulse current is 2 mA, and the average power is kept low by maintaining a short (several μs) pulse length and a low repetition rate. In addition, a Low Emittance mode with bunch population decreased by heavy scraping in the MEBT needs to be made operational.

Since the warm front end is separated from the main tunnel by a radiation wall, installation in the tunnel can proceed in parallel with the WFE commissioning.

21.2.2 SC Linac and the beam line to low power beam dump

When occupational readiness of the main tunnel is declared, installation of the cryomodules and the portion of the transport line that goes straight to a low power dump will begin. This installation might be performed in several stages as well, being either interleaved with commissioning of the Linac sections or performed sequentially with the commissioning stages, which specifics will be determined later. The need for the intermediate stages is dictated by the large betatron phase advance per cryomodule at low energies. In SNS and ESS, these stages correspond to the warm part of the Linac and were/are planned to be commissioned separately.

In PIP-II the low-energy part of the Linac is already superconducting. While it similar to FRIB [146] where a multi-stage commissioning approach is chosen, unlike the FRIB design, large warm inserts are not foreseen at PIP-II. As a result, using insertable devices is highly discouraged. On the other hand, the main diagnostics envisioned for transverse profiling during Linac

operation is the laser wire. It is a sophisticated tool that, according to SNS's experience, is not likely to be fully functional at the beginning of commissioning. The choice of either permanently installing insertion devices between cryomodules that would be used only during commissioning or commissioning in stages using a warm diagnostic line movable between sections is presently debated.

Commissioning of the Linac at these stages will be performed only in a Diagnostic mode with a very low duty factor to avoid radioactive contamination of the tunnel and minimize the risk of equipment failures.

The tunnel will be interlocked for the time of conditioning the cryomodules and running the beam.

21.2.3 Transport line to the main Linac dump

When the tunnel for the transport line to the main Linac dump is declared ready for occupancy, the transfer line is installed there. Whether the installation work can proceed in parallel in the transfer line to the main dump is under discussion. After installation and subsystem commissioning is finished, the beam will be delivered to the main dump. In addition to measuring the transverse optics of the transfer line in Diagnostic mode, one of the main goals at this stage is to demonstrate for the first time Linac operation at longer pulses (up to 0.1 ms). It requires the LLRF system to be fully functional, including beam loading compensation. In addition, the technique of beam energy stabilization needs to be commissioned.

21.2.4 Booster injection

Installation in the Booster injection area can proceed in parallel with commissioning in the previous stages. When these stages are completed, and the Booster receives ORC, the beam is injected into the ring, first at a low duty factor. The duty factor will be increased as the Booster is being recommissioned, to the point of reaching the nominal parameters indicated in Table 3.1, which will mark the completion of the Linac commissioning campaign.

References

[1] **HEPAP Subcommittee** Collaboration, S. Ritz *et al.*, "Building for Discovery: Strategic Plan for U.S. Particle Physics in the Global Context,".

[2] **Mu2e** Collaboration, F. Abusalma *et al.*, "Expression of Interest for Evolution of the Mu2e Experiment," arXiv:1802.02599 [physics.ins-det].

[3] F. Garcia, S. Chaurize, C. Drennan, K. Gollwitzer, V. Lebedev, W. Pellico, J. Reid, C.-Y. Tan, and R. Zwaska, "Fermilab - The Proton Improvement Plan (PIP)," in *Proceedings, 61st ICFA Advanced Beam Dynamics Workshop on High-Intensity and High-Brightness Hadron Beams (HB2018): Daejeon, Korea, June 17-22, 2018*, p. WEP2PO010. 2018. http://lss.fnal.gov/archive/2018/conf/fermilab-conf-18-430-ad.pdf.

[4] M. Plum *et al.*, "Status of the SNS Ring Power Ramp Up, Proceedings of EPAC08, p. 3560-3562..".

[5] I. Kourbanis *et al.*, "Progress Toward Doubling the Beam Power at Fermilab's Accelerator Complex, Proceedings of IPAC 2014 (FERMILAB-CONF-14-187-AD).".

[6] "Project X LEBT: Functional Requirement Specifications.". TeamCenter Document ED0001289; uncontrolled copy in Project X Document 912: http://projectx-docdb.fnal.gov/cgi-bin/ShowDocument?docid=912.

[7] S. Nagaitsev *et al.*, "The Project-x Injector Experiment: A Novel High Performance Front-end For A Future High Power Proton Facility At Fermilab," in *1st North American Particle Accelerator Conference (NAPAC2013) Pasadena, CA, USA, September 29-October 4, 2013*. 2013. arXiv:1409.5470 [physics.acc-ph]. http://lss.fnal.gov/archive/2013/conf/fermilab-conf-13-415-ad-apc-td.pdf.

[8] **PIP-II** Collaboration, A. Shemyakin, M. Alvarez, R. Andrews, J. P. Carneiro, A. Chen, B. Hanna, L. Prost, V. Scarpine, R. D'Arcy, and C. Wiesner, "PIP-II Injector Test's Low Energy Beam Transport: Commissioning and Selected Measurements," *AIP Conf. Proc.* **1869** no. 1, (2017) 050003, arXiv:1704.08744 [physics.acc-ph].

[9] L. Prost, J. P. Carneiro, and A. Shemyakin, "Low Emittance Growth in a LEBT with Un-Neutralized Section," *Phys. Rev. Accel. Beams* **21** no. 2, (2018) 020101,

arXiv:1805.01920 [physics.acc-ph].

[10] Q. Ji and J. Staples, "Project X H^- Ion Source Acceptance Test and Future Plan." Project X Document 897, http://projectx-docdb.fnal.gov/cgi-bin/ShowDocument?docid=897.

[11] **ProjectX** Collaboration, G. Romanov, M. Hoff, D. Li, J. Staples, and S. Virostek, "Project X RFQ EM Design," *Conf. Proc.* **C1205201** (2012) 3883–3885.

[12] K. Crandall *et al.*, "RFQ Design Codes." Los Alamos Report LA-UR-96-1836 (1996, Revised, Dec. 7 2005).

[13] A. Shemyakin *et al.*, "Design of MEBT for the Project X Injector Experiment at Fermilab," in *Proceedings, 26th International Linear Accelerator Conference (LINAC12): Tel Aviv, Israel, September 9-14, 2012*, p. MOPB095. 2013. arXiv:1301.7698 [physics.acc-ph]. http://lss.fnal.gov/cgi-bin/find_paper.pl?conf-12-496.

[14] V. Lebedev, A. Chen, R. Pasquinelli, D. Peterson, G. Saewert, A. Shemyakin, D. Sun, M. Wendt, and T. Tang, "Progress with PXIE MEBT Chopper," *Conf. Proc.* **C1205201** (2012) 2708–2710, arXiv:1301.5649 [physics.acc-ph].

[15] M. H. Awida, C. M. Baffes, A. Z. Chen, Y. I. Eidelman, V. A. Lebedev, L. R. Prost, A. V. Shemyakin, N. Solyak, and V. P. Yakovlev, "Design Considerations for an MEBT Chopper Absorber of 2.1 MeV H- at the Project X Injector Experiment at Fermilab," *Conf. Proc.* **C1205201** (2012) 2585–2587.

[16] "PXIE MEBT Functional Requirements Specification." TeamCenter Document ED0001303; uncontrolled copy in Project X Document 938: http://projectx-docdb.fnal.gov/cgi-bin/ShowDocument?docid=938.

[17] A. Saini, C. Baffes, A. Chen, V. Lebedev, L. Prost, and A. Shemyakin, "Design of PIP-II Medium Energy Beam Transport," in *Proceedings, 9th International Particle Accelerator Conference (IPAC 2018): Vancouver, BC Canada*, p. TUPAF076. 2018.

[18] **PIP-II** Collaboration, L. R. Prost *et al.*, "PIP-II Injector Test Warm Front End: Commissioning Update," in *Proceedings, 9th International Particle Accelerator Conference (IPAC 2018): Vancouver, BC Canada*, p. THYGBF2. 2018. arXiv:1806.05708 [physics.acc-ph]. http://lss.fnal.gov/archive/2018/conf/fermilab-conf-18-017-ad.pdf.

[19] "Functional specifications for PXIE MEBT scrapers." TeamCenter Document ED0001306; uncontrolled copy in Project X Document 1067: http://projectx-docdb.fnal.gov/cgi-bin/ShowDocument?docid=1067.

[20] A. Saini and A. Shemyakin, "Optical Design of the PI-Test MEBT Beam Scraping System," in *Proceedings, 28th International Linear Accelerator Conference (LINAC16): East Lansing, Michigan, September 25-30, 2016*, p. THPRC026. 2017.

[21] T. P. Wangler, *RF linear accelerators*, p. 203. 2008.

[22] V. Yakovlev and C. Ginsburg, "SRF Linac Technology Development at Fermilab," in *Proceedings, 26th International Linear Accelerator Conference (LINAC12): Tel Aviv, Israel, September 9-14, 2012*, p. MO1A03. 2013. http://accelconf.web.cern.ch/AccelConf/LINAC2012/papers/mo1a03.pdf.

[23] G. Ciovati, "Review of high field q slope, cavity measurements." in Proc. SRF2009: 90 (2009).

[24] "Assumption about Q values in CW linac.". Project X Document 590, http://projectx-docdb.fnal.gov/cgi-bin/ShowDocument?docid=590.

[25] O. Brunner *et al.*, "Assessment of the basic parameters of the CERN SPL," *Phys. Rev. ST Accel. Beams* **12** (2009) 070402.

[26] LANSCE, http://lansce.lanl.gov/.

[27] **Proton Driver** Collaboration, A. Saini, J. P. Carneiro, D. Johnson, J. F. Ostiguy, N. Solyak, and V. P. Yakovlev, "Layout of Project-X Facility: A Reference Design," in *1st North American Particle Accelerator Conference (NAPAC2013) Pasadena, CA, USA, September 29-October 4, 2013*. 2013. http://lss.fnal.gov/archive/2013/conf/fermilab-conf-13-428-apc.pdf.

[28] **Proton Driver** Collaboration, A. Saini, N. Solyak, and V. P. Yakovlev, "Design Issues of High Intensity SC CW Ion Linac for Projet-X facility.," in *1st North American Particle Accelerator Conference (NAPAC2013) Pasadena, CA, USA, September 29-October 4, 2013*. 2013. http://lss.fnal.gov/archive/2013/conf/fermilab-conf-13-430-ad.pdf.

[29] A. Saini, V. Lebedev, J.-F. Ostiguy, N. Solyak, and V. Yakovlev, "Design of Superconducting CW linac for PIP-II," in *Proceedings, 6th International Particle Accelerator Conference (IPAC 2015): Richmond, Virginia, USA, May 3-8, 2015*, p. MOPMA014. 2015. http://accelconf.web.cern.ch/AccelConf/IPAC2015/papers/mopma014.pdf.

[30] A. Saini, "Design Considerations for the Fermilab PIP-II 800 MeV Superconducting Linac," in *Proceedings, 2nd North American Particle Accelerator Conference (NAPAC2016): Chicago, Illinois, USA, October 9-14, 2016*, p. WEPOA60. 2017. http://accelconf.web.cern.ch/AccelConf/napac2016/papers/wepoa60.pdf.

[31] I. Hofmann, "Challenges in Benchmarking of Simulation Codes Against Real High Intensity Accelerators," in *Proceedings, 52nd ICFA Advanced Beam Dynamics Workshop on High-Intensity and High-Brightness Hadron Beams (HB2012)*. 2013. http://accelconf.web.cern.ch/AccelConf/HB2012/papers/moi1c02.pdf.

[32] P. Ostroumov *et al.*, "Accelerator Physics Advances in FRIB (Facility for Rare Isotope Beams)," in *Proceedings, 9th International Particle Accelerator Conference (IPAC 2018):*

Vancouver, BC Canada, April 29-May 4, 2018, p. THYGBF4. 2018.

[33] N. Pichoff, D. Uriot, S. Nath, J. Qiang, J. Stovall, H. Takeda, L. Young, R. D. Ryne, and K. Crandall, "Comparison of Linac Simulation Codes," *Conf. Proc.* **C0106181** (2001) 264–266. [,264(2001)].

[34] Technical Specifications for High RRR Grade Niobium Sheet for Use in Superconducting Radio Frequency Cavities, Fermilab Specification: 5500.000-ES-371037 Rev B, Fermilab, Technical Division.

[35] O. E. Krivosheev and N. V. Mokhov, "Tolerable beam loss at high intensity proton machines," in *Beam halo and scraping. Proceedings, 7th ICFA Mini-Workshop on High Intensity High Brightness Hadron Beams, Lake Como, Wisconsin, September 13-15, 1999*, pp. 85–88. 2000. http://lss.fnal.gov/cgi-bin/find_paper.pl?conf-00-192.

[36] V. Lebedev, J.-F. Ostiguy, N. Solyak, A. Aleksandrov, and A. Shishlo, "Intrabeam Stripping in H^- Linacs," in *Proceedings, 25th International Linear Accelerator Conference, LINAC2010: Tsukuba, Japan, September 12-17, 2010*, p. THP080. 2011. arXiv:1207.5492 [physics.acc-ph]. http://lss.fnal.gov/cgi-bin/find_paper.pl?conf-10-382.

[37] A. Shishlo, J., et.al. "First Observation of Intrabeam Stripping of Negative Hydrogen in a Superconducting Linear Accelerator" Plum, Phys. Rev. Lett. 108, 114801 (2012).

[38] A. Sullivan, "A Guide to Radiation and Radioactivity Levels Near High Energy Particle Accelerators, Nuclear Technology Publishing, (1992).".

[39] "PIP-II Conceptual Design Report," April 2018. https://pip2-docdb.fnal.gov/cgi-bin/private/RetrieveFile?docid=113&filename=PIP-II_CDR_v.0.3.pdf&version=10.

[40] A. F. A. Ferrari, P.R. Sala and J. Ranft, "FLUKA: a multi-particle transport code, CERN 2005-10 (2005), INFN/$TC_0$5/11, $SLAC - R - 773.''$.

[41] G. Battistoni *et al.*, "Overview of the FLUKA code, Annals of Nuclear Energy 82 (2015) 10-18.".

[42] G. Battistoni *et al.*, "Overview of the FLUKA code, Annals of Nuclear Energy 82 (2015) 10-18.".

[43] N. Mokhov *et al.*, "Fermilab-FN-628 (1995), Prog. Nucl. Sci. Technol., vol. 4, 496-501 (2014).".

[44] I. R. Y. E. N.V. Mokhov, I. Tropin and L. Tchelidze, "ESS Accelerator Prompt Radiation Shielding Design Assessment, ESS Report No. 0052477, 2016.".

[45] K. Seiva *et al.*, "Proceedings of the 2007 Particle Accelerator Conference, edited by C. Petit-Jean-Ganaz (IEEE, Piscataway, NJ, 2007), pp. 742-744,

DOE:10.1109/PAC.2007.4440760.".

[46] "Building for Discovery: Strategic Plan for U.S. Particle Physics in the Global Context." http://science.energy.gov/~/media/hep/hepap/pdf/May-2014/FINAL_P5_Report_053014.pdf.

[47] "LBNE Conceptual Design Report: The Beamline at the Near Site," October 2012. http://lbne2-docdb.fnal.gov/cgi-bin/RetrieveFile?docid=4317;filename=CDR-beam-volume-101812-reduced.pdf.

[48] J. Carneiro, "H- Stripping Equations and Application to the High Intensity Neutrino Source, Beams-doc-2740," tech. rep. http://beamdocs.fnal.gov/AD-public/DocDB/DocumentDatabase.

[49] G. Gillespie. Phys. Rev. A 15, 563 (1977) and 16, 943 (1977), Nucl. Intr. and Meth. B 2, 231 (1984) and B 10/11, 23 (1985).

[50] A. Drozhdin, "H- beam collimation in the transfer line from 8 GeV linac to the Main Injector Beams-doc-2740, June 2008," tech. rep. https://beamdocs.fnal.gov/AD-private/DocDB/ShowDocument?docid=2201.

[51] S. Nagaitsev *et al.*, "The Project-X Injector Experiment: A Novel High Performance Front-end for a Future High Power Proton Facility at Fermilab," tech. rep. Proceedings of PAC-2013, p. 374.

[52] Q. Ji and J. Staples, "Project X H- Ion Source Acceptance Test and Future Plan," tech. rep. http://projectx-docdb.fnal.gov/cgi-bin/ShowDocument?docid=897.

[53] http://www.d-pace.com/.

[54] R. D'Arcy *et al.*, "Nuclear Instrumentation And Methods in Physics, Res. A 815 (2016) 7-17..".

[55] H.-F. Ouyang *et al.*, "Study on the pre-chopper in CSNS LEBT, 2010 Chinese Phys., C341122.".

[56] "Scheme for Low Energy Beam Transport with a non-neutralized section, FERMILAB-TM-2599-AD (2015); arXiv:1504.06302 [physics.acc-ph]," tech. rep.

[57] "PXIE LEBT Beam Transverse Emittance Station FRS," tech. rep. TeamCenter Document ED0001294; uncontrolled copy in Project X Document 1077: http://projectx-docdb.fnal.gov/cgi-bin/ShowDocument?docid=1077.

[58] "Project-X RFQ EM-design," tech. rep. IPAC2012, New Orleans, May 2012; FERMILAB-CONF-128-TD.

[59] "Project X RFQ functional physics requirements," tech. rep. TeamCenter Document

ED0001300; uncontrolled copy in Project X Document 894, http://projectx-docdb.fnal.gov/cgi-bin/ShowDocument?docid=894.

[60] S. Virostek *et al.*, "Design and analysis of the PXIE CW Radio-Frequency Quadrupole (RFQ)," tech. rep. in Proc. of IPAC2012, New Orleans, Louisiana, USA, 2012, THPPC034.

[61] A. Ratti *et al.*, "The Design of a High Current, High Duty Factor RFQ for the SNS, in Proc. of EPAC '00, Vienna, Austria, 2000, pp. 495-497.," tech. rep.

[62] S. Kazakov *et al.*, "Design of 162.5 MHZ CW MAIN COUPLER FOR RFQ," tech. rep. LINAC 2014, Geneva, Switzerland, THPP049, p. 960.

[63] S. ho Kim *et al.*, "DeStabilized operation of the Spallation Neutron Source radio-frequency quadrupole," tech. rep. Phys. Rev. ST Accel. Beams 13, 070101 (2010).

[64] "PXIE MEBT Functional Requirements Specification." `http://projectx-docdb.fnal.gov/cgi-bin/ShowDocument?docid=938`. TeamCenter Document ED0001303; uncontrolled copy in Project X Document 938.

[65] "PXIE MEBT quadrupoles specifications." TeamCenter Document ED0001312; uncontrolled copy in Project X Document 933", url = http://projectx-docdb.fnal.gov/cgi-bin/ShowDocument?docid=933.

[66] "FRS for Bunching cavity for PXIE MEBT.". TeamCenter Document ED0001307; uncontrolled copy in Project X Document 1071, http://projectx-docdb.fnal.gov/cgi-bin/ShowDocument?docid=1071.

[67] G. Romanov *et al.*, "CW Room Temperature Re-Buncher for the Project X Frontend, in Proc. of IPAC'12 New Orleans USA 2012 THPPP063.".

[68] R. Webber *et al.*, "Overview of the High Intensity Neutrino Source Linac RD Program at Fermilab, LINAC'08, Victoria, BC, Canada, 2008," tech. rep.

[69] I. Terechkine *et al.*, "Cw Room Temperature Re-Buncher for the PIP-II Linac, IPAC2014, Dresden, Germany, 2014," tech. rep.

[70] R. Webber *et al.*, "Functional specifications for PXIE MEBT scrapers," tech. rep. `http://projectx-docdb.fnal.gov/cgi-bin/ShowDocument?docid=1067`. TeamCenter Document ED0001306; in controlled copy in Project X Document 1067.

[71] "Pxie mebt kicker specification." `http://projectx-docdb.fnal.gov/cgi-bin/ShowDocument?docid=977`. TeamCenter Document ED0001305; uncontrolled cone in Project X Document 977.

[72] "Experimental study of the SNS MEBT chopper performance, in Proc. of IPAC'10, Kyoto, Japan, 2010, MOPD063," tech. rep.

[73] "Progress with PXIE MEBT chopper, in Proc. of IPAC'12, New Orleans, USA, 2012, WEPPD078," tech. rep.

[74] "Functional specifications for PXIE MEBT absorber.". TeamCenter Document ED0001304; uncontrolled copy in Project X Document 964, http://projectx-docdb.fnal.gov/cgi-bin/ShowDocument?docid=964.

[75] A. Shemyakin and C. Baffes, "High power density test of PXIE MEBT absorber prototype, Proceedings of Linac 2014 August 31 - September 5, 2014 Geneva, Switzerland, THPP055.".

[76] J. Fuerst *et al.*, "Assembly Installation and Commissioning of the ATLAS Upgrade Cryomodule, in Advances in Cryogenic Engineering 55A, edited by J.G. Weisend et al., American Institute of Physics, New York, New York, 2010, Pg. 815..".

[77] Z. Conway *et al.*, "Assembly and Commissioning of a new SRF Cryomodule for the ATLAS Intensity Upgrade, in Advances in Cryogenic Engineering 59,edited by J.G. Weisend et al., Anchorage, Alaska, USA, 2013, Pg. 1829..".

[78] J. Fuerst, "The ATLAS Energy Upgrade Cryomodule, in Proc. of SRF'09, Berlin, Germany, 2009, Pg. 52..".

[79] Z. Conway *et al.*, "Achieving High Peak Fields and Low Residual Resistance in Half-Wave Cavities, Proceedings of SRF'15, Whistler, British Columbia, Canada, 2015, WEBA05.".

[80] "Process Piping: American Society of Mechanical Engineers Code for Pressure Piping, B31.3-2012..".

[81] T. Nicol *et al.*, "SSR1 Cryomodule Design for PXIE.". Proceedings of PAC2013, Pasadena, CA, USA, THPMA09.

[82] L. Ristori *et al.*, "Design, Fabrication and Testing of Single Spoke Resonators at Fermilab, in Proc. of SRF2009, Berlin, Germany, THPPO011.".

[83] "325 MHz SSR2 Superconducting RF Cavities Functional Requirements Specification: Teamcenter ED0001854.".

[84] "Guidelines for the Design, Fabrication, Testing and Installation of SRF Cavities, FESHM Chapter 5031.6, TD-09-005, Fermi National Accelerator Laboratory," tech. rep.

[85] D. Passarelli *et al.*, "Methodology for the Structural Design of Single Spoke Accelerating Cavities at Fermilab, in Nuclear Instruments and Methods in Physics Research Section A, Volume 834C, 2016, Pages 1-9.".

[86] A. Sukhanov *et al.*, "Result of Cold Tests of The Fermilab SSR1 Cavities, in Proc. Of LINAC2014, Geneva, Switzerland, THPP057.".

[87] A. Hocker *et al.*, "RF Tests of Dressed 325 MHz Single Spoke Resonators at 2 K, in Proc.

of LINAC2014, Geneva, Switzerland, MOPP055.".

[88] R.Paparella, "Overview of Recent Tuner Development on Elliptical and Low-Beta Cavities, in Proc. of SRF2015, Whistler, BC, Canada, FRAA01..".

[89] Y. Pischalnikov *et al.*, "Tests of a Tuner for a 325MHz SRF Spoke Resonator, in Proc. of 2011 Particle Accelerator Conference, New York, NY, USA, TUP080..".

[90] D. Passarelli *et al.*, "SSR1 Tuner Mechanism: Passive and Active Device, in Proc. of LINAC2014, Geneva, Switzerland, TUPP052..".

[91] D. Passarelli and others., "Performance of the Tuner mechanism for SSR1 Resonators During Fully Integrated Tests at Fermilab, in Proc. of SRF2015, Whistler, Canada, THPB061..".

[92] W. Schappert and others., "Resonance Control for Narrow-Bandwidth, Superconducting RF Applications, in Proc. of SRF2015, TUPB095, Whistler, BC, Canada.".

[93] "Focusing Lens for SSR1 Cryomodule Project X Injector Experiment (PXIE) Functional Requirements Specification: Teamcenter ED0001315.".

[94] A. Lunin *et al.*, "Development of a Low-Beta Button BPM for PXIE Project,in Proc. of IBIC2013, Oxford, UK.,".

[95] "Focusing Lens for SSR2 Cryomodule Project X Injector Experiment (PXIE) Functional Requirements Specification.". Teamcenter ED0003642.

[96] K. Singh, "PIP-II Solenoid Focusing lens for SSR2 Cryomodule.".

[97] D. Passarelli *et al.*, "High-Vacuum Simulations and Measurements on the SSR1 Cryomodule Beam-line, in Proc. of SRF2015, Whistler, Canada, TUPB074.,".

[98] P. Kneisel, "Effect-Cavity Vacuum on Performance of Superconducting Niobium Cavities, in Proc. of the 1995 Workshop on RF Superconductivity, Gif-sur-Yvette, France.,".

[99] J. Knobloch and H. Padamsee, "Reduction, of the surface resistance in superconducting cavities due to gas discharge, in Proc. of 8th Workshop on RF Superconductivity, Padova, Italy.,".

[100] T. Nicol *et al.*, "Design and Analysis of the SSC Dipole Magnet Suspension System.". in Supercollider 1, p. 637 (1989).

[101] "Design of 650 MHz Tuner for PIP-II Project, IPAC2018, Vancouver, BC, Canada.".

[102] Y. Pischalnikov *et al.*, "Design and Test of Compact Tuner for Narrow Bandwidth SRF Cavities, IPAC2015, Richmond, VA, USA.".

[103] I. Gonin *et al.*, "Design of a Compact Lever Slow/Fast Tuner for 650MHz Cavities for Project X, LINAC2014, Geneva, Switzerland.".

[104] `https://www.phytron.eu/products/motors-actuators/cavity-tuner/`.

[105] Y. Pischalnikov *et al.*, "Reliability of the LCLS II SRF Cavity Tuner.". SRF2015, Whistler, BC, Canada.

[106] Y. P. N. Huque, E.F. Daly, "Results of Accelerated Life Testing of LCLS II Cavity Tuner Motor, SRF2017, Lanzhou, China.".

[107] `https://www.physikinstrumente.com/en/products`.

[108] A. Lunin *et al.*, "Development of a Low-Beta Button BPM for the PXIE Project." TUPC14, IBIC2013, Oxford, UK.

[109] J. Crisp *et al.*, "Position and Phase Measurements of Microampere Beams at the Michigan State University REA3 Facility." THPAC20, PAC2013, Pasadena, CA.

[110] C. Drennan. Private communication.

[111] W. Blokland and C. Peters, "A New Differential and Errant Beam Current Monitor for the SNS Accelerator." THAL2, IBIC2013, Oxford, UK.

[112] R. Connolly *et al.*, "Beam-Energy and Laser Beam-Profile Monitor at the BNL Linac." TUPSM011, BIW2010, Santa Fe, NM.

[113] Y. Liu, A. V. Aleksandrov, W. Blokland, C. Deibele, C. D. Long, A. A. Menshov, J. Pogge, A. Webster, A. P. Zhukov, and R. A. Hardin, "Laser Based Diagnostics for Measuring H^- Beam Parameters," *Conf. Proc.* **C110328** (2011) 1433–1437.

[114] Y. Liu *et al.*, "Laser Applications: H^- Beam Photo-Detachment and Push Button Diagnostics." TUCP02, BIW2012, Newport News, VA.

[115] R. B. Wilcox *et al.*, "A Low-Power Laser Wire with Fiber Optic Distribution." TUPD53, DIPAC2011, Hamburg, Germany.

[116] A. Zhukov *et al.*, "Longitudinal Laser Wire at SNS." MOCYB3, IBIC2014, Monterey, CA.

[117] P. W. Allison, J. D. Sherman, and D. B. Holtkamp, "An Emittance Scanner for Intense Low-Energy Ion Beams," *IEEE Trans. Nucl. Sci.* **30** (1983) 2204.

[118] M. P. Stockli *et al.*, "Emittance Studies with an Allison Scanner," *Rev. Sci. Instrum.* **77** (2006) 03B706.

[119] R. D'Arcy, M. Alvarez, J. Gaynier, L. Prost, V. Scarpine, and A. Shemyakin, "Characterisation of the PXIE Allison-Type Emittance Scanner," *Nucl. Instrum. Meth.*

A815 (2016) 7–17.

[120] Y. Liu, A. Aleksandrov, C. Long, A. Menshov, and A. Zhukov, "Laser Wire Based Transverse Emittance Measurement of HâĄż Beam at Spallation Neutron Source," in *Proceedings, 6th International Particle Accelerator Conference (IPAC 2015): Richmond, Virginia, USA, May 3-8, 2015*, p. MOPHA041. 2015. http://accelconf.web.cern.ch/AccelConf/IPAC2015/papers/mopha041.pdf.

[121] T. Hofmann, G. Boorman, A. Bosco, E. Bravin, S. Gibson, E. Griesmayer, U. Raich, and F. Roncarolo, "Design of a Laser-based Profile Monitor for LINAC4 Commissioning at 50 MeV and 100 MeV," in *Proceedings, 4th International Beam Instrumentation Conference, IBIC2015*, p. TUPB055. 2016.

[122] R. Thurman-Keup *et al.*, "Longitudinal bunch monitoring at the Fermilab Tevatron and Main Injector synchrotrons," *JINST* **6** (2011) T10004, arXiv:1110.3086 [physics.ins-det].

[123] A. Aleksandrov, "Beam Halo Characterization and Mitigation," in *Proceedings, 7th International Particle Accelerator Conference (IPAC 2016): Busan, Korea, May 8-13, 2016*, p. FRXBA01. 2016.

[124] K. Cahill *et al.*, "The Fermilab accelerator control system," *ICFA Beam Dyn. Newslett.* **47** (2008) 106–124.

[125] J. Patrick and S. Lackey, "Control Systems for Linac Test Facilities at Fermilab," in *Proceedings of the XXIV Linear Accelerator Conference 29 September - 3 October 2008. Victoria, British Columbia, Canada*. 2008.

[126] R. Schmidt, "Machine Protection," in *CAS - CERN Accelerator School: Advanced Accelerator Physics Course: Trondheim, Norway, August 18-29, 2013*, pp. 221–244. 2014. arXiv:1601.05207 [physics.acc-ph].

[127] C. Sibley, D. J. Armstrong, A. Jones, A. Justice, and D. Thompson, "The SNS machine protection system: Early commissioning results and future plans," *Conf. Proc.* **C0505161** (2005) 1727. [,1727(2005)].

[128] A. Warner, L. Carmichael, B. Harrison, N. Liu, R. Neswold, A. Saewert, and J.-Y. Wu, "Machine Protection System Research and Development for the Fermilab PIP-II Proton Linac," in *Proceedings, 16th International Conference on Accelerator and Large Experimental Physics Control Systems (ICALEPCS 2017): Barcelona, Spain, October 8-13, 2017*, p. THPHA110. 2018. http://lss.fnal.gov/archive/2017/conf/fermilab-conf-17-666-ad-apc.pdf.

[129] L. Carmichael, D. Crawford, N. Liu, R. Neswold, A. Warner, and J.-Y. Wu, "Commissioning and Design of the Machine Protection System for Fermilab's Fast Facility," in *Proceedings, 15th International Conference on Accelerator and Large Experimental Physics Control Systems (ICALEPCS 2015): Melbourne, Australia, October*

17-23, 2015, p. MOPGF145. 2015.

[130] J. Wu, A. Warner, N. Liu, R. Neswold, and L. Carmichael, "The Machine Protection System for the Fermilab Accelerator Science and Technology Facility," in *Proceedings, 2015 IEEE Nuclear Science Symposium and Medical Imaging Conference (NSS/MIC 2015): San Diego, California, United States*, p. 7581882. 2016. http://lss.fnal.gov/archive/2015/conf/fermilab-conf-15-506-ppd.pdf.

[131] S. Claudet, "Recent Progress in Power Refrigeration Below 2 K for Superconducting Accelerators.". Invited paper at the Particle Accelerator Conference", Knoxville, TN, USA, 2005.

[132] "European X-Ray Free-Electron Laser Technical Design Report.".

[133] "ESS Technical Design Report," tech. rep. Invited paper at the Particle Accelerator Conference, Knoxville, Tn, USA, 2005.

[134] "Specification of the ESS Accelerator Cryoplant," tech. rep. Physics Procedia, Vol. 67, pp 89-94, 2015.

[135] H.Quack *et al.*, "The TESLA Cryo Plants,". TESLA Report, 38, 2001.

[136] "Functional Requirement Specification 650 MHz, Beta .61 CRYOMODULE CAVITIES," tech. rep., FNAL. Teamcenter ED0001830.

[137] "Functional Requirement Specification 650 MHz, Beta .92 CRYOMODULE CAVITIES," tech. rep., FNAL. Teamcenter ED0001322.

[138] "Functional Requirement Specification: Half Wave Resonator Cryomodule," tech. rep., FNAL. Teamcenter ED0001313.

[139] "Functional Requirement Specification: 325 MHz SSR1 cryomodule," tech. rep., FNAL. Teamcenter ED0001316.

[140] "Functional Requirement Specification: 325 MHz SSR2 cryomodule," tech. rep., FNAL.

[141] "Producing Very Low Particulate UHV Components: Teamcenter ED0003571.".

[142] "PIP-II Systems Engineering Management Plan: Teamcenter ED0008164.".

[143] "PIP-II Review Plan: Teamcenter ED0008163.".

[144] S. Henderson, "Recent beam commissioning results from the Spallation Neutron Source," *Conf. Proc.* **C0605295** (2006) 6–10.

[145] "ESS Technical Design Report," 2013. ESS Document 274, http://eval.esss.lu.se/cgi-bin/public/DocDB/ShowDocument?docid=274.

[146] M. Ikegami, L. Hoff, S. Lidia, F. Marti, E. Pozdeyev, T. Russo, R. Webber, J. Wei, and Y. Yamazaki, "Commissioning Plan for the FRIB Driver Linac*," in *Proceedings, 27th Linear Accelerator Conference, LINAC2014: Geneva, Switzerland, August 31-September 5, 2014*, p. MOPP041. 2014. http://jacow.org/LINAC2014/papers/mopp041.pdf.